Adama Science and Technology University

Research and Centre of Excellence Diroctorate

Proceedings of the Fourth International Research Symposium

"*Promoting Digital Economy through Research and Innovation*"

April 28 – 29, 2023, Adama, Ethiopia

Organizing Committee

Chairperson

Dr. Alemu Disassa

Secretary

Dr. Yadeta Chimdessa

Members

Dr. Fedlu Kedir	**Mr. Tadesse Hailu**
Dr. Tegene Desalegn	**Dr. Alemgena Abdeta**
Dr. Belay Brehane	**Dr. Temesgen Debelo**
Mr. Mitiku Kinfe	**Dr. Alemu Gonfa**
Dr. Shimelis Lemma	**Mr. Bejiga Yadecha**
Dr. Bedasa Abdisa	

Main Theme of the Symposium

Promoting Digital Economy through Research and Innovation

Sub-Themes of the Symposium

- **Manufacturing**
- **Smart Materials & Technology**
- **Energy**
- **Environment & Natural Resources**
- **Industrial Park**
- **Infrastructure and Construction**
- **Computational Sciences**
- **Social Development**

Disclaimer

Adama Scienec and Technology University is not responsible for the contents refelected in the articles published in the proceedings of this International Research Symposium. The contents of this document are solely the responsibility of the authors.

Inquires should address to:
Research and Centre of Excellence Directorate
Adama Scienec and Technology University
P.O.Box 1888, Adama, Ethiopia
Tel: +251-22-211-1797

Table of Contents

Preface

The transformation of a nation can basically be achieved through the advancement of science and technology. Ethiopia has long recognized the role of science and technology in bringing about sustainable development. The country has invisioned transforming itself into a middle-income country in 2025. To this end, the country has exerted relentless efferts to materialize science and technology in the country. Thus, it has made science and technology the pillar of its top priorities for transformation of the economy.

As one of the universities mandated to spearhead the transformation process, Adama Science and Technology University (ASTU) is looking forward to excel in science and technology. Its goal is to develop highly qualified, capable, competent, and innovative human resource in the field of science and technology so as to transfer relevant scientific knowledge and skills required for nation building. The university also committed to conduct need based problem solving researches for alleviating the problems of the region and the country at large. To this end, the university is working in collaboration with industries in its vicinity whereby its staff members are contributing a great deal in alleviating problems. Moreover, ASTU has set centers of excellence as a platform where academia can meet stakeholders.

ASTU's development into a full-fledged science and technology university has helped it to forge strong linkage, coopration, and partnership with various national and international universities, development sectors, stake-holders, and relevant personalities. To showcase its all-round efforts, ASTU has organized its fourth international research symposium on "***Promoting Digital Economy through Research and Innovation***". This is a timely and broad agenda that is seen as a part of the national plan of transformation of the country. Thus, this research symposium aims to further strengthen the contribution of ASTU in development endeavours of the country at large.

Message from Organizing Committee

Alemu Disassa Muleta (PhD)
Vice President, RTT
Chair of the Organizing Committee

Honorable Guests, Dear Participants, on behalf of the organizing committee, I would like to welcome you all to the 4th International Research Symposium of Adama Science and Technology University organized on the theme **"*Promoting Digital Economy through Research and Innovation*"**.

Since its establishment as full-fledged Science and Technology University, ASTU has been exerting tremendous effort to foster research culture among its staff. Over the last five years, it has conducted various national and regional researches, community service and consultancy service projects that led to new policy initiatives and generation of new development insights. The establishment of eight centers of excellence and the construction state-of-the-art research park in ASTU also witnesses the commitment of the university towards nurturing research culture.

In the effort to disseminate its research outputs and create a platform which allows the academia in ASTU share scientific knowledge and thought with national and international scholars, ASTU had successfully held three international research symposiums so far. The 1st International Research Symposium was held in September 2012 on the theme "*Sustainable Development through Science and Technology: Lessons from Emerging Economies*", the 2nd in June 2017 on the theme "*Ensuring Sustainable Development through Research in Science and Technology*" while the 3rd one was held in May 2019 on the theme "*Emerging Technology and Energy for Sustainable Development*. These three symposiums have helped a lot in increasing our national and international collaborations besides nurturing better research culture in our university.

The 4th International research symposium is also aimed at consolidating our national and international research collaboration and eventually helping ASTU achieve its vision of becoming a national hub for science and technology researches. The overwhelming response that we have received from several senior and young researchers and scientists to our "Call-for-paper" witnesses the relevance and timely nature of the theme of this symposium. The theme of ASTU's 4th International Research Symposium was designed to offer comprehensive range of sessions that include: Manufacturing and Computational Science, Environment and Natural Resources, Smart Materials and Technology, Energy and Infrastructure. A total of 37 researchers, including 5 international speakers, are expected to present their works at plenary and syndicate sessions. Nearly 300 participants from higher learning institutions, industries, research institutions, federal and regional sector offices are expected to take part in this symposium. Thus, I am very much confident that the participants can learn a lot from the symposium.

Finally, I would like to thank you all for accepting our invitation to share us your scientific knowledge and expertise. I wish you all a fruitful scientific deliberations and a very pleasant stay in Adama City.

Welcoming Speech

Lemi Guta (PhD)
Presiden of ASTU

H.E. Dr. Samuel Kifle, State Minister, Ministry of Education

Dear Board Members

Dear Senate members

Dear Presidents and Vice Presidents of various universities

Dear Invited Guests from various industries

Dear our Academic and Admin Staff Members

Dear Keynote Speaker, Prof. Dr. Oliver Sholtz

Dear Plenary Speakers: Prof. Alemayehu Gebisa, Prof. Samuel Kinde, Prof. Wilhelm Stork and Prof. Jaebeom Lee

Dear Researchers and paper presenters

Dear Religious Leaders

Dear Invited Students

Dear Media Representatives

Ladies and gentlemen!

I would like to warmly welcome you all to our 4th International Research Symposium with a theme '**Promoting Digital Economy through Research and Innovation**'.

Adama Science and Technology University is one of the two leading and a special mission driven science and technology universities in Ethiopia. Since it was re-established as a model Science and Technology University under the former Ministry of Science and Technology (MoST), ASTU has been working hard by concentrating on teaching science, innovation, research and technology transfer with the prime objective of playing a leading role in supporting the country's endeavor to climb up the technology development ladder.

Ladies and gentlemen!

Every year the university admits high caliber and talented students in science and technology through a special entrance exam using its own online and live software. In doing so, the university has been producing qualified and internationally competent graduates in Applied Science and Technology fields.

Since 2018, the university has re-designed all its undergraduate curricula based on international curriculum accreditation principles called ABETS. In addition to that the university has launched 14 postgraduate programs with 35 fields of specialization where over 300 PhD students are admitted to the programs.

Among our graduates, I would like to mention one extra ordinary performing student from OROMIA Boarding School who graduated with two majors (Physics and Mathematics) scoring all the 60 course A^+ and who got admission at MIT, USA directly for PhD program. This shows that we are preparing a curriculum that can accommodate students with extraordinary talents and unique academic interests.

ASTU has 5 major schools and has established 8 CoEs, all working aggressively to realize its vision and mission. The drones designed and tested in our Space Technology Institute and the ongoing research regarding space technology is one of the encouraging achievements of our CoEs. The university has transferred technologies, participated in technology based community services and our academic staff members have published many articles on international reputable journals. Our global visibility has been increasing remarkably from time to time. ASTU has also embarked on technology transfer activities and consultancy services.

Since 2017, the university has consulted more the 20 national and regional mega projects and developed software for federal and regional government institutions based on their request. Every year, the university conducts job expos in order to bring together industry owners, employers and graduating students to the same stage. Our students sell their best ideas and projects to the industry owners thereby facilitate employment opportunities for themselves. The tracer study result conducted every year shows that 82.5 % of our graduates get employment within a year of their graduation. This is really an encouraging achievement that can be a model for other universities.

Ladies and gentlemen!

The university is undergoing a massive landscaping and greenery works to make the compound attractive and green campus for its community. In this academic year, the university is working aggressively on exit exam, institutional autonomy, curriculum accreditation, internationalization & partnership, establishment of strong university enterprise, completing ongoing construction projects, etc..

With the intention of creating a favorable platform for industry owners, employment organizations and graduating students, ASTU has been successfully organizing Job fairs for the last three consecutive years. Earlier to our today's international research symposium, we have successfully conducted three international research symposia. Our university has been conducting research conferences in order to create a conducive platform for academicians to exchange knowledge and experience about global phenomenon.

The theme of this research symposium is 'Promoting Digital Economy through Research and Innovation'. Digital technologies are transforming how people interact, how businesses operate and how economies are configured. Digitalization represents a key solution to narrowing the vast trade distances; digital platforms can provide opportunities to open or expand access to local, regional and international markets and knowledge networks. Digital businesses also benefit from lower start-up and operating costs. From a broader perspective, digital transformation offers opportunities for the nation to accelerate progress towards virtually all the Sustainable Development Goals (SDGs).

I am confident that many publications, problem solving research findings and policy issues will come out of our today's International Research Symposium. Taking this opportunity, I would like to express my utmost appreciation to the office of vice president for research and technology transfer and various committee members under this wing for organizing this grand event.

Once again, I would like to welcome you all to our 4th International Research Symposium and I wish you a beautiful and successful stay in ASTU .

Following this, I would like to invite H.E. Dr. Samuel Kifle, State Minister, Ministry of Education to make an opening remarks.

Thank you! Galatoomaa!

Key Note Address

Prof. Oliver Scholz

HTW Berlin - University of Applied Science
Berlin, Germany

Keynote Title: Digital Economy

Plenary Session

Prof. Wilhelm Stork

Karlsruhe Institute of Technology
Karlsruhe, Germany

Topic: Utilizing Artificial Intelligence to Implement Smart Grid Solutions

Prof. Samuel Kinde Kassegne

San Diego State University
San Diego, California, USA

Topic: Smart Materials

Prof. Alemayehu Gebissa

Rostock University
Rostock, Germany

Topic: The Role of Building Information Modeling (BIM) in Transforming Highway Construction and Services

Prof. Jaebeom Lee

Chungnam National University
Daejeon, South Korea

Topic: Magnetoplasmonic Nanoparticles and Assembles: Biomedical and Energy Application

Syndicate 1:

Energy and Infrastructure

Novel Organic Materials Discovery for Green and Renewable Energies with Generative Adversarial Network (GAN)

Mesfin Diro Chaka [1,3,*], Chernet Amente Geffe[1], Yedilfana Setarge Mekonnen[2]

[1]*Department of Physics, Addis Ababa University, P. O. Box 1176, Addis Ababa, Ethiopia,*
[2]*Center for Environmental Science, Addis Ababa University, P. O. Box 1176, Addis Ababa, Ethiopia,*
[3]*Computational Data Science, Addis Ababa University, P. O. Box 1176, Addis Ababa, Ethiopia,*
**Corresponding author, e-mail: mesfin.diro@aau.edu.et*

ABSTRACT

One of the main contributors to greenhouse gas emissions is the generation of electricity from fossil fuels. Redox flow batteries (RFBs) are promising candidates for energy storage systems generated from green and renewable energy sources such as wind and solar to mitigate their intermittent nature. Organic redox-active materials have become emerging alternatives to RFB technology due to their low manufacturing costs and environmental sustainability. Adversarial generation is a key tactic in computational molecular design for generating molecular species that are comparable to a given molecular dataset. Due to the various hidden layers of nonlinear processing units, deep learning algorithms may understand complex patterns and correlations from unstructured molecular input data to find new materials for RFB applications. A class of generative models known as generative adversarial networks (GANs) uses two neural networks (a discriminator and a generator) to approximate the model distribution with an empirical distribution in order to produce samples that are comparable to a training set. The generator creates samples based on existing molecular data while the discriminator tries to distinguish between real data and fraudulently generated data. GANs have been effectively used in a variety of fields, including text-to-speech synthesis, style transfer, super-resolution, and image production. This paper provies a method for discovering novel organic compounds with desired properites that are applicable to RFBs technologies for green and renewable energy sources.

Keywords: *Graph Neural Networks, Molecular Graph Attention, Aqueous Solubility, Redox Flow Batteries*.

1. INTRODUCTION

Electricity production from fossil fuel sources is one of the major factors causing greenhouse gas emissions [1]. Wind and solar energy sources are regarded as promising alternatives to future energy sources due to their environmentally friendly characteristics. These renewable-energy sources are being deployed in larger numbers than ever before [2]. As global interest and investment in renewable energy resources has grown rapidly, so has the demand for effective energy storage technologies [3]. Modern electrical energy storage devices are required for the electrical grid system to smooth out the inconsistencies in power supply and ensure the robustness of intermittent wind and solar energy sources [4]. Because of their high stability and storage capacity, lithium-ion batteries have become the most popular and widely used type of energy storage device [5]. Redox flow batteries (RFBs) are, however, the most promising candidates for efficient green energy storage systems like wind and solar. Organic redox-active materials have become emerging alternatives to battery technology due to their low manufacturing cost, adjustable electrochemical performance, and environmental sustainability [6].

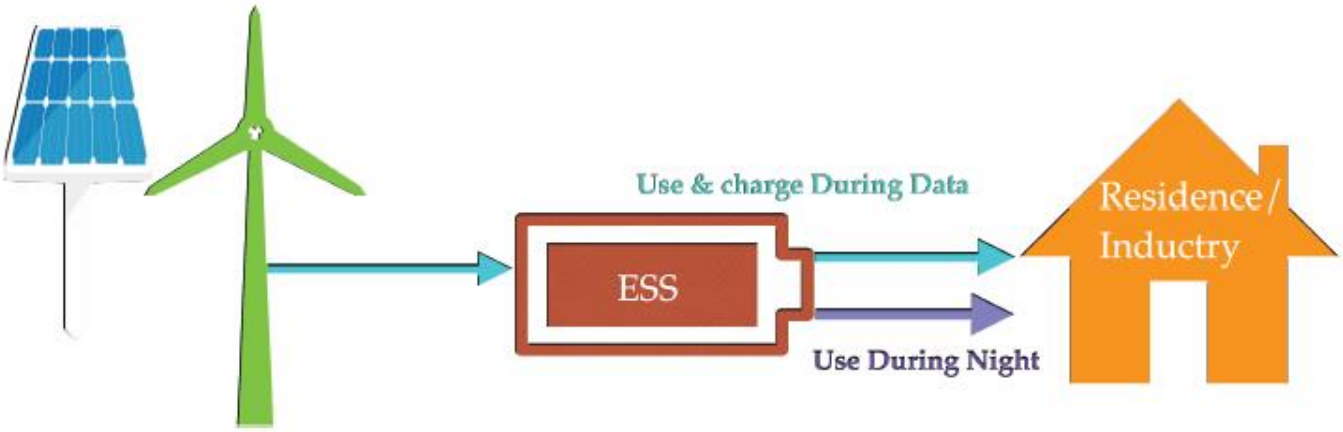

Figure 1: Schematic representation of Energy storage systems (ESS)

Redox flow batteries are a type of battery technology that is increasingly being used in renewable energy applications. These batteries are usually composed of two tanks that contain electrolytes, or liquid solutions of different chemicals, that contain ions such as hydrogen and oxygen. The ions in the electrolyte can be exchanged between the tanks via a membrane which prevents other materials from passing through it. This exchange allows the battery to store and release energy thus making them highly efficient, long-lasting and reliable battery storage systems. Redox flow batteries can also be safely cycled multiple times which increases their versatility and adaptability for use in renewable energy applications such as wind farms or solar arrays, where intermittent and fluctuating power sources are present. Additionally, redox flow batteries have a low environmental impact and do not require any hazardous metals or chemicals to operate, making them an ideal choice for environmentally conscious users. The redox flow battery system is shown in Figure 2.

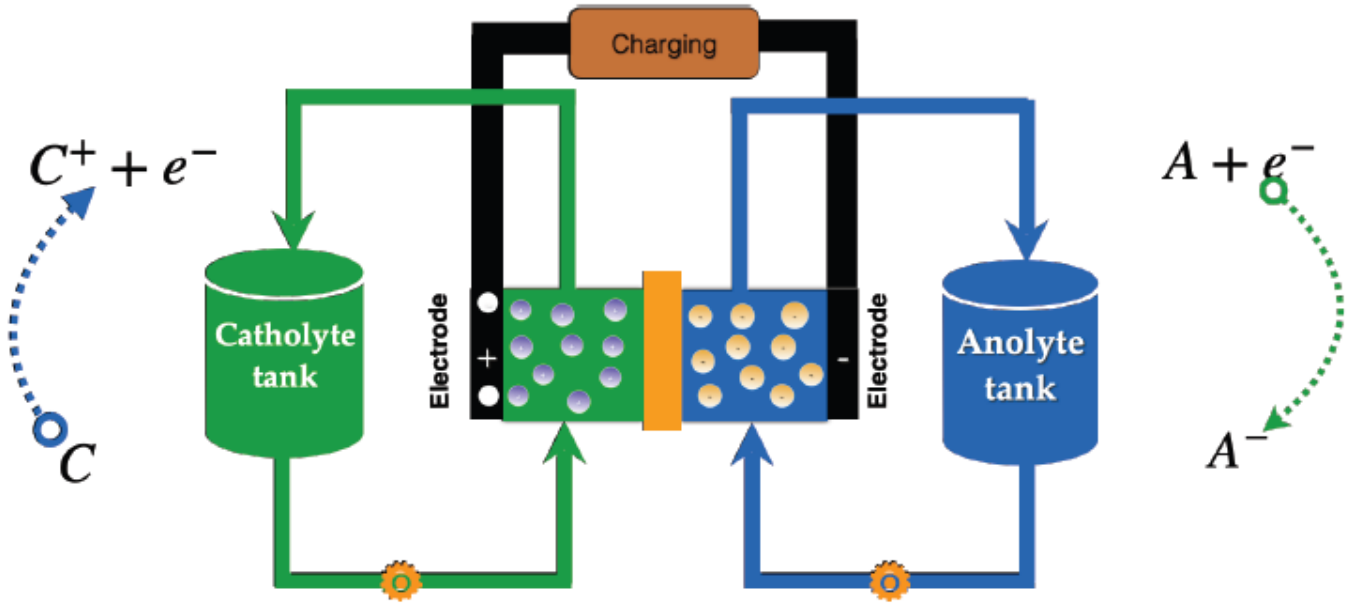

Figure 2: Schematic representation of redox flow batteries (RFBs)

The basic process of a redox flow battery (RFB) is illustrated in the Figure 2 requires four main components: (1) two electro-chemical cells, each consisting of two electrodes connected to a load by means of wire conduits; (2) pumps, used to circulate electrolytes between the two electrodes; (3) storage tanks that store the electrolyte

solutions; (4) a charge controller, with an electrical circuit and a switch, controls the direction of current during charging and discharging of the RFB. During charging, one tank acts as an anode while the other tank acts as a cathode in producing electricity through a redox reaction between two different ions (anions and cations). The ions move from one cell to another in loose form or in solution (electrolyte) under pressure generated by positively charged electrodes (anodes). During discharge, this process reverses itself so that negative ions move from one cell to another under the control of negatively charged electrodes (cathodes). This causes electric current to flow from one electrode to its opposite through the load which then powers energy consuming devices or stored back into batteries for later use.

Redox-active organic compounds are essential ingredients to redox flow batteries. They are used as part of the two electrolyte solutions of a redox flow battery and play an important role in transferring charge from one electrode to the other. Without them, there would be no electrochemical reaction taking place and thus no energy storage or release. Redox-active organic compounds also have advantages over traditional metal-based electrodes such as increased energy density, longer life cycle, and lower cost. As such, they are key components of these advanced battery technologies and offer a viable alternative to conventional rechargeable batteries for grid stabilization applications.

Materials science research has been influenced by the growing interest in artificial intelligence and machine learning. AI/ML has accelerated and improved the efficiency of materials discovery by developing databases, algorithms, and initiatives such as the Materials Genome Initiative (MGI) [7], Automatic Flow for Materials Discovery (AFLOWLIB) [8], and the Joint Automated Repository for Various Integrated Simulations (JARVIS) [9] to discover structure-property relationships [10].

Deep generative models (GMs) can be used to encode materials structure and/or properties into a latent space, which can then be explored and manipulated in order to generate new materials with targeted properties. GMs differ from traditional machine learning methods in that they learn representations of a materials structures and its corresponding physics or chemistry to accelerate materials discovery rather that using statistical and combinatorial screening of existing materials. This approach could help speed up research related to discovering novel compounds or structures as well as aid researchers looking for specific characteristics such as improved performance or cost-effectiveness when designing new products using existing components [10].

Graph Neural Networks (GNNs) are a type of graph networks (GNs) which have recently been used to learn representations of graphs [11–13]. GNNs are a type of neural network that generalizes convolutions to graphs, such as graph convolutional netwroks (GCNs) [14] and message passing neural networks (MPNNs) [15]. Graphs are data structure which are composed of nodes and vertices and edges (connections between nodes). GNs take graph-structures data as input and output a latent representation of the input graph. This output graph representation is the result fo combining the hidden node states (vectors) obtained in the different propagation blocks of the GN. The learned graph representation are node-order invariant, meaning that the order of the nodes does not affect the representation. Additionally, a smaller distance between two graph representations implies a greater degree of similarity.

Molecular generative models are a promising method used to explore the chemical space through de novo molecular design [11,16,17]. This means that they are used to create new molecules from scratch. These models have largely focused on string-based approaches but graph-based approaches are models that use graphs to represent molecules, and they are built using graph neural networks (GNNs) [18], variational autoecoders (VAEs), generative adversarial networks (GANs), or combinations of these. Graph-based molecular generative models can be classified into two types: single shoot and iterative models. In single-shot molecular graph generation, new graphs $G = (A, X)$ are generated in one or two steps. This is done by first generating an adjacency tensor A from a corresponding latent graph representation, and then generating a node features tensor X which "fills in" the identities of the nodes in A. On the other hand, in iterative molecular graph generation, the molecular graph is generated in a step-by-step fashion, typically starting from an empty graph $G_0 = (A_0, X_0)$. Then, nodes and/or edges are added sequentially by sampling from a learned distribution until the graph is complete.

The use of Graph Adversarial Networks (GANs) with Representation Learning on Molecular Graphs has shown to be effective in discovering novel organic materials for Redox Flow Battery applications. In particular, GAN-based representation learning has been applied to the prediction of solid-state properties, such as total energy, band gap energy and dielectric constants, from molecular graphs [19]. Additionally, GAN-based methods have been successful in discovering promising electrochemical materials from a dataset of over 3 million molecules [20]. One application even used GANs to design and optimize electrochemically active material structures for Li-ion battery applications. Overall, the use of GANs with representation learning on molecular graphs has been seen as an effective solution to discover novel organic materials for redox flow battery applications.

In this work, we applied deep generative model based on iterative graph generation with Generative Adversarial Networks (GANs) model to discovery novel redox-active organic molecules that can be applied on redox-flow batteries.

2. MATERIALS AND METHODS

2.1. Variational Autoecnoder (VAE)

A variational autoencoder (VAE) is an unsupervised learning model that employs deep generative models to develop useful latent representations of molecular data. VAEs are increasingly being applied to molecular discovery applications, such as novel organic material discovery, by leveraging generative adversarial networks (GANs) to generate more realistic molecules.

VAEs appear promising for improving various tasks related to organic materials synthesis and discovery. The VAE captures the complex data distributions of underlying chemical properties from large datasets, which can then be transformed into a simplified set of underlying features that control certain behavior. These features can then be used to generate a range of new compounds with desired properties, eliminating the need for blocking groups or exhaustive enumeration schemes for new compounds. With GANs, these VAEs are able to produce samples such as candidate molecules with their known analytical fingerprints for accurate prediction and validation purposes. We employed the VAE technique to encode discrete molecular representations into a continuous lower-dimensional vector called latent space, as shown in Figure 3. This continuous latent space can also enable in the prediction of electrochemical properties of redox-active organic molecules such redox potential, solubility, and stability.

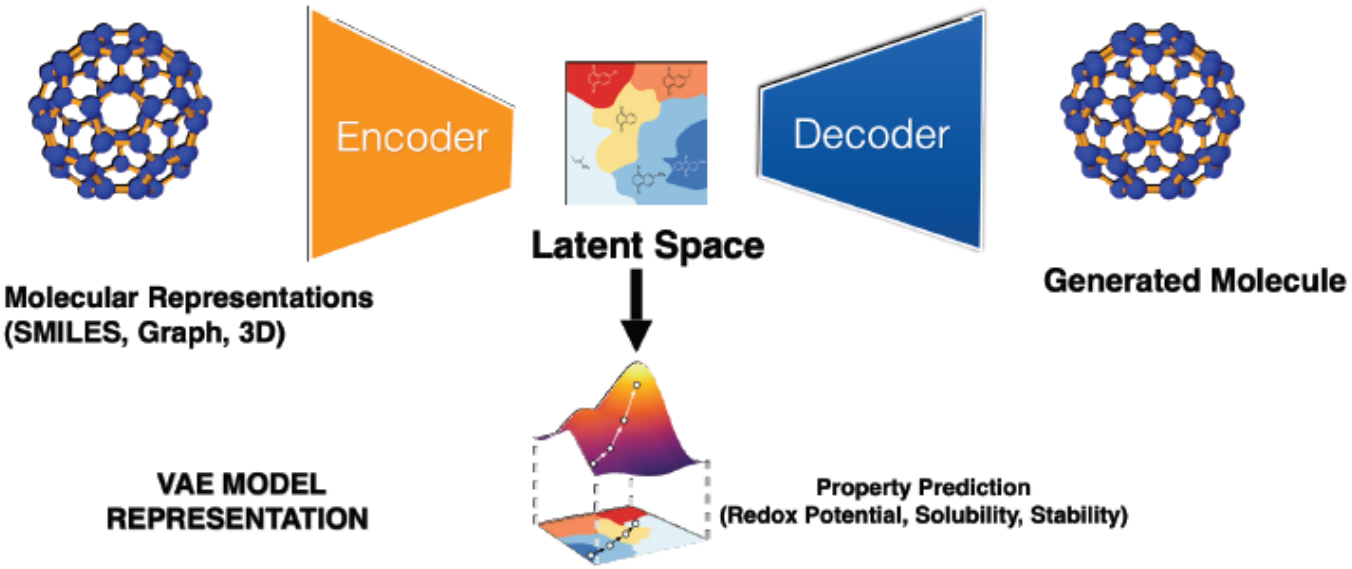

Figure 3: Schematic representation VAE model for molecular representation

2.2. Generative Adversarial Networks (GANs)

Generative Adversarial Networks (GANs) are a type of deep neural network used for unsupervised learning problems. They are composed of two competing neural networks that work together to generate realistic data from a given distribution. The two networks, the generative and the discriminative, have alternating roles in training. The generative network creates synthetic data by transforming noise into samples, while the discriminative network assesses their quality and attempts to distinguish them from real data. By playing off each other in this way, both networks improve until the discriminator can no longer detect any meaningful difference between real and generated data samples. Thus, GANs could help discover new materials for energy storage by learning complex distribution from training data and generating promising materials by exploring those regions of chemical space that would otherwise be unreachable via traditional methods.

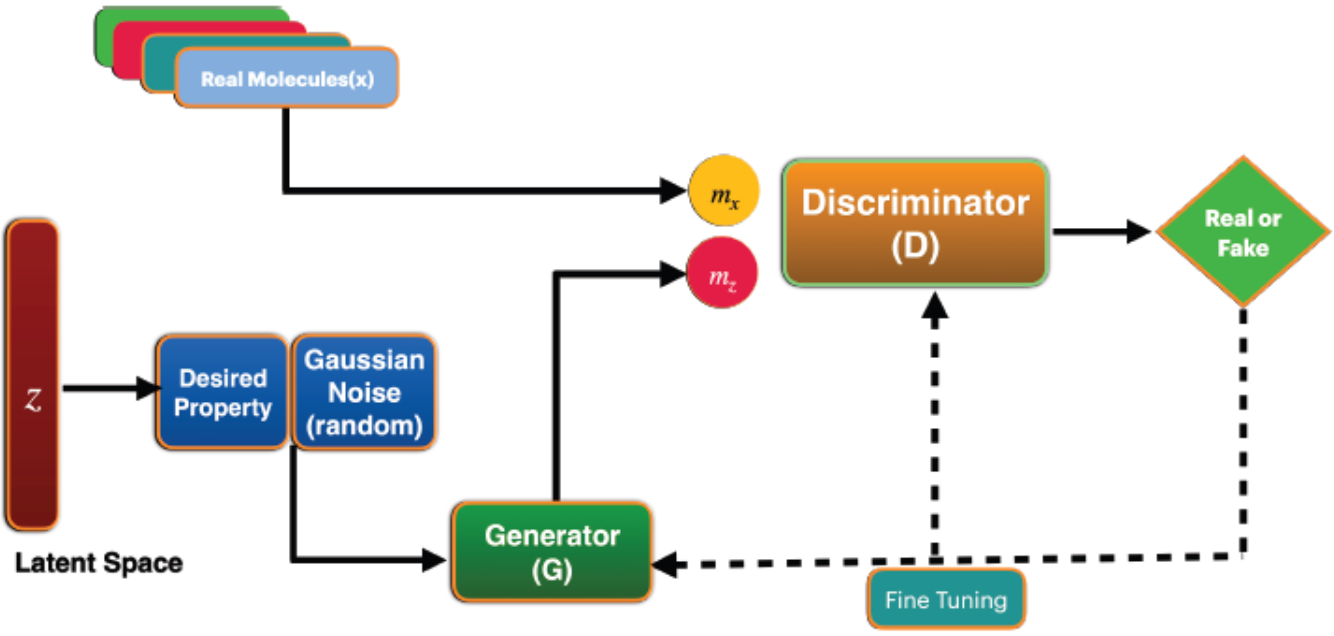

Figure 4: Schematic representation GAN model

The GAN model for molecular data consists of three main components: a generator (z), a discriminator (x) and a reward network $R\psi$. The generator takes a sample from a normal distribution N (0, I) latent space z encoded by VAE and generates an annotated graph G representing a molecule with adjacency matrix $\hat{A}$ and the node feature matrix $\hat{X}$ of the molecular graph. The architecture of these two neural networks, discriminator and reward network, were implemented by a simple MLP with three layers. The reward network is used to approximate the reward function of a sample and optimize molecule generation towards non-differentiable metrics using reinforcement learning. The discriminator model (x) and the generator model (z) are playing minmax zero-sum game with the comprehensive objective loss function(min-max loss) from cross-entropy distribution is

$$\min_G \max_D V(G,D) = E_x\left[\log D(x)\right] + E_z\left[\log(1 - D(G(z))\right]$$

- D is accurate over real data by maximizing E_x [log (x)].
- G is trained to increase D's probability for fake molecules by minimizing E_z [log(1 − $D(G(z))$].

In general, D and G play a two-player minimax game with value function of V (G, D) with the goal of the discriminator is to maximize V (D, G) when $D(x)$ = 1 and $D(G(z))$ = 0. While log probability of D predicting that real-world data is genuine, the log probability of D predicting that G's generated data is not genuine. Hence, the

discriminator is a binary classifier that returns 1 for real molecule and 0 for a fake molecule from the generator model.

2.3. Data Sources and Representation

The rise of big-data repositories sparks the expansion of online availability of chemical and materials datasets such as Crystallography of Database(COD), Inorganic Crystal Structure Database, AFLOW, Materials Project, Open Quantum Materials Database (OQMD), ChemSpider, Pubchem etc. PubChemQC is also a recent attempt to create training data for ML with calculated ground-state electronic structure of 3 million molecules based on DFT at B3LYP/6-31G* level. Furthermore, GDB-11 lists 26.4 million small organic molecules of up to 11 atoms of CNOF with energies and DFT-level properties [21]. GDB-13 enumerates 978 billion molecules with up to up to 13 atoms of CNOSCl [22] and GDB-17 contains 166.4 billion molecules of up to 17 atoms of CNOS, and halogens. However, RedDB [23] and QM9 [24] are the two main dataset utilized to train the GAN model.

There are four commonly used in molecular data representation. These are: fingerprints, Graph, SMILES and 3D. From these data representation formats, we have used both SMILES and graph representation to build library of organic molecules that could be transformed into continuous representation to train GAN model and then feed to our deep generative model to discovery a new material. Many molecular data are not organized on regular grids to model relationships between objects. However, recent development of deep learning models are depend on graph based computational frameworks. Making deep learning models to fit a complex real world applications needs the modeling framework dynamic, flexible and adaptable to other frameworks. These frameworks promise a better experience in creation of models using the combination of convolutions neural networks, recurrent neural networks, and deep leaning networks. Hence, graph convolutional deep learning is used to generalize a graph neural network for non-Euclidean data. A graph is represented as $G = (V, E, A)$ where V is the set of nodes (objects) and E is the set of edges (relationships) with the adjacency matrix A between node i and node j. Let $vi \in V$ to denote a node and $e_{ij} = (v_i, v_j) \in E$ to denote an edge pointing from vj to vi. The neighborhood of a node V is defined as $N(v) \in E$.

2.4. Model Training

Data preprocessed: To reduce overfitting, effective preprocessed data strategies were employed. This included adding random perturbations to the inputs and labels during training, as well as augmenting the training set by applying randomly sampling node attributes, edge weights and graph structures. These preprocessed data allowed the model to effectively generalize beyond the original dataset. This allowed for better exposure and better performance on unseen datasets during test phase. Overall, a great deal of research went into studying the best practices for this type of supervised learning problem. Finding an adequate hyperparameter configuration, managing block sizes when reading in data, not using early stopping criteria, and applying effective data augmentation techniques all helped to make training more robust for this model.

The model was trained using the Adam optimizer with a learning rate of 0.0001. To maintain the learning, mini-batch training was carried out with a batch size 32. With an early ending strategy, the model training was stopped once the maximum allowed number of epochs (350) had been reached or when the average change in loss over 10 epochs was less than 1.0%. Generally, the molecular generation model was evaluated using the indices of validity, novelty, and uniqueness. The proportion of chemically valid molecules among newly generated compounds is known as validity. Be aware that validity only considers the valence of atoms and not the connectivity of molecules. The fraction of legitimate molecules among the generated molecules that were excluded from the training set is known as novelty. These compounds met the criteria for new molecules in this investigation. The proportion of newly created molecules that are both unique and valid is known as uniqueness.

3. RESULTS

The proposed method for generating molecules based GANs model consists of two components: a generator network and discriminator network. The goal of the generator is to produce realistic molecules given a molecular formula. The discriminator aims at distinguishing between real molecules and synthesized ones. The generator takes a molecular graph as input and produces a molecular latent space of their representation. The trained a GAN model using molecular graph was aimed to learn how to generate molecules given only their smiles. To achieve this goal first need to represent the molecular graph of molecules in a way that makes them amenable to training a GAN

model. The result shows that the suggested strategy is effective in generating effective compounds with desired properties for redox flow batteries applications as shown in Figure 5.

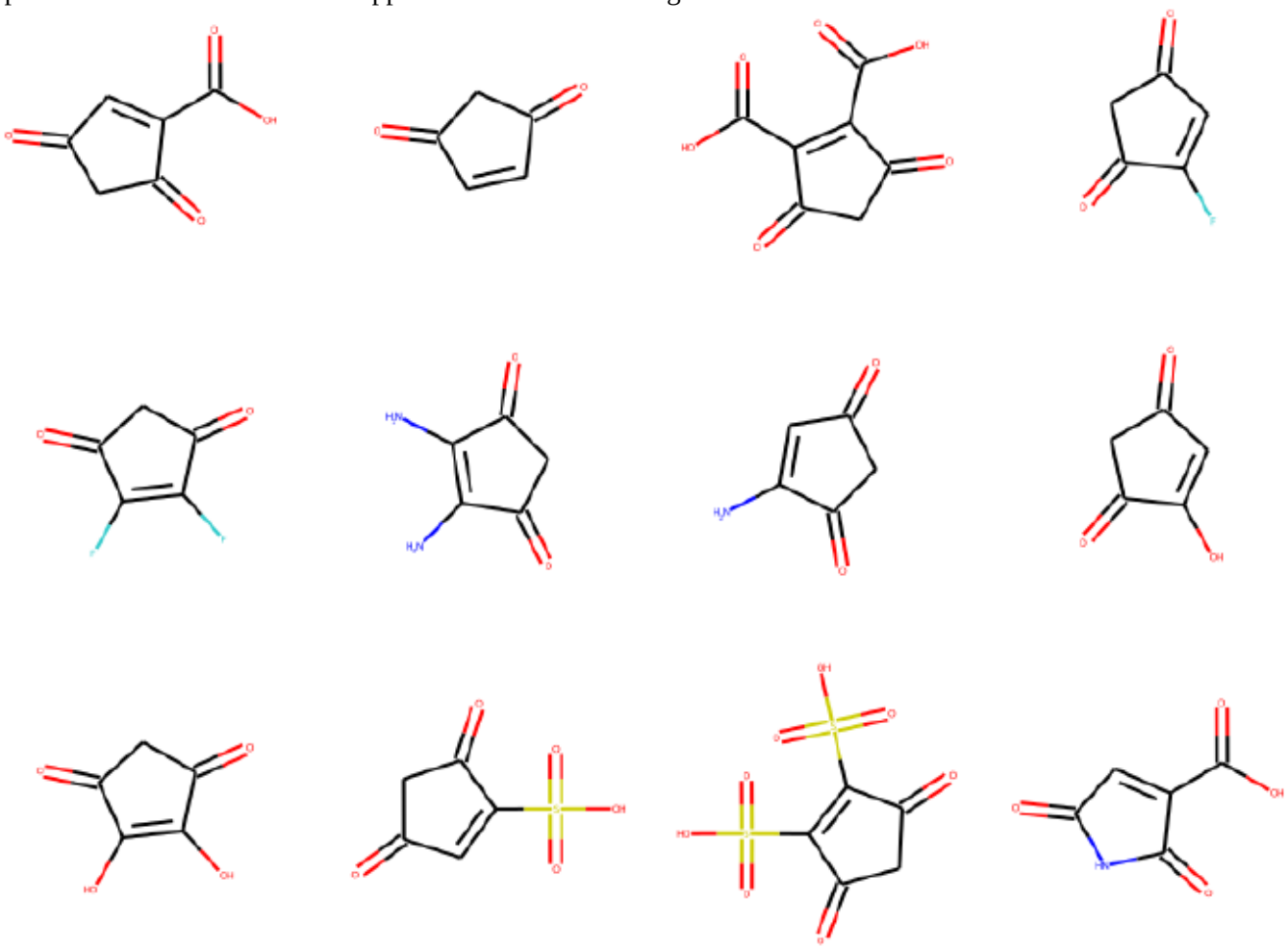

Figure 5: Sampled novel organic molecules generated with GAN model

4. CONCLUSION

This paper illustrated the potential of adversarial generation and machine learning algorithms in discovering novel organic materials for redox flow batteries. By exploiting the generative adversarial networks (GANs), new classes of molecules with desired properties were successfully generated from existing training set data. Our results showed great promise for future generations of energy storage systems derived from green and renewable sources. With continued development, GANs-based molecular design that mimics organic chemistry may become a powerful tool for finding new molecules for battery technologies such as RFBs. Furthermore, by combining VAEs with GANs and incorporating prior knowledge, novel molecular discovery applications can be significantly accelerated.

REFERENCES

[1] T. M. Gür, Review of Electrical Energy Storage Technologies, Materials and Systems: Challenges and Prospects for Large-Scale Grid Storage, Energy & Environmental Science 11, 2696 (2018).
[2] A. Z. Weber, M. M. Mench, J. P. Meyers, P. N. Ross, J. T. Gostick, and Q. Liu, Erratum to: Redox Flow Batteries: A Review, Journal of Applied Electrochemistry 41, 1165 (2011).
[3] E. O. Pyzer-Knapp, K. Li, and A. Aspuru-Guzik, Learning from the Harvard Clean Energy Project: The Use of Neural Networks to Accelerate Materials Discovery, Advanced Functional Materials 25, 6495 (2015).

[4] L. Cheng, R. S. Assary, X. Qu, A. Jain, S. P. Ong, N. N. Rajput, K. Persson, and L. A. Curtiss, Accelerating Electrolyte Discovery for Energy Storage with High-Throughput Screening, The Journal of Physical Chemistry Letters 6, 283 (2015).
[5] N. Nitta, F. Wu, J. T. Lee, and G. Yushin, Li-Ion Battery Materials: Present and Future, Materials Today 18, 252 (2015).
[6] R. Chen, Redox Flow Batteries for Energy Storage: Recent Advances in Using Organic Active Materials, Current Opinion in Electrochemistry 21, 40 (2020).
[7] J. J. de Pablo, B. Jones, C. L. Kovacs, V. Ozolins, and A. P. Ramirez, The Materials Genome Initiative, the Interplay of Experiment, Theory and Computation, Current Opinion in Solid State and Materials Science 18, 99 (2014).
[8] S. Curtarolo et al., AFLOW: An Automatic Framework for High-Throughput Materials Discovery, Computational Materials Science 58, 218 (2012).
[9] K. Choudhary et al., The Joint Automated Repository for Various Integrated Simulations (JARVIS) for Data-Driven Materials Design, Npj Computational Materials 6, (2020).
[10] A. S. Fuhr and B. G. Sumpter, Deep Generative Models for Materials Discovery and Machine Learning-Accelerated Innovation, Frontiers in Materials 9, (2022).
[11] R. Mercado, T. Rastemo, E. Lindelöf, G. Klambauer, O. Engkvist, H. Chen, and E. Jannik Bjerrum, GraphNetworks for Molecular Design, Machine Learning: Science and Technology 2, 025023 (2021).
[12] W. L. Hamilton, Graph Representation Learning, Synthesis Lectures on Artificial Intelligence and Machine Learning 14, 1 (2020).
[13] D. Fooshee, A. Mood, E. Gutman, M. Tavakoli, G. Urban, F. Liu, N. Huynh, D. Van Vranken, and P. Baldi, Deep Learning for Chemical Reaction Prediction, Molecular Systems Design & Engineering 3, 442 (2018).
[14] H. Pei, B. Wei, K. C.-C. Chang, Y. Lei, and B. Yang, Geom-{{GCN}}: {{Geometric Graph Convolutional Networks}}, ArXiv200205287 Cs Stat (2020).
[15] J. Gilmer, S. S. Schoenholz, P. F. Riley, O. Vinyals, and G. E. Dahl, Neural Message Passing for Quantum Chemistry, (2017).
[16] B. Sanchez-Lengeling, C. Outeiral, G. L. Guimaraes, and A. Aspuru-Guzik, Optimizing Distributions over Molecular Space. An Objective-Reinforced Generative Adversarial Network for Inverse-Design Chemistry (ORGANIC), (2017).
[17] T. Blaschke, J. Arús-Pous, H. Chen, C. Margreitter, C. Tyrchan, O. Engkvist, K. Papadopoulos, and A. Patronov, REINVENT 2.0 – an AI Tool for de Novo Drug Design, (2020).
[18] N. De Cao and T. Kipf, MolGAN: An Implicit Generative Model for Small Molecular Graphs, arXiv:1805.11973 [Cs, Stat] (2018).
[19] S. Kim, J. Noh, G. H. Gu, A. Aspuru-Guzik, and Y. Jung, Generative Adversarial Networks for Crystal Structure Prediction, ACS Central Science 6, 1412 (2020).
[20] A. E. Blanchard, C. Stanley, and D. Bhowmik, Using GANs with Adaptive Training Data to Search for New Molecules, Journal of Cheminformatics 13, (2021).
[21] T. Fink and J.-L. Reymond, Virtual Exploration of the Chemical Universe up to 11 Atoms of C, N, O, F: Assembly of 26.4 Million Structures (110.9 Million Stereoisomers) and Analysis for New Ring Systems, Stereochemistry, Physicochemical Properties, Compound Classes, and Drug Discovery, Journal of Chemical Information and Modeling 47, 342 (2007).
[22] L. C. Blum and J.-L. Reymond, 970 Million Druglike Small Molecules for Virtual Screening in the Chemical Universe Database GDB-13, Journal of the American Chemical Society 131, 8732 (2009).
[23] E. Sorkun, Q. Zhang, A. Khetan, M. C. Sorkun, and S. Er, RedDB, a Computational Database of Electroactive Molecules for Aqueous Redox Flow Batteries, (2021).
[24] R. Ramakrishnan, P. O. Dral, M. Rupp, and O. A. von Lilienfeld, Quantum Chemistry Structures and Properties of 134 Kilo Molecules, Scientific Data 1, 140022 (2014).

A Comprehensive Review of Energy Storage Technologies Application Potential for Grid-connected Renewable Source

Henok Ayele Behabtu*, Abraham Alem Kebede, Kinde Anlay Fanta

Faculty of Electrical and Computer Engineering, Jimma University, P.O.Box 378, Jimma, Ethiopia
**Corresponding author, e-mail: henok.ayele@ju.edu.et*

ABSTRACT

Renewable energy sources (RESs) such as wind and solar are frequently hit by fluctuations due to, for example, insufficient wind or sunshine. Energy storage technologies (ESTs) mitigate the problem by storing excess energy generated and then making it accessible on demand. While there are various EST studies, the literature remains isolated and dated. The comparison of the characteristics of ESTs and their potential applications is also short. This paper fills this gap. Using selected criteria, it identifies key ESTs and provides an updated review of the literature on ESTs and their application potential to the renewable energy sector. The critical review shows a high potential application for Li-ion batteries and the most fit to mitigate the fluctuation of RESs in utility grid integration sector. However, for Li-ion batteries to be fully adopted in the RESs utility grid integration, their cost needs to be reduced.

Keywords: *Intermittent energy sources; energy storage application; characteristics of ESTs; comparison of ESTs; selection criteria of ESTs.*

1. INTRODUCTION

Nowadays, renewable energy generation capacity is growing at a rapid rate globally. Data from the International Renewable Energy Agency (IRENA) showed that, at the end of 2019, global RESs generation capacity amounted to 2537 GW. Hydropower accounted for the largest share of the global total, with a capacity of 1190 GW (excluding pure pumped storage); this is followed by wind energy (623 GW), solar energy (586 GW), bioenergy (124 GW), geothermal energy (14 GW), and marine energy (500 MW) [1]. Among renewable energy sources (RESs') generation capacity, wind and solar energy continued to dominate renewable capacity addition in 2019 [1]. However, energy supply from such sources is often hit by fluctuations due to, for example, insufficient wind or sunshine. It is, therefore, necessary to maintain the power fluctuation of a power system integrated with a large amount of RESs such as wind and solar. Energy storage is a crucial means that mitigates such increased fluctuations or power quality problems by providing voltage support, smoothing their output fluctuations, balancing the power flow in the network, and matching supply and demand. Moreover, with the increase of the production of power or energy from RESs, it becomes much important to look at methods or techniques of selecting the appropriate type of ESTs for RESs grid integration application. Hence, the relationship between ESTs and its application is interdependent; knowledge of the technical characteristics of each ESTs as well as their application potential in RESs are very important toward technology adoption. Our key research questions are, therefore, what are the major ESTs and how can their technical, economic, and environmental fit be evaluated? This paper addresses central questions and provides to date review for researchers, industry, and policymakers on technical, economic, and environmental characteristics of ESTs for RESs utility grid integration application.

This review paperwork is different from other literature work reviewed before in the following way. A literature review is conducted to understand better the advantage and disadvantages of ESTs, and their potential applications in RESs grid integration applications sector. Even though there are various ESTs already reviewed in the literature, there is limited information and updated data on characteristics of ESTs and their application potential for RESs grid integration. There is also a lack of evaluating ESTs with the help of graphic comparison from a complete selection criteria perspective such as technical, environmental, and economic. Therefore, this review paper aims to

address this gap by evaluating the application potential of ESTs for RESs utility grid integration based on up-to-date selected criteria such as technical, economic and environmental impacts.

2. MATERIALS AND METHODS

Among different ESTs, pumped hydro storage (PHS), compressed air energy storage (CAES), flywheel energy storage (FES), supercapacitor energy storage (SCES), superconductive magnetic energy storage (SMEs), lead-acid (Pb-A), nickel-cadmium (Ni-Cd), sodium-sulfur (Na-S), sodium nickel chloride ($NaNiCl_2$), lithium-ion (Li-ion), and flow battery energy storage (FBES) were selected based on their advantages, disadvantages, application potential for RESs and availability of characteristics data in the literature. Those characteristics data are energy and power density, lifetime, cost, efficiency, technology maturity, response time, self-discharge time, power rating, discharge time, and environmental impacts shown in Tables 1 and 2.

The procedures followed to select the most suited ESTs for RESs utility grid integration is as follows:

- Up-to-date technical details and characteristics data for all selected ESTs have been collected from several peer-reviewed journal papers.
- To evaluate the application potential of ESTs for RESs utility grid integration clearly, all selected characteristics of ESTs are graphically compared and analyzed.
- Using graphic comparison results, the application potential of ESTs categorizations has been decided by considering the common characteristics of ESTs and their application area requirements.

Table 1: Technical characteristics of all studied ESTs

ESTs	Power Range (MW)	Energy Density (Wh/l)	Power Density (W/l)	Round Trip Efficiency (%)
PHS	10–5000 [2,5,6,8]	0.5–1.5 [5–17,8]	0.5–1.5 [4,9]	75–85 [2], 65–87 [5,8] 70–85 [7]
FES	0.1–20 [2], < 0.25 [4], 0–0.25 [5,8] 0.01–0.25 [7]	20–80 [4,8]	1000–2000 [4,8]	93–95 [2] 90–95 [7] 90–93 [9]
CAES	5–1000 [2], 5–300 [5,6,8]	3–6 [5,6,8]	0.5–2 [5,6]	70–89 [2] 50–89 [5,6] 70–79 [9]
Pb-A	0–40 [2], 0–20 [5,6]	50–80 [5,6]	10–400 [5,6]	70–90 [2] 75–80 [5]
Ni-Cd	0–40 [2,6]	60–150 [2,6]	150–300 [2]	60–65 [2] 85–90 [5]
Na-S	0.05–34 [2] 0.05–8 [6]	150–250 [5,8]	150–230 [5,8]	85–90 [2] 80–90 [5,8]
NaNiCl2	0–3 [26]	150–180 [26]	220–300 [26]	85–90 [26]
Li-ion	0–100 [2], 0–1 [5,6]	200–500 [6,8]	500–2000 [8]	85–90 [2,8] ~90–97 [4]
VRFB	0.3–3 [5]	16–33 [5] 20–70 [10]	0.5–2 [10]	85–90 [5] 75–82 [9]
SCES	0–0.3 [5,6]	2.5–15 [8]	500–5000 [8]	90–95 [2,8] 95–98 [9]
SMES	0.1–10 [5,6]	0.2–2.5 [8]	1000–4000 [8]	95–98 [2,8] 95 [9]

Source: Authors' (collated from difference source)

Table 2: Additional technical characteristics of all studied ESTs

ESTs	Discharge Time (ms-hr)	Response Time (ms-h)	Lifetime (yr)	Daily Self-Discharge (%)	Technology Maturity
PHS	1–24 hr+ [2,5–7,8]	sec-min [2], min [4,7], 1–2 min [12]	40–60 [2,4]–[6,8]	Very small [4,5] 0.00 [3]	Very mature/Fully commercialized [2,3,4,7]
FES	ms–15 min [2,7,8]	< 4 ms-sec [2], sec [7]	15 + [2], 15 [5,6,8]	100 [6] 24–100 [3]	Mature/Commercializing [3,4,5,7,8]
CAES	1–24 hr+ [2,5,8]	1–15 min [2], 1–2 min [5]	20–40 [2]	Small [4–6] 0.00 [3]	Proven/Commercializing [3,5]
Pb-A	sec-hr [2,5,6]	5–10 ms [2], sec [5]	3–15 [2], 5–15 [5,6]	0.1–0.3 [5,6] 0.033–1.10 [3]	Very mature/Fully Commercialized [3,4,7]
Ni-Cd	sec-hr [5]	20 ms-sec [2], sec [5]	10–20 [2,5]	0.2–0.6 [5,6] 0.07–0.71 [3]	Very mature/Fully commercialized [2,3,5]
Na-S	sec-hr [2,5,8]	1 ms [2], sec [5]	10–15 [2,5,8]	20 [3,5,8]	Proven/Commercializing [2,3,5]
NaNiCl2	sec–hr [8]	< sec [10]	10–14 [8]	11.89–26.25 [3]	Proven/Commercializing [3,8]
Li-ion	min–hr [2,5,8]	20 ms-s [2]	5–15 [2,5]	0.1–0.3 [5,6] 0.03–0.33 [3]	Proven/Commercializing [2,5]
VRFB	sec-10 hr [5]	Sec [5]	5–10 [5]	Small [5]	Proven/Commercializing [3,5]
SCES	ms–hr [2]	8 ms [2],	20 + [2,5]	20–40 [2,5] 0.46–40 [3]	Proven/Commercializing [2,3]
SMES	ms–8 sec [2]	< 100 ms [2]	20 + [2,5]	10–15 [2,5] 1–15 [3]	Proven/Commercializing [2,3]

Source: Authors' (collated from difference source).

3. RESULTS AND DISCUSSION

To evaluate the potential applications of ESTs for RESs grid integration application clearly, all selected criteria of ESTs are graphically compared and analyzed in detail. The purpose of analyzing and comparing all studied ESTs is to offer an updated comparison for all selected ESTs. Among the technical characteristics of ESTs the following selected result has been presented:

3.1 Energy and Power Density of ESTs Comparison

As shown in Figure 1, compared to all studied ESTs, electrochemical energy storage systems (Pb-A, Ni-Cd, Na-S, $NaNiCl_2$ & Li-ion) have higher energy density than others. On the other hand, the power density of FES, SMES, and SCES are higher than other types of ESTs. Among electrochemical energy storage, Li-ion, Na-S, and $NaNiCl_2$ have higher energy density than other selected rechargeable batteries.

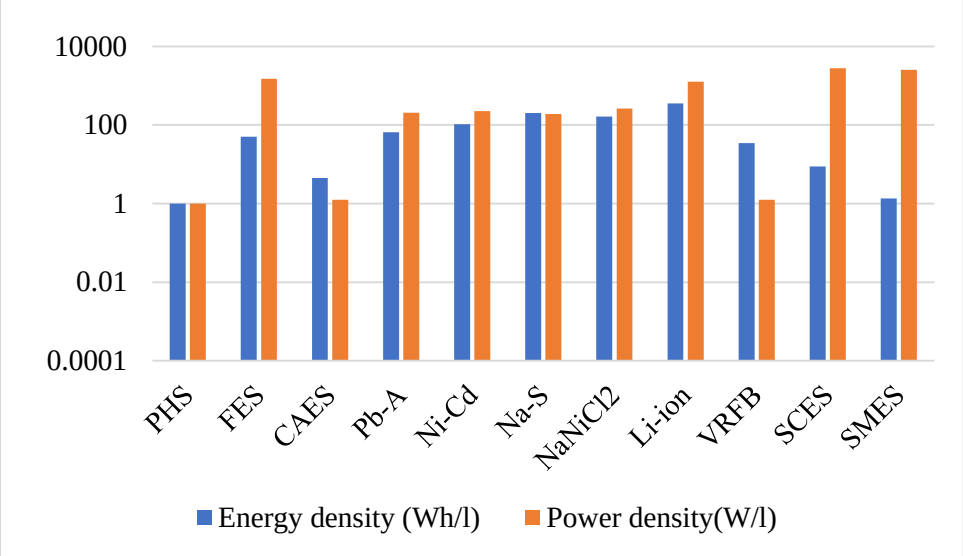

Figure 1: Comparison of energy and power density for the studied ESTs, according to the average data of Table 1

3.2 Power Rating and Discharge Time of ESTs Comparison

The power ratings and discharge time (E/P) of various ESTs are compared in Figure 2 using the bubble chart. Among all studied ESTs, PHS, and CAES have a higher power range and longer discharge time than others. On the contrary, SMES, FES, and SCES have a low power range and a very short discharge time.

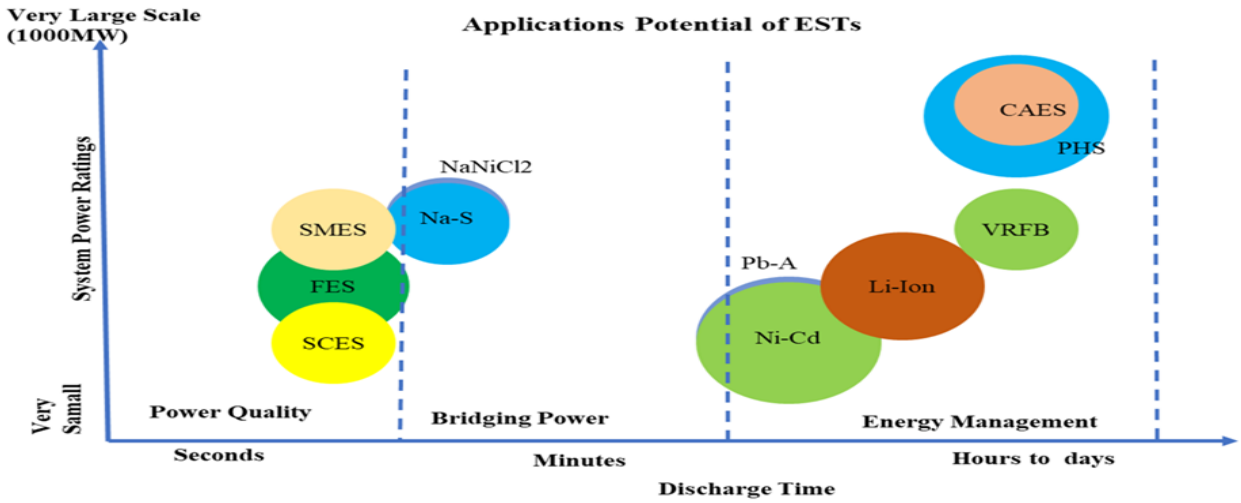

Figure 2: Comparison of power rating and discharge time for the studied ESTs, according to the average data of Tables 1 and 2

3.3 Self-Discharge Time of ESTs Comparison

The portion of the energy in a storage device, stored initially after charging and has dissipated over a certain amount of non-use time refers to the self-discharge of the storage device. Figure 3 illustrates the daily self-discharge (energy dissipation) of the ESTs. PHS, CAES, and flow batteries have a very small (almost negligible) daily self-discharge ratio compared to other ESTs. Therefore, such energy storage systems are suitable for long storage period applications. Among electrochemical energy storage systems, Na-S and NaNiCl2 have the highest self-discharge rate of 20% and 19.07% per day, respectively. Compared to the other ESTs, FES has the highest self-

discharge rate of 74.67% per day. Similarly, SMEs and SCES have the highest self-discharge rate for electrical energy storage systems at 10.25% and 25.115% per day, respectively.

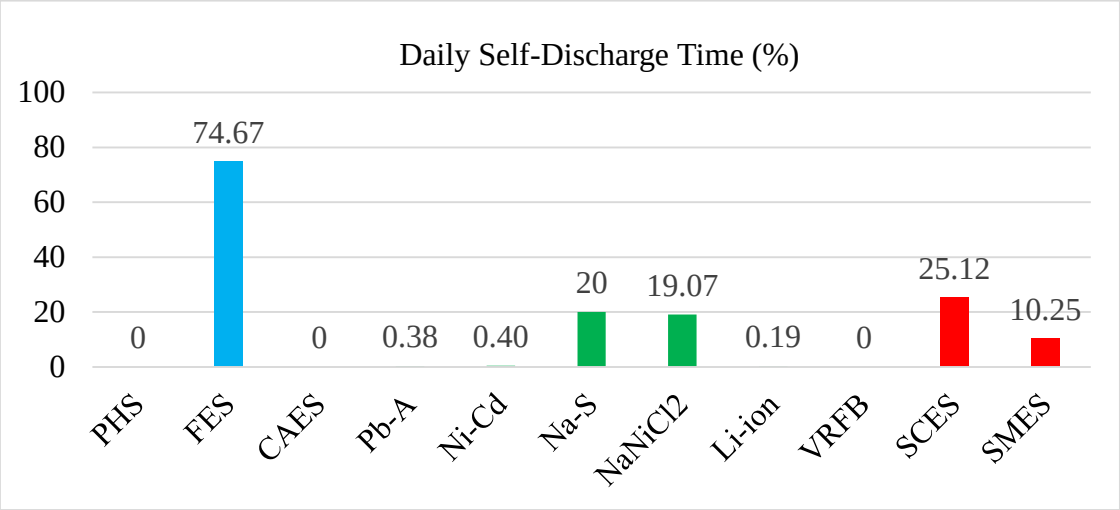

Figure 3: Comparison of self-discharge time for the studied ESTs, according to the average data of Table 2

3.4 The lifetime of ESTs Comparison

The lifetime of a storage system can be expressed both in terms of calendar life (years) and cycle life (number of charge/discharge cycles). Before selecting/adopting any EST for any application, identifying the life span of the EST plays a significant role in terms of investment. With all things being equal, EST with long life spans is usually preferred from an investment point of view over those with short life spans. Figure 4 compares the life span in years for different types of ESTs. Compared to the other ESTs, PHS has the largest life span of 50 years, while electrochemical energy storage systems fall within the range of 7.5-15 years depending on the quality of materials used coupled with the rate of chemical deterioration of the electrolyte used. Generally, mechanical energy storage systems (PHS and CAES) have longer lifetimes than electrochemical and electrical energy storage systems; as their lifetime is mainly determined by the lifetime of the mechanical components. On the other hand, compared to mechanical and electrical energy storage systems, electrochemical energy storage system usually has a short lifetime due to chemical deterioration with the operating time, rapid recharging and the effect of working in high temperatures.

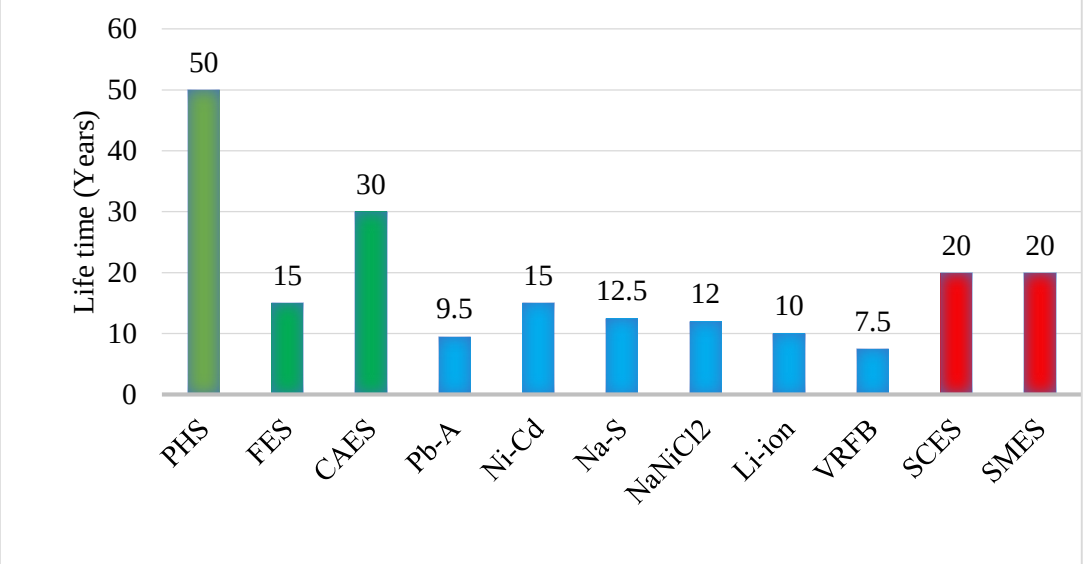

Figure 4: Comparison of a lifetime for the studied ESTs, according to the average data collected in Table 2

3.5 Round-Trip Efficiency of ESTs Comparison Result

Round-trip efficiency or cycle efficiency is the ratio of electricity output from the storage device to the electricity input to the device during the charge/discharge cycle; efficiency has expressed as the ratio of released energy to stored energy. Round-trip efficiency also considers energy losses during storing and withdrawing from the energy storage device. The actual discharge energy is less than the energy storage capacity due to losses that could be due to the transformer, pumping equipment, power control system, wiring, etc. As shown in Figure 5, FES, SMEs, SCES, and Li-ion batteries have a very high cycle efficiency (>90%), ranking them top among the other ESTs. Similarly, PHS, CAES, batteries (except for Li-ion) and flow batteries have a cycle efficiency of 74.5-90%.

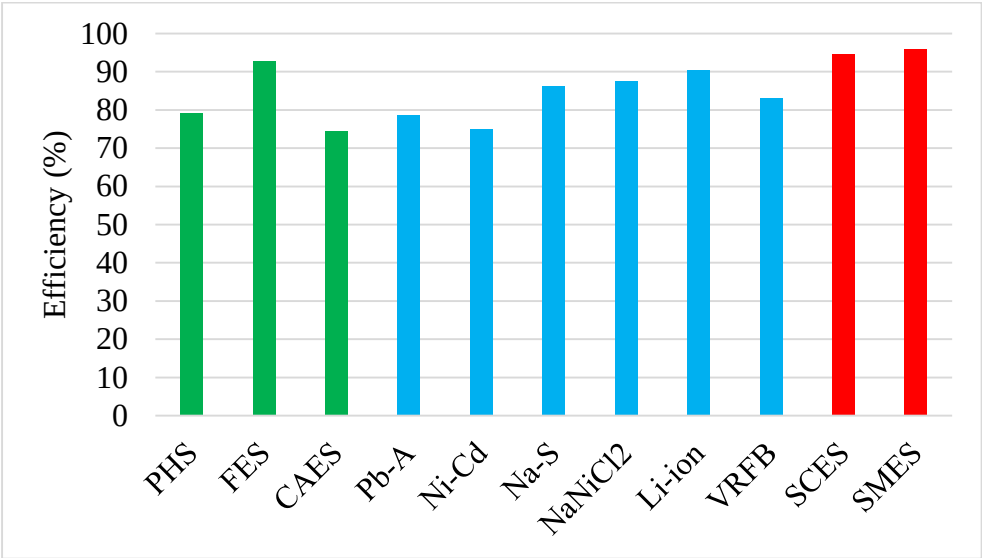

Figure 5: Comparison of round-trip efficiency for the studied ESTs, according to the average data of Table 1

4. CONCLUSIONS

According to the study result, electrochemical energy storage systems (batteries) are the dominant ESTs to be used when high energy and power densities, high power range, longer discharge time, fast response time, high cycle efficiency are paramount. Such types of ESTs have application potential in the renewable energy sector as well as in the power system in general such as, for energy management and bridging power application. Among electrochemical energy storage system, Li-ion batteries are considered as a more competitive option for grid-scale energy storage applications such as RESs utility grid integration due to their high energy density (350 Wh/l) and power density (1250 W/l), being lighter in weight and smaller in size, high cycle efficiency (90.5%), low daily self-discharge rate (0.19), the rapid response time (sec), and low environmental impacts. However, for Li-ion batteries to be fully adopted in the renewable energy sector, the cost of the storage device needs to be reduced.

REFERENCES

[1]. IRENA. Renewable Energy Capacity Highlights; Irena: New York, NY, USA, 2020.
[2]. Das, C.K.; Bass, O.; Kothapalli, G.; Mahmoud, T.S.; Habibi, D. Overview of energy storage systems in distribution networks: Placement, sizing, operation, and power quality. Renew. Sustain. Energy Rev. 2018, 91, 1205–1230, doi:10.1016/j.rser.2018.03.068.
[3]. Sabihuddin, S.; Kiprakis, A.E.; Mueller, M. A numerical and graphical review of energy storage technologies. Energies 2015, 8, 172–216, doi:10.3390/en8010172.
[4]. Luo, X.; Wang, J.; Dooner, M.; Clarke, J. Overview of current development in electrical energy storage technologies and the application potential in power system operation. Appl. Energy, 2015, 137, 511–536, doi:10.1016/j.apenergy.2014.09.081.
[5]. Rohit, A.K.; Rangnekar, S. An overview of energy storage and its importance in Indian renewable energy sector: Part II—Energy storage applications, benefits and market potential. J. Energy Storage 2017, 13, 447–456, doi:10.1016/j.est.2017.07.012.
[6]. Chen, H.; Cong, T.N.; Yang, W.; Tan, C.; Li, Y.; Ding, Y. Progress in electrical energy storage system: A critical review. Prog. Nat. Sci. 2009, 19, 3, 291–312, doi:10.1016/j.pnsc.2008.07.014.
[7]. Nadeem, F.; Hussain, S.M.S.; Tiwari, P.K.; Goswami, A.K.; Ustun, T.S. Comparative review of energy storage systems, their roles, and impacts on future power systems. IEEE Access 2019, 7, 4555–4585, doi:10.1109/ACCESS.2018.2888497
[8]. Aneke, M.; Wang, M. Energy storage technologies and real life applications—A state of the art review. Appl. Energy 2016, 179, 350–377, doi:10.1016/j.apenergy.2016.06.097.
[9] Ben Elghali, S.; Outbib, R.; Benbouzid, M. Selecting and optimal sizing of hybridized energy storage systems for tidal energy integration into power grid. J. Mod. Power Syst. Clean Energy 2019, 7, 113–122, doi:10.1007/s40565-018-0442-0.
[10] IEC. IEC Electrical Energy Storage White Paper. 2009. Available online: https://www.iec.ch/whitepaper/energystorage/ (accessed on 24 October 2020).

Synthesis of Resorcinol–formaldehyde Resins Doped with TiO_2 as Semiconductor Photocatalysts for Solar-to-hydrogen Peroxide Energy Conversion and Post-synthesis Organic Transformation

Addisalem Abebe Godana, Aditi Halder*, Subrata Ghosh*

School of chemical sciences, Indian Institute of Technology, IIT Mandi, India
**Corresponding author, e-mail:* aditi@iitmandi.ac.in *and* subrata@iitmandi.ac.in

ABSTRACT

Photocatalytic generation of hydrogen peroxide (H_2O_2) from water and O_2 under sunlight is a promising artificial photosynthesis reaction to generate renewable fuel. The generation of H_2O_2 from water and dioxygen ($H_2O + 1/2\ O_2 \rightarrow H_2O_2$, $\Delta G° = 117\ kJ\ mol^{-1}$) by sunlight-driven heterogeneous photocatalysis is a promising method for the artificial photosynthesis of a liquid solar fuel. TiO_2 doped resorcinol–formaldehyde (RF) resin powders prepared by high-temperature hydrothermal synthesis act as highly active semiconductor photocatalysts for H_2O_2 generation. The resin activity increases with an increase in the amount of TiO_2 until x = 1.2% w/w. The H_2O_2 produced is used as an oxidant to convert aryl sulfides to corresponding sulfoxides and sulphones and is further utilized for Baeyer-Villiger oxidation of acyclic ketones to corresponding esters and lactones. In this research, many electroanalytical techniques, thermal annealing and several characterization techniques like: SEM, XPS, BET, NMR, DRs, UV-Vis, Raman spectroscopy, FT IR, EIS, Photocurrent study, TGA, DLS were used.

Keywords: *Artificial photosynthesis, liquid solar fuel, hydrogen peroxide, organic transformation, solar-to-chemical energy conversion.*

1. INTRODUCTION

Artificial photosynthesis, which converts earth-abundant resources into fuels using sunlight, is a critical challenge in moving towards a sustainable future[1]. H2 generation by overall water splitting (equation 1) has been studied extensively for this purpose using photovoltaic electrolysis[2], photo electrochemical cells[3] and photocatalysts[4], with simple suspensions of powder photo catalysts being the most practical system for large-scale applications. In the past half century, only two types of powder catalyst, Rh_2–$yCryO_3$-(Ga1–xZnx)(N1–xOx) [5,6] and Ru-$SrTiO_3$/$BiVO_4$:Rh [7], have been found to split water under simulated sunlight with high solar-to-chemical conversion (SCC) efficiency (~0.2%), which is higher than the average solar-to-biomass conversion efficiency of natural photosynthesis by typical plants (~0.1%)[8]. Recently, a photo catalyst panel prepared by fixation of two kinds of powder catalyst (Ru_2–$yCryO_3$-$SrTiO_3$:La,Rh and $BiVO_4$:Mo) onto an Au sheet succeeded in splitting water with 1.1% SCC efficiency, although special fabrication techniques were necessary[9].

Furthermore, all water-splitting systems suffer from two unavoidable issues: (1) the catalysts are noble and expensive metals, (2) the systems need low-pressure or inert-gas atmosphere conditions and (3) the H_2 formed has low energy density and needs to be converted to a transportable liquid carrier such as ammonia. The photosynthesis strategy that generates liquid solar fuels on inexpensive powder catalysts under ambient conditions is thus a challenge. Hydrogen peroxide (H_2O_2) has received growing interest as a new liquid solar fuel because it is storable and transportable and it generates electricity in a direct peroxide–peroxide fuel cell (DPPFC)[10]. Theoretically, H_2O_2 can be generated from earth-abundant water and O_2 by semiconductor photocatalysis[11]. The photo generated valence band holes (VB h^+) oxidize water, producing O_2 (equation 2), and the conduction band electrons (CB e^-) promote the two-electron reduction of O_2, producing H_2O_2 (equation 3). These redox reactions generate H_2O_2 by sunlight irradiation under ambient conditions with a positive free energy change (equation 4). Photocatalytic H_2O_2 generation is therefore a potentially promising new candidate for artificial photosynthesis:

$$H_2O \rightleftharpoons H_2 + \tfrac{1}{2} O_2 \quad (\Delta G = +237 \text{ kJ mol}^{-1}) \quad (1)$$

$$H_2O \rightleftharpoons 1/2O_2 + 2H^+ + 2e^- \ (+1.23 \text{ V vs NHE, pH 0}) \quad (2)$$

$$O_2 + 2H^+ + 2e^- \rightleftharpoons H_2O_2 \ (+0.68 \text{ V vs NHE, pH 0}) \quad (3)$$

$$H_2O + 1/2O_2 \xrightleftharpoons{h\nu} H_2O_2 \ (\Delta G = +116 \text{ kJ mol}^{-1}) \quad (4)$$

Scheme 1: Mechanism of Hydrogen peroxide production

Several inorganic powder catalysts have been proposed but have been found to generate only small amounts of H_2O_2 (<0.4mM)[12-16]. This is because (1) they exhibit low activity for water oxidation (equation 2), (2) they exhibit low selectivity for two-electron reduction of O_2 (equation 3) due to one- or four-electron reductions and (3) they subsequently decompose the formed H_2O_2 by disproportionation or oxidation by the VB h^+ on the metal or semiconductor surface (equation 3). In contrast, the current research has revealed that metal-free polymeric semiconductors based on graphitic carbon nitride (g-C_3N_4)[17] produce H_2O_2 with much higher efficiency (>2mM)[18–21], with a pyromellitic-diimide-doped g-C_3N_4 hybridized with reduced graphene oxide (g-C_3N_4/PDI-rGO) exhibiting the highest efficiency[20]. The catalyst is photo excited by visible light (λ450nm), although several modifications have been studied[22]. Creating new low-bandgap semiconductors that can efficiently promote water oxidation and O_2 reduction with longer-wavelength light is necessary for artificial photosynthesis of H_2O_2.

Earlier, authors reported that resorcinol−formaldehyde (RF) resins,[23] which have been used as insulators for a quarter of a century,[24–25] become n-type semiconductors when prepared under high-temperature hydrothermal conditions and exhibit high activities in the photocatalytic generation of H_2O_2.[27] This synthesis route produces methylene-linked resin powders comprising the quinoid forms of resorcinol, which are π-conjugated with the inherent benzenoid forms of resorcinol via methine bridges.[28] As shown in Figure 1a, this resin consists of benzenoid−quinoid π-conjugated donor−acceptor (D−A) units linked by non-π-conjugated (insulated) methylene linkers. These D−A interactions create small highest molecular orbital−lowest unoccupied molecular orbital (HOMO−LUMO) gaps. The π-stacking of the D−A units (Figure 1b) hybridizes their energy levels and create a semiconducting band (Figure 1e) with a low bandgap energy (Ebg= 1.69 eV). The resins absorb long-wavelength light up to ~800 nm and efficiently promote the oxidation of water and reduction of O2 while being less active in decomposing the produced H_2O_2. The resins irradiated by simulated sunlight in water under O_2 atmosphere.

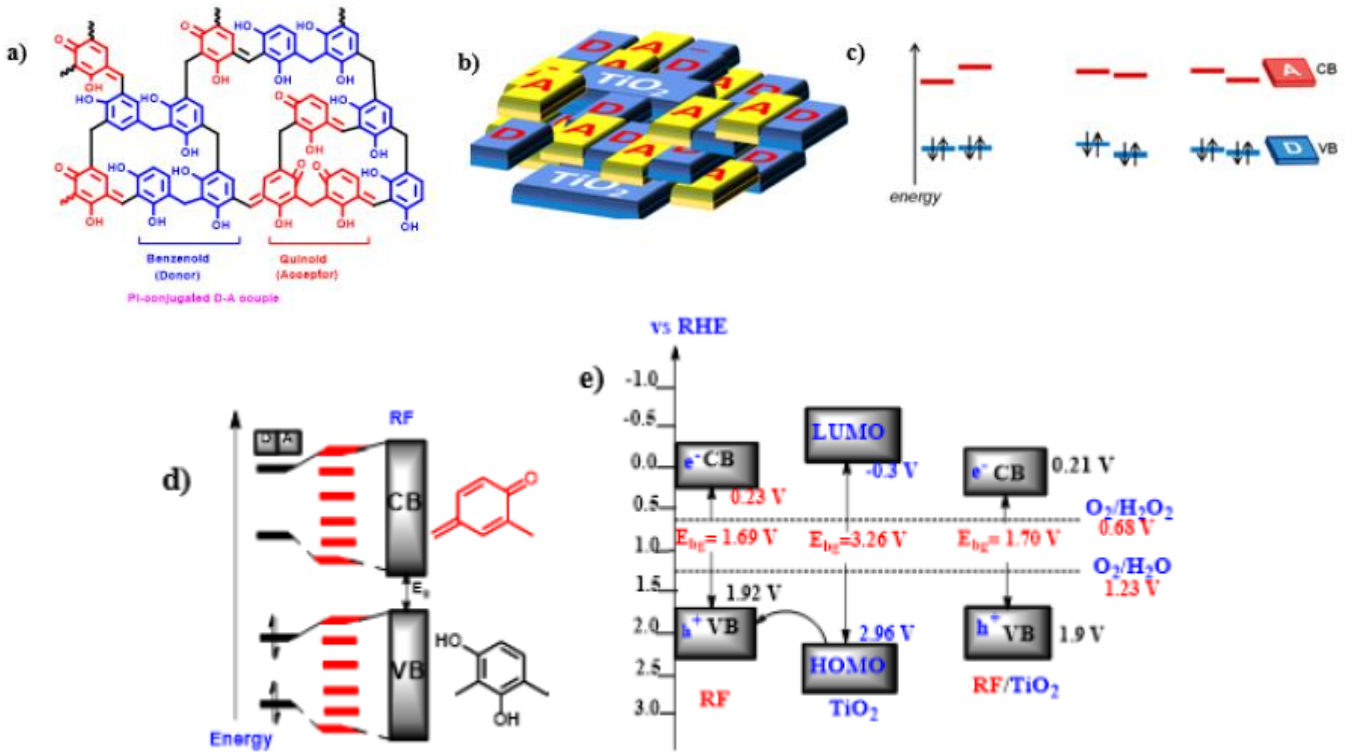

Figure 1: Physical and electronic structure of the materials. (a) Cross-linking structure of the RF resins; (b) Electronic band structure of the undoped RF resins; (c) Architecture of the TO2-doped RF resins; (d) and (e) Electronic band structure of π-conjugated D-A couples.

Structure and synthesis of Resin

Resorcinol–formaldehyde (RF) resins are inexpensive cross-linked polymers, first synthesized by Pekala in 1989[29] with a simple base-catalysed polycondensation of resorcinol with formaldehyde by low-temperature hydrothermal synthesis (200 °C). In this study, high-temperature hydrothermal synthesis at ~200 °C creates RF resins that behave as highly active D–A polymer photo catalysts. This synthesis produces methylene-crosslinked RF resins consisting of quinoid forms of resorcinol, each of which is π-conjugated with inherent benzenoid forms of resorcinol (Fig. 1a). With π-stacking of the benzenoid–quinoid D–A couples (Fig. 1e) low-bandgap (~1.69 eV) semiconductors are created that are capable of promoting water oxidation and O_2 reduction.

2. MATERIALS AND METHODS

2.1 Materials Used

Commercially available cheap chemicals resorcinol, 37 % formaldehyde, titanium (IV) oxide, oxalic acid dihydrate were purchased and used for experiments without any further purification. Various solvents of 99% purity were also used; namely, acetone, ethanol, isopropanol, and methanol for this study. Instruments used for characterization and the detailed studies were:

- ✓ UV-Vis-NIR spectrophotometer (Make: Perkin Elmer, Model: UV -2450)
- ✓ Dynamic Light Scattering (Make: MALVERN INSTRUMENTS LTD. Model: Zetasizer Nano ZS)
- ✓ Fourier Transform Infrared Spectrometer (Make: Agilent Technologies, Model: L1600312 spectrum TWOLITA/ZnSe)

- ✓ Electrochemical Analyzer (Make: Sherwood Scientific 1The Paddocks, Model: MK1 MSB, (220V, 50Hz))
- ✓ Thermo Gravimetric Analyzer coupled with Differential Scanning Calorimetry (Make: NETZSCH Geratebau GmbH. Model: STA 449 F1 Jupiter)
- ✓ Thermogravimetric analysis (Make: Perkin Elmer Model: Pyris 1)
- ✓ Nuclear Magnetic Resonance Spectrometer (PECX 500MHz Jeol)
- ✓ Powder X ray diffractometer (Smart Lab Rigaku)
- ✓ High-resolution mass spectrometer (Impact HD Bruker)
- ✓ Field emission scanning electron microscopy (Nova Nano SEM 450 FEI)
- ✓ BET surface area measuring unit (Autosorb iQ3 Quanta chrome Instrument).
- ✓ X-ray photoelectron spectroscopy

2.2 Methods

The RF/TiO_2-X resins were prepared by an acid-catalyzed high-temperature hydrothermal approach.[28] Resorcinol, formaldehyde, and $(COOH)_2$ were added to water (20:40:1 molar ratio), and the desired amount of the commercially available TiO_2 was added to the solution [x (wt %) = TiO2/resorcinol × 100; x = 0.4−4.8]. The resulting solution was then subjected to hydrothermal reaction at 200 °C for 12 h. Thereafter, 24 h Soxhlet extraction of the obtained solids with acetone and subsequent drying produced the RF/TiO_2-x resin powders. The overall schematic experimental design is shown in Figure 2.

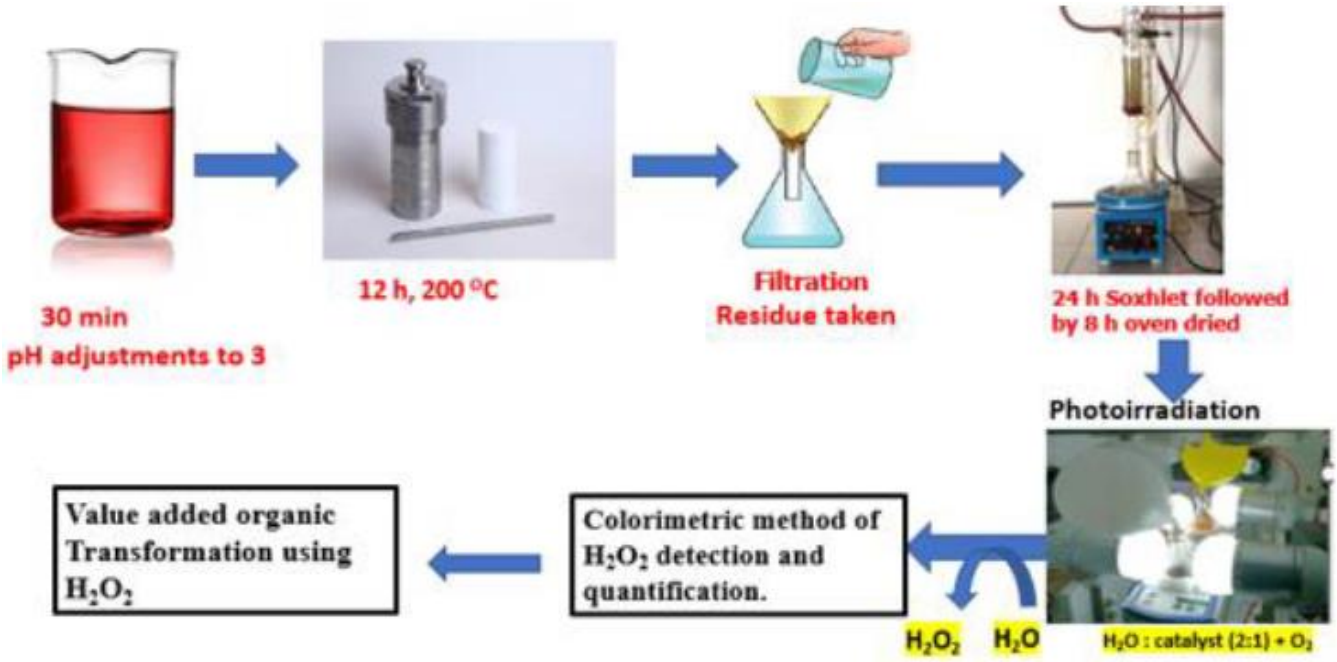

Figure 2: The overall design of experiment and synthetic scheme (catalysis and post catalysis)

Photocatalytic Reaction. Catalyst (40 mg) was added to water (20 mL) in a glass bottle (φ 35 mm; capacity, 50 mL), which was sealed with a rubber cap. After bubbling O_2 through the mixture for 15 min, the bottle was photoirradiation at λ > 420 nm using visible light two bulbs (40 W each) with a constant magnetic stirring. A series of TiO_2 doped RF (0.4, 0.8, 1.2, 2.4, 3.6 and 4.8) was prepared and subjected to photoirradiation for 5 h and each time triplicates of aliquots each 300 µL were collected and centrifuged to recover the catalyst for next round reaction. H_2O_2 was detected and quantified by colorimetric detection method. 200 µL of the aliquot collected was titrated with 400 µL of 0.1 M potassium hydrogen phthalate (KHP) and 400 µL of 0.4 M Potassium Iodide (KI).

Then UV-Vis reading was done and a peak observed at a wavelength 350 nm is characteristic peak of H_2O_2. Finally, the solar-to-chemical efficiency and other concentration calculations were performed based on the absorbance obtained from the UV-Vis spectra.

Analysis. Electrochemical analysis was performed with a Pt wire and Ag/AgCl electrode as the counter and reference electrodes, respectively. The working electrodes were composed of FTO.[28] All potential values were expressed with respect to the RHE using the following equations:

$$E \text{ (vs RHE)} = E \text{ (vs Ag/AgCl} + E_{Ag/AgCl}) + 0.0591 \text{ V x pH}$$

(E_{AgCl} = 0.1976 V vs NHE at 25 °C)

3. RESULTS AND DISCUSSION

All prepared RF/TiO_2-x resins were red-black powders similar to the undoped RF (Figure 3). Scanning electron microscopy (SEM) observations of RF/TiO_2-1.2 (Figure q,r) exhibited spherical particles size of 20 μm before and after catalysis, as also compared to original RF. These data demonstrated that the morphology and performance of the RF resin did not change during the photoreaction, thereby promoting stable H_2O_2 generation. N_2 adsorption/desorption analysis of RF/TiO_2-1.2 (Figure 3d) showed a type III isotherm, indicating a nonporous character, and its specific surface area (20.41 m^2g^{-1}) was similar to that of RF (20.39 m^2g^{-1}). These findings suggest that the high-temperature hydrothermal synthesis of RF resin in the presence of 1.2 wt % TiO_2 produces spherical nonporous particles that are slightly larger in size than the original RF resin.

The undoped RF resin were synthesize at four different hydrothermal temperatures 150 °C, 200 °C, 250 °C and 300 °C. The photocatalytic solar-to-chemical H_2O_2 conversion was studied for the four resins; RF which was synthesized at 200 °C was showing better activity. The TiO_2 doping was then done based on this temperature and photocatalytic studies were carried out intensively. The resins are thermally stable up to 400 °C as shown in Figure 3 c (Thermal gravimetric analysis).

The photocatalytic reactions were then conducted under visible-light irradiation (λ > 420 nm) of the resin catalysts suspended in pure water using a white bulb. As shown in Figure 4 c, d, f, g, h and I, which indicate the amount of H_2O_2 produced after 5 h photo irradiation with magnetic stirring under an O_2 atmosphere at 298 K. The resin activity increases with an increase in the amount of TiO_2 until x = 1.2, beyond which point (i.e., x = 2.4, 3.6, and 4.8) it shows decreased activities, thereby indicating that an optimal TiO_2 doping is required to maximize the activity for photocatalytic generation of H_2O_2.

Powder X-ray diffraction (XRD) analysis of RF (Figure 3 I, j, k, l, m,) showed a broad peak at 2θ = ∼23° (d = ∼3.9 Å) assigned to the π-stacked aromatics; the RF/TiO_2-1.2 resin exhibited a peak at an identical position, indicating that the π-stacking distances of the D−A units are unaffected by TiO_2 doping. These data indicate that methylene-and methine bridged RF resins with similar cross-linking degrees, carbon compositions, numbers of D and A units, and π-stacking distances are produced even in the presence of TiO_2. Additional peak appearing at around 2θ = ∼28° revealed the presence of TiO_2. After one-time photocatalytic reaction, the intensity of the peak diminishes slightly but its 2θ value does not shift. It still remains amorphous nearly equal intensity as shown in Figure 3 a-c.

Diffuse-reflectance ultraviolet−visible (DR UV−vis) spectroscopic examinations of RF/TiO_2-x (Figure 3 e) showed absorption bands extending to 800 nm, which are similar to those of RF and are related to the π-conjugated and π-stacked D−A units. The increased absorbance at 600−750 nm for RF/TiO_2-1.2% may originate from the TiO_2 component. In addition, the Ebg values of both RF and RF/TiO_2 calculated by the Tauc plots (Figure 3 f) are similar (1.69 eV and 1.9 eV, respectively). The obtained flat band potential and Ebg provided the electronic band

structure of RF/ TiO_2 (Figure 1 e), which is comparable to that of RF where the CB bottom [+0.21 V vs reversible hydrogen electrode (RHE)] and VB top (+1.90 V vs RHE) are sufficient to permit the reduction of O_2 (+0.68 V, eq 3) and oxidation of water (+1.23 V, eq 2). These findings suggest that the band structure of the resin is unaffected by TiO_2 doping.

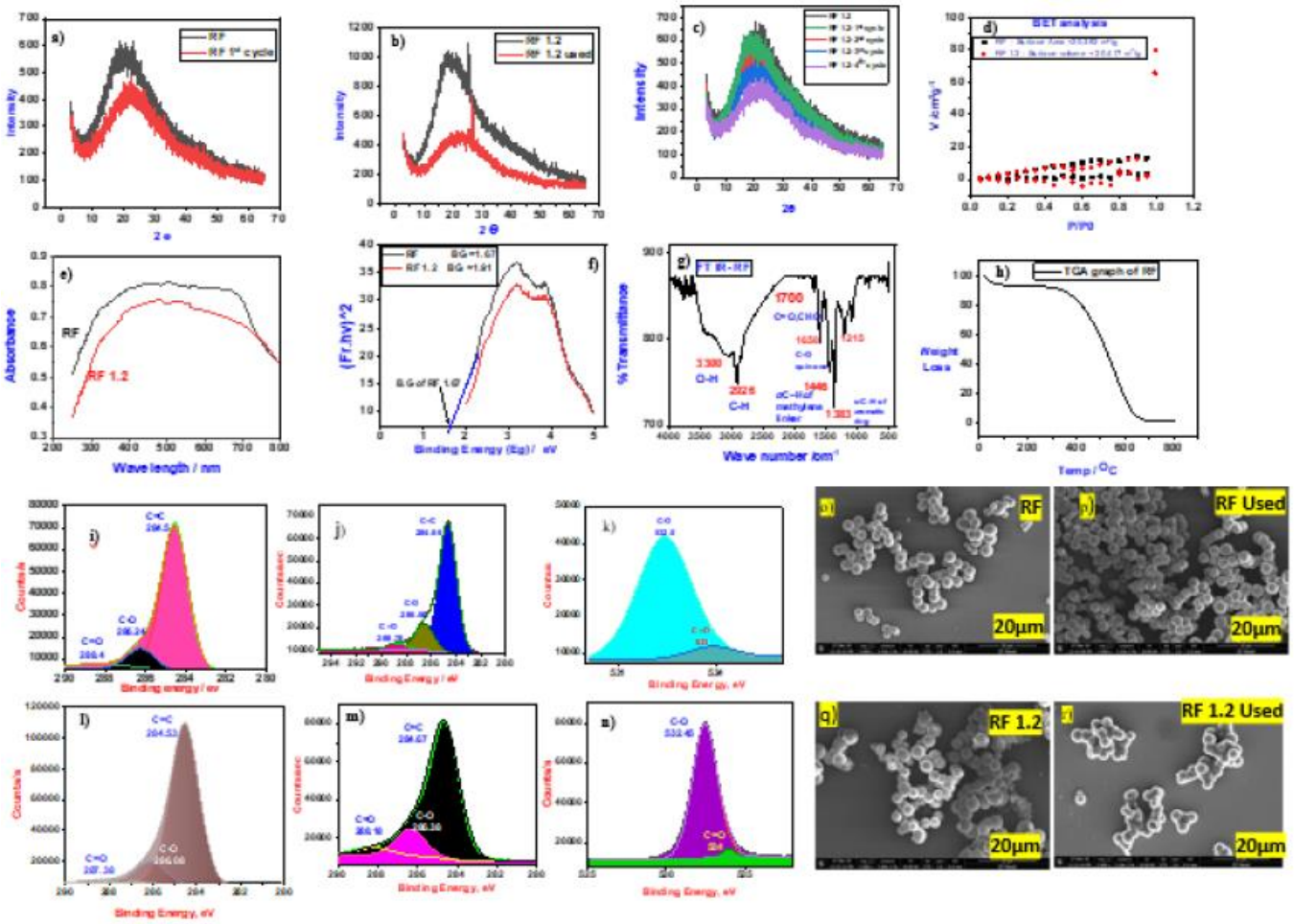

Figure 3: (a-c) XRD patterns of the resins; (d) N_2 adsorption/desorption isotherms of the resins; (e) DRs UV-Vis absorption spectra; (f) Tauc plot for band gap; (g) FT IR spectra of the resin; (h) TGA of the resin; (i, j, l,m) XPS charts (C 1s level) of the resins; (k, n) XPS charts (O 1s level) of the resins; (o-r) SEM images of RF and RF/TiO_2-1.2 before and after photoreaction

In addition to the aforementioned evidences from band structure for the activity enhancement of TiO_2 doped RF, the photoirradiation of RF/TiO_2 increases the signal intensity, suggesting that its photoexcitation generates h^+–e^- pairs. As shown in Figure 4 b, the photocurrent responses of the resins measured on a fluorine tin oxide (FTO) electrode revealed that the current density of RF/TiO_2-1.2 is larger than that of RF, indicative of enhanced h^+–e^- separation. This is supported by the electrochemical impedance spectra (EIS) of the resins obtained under photoirradiation (Figure 4 a), wherein the Nyquist plots showed that RF/TiO_2-1.2 exhibited a lower CT resistance (RCT) than RF. These data support the assumption that the enhanced e^- conductivity resulting from TiO_2 doping promotes efficient h^+–e^- separation, thereby enhancing the photocatalytic activity.

As shown in Figure 4 k, l, the rate of H_2O_2 formation on RF/TiO_2-1.2 was higher than that on RF, again confirming the doping effect of TiO_2. We can observe that the high initial formation rate becomes constant after

prolonged irradiation (~3 h), as in the case of RF. Importantly, this SCC efficiency is higher than that obtained for RF and is the highest value reported for previous powder catalysts used in artificial photosynthesis reactions.1−8 These results thus indicate that the present doped catalyst exhibits a very high activity for solar-to-chemical energy conversion.

Fourier-transformed IR charts of the resins (structure given Figure 1 a) in (a) 1000–4000 cm^{-1} and (b) 1000–1800 cm–1 regions. Peak assignments: 3300 cm^{-1} (*ν*O–H of resorcinol or methylol), 2926 cm^{-1} (νC–H of methylene linker), 1700 cm^{-1} (νC=O of –CHO residue), 1650 cm^{-1} (νC=O of quinone), 1620 cm^{-1} (νC=C of aromatic ring), 1490, 1450 cm^{-1} (σC–H of methylene linker), 1370, 1300 cm^{-1} (σC–H of aromatic ring), 1240, 1100 cm^{-1} (νC–O of resorcinol and methylol). The X-ray photoelectron spectroscopy (XPS) analyses of the resins at the C 1s (Figure 3 i, j, l, m) and O 1s levels (Figure 3 k, n) confirmed the presence of C–O and C=O bonds. The SCC efficiency was determined using the following equation[27]:

$$SCC\ effeciency\ (\%) = \frac{[\Delta G\ for\ H_2O_2\ generation\ (Jmol^{-1})] * [Amount\ of\ H_2O_2\ formed\ (mol) * 100}{[Total\ input\ energy\ (W)] * [Reaction\ time\ (s)]}$$

The free energy for H_2O_2 generation is 117 kJ mol^{-1} (Eq. 4); while the total input energy was 0.314 W[30].

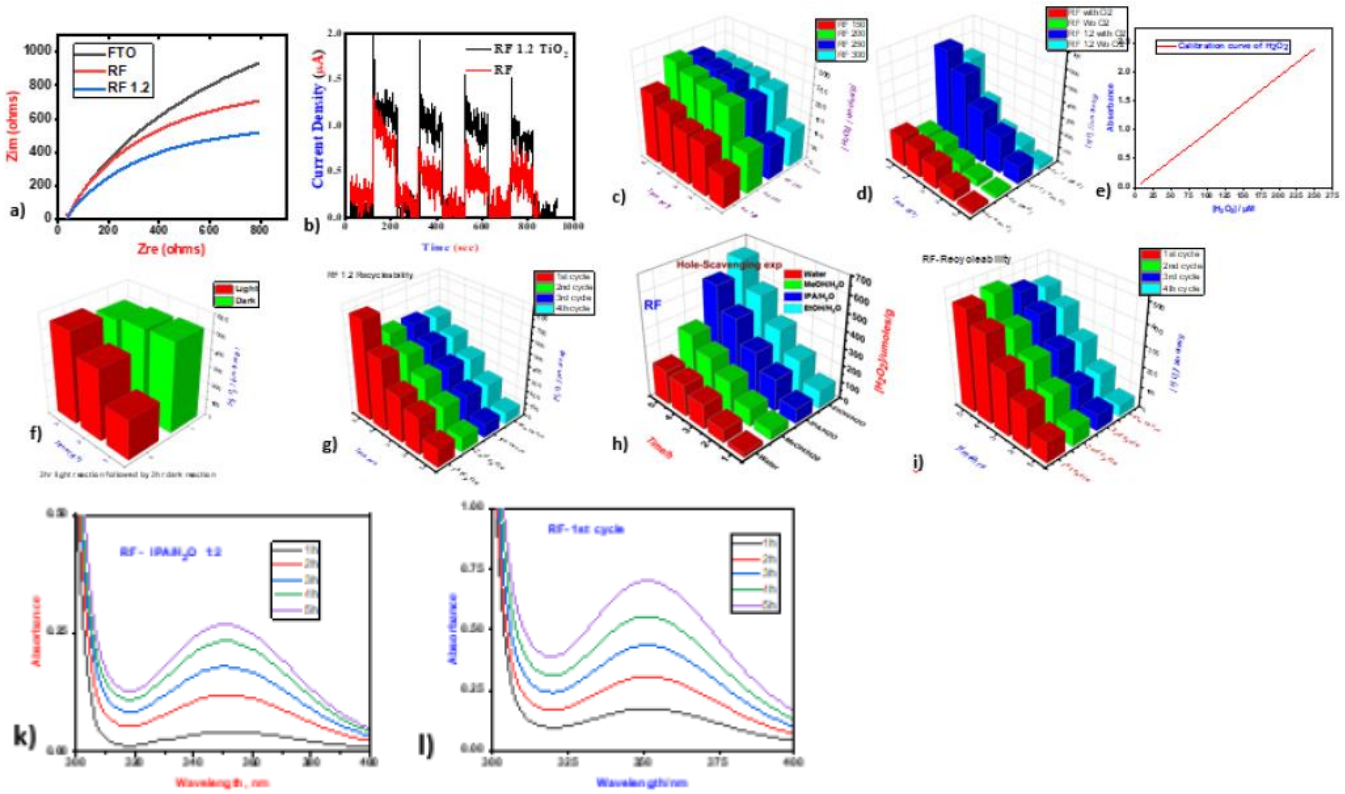

Figure 4: (a) Electron impedance spectroscopy (Nyquist plot); (b) Photocurrent study of the resins; (c) H_2O_2 conversion efficiency made at d/t temperature; (d) O_2 dependent study of resins for H_2O_2 conversion; (e) Calibration curve of H_2O_2; (f) Light and dark reaction; (g,l) Recyclability of catalysts; (h) 5 h hole-scavenging study; (k,l) UV-vis spectra of H2O2 after 5 h photoirradiation

The resins are four times recyclable without losing its activity and morphology as depicted in Figure 4 g, j. Another study indicated the efficiency of RF and RF/TiO_2-1.2. is enhanced in proton donor alcohols like isopropyl

alcohol, methanol and ethanol as hole-scavenging agents. Scavenger to water ratio is taken in 1:2 ratio. The order of H_2O_2 conversion efficiency as shown in Figure 4 h is $EtOH/H_2O > IPA/H_2O > MeOH/H_2O > H_2O$.

Mechanism of polycondensation of RF resin

The acid-catalysed condensation (Scheme 2) is triggered by the protonation of formaldehyde, which promotes the hydroxymethylation of resorcinol. The protonation of the methylols and the subsequent dehydration produce benzyl carbonium ions, which react with methylols, leading to the formation of methylene linkers. In this case, slow hydroxymethylation produces a smaller number of few-substituted methylols and benzyl carbonium ions, thus resulting in the formation of lower-degree-crosslinked resins28. In addition, the high-temperature hydrothermal process promotes the deprotonation of the benzyl carbonium ions, which results in quinone methides, leading to the formation of quinoid units. These reactions create a lower-degree-crosslinked D–A architecture.

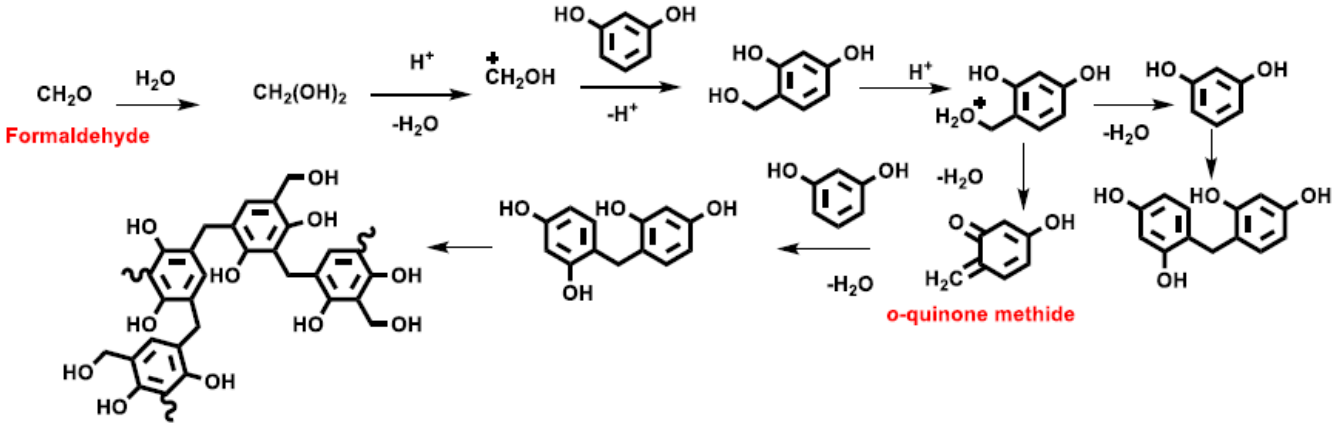

Scheme 2: Mechanism of acid-promoted polycondensation of resorcinol-formaldehyde resins

Post Catalytic Organic Transformation (Value Added Products)

A) General Procedure for Sulfoxidation of Sulfides[31]:

A 10 mL flask was charged with 100 µL (8.0 mmol) of aqueous solution of H_2O_2, and 2 mmol sulfide. Acetonitrile (3 mL) was added as solvent to increase solubility of sulphide. 50 mg Aluminium oxide was added. The reaction mixture initially added on ice bath the stirred at room temperature for 3 h. The progress of the reaction was followed by TLC. After complete disappearance of the reactant, the excess amount of H_2O_2 was destroyed by the addition of saturated aqueous solution of Na_2SO_3 to the reaction mixture. The product was extracted with EtOAc which was separated and dried over anhydrous Na_2SO_4. Evaporation of the solvent under diminished pressure resulted in almost pure product.[31]

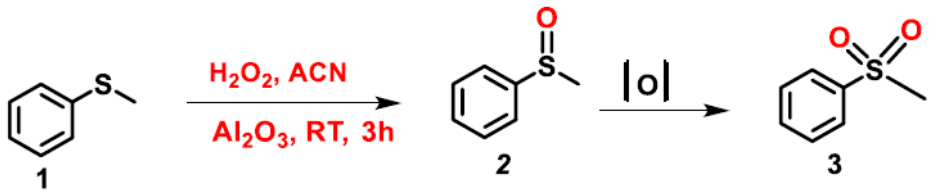

Scheme 3: Insitu Sulfoxidation of organic methyl phenyl sulphide to corresponding sulphides and sulfoxides

^{1}H NMR and ^{13}C NMR of compound 3 [31, 32]

Methyl phenyl sulfone (compound 3). [31] ^{1}H NMR (500 MHz, $CDCl_3$, δ): 7.95-7.87 (*m*, 2H), 7.71-7.61 (*m*, 2H), 7.59-7.52 (*m*, 1H), 3.02 (*s*, 3H); ^{13}C NMR (500 MHz, CDCl3, δ): 137.44, 133.21, 128.54, 126.23, 44.88;

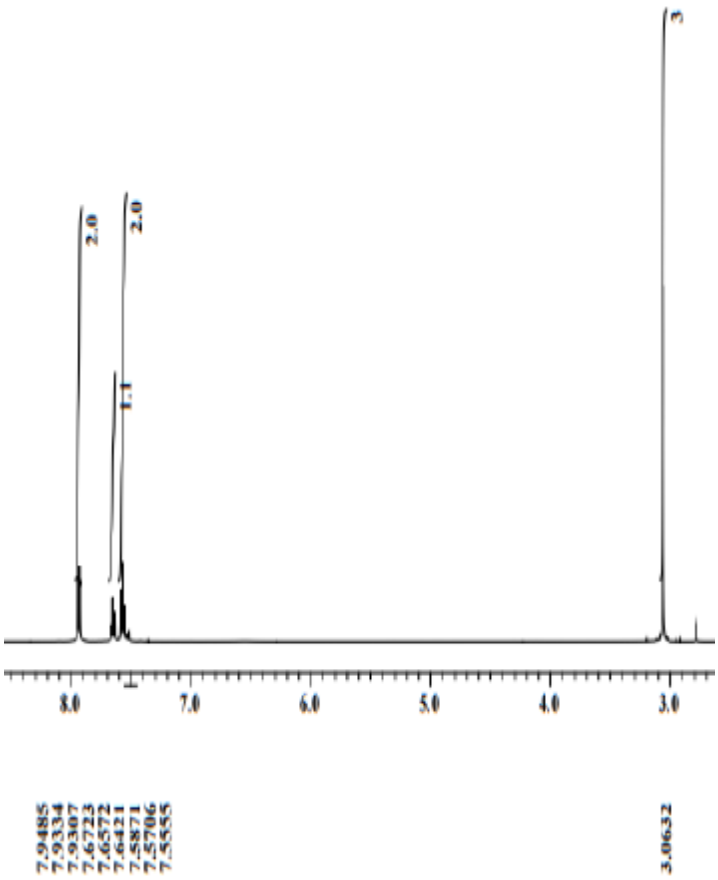

Figure 5: ^{1}H NMR of methyl phenyl sulphone (3)

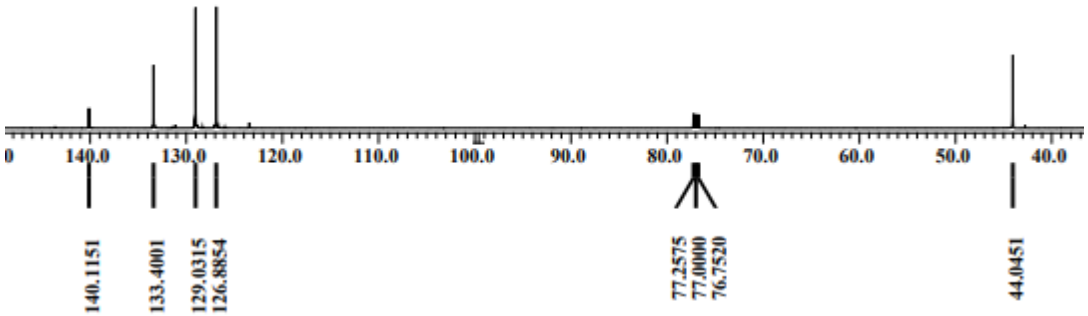

Figure 6: ^{13}C NMR of methyl phenyl sulphone (3)

B) Insitu Baeyer-Villiger oxidation of ketone (4) to Ester (5)

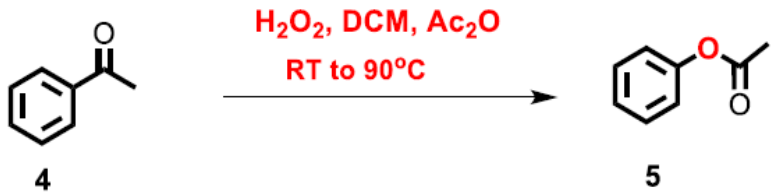

General Procedure for Insitu Oxidation of Methyl Phenyl Ketone (4):

Hydrogen peroxide (H_2O_2) (8 mmol) which was collected from the reaction medium of volume 60 mL which is expected to produce 2.1 mM H_2O_2 is subjected to undergo oxidation reaction *insitu* with acyclic ketones (2 mmol) at RT (25 ^oC). Slowly acetic anhydride was added dropwise at RT. After the addition of all the necessary reagents the reaction temperature was increased gradually to 90 ^oC and maintained at this temperature for 18 h. The resulting reaction mixture was cooled to RT and organic layer was extracted with ethyl acetate and the trace amount of acetic acid formed is evaporated in Rota vapor. The progress of the reaction was followed by TLC. After complete disappearance of the reactant, the excess amount of H_2O_2 was destroyed by the addition of saturated aqueous solution of Na_2SO_3 to the reaction mixture. The product was extracted with EtOAc which was separated and dried over anhydrous Na_2SO_4. Evaporation of the solvent under diminished pressure resulted in almost pure product.

The resulting organic compound was characterized using ^1H- and ^{13}C- NMR. The yield was very low (approx. 17%) because the amount of H_2O_2 obtained from oxidation water is very dilute.[33]

^1H and ^{13}C NMR analysis of phenyl ethanoate (compound 5)[31]

^1H NMR (500 MHz, $CDCl_3$, δ): 7.96-7.95 (*m*, 2H), 7.47-7.44 (*m*, 2H), 7.57-7.54 (*m*, 1H), 2.6 (*s*, 3H);

^{13}C NMR (500 MHz, $CDCl^3$, δ): 199, 136, 133, 128.8, 128.54, 26.

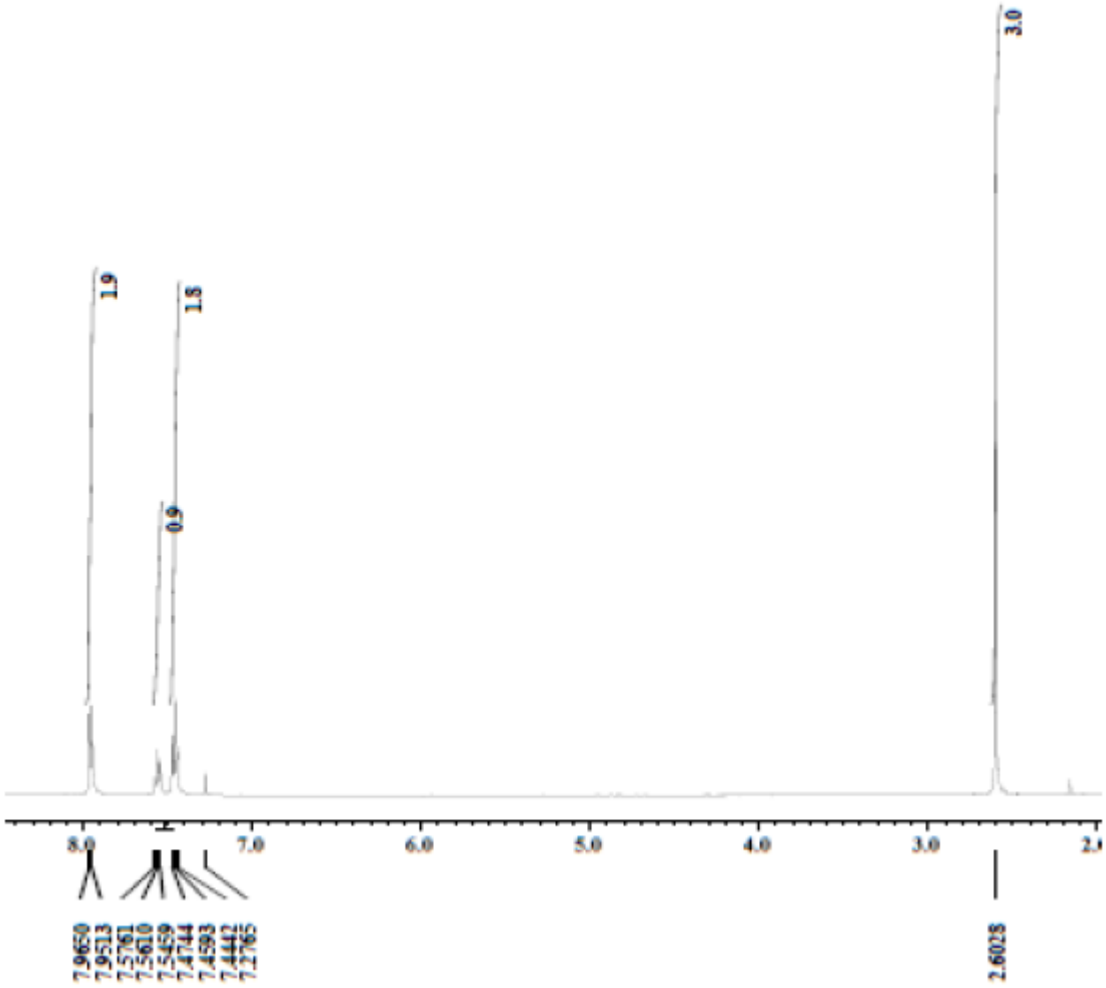

Figure 7: ^1H NMR of Phenyl ethanoate (5)

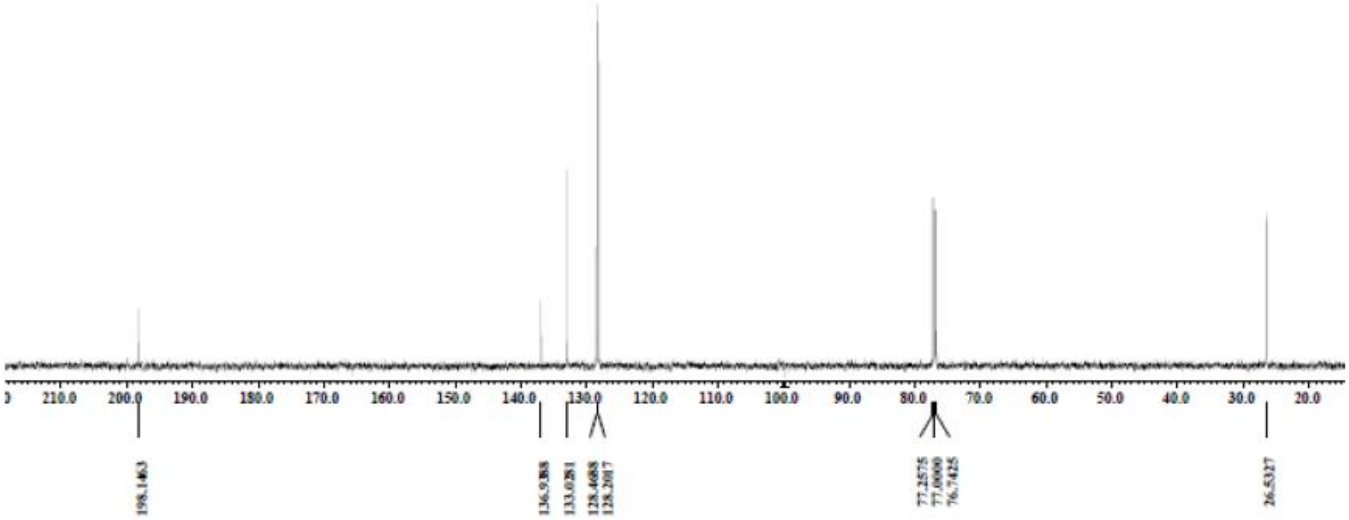

Figure 8: ^{13}C NMR of phenyl ethanoate (5)

4. CONCLUSION

The preparation of low-Ebg resins using readily available and inexpensive reagents may open a new route for H_2O_2 generation. The Synthesis of RF at lower pH (<4) results in lower cross-linked RF resins with a strong Pi-stacked benzenoid-quinoid D-A architecture, this in turn results in highly conductive, lower band gap (1.7 eV) that is efficiently promote water oxidation and O_2 reduction under visible light irradiation. The photoirradiation of RF/TiO_2-1.2 in water and ethanol or 2-propanol as an electron donor for 5 h under O_2 produced higher amount of H_2O_2 as compared to pure water. This clearly indicates water oxidation is the rate-determining step for H_2O_2 production. We synthesized RF doped with TiO_2 in %w/w= 0.4, 0.8, 1.2, 2.4, 3.6 and 4.8. Our material exhibited the highest activity till TiO_2 1.2 w/w%, after this optimum TiO_2 doping activity decreases. The high activity seen immediately after photoirradiation is because the photo formed VB h^+ is consumed not only by the water oxidation but also by self-oxidation of the resin. Post-catalytic Sulfoxidation and Baeyer-Villiger oxidation were also successful giving from low to medium percentage yield 20% conversion. Generally, we are able to convert thermodynamically non-spontaneous reaction water to liquid solar fuel hydrogen peroxide. Besides this achievement we proved the formation of hydrogen peroxide by performing organic transformation using H_2O_2 as oxidant.

ACKNOWLEDGMENTS

I would like thank Ministry of Education of India (MoE) for the fellowship and financial support. My extended thank goes to Advanced Materials research centre (AMRC), IIT Mandi for sophisticated instrument facility and characterization. I would like to thank my supervisors Professor Subrata Ghosh (synthesis of advanced materials group) and Professor Aditi Halder (from Renewable energy groups).

REFERENCES

1. Hisatomi, T., Kubota, J. & Domen, K. Recent advances in semiconductors for photocatalytic and photoelectrochemical water splitting. *Chem. Soc. Rev.* 43, 7520–7535 (**2014**).
2. Jia, J. et al. Solar water splitting by photovoltaic-electrolysis with a solar-to hydrogen efciency over 30%. *Nat. Commun*. 7, 13237 (**2016**).
3. Walter, M. G. et al. Solar water splitting cells. *Chem. Rev.* 110, 6446–6473 (**2010**).
4. Kudo, A. & Miseki, Y. Heterogeneous photocatalyst materials for water splitting. *Chem. Soc. Rev.* 38, 253–278 (**2009**).

5. Maeda, K. et al. Photocatalyst releasing hydrogen from water. *Nature* 440, 295 (**2006**).
6. Kubota, J. & Domen, K. Photocatalytic water splitting using oxynitride and nitride semiconductor powders for production of solar hydrogen. *Electrochem. Soc. Interface* 22, 57–62 (**2013**).
7. Sasaki, Y., Nemoto, H., Saito, K. & Kudo, A. Solar water splitting using powdered photocatalysts driven by Z-schematic interparticle electron transfer without an electron mediator. *J. Phys. Chem.* C 113, 17536–17542 (**2009**).
8. Reijnders, L. & Huijbregts, M. Biofuels for Road Transport: A Seed to Wheel Perspective (Springer, **2009**).
9. Wang, Q. et al. Scalable water splitting on particulate photocatalyst sheets with a solar-to-hydrogen energy conversion efficiency exceeding 1%. *Nat. Mater.* 15, 611–615 (**2016**).
10. Fukuzumi, S. Production of Liquid solar fuels and their use in fuel cells. *Fuel Cells.* Joule 1, 689–738 (**2017**).
11. Fukuzumi, S., Lee, Y. M. & Nam, W. Solar-driven production of hydrogen peroxide from water and dioxygen. *Chem. Eur. J.* 24, 5016–5031 (**2018**).
12. Teranishi, M., Naya, S. & Tada, H. In situ liquid phase synthesis of hydrogen peroxide from molecular oxygen using gold nanoparticle-loaded titanium (iv) dioxide photocatalyst. *J. Am. Chem. Soc.* 132, 7850–7851 (**2010**).
13. Kato, S., Jung, J., Suenobu, T. & Fukuzumi, S. Production of hydrogen peroxide as a sustainable solar fuel from water and dioxygen. *Energy Environ. Sci.* 6, 3756–3764 (**2013**).
14. Moon, G.-H. et al. Solar production of H2O2 on reduced graphene oxide–TiO2 hybrid photocatalysts consisting of earth-abundant elements only. *Energy Environ. Sci.* 7, 4023–4028 (**2014**).
15. Kaynan, N., Berke, B. A., Hazut, O. & Yerushalmi, R. Photocatalytic production of hydrogen peroxide from water and molecular oxygen. *J. Mater. Chem. A* 2, 13822–13826 (**2014**).
16. Kim, H., Kwon, O. S., Kim, S., Choi, W. & Kim, J.-H. Harnessing low energy photons (635nm) for the production of H2O2 using up conversion nanohybrid photocatalysts. *Energy Environ. Sci.* 9, 1063–1073 (**2016**).
17. Wang, X. et al. A metal-free polymeric photocatalyst for hydrogen production from water under visible light. *Nat. Mater.* 8, 76–80 (**2009**).
18. Shiraishi, Y. et al. Sunlight-driven hydrogen peroxide production from water and molecular oxygen by metal-free photocatalysts. *Angew. Chem. Int. Ed.* 53, 13454–13459 (**2014**).
19. Kofuji, Y. et al. Graphitic carbon nitride doped with biphenyl diimide: efficient photocatalyst for hydrogen peroxide production from water and molecular oxygen by sunlight. *ACS Catal.* 6, 7021–7029 (**2016**).
20. Kofuji, Y. et al. Carbon nitride–aromatic diimide–graphene nanohybrids: metal-free photocatalysts for solar-to-hydrogen peroxide energy conversion with 0.2% efficiency. *J. Am. Chem. Soc.* 138, 10019–10025 (**2016**).
21. Kofuji, Y. et al. Mellitic triimide-doped carbon nitride as sunlight-driven photocatalysts for hydrogen peroxide production. *ACS Sustain. Chem. Eng.* 5, 6478–6485 (**2017**).
22. Ong, W. J., Tan, L. L., Ng, Y. H., Yong, S. T. & Chai, S. P. Graphitic carbon nitride (g-C3N4)-based photocatalysts for artificial photosynthesis and environmental remediation: are we a step closer to achieving sustainability? *Chem. Rev.* 116, 7159–7329 (**2016**).
23. Pekala, R. W. Organic aerogels from the polycondensation of resorcinol with formaldehyde. *J. Mater. Sci.* **1989**, 24, 3221−3227.
24. Al-Muhtaseb, S. A.; Ritter, J. A. Preparation and properties of resorcinol-formaldehyde organic and carbon gels. *Adv. Mater.* **2003**, 15, 101−114.
25. ElKhatat, A. M.; Al-Muhtaseb, S. A. Advances in Tailoring Resorcinol-Formaldehyde Organic and Carbon Gels. **Adv. Mater. 2011**, 23, 2887−2903.
26. Durairaj, R. B. Resorcinol, Chemistry, Technology and Applications; Springer-Verlag Berlin Heidelberg: New York, **2005.**
27. Shiraishi, Y.; Takii, T.; Hagi, T.; Mori, S.; Kofuji, Y.; Kitagawa, Y.; Tanaka, S.; Ichikawa, S.; Hirai, T. Resorcinol-Formaldehyde Resins as Metal-Free Semiconductor Photocatalysts for Solar-to-Hydrogen Peroxide Energy Conversion. *Nat. Mater.* **2019**, 18, 985− 993.
28. Shiraishi, Y.; Hagi, T.; Matsumoto, M.; Tanaka, S.; Ichikawa, S.; Hirai, T. Solar-to-hydrogen peroxide energy conversion on resorcinol−formaldehyde resin photocatalysts prepared by acid-catalysed polycondensation. *Commun. Chem.* **2020**, 3, 169.
29. Seabold, J. A.; Choi, K. S. Efficient and stable photo-oxidation of water by a bismuth vanadate photoanode coupled with an iron oxyhydroxide oxygen evolution catalyst. *J. Am. Chem. Soc.* **2012**, 134, 2186−2192.
30. Li, T., Cao, M., Liang, J., Xie, X. & Du, G. Mechanism of base-catalyzed resorcinol-formaldehyde and phenol-resorcinol-formaldehyde condensation reactions: A theoretical study. *Polymers* 9, 426 (**2017**).
31. V. G. Shukla, P. D. Salgaonkar, K G. Akamanchi, *J. Org. Chem.* **2003**, 68, 5422.
32. (a) J. J. Boruah, S. P. Das, S. R. Ankireddy, S. R. Gogoi, N. S. Islam, *Green Chem*. **2013**, 15, 2944- 2959. (b) X. Qu, X. Li, Y. Chai, Q. Yang, P. Li, Y. Yao, *Green Chem*., **2013**, 15, 357–361.
33. Ulf Schuchardt., *et.al*, *Journal of Molecular Catalysis A*: chemical volume 287, issues 1-2, **2008**, 41-44.

Non-Thermal Plasma Assisted Fabrication of Ultrathin NiCoOx Nanosheets for High-Performance Supercapacitor

Birhanu Bayissa Gicha[1,2], Lemma Teshome Tufa[3,4], Mahendra Goddati[5], Samira Adhikari[6], Juyoung Gwak[3], Jaebeom Lee[1,5,*]

[1]*Department of Chemistry, Chungnam National University, Daejeon, 34134, Republic of Korea*
[2]*Environmental Science Program, Haramaya University, Dire Dawa, 138, Ethiopia*
[3]*Research Institute of Materials Chemistry, Chungnam National University, Daejeon, 34134, Republic of Korea*
[4]*Department of Applied Chemistry, Adama Science and Technology University, P.O.Box 1888, Adama, Ethiopia*
[5]*Department of Chemical Engineering and Applied Chemistry, Chungnam National University, Daejeon, 34134, Republic of Korea*
[6]*Institute of Quantum Systems, Chungnam National University, Daejeon, 34134, Republic of Korea*
**Corresponding author, e-mail: nanoleelab@gmail.com*

ABSTRACT

Transition metal based layered double hydroxides (TMLDHs) are potential candidates for supercapacitors; however, their structural staking often limits their energy density, one of the major pending obstacles in the sector. Simple, fast, and safe modification strategies such as exfoliation of jammed layers into single sheets can be a viable option to overcome those challenges. This work reports fabrication of ultrathin nanosheets from bulk TMLDHs using superficial non-thermal Ar-plasma exfoliation strategy. Electrochemical characterizations have confirmed that capacitive performance of pristine $NiCoO_x$ nanosheets has improved because of Ar-plasma induced exfoliation. A remarkable 5.7 $F\,cm^{-2}$ areal capacitance was achieved at a current density of 5 $mAcm^{-2}$ for ultrathin Ar-$NiCoO_x$ nanosheets. The material also exhibited excellent cyclic stability with over 88 % capacitance retention after 5000 cycles. The electrode material assembled into symmetric supercapacitor device delivering an energy density of 85.9 $\mu Whcm^{-2}$ at a power density of 500 μWcm^{-2} .The higher super capacitive performance is attributed to increased electrochemical surface area and improved capability of electron and ion transport induced by Ar-plasma exfoliation, demonstrating an opportunity for further use of TMLDHs in the energy conversion and storage sector.

***Key words**: ultrathin nanosheet, supercapacitor, NiCo LDHs, cycle stability, Ar-plasma exfoliation.*

1. INTRODUCTION

Breakthrough advancement of renewable energy-storage technologies are indispensable to curtail the severe environmental disaster stemming from ever-increasing global energy consumption.[1,2] Recently, supercapacitors (SCs) have shown remarkable potential as energy storage device due to their higher power density, short charging time, and excellent rate capablity.[3-5] However, the major pending obstacle pertaining to their low energy density compared to batteries have considerably limited their commercialization in wide-scale energy storage systems.[6] Efforts are poured to enhance the energy storage performance of SCs while maintaining its higher power density through rational design of electrode materials mainly sourcing from transition metals.

As an imminent class of 2D nanomaterial, layered double hydroxides of transition metals (TMLDHs) have drained growing attention as promising electrode materials for SCs.[7,8] TMLDHs are group of anionic lamellar with brucite-like host layers generally represented as $[M_{1-x}^{2+}M_x^{3+}(OH)_2]$-$A_{x/n}^{n-}\cdot mH_2O$, where M^{2+} stands for bivalent metal cations, and M^{3+} stands for trivalent metal cations, A^{n-} is anionic interlayer.[9,10] TMLDHs are exalted for their high catalytic activity, ease of fabrication, and their low cost sourcing from abundant precursors.[11] Their unique lamellar structure endows them with flexibility of the metal cation host layers and tunable interlayer distance resulting with many fascinating electrochemical features.[12] Nevertheless, the application of TMLDHs as electrode materials for SCs is limited mainly due to its poor electrical conductivity and inaccessibility of the active sites because of its jammed layers manifested as poor cycling stability, low specific capacitance, and inferior rate

capability.[13] To address these issues and expand the scope of its application, it is essential to modify jammed layers of TMLDHs to thin nanosheets, enhancing electrochemical surface area for high charge storage.

Numerous modification strategies such as exfoliation and doping have been widely employed to manipulate the structure and composition of TMLDHs to enhance their capacitive performances.[14, 15] In particular, exfoliation is widely used to obtain an ultrathin nanosheet layers exposing more active sites and enhance surface area, creating abundant storage sites for the guest ions to attain higher capacitance.[16] For instance, Quan et al.[17] employed exfoliation technique to restack Ni-Mn LDH and MnO_2 nanosheet composites with improved capacitive performances. The as-synthesized material has demonstrated higher energy density of 16 Wh/Kg at a power density of 15 KW/Kg. Li and co-workers [18] were also able to exfoliate Co-Al LDH and Go into Co-Al LDH-NS/GO-NS with improved electrochemical performance as asymmetric supercapacitor. Nevertheless, conventional exfoliation techniques are not safe, requiring longer treatment time and toxic chemicals.[16] On the other hand, difficulty to remove solvents after exfoliation process due the strong affinity of TMLDHs lead to blockage of active sites, degrading capacitive performance.[19] To overcome these challenges, new exfoliation approaches are desirable. In this regard, plasma-induced exfoliation is highly hailed for its efficiency, timesaving, environmentally friendly, and the final products are free of surfactants minimizing interference.[20]

Based on the above idea, we have employed a facile and safe superficial non-thermal Ar-plasma exfoliation strategy to fabricate an ultrathin NiCo LDHs nanosheets from its counter bulk state. A remarkable areal capacitance of 5.7 F cm^{-2} was achieved at a current density of 5 A cm^{-2} for ultrathin Ar-NiCo nanosheets. The material also exhibited excellent cyclic stability with over 88% capacitance retention after 5000 cycles. Remarkably, the results confirmed that the exfoliation process led to the modifications of morphological and electronic structure, further enhancing the capacitive performance of TMLDHs.

2. MATERIALS AND METHODS

2.1 Material synthesis

NF was first cleaned as reported elsewhere.[1] The NiCo-LDHs nanosheet was synthesized using electrodeposition method. The electrodeposition was carried using a standard three-electrode system from a solution containing $Ni(NiO_3)_2.6H_2O$ and $Co(NO_3)_2.6H_2O$ salts. The electrodeposition was carried at -1.0 V vs. Ag/AgCl for 400 s. Once the deposition was completed, the material was rinsed with DI water and left to dry in air. Finally, the dried sample was treated using non-thermal Ar-plasma of 100 W polarization for a defined period.

2.2 Physical characterization

SEM and TEM images were taken using FE-SEM S-4700, Hitachi, and TEM, JEM-2100F, JEOL Ltd., Tokyo, Japan, respectively. Material composition and surface electronic characterization were done using XPS with K-α XPS (Themo Scientific), XRD data was obtained by Empyrean series-2; PANalytical, Netherlands, and AFM (Veeco diInnova, USA).

2.3 Electrochemical analysis

Electrochemical characterization was performed using an Iviumstat (Eindhoven, Netherlands) workstation at room temperature. Ar-NiCo, NiCo, and NF (1 cm2 in area) were directly used as the working electrode, platinum wire and Ag/AgCl (3M KOH) were used as a counter electrode and reference electrode, respectively. Cyclic voltammetry (CV) curves and galvanostatic charge-discharge tests were carried out using a classical three-electrode configuration. The cyclic voltammetry curves were measured in a potential range between 0.0 and 0.6 V at different scan rates, and the charge/discharge processes were performed by cycling the potential from -0.1 to 0.45 V at different current densities in 3M KOH electrolyte. The cyclic stability was evaluated by cyclic voltammetry

measurements at a current density of 100 mA cm^{-2} for over 5000 cycles. The areal capacitance (F cm^{-2}) of the electrode was calculated according to the following Equation 1.

$$C = \frac{Jt}{\Delta V} \text{ ---------- (1)}$$

where J is the current density (Acm^{-2}), t is discharge time (s), and ΔV (V) is potential window for the cycling test.

3. RESULTS AND DISCUSSIONS

An ultrathin NiCo nanosheets was fabricated using nickel foam (NF) as a support material via electrodeposition method followed by superficial nonthermal Ar-plasma exfoliation strategy (Figure 1a). The morphology and the microstructure of the as-synthesized electrode materials were characterized by scanning electron microscopy (SEM). The entire surface of NF was covered by a vertically grown interconnected nanosheet arrays (Figure 1b, c).

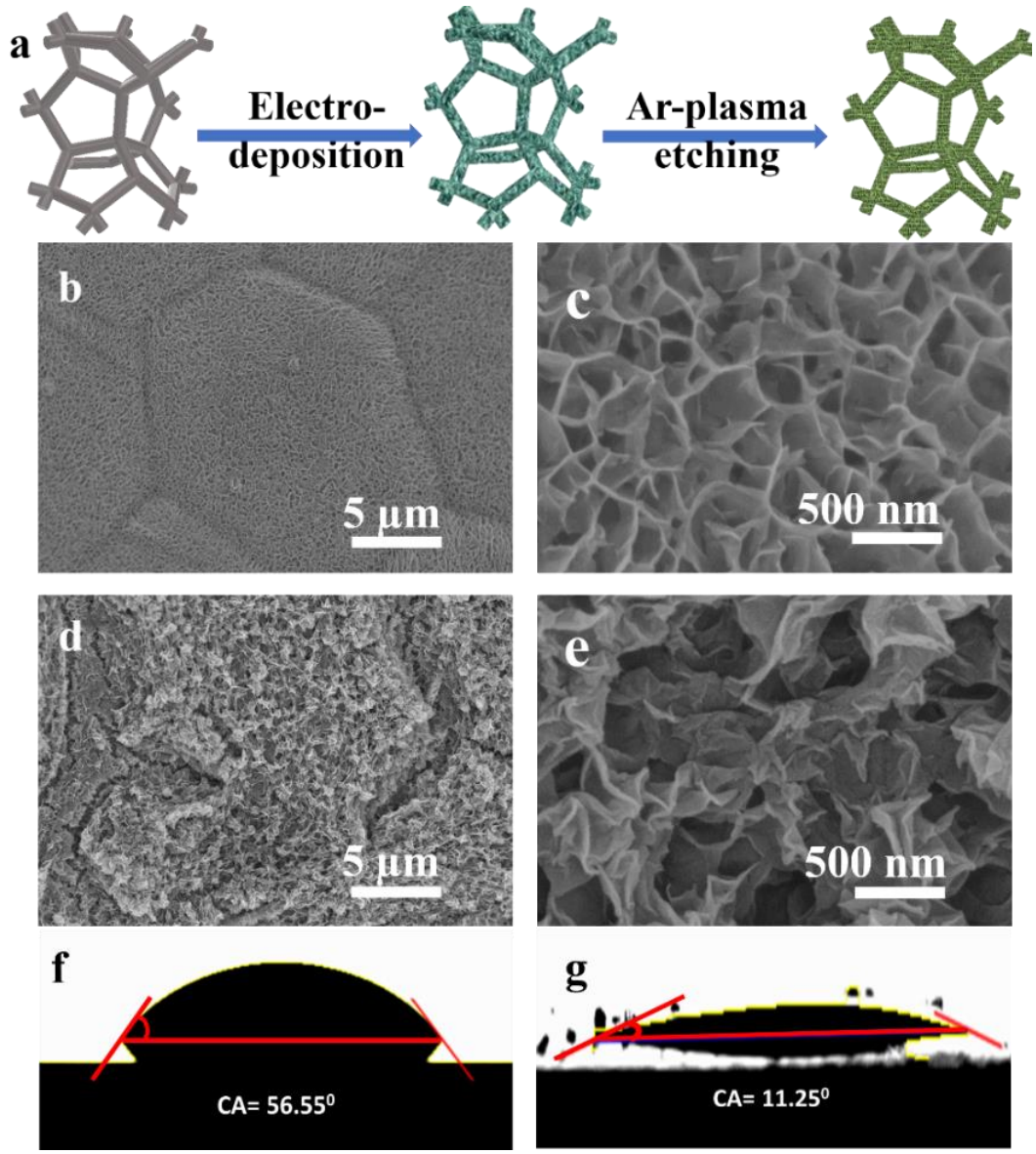

Figure 1: (a) Illustration of the synthesis of Ar-NiCo nanosheets, SEM images of (b, c) NiCo, (d, e) Ar-NiCo, and contact angle for (f) NiCo, and (g) Ar-NiCo nanosheets.

After the surface of the NiCo bulk LDHs was treated with Ar-plasma (100 W) for 20 min, rippled silk like morphology with enlarged intercalated space were appeared, indicating the successful exfoliation of the bulk material (Figure 1d, e). These as-formed nanosheet with a lateral size of several hundred nanometers are interconnected with each other, creating loose porous nanostructures with abundant electroactive surface sites.[21] The surface wettability of the samples was measured by using water droplet contact angle (CA) test. As shown in Figure 1f, g, Ar-NiCo nanosheets exhibited lower contact angle value of 11.25^0 compared to bulk NiCo with contact angle value of 56.55^0 revealing a much electrolyte-hydrophilic surface. The improved surface wettability enhances the exposure rates of the interaction between the hydroxide ions of the electrolyte and Ni^{2+}/Co^{2+}, accelerating rapid electrolyte ion penetration and improves utilization of active sites of the LDHs nanosheets.[22]

Transmission electron microscopy (TEM) measurement was carried out to further investigate the morphology of the as-synthesized NiCo LDH nanosheets. Compared to bulk NiCo (Figure 2a), a typical TEM image of Ar-NiCo nanosheets (Figure 2b) shows a homogenous transparent feature, indicating ultrathin nature of the exfoliated nanosheets. Furthermore, the higher resolution (HR) TEM image insets in Figure 2a, b reveal no measurable lattice fringes revealing that the basic architecture of the layer remained unchanged after exfoliation. Moreover, the uniform distribution of Ni, Co, and O was confirmed from the separate elemental mapping recorded from energy dispersive X-ray spectroscopy (EDX) TEM images (Figure 2c). The SEM EDX for the bulk NiCo also confirms the presence of the desired elements in the composition.

A tapping-mode atomic force microscope (AFM) images further verified the exfoliation of bulk NiCo LDHs to ultrathin nanosheets. As shown in Figure 2 d, e the thickness of NiCo LDHs is decreased from ~53.7 nm to ~1.3 nm (Figure 2f), which corresponds to monolayer.

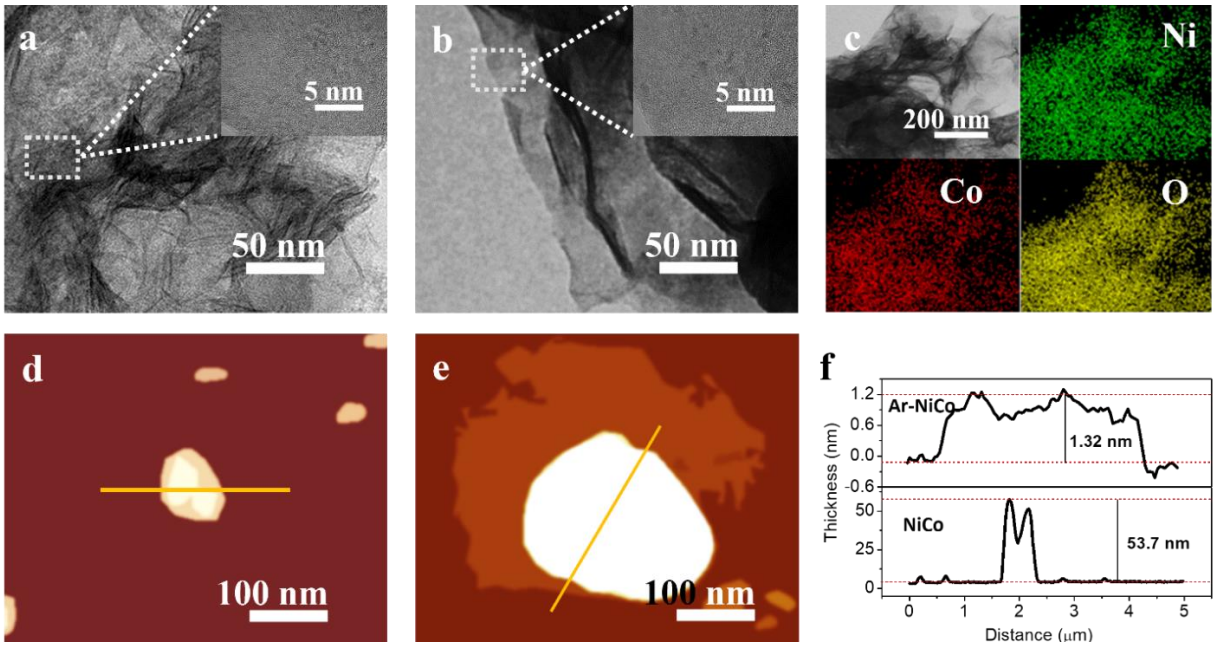

Figure 2: TEM (inset: HRTEM) for (a) NiCo, (b) Ar-NiCo, (c) EDX mapping images of Ar-NiCo, AFM images of (d) NiCo, (e) Ar-NiCo, and (f) corresponding height curves.

The powder X-ray diffraction (XRD) patter of Ar-NiCo nanosheet is presented in Figure 3a, where no diffraction peaks corresponding to oxide/hydroxides of Ni, Co or their composites were detected, showing amorphous nature of the material at room temperature.[23] The valence state and chemical composition of the as-synthesized materials were further investigated by high resolution X-ray photoelectron spectroscopy (XPS). As shown in Figure 3b-d, the desired elements were detected in the samples. For Ni 2p XPS spectrum (Figure 3b),

main peaks at 856.1 eV corresponding to Ni $2p_{3/2}$ and 873.7 eV for Ni $2p_{1/2}$ are clearly visible. These main peaks are followed by shakeup satellites, clearly indicating the existence of $Ni(OH)_2$.

The spin-orbit splitting values of Ni 2p spectra of the samples are almost the same, indicating that the nickel ions maintained the divalent state before and after Ar plasma treatment.[24] The Co 2p XPS (Figure 3c) spectrum split into Co $2p_{3/2}$ (781.5 eV) and Co $2p_{1/2}$ (797.2 eV) peaks accompanied by satellite bands around 786.1 and 803.1 eV, which corresponds to $Co(OH)_2$.[25] After Ar-plasma treatment, slight peak shifts to lower energy in the region of Co $2p_{3/2}$ (781.2 eV) and Co $2p_{1/2}$ (797.0 eV) were prevalent, indicating the partial oxidation of Co^{2+} to Co^{3+}.[26] Meanwhile, the signal in the O 1s region at 532.0 eV (Figure 3D) matched with -OH phase, further indicating the hydroxide structure of samples.[27]

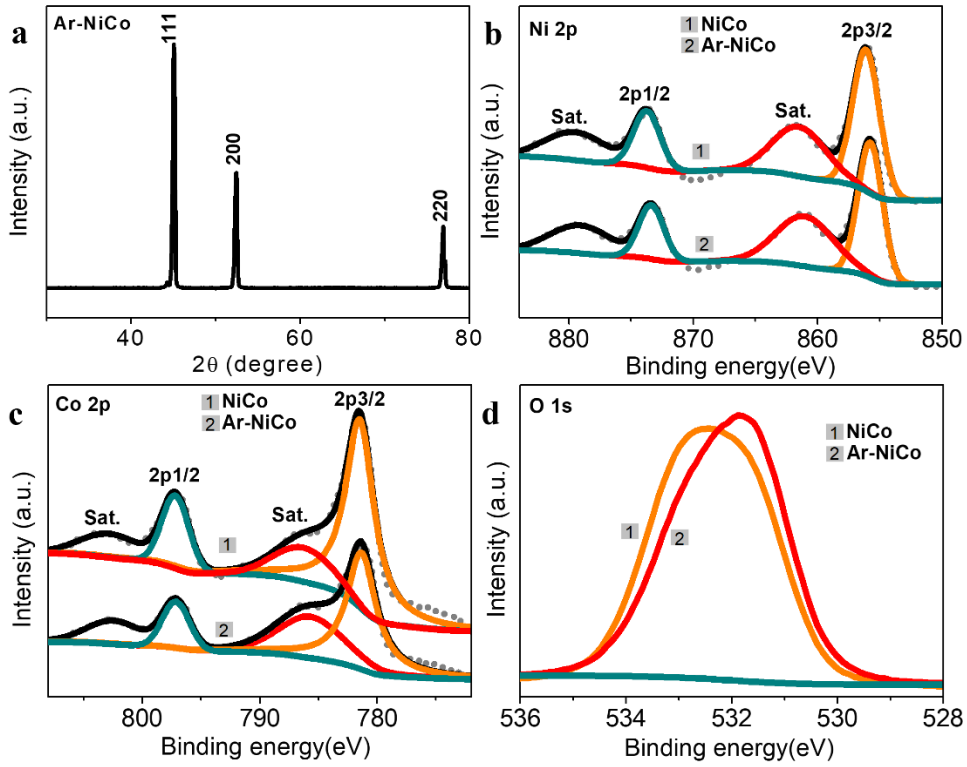

Figure 3: (a) XRD patterns of Ar-NiCo, (b-d) High-resolution XPS spectra of NiCo and Ar-NiCo nanosheets

The capacitive performance of the as-synthesized electrode materials was investigated through cyclic voltammetry (CV) and galvanostatic charge-discharge (GCD) using a standard three-electrode system in 3M KOH electrolyte. Figure 4a shows typical CV curves of Ar-NiCo, NiCo, and NF substrate in the potential range of 0.0-0.6 V at scan rate of 60 mV s^{-1}. It is apparent that the integrated area of Ar-NiCo nanosheets and its redox current is higher than bulk NiCo and NF. For Ar-NiCo and NiCo, there is a pair of redox peaks located around 0.1 and 0.4 V respectively, which mainly attributed to the Faradaic reactions related to M-O/M-O-OH (M represents Ni or Co).[28]

Compared to bulk NiCo LDHs, Ar-NiCo nanosheets demonstrated a smaller oxidation-reduction energy barrier because of fast ion diffusion across the ultrathin and enlarged interlayer spacing resulting from Ar-plasma assisted exfoliation of the bulk material. The larger the integral area enclosed under the same scan rate and voltage window, the better the capacitive performance of the material.[29] Compared to others, the area from CV curves of NF is negligible indicating the capacitive contribution of NF is quite small. The high-capacitive characteristic of the Ar-NiCo electrode material can be identified from its voltametric response at various scan rates. Apparently, all curves exhibit a similar shape with a pair of well-defined redox peaks, and the current density increases with increasing

scan rate, which is an indicator of a good electrochemical reversibility (Figure 4b). Like Ar-NiCo, the shapes of CV curves for NF and bulk NiCo were maintained and peak current increases with increase in sweep rates.

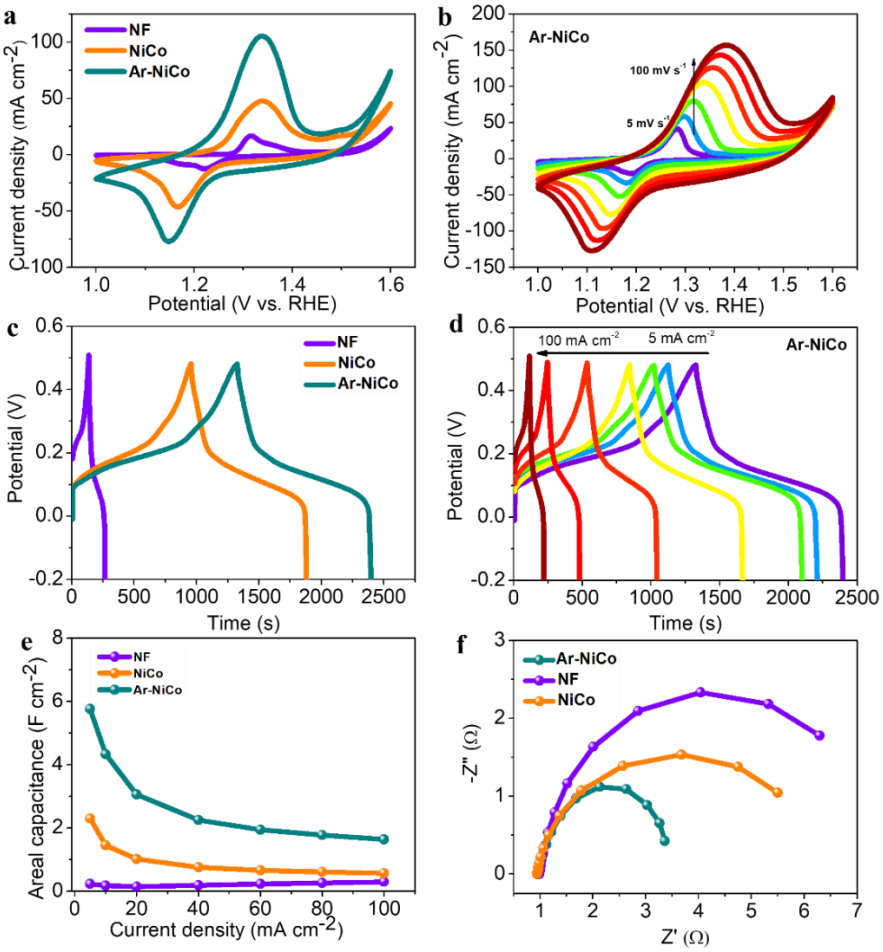

Figure 4: Electrochemical characterization of Ar-NiCo nanosheets in the positive potential range. (a) Comparison of the CV profiles of NF, NiCo, and Ar-NiCo, (b) CV profiles of Ar-NiCo at different scan rates, (c) Comparison of GCD profiles of NF, NiCo, and Ar-NiCo at 5 mA cm^{-2}, (c) GCD profiles of Ar-NiCo nanosheets at different current densities, (e) Areal capacitance estimated from GCD (f) EIS Nyquist plots.

To further evaluate the performance of the electrode material, galvanostatic charge discharge (GCD) tests were performed in the potential range of 0-0.5 V under a variable areal current density ranging from 5 mA cm^{-2} to 100 mA cm^{-2}. Figure 4c depicts the GCD curves of Ar-NiCo, NiCo, and NF electrode materials at a current density of 5 mA cm^{-2}. Evidently, the GCD curves were featured by a rapid potential drop due to the internal resistance and a sluggish potential decay because of the Faradaic redox reaction. Under the same current density and potential window, the discharge of Ar-NiCo electrode is longer than those of NiCo, and NF electrode materials, manifesting good reversibility and high capacitance. The GCD curves of Ar-NiCo recorded at different current densities is shown in Figure 4d. The observation of nearly symmetric potential-time curves at all current densities implies the high charge-discharge coulombic efficiency and low polarization of the electrode material. The areal capacitance of Ar-NiCo, NiCo, and NF electrode materials were calculated based on charge-discharge curves from Figure 4d and the results are plotted against discharging current density in Figure 4e. Encouragingly, the Ar-NiCo nanosheet electrode exhibits excellent areal capacitance of 5.7, 4.3, 3.0, 2.2, 1.9, 1.7, and 1.6 F cm^{-2} at current densities of 5,

10, 20, 40, 60, 80 and 100 A cm^{-2}. Compared to Ar-NiCo nanosheets, NiCo LDHs and NF demonstrated lower areal capacitance at the same current densities, indicating the effectiveness of Ar-plasma-induced exfoliation. Figure 4F shows the electrochemical impedance spectrum of Ar-NiCo, NiCo, and NF electrode materials in the frequency range of 0.01 Hz ~ 10 kHz. Clearly, Ar-NiCo nanosheet demonstrated shorter diameter semicircle compared to bulk NiCo and NF, an indicator enhanced ion diffusion and effective electron transfer.[29]

It can also be observed that the electrochemical characteristics of Ar-NiCo nanosheets are also affected by the duration of the Ar-plasma treatment. The electrode material has demonstrated enhanced capacitive activity with increase in treatment time, where maximum activity was attained at around 20 min treatment time (Figure a, b, c). The areal capacitances of Ar-NiCo nanosheets with prolonged Ar-plasma treatment period of 20 minutes can reach as high as 5.7 F cm^{-2} (Figure 5a). Furthermore, the long-term charge/discharge performance of NiCo and Ar-NiCo nanosheets were tested at a current density of 100 mA cm^{-2} (Figure 5b). After 5000 cycles, NiCo, and Ar-NiCo nanosheets maintained 84%, and 88% of their initial capacitance, respectively, indicator of good electrochemical stability.

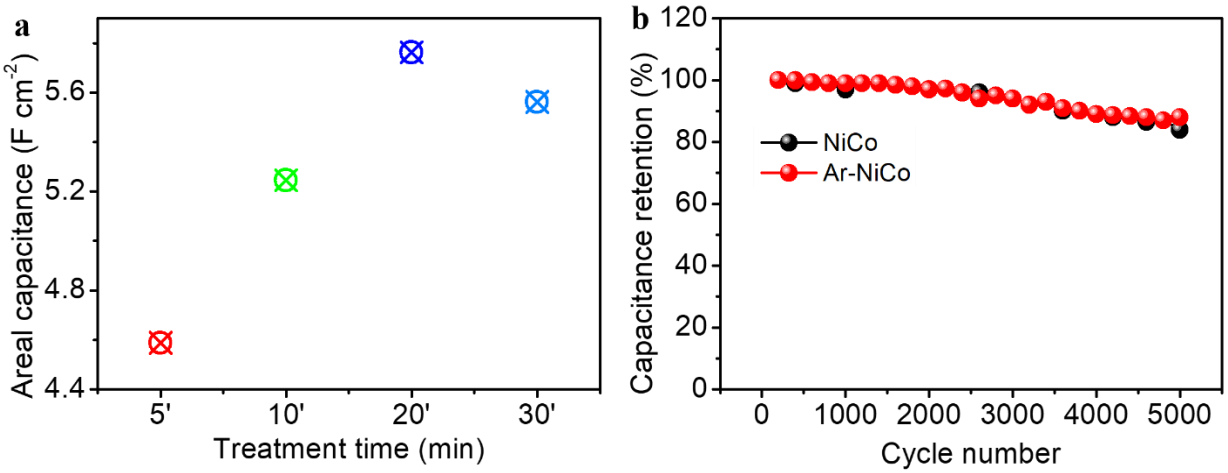

Figure 5: (a) Areal capacitance of Ar-NiCo nanosheets at different Ar-plasma treatment times obtained at a current density of 5 mA cm^{-2}, (b) Cycling stability of NiCo and Ar-NiCo nanosheets.

4. CONCLUSION

In summary, we have demonstrated an effective and environmentally friendly strategy to exfoliate bulk LDHs into ultrathin nanosheets. By using non-thermal Ar-plasma exfoliation technique, we were able to fabricate a single layer of nanosheets from bulk NiCo LDHs. As a result, the electrode material exhibited an areal capacitance of 5.7 F cm^{-2} at current density of 5 A cm^{-2} and excellent cycling stability with over 88% capacitance retention after 5000 cycles. Such a high-capacity density and cycle stability is mainly attributed to increased surface area and improved charge transport induced by Ar-plasma exfoliation of the bulk LDHs. The concept proposed in this work may open opportunities to tune the structural and electrochemical properties of LDHs for their use as high-energy supercapacitors.

ACKNOWLEDGEMENTS

This work was supported by National Research Foundation of Korea (NRF-2021H1D3A2A01099457, 2021K1A3A1A16096990, 2019R1A2C2007825).

REFERENCES

[1] B.B. Gicha, L.T. Tufa, Y. Choi, J. Lee. Amorphous Ni1–xFex Oxyhydroxide Nanosheets with Integrated Bulk and Surface Iron for a High and Stable Oxygen Evolution Reaction, ACS Appl.Energy Mater. 4(5) (2021) 6833-6841.
[2] L.T. Tufa, B.B. Gicha, H. Wu, J. Lee. Fe-Based Mesoporous Nanostructures for Electrochemical Conversion and Storage of Energy, Batter. Supercaps 4, (2020) 429-444.
[3] W. Jiang, D. Yu, Q. Zhang, K. Goh, L. Wei, Y. Yong, R. Jiang, J. Wei, Y. Chen. Ternary Hybrids of Amorphous Nickel Hydroxide–Carbon Nanotube-Conducting Polymer for Supercapacitors with High Energy Density, Excellent Rate Capability, and Long Cycle Life, Adv. Funct. Mater. 25(7) (2015) 1063-1073.
[4] K. Saravanan, C.W. Mason, A. Rudola, K.H. Wong, P. Balaya. The First Report on Excellent Cycling Stability and Superior Rate Capability of Na3V2(PO4)3 for Sodium Ion Batteries, Adv. Energy Mater. 3(4) (2013) 444-450.
[5] Y. Liao, H. Wang, M. Zhu, A. Thomas. Efficient Supercapacitor Energy Storage Using Conjugated Microporous Polymer Networks Synthesized from Buchwald–Hartwig Coupling, Adv. Mater. 30(12) (2018) 1705710.
[6] N. Wu, X. Bai, D. Pan, B. Dong, R. Wei, N. Naik, R.R. Patil, Z. Guo. Recent Advances of Asymmetric Supercapacitors, Adv. Mater. Interfaces 8(1) (2021) 2001710.
[7] M.-Q. Zhao, Q. Zhang, J.-Q. Huang, F. Wei. Hierarchical Nanocomposites Derived from Nanocarbons and Layered Double Hydroxides - Properties, Synthesis, and Applications, Adv. Funct. Mater. 22(4) (2012) 675-694.
[8] L. Lv, Z. Yang, K. Chen, C. Wang, Y. Xiong. 2D Layered Double Hydroxides for Oxygen Evolution Reaction: From Fundamental Design to Application, Adv. Energy Mater. 9(17) (2019) 1803358.
[9] X. Gao, P. Wang, Z. Pan, J.P. Claverie, J. Wang. Recent Progress in Two-Dimensional Layered Double Hydroxides and Their Derivatives for Supercapacitors, ChemSusChem 13(6) (2020) 1226-1254.
[10] B.B. Gicha, L.T. Tufa, S. Kang, M. Goddati, E.T. Bekele, J. Lee. Transition Metal-Based 2D Layered Double Hydroxide Nanosheets: Design Strategies and Applications in Oxygen Evolution Reaction, Nanomaterials 11(6) (2021) 1388.
[11] H. Yi, S. Liu, C. Lai, G. Zeng, M. Li, X. Liu, B. Li, X. Huo, L. Qin, L. Li, M. Zhang, Y. Fu, Z. An, L. Chen. Recent Advance of Transition-Metal-Based Layered Double Hydroxide Nanosheets: Synthesis, Properties, Modification, and Electrocatalytic Applications, Adv. Energy Mater. 11(14) (2021) 2002863.
[12] Y. Wang, D. Yan, S. El Hankari, Y. Zou, S. Wang. Recent Progress on Layered Double Hydroxides and Their Derivatives for Electrocatalytic Water Splitting, Adv. Sci. 5(8) (2018) 1800064.
[13] T. Wang, F. Yu, X. Wang, S. Xi, K.-J. Chen, H. Wan. Enhancing cycling stability of transition metal-based layered double hydroxides through a self-sacrificial strategy for hybrid supercapacitors, Electrochim. Acta 334 (2020) 135586.
[14] C. Jing, B. Dong, Y. Zhang. Chemical Modifications of Layered Double Hydroxides in the Supercapacitor, Energy Env. Mater. 3(3) (2020) 346-379.
[15] Y. Shabangoli, M.S. Rahmanifar, A. Noori, M.F. El-Kady, R.B. Kaner, M.F. Mousavi. Nile Blue Functionalized Graphene Aerogel as a Pseudocapacitive Negative Electrode Material across the Full pH Range, ACS Nano 13(11) (2019) 12567-12576.
[16] C. Chen, L. Tao, S. Du, W. Chen, Y. Wang, Y. Zou, S. Wang. Advanced Exfoliation Strategies for Layered Double Hydroxides and Applications in Energy Conversion and Storage, Adv. Funct.Mater. 30(14) (2020) 1909832.
[17] W. Quan, C. Jiang, S. Wang, Y. Li, Z. Zhang, Z. Tang, F. Favier. New nanocomposite material as supercapacitor electrode prepared via restacking of Ni-Mn LDH and MnO2 nanosheets, Electrochim. Acta 247 (2017) 1072-1079.
[18] J. Li, P. Zhang, X. Zhao, L. Chen, J. Shen, M. Li, B. Ji, L. Song, Y. Wu, D. Liu. Structure-controlled Co-Al layered double hydroxides/reduced graphene oxide nanomaterials based on solid-phase exfoliation technique for supercapacitors, J. Colloid Interface Sci. 549 (2019) 236-245.
[19] Y. Wang, Y. Zhang, Z. Liu, C. Xie, S. Feng, D. Liu, M. Shao, S. Wang. Layered Double Hydroxide Nanosheets with Multiple Vacancies Obtained by Dry Exfoliation as Highly Efficient Oxygen Evolution Electrocatalysts, Angew. Chem. Int. Ed. 56(21) (2017) 5867-5871.
[20] H. Liang, F. Ming, H.N. Alshareef. Excellence in Energy: Applications of Plasma in Energy Conversion and Storage Materials, Adv. Energy Mater. 8(29) (2018) 1870126.
[21] C. Yuan, J. Li, L. Hou, X. Zhang, L. Shen, X.W. Lo. Ultrathin Mesoporous NiCo2O4 Nanosheets Supported on Ni Foam as Advanced Electrodes for Supercapacitors, Adv. Func. Mater. 22(21) (2012) 4592-4597.
[22] H. He, J. Lian, C. Chen, Q. Xiong, M. Zhang. Super hydrophilic carbon fiber film for freestanding and flexible cathodes of zinc-ion hybrid supercapacitors, Chem. Eng. J. 421 (2021) 129786.
[23] X. Lu, C. Zhao. Electrodeposition of hierarchically structured three-dimensional nickel–iron electrodes for efficient oxygen evolution at high current densities, Nat. Commun. 6(1) (2015) 6616.
[24] M.C. Biesinger, B.P. Payne, A.P. Grosvenor, L.W.M. Lau, A.R. Gerson, R.S.C. Smart. Resolving surface chemical states in XPS analysis of first row transition metals, oxides, and hydroxides: Cr, Mn, Fe, Co and Ni, Appl. Surf. Sci. 257(7) (2011) 2717-2730.

[25] R. Liu, Y. Wang, D. Liu, Y. Zou, S. Wang. Water-Plasma-Enabled Exfoliation of Ultrathin Layered Double Hydroxide Nanosheets with Multivacancies for Water Oxidation, Adv. Mater. 29(30) (2017) 1701546.
[26] M.C. Biesinger, B.P. Payne, L.W.M. Lau, A. Gerson, R.S.C. Smart. X-ray photoelectron spectroscopic chemical state quantification of mixed nickel metal, oxide and hydroxide systems, Surf. Interface Anal. 41(4) (2009) 324-332.
[27] H. Wang, Q. Gao, L. Jiang. Facile Approach to Prepare Nickel Cobaltite Nanowire Materials for Supercapacitors, Small 7(17) (2011) 2454-2459.
[28] L.T. Tufa, S. Oh, J. Kim, K.-J. Jeong, T.J. Park, H.-J. Kim, J. Lee. Electrochemical immunosensor using nanotriplex of graphene quantum dots, Fe3O4, and Ag nanoparticles for tuberculosis, Electrochim. Acta 290 (2018) 369-377.
[29] L. Zhang, H. Xia, S. Liu, Y. Zhou, Y. Zhao, W. Xie. Nickel–Cobalt Hydroxides with Tunable Thin-Layer Nanosheets for High-Performance Supercapacitor Electrode, Nanoscale Res. Lett. 16(1) (2021) 83.

Electrocatalytic Study of Pd/CeO_2 -N, S-rGO for Hydrogen and Oxygen Evolution Application

MengistuWoldetinsay[1,2], Tesfaye R. Soreta[3,]*, Krishnamurthy Palani[4], ThandavarayanMaiyalagan[4], Olu Emmanuel Femi[1]

[1]*Faculty of Material Science and Engineering, Jimma Institute of Technology (JIT), Jimma University, P.O. Box 378, Jimma, Ethiopia*
[2]*Department of Chemistry, Wollega University, P.O. Box 395, Nekemte, Ethiopia*
[3]*Center for Materials Engineering, Addis Ababa Institute of Technology, Addis Ababa University, P.O. Box 1176 Addis Ababa, Ethiopia*
[4]*Electrochemical Energy Laboratory, Department of Chemistry, SRM Institute of Science and Technology, Kattankulathur 603203, India*
**Corresponding author, e-mail: tesfaye.refera@aait.edu.et*

ABSTRACT

The sustainable production of hydrogen and oxygen through electrolysis of water requires the development of an efficient electrocatalyst. In this work we report the electro catalytic activity of Pd nanoparticles dispersed on CeO_2/N, S-rGO (where N, S-rGOrepresents nitrogen and sulfur doped reduced graphene oxide).The CeO_2/N, S-rGO and Pd nanoparticle were synthesized by hydrothermal and chemical reduction methods respectively. Electrochemical measurements towards hydrogen evolution reaction (HER) and oxygen evolution reaction (OER) show a high electrocatalytic activity of the catalyst. Among the synthesized electrocatalystsPd/CeO_2/N, S-rGO exhibits lower overpotential (75 mV and 240 mV) at 10 $mAcm^{-2}$ and lower Tafel slope value (44 mV dec^{-1} and 42 mV dec^{-1}) for HER and OER, respectively. The chronoamperometric and linear sweep voltammetry (LSV) of the electrocatalyst shows a negligible decrease in the current density for twelve hours and a minor change in the polarization curve after 10,000 cycles, respectively. The high electrocatalytic activity and superior stability of the synthesized electrocatalyst could be attributed to the synergetic effect between Pdnanoparticlesand CeO_2/N, S-rGO support. This work demonstrates a facile way to develop effective and stable electrocatalysts by exploiting the Pd/Metal oxide interface.

Keywords: *Electrocatalyst, Hydrogen Evolution Reaction (HER), Oxygen Evolution Reaction, Pd nanoparticle, CeO_2*

1. INTRODUCTION

Hydrogen has been a promising clean energy source for the future (Dresselhaus and Thomas, 2001). Currently, the production of hydrogen through water splitting sustainably by using an effective electro catalyst is attracting more attention (Bard and Fox, 1995; Walter et al, 2010). The electrochemical water splitting in acidic polymer electrolyte water electrolyzers (PEWEs) has many advantages than the alkaline system. This includes higher kinetics of the cathodic hydrogen evaluation reaction, high electrolyte conductivity, and higher pressure above 50 bar (Paoli et al., 2014).

Pt and Pt-based electro catalyst are mostly used for hydrogen production (Greeley et al., 2006). However, low natural abundance of Pt and posing of electrode hinders large-scale applications. These limitations forced the research community to find a non-Pt or less Pt content electro catalyst (Zhou et al., 2004; Antolini et al., 2006) or Pt alloys with other metals such as Pd (Xu et al., 2007; Gao et al. 2011), Ni (Wind et al. 2002; Park et al., 2003), etc. Recently Pd and Pd-based electro catalysts are attracting more attention because Pd has a similar property with Pt, relatively more abundant than Pt and less poisonous during processing (Axon and Casci, 2007. Moreover, Pd has very close adsorption energy and exchange current density to Pt towards HER (Ji et al., 2017).

Pd and Pd-based electrocatalysts are mostly used in catalytic reactions related to hydrogen both for storage and evolution (Fan et al., 2020; Liao et al., 2017). However, the strong binding energy between Pd and hydrogen in Pd-

H bonding makes the Pd electro catalyst inactive towards hydrogen evolution reaction. Many strategies have been employed to alter hydrogen binding energy on the Pd surface (Wang et al., 2017).These include the combining of Pd with heteroatomic metallic elements that could affect the lattice strain (Bai et al., 2014) and the dispersion of Pd on high surface area support that could weaken the bond between Pd and Hydrogen (Trimpalis et al., 2019; Wang et al., 2019). An additional reason for the special attention given to Pd based materials towards hydrogen evolution reaction is because of its fast adsorption kinetics, selectivity, and reversible hydrogen formation (Sarkar and Peter, 2018). However, desorption of hydrogen from the palladium catalyst surface is very difficult.The hydrogen evolution performance of Pd nanoparticle can be improved by affecting the electronic properties and crystal parameters, which could be achieved by reducing the size of Pd.

The noble metal content in the electro catalyst can be reduced without compromising the HER performance using support materials that have a higher surface area and good electrical conductivity (Cardoso et al., 2006). Good electrical conductivity, higher surface area, optimum porosity, and higher stability in an acidic environment are the main characteristics of good support material. They should also possess high energy density and corrosion resistance under oxidizing conditions (Meier et al., 2014; Bhowmik et al., 2016).

The morphology, size, structure, and nature of the support materials may influence the metal nanoparticles' catalytic activity. In addition to these, the low coordination of metal nanoparticles, quantum size effect, and better metal support interactions could have a more significant impact (Ojani et al., 2014).

Among the carbon support materials, graphene can best fit the above criteria (Fan et al., 2017; Fan et al., 2014). However, due to the Van der Waals attraction between graphenenanosheets, the effective surface area and conductivity could be affected (Guo et al., 2013; Ratso et al., 2016). To solve this problem, doping of electron-rich specious on graphene is the best option to help the carbon π electrons conjugate with electrons of doped element to increase the material's donor properties (More et al., 2010).

Generally, various carbon-supported catalysts have significant limitations, such as low electro catalytic stability due to the rapid depletion of carbon (Perini et al., 2014). Many attempts have been devoted to overcoming this problem, such as the incorporation of heteroatom example, nitrogen, and sulfur that coordinates with different nano particles (NPs) (Noto et al., 2012; He et al., 2015).

Doping of a small amount of cerium oxide (CeO_2) can improve the catalytic activity of metal catalyst (Zou and Zhang, 2015; Ge et al., 2012), for example, Au-CeO_2 (Kayama et al., 2010), Ag-CeO_2 (Yu et al., 2012), and Pt-CeO_2 (Wang et al., 2012). This is due to the high capability of CeO_2 in adsorbing OH-species, which is closely related to the redox process between the different possible oxidation states of cerium (Ce) (Wang et al., 2013b; Wang et al., 2013a; Urayama et al., 2016). To increase both the activity and stability of metal-CeO_2 suitable support that can disperse metal NP is required. In this respect, reduced graphene oxide (rGO) is the best choice due to its high surface area, good conductivity, and thermal and chemical stability (Wang et al., 2014; Zhang et al., 2015). Combining N, S-rGO, and CeO_2 may optimize both the dispersion and catalytic activity of Pdnanoparticles and stability.

Recently, we reported M-Pd (M=Ni, Cu, Co) core-shell nanostructures supported on N, S-rGO (MengistuWoldetinsay et al., 2020b) and Pd/MOS_2/N,S-rGO (MengistuWoldetinsay et al. 2020a) to demonstrate a higher electro catalytic activity with small over potential, stability, and lower Tafel slope value towards hydrogen evolution reactions due to the synergetic effect between Pdnanoparticles and supports. In this report, we synthesized Pd/CeO_2/N,S-rGO, and Pd-Ni/CeO_2/N, S-rGO by hydrothermal, and wet chemical reduction method. The characterization of the as prepared composites and their application in electrochemical activities towards hydrogen evolution reaction and oxygen evolution reaction was studied. Among the synthesized electro catalysts, Pd/CeO_2/N,S-rGO demonstrated the highest electro catalytic activity than Pd-Ni/CeO_2/N, S-rGO, and CeO_2/N, S-rGO.

2. MATERIALS AND METHODS

2.1 Reagents

All chemicals used for this analysis were analytical grade and utilized without further purification.Graphite powder (99.9%); Nickel nitrate hexahydrate ($Ni(NO_3)_2.6H_2O$) (99%); Ceriumnitrate $Ce(NO_3)_3.6H_2O$ (99%); Ethylene glycol (99%); Palladium chloride ($PdCl_2$, 98%); hexadecyltrimethyl ammonium bromide (CTAB) (>99% solubility in water); Sulfuric acid (H_2SO_4, ≥ 95-98%,); Potassiumpermanganate ($KMnO_4$) (99.4%); Sodium nitrate ($NaNO_3$) (99.0%) and Thiourea (N_2H_4SC) (99.0%), Ethanol (98%); Hydrogen peroxide (H_2O_2, ≥ 30% (w/w), sodium borohydride ($NaBH_4$) (99.9%). De-ionized water was used for all aqueous sample preparation.

2.2 Characterization of Instruments

X-ray diffraction (XRD) was used to investigate the crystalline structure of the crystals using Cu kα radiation. Raman spectra with 633 nm Ar Laser source was used to evaluate the prepared sample's defect structure. High transmission electron microscope (HRTEM) image was taken with a LaB6 electron gun. The X-ray Photoelectron Spectroscopy (XPS) with soft x-ray (Al k-alpha) and XPSPEAK4.1 software were used to analyze the synthesized sample's surface chemistry. Scanning electron microscope (SEM) and field emission scanning electron microscope (FESEM) was used to study the surface morphology.

2.3 Methods

2.3.1 Graphene oxide (GO) and nitrogen and sulfur doped reduced graphen oxide (N, S-rGO) Synthesis

Graphene oxide was synthesized from graphite powder by the modified Hummer method as described in our previous report (MengistuWoldetinsay et al., 2020a). N, S-rGO was synthesized by the hydrothermal method as we have previously reported (MengistuWoldetinsay et al., 2020a). Briefly, GO (70 mg) was added to de-ionized water (70 ml), followed by sonication for an hour. Thiourea (1 g) was added to the above mixture as a source of both N and S, followed by sonication for 30 minutes. The mixture was transferred into 100 ml Teflon lined stainless steel autoclave for the hydrothermal reaction at 180 ^oC for 12 h. Finally, the product was collected by washing with de-ionized water and ethanol, followed by drying at 60 ^0C for 12 h.

2.3.2 Cerium doped on nitrogen and sulfur doped reduced graphen oxide (CeO_2/ N, S-rGO) Synthesis

CeO_2/N, S-rGO was synthesized by following the procedure reported by Gao et al. (2018). Briefly, $Ce(NO_3)_3.6H_2O$ (10.1 g) dissolved in 250 ml of de-ionized water and N, S-rGO (4 g) was added to the above solution, followed by sonication of the whole solution for 30 minutes. The solution's pH was adjusted to neutral value using 0.1 M KOH, followed by stirring the solution for 2 h. Finally, the product was collected by filtration and washed with de-ionized water until the pH becomes neutral and dried at 60 ^oC. The powder was further heated in a tube furnace at 250 ^oC for two hours.

2.3.3 Pd/CeO_2/ N, S-rGOandPd-Ni/CeO_2/ N, S-rGO Synthesis

Palladium nanoparticle anchored on CeO_2/ N, S-rGO, was synthesized using the method reported by Gao et al. (2018) with minor modification. Accordingly, CeO_2/ N, S-rGO (500 mg) was dissolved in 100 ml of de-ionized water followed by vigorous stirring (for one hour) and sonication (for 30 minutes). A solution of K_2PdCl_4 (0.17 g) in 20 ml of de-ionized water was added to the above mixture under stirring and stirred for an additional one hour. The solution's pH was adjusted by adding 2 ml of 2.5 M KOH solution dropwise, followed by addition of 15 ml of Ethylene glycol (1 ml /min) and sodium borohydride(10 mg/ml) drop wise. The whole solution was heated for one hour at 80 ^oC. Finally, the product was collected by cooling, filtering, and washing until the pH becomes neutral, and dried at 60 ^oC. The Pd-Ni/CeO_2/ N, S-rGO composite was synthesized by co-reduction of the metal salts.

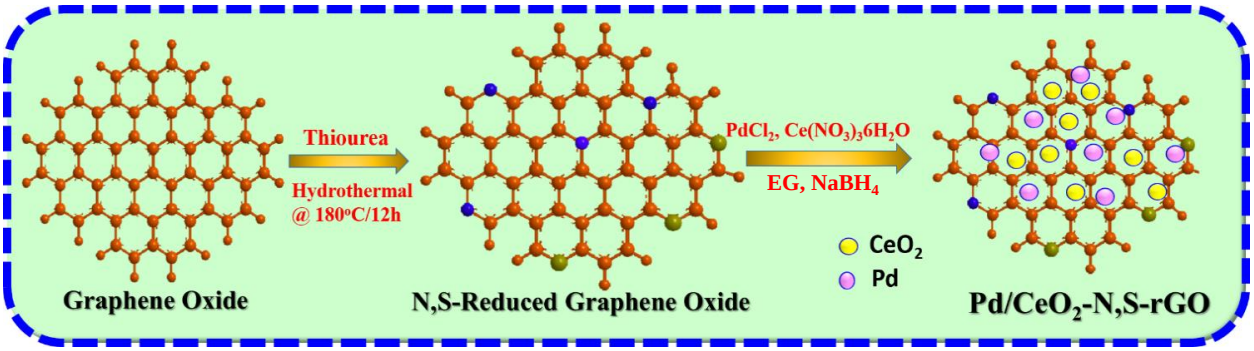

Figure1: Graphical representation for synthesis of electro catalysis

2.3.4 Electrode fabrication

The glassy carbon electrode was polished with different particle size alumina polishing slurry. The geometric area of the electrode was 0.0706 cm^2. The Pd loading amount on the glassy carbon was 0.14 mg/cm^2. The catalyst ink was prepared by dissolving 5 mg of electro catalyst sample in water/ethanol (1:1) and 10 µl 5% Nafion solution (used as a binder). The suspension was ultrasonicated for 30 minutes. The ink (5 µl) dropped cast on the polished glassy carbon.

2.3.5 Electrochemical measurements

All electrochemical measurements were carried out using a potentiostat with EC-Lab (V11.10) software with a three-electrode configuration. The electro catalyst modified glassy carbon electrode was used as a working electrode, Ag/AgCl (saturated KCl) as a reference electrode. A graphite electrode was used as a counter electrode in N_2 saturated 0.5 M H_2SO_4 for hydrogen evolution and in 0.1M KOH for oxygen evolution.

The electro catalytic performance evaluated using linear sweep voltammetry (LSV) measurement due to the ohmic resistance (iR) the current measured may not indicate the intrinsic behavior so iR correction was done LSV measurement. Stability is essential criteria for a practical applications. Commonly there are two ways of study the stability of electro catalyst. One way is measuring the change in current with time in the I-t curve. In this case the current was set at current density of 10 mA cm^{-2} for twelve hours. The second method was by conducting cycling experiment for 10,000 cycles at 25 ^oC in 0.5 M H_2SO_4 and 0.1 M NaOH, for HER and OER respectively.

The electrochemical impedance spectroscopy (EIS) used to evaluate the charge transfer resistance of the solution which was conducted at a frequency range of 100 kHz to 0.01 HZ at open circuit potential with perturbation 5 mV. All the potential mentioned in this report converted to RHE by using

$$E_{RHE} = E_{Ag/AgCl} + 0.059pH + E^o_{Ag/AgCl} \quad (0.197)$$

3. RESULTS AND DISCUSSIONS

3.1 X-ray diffraction (XRD)

The XRD pattern was used to analyze the crystalline nature of the synthesized sample. Accordingly, the diffraction peak of Pd/CeO_2/N,S-rGO electrocatalyst displayed in Fig. 2(a) shows Bragg diffraction peak located at 2Θ= 39.61,46.05 and 66.94 corresponds to Pd(111), Pd(220) and Pd(200) planes of palladium respectively which was comparatively lower 2Θ value than diffraction peak of Pd-Ni/CeO_2/N, S-rGO. This could be due to the highest degree of desperation of Pd in the former case. Commonly there are two type of interaction between Pd_{NP} and CeO_2 those are spillover effect or reverse spillover effect. The presence of Pd peak and the absence of PdO peak confirm the interaction occurs through the reverse spillover effect in which electrons transfer between Pd_{NP} and CeO_2 in Pd/CeO_2/N,S-rGO. The diffraction peak of Ce at 29.76 corresponds to miller indices Ce (111) in CeO_2/N,S-rGO, which indicates the higher crystalline nature of the sample. The characteristic peak of Ce at 29.76

was diminished in Pd/CeO_2/N,S-rGO composite result from interaction between Pd and Ce that may reduce the existence of CeO_2 as CeO_2 nanoparticles (Zhang et al., 2018).

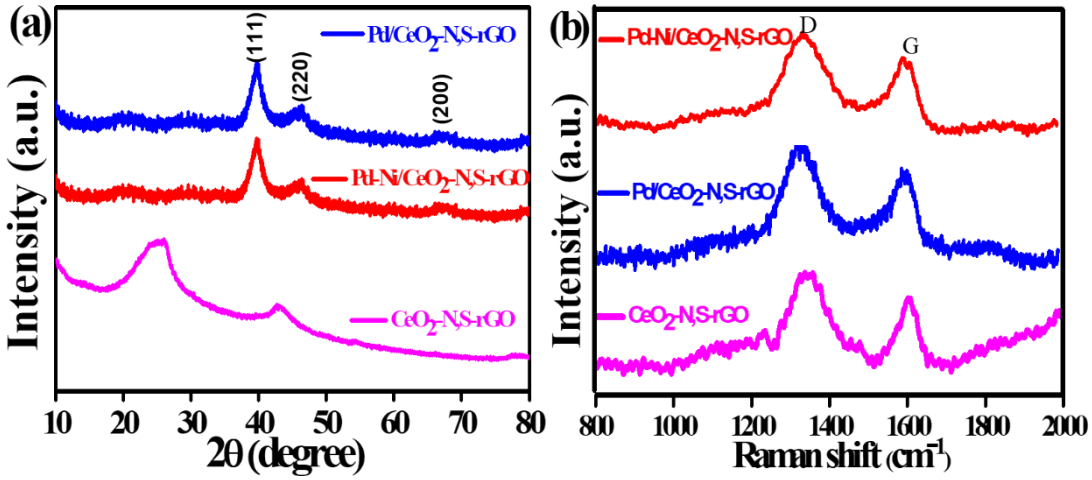

Figure 2: (a) XRD pattern of Pd/CeO_2/N,S-rGO, Pd-Ni/CeO_2/N,S-rGO and CeO_2/N,S-rGO respectively; (b) the Raman shift spectra of Pd-Ni/CeO_2/N,S-rGO, Pd/CeO_2/N,S-rGO and CeO_2/N,S-rGO

3.2 Raman spectroscopy

The Raman spectroscopy was used to analyze the defect in the synthesized sample in a non-distractive way. The presence of more defects in the structure of nano composite helps for creating more active site for electrochemical reactions. The two bands in the Raman spectrum are D-band which related to out of plane vibration of SP^2 bonded carbon associated with the presence of structural defect and G-band due to in-plane vibrations of SP^2 bonded carbon. Moreover, the I_D/I_G ratio is very useful in indicating the degree of defect in the synthesized sample. The Raman analysis result of the electrocatalyst displayed in Fig. 2 (b) shows a peak at (1322.6) corresponding to D-band and (1594.2) G-band for Pd/CeO_2/N, S-rGO and a peak at (1337.2) corresponding to D-band and (1596.3) G-band for, Pd-Ni/CeO_2/N, S-rGO and a peak at (1341.3) corresponding to D-band and (1602.5) G-band for CeO_2/N, S-rGO. The increase in intensity ratio (I_D/I_G) after incorporating heteroatoms related to rGO indicates the formation of more defects in the synthesized sample. The defect in the structure result more active site that enhance the interaction between palladium particle and the support and which may contribute the increase in palladium nano particle dispersion.Relative to rGO the peak position shifted by 2.8, 4.98 and 16.44 for CeO_2/N, S-rGO, Pd-Ni/CeO_2/N, S-rGO and Pd/CeO_2/N, S-rGO, respectively. The observed higher shift in peak position of Pd/CeO_2/N,S-rGO could indicate the stain effect and formation more defect in the structure that contribute availability more active site for electrochemical reactions.

Table 1: Raman parameters for the synthesized electrocatalyst

Electrocatalyst	D-band	G-band	ID/IG
rGO	1338	1597	0.83
N,S-rGO	1340	1600	0.91
CeO_2/N,S-rGO	1341.3	1602.5	1.24
Pd/CeO_2/N,S-rGO	1322.6	1594.2	1.25
Pd-Ni/CeO_2/N,S-rGO	1337.2	1596.3	1.22

3.3 X-ray Photoelectron Spectroscopy (XPS)

The X-ray Photoelectron Spectroscopy (XPS) measurement was conducted to investigate the chemical composition and state of elements in synthesized nano composite. The survey of the XPS spectra of the best performing electro catalyst revels the existence of Palladium (Pd), Cerium (Ce), Carbon (C), Nitrogen (N), Sulfur (S), and Oxygen (O) as shown in Fig. 3. The XPS spectrum of palladium (Pd) displayed in figure 2(a) the peak around 336.6 eV and 341 eV corresponding to Pd $3d_{3/2}$ andPd $3d_{5/2}$ level of Pd^0, respectively (Akbayrak et al., 2017; Liu et al., 2015). The observed positive shift in the binding energy of Pd could be due to the strong electronic interaction between Pd and CeO_2, which resulted from electron transfer between Pd and CeO_2 (Mamontov and Egami, 2000). The Peak at 337.0 eV and 342.2 eV corresponds to palladium (II).The higher intensity of the former peak indicates the higher dispersion of palladium nanoparticles.

The XPS spectrum of Ce3d is displayed in figure 2 (b). The highest peaks at 905.3 eV and 886.1 eVis associated with Ce (Ce^{4+}). The satellite peaks relatively lower binding energies are related to trivalent Ce (Ce^{3+}). The interaction of Pd with CeO_2 shifts the binding energy palladium positively. Since the interaction is through electron transfer from Pd to CeO_2 the oxidation state palladium will be increased. The satellite peaks of Ce 3d such as at 888.1, 885.4 and 904.2 eV associate with (Ce^{3+}) that indicate the existence of oxygen vacancy in CeO_2 (Zhang et al., 2018).

The peak at 284.7 of C 1s shown in Fig.3(c) corresponds to graphitic carbon due to distortion in the sp^3 carbon structure. The peak at 289.4 eV corresponds to the oxygen-containing carbon functional group (O-C=O) (Tedsree et al., 2011). The XPS spectrum of S 2p displayed in Fig.3 (d) with a peak at 162.3 eV, and 163.03 eV corresponds to S $2p_{3/2}$ and S $2p_{5/2}$. The N 2p XPS spectrum shown in Fig.3(e) shows major peaks around 398.6 eV and 399.0 eV associated with nitrogen bonded to Sp2- hybridized carbon (C-C=N-C) (Vinayan et al., 2012; Vinayan et al., 2013). The High-resolution O 1s XPS spectrum at 540.1 eV could indicate the electron cloud density change. The XPS analysis confirms the successful incorporation of N and S in Pd/CeO_2/N, S-rGO.

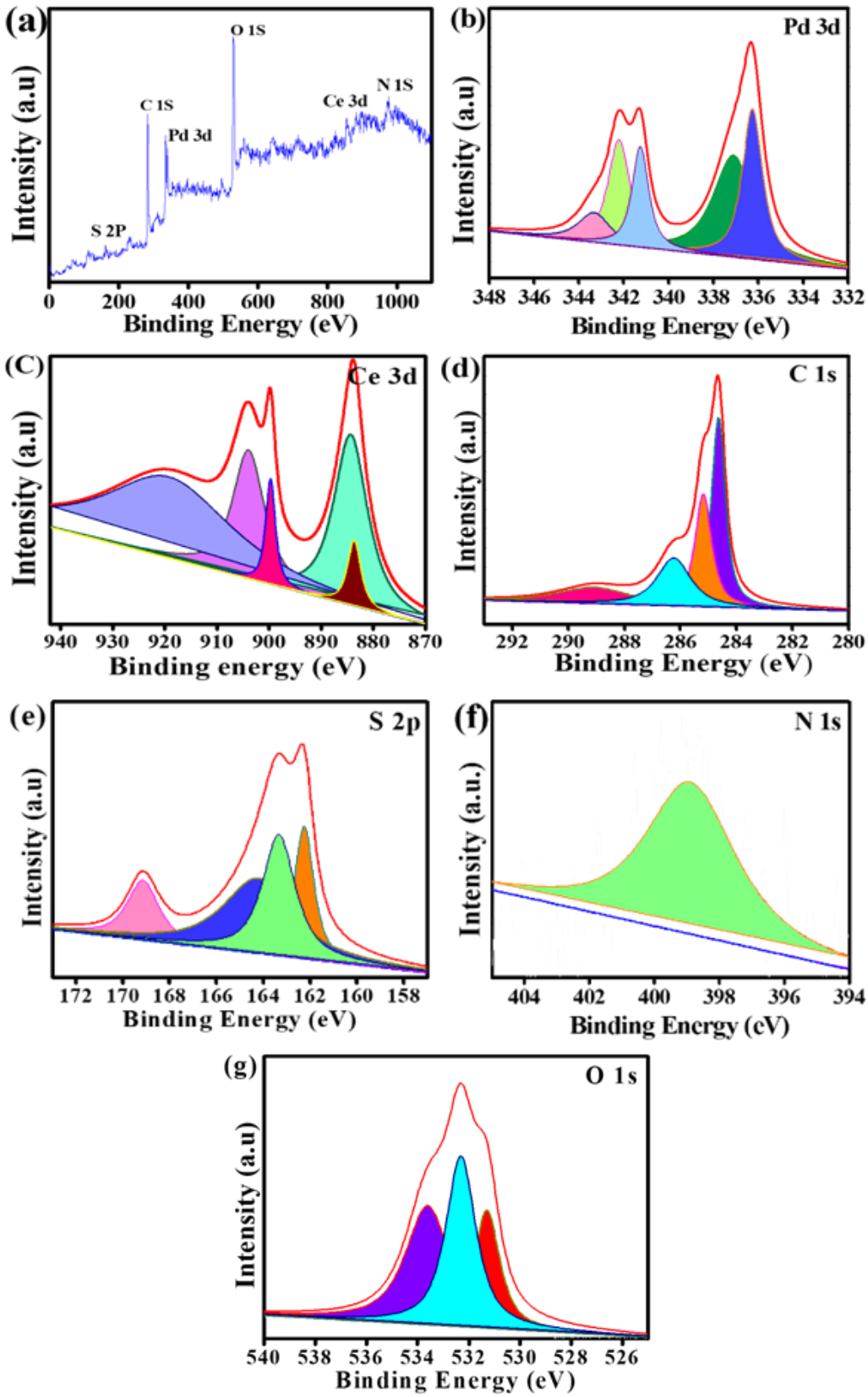

Figure 3: XPS plot for Pd/CeO_2/N, S-rGO nanostructure (a) Pd/CeO_2/N,S-rGO; (b) Pd3d; (c) Ce3d; (d) C1s; (e) S 2P; (f) N 1S; (g).O 1s

3.4 High Transmission Electron Microscope (HRTEM)

The HRTEM and FESEM analysis was conducted to study the morphology and microstructure of the best performing electro catalyst Pd/CeO_2-N,S-rGO. The FE-SEM analysis in Fig. 4 (a&b) shows the particles are randomly distributed and no agglomeration. The HRTEM images (Fig. 4 c) shows uniform dispersion of Pd nanoparticle on CeO_2-N,S-rGO. The result suggests the nano composite was formed by transferring an electron from Pd nanoparticle to CeO_2 by reverse spillover effect (Lykhach et al., 2019). The EDX spectra in Fig.4 (d) confirms the presence of Pd, Ce, O, N, C, S in the Pd/CeO_2-N, S-rGO.

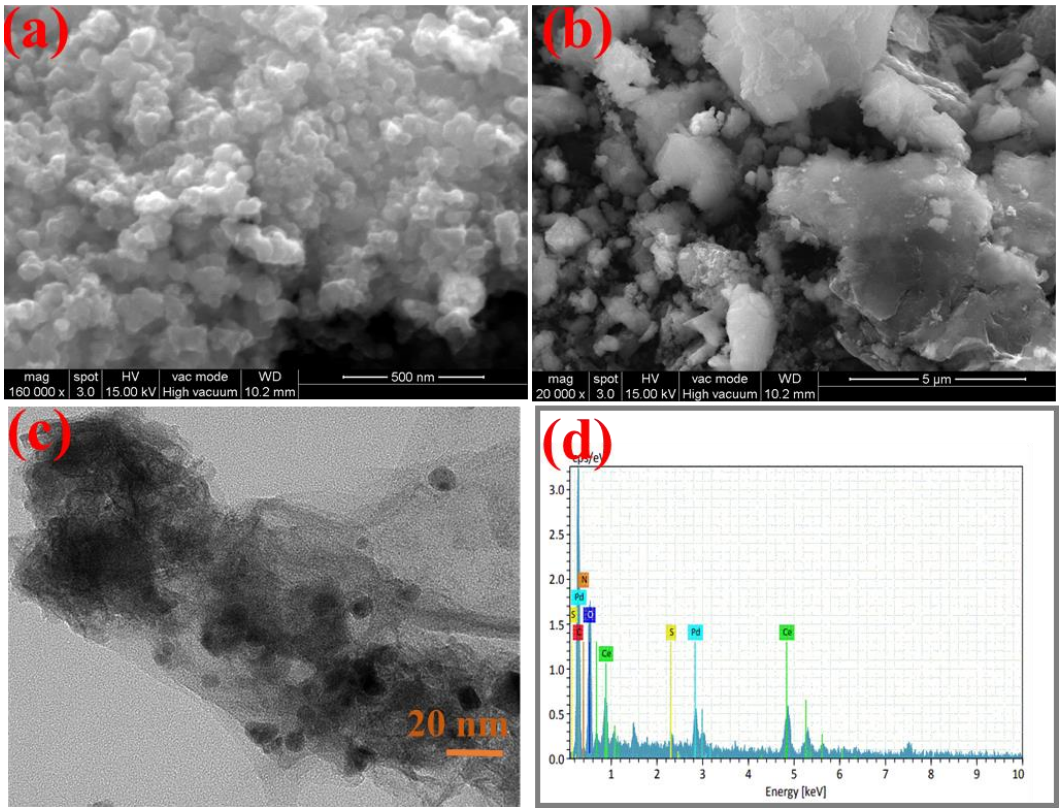

Figure 4: (a) & (b) FESEM, (c) TEM image and (d) EDX spectra of Pd/CeO_2-N, S-rGO

3.5 Electrochemical Activity Measurement

The electrochemical hydrogen evolution reaction (HER) activity was investigated in 0.5 M H_2SO_4. Fig. 5 shows the iR-corrected polarization curve (LSV) of the synthesized electro catalyst. The CeO_2/N, S-rGO exhibit very weak activity with an onset potential of 261 mV and over potential of 197 mV at 10 mA cm^{-2}. Pd/CeO_2/N, S-rGO demonstrates the highest HER activity with onset potential 45 mV, overpotential of 75 mV at 10 mA cm^{-2}, which could be resulted from the strong interaction between Pd and CeO_2. Comparatively, Pd-Ni/CeO_2/N, S-rGO exhibited lower HER activity than Pd/CeO_2/N, S-rGO with an onset potential of 75 mV, over potential of 105 mV at 10 mA cm^{-2} under the same condition. This could be related to the availability of less active sites in Pd-Ni/CeO_2/N,S-rGO for electro catalytic reaction.

The Tafel slope value derived from the polarization curve indicate the rate of increase in current against over potential the increase in current density with small change in over potential signifies faster electro catalyst kinetics and it also used to estimate hydrogen desorption mechanism from the electrocatalyst's surface. Accordingly, Pd/CeO_2/N, S-rGO reveals 49 mV dc^{-1}, Pd-Ni/CeO_2/N, S-rGO 64 mV dc^{-1} and CeO_2/N, S-rGO 101 mV dc^{-1}.

Therefore, the hydrogen evolution follows the Volmer-Heyrovsky mechanism in which hydrogen desorption was the rate-determining step (Cardoso et al., 2016).

The EIS was measured in 0.5 M H_2SO_4 with a frequency range from 100 kHz to 0.01 HZ and displayed in Fig. 5 (e) the smallest semicircle obtained for Pd/CeO_2/N, S-rGO indicates the high kinetics of HER resulted from strong metal-support interactions.

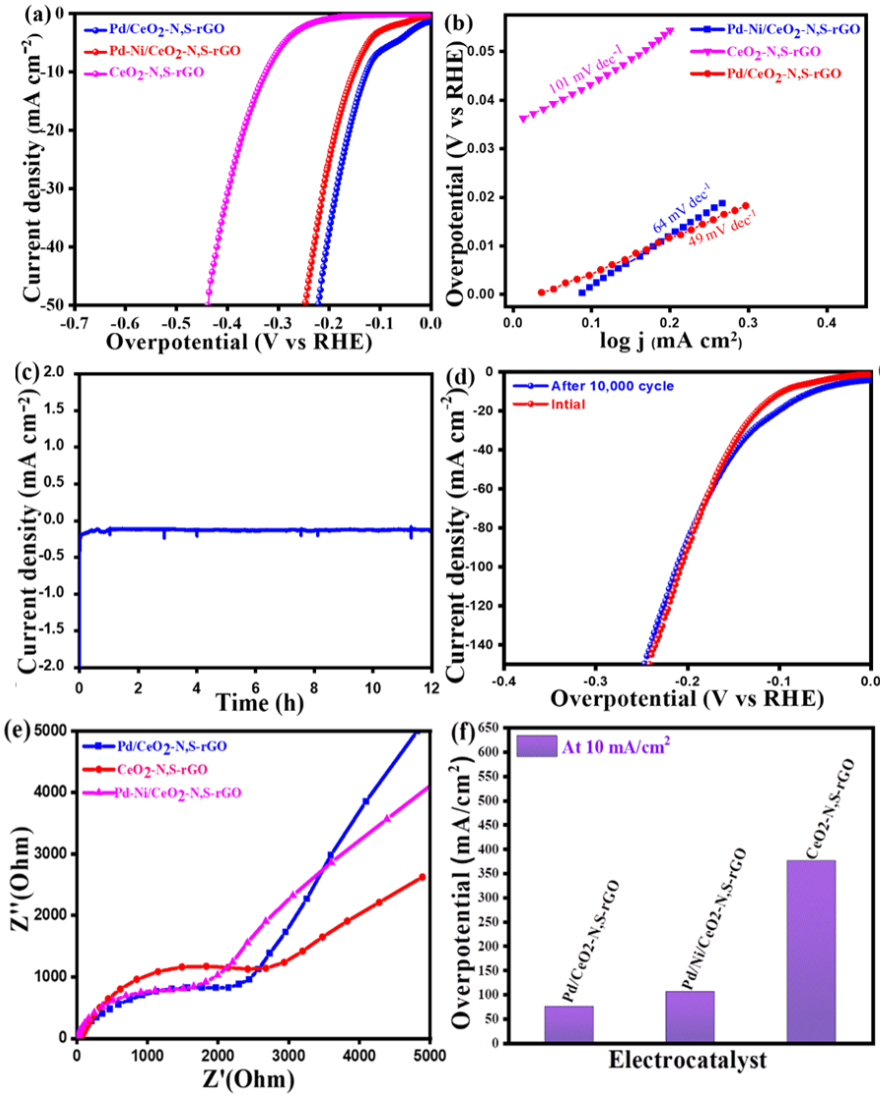

Figure 5: (a) HER polarization curves forPd/CeO_2/N,S-rGO,Pd-Ni/CeO_2/N,S-rGO and CeO_2/N,S-rGO in 0.5 M H_2SO_4 with scan rate 5 mVs^{-1}. (b) The corresponding Tafel plot derived from the polarization curve, (c) and (d) are the stability test of Pd/CeO_2/N, S-rGOby Linear Sweep Voltammetry (LSV) and chronoamperometry respectively (e) electrochemical impedance spectroscopy of the prepared catalysts (f) Comparison of overpotential at 10 mA for the prepared catalysts.

3.6 Electrochemical measurement of oxygen evolution reaction activity

Oxygen evolution reaction (OER) involves a complex process in which the O-H bond is broken, and the O = O bond is formed through the transfer of four electrons. The OER activity of the synthesized electro catalysts evaluated by using linear sweep voltammetry (LSV) in N_2-saturated 1M KOH solution at scan rate of 5 mVs^{-1}. As

displayed in Fig.6. $Pd/CeO_2/N$, S-rGO demonstrate lower over potential and Tafel slop value 0.24 V at 10 mA/cm^2 and 42 mv dec^{-1} respectively. The incorporation of Ni resulted less activity of OER compared to the former (0.29 V and 44 mv dec^{-1}) that could be due to the availability of less active site for electro chemical reaction. The least electrochemical activity observed for CeO_2/N, S-rGO (0.41 V and 78 mv dec^{-1}). Moreover the chronoamperometric stability study shows good stability for 12 h and EIS measurement was conducted in 0.1 M KOH with a frequency range from 100 kHz to 0.01 HZ and amplitude 5 mV. The small semicircle demonstrated by $Pd/CeO_2/N$, S-rGO shows faster electron transfer rate.

The physicochemical analysis result such as XRD, Raman, XPS revels strong interaction between palladium nanoparticles and CeO_2 that may affect the binding energy and the presence N,S-rGO favors the formation more active site for electro chemical reaction. The cumulative effect result higher electro catalytic activity of $Pd/CeO_2/N$,S-rGO towards hydrogen evolution and oxygen evolution reaction.

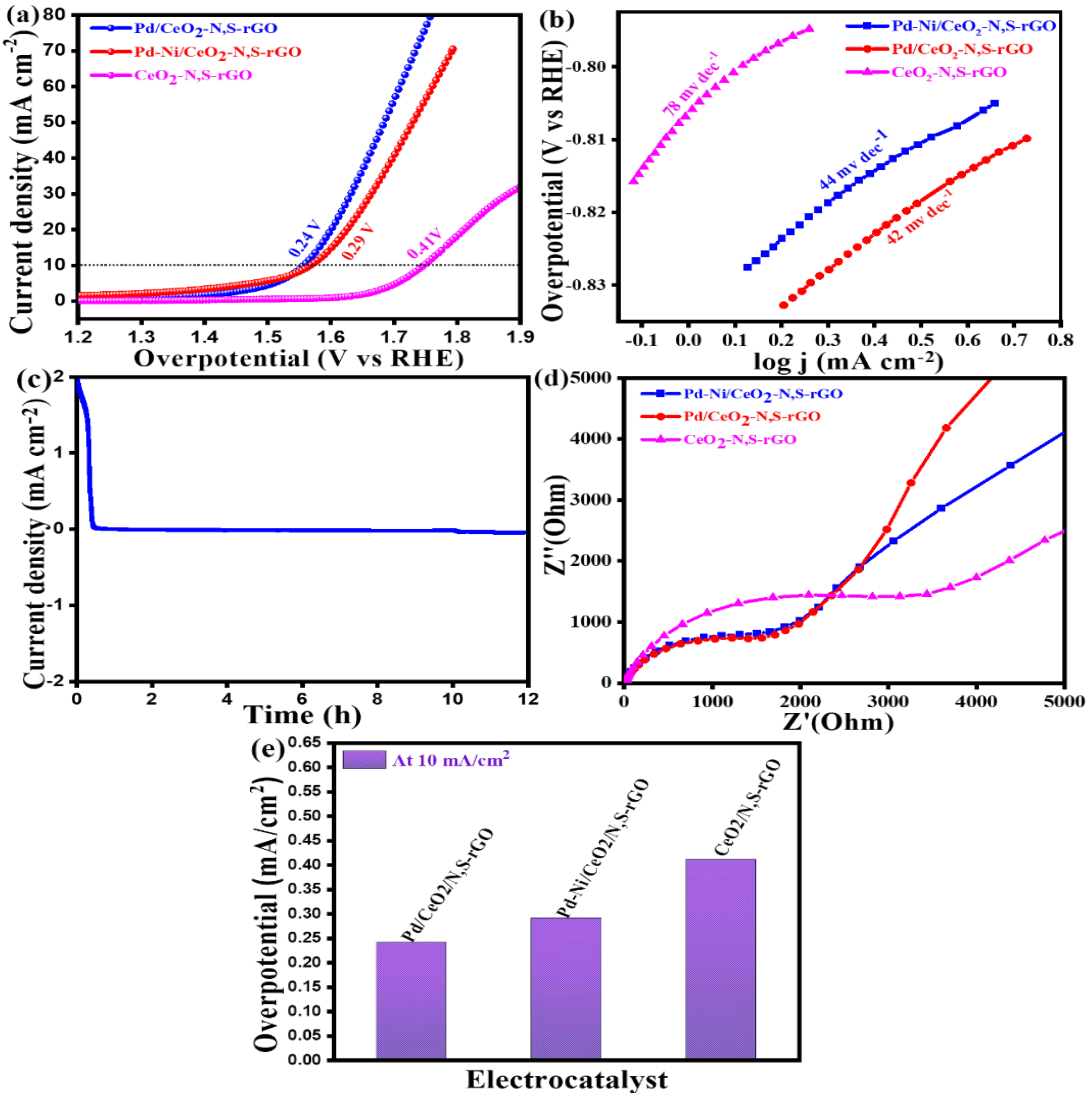

Figure 6: (a) OER polarization curves of the$Pd/CeO_2/N$,S-rGO, Pd-Ni/CeO_2/N,S-rGO, and CeO_2/N, S-rGOin 0.1 M KOH at a scan rate of 5 mVs^{-1}(The number marked in LSV curve indicate the over potential at 10 mA/cm^2).(b) The corresponding Tafel plot derived from the polarization curve, (c) the stability test of $Pd/CeO_2/N$, S-rGObyChronoamperometry for 12 h in 0.1 M KOH (d) Nyquist plot of electrochemical impedance spectroscopy of the prepared catalysts in 0.1 M KOH(e) Comparison of overpotential at 10 mA for the prepared catalysts.

Table 2 compares the electrochemical performance of the synthesized electro catalyst towards HER with other previously reported among the list $Pd/CeO_2/N,S$-rGO demonstrate lower potentials and Tafel slope value.

Table 2: Comparison of HER electrocatalytic performance of the electrocatalyst in 0.5 M H_2SO_4

Electro catalyst	Onset potential(mv)	Over potential(mv)	Tafel slope ($mv.dec^{-1}$)	Reference
$Pd/CeO_2/N,S$-rGO	64	75	49	This work
Pd-Ni/CeO_2/N, S-rGO	69	105	64	This work
GO-$Au_{48}Pd_{52}$	80	130	149	Zeid and Ibrahem (2017)
rGO-$Fe_{48}Pd_{52}$	140	250	370	Zeid and Ibrahem (2017
PdNiMo film	85	110	227	Huang et al.(2017)
Co-Pd/N,S-rGO	94	58	54	Woldetinsay et al.(2020b)
Pd16-CoCNTs	-	120	79	Huang et al.(2017)
Pd/MoS_2/CB		78	57	Woldetinsay et al.(2021)
Pd/g-C_3N_4		105	69	Woldetinsay et al.(2021)

4. CONCLUSION

In this study, we synthesized $Pd/CeO_2/N,S$-rGO, Pd-Ni/CeO_2/N,S-rGO and $CeO_2/N,S$-rGO successfully by hydrothermal and chemical reduction method. The $Pd/CeO_2/N,S$-rGO, demonstrates a higher electro catalytic activity with lower over potential (75 mV) and Tafel slope value(49 mV/dec) than Pd-Ni/CeO_2/N, S-rGO, and CeO_2/N, S-rGO. The observed decrease in electro catalytic activity after incorporation of Ni in Pd/CeO_2/N, S-rGO, could be due to decrease active cite for electrochemical reactions. The XRD, Raman, XPS, HRTEM result demonstrate modification of the surface electronic structure that might have potential contribution to enhance the catalytic activity towards hydrogen evolution reaction and oxygen evolution reactions. Furthermore, the coexistence of CeO_2 and N,S-rGO in the support was beneficial for anchoring and stabilizing the metal nanoparticles. It is also evident that interaction exists in the nano composite metals with the support. This study contributes investigations for the further development of improved electro catalysts of non-Pt based through Pd/Metal oxide interface.

ACKNOWLEDGEMENTS

The authors acknowledge the financial support from Jimma University Institute of Technology, Jimma, Ethiopia.. The authors also acknowledge Department of Science and Technology-Science and Engineering Research Board [DST-SERB; No. ECR/2016/002025], India through Early Career Research Awarded toSRM Institute of Science and Technology for the provision of research facilities and chemicals to carry out this research work.

REFERENCES

Akbayrak, S., Tonbul, Y. & Özkar, S. (2017): Nanoceria Supported Palladium(0) Nanoparticles: Superb Catalyst in Dehydrogenation of Formic Acid at Room Temperature. Appl.Catal. B: Env., 1-31.

Antolini, E., Salgado, J. R. C. & Gonzalez, E. R. (2006): The stability of Pt–M (M= first row transition metal) alloy catalysts and its effect on the activity in low temperature fuel cells A literature review and tests on a Pt–Co catalyst. J. Power Sources,160: 957–968.

Axon, S. A. & Casci, J. L. (2007): Recycling ofSpent Catalysts Containing Base Metals. Metal, 1871.

Bai, S., Wang, C., Deng, M., Gong, M., Bai, Y., Jiang, J. & Xiong, Y. (2014): Surface Polarization Matters: Enhancing the Hydrogen-Evolution Reaction by Shrinking Pt Shells in Pt–Pd–Graphene Stack Structures. Angew. Chem. Int. Ed. , 53: 1 – 6.

Bard, A. J. & Fox, M. A. (1995): Artificial Photosynthesis: Solar Splitting of Water to Hydrogen and Oxygen. Acc. Chem. Res., 28: 141-145.

Bhowmik, T., Kundu, M. K. & Barman, S. (2016): Palladium Nanoparticle-Graphitic Carbon Nitride Porous Synergistic Catalyst for Hydrogen Evolution/Oxidation Reactions in Broad Range of pH and Correlating its Catalytic Activity with Measured Hydrogen Binding Energy. ACS Catal., 1-16.

Cardoso, J. A. S. B., Amaral, L., Metin, O., Cardoso, D. S. P., Sevim, M., Sener, T., Sequeira, C. A. C. & Santos, D. M. F. (2006): Reduced graphene oxide assembled Pd-based nanoalloys for hydrogen evolution reaction. Int. J. Hydrog. energy, I-6.

Cardoso, J. A. S. B., Amaral, L., Metin, O., Cardoso, D. S. P., Sevim, M., Sener, T., Sequeira, C. A. C. & Santos, D. M. F. (2016): Reduced graphene oxide assembled Pd-based nanoalloys for hydrogen evolution reaction. Int. J.Hydrog. Energy, I-10.

Dresselhaus, M. S. & Thomas, I. L. (2001): Alternative energy technologies Nature, 414, 332-337.

Fan, A., Zheng, P., Qin, C., Zhang, X., Dai, X., Ren, D., Fang, X., Luan, C. & Yang, J. (2020): Few-layer MoS2 and Pt Nanoparticles Co-anchored on MWCNTs for Efficient Hydrogen Evolution over a Wide pH Range. Electrochim. Acta, 1-35.

Fan, J., Qi, K., Zhang, L., Zhang, H., Yu, S. & Cui, X. (2017): Engineering the Pt/Pd Interfacial Electronic Structures for Highly-efficient Hydrogen Evolution and Alcohol Oxidation. ACS Appl. Mater. Interfaces, 1-21.

Fan, L.-Z., Chen, T.-T., Song, W.-L., Li, X. & Zhang, S. (2014): High nitrogen-containing cotton derived 3D porous carbon frameworks for high-performance supercapacitors. Scientific RepoRts, 5:15388.

Gao, T., Yang, J., Nishijima, M., Miller, H. A., Vizza, F., Gu, H., Chen, H., Hu, Y., Jiang, Z., Wang, L., Shuai, L., Qiu, M., Lei, C., Zhang, A., Hou, Y. & He, Q. (2018): Evidence of the Strong Metal Support Interaction in a Palladium-Ceria Hybrid Electrocatalyst for Enhancement of the Hydrogen Evolution Reaction. J. Electrochem. Soc., 165: F1147-F1153.

Gao, Z., Wang, J., Li, Z., Yang, W., Wang, B., Hou, M., He, Y., Liu, Q., Mann, T., Yang, P., Zhang, M. & Liu, L. (2011): Graphene Nanosheet/Ni2+/Al3+ Layered Double-Hydroxide Composite as a Novel Electrode for a Supercapacitor. Chem. Mater, 23: 3509–3516.

Ge, M., Cao, C., Huang, J., Li, S., Chen, Z., Zhang, K., Al-Deyab, S. S. & Lai, Y. (2012): A Review of One-dimensional TiO2 Nanostructured Materials for Environmental and Energy Applications. J. Mater. Chem. A, 136.

Greeley, J., F.Jaramillo, T., Bonde, J., Chorkendorff, I. & Nørskov, J. K. (2006): Computational high-throughput screening of electrocatalytic materials for hydrogen evolution. Nat. mater. , 5: 909-913.

Guo, S., Dong, S. & Wang, E. (2013): Pt/Pd bimetallic nanotubes with petal-like surfaces for enhanced catalytic activity and stability towards ethanol electrooxidation. Energy Environ. Sci., 3: 1307–1310.

He, L., Liang, B., Li, L., Yang, X., Huang, Y., Wang, A., Wang, X. & Zhang, T. (2015): Cerium-Oxide-Modified Nickel as a Non-Noble Metal Catalyst for Selective Decomposition of Hydrous Hydrazine to Hydrogen. ACS Catal., 5: 1623−1628.

Huang, B., Chen, L., Wang, Y., Ouyang, L. & Ye, J. (2017): Paragenesis of palladium-cobalt nanoparticle in nitrogen-rich carbon nanotubes as bifunctional electrocatalyst for hydrogen evolution reaction and oxygen reduction reaction. Chem. Eur. J., 1-30.

Ji, J., Li, Y., Fu, W., Cui, Z., Shen, J. & Ye, M. (2017): Self-assembled three-dimensional Pd/MoS2/reduced graphene oxide nanocatalyst: A case for homogeneous leaching mechanism. J. Colloid Inter. Sci., 505: 983–994.

Kayama, T., Yamazaki, K. & Shinjoh, H. (2010): Nanostructured Ceria-Silver Synthesized in a One-Pot Redox Reaction Catalyzes Carbon Oxidation. J. Am. Chem. Soc., 132: 13154–13155.

Liao, H., Wei, C., Wang, J., Fisher, A., Sritharan, T., Feng, Z. & Xu, Z. J. (2017): A Multisite Strategy for Enhancing the Hydrogen Evolution Reaction on a Nano-Pd Surface in Alkaline Media. Adv. Energy Mater, 1701129.

Liu, T., Qingtaowang, Yan, B., Zhao, M., Li, W. & Bie, H. (2015): Ru Nanoparticles Supported on MIL-101 by Double Solvents Method as High-Performance Catalysts for Catalytic Hydrolysis of Ammonia Borane. J.Nanomater., 1-6.

Lykhach, Y., Kubát, J., Neitzel, A., Tsud, N., Vorokhta, M., Skála, T., Dvoˇrák, F., Kosto, Y., Prince, K. C., Matolín, V., Johánek, V., Mysliveˇcek, J. & Libuda, J. (2019): Charge transfer and spillover phenomena in ceria-supported iridium catalysts: A model study. J. Chem. Phys., 151: 204703.

Mamontov, E. & Egami, T. (2000): Lattice Defects and Oxygen Storage Capacity of Nanocrystalline Ceria and Ceria-Zirconia. J. Phys. Chem. B, 104: 11110-11116.

Meier, J. C., Galeano, C., Katsounaros, I., Witte, J., Bongard, H. J., Topalov, A. A., Baldizzone, C., Mezzavilla, S., Schüth, F. & Mayrhofer, K. J. J. (2014): Design criteria for stable Pt/C fuel cell catalysts. Beilstein J. Nanotechnol., 5: 44–67.

More, K. L., Perry, K. A., Chi, M. & Reeves, K. S. (2010): Carbon Support Structural Degradation Observed in Aged PEM Fuel Cells. Electrochem. Soc., 1-2.

Noto, V. D., Negro, E., Polizzi, S., Agresti, F. & Giffin, G. A. (2012): Synthesis–Structure–Morphology Interplay of Bimetallic "Core–Shell" Carbon Nitride Nano-electrocatalysts. ChemSusChem, 5: 2451 – 2459.

Ojani, R., Valiollahi, R. & Raoof, J.-B. (2014): Comparison between graphene supported Pt hollow nanospheres and graphene supported Pt solid nanoparticles for hydrogen evolution reaction. Energy Environ. Sci., 1-6.

Paoli, E. A., Masini, F., Frydendal, R., Deiana, D., Schlaup, C., Malizia, M., Hansen, T. W., Horch, S., Stephens, I. E. L. & Chorkendorff, I. (2014): Oxygen evolution on well-characterized massselected Ru and RuO2 nanoparticles. Chem. Sci., 1-7.

Park, K.-W., Choi, J.-H. & Sung, Y.-E. (2003): Structural, Chemical, and Electronic Properties of Pt/Ni Thin Film Electrodes for Methanol Electrooxidation. J. Phys. Chem. B, 107: 5851-5856.

Perini, L., Durante, C., Favaro, M., Perazzolo, V., Agnoli, S., Schneider, O., Granozzi, G. & Gennaro, A. (2014): Metal-Support Interaction in Platinum and Palladium Nanoparticles Loaded on Nitrogen Doped Mesoporous Carbon for Oxygen Reduction Reaction. ACS Appl. Mater. Interfaces, 1-34.

Ratso, S., Kruusenberg, I., Joost, U., Saar, R. & Tammeveski, K. (2016): Enhanced oxygen reduction reaction activity of nitrogen-doped graphene/multi-walled carbon nanotube catalysts in alkaline media. Int. J.Hydrog. ENergy, 1-10.

Sarkar, S. & Peter, S. C. (2018): An Overview on Pd Based Electrocatalysts for Hydrogen Evolution Reaction. Inorg.Chem. Front., 1-48.

Tedsree, K., Chan, C. W. A., Jones, S., Cuan, Q., Li, W.-K., Gong, X.-Q. & Tsang, S. C. E. (2011): 13C NMR Guides Rational Design of Nanocatalysts via Chemisorption Evaluation in Liquid Phase. Sci., 332: 224-228.

Trimpalis, A., Giannakakis, G., Cao, S. & Flytzani-Stephanopoulos, M. (2019): NiAu single atom alloys for the selective oxidation of methacrolein with methanol to methyl methacrylate. Catal. Today 19: 30169-5.

Urayama, T., Mitsudome, D. T., Maeno, D. Z., Mizugaki, D. T., Jitsukawa, P. D. K. & Kaneda, P. D. K. (2016): Green One-Step Synthesis of Core-Shell Nanocomposites in Water and Their Catalytic Application to Chemoselective Hydrogenations. Chem. Eur. J., 1-16.

Vinayan, B. P., Nagar, R., Rajalakshmi, N. & Ramaprabhu, S. (2012): Novel Platinum–Cobalt Alloy Nanoparticles Dispersed on Nitrogen-Doped Graphene as a Cathode Electrocatalyst for PEMFC Applications. Adv. Funct. Mater., 1-6.

Vinayan, B. P., Nagar, R. & Ramaprabhu, S. (2013): Solar light assisted green synthesis of palladium nanoparticle decorated nitrogen doped graphene for hydrogen storage application. J. Mater. Chem. A, 1-29.

Walter, M. G., Warren, E. L., Mckone, J. R., Boettcher, S. W., Mi, Q., Santori, E. A. & Lewis, N. S. (2010): Solar Water Splitting Cells. Chem. Rev. , 110: 6446–6473.

Wang, G., Liu, J., Sui, Y., Wang, M., Qiao, L., Du, F. & Zou, B. (2019): Palladium structure engineering induced by electrochemical H intercalation boosts hydrogen evolution catalysis. J. Mater. Chem. A, 7: 14876.

Wang, J., Tan, H., Jiang, D. & Zhou, K. (2017): Enhancing H2 evolution by optimizing H adatom combination and desorption over Pd nanocatalyst. Nano Energy, 33: 410–417.

Wang, K., Yao, Q., Qing, S. & Lu, Z.-H. (2013a): La(OH)3 nanosheet supported CoPt nanoparticles: Highly efficient and magnetically recyclable catalyst for hydrogen production from hydrazine in aqueous solution. J. Mater. Chem. A, 1-9.

Wang, X., Liu, D., Song, S. & Zhang, H. (2012): Synthesis of highly active Pt–CeO2 hybrids with tunable secondary nanostructures for the catalytic hydrolysis of ammonia borane. Chem. Commun, 48:10207–10209.

Wang, X., Liu, D., Song, S. & Zhang, H. (2013b): Pt@CeO2 Multicore@Shell Self-Assembled Nanospheres: Clean Synthesis, Structure Optimization and Catalytic Applications. J. A. Chem. Soc., 1-34.

Wang, Y., Liu, G., An, C., Li Li, F. Q., Wang, Y., Jiao, L. & Yuan, H. (2014): Bimetallic NiCo Functional Graphene: An Efficient Catalyst for HydrogenStorage Properties of MgH2. Chem. Asian J., 9: 2576 – 2583.

Wind, J., Spa¨H, R., Kaiser, W. & Bo¨Hm, G. (2002): Metallic bipolar plates for PEM fuel cells. J. Power Sources,105: 256–260.

Woldetinsay, M., Refera, T., Olu, F. & Maiyalagan, T. (2020a): Synergetic effect between MoS2 and N, S- doped reduced graphene oxide supported palladium nanoparticles for hydrogen evolution reaction. Mater. Chem. Phys. , 251: 123106.

Woldetinsay, M., Soreta, T. R., Maiyalagan, T. & Femi, O. (2020b): Electrocatalytic Investigation of M@Pd (M=Ni, Co, Cu) Core-Shell Nanostructure Supported on N, S-Doped Reduced Graphene Oxide towards Hydrogen and Oxygen Evolution Reaction. ChemistrySelect, 5: 9989–9998.

Woldetinsay, M., Soreta, T. R., Maiyalagan, T. & Femi, O. E. (2021): Effect of Support Material on the Electrocatalytic activity of PdNP toward Hydrogen Evolution reaction. Mater. Res. Express in press, 1-17.

Xu, C., Wang, H., Shen, P. K. & Jiang, S. P. (2007): Highly Ordered Pd Nanowire Arrays as Effective Electrocatalysts for Ethanol Oxidation in Direct Alcohol Fuel Cells. Adv. Mater., 19: 4256–4259.

Yu, H., Wang, T., Wen, B., Lu, M., Xu, Z., Zhu, C., Chen, Y., Xue, X., Sun, C. & Cao, M. (2012): Graphene/polyaniline nanorod arrays: synthesis and excellent electromagnetic absorption properties. J. Mater. Chem. A, 22: 21679.

Zeid, E. F. A. & Ibrahem, I. A. (2017): Preparation, characterization and electrocatalytic activity for oxygen reduction reaction in PEMFCs of bimetallic PdNi nanoalloy. Mater Renew Sustain Energy, 1-7.

Zhang, L., Fang, Q., Huang, Y., Xu, K., Chu, P. K. & Ma, F.(2018): Oxygen Vacancy Enhanced Gas-Sensing Performance of CeO2/Graphene Heterostructure at Room Temperature. Analytical Chem., 90: 9821-9829.

Zhang, Z., Lu, Z.-H. & Chen, X. (2015): Ultrafine Ni−Pt Alloy Nanoparticles Grown on Graphene as Highly Efficient Catalyst for Complete Hydrogen Generation from Hydrazine Borane. ACS Sustain. Chem. Eng, 1-7.

Zhou, W. J., Li, W. Z., Song, S. Q., Zhou, Z. H., Jiang, L. H., Sun, G. Q., Xin, Q., Poulianitis, K., Kontou, S. & Tsiakaras, P. (2004): Bi- and tri-metallic Pt-based anode catalysts for direct ethanol fuel cells. J. Power Sources, 131: 217–223.

Zou, X. & Zhang, Y. (2015): Noble metal-free hydrogen evolution catalysts for water splitting. Chem. Soc. Rev, 44:5148.

Metal Oxide Semiconductors Nonmaterials Electron Transport Blaiyer to Improve the Interface in the Planar Perovskite Solar Cells

Wegene Lema Lachore[1,*], Fekadu Gashaw Hone[2,*], Dinsefa Mensur Andoshe[3], Mulualem Abebe Mekonnen[1]

[1]*Faculty of Materials Science and Engineering, Jimma Institute of Technology, Jimma University, P.O.Box 1041, Jimma, Ethiopia*
[2]*Department of Physics, Addis Ababa University, P.O.Box 1176, Addis Ababa, Ethiopia*
[3]*Department of Materials Science and Engineering, Adama Science and Technology University, P.O.Box 1888, Adama, Ethiopia*
**Corresponding author, e-mail: fekeye@gmail.com or wegekx@gmail.com*

ABSTRACT

In this study, we investigate the influence of a bilayer electron transport included of ZnO/SnO_2 , ZnO/WO_3 , and SnO_2/WO_3 on the interface between electron transport layers (ETLs) and perovskite layers to reduce energy loss in planar perovskite solar cells (P-PSCs).The structural, optical, and electrical properties, as well as the surface morphology, of perovskitethin film on different ETLs were investigated systematically by various characterization techniques. Impedance analysis of charge dynamics with PSC and without on metal oxide (MOs) were also studies. The X-ray diffraction (XRD) study confirmed that the prepared sample had a tetragonal rutile crystal structure for perovskite thin film on differentETLs. UV-visible spectra analysis revealed that perovskitethin films on various ETLs almost identical absorption onset at 752 nm were observed. The photoluminescence (PL) spectra study revealed that perovskite thin film on various ETLsan emissive band peaked at around 781 nm. The emission of the perovskite was quenched by 35.8%, for $ZnO/MAPbI_3$ to 72.8 % for ZnO/WO_3 /$MAPbI_3$ to respectively. I–V studies confirmed that the prepared bilayer and singly layer had a good ohmic contact behavior and the resistivity decreased significantly from 128.87 Ω for WO_3 to 112.49 Ω for ZnO/WO_3 thin film respectively. These results revealed that bilayer electron transport has better charge transfer and charge collection properties, as well as suppressing trap-assisted recombination at the P-PSC interface. Overall, the results indicate that a bilayer of electron transport layers is an effective method for improving the interface and fabricating efficient planar perovskite solar cells.

Keywords: *Solar cells, Perovskite, Electron transport bilayer, Charge dynamics*

1. INTRODUCTION

Organic-inorganic hybrid perovskite solar cells (PSCs) were first introduced by Miyasaka in 2009, and their low cost, easy fabrication, and outstanding photovoltaic properties, such as excellent light harvesting, high charge carrier mobility, and long diffusion length, have had a significant impact on solar energy research [1-5]. Today, the highest efficiency of PSCs have achieved certified power conversion efficiencies (PCE) exceeding 25.5% [6]. In a typical structure, PSCs have a working electrode (cathode), electron transport layer (ETL), perovskite layer, hole-transport layer (HTL), and counter electrode (anode) [7]. The ETL and HTL play key roles in photovoltaic performance because they are capable of collecting photon-generated electrons and holes from perovskites and delivering them to the anode and cathode, respectively [8]. However, the regular (n-i-p type) device structure uses the two most common electron transport layer and the hole transport layer such as compact titanium dioxide (TiO_2) and spiro-OMeTAD. This electron transport layer has a good band alignment, but it has a low electron mobility, which results in insufficient charge separation at the perovskite layer interface [9].

A few solutions have been adopted to overcome the limits of TiO_2, such as doping TiO_2 with inorganic elements such as Y, Mg, Li, Zn etc and passivation of TiO_2 surfaces using reduced graphene oxide and PCBM [10–20]. In fact, none of these procedures are sufficient to create a perfect planar perovskite device. However, SnO_2 as an ETL in planar PSCs has recently emerged as a viable alternative to TiO_2. The benefits of SnO_2 ETL features such as good charge extraction, high carrier mobility, low temperature procedure, and appropriate band alignment with perovskite absorber layer allow planar PSCs to function better [21,22]. The typical hysteresis as well as high PCE concerns can be handled using SnO_2 as an ETL. WO_3 is a promising candidate for the creation of PSCs in addition to TiO_2, ZnO, and SnO_2. WO_3 is an n-type material with electron mobility of 10–20 cm^2/V s that is in the middle of TiO_2 and ZnO [23, 24]. The optical band gap of WO_3 ranges from 2.7 to 3.2 eV depending on different crystalline structures [25]. Furthermore, WO_3 has high transmission in the visible region and excellent chemical stability

which is better than that of ZnO [26]. After surveying previous literatures, we notice that electron transporting WO_3 is less reported in the area of PSCs. However, they created an interlayer between electron-transporting and perovskite layers to minimize interfacial defects.

The high-concentration defects in the interfaces between the perovskite and charge-transporting layers significantly reduce the power conversion efficiency of the devices.The most crucial approach for addressing the aforementioned issues is bilayer electron transport, which is used to increase electrical conductivity, intrinsic carrier mobility, and decrease charge recombination and defects at the surface and grain boundaries. We introduce a bilayer electron transport structure based on methylammonium lead triiodide ($MAPbI_3$) for reducing energy loss in P-PSCs. To address these issues, no one still reported of compared studies charge dynamics three metal oxide semiconductors bilayer electron transport for planner perovskite solar cells. In this paper we developed a ZnO/SnO_2, ZnO/WO_3, SnO_2/WO_3 bilayer structure as a potential ETL for $MAPbI_3$-based PSCs through simple solution process method (sol-gel and co-precipitation method). The addition of SnO_2 and WO_3 between the ZnO and the perovskite active layer allows for more well-matched energy levels and efficient electron transport, resulting in a more advantageous energy level alignment and charge transport channel than a single ETL comprising ZnO, SnO_2, and WO_3. We prepared a perovskite solar cell with the following device architecture: glass/ITO/ZnO/SnO_2/$MAPbI_3$/MoO_3/Al, ITO/ZnO/WO_3/$MAPbI_3$/MoO_3/Al, ITO/SnO_2/WO_3/$MAPbI_3$/MoO_3/Al, ITO/WO_3/$MAPbI_3$/MoO_3/Al, and ITO/ZnO/$MAPbI_3$/MoO_3/Al. Furthermore, we used various microscopic and spectroscopic techniques to conduct extensive evaluations on all prepared devices.

2. MATERIALS AND METHODS

2.1 Experimental Procedure

The representative bilayer ZnO/WO_3/$MAPbI_3$ solar cell device was fabricated in the following way. The indium tin oxide (ITO,Pilkington, thickness of 1.1mm)-coated glass substrates were sonicated for 30 minutes and then cleaned with water, acetone, and isopropanol before being treated with UV-O_3. After the ZnO layer was formed by spin-coating onto the ITO-coated glass (3000 rpm for 30 s), the substrate was annealed at 150 °C for 1 hrs under an ambient environment. After the substrates were cooled to room temperatures the WO_3 solution via spin-coating at 3000 rpm for 30 s at top ZnO layer and annealing at 350^{O}C for 1 h under an ambient environment, the perovskite layer was spin-coated at 1000 rpm for 15 s. The spinning rate was increased up to 3000 rpm for the next 15 s, and 60μL chlorobenzene was dripped on top of the substrates. The dark-brown films were thermally annealed at 100°C for 10 min and MoO_3 as vapor-deposited under pressure (10^{-5}Torr). Finally, Al was evaporated under high vacuum ($<5 \times 10^{-6}$Torr). The active area was defined by shadow mask to be 0.04 cm^{-1}. This is a similar procedure to each six prepared device.

2.2 Characterizations

A Shimadzu-7000 X-ray diffractometer with CuK (= 1.5406) radiation was used to perform the structural investigation at room temperature. UV-Vis spectrophotometer analysis was carried out absorbance of the prepared samples using a wavelength ranging from 250 nm to 900 nm.. Thin film surface morphology was observed using field-emission scanning electron microscopy (FE-SEM). The photoelectric characteristics of the prepared PSC device, were measured using a solar simulator and a Keithley source metre unit (model-2400) under AM 1.5G (100Mwcm^{-2}) illumination in which the light intensity was carefully calibrated using a reference cell (filtered Silicon).

3. RESULTS AND DISCUSSION

3.1 The XRD Analysis

The prepared samples were analyzed by x-ray diffraction using the CuKα wavelength of 0.15406 nm. The XRD patterns show the phase compositions and crystallinities of the perovskite thin films and the perovskite thin films on different metal oxide ETLs. As shown in Fig. 1(a-g), all films exhibited the same dominant diffraction peaks from the (110) and (220) planes at around 14.02^{O}C and 28.31^{O}C, respectively, which are the peaks indicating a tetragonal structure of perovskite [28,29]. There is no obvious difference in the XRD patterns, suggesting that the crystal structures of the perovskite films are almost identical with ZnO, SnO_2, WO_3, ZnO/SnO_2, ZnO/WO_3 and SnO_2/WO_3 ETLs. The perovskite film exhibits a high degree of crystallinity and purity, and there is no phase apparent in the XRD data, such as PbI_2 or CH_3NH_3I. Moreover, the perovskite film on ITO/ZnO/SnO_2/$MAPbI_3$ and

ITO/ZnO/WO_3/$MAPbI_3$ architectures shows high intensity than other films due to highly crystalline and larger grainsizes as shown in Table 1. However, the crystallinity of perovskite films on the ZnO singly layered thin films decreased as compared to both ZnO/SnO_2 and ZnO/WO_3 bilayer thin films. This indicates that the surface morphology of the ZnO singly layered thin films has cracks and pinholes in the grains' boundaries, as shown in Fig.4a.The improved crystallinity of $MAPbI_3$ perovskite films due to the metal oxide (MOs) layer is indicated by the increased peak intensity [32].

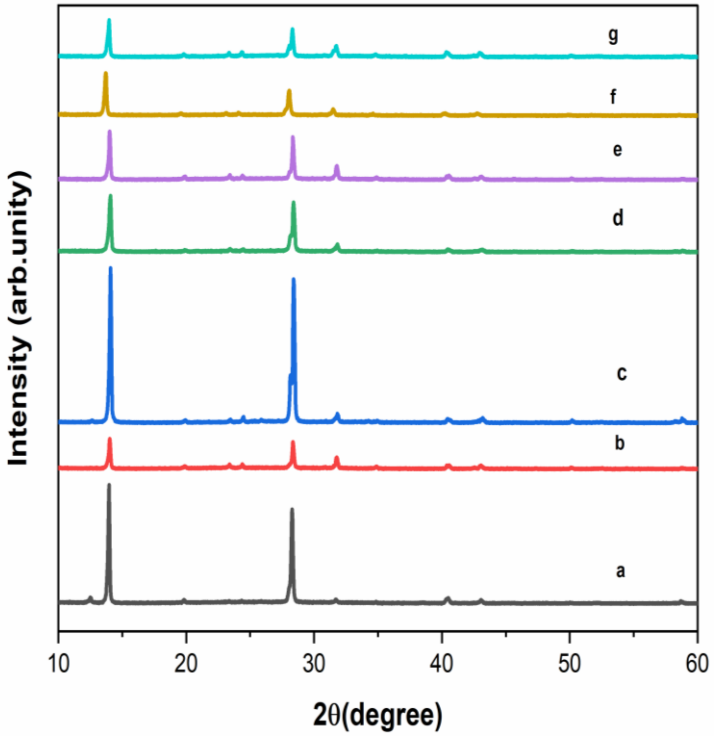

Figure1: The XRD patterns: (a) $MAPbI_3$; (b) ZnO/$MAPbI_3$; (c) SnO_2/$MAPbI_3$; (d) WO_3 /$MAPbI_3$; (e) ZnO/SnO_2/$MAPbI_3$; (f) ZnO/WO_3/$MAPbI_3$; (g) SnO_2/WO_3/$MAPbI_3$

The average crystallite size (D) of perovskite thin film and perovskite based ETLs thin films were calculated from (110) and (220) planar orientation using the Debye Scherer relation given in Eq. (1) [33].

$$D = \frac{K\lambda}{\beta \cos\theta} \quad \ldots\ldots\ldots\ldots\ldots\ldots\ldots\ldots\ldots\ldots (1)$$

where D is the average crystallite size of two dominate peak, K is constant for the shape factor equal to 0.9, and λ is the wavelength of X-ray used (CuKα, 0.15406 nm), β is the full width at half maximum of two dominant peaks, and θ is the angel of diffraction of two dominant peaks.

Table 1 lists the numerical values for the crystal size, micro-strain, and dislocation density of perovskite films on ETLs calculated from XRD spectral fitting results.

Table 1: Crystallographic parameters of the perovskite film on different metal oxide ETLs.

Thin film	Average Crystal size (nm)	Dislocation density ($\times 10^{-3}$) lines/m^2	Micro-strain ($\times 10^{-2}$)
$MAPbI_3$	46	0.4776	26.03
ZnO/ $MAPbI_3$	32	0.9536	36.80
SnO_2/ $MAPbI_3$	41	0.5943	28.99
WO_3/ $MAPbI_3$	32	0.9284	36.22
ZnO/SnO_2/ $MAPbI_3$	43	0.5347	28.00
ZnO/WO_3/ $MAPbI_3$	41	0.5828	29.43
SnO_2/WO_3/ $MAPbI_3$	35	0.8098	34.24

The dislocation density (δ), which is inversely proportional to the square of the usual crystalline size and is responsible for the mismatch in crystalline structure, by the following Eq. (2).

$$\delta = \frac{1}{D^2} \quad \ldots\ldots\ldots\ldots\ldots\ldots\ldots\ldots\ldots\ldots (2)$$

The micro-strain (ε) of perovskite based ETLs can be calculated by the following Eq. (3) [34].

$$\varepsilon = \frac{\beta}{4\,tan\theta} \quad \ldots\ldots\ldots\ldots\ldots\ldots\ldots\ldots\ldots\ldots (3)$$

where, β is FWHM and θ is diffraction angle.

Micro-strain is a measureable evaluation of the local change in atoms' equilibrium position at the crystalline lattice brought on by the presence of pores, point defects, or dislocations at the grain boundaries [35,36]. Higher levels of micro-strain and dislocation density in perovskite on ETLs suggest more crystalline disorientation [37]. Therefore, perovskite films on bilayer ZnO/SnO_2 and ZnO/WO_3 display stronger crystallinity, largercrystallite size, better crystallographic orientation, and lower dislocation density when compared to perovskite on single layers ZnO and WO_3, according to the XRD data and SEM micrograph.

3.2 UV-Visible Spectrophotometer Analysis

UV-Vis spectrophotometer used to study the absorbance and transmittance properties of perovskite thin film and the perovskite thin film on different metal oxides ETLs (Glass/$MAPbI_3$, Glass/ZnO/$MAPbI_3$, Glass/SnO_2/$MAPbI_3$, Glass/WO_3/$MAPbI_3$, Glass/ZnO/SnO_2/$MAPbI_3$, Glass/ZnO/WO_3/$MAPbI_3$, and Glass/SnO_2/WO_3/$MAPbI_3$). In Fig.3, the absorption of perovskite films shows a stronger light absorption at full wavelength ranging from 400-900 nm. The perovskite films on glass or different ETLs substrates show almost identical absorption spectra onset at 752 nm was observed, which are the characteristics of $MAPbI_3$ active layer.

The absorption intensity perovskite film on different metal oxides ETLs substrates in the visible region is also slightly better than $MAPbI_3$ films. We confirmed that these enhanced light absorption intensities are closely related to the disappearance of PbI_2 phase in perovskite active layer [30].

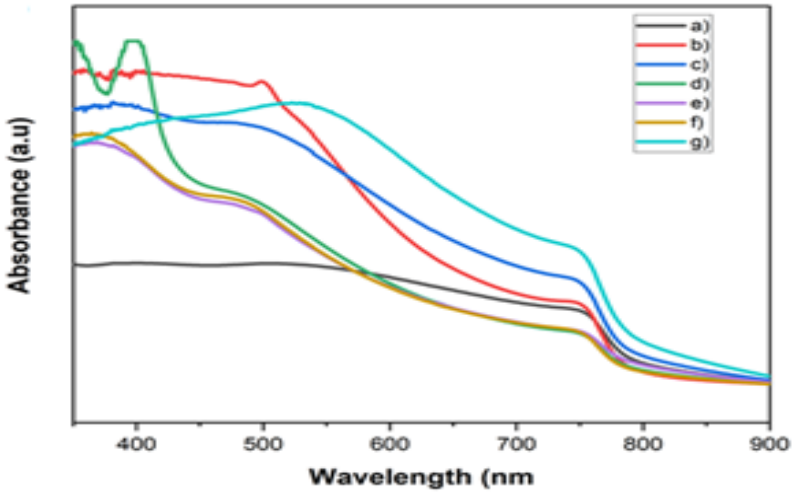

Figure 2: UV-vis- NIR absorption spectra of perovskite film deposited on different ETLs, (a) $MAPbI_3$, (b) ZnO/$MAPbI_3$, (c) SnO_2/$MAPbI_3$, (d) WO_3/$MAPbI_3$, (e) ZnO/SnO_2/$MAPbI_3$, (f) ZnO/WO_3/$MAPbI_3$, (g) SnO_2/WO_3/$MAPbI_3$

3.3 Photoluminescence (PL) Studies

The charge transport and charge recombination process of PSCs was studied using photoluminescence in order to completely evaluate the impacts of ZnO/SnO_2, ZnO/WO_3, SnO_2/WO_3ETL on device performance (PL). The excitation wavelength for PL measurement was of 485 nm. As shown in Fig. 3a, perovskite film exhibits an emissive emission peak around 781 nm. Fig.3 shows PL spectra of $ZnO/MAPbI_3$, $SnO_2/MAPbI_3$, $WO_3/MAPbI_3$ and $ZnO/SnO_2/MAPbI_3$, $ZnO/WO_3/MAPbI_3$, and $SnO_2/WO_3/MAPbI_3$ on glass substrate respectively. However, from the intensity of the peak, it can be estimated the quenching effect of perovskite on different ETLs such as ZnO for 35.8%, SnO_2 for 41.1%, WO_3 for 36.5% and 72.8% for ZnO/WO_3, 55.8% for ZnO/SnO_2, and 50.0% for SnO_2/WO_3, respectively. Therefore the bilayer $ZnO/SnO_2/MAPbI_3$, $ZnO/WO_3/MAPbI_3$, and $SnO_2/WO_3/MAPbI_3$ thin films exhibits a much stronger quenching effect then $ZnO/MAPbI_3$, $SnO_2/MAPbI_3$, and $WO_3/MAPbI_3$ singly layered thin films.

This indicates that $ZnO/SnO_2/MAPbI_3$, $ZnO/WO_3/MAPbI_3$, $SnO_2/WO_3/MAPbI_3$ double layer ETL has better charge extraction properties at ETL/perovskite interface than that of $ZnO/MAPbI_3$,$SnO_2/MAPbI_3$, and $WO_3/MAPbI_3$.

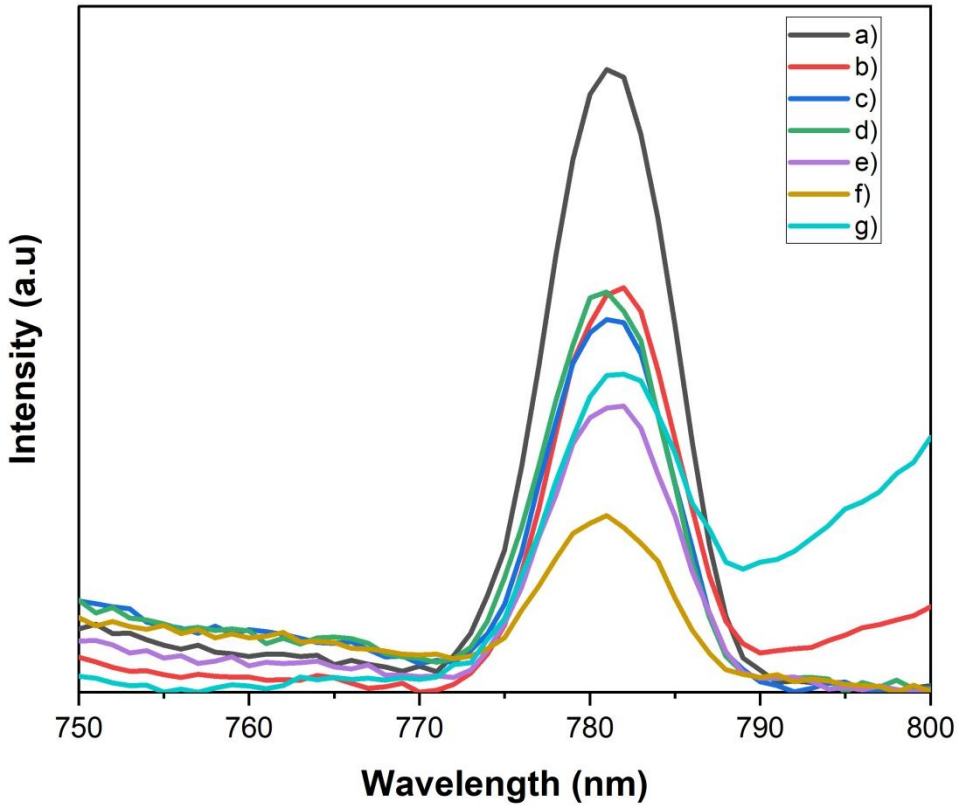

Figure 3: Steady-state photoluminescence of perovskite with ETLs a) $MAPbI_3$, b) ZnO,c) SnO_2, d)WO_3, e) ZnO/SnO_2, f) ZnO/WO_3, g) SnO_2/WO_3

3.4 Surface Morphology Analysis

The surface morphology of perovskite film plays important roles in the performances of planer perovskite solar cells. We investigated the surface morphology of glass substrate/ZnO, glass/$ZnO/MAPbI_3$, glass/$ZnO/SnO_2/MAPbI_3$, and glass/$ZnO/WO_3/MAPbI_3$ films using the scanning electron microscope and the images are shown in Fig.4a-d, respectively. The perovskite films deposited on ZnO/SnO_2 bilayer electron transport with a few pinholes and aggregates are observed on the surface when we compare them with the single electron transport layer.Furthermore, the perovskite films on the ZnO/WO_3 thin film bilayer have a smooth and uniform

surface morphology without any pinholes or cracks. This indicates perovskite film on ZnO/SnO_2 and ZnO/WO_3 thin film's bilayer to prevent trapping of electrons and direct contact of ITO electrode and the perovskite layer. The perovskite films with high coverage and quality can effectively absorb and utilize light, which in turn facilitates charge excitation, contributing to the photoelectric conversion and photovoltaic performance [27].

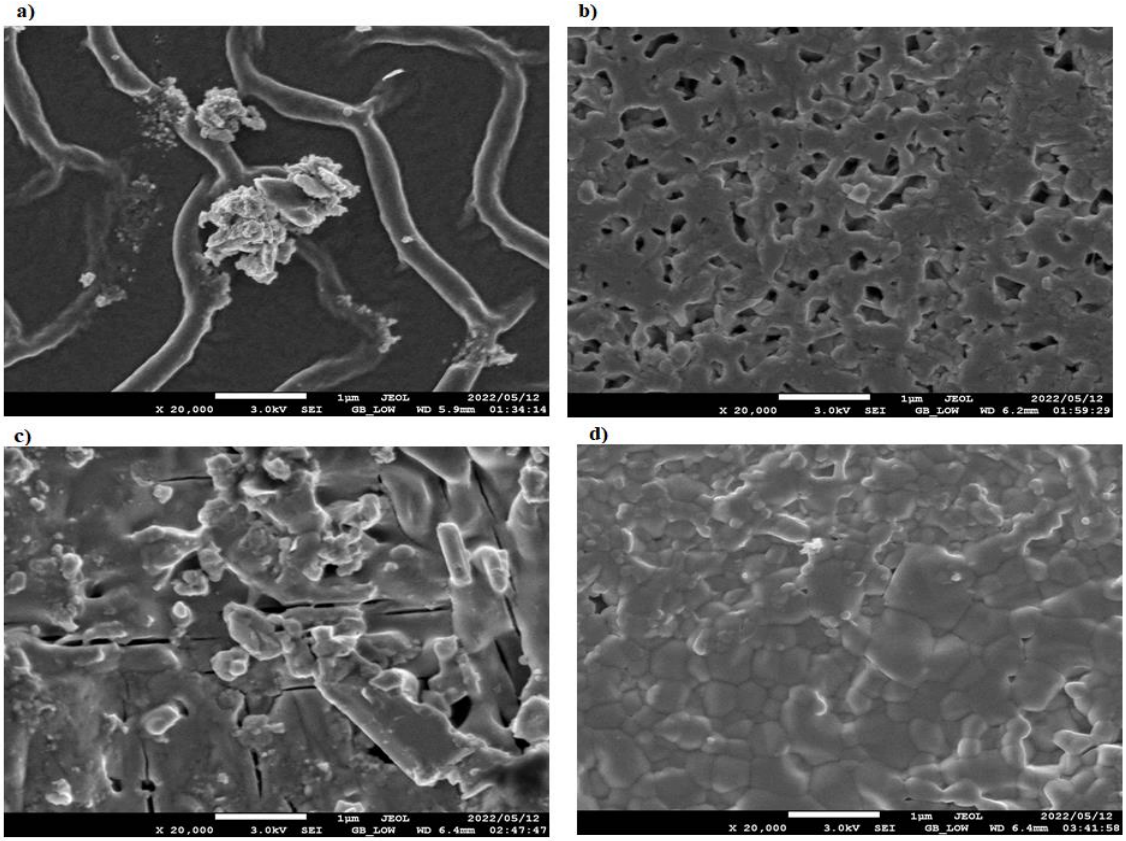

Figure 4: SEM images of (a) Glass/ZnO film, (b) Glass/ZnO/ $MAPbI_3$ film, (c) Glass/ZnO/SnO_2/$MAPbI_3$ film, (d) Glass/ZnO/WO_3/$MAPbI_3$ film

3.5 Thin film and Solar Cell Characterization Techniques

3.5.1 J-V Characteristics

To investigate their photovoltaic performance, a variety of metal oxides ETLs were used to fabricated planar perovskite solar cell devices based on single layer (ZnO, SnO_2, WO_3) and bilayer (ZnO/SnO_2, WO_3, SnO_2/WO_3) metal oxides materials. Fig.5 displays the current density-voltage (J-V) curves for the six devices under 100 mW/cm^2 of solar irradiation, and the corresponding parameters are summarized in Table 2. We can observe that the ITO/ZnO/WO_3/$MAPbI_3$/MoO_3/Al device exhibits a good I-V performances with a short-circuit current density (J_{SC}) of 14.9 mA cm^{-2}, an open-circuit voltage (V_{OC}) of 481.9mV, a fill factor (FF) of 0.390, and a power-conversion efficiency (PCE) of 2.80%, respectively. The performance of the ITO/ZnO/$MAPbI_3$/MoO_3/Al and ITO/WO_3/$MAPbI_3$/MoO_3/Al devices is significantly lower, principally because of the reduced V_{OC} and fill factor.

This is due to the smooth and few pinholeinterfaces between the ZnO/WO_3 ETL and the perovskite absorber, which suggests fewer defects and recombination sites [37] and supports the higher current density and FF of the ZnO ETL-based device. The result shows that direct contact between the ITO electrode and the $MAPbI_3$ absorber layer may result in a sizable recombination shunt diode. As a result, by adding a WO_3 layer between ZnO and the $MAPbI_3$ absorber layer interface, the shunt recombination at the ITO/$MAPbI_3$ interface was enhanced. From the result we conclude that all the bilayer based devices show enhanced FF, Voc, Jsc, and PCE compared with the

single layer based cells. The J_{SC} and FF improvements of the bilayer can be realized from several experimental observations, including higher visible-range absorbance, larger perovskite crystal grain size from SEM, and suppression of carrier recombination from PL quenching. Additionally, we confirmed from XRD and SEM higher crystallization, smooth and uniform with some pinhole surface, lower recombination rate and prohibited leakage current.

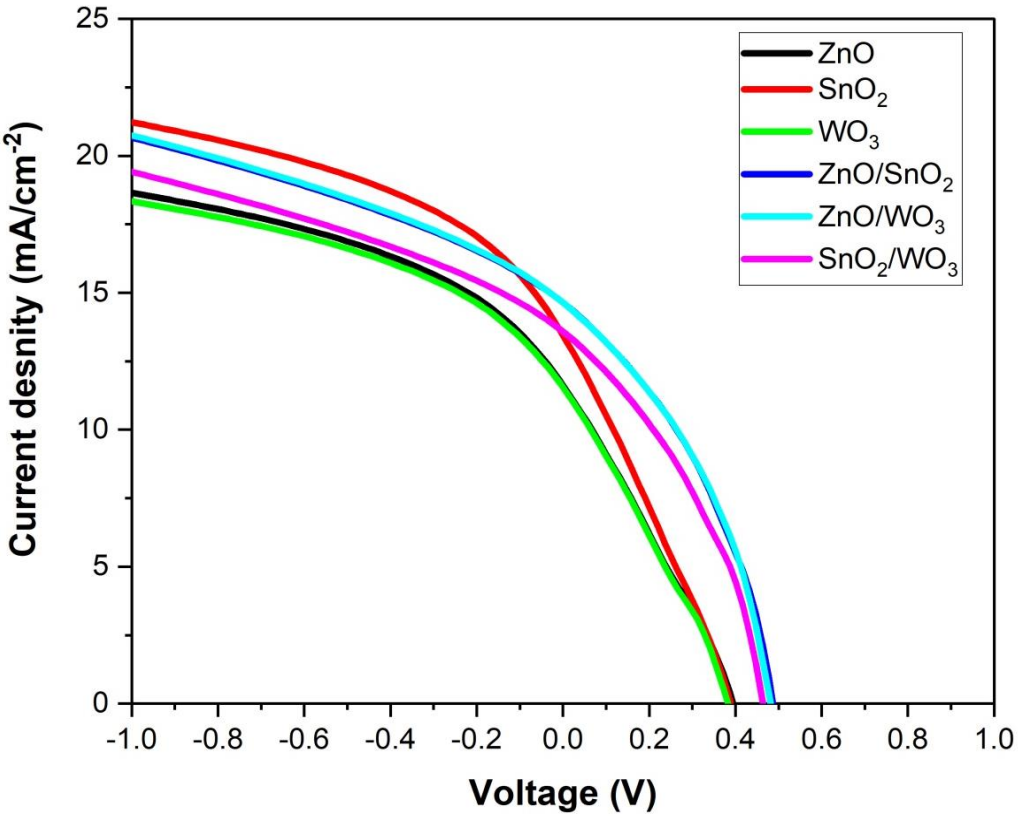

Figure 5: Current density –voltage (J-V) curves of perovskite devices with different metal oxide ETLs

Table 2: Photovoltaic performancesof the six PSCs with different configurations

Devices	V_{OC} (V)	J_{SC} (mA/cm^2)	FF	PCE (%)
ITO/ZnO/$MAPbI_3$/MoO_3/Al	0.386	11.591	0.291	1.310
ITO/SnO_2/$MAPbI_3$/MoO_3/Al	0.384	13.617	0.277	1.450
ITO/WO_3/$MAPbI_3$/MoO_3/Al	0.399	10.577	0.292	1.234
ITO/ZnO/SnO_2/$MAPbI_3$/MoO_3/Al	0.492	14.789	0.382	2.777
ITO/ZnO/WO_3/$MAPbI_3$/MoO_3/Al	0.482	14.896	0.390	2.801
ITO/SnO_2/WO_3/$MAPbI_3$/MoO_3/Al	0.466	13.643	0.379	2.407

4. CONCLUSION

In this study, the simple solution-processed approach was used to demonstrate the synthesis of ZnO, WO_3, and SnO_2 semiconductor metal oxides nanomaterials. For improved photovoltaic performance in $MAPbI_3$-based P-PSCs, we introduced to design of a bilayer ETL based ZnO/SnO_2, ZnO/WO_3, and SnO_2/WO_3 thin films. The structures, optical and electrical, as well as the morphology of the perovskite thin film on different ETLs were investigated. The XRD spectra revealed that perovskite incorporated different metal oxide ETLs such as ZnO,

WO_3, SnO_2 and ZnO/SnO_2, ZnO/WO_3 and SnO_2/WO_3 are tetragonal structures. According to the SEM results, the bilayer ETL made of ZnO/SnO_2 and ZnO/WO_3 improved exceptional film quality, reduced trap density, and reduced charge accumulation at the ETL/perovskite interface of the resulting devices.

Additionally, the surface morphology of the bilayer is homogeneous, smooth, and some of pinholes, which improves charge extraction at the junction between the ETL and perovskite layer in comparison to a single layer. The PL spectra confirmed that the quenching effect of perovskite on ZnO/SnO_2 and ZnO/WO_3 is better than the ZnO layer. This implies better charge transportation and extraction at the interface between ETL layers and perovskite layers than at the ZnO layer. These advantages lead to a significant decrease in front surface recombination and a high efficiency of more than 2.8% in the cell.

REFERENCE

1. Chang J, Zhu H, Li B, Isikgor FH, Hao Y, Xu Q, Ouyang J. Boosting the performance of planar heterojunction perovskite solar cell by controlling the precursor purity of perovskite materials. Journal of Materials Chemistry A. 2016;4(3):887-93.
2. Min H, Lee DY, Kim J, Kim G, Lee KS, Kim J, Paik MJ, Kim YK, Kim KS, Kim G, Shin TJ. Perovskite solar cells with atomically coherent interlayers on SnO_2 electrodes. Nature. 2021 Oct;598(7881):444-50.
3. Liu M, Johnston MB, Snaith HJ. Efficient planar heterojunction perovskite solar cells by vapour deposition. Nature. 2013 Sep;501(7467):395-8.
4. Kim GW, Kang G, Kim J, Lee GY, Kim HI, Pyeon L, Lee J, Park T. Dopant-free polymeric hole transport materials for highly efficient and stable perovskite solar cells. Energy & Environmental Science. 2016;9(7):2326-33.
5. Ke W, Fang G, Wang J, Qin P, Tao H, Lei H, Liu Q, Dai X, Zhao X. Perovskite solar cell with an efficient TiO_2 compact film. ACS applied materials & interfaces. 2014 Sep 24;6(18):15959-65.
6. Manseki K, Ikeya T, Tamura A, Ban T, Sugiura T, Yoshida T. Mg-doped TiO_2nanorods improving open-circuit voltages of ammonium lead halide perovskite solar cells. RSC Advances. 2014;4(19):9652-5.
7. Han GS, Chung HS, Kim BJ, Kim DH, Lee JW, Swain BS, Mahmood K, Yoo JS, Park NG, Lee JH, Jung HS. Retarding charge recombination in perovskite solar cells using ultrathin MgO-coated TiO_2nanoparticulate films. Journal of Materials Chemistry A. 2015;3(17):9160-4.
8. Tavakoli MM, Simchi A, Fan Z, Aashuri H. Chemical processing of three-dimensional graphene networks on transparent conducting electrodes for depleted-heterojunction quantum dot solar cells. Chemical Communications. 2016;52(2):323-6.
9. Qin P, Domanski AL, Chandiran AK, Berger R, Butt HJ, Dar MI, Moehl T, Tetreault N, Gao P, Ahmad S, Nazeeruddin MK. Yttrium-substituted nanocrystalline TiO_2photoanodes for perovskite based heterojunction solar cells. Nanoscale. 2014;6(3):1508-14.
10. Bu T, Wen M, Zou H, Wu J, Zhou P, Li W, Ku Z, Peng Y, Li Q, Huang F, Cheng YB. Humidity controlled sol-gel Zr/TiO_2 with optimized band alignment for efficient planar perovskite solar cells. Solar Energy. 2016 Dec 1;139:290-6.
11. Shin SS, Yang WS, Noh JH, Suk JH, Jeon NJ, Park JH, Kim JS, Seong WM, Seok SI. High-performance flexible perovskite solar cells exploiting Zn_2SnO_4 prepared in solution below 100° C. Nature communications. 2015 Jun 22;6(1):1-8.
12. Tavakoli MM, Giordano F, Zakeeruddin SM, Gratzel M. Mesoscopic oxide double layer as electron specific contact for highly efficient and UV stable perovskite photovoltaics. Nano letters. 2018 Mar 12;18(4):2428-34.
13. Li Y, Zhao Y, Chen Q, Yang Y, Liu Y, Hong Z, Liu Z, Hsieh YT, Meng L, Li Y, Yang Y. Multifunctional fullerene derivative for interface engineering in perovskite solar cells. Journal of the American Chemical Society. 2015 Dec 16;137(49):15540-7.
14. Tavakoli MM, Zakeeruddin SM, Grätzel M, Fan Z. Large-grain tin-rich perovskite films for efficient solar cells via metal alloying technique. Advanced Materials. 2018 Mar;30(11):1705998.
15. Zhou H, Chen Q, Li G, Luo S, Song TB, Duan HS, Hong Z, You J, Liu Y, Yang Y. Interface engineering of highly efficient perovskite solar cells. Science. 2014 Aug 1;345(6196):542-6.
16. Tavakoli MM, Tavakoli R, Hasanzadeh S, Mirfasih MH. Interface engineering of perovskite solar cell using a reduced-graphene scaffold. The Journal of Physical Chemistry C. 2016 Sep 8;120(35):19531-6.
17. Anaraki EH, Kermanpur A, Steier L, Domanski K, Matsui T, Tress W, Saliba M, Abate A, Grätzel M, Hagfeldt A, Correa-Baena JP. Highly efficient and stable planar perovskite solar cells by solution-processed tin oxide. Energy & Environmental Science. 2016;9(10):3128-34.
18. J. P. C. Baena, L. Steier, W. Tress, M. Saliba, S. Neutzner, T. Matsui, F. Giordano, T. J. Jacobsson, A. R. S. Kandada, S. M. Zakeeruddin, A. Petrozza, Energy Environ. Sci. 2016, 8, 2928.

19. Wang K, Shi Y, Dong Q, Li Y, Wang S, Yu X, Wu M, Ma T. Low-temperature and solution-processed amorphous WO_X as electron-selective layer for perovskite solar cells. The journal of physical chemistry letters. 2015 Mar 5;6(5):755-9.
20. Ramana CV, Utsunomiya S, Ewing RC, Julien CM, Becker U. Structural stability and phase transitions in WO_3 thin films. The Journal of Physical Chemistry B. 2006 Jun 1;110(21):10430-5.
21. Weinhardt L, Blum M, Bär M, Heske C, Cole B, Marsen B, Miller EL. Electronic surface level positions of WO_3 thin films for photoelectrochemical hydrogen production. The Journal of Physical Chemistry C. 2008 Feb 28;112(8):3078-82.
22. Szilagyi IM, Madarász J, Pokol G, Király P, Tárkányi G, Saukko S, Mizsei J, Toth AL, Szabó A, Varga-Josepovits K. Stability and controlled composition of hexagonal WO_3. Chemistry of Materials. 2008 Jun 24;20(12):4116-25.
23. Dong J, Zhao Y, Shi J, Wei H, Xiao J, Xu X, Luo J, Xu J, Li D, Luo Y, Meng Q. Impressive enhancement in the cell performance of ZnOnanorod-based perovskite solar cells with Al-doped ZnO interfacial modification. Chemical Communications. 2014;50(87):13381-4.
24. Noh YW, Jin IS, Kim KS, Park SH, Jung JW. Reduced energy loss in SnO_2/ZnO bilayer electron transport layer-based perovskite solar cells for achieving high efficiencies in outdoor/indoor environments. Journal of Materials Chemistry A. 2020;8(33):17163-73.
25. Li Z, Kulkarni SA, Boix PP, Shi E, Cao A, Fu K, Batabyal SK, Zhang J, Xiong Q, Wong LH, Mathews N. Laminated carbon nanotube networks for metal electrode-free efficient perovskite solar cells. ACS nano. 2014, 22;8(7):6797-804.
26. Yu M, Wang Y, Wang HY, Han J, Qin Y, Zhang JP, Ai XC. The influence of morphology on charge transport/recombination dynamics in planar perovskite solar cells. Chemical Physics Letters. 2016 Oct 1;662:257-62.
27. Wang S, Liu H, Bala H, Zong B, Huang L, Guo ZA, Fu W, Zhang B, Sun G, Cao J, Zhang Z. A highly stable hole-conductor-free CsxMA1-xPbI3 perovskite solar cell based on carbon counter electrode. ElectrochimicaActa. 2020 Mar 1;335:135686.
28. Dualeh A, Moehl T, Tétreault N, Teuscher J, Gao P, Nazeeruddin MK, Grätzel M. Impedance spectroscopic analysis of lead iodide perovskite-sensitized solid-state solar cells. ACS nano. 2014 Jan 28;8(1):362-73.
29. Janáky C, Rajeshwar K. The role of (photo) electrochemistry in the rational design of hybrid conducting polymer/semiconductor assemblies: From fundamental concepts to practical applications. Progress in Polymer Science. 2015 Apr 1;43:96-135.
30. Huang X, Qi X, Boey F, Zhang H. Graphene-based composites. Chemical Society Reviews. 2012;41(2):666-86.
31. Mahmud, M. A.; Elumalai, N. K.; Upama, M. B.; Wang, D.; Haque, F.; Wright, M.; Xu, C.; Uddin, A., Controlled Nucleation Assisted Restricted Volume Solvent Annealing for Stable Perovskite Solar Cells. Sol. Energy Mater. Sol. Cells 2017, 167, 70-86.
32. Qian LH, Wang SC, Zhao YH, Lu K. Microstrain effect on thermal properties of nanocrystalline Cu. Actamaterialia. 2002 Aug 1;50(13):3425-34.
33. Padiyan DP, Marikani A, Murali KR. Influence of thickness and substrate temperature on electrical and photoelectrical properties of vacuum-deposited CdSe thin films. Materials Chemistry and Physics. 2003 Feb 3;78(1):51-8.
34. Sherkar TS, Momblona C, Gil-Escrig L, Avila J, Sessolo M, Bolink HJ, Koster LJ. Recombination in perovskite solar cells: significance of grain boundaries, interface traps, and defect ions. ACS energy letters. 2017 May 12;2(5):1214-22.
35. Yang D, Yang R, Zhang J, Yang Z, Liu SF, Li C. High efficiency flexible perovskite solar cells using superior low temperature TiO_2. Energy & Environmental Science. 2015;8(11):3208-14.
36. Qian, L. H.; Wang, S. C.; Zhao, Y. H.; Lu, K., Microstrain Effect on Thermal Properties ofNanocrystalline Cu. Acta Mater. 2002, 50 (13), 3425-3434.
37. Williamson, G. K.; Smallman, R. E., III. Dislocation Densities in Some Annealed and Cold-workedMetals from Measurements on the X-ray Debye-scherrer Spectrum. Philos. Mag. (1798-1977) 1956, 1(1), 34-46.

Clean Energy Uptakes and Its Determinants in Rural Ethiopia: Evidence from Ethiopian Rural Household Survey

Obsa Urgessa*

Department of Economics, School of Business& Economics, Ambo University, P.O.Box 217, Ambo, Ethiopia
**Corresponding author, e-mail: obsa.ur@gmail.com*

ABSTRACT

This study is aimed to analyze the determinants of rural households' clean energy choices relative to traditional sources of energy for household lighting. To conduct the study, samples of 2,021 were taken from 4th round Ethiopian Socio-Economic Survey (ESS4-2018/19). The study categorized household's energy choices in to five categories: Electricity, fuelwood, kerosene, solar and simple rechargeable tools. To estimate the determinants of households' likelihood to uptake clean energy sources, multinomial model is employed. All estimation results are compared to kerosene alternative choice. The study finds that household's average years of education, household size, mobile ownership and income proxied by household annual consumption are the significant factors affecting the likelihood of adopting electricity. Similarly, household access to finance, monogamous marital status, mobile ownership and number of livestock owned are the significant factors determining the adoption of solar energy sources. The study also found that household income and the number of livestock owned are the driving force to determine the probability of choosing simple rechargeable tools as a source of household lighting. The study suggests that to increase rural household clean energy uptakes, expanding education, increasing rural income, empowering them in terms of assets and reducing fertility rate to reduce household size are important.

Keywords: *clean energy, multinomial, logit, Ethiopia*

1. INTRODUCTION

Energy is an important requisite of life. Sustainable development and attempts to reduce rural poverty highly depend on the sustained availability and access of modern sources of energy (Bisaga, 2018; Shahbaz et al., 2018; Sarker et al., 2019; Guta, 2014; Blimpo & Cosgrove-Davies, 2019). Earlier studies on the relation between energy, economic growth and household welfare at the micro and macro level reveal that the provision of energy alternatives contribute to economic growth as well as enhances household welfare (Khobai, et al., (2016); Raza, et al., (2016); Best & Burke, (2018); Stern, et al., (2019); Alam & Kaneko, (2019). Due to the crucial role it plays in the development process, increasing access to alternative energy sources has become the central development agenda globally. For example, United Nations (UN) is dedicated to "ensuring access to affordable, reliable, sustainable and modern energy for all" as its 7th sustainable development goal (UN, 2016).

Households get energy either from traditional or modern sources. Due to its health, economic and environmental impacts, there is a growing interest towards the adoption of the modern form of energy use in LDCs (Abate & Chawla, 2016; Geddafa et al., 2021; Shallo et al., 2020). Thus, renewable energy sources are believed to have a dual role in combatting climate change and improving the living conditions of rural households. Against these benefits, 789 million people globally (IEA et al., 2020) and 550 million in sub-Saharan Africa lives without access to electricity in 2018 (Nash & Khinmaung-Moore, 2020). Being part of sub-Saharan Africa (SSA), Ethiopia is not only the poorest country in terms of per capita income, but also poor in terms of per capita energy consumption. Access to modern energy is drastically low in rural Ethiopia where more than 80 million population rely on the traditional, pollutant, danger for health and unreliable source of energy (Yonas, 2016; Barnes et al., 2016). The total per capita energy consumption in Ethiopia was about 86 kWh per year by 2019 (Hilawe, 2019; Mekonnen & Abera, 2019), much lower than the African countries average of 591.87 kWh by 2015 (Blimpo & Cosgrove-Davies, 2019; Quansah et al., 2016).

Electrification in Ethiopia is currently available for 45% of the total population, which includes 97% of the urban population and 31% of the rural population (Kruger et al., 2019; IEA, 2019). Recently the country is generating 4.5GW power energy of which 85% (3.8 GW) is obtained from 14 hydro plants (Suntrace, 2017). Similarly, solar energy is serving the country's energy demand by generating 14MW in 2018. Besides that, in order to meet its energy shortfalls, the country planned to add 10GW hydropower and 3 GW from other sources of renewable projects. In order to achieve universal access by 2025, Ethiopia initiated a national electrification program (NEP) in 2017 in which 65% is targeted from grid solutions and 35% from off-grid technologies.

Despite the efforts made by the government to improve access of energy alternatives nationwide, Ethiopia's energy system remained one of the least diversified even by African standards (Akrofi, 2021). For example, Yalew, (2022) shows that 88%, 9.5% and 2.7% of Ethiopia's energy supply comes from bioenergy, petroleum and electricity respectively. In Ethiopia, about 81.4%, 11.5% and 2.4% of households use firewood, leaves & dung cakes and kerosene for cooking respectively (Shallo et al., 2020). This indicates that even though the country is striving to transit to alternative renewable energy sources, it is still reliant on a traditional source of energy. Therefore, this study is intended to investigate what factors determine household energy choices among renewable sources of energy instead of traditional sources of energy.

Previous studies show that households decision to choose alternative energy sources is determined by household income and family size (Shahi et al, 2020; Wassie et al., 2021; Baiyegunhi & Hassan, 2014); age of household head (Özcan et al., 2013; Zou & Luo, 2019; Mulugeta & Leta, 2021), educational achievements (Rahut et al., 2014; Baiyegunhi & Hassan, 2014; Zou & Luo, 2019; Twumasi, et al., 2021); private house and ICT device ownership (Wassie et al., 2021; Acharya & Marhold, 2018; Baiyegunhi & Hassan, 2014); credit and off-farm job (Twumasi, et al., 2021; Zou & Luo, 2019), location (Rahut et al., 2014; Wassie et al., 2021). These studies adopted various approaches to estimate the effect of those variables identified on household energy choices. For example, Shahi et al., (2020) employed binary logit model to analyze the effect of education on electricity use in rural Nepal; while Acharya & Marhold, (2018) employed multiple discrete continuous extreme value (MDCEV) model to examine the determinants of household energy choices. Similarly, Rahut et al., (2014); Özcan et al., (2013) and Baiyegunhi & Hassan, (2014) employed multinomial logit to model determinants of fuel energy choices; and Twumasi, et al., (2021) used endogenous switching (ESM) model while Wassie et al., (2021) employed multivariate Probit in their studies. Majorities of these studies mainly focused on and modeled one dimension of clean energy. However, rural households have different renewable energy options from which they choose and hence, cannot be estimated using binary choice models. Besides that, these studies are also based on case studies that may overlook the heterogeneity of factors influencing household alternative energy choices. Thus, this study fills the limitations of previous studies by using national data, taking in to account all available clean energy alternatives to rural households and focus on clean energy for household lighting.

2. Literature Review

2.1 Theoretical Framework

In energy economics literature, there are two widely discussed kinds of energy choice models by households: energy ladder and energy stacking model (Campbell et al., 2003; Heltberg, 2004). The concept of energy ladder hypothesis first appeared in a paper produced by Hosier and Dowd's in 1987 (Arthur et al., 2010). The model is based on the utility-maximizing behavior of household. The demand for better energy options is assumed to be a normal good. An increase in household income/welfare causes demand for more of some goods and less of inferior goods. In this regard, the energy ladder posits that as household income increases households will leapfrog to a higher energy ladder (Hosier & Dowd, 1987). The model depicts three stages of transition processes: stage one involves the use of traditional sources such as fuel woods, dung cake and crop residue; stage two also called the "transitional" stage involves the use of kerosene, charcoal and coal. In the third stage, society uses modern sources

such as electricity, liquid petroleum gas (LPG) or natural gas (Wassie et al., 2021; Inayatullah et al., 2011). Stage one is related to low level of income while stage three is achieved when per capita income is high.

However, the energy ladder hypothesis is criticized by different scholars on the following dimensions. First, it assumes that households abandon traditional sources as their income increases. However, there are substantial pieces of evidence suggesting that even if household income is increasing, households continue to use traditional sources along with modern energy (Masera et al.,2000; Heltberg, 2003; Peng et al., 2010; Taylor et al., 2013). This condition is termed as "fuel stacking" instead of full transition (Baiyegunhi & Hassan, 2014). The fuel stacking hypothesis argues that households would like to enjoy the complementarities of traditional and modern energy sources and thus utilize them simultaneously (Masera et al., 2000). Second, evidence also shows that besides household income, cultural and habitual factors, distance from biomass sources, fuel wood availability, and its shortage due to deforestation can push households to shift towards modern energy sources (Veld et al., 2006; Campbell, 2003; Nansairo et al., 2011).

However, there are some exceptions to the 'energy ladder' paradigm that must be considered. Many middle-income households in rural parts of developing countries continue to rely entirely or partially on traditional biomass fuels, despite the fact that they could theoretically purchase modern and convenient fuels (Heltberg, 2003). Household energy choices are influenced by household demographic factors such as age, education of household head, family size and non-demographic factors like tests and preference for food cooked with fuelwoods and private ownership of dwellings (Osiolo, 2009). Thus, even though income is the primary determinant, it is not the only factor influencing household energy choices. Therefore, the failure of the energy ladder hypothesis through several pieces of evidence suggests that household energy choices are explained as a portfolio choice (Baiyegunhi & Hassan, 2014).

Household energy choice can be explained using the theory of consumer behavior. Accordingly, household energy choices from alternative energy sources are driven by utility maximization (Hensher et al., 2005). Households' decision to choose from alternative energy sources is determined by the availability of information at their disposal, economic and non-economic factors (Baiyegunhi & Hassan, 2014). The economic factors may include household income and expenditure, fuel price and its availability, whereas the non-economic factors may include factors such as household size, gender, age, type of dwelling, house ownership, distance to fuel source, location of residence and access to electricity. This study adopts variables that have been identified by previous studies as determinants of household energy choices.

In this study, following Hensher et al., (2005), it is assumed that the individual household is considered to assess the whole set of provided alternative energy types in a choice situation and must choose the option that maximizes utility. Consider a households' choice of energy type and assume that utility is derived from a set of choices in a set (C) i.e., the choice set that incorporates all the conceivable fuel choices. In this way, a household is expected to have a utility:

$$U_{i,j} = Q(Z_{j,}S_i) + \varepsilon(Z_jS_i) \quad \ldots\ldots\ldots\ldots\ldots\ldots\ldots (1)$$

Where $U_{i,j}$ is ith household utility from jth alternative energy source, $Z_{j,}$ is the characteristics of the energy type, S_i is socio-economic and other factors affecting household decision to use alternative energy sources. Equation 1 implies that the probability that household choose alternative j over another energy source is a function of utility embodied in j. Following Baiyegunhi & Hassan, (2014) the mathematical expression for this argument is given as:

$$P_{ij} = prob(U_{ij} > U_{ia}), \quad a = 1,2,3,\ldots\ldots,j; a \neq j$$

Therefore, if the jth alternative energy is chosen, then it implies that ith household gets the highest utility from it. This is the conceptual framework on which this research is founded.

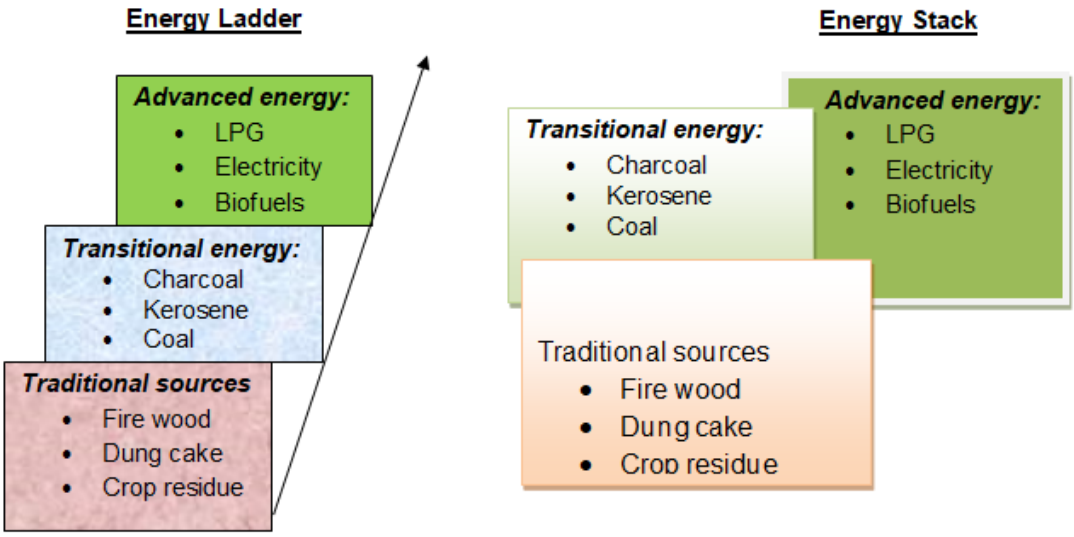

Figure 1: Theoretical framework (Source: Schlag and Zuzarte (2008))

2.2 Empirical Review

There are various studies conducted to investigate the determinants of household energy choices globally. Most of these studies were conducted in Asia and sub-Saharan Africa. These studies reveal that household transition to modern energy options are determined by socio-economic and ecological factors. For example, Sharma & Dash, (2022) shows that age and education of household head, household monthly expenditure and decision-making power between male and female discourage the use of traditional fuel in India. Aziz et al., (2022) also reveals that in houses with more ventilation, male headed and age of household tend to use less clean fuels. Likewise, Qing, et al., (2022) find that biogas adoption in rural China is determined by peer influence from friends and relatives. Similar study in China by Zou & Luo, (2019) find that healthy and old household head relies on coal energy while more educated households with large family size and participating in off-farm job uses electricity and liquid petroleum gas (LPG).

Another study from Asia is produced by Shahi et al., (2020) and Acharya & Marhold, (2018); Rahut et al., (2014). For example, Acharya & Marhold, (2018) find that households with lower education achievements and owning private houses relies on traditional fuel energy while ICT product ownership encourage the usage of clean energy in Nepal. Similarly, Shahi et al., (2020) shows that household tendency to use clean energy is determined by household income, occupation, family size and educational attainments. Rahut, et al., (2014) find that household with higher income and better education relies on cleaner energy sources while poorer household remained to depend on unclean sources of energy for cooking, lighting and heating in Bhutan. Their study also suggest that female headed households uses more cleaner energy sources than male headed households. In Turkey, Özcan et al., (2013) also examined factors affecting households' energy uses. Their finding reveals that monthly income, age and health status of household head determines their preference for energy alternative sources.

There are also some recent studies conducted in Africa. For example, Waweru et al., (2022) find that household energy choices are influenced by household income, cost of the fuel and household socio-economic factors in Kenya. Similarly, Martey et al., (2022) shows that off-farm job reduce the use of dirty fuel and encourage the use of clean energy in Ghana. Twumasi, et al., (2021) also find that household education, off-farm work, access to the internet, non-fixed assets and credit, and a household having a member residing in an urban area are the main determinants of fuel energy in rural Ghana. Other study by Bofah et al., (2022) reveals that housing quality, education and paid employment encourage household transition to clean energy whereas employment in informal

sector and dependency ratio encouraged reliance on unclean energy. Further, Baiyegunhi & Hassan, (2014) shows that household head's age, educational attainment, type of dwelling unit, income, household size, the duration of food cooked and price of fuelwood determine households' choice of cooking fuel in Nigeria.

There are also few studies conducted in Ethiopia, especially with regard to fuel energy choice in rural Ethiopia. For instance, using binary logit model, Guta, (2018) find that wealthy and more educated households are more likely to adopt solar energy whereas male headed are less likely to adopt. Likewise, Wassie et al., (2021) reveals that family size, income, access to road, education, location, cost of the technology and distance to market are the significant determinant of energy choice in southern Ethiopia. Another study by Mulugeta & Leta, (2021) shows that age, family size, income, education, landholding size, number of livestock owned and participation in training were significant to determine household adoption of clean and mixed energy sources. Similarly, Geddafa et al., (2021) and Shallo et al., (2020) reveals that livestock holding size, access to credit, distance to fire wood source, education, household income, access to technical support and level of awareness encourages the adoptions of biogas in rural Ethiopia.

These previous studies focus on only some aspects of household energy choices and identify its determinants. Specially, studies conducted in Ethiopia mainly emphasized on household biogas and solar energy adoptions. But households when they choose, they consider all energy alternatives available to them. Thus, previous studies overlooked household tendency to consider and choose the one that maximize their interest. This study tries to include all household energy choices including the traditional sources of energy. There is no sufficient evidence on the factors determining household lighting energy choices in rural Ethiopia.

2.3 Conceptual Framework

Based on the theoretical and empirical works done so far, the study developed the following conceptual framework of the study.

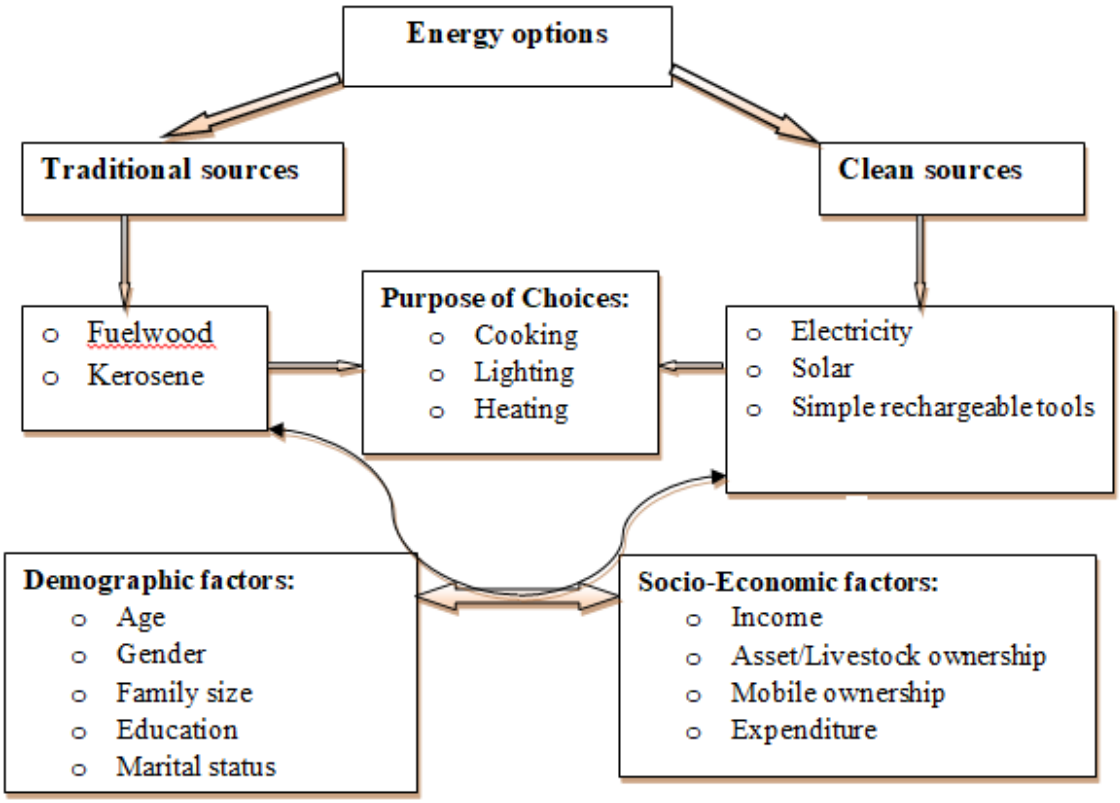

Figure 2: Conceptual Framework (Source: Nikus and Wayessa (2022))

3. MATERIALS AND METHODS

3.1 Model Development

To estimate the determinants of household alternative energy adoptions, multinomial logit model is employed. This model is preferred since there are more than two categories of household's energy options in the survey data. It is employed when outcomes are unordered and labeling of outcomes has no ordinal meaning. For the sake of analysis, the study categorized household's main sources of energy for lighting in to five categories: grid-based sources (electricity), fuelwood, kerosene, solar and simple clean sources (biogas, flashlight, rechargeable battery, and lantern). Each of these categories are labeled as:1 for electricity, 2 for fuelwoods, 3 for kerosene, 4 for solar and 5 for simple clean sources. These sources are mutually exclusive since each household reported only one main sources of energy for light. The probability that household i adopt energy choice j is given by $P_r(Y = j|X)$.

The general multinomial logit model is specified as follows:

$$P_r(Y_i = j|X) = \frac{\exp(X\beta_j)}{[1+\sum_{i=1}^{5}\exp(X\beta_h)]}, j = 1, \ldots, 5 \quad \ldots\ldots\ldots\ldots\ldots\ldots\ldots\ldots (2)$$

Equation (2) is usually estimated using the maximum likelihood estimation method and it is done using the Stata package.

3.2 Data Source and Its Collection

This study is based on cross-sectional data compiled from 4th round Ethiopian Socio-Economic Survey (ESS4-2018/19) collected by World Bank in collaboration with Ethiopian Central Statistical Authority (CSA) with funding from the Bill and Melinda Gates Foundation (BMGF). ESS4 was conducted in 565 enumeration areas (EAs), of which 316 are rural and 219 are urban. The survey contains three types of datasets: household dataset, community dataset and agricultural related datasets. From the survey, a sample of 2,021 rural households is taken after the data is cleaned based on the availability of information for all variables of the study. To ensure the representativeness, sample is taken from each region in proportion to their population size (Table 2). Largest sample is taken from Oromia (17%) followed by Amhara (16%) and southern nation and nationalities (SNNP) (15%). The least sample was from Diredawa and Gambela. The study identified nine variables as the potential factors affecting household's alternative clean energy sources. Table 1 shows the descriptions of variables used in this study.

Table 1: Descriptions of explanatory variables used in the study

Variable	**Description & Measurement**	
Energy options	Dependent and categorical variable:1 = electricity 2 = fuel wood, 3 = kerosene, 4 = traditional, and 5 = simple clean sources	
	Explanatory variables	***Expected sign***
Age of head	Age of household head in years	-
Household size	Number of individual/s living under one roof	±
Average education	Average education of household members in year	+
Annual consumption	Household's annual total consumption expenditure in birr	+
Gender head	Sex of household head and dummy: 1=male, 2=female	-
No. of livestock owned	Number of cattle owned by the household	+
Mobile ownership	Dummy:1= own, 2 = not own	+
Marital status	Respondent marital status and dummy: 1= never married, 2 = married (monogamous), 3 = married (polygamous), 4=divorced, 5=separated, 6=widowed	+
Financial access	Dummy: 1= has access to financial services, 2= has no access to financial services	+

For the sake of analysis, the study divided household's main sources of energy for lighting in to five categories. Among rural sample households, 245 of them use electricity, 232 use fuelwood, 370 use kerosene, 666 use solar products and 508 uses other simple tools of clean anergy products as a source of household lighting. The data reveals that around 30% of the sample household still depends on traditional energy sources as their main lighting of household during nighttime. Figure 1 below compares lighting energy by sources and regions. In Tigray, Amhara, Oromia and Harari rural households, solar is the primary source of lighting energy. Similarly, in Benishangul and Gambela, fuelwood is the main source of lighting households, while Kerosene is primary source of lighting households in SNNP.

Table 2: Household sample distribution by region

Region	Sample Household (No)	In percent
Tigray	251	12.4
Afar	156	7.7
Amhara	321	15.9
Oromia	339	16.8
Somali	231	11.4
Benishangul	115	5.7
SNNP	296	14.7
Gambela	105	5.2
Harari	114	5.6
Diredawa	93	4.6
Total	2,021	

Further, simple rechargeable hand tools are primarily used in Afar and Somali region. Even though solar is the primary source in Oromia and Tigray, substantial percent of rural households are also relying on traditional sources of energy.

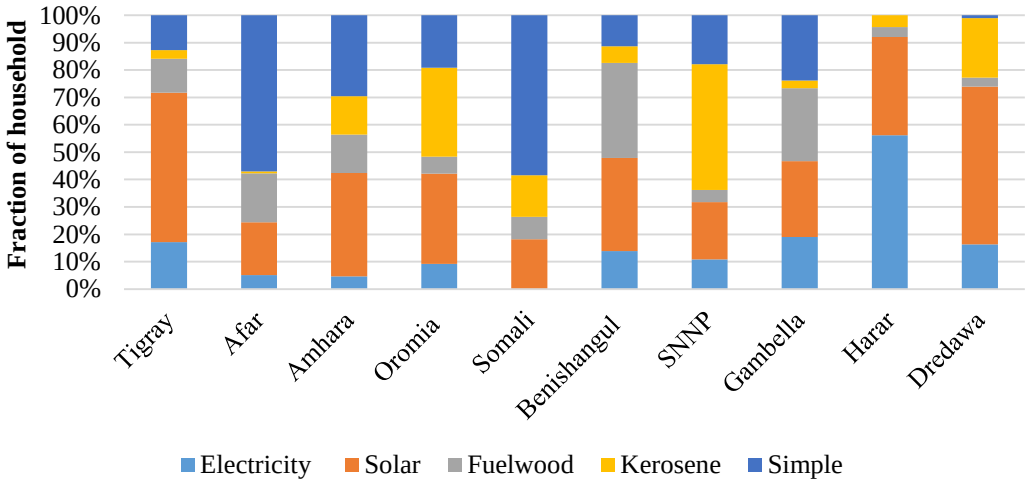

Figure 3: Rural household light energy sources by region

4. RESULTS AND DISCUSSION

4.1 Descriptive Analysis

Table 3 reveals the descriptive statistics for the main variables used in this study. The dependent variable is the energy choices of household for lighting. The study divided the main sources of light in to five categories as:

electricity, fuelwood, kerosene, solar and simple renewable sources (solar, flash rechargeable light, lantern lamp and biogas). Among these energy options, solar is the primary source of lighting (33%) followed by simple renewable sources (25%), while only 12% of sample household are using grid-based electricity for lighting purpose. Significant percent (30%) of the households are also still relying on traditional sources of energy. This result is different from the result obtained by Wassie et al, (2021) in which they obtained that 50% of rural household rely on traditional energy sources for lighting. Their result might be exaggerated since it was based on case study.

Table 3: Characteristics of variables used in the multinomial model

Variable	Mean/Percent	S\devn.
Lighting energy sources (dependent variables)	***Households in percent***	
Electricity	12.12	
Fuelwood	11.48	
Kerosene	18.31	
Solar	32.95	
Simple green	25.14	
Continuous explanatory variables	*Mean*	*S/Deviation*
Average education	7.03	10.40
Household size	5.46	2.09
No. of livestock owned	35.35	63.6
Age of household head	44.72	14.20
Log (annual consumption expenditure)	10.66	0.64
Dummy variables (independent variables)	***Households in percent***	
Access to financial service	23.06	
Mobile ownership	36.96	
Male headed household	79.71	
Household marital status	***Percents of Households***	
Never married	2.18	
Married (Monogamous)	79.12	
Married (Polygamous)	3.86	
Divorced	3.66	
Separated	1.19	
Widowed	9.90	
N	*2,021*	

The other characteristic of sample household is the education attainment. On average, the sample household attained primary education (7 years of schooling) with 10 standard deviations. This implies that, sample households are relatively literate. The average household size is 5 members with a maximum of 14 members and minimum of 1 member. Similarly, the average age of sample household is 45 years with standard deviation of 14 years. This implies that on average, the sample households are in the productive age. The minimum and maximum ages in the sample are 18 years and 99 years, respectively. Asymmetry is also observed in terms of the ownership of livestock. The characteristics of categorical variables also shows that 80% are male headed, 37% owns mobile cellphone and 23% have access to financial services. Most households are male-headed and engaged in monogamous marriages. Another striking issue from the data is that majority of households have no access to financial services. Detailed descriptions of the study variables are shown in Table 3.

Next, the study analyzed the correlation between study variables. In Table 4, the correlation between dependent response variables shows that they are negatively and significantly related to one another. This implies that energy

options adopted by each household are a close substitute for one another. The correlation between continuous variables used and alternative energy options is also described in Figure 4 to 7.

Table 4: correlations between household lighting energy choices

	Electricity	Kerosene	Solar	simple clean	Fuelwood
Electricity	1.00				
Kerosene	-0.1758*	1.00			
Solar	-0.2604*	-0.3319*	1.00		
Simple clean	-0.2152*	-0.2743*	-0.4062*	1.00	
Fuelwood	-0.1338*	-0.1705*	-0.2525*	-0.2087*	1.00

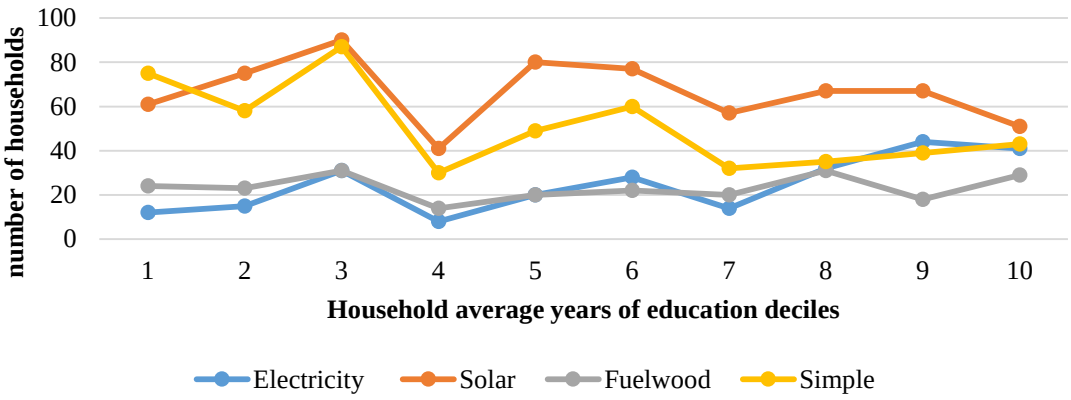

Figure 4: Average education and energy type for lighting

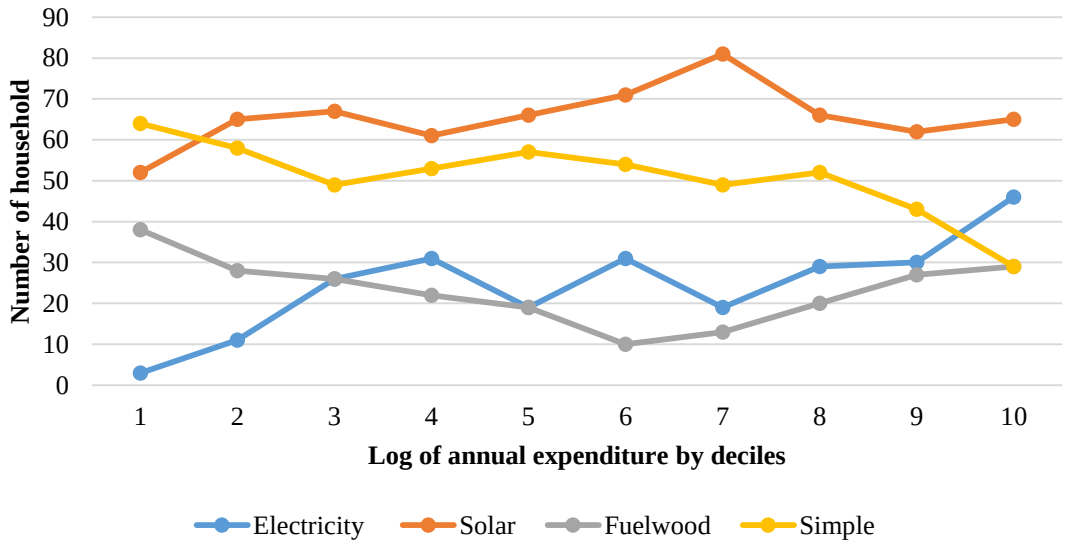

Figure 5: Log of annual expenditure and sources of household lighting energy

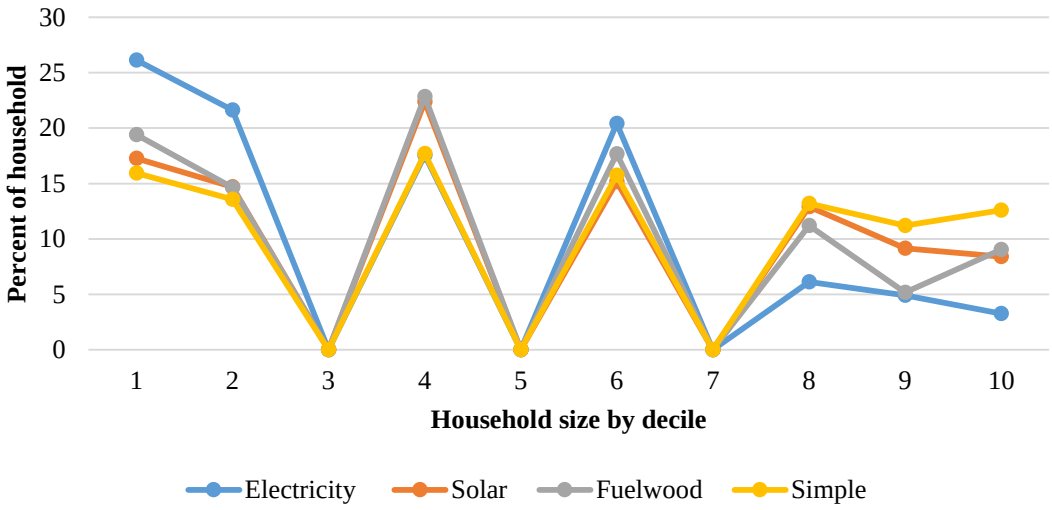

Figure 6: Household size and sources lighting energy

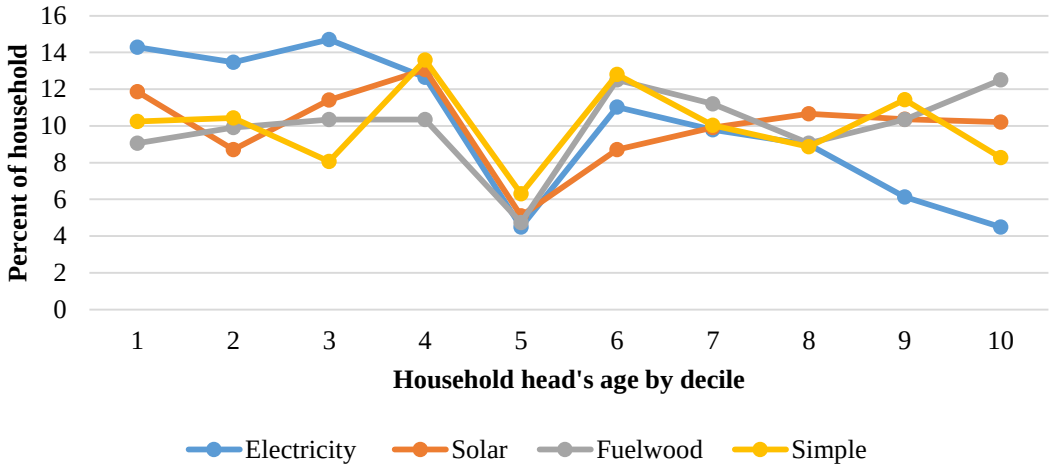

Figure 7: Household age and sources of lighting energy

From Figures 4 and 5, we observe that there is a clear movement between average household years of education, annual household consumption expenditure and alternative energy sources. The movement is in the same direction with energy options for both variables. The relationship is relatively strong with solar energy and low for fuelwood source. With respect to household head age decile from Figure 7, there is also positive relationship with alternative energy options. However, the co-movement of household size decile with energy sources is not strong. The result implies that even though household welfare in terms of consumption and education is improving, household continue to combine and use both in rural areas.

Before conducting any formal regression, the study conducted diagnostic test to evaluate whether there is multicollinearity between the regressors or not. The test result shows that there is no serious multicollinearity between explanatory variables, since VIF result is less than 10 for all variables.

Table 5: Multicollinearity test for the predictor variable in the multinomial model

Variable	VIF	1/VIF
Average Education	1.03	0.967259
Accesses to financial service	1.06	0.941592
Household size	1.22	0.816975
Marital status		
Married (Monogamous)	7.91	0.126490
Married (Polygamous)	2.72	0.367476
Divorced	2.88	0.346977
Separated	1.62	0.617666
Widowed	5.92	0.168859
Cohabiting	1.05	0.951730
Mobile ownership	1.02	0.984175
Number of livestock owned	1.07	0.936526
Age of household head	1.14	0.874499
Gender of household head	2.19	0.455795
Log (annual consumption)	1.10	0.908632
Mean VIF	2.28	

4.2 Estimation Results

The multinomial MLE estimation result is presented in Table 6. The parameter only tells the direction of the effects of those explanatory variables. The estimated coefficients are interpreted in comparison with Kerosene source of lighting as a reference energy choice. The model is estimated using robust standard error.

The overall percent correctly predicted by the model is 38.5%. The model correctly predicted about 76.3%, 29.4%, 29.1%, 12.7% and 0.9% of rural household choice of solar, electricity, simple rechargeable tools, kerosene and fuelwood as source of lighting energy respectively. Besides this, the joint significance of variables included in the model are highly significant at 5% level of significance.

From the explanatory variables included in the model, average household education positively influences the likelihood of adopting electricity and fuelwood for household lighting. From Table 6, the effect of average education on the likelihood of adopting electricity and fuelwood is statistically significant. This result is consistent with the finding of Rahut et al., (2017) where they found that more wealthy and more educated households are more likely to adopt less kerosene and more electricity. The marginal effect shows that each additional year of education increases the likelihood of adopting electricity by 0.14% than Kerosene. However, its effect on the likelihood of adopting off-grid energy sources is insignificant.

Table 6: Multinomial logit estimation result (dependent variable: household's energy choices)

VARIABLES	(1) Electricity	(2) Fuelwood	(4) Solar	(5) simple clean
Average education	0.0244***	0.0198**	0.0092	0.0114
	(0.0089)	(0.0098)	(0.0090)	(0.0097)
Financial access	-1.5182***	0.3626	-0.8803***	-0.4236**
	(0.2088)	(0.2809)	(0.1826)	(0.2022)
Household size	-0.1416***	-0.0374	-0.0300	0.0709*
	(0.0489)	(0.0484)	(0.0380)	(0.0386)
Marital status				
Married(monogamous)	0.2399	0.1677	1.1999**	0.8315*
	(0.4795)	(0.5439)	(0.5215)	(0.4876)
Married(polygamous)	-0.9449	-0.1618	0.8751	0.9958*
	(0.8032)	(0.7099)	(0.6205)	(0.5859)
Divorced	0.5642	0.6922	1.3961**	0.4793
	(0.6479)	(0.7142)	(0.6718)	(0.6486)
Widowed	1.5084*	1.0103	1.6783*	0.8402
	(0.9013)	(0.9479)	(0.8873)	(0.9068)
Separated	-0.0284	-0.3023	0.7265	0.0296
	(0.5839)	(0.6353)	(0.6065)	(0.5662)
Mobile ownership	0.0179*	0.0220***	0.0273***	-0.1044
	(0.0095)	(0.0080)	(0.0052)	(0.1206)
No. of livestock owned	-0.0144**	0.0126***	0.0103***	0.0118***
	(0.0066)	(0.0031)	(0.0031)	(0.0030)
Age of head	-0.0091	0.0045	0.0028	0.0011
	(0.0064)	(0.0061)	(0.0050)	(0.0053)
Gender of head	-0.1075	0.1882	-0.4038	0.4121*
	(0.2836)	(0.3087)	(0.2544)	(0.2465)
Log (annual consumption)	0.7956***	-0.2444	-0.1495	-0.5026***
	(0.1477)	(0.1649)	(0.1177)	(0.1236)
Constant	-5.2476***	0.5039	2.7378*	4.4912***
	(1.6981)	(1.9099)	(1.4364)	(1.5045)
Observations	2,019			
Percent correctly predicted	38.5%	Wald chi2(52) =	325.74	
Log-likelihood	-2874.7982	Prob > chi2 =	0.0000	
Pseudo R^2	0.0679			

*** p<0.01, ** p<0.05, * p<0.1, Robust standard errors in parentheses

The effect on energy from solar and simple rechargeable tools is not significant. Similarly, its marginal effect on the probability of adopting both types of energy source is practically insignificant (Table 7). Relative to kerosene, households with access to financial services are less likely to use light energy from electricity, solar and simple clean sources. This can be due to the fact that from the sample household only 23% have received services from financial institutions. The marginal effect reveals that household having access to financial services are 10.1%, 9.6% and 10.8% less likely to choose electricity, fuelwood and solar energy sources over kerosene respectively (Table 7).

The estimated coefficient for household size is negative and statistically significant in affecting the likelihood of choosing electricity compared to Kerosene. Each additional unit of household size reduces the probability to adopt electricity by 1.3% than kerosene (Table 7). However, it increases the probability to adopt simple tools positively and significantly with marginal effect of 2% relative to kerosene. From the categories of marital status, relative to kerosene, a household with monogamous marriage are more likely to adopt solar energy sources than unmarried individuals. When we move from unmarried households to monogamously married households, the likelihood of adopting solar energy over kerosene increases by 15.5% (Table 7). The number of livestock owned reduces the

probability of adopting grid-based energy sources (electricity) relative to choosing kerosene as a source of household lighting. This is an unexpected result. However, it increases the likelihood of adopting fuelwood, solar and simple tools (table 6). Each additional unit of livestock owned reduces the likelihood to adopt electricity over kerosene by 0.21% while it increases the probability of using fuelwood, solar and simple rechargeable tools by 0.1%, 0.13%, and 0.12% respectively. The result aligns with the finding of Guta (2018) where more wealthy households are more probable to adopt solar energy than poorer households.

Table 7: Marginal effect estimates

Marginal Effects				
	(1)	(2)	(3)	(4)
Variables	Electricity	Fuelwood	Solar	Simple green
Average education	0.0014***	0.0010	-0.0006	0.0002
	(0.0005)	(0.0006)	(0.0011)	(0.0013)
Accesses to financial service	- 0.1005***	0.0964***	-0.108***	0.0194
	(0.0137)	(0.0232)	(0.0243)	(0.0247)
Household size	-0.0131 **	-0.0033	-0.0054	0.0196***
	(0.0040)	(0.0037)	(0.0055)	(0.0048)
Marital status				
Married(monogamous)	-0.0390	-0.0532	0.1552***	0.0601
	(0.0465)	(0.0580)	(0.0587)	(0.0641)
Married(polygamy)	-0.1088**	-0.0710	0.1128	0.1580*
	(0.0532)	(0.0657)	(0.0770)	(0.0829)
Divorced	-0.0154	0.0019	0.1856**	-0.0346
	(0.0616)	(0.0749)	(0.0890)	(0.0776)
Separated	0.0714	-0.0037	0.1523	-0.0339
	(0.0953)	(0.0906)	(0.1223)	(0.0964)
Widowed	-0.0244	-0.0592	0.1385*	-0.0209
	(-0.0562)	(0.0639)	(0.0758)	(0.0719)
Mobile ownership	0.0027	0.0042	0.0129	-0.0221
	(0.0028)	(0.0037)	(0.0098)	(0.0211)
Number of livestock owned	-0.0021***	0.0007***	0.0013***	0.0012***
	(0.0004)	(0.0001)	(0.0003)	(0.0002)
Age of household head	-0.001*	0.0004	0.0007	0.00003
	(0.0005)	(0.0005)	(0.0008)	(0.0007)
Male headed household	-0.0056	0.0244	-0.123***	0.1042***
	(0.0257)	(0.0238)	(0.0412)	(0.0334)
Log (annual consumption)	0.0932***	-0.0125	-0.0126	-0.0888***
	(0.0111)	(0.0112)	(0.0169)	(0.0157)
N	2,019	2,019	2,019	2,019

t statistics in parentheses * $p < 0.05$, ** $p < 0.01$, *** $p < 0.001$

Male-headed households are more likely to use simple clean energy over kerosene relative to female-headed households. The marginal effect suggests that males are 10.4% more likely than female-headed households to choose simple rechargeable tools over kerosene. On the other hand, male-headed households are less likely to adopt electricity and solar, though it is statistically insignificant. Lastly, household income proxied by household annual consumption increases the likelihood of using grid-based energy sources. However, its effect on the probability of adopting simple rechargeable sources is negative and statistically significant. The marginal effect indicates that each additional expenditure of a household increases the chances of adopting electricity over kerosene as a source of household lighting by 9% (table 7) and reduces the choice of simple tools by the same magnitude. Similarly, mobile phone ownership is found to be one significant factor influencing lighting energy choice among the sample

household. Households owning mobile phone are more likely to choose electricity, solar and fuelwood over kerosene as a source of energy (Table 6).

4.3 Robustness Check

Table 8: Logit regression result

VARIABLES	(1) Electricity	(2) Kerosine	(3) Solar	(4) Simple green	(5) Fuelwood
Average education	0.0144**	-0.0154**	-0.0055	-0.0012	0.0084
	(0.0059)	(0.0075)	(0.0050)	(0.0053)	(0.0057)
Financial access	-1.0574***	0.7792***	-0.3616***	0.2782**	1.1302***
	(0.1539)	(0.1668)	(0.1137)	(0.1382)	(0.2388)
Household size	-0.1430***	0.0171	-0.0112	0.1237***	-0.0194
	(0.0438)	(0.0321)	(0.0254)	(0.0274)	(0.0375)
Marital status					
Married (monogamous)	-0.4041	-0.6757*	0.8982**	0.3607	-0.4731
	(0.4156)	(0.3687)	(0.4002)	(0.4056)	(0.4351)
Married (polygamous)	-1.4754**	-0.5040	0.6509	0.8341*	-0.6786
	(0.7439)	(0.4737)	(0.4710)	(0.4682)	(0.5720)
Divorced	-0.1173	-0.7433	1.0267**	-0.2208	0.0354
	(0.5622)	(0.5074)	(0.4985)	(0.5173)	(0.5547)
Widowed	0.5328	-1.1890	0.9065	-0.2378	-0.0562
	(0.6998)	(0.7333)	(0.6378)	(0.6639)	(0.6850)
Separated	-0.2335	-0.0950	0.8113*	-0.1468	-0.5384
	(0.5191)	(0.4331)	(0.4619)	(0.4641)	(0.5175)
Mobile ownership	-0.0011	-0.0216	0.0146**	-0.1357	0.0028
	(0.0099)	(0.0187)	(0.0068)	(0.1176)	(0.0084)
No. of livestock owned	-0.0234***	-0.0093***	0.0006	0.0023**	0.0027**
	(0.0043)	(0.0021)	(0.0008)	(0.0010)	(0.0011)
Age of head	-0.0108*	-0.0000	0.0049	0.0012	0.0047
	(0.0058)	(0.0044)	(0.0036)	(0.0041)	(0.0051)
Gender of head	-0.1025	-0.0425	-0.5786***	0.5402***	0.2172
	(0.2765)	(0.2083)	(0.1924)	(0.1852)	(0.2401)
Log (annual consumption)	1.0078***	0.1358	-0.0397	-0.4631***	-0.1076
	(0.1232)	(0.0960)	(0.0790)	(0.0889)	(0.1148)
Constant	-8.8960***	-3.3838***	-0.0084	1.7875*	-3.0811**
	(1.4125)	(1.1608)	(0.9761)	(1.0806)	(1.3998)
Observations	2,019	2,019	2,019	2,019	2,019
Percent correctly predicted	88.40%	81.71%	67.24%	74.43%	88.55%
Log-likelihood	-630.1	-923.3	-1255.5	-1092.6	-686.5

Standard errors in parentheses
*** p<0.01, ** p<0.05, * p<0.1

Overall, out of explanatory variables included in the model, most of them have statistically significant effect in determining household's adoptions of alternative energy sources. Age of the household head is the only insignificant variable to affect at least one of energy choices.

5. CONCLUSION AND POLICY IMPLICATIONS

This study focused on the factors determining rural household adoptions of clean light energy choices in Ethiopia. The study adopted multinomial logit model in order to estimate factors affecting the probability of adopting clean sources of light energy. The study finds that household average years of education, household size, mobile ownership and income proxied by household annual consumption are the significant factors affecting the likelihood of adopting electricity. Similarly, household access to finance, monogamous marital status, mobile ownership and number of livestock ownership are the significant factors determining the adoption of solar energy

sources. Further, the study also find that household income and the number of livestock owned are the deriving force to determine the probability of choosing simple rechargeable tools as a source of household lighting.

Based on the finding of the study, we recommend that in order to expand the adoption of clean energy among rural households, expand education, reduce family size, capacitate household town mobile phones, encourage the ownership of assets like livestock, and increase/diversify the sources of household income are necessary to encourage them to adopt renewable clean sources.

REFERENCES

Acharya, B., & Marhold, K. (2018). Determinants of Household Energy Use and Fuel Switching Behavior in Nepal. Energy, doi: 10.1016/j.energy.2018.12.109.

Abate, W. L., & Chawla, A. S. (2016). Determinants of Adoption of Renewable Energy Sources towards Reducing Deforestation in Ambo district, West Shoa, Oromia Regional State, Ethiopia. Journal of Energy Technologies and Policy, 6(1),, 23-41.

Akrofi, M. M. (2021). An analysis of energy diversification and transition trends in Africa. Int J Energ Water Res (5). https://doi.org/10.1007/s42108-020-00101-5, 1-12.

Alam, M. J., & Kaneko, S. (2019). The Effects of Electrification on School Enrollment in Bangladesh: Short-and Long-Run Perspectives. Energies, 12(4), 629., 12(4), 629.

Arthur, M.S., Zahran, S., & Bucini, G. (2010). On the Adoption of Electricity as a Domestic Source by Mozambican Households. Energy Policy 38 (11):, 7235-7249.

Aziz, S., Barua, S., & Chowdhury, S. A. (2022). Cooking energy use in Bangladesh: Evidence from technology and fuel choice. Energy, 250, 123696.

Baiyegunhi , L. J., & Hassan, M. B. (2014). Rural household fuel energy transition: Evidence fromGiwa LGA Kaduna State, Nigeria. Energy for Sustainable Development, (20),, 30-35.

Barnes, D. F., Golumbeanu, R., & Diaw, I. (2016). Beyond Electricity Access: Output-Based Aid and Rural Electrification in Ethiopia. Washington DC: World Bank.

Best, R., & Burke, P. J. (2018). Electricity availability: A precondition for faster economic growth?. Energy Economics,, 74, 321-329.

Bisaga, I. M. (2018). Scaling up off-grid solar energy access through improved understanding of customers' needs, aspirations and energy use of decentralised (SMART) Solar Home Systems – a case study of BBOXX customers in Rwanda. Thesis Submitted for the Degree of Philosophy.

Blimpo, M., & Cosgrove-Davies, M. (2019). Electricity Access in Sub-Saharan Africa: Uptake, Reliability, and Complementary Factors for Economic Impact. Africa Development Forum series. Washington, DC: World Bank. doi:10.1596/978-1-4648-1361-0. License: Creative Commons Attribution CC BY 3.0 IGO.

Bofah,, R. O., Appiah-Konadu, P., & Ngwu, F. N. (2022). Transition to cleaner cooking energy in Ghana. . Clean Energy, 6(1), 957-966., 957-966.

Campbell , B. M., Vermeulen , S. J., Mangono , J. J., & Mabugu , R. (2003). The energy transition in action: urban domestic fuel choices in a changing Zimbabwe. . Energy Policy;31(6), 553-562.

Campbell , B. M., Vermeulen , S. J., Mangono , J. J., & Mabugu , R. T. (2003). The energy transition in action: urban domestic fuel choices in a changing Zimbabwe. . Energy Policy, 31(6), 553-562.

Dorothal, M. (2019). The solar future Deserts of Africa. Addis Ababa, Ethiopia: Solarplaza.

Geddafa, T., Melka, Y., & Sime, G. (2021). Determinants of Biogas Technology Adoption in Rural Households of Aleta Wondo District, Sidama Zone, Southern Ethiopia. Journal of Energy, https://doi.org/10.1155/2021/9934942.

Geddafa, T., Melka, Y., & Sime, G. (2021). Determinants of Biogas Technology Adoption in Rural Households of Aleta Wondo District, Sidama Zone,Southern Ethiopia. Journal of Energy,, 1-7.

Guta, D. (2018). Determinants of household adoption of solar energy technology in rural Ethiopia. Journal of Cleaner Production 204, DOI:10.1016/j.jclepro.2018.09.016.

Guta, D. D. (2014). Bio-Based Energy, Rural Livelihoods and Energy Security in Ethiopia. Department of Economic and Technological Change Centre for Development Research (ZEF): Doctoral Dissertation.

IEA, IRENA, UNSD, World Bank, & WHO. (2020). Tracking SDG 7: The Energy Progress Report. World Bank, Washington DC. © World Bank. License: Creative Commons Attribution—NonCommercial 3.0 IGO (CC BY-NC 3.0 IGO).

Heltberg , R. (2003). Household energy use in developing countries: amulti-country study. . Oil and gas policy division, discussion paper.Washington, DC, New York:World Bank;.

Heltberg , R. (2003). Household energy use in developing countries: amulti-country study. . Oil and gas policy division, discussion paper.Washington, DC, New York:World Bank; .

Heltberg , R. (2004). Fuel switching: evidence from eight developing countries. Energy. Energy Economics, 26,, 869-887.

Hensher , D., Rose , J., & Greene , W. (2005). Applied choice analysis: a primer. . Cambridge:: Cambridge University Press; 2005.

Hilawe , L. (2019). Solar and Wind Energy Resources for Off-Grid Electricity Access in Ethiopia. The 8th Climate Change and Development in Africa CCDA 8):. Addis Ababa: Ministry of Water, Irrigation and Electricity.

Hosier , R. H., & Dowd , J. (1987). Household fuel choice in Zimbabwe: an empirical test of the energy ladder hypothesis. . Resource Energy ;9(4):, 347-361.

Inayatullah , J., Khan , H., & Hayat , S. (2011). Determinants of rural household energy choices: an example from Pakistan. . Pol J Environ Stud, 21(30),, 635-641.

Khobai, H., Abel, S., & Le Roux, P. (2016). Co-integration between electricity supply and economic growth in South Africa. International Journal of Energy Economics and Policy, 6(3).

Kruger, W., Stuurman , F., & Alao, O. (2019). Ethiopia Country Report: Energy and Economic Growth Research Programme, Report 5, (W01 and W05) PO Number: PO00022908.

Martey, E., Etwire, P. M., Adusah-Poku, F., & Akoto, I. (2022). Off-farm work, cooking energy choice and time poverty in Ghana: An empirical analysis. . Energy Policy, 163, 112853.

Masera , O. R., Saatkamp , B. D., & Kammen , D. M. (2000). From linear fuel switching to multiple cooking strategies: a critique and alternative to the energy ladder model. World Dev, 28(12). World Devolopment, 28(12), 2083-103.

Mekonnen, K. F., & Abera, Y. (2019). Determinants of Lighting Energy Transitions in Rural Ethiopia: Lessons from Mida Oromo and Wonisho Districts of Ethiopia. Environmental Management and Sustainable Development, 13-37.

Mulugeta, S., & Leta, A. (2021). Adoption of Renewable Energy Technologies and Energy Source Choice of Households. Grassroots Journal of Natural Resources, 4 (3); doi.org/10.33002/nr2581.6853.040303.

Nansairo , A., Rambo , A. T., & Simaraks , S. (2011). Climbing the energy ladder or diversifying energy sources? The continuing importance of household use of biomass energy in urbanizing communities in northeast Thailand. Biomass Energy;35(10):, 4180-8.

Nash, S., & Khinmaung-Moore, J. (2020). Designing Sustainable Subsidies to Accelerate Universal Energy Access: A briefing paper on key principles for the design of pro-poor subsidies to meet the goal of sustainable energy for all. tearfund.

Osiolo , H. H. (2009). Enhancing household fuel choice and substitution in Kenya. . Discussion paper no. 102. Kenya Institute for Public Policy Research and Analysis (KIPPRA).

Özcan, K. M., Gülay , E., & Üçd, S. (2013). Economic and Demographic determinants of household energy use in Turkey. Energy Policy (60), 550–557.

Peng, W., Hisham, Z., & Pan, J. (2010). Household Level Fuel Switching in Rural Hubei. Energy for Sustainable Development , 14 (3): , 238-244.

Qing, C., He, J., Guo, S., Zhou, W., Deng, X., & Xu, D. (2022). Peer effects on the adoption of biogas in rural households of Sichuan Province, China. Environmental Science and Pollution Research,, 1-14.

Quansah, D. A., Adaramola, M. S., & Mensah, L. D. (2016). Solar Photovoltaics in sub-Saharan Africa – Addressing Barriers, Unlocking Potential. 1st Energy Economics Iberian Conference, EEIC | CIEE 2016, February 4-5, Lisbon, APEEN (www.apeen.org) and AEEE (www.aeee.es).

Rahut, D. B., Mottaleb, K. A., & Ali, A. (2017). Household energy consumption and its determinants in timor-leste. Asian Development Review, 34(1), 167–197. https://doi.org/10.1162/ADEV_a_00085

Rahut, D. B., Das, S., Groote, H. D., & Behara, B. (2014). Determinants of household energy use in Bhutan. Energy, 1-12.

Raza, S. A., Jawaid, S. T., & Siddiqui, M. H. (2016). Electricity consumption and economic growth in South Asia. South Asia Economic Journal,, 17(2), 200-215.

Sarker, S. A., Wang, S., & Adnan, K. M. (2019). Energy Consumption and Economic Growth Nexus in Bangladesh. Journal of Systems Science and Information, 497-509.

Shahbaz, M., Zakaria, M., Hussain, S. J., & Mahalik, M. K. (2018). The energy consumption and economic growth nexus in top ten energy-consuming countries: Fresh evidence from using the quantile-on-quantile approach. Energy Economics., 282-301.

Shahi, D. K., Rijal, H. B., & Shukuya, M. (2020). A study on household energy-use patterns in rural, semi-urban and urban areas of Nepal based on field survey. Energy & Buildings, doi: https://doi.org/10.1016/j.enbuild.2020.110095.

Shallo, L., Ayele, M., & Sime, G. (2020). Determinants of biogas technology adoption in southern Ethiopia. Energy, Sustainability and Society; https://doi.org/10.1186/s13705-019-0236-x.

Shallo, L., Ayele, M., & Sime, G. (2020). Determinants of biogas technology adoption in southern Ethiopia. Energy, Sustainability and Society, 1-13.

Sharma, V., & Dash, M. (2022). Household energy use pattern in rural India: A path towards sustainable development. Environmental Challenges, 6, 100404.

Stern, D. I., Burke, P. J., & Bruns, S. B. (2019). The impact of electricity on economic development: a macroeconomic perspective.

Suntrace. (2017). Solar Market Brief: Ethiopia. www.suntrace.de.

Taylor, M. J., Moran-Taylor, M. J., Castellanos, E. J., & Elías, S. (2013). Burning for Sustainability: Biomass Energy, International Migration, and the Move to Cleaner Fuels and Cookstoves in Guatemala. Annals of the Association of American Geographers 101 (4):, 918-928.

Twumasi, M. A., Jiang, Y., Addai, B., Asante, D., Liu, D., & Ding, Z. (2021). Determinants of household choice of cooking energy and the effect of clean cooking energy consumption on household members' health status: The case of rural Ghana. Sustainable Production and Consumption,(28),, 484–495.

Veld , V. K., Narain , U., Gupta , S., Chopra , N., & Singh , S. (2006). India's firewood crisis reexamined. . RFF Discussion Paper 06-25. Washington D.C.: Resource for the Future (RFF); .

Wassie, Y. T., Rannestad, M. M., & Adaramola, M. S. (2021). Determinants of household energy choices in rural sub-Saharan Africa: An example from southern Ethiopia. Energy,(221),doi.org/10.1016/j.energy.2021.119785.

Waweru, D., Mose, N., & Otieno, S. (2022). Household Energy Choice in Kenya: An Empirical Analysis of the Energy Ladder Hypothesis. . Journal of Energy Research and Reviews, 10(4), , 12-19.

Yalew, A. W. (2022). The Ethiopian energy sector and its implications for the SDGs and modeling. Renewable and Sustainable Energy Transition, 2, 100018.

Yonas, W. (2016). SUN TRANSFER:Sustainable Off-grid energy solutions. Seminar on Ensuring Access to Affordable, Reliable, Sustainable and Modern Energy for All (SDG 7). Addis Ababa: UNDESA.

Zou, B., & Luo, B. (2019). Rural Household Energy Consumption Characteristics and Determinants in China. Energy, doi: 10.1016/j.energy.2019.06.048.

Influence of Maize Cob Ash as a Filler Material in Asphalt Concrete Mixes

Destaw Kifile Endashaw

Civil Engineering Department, Faculty of Technology, Debretabor University, Debretabor, Ethiopia
**Corresponding author, e-mail: destaw02@gmail.com*

ABSTRACT

In this study, an attempt has been made to assess the influence of Maize Cob Ash (MCA) as filler in asphalt concrete mix. The effect of Maize cob ash on mechanical properties of the asphalt concrete such as Marshall stability, flow, volumetric properties, and Indirect Tensile Strength of asphalt binder courses for heavy traffic roads has been evaluated. A total of thirty (30) asphalt concrete specimens were prepared with basaltic stone dust (BSD) and Maize cob ash as a filler with bitumen content between 3.5% and 5.5% at varying increments of 0.5% and the Marshall Stability test was performed on full mixes to determine the Optimum Bitumen Content (OBC) of the mixtures. From the test results, it is seen that specimens made with Maize cob ash and basaltic stone dust are found to have satisfactory Marshall properties and moisture susceptibility showed that mixes using MCA filler provide better resistance to moisture effect than mixtures using BSD filler. The optimum asphalt content (4.69%) in the case of MCA and BSD are (4.86%), the same is slightly higher. It is seen that maximum stability is observed by MCA filler materials. The value of stability of the asphalt concrete mixture using MCA and BSD is 11.4KN and 10.9KN respectively which satisfies the limiting value of 8.006 KN. Research findings indicated that the Indirect Tensile Strength Ratio (ITSR) of the paving mixes using basaltic stone dust was 93.71%, and Maize cob ash was 97.04% which satisfies the criteria provided in the ERA and Asphalt Institute Standard Specifications. Hence, it is generally concluded that the Maize cob ash can effectively be used as filler in paving mixes in place of the most commonly used filler such as basaltic stone dust. Maize cob ash is a viable agriculture waste product that can be used as filler materials in the production of asphaltic binder courses for heavy-trafficked roads. Overall, the use of Maize cob ash as filler in hot mix asphalt concrete partly solves the significant agricultural waste disposal problem of the environment.

Keywords: *Basaltic Stone Dust, Flow, Marshall Stability, Tensile Strength, Heavy Traffic*

1. INTRODUCTION

Asphalt mixture is the most widely used material in road pavement due to its superior in-service performance (Seyed , et al., 2018). Asphalt mixture is a combination of aggregate, asphalt binder, and filler (Seyed , et al., 2018; Fisseha , et al., 2018). Asphalt concrete is a well-graded mixture containing coarse aggregate (50-65%), fine aggregate and filler (35-50%), asphalt (5-8%) of the total mass of aggregate (Rocksana & Kamal, 2017). Among them, the filler is one of the most important components of asphalt concrete (Asmael, 2010) The filler plays a major role in the properties and behavior of bituminous paving mixtures (Asmael, 2010; Rahman, et al., 2012; Jain, et al., 2013). A good design of asphaltic concrete is expected to result in a mix that is adequately strong, durable, resistant to fatigue and permanent deformation, and at the same time environmentally friendly and economical (Osuya & Mohammed, 2017). Suitable material combination and modified asphaltic concrete have been found to result in longer life for wearing courses depending on the type and percentage of mineral filler used (Tomar, et al., 2013).

A lot of studies have been done on using solid waste as a modified material in Hot Mix Asphalt Concrete (HMAC). In general, Modifying HMAC for waste material can be done in three ways. One innovation is to employ waste material as a modifier for the asphalt binder. HMAC has improved qualities when the asphalt binder is amended with the inclusion of rubber, polymer, and a variety of other waste materials, according to studies (Ghasemi & Marandi, 2013; Yildirim, 2007). The second advancement is the utilization of solid waste material as a filler and aggregate substitute in HMAC. The importance of the filler used in asphalt concrete was revealed in the findings of various investigations (Rocksana & Kamal, 2017). The third method is to use additives such as polymers and fibers to HMAC in addition to the binders and aggregates. The performance of HMAC with PET and

HDP in stone mastic asphalt was tested in many studies (Singh & Sakale, 2018). The results reveal that the replacement or addition makes the mix better.

With the rapid economic growth and continued increased consumption, a large number of waste materials are generated. One of the main problems in the construction of bituminous paving mixture is the insufficient amount of filler from crushing stone aggregate, and cement supply is low (Fisseha , et al., 2018; Destaw, et al., 2020). The shortage is to be filled by importing supplies from other locations such as blasting of more quarry areas. This could result in the deterioration or depletion of naturally available materials like sand and rock, making the production of mineral fillers more challenging. Meanwhile, as natural sources of high-quality granular materials for highway construction have grown scarce, the problem for the highway engineer is to identify alternate materials that meet the specifications for these materials. Some of these alternative materials are marble dust (Mustafa & Serdal , 2007), fly Ash (Raja & Tapas, 2016), Stone sawdust ash (Osuya & Mohammed, 2017), Rice Husk Ash and Slag (Rocksana & Kamal, 2017). There would be three advantages to using waste or by-product materials in construction projects instead of natural materials: saving natural resources, disposing of waste materials (which are sometimes ugly), and freeing up precious land for other uses. As a result, it is advisable to preserve and reduce the use of natural materials, as well as to consider how to reuse and recycle waste materials that can be used to replace natural materials. In the present study, evaluate the influence of maize cob ash on the characteristics of asphaltic concrete to investigate its suitability as an additive in asphaltic concrete. The objective of the study is to evaluate the Marshall and mechanical properties of basaltic stone dust and maize cob ash as a filler material in hot mix asphalt concrete, according to the test procedure specified by ASTM.

2. MATERIALS AND METHODS

Asphalt concrete is a well-graded mixture containing coarse aggregate (50-65%), fine aggregate and filler (35-50%), asphalt (5-8%) of the total mass of aggregate (Rocksana & Kamal, 2017). Materials used in the Mix design of asphalt include BSD and MCA as a filler material, the crushed basaltic rock as a coarse and fine aggregate, and 85/ 100 penetration grade of bitumen as binder material. The maize cob ash used in this study was collected from local farms after threshing of the kernel maize. The maize cob was exposed to air for 8 hours by spreading the cobs in an open space to reduce the moisture content. The maize cobs were burnt into ash at a temperature of 700°C, allowed to cool, and sieved through a sieve No.200 (0,075 mm) to remove pebbles and unburnt shaft before being added to the mix. The basaltic rock of coarse aggregate, fine aggregate, and BSD filler are supplied from International First Highway (IFH) Engineering PLC construction quarry in four different sizes: 14-25mm, 6-14mm, 3-6mm, and 0-3mm. The bitumen used was also collected from IFH engineers PLC batching plant. The methodology involves the experimental tests carried out to determine the physical properties of bitumen, coarse aggregate, fine aggregate, BSD, and MCA. All the testing is conducted using equipment and devices available in the laboratories of IFH Engineering PLC.

2.1 Physical Properties of Mineral Filler

Mineral filler is defined as that portion of the aggregate passing the 0.075-mm sieve. Mineral filler is a very fine material with the consistency of flour and is also referred to as mineral dust or rock dust. Moreover; at least 70 percent of this material passes the No. 200 (0,075 mm) standard sieve (Destaw, et al., 2020). Filler is one of the most important components of asphalt concrete. It plays a significant role in the properties of asphalt concrete (Asmael, 2010; Tomar, et al., 2013). The fillers used in the current study namely Basaltic Stone Dust (BSD) and Maize Cob Ash (MCA). The amount of these fillers was selected as equal to 6% by the total mass of aggregates. Laboratory tests have been conducted to evaluate the physical properties of each type of filler, which consist of the gradation parameters, absorption plasticity index, and specific gravity. Table 1, illustrates the physical properties of each type of filler.

Table 1: Physical Properties of the used mineral filler with standard specifications

Sieve No.	Percentage of Passing		ASTM D242
	MCA	BSD	
No. 30	100	100	100
No. 50	96	98	95-100
No. 200	80	89	70-100
Plasticity Index	NP	NP	Max 4
Absorption (%)	0.2	1.2	Max 2
Specific gravity	2.60	2.70	--

2.2. Physical Properties Mineral Aggregate

Aggregate structures provide the largest portion of the resistance to permanent deformation, repeated load applications, degradation, and structural instability of asphalt pavement mixture. To investigate the physical properties of the aggregates and their suitability in road construction, various lab tests were conducted on basaltic aggregate, including sieve analysis, specific gravity, and Los Angeles abrasion tests. Table 2 summarizes the physical properties of the fine and coarse aggregates used in this research. The results indicate that all aggregate materials conform to specifications. The aggregate gradation used in this study is given in Table 3 with ASTM specifications for asphalt binder course gradation. Fig. 1 shows the result of the grain size distribution of the mixture used in this research. It can be seen that the selected aggregate gradation curve is found to be satisfying ASTM specification for asphalt binder course gradation.

Table 2: Properties aggregates and standard specifications

Test	Test Method	Test Result				Specification
		14-25 mm	6-14 mm	3-6 mm	0-3 mm	
Bulk dry S. G	AASHTO T 85-91	2.66	2.68	2.60	2.60	-
Sand Equivalent, %	AASHTO T176-86	73.9	-	-	-	Min 40
Bulk SSD S. G	AASHTO T 85-91	2.65	2.67	2.61	2.67	-
Water absorption %	BS 812, Part 2	1.9	1.9	1.9	-	Max 2
Apparent S. G	AASHTO T 85-91	2.71	2.73	2.79	2.77	-
ACV, %	BS:812 Part 110	16	-	-	-	Max 25
Flakiness Index	BS 812 Part 105	21	-	-	-	Max 45
LAA %	AASHTO T 96	15	-	-	-	Max 30

Table 3: Aggregates graduation and specification

Sieve Size (mm)	Gradation of aggregates and Weight			ASTM D3515 Specification
	Passing (%)	% Used	weight (g)	
25	100	0	0	100
19	94.49	5.5	66.13	90-100
12.5	77.79	17	200.4	71-88
9.5	67.22	11	126.8	56-80
4.75	46.43	21	249.5	35-65
2.36	31.25	15	182.2	23-49
1.18	21.47	9.8	117.3	15-37
0.6	14.71	6.8	81.18	10-28
0.3	10.3	4.4	52.92	5-19
0.15	7.934	2.4	28.38	4-13
0.075	6.0	1.9	23.2	2-8

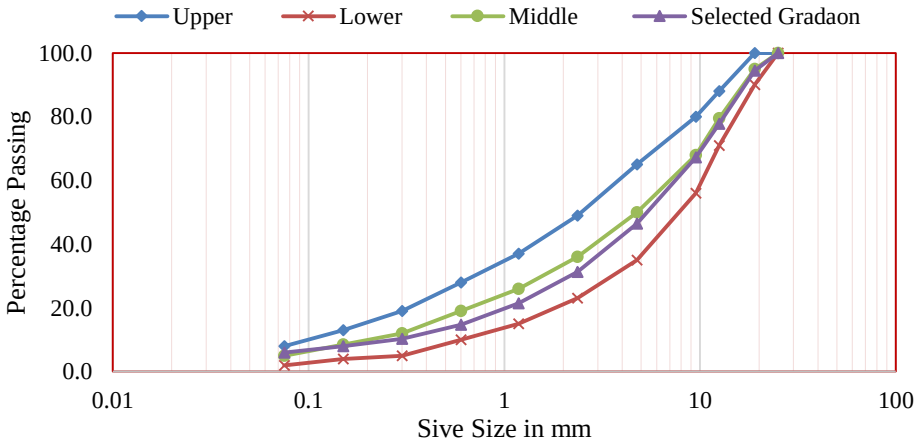

Figure 1: Combined aggregate gradation curve containing 6.0% CSD fill

2.3. Asphalt Binder Properties

Asphalt binders, sometimes referred to as asphalt cement binders or simply asphalt cement, are an essential component of asphalt concrete they are the cement that holds the aggregate together. One penetration-grade asphalt cement 85/100 is widely used in Ethiopia. This asphalt was obtained from IFH engineers PLC batching plant, kality. This type of asphalt was chosen because it is widely used in road construction in the country of Ethiopia. A series of bitumen quality tests were conducted before the start of the mix design. The specific gravity of asphalt cement used was 1.025. Table 4 gives a summary of the test results of 85/100 penetration grade binder obtained from the asphalt binder in the laboratory.

Table 4: Properties of the 85/100 Penetration Grade Bitumen

Property	Unit	Test Method	Test Result	Specification
Penetration (25°C)	(0.1mm)	AASHTO T49	92.3	85-100
Ductility	(cm)	AASHTO T51	108	Min 100
Softening point	(°C)	AASHTO T53	46.4	42-51
Solubility	(%)	AASHTO T44	99.4	Min 99%
Specific gravity at (25°C)	(g/cm^3)	AASHTO T228	1.025	-

2.4. Mix Design and Preparation of Specimens

In this study, the Marshall method was used to determine the optimum bitumen content and prepare HMA according to ASTM D1559 standard method (ASTM, 2000). Three Marshall specimens for each combination were prepared at five different bitumen contents between 3.5% and 5.5% by total weight of mixture at 0.5% increments and the average of these results has been reported. The amount of filler for all mixture proportions was fixed to 6%. As a first step in the procedures, well-blended aggregates and filler were put together in the oven to a temperature of 175°C for 16hr to become completely dry before preparing HMA mixtures. Then, the asphalt binder was heated to the temperature of 155–160°C before being mixed with aggregates. Starting from the first trial, the required amount of heated asphalt binder was added to heated aggregates and then thoroughly mixed by a mechanical mixer at the desired temperature of 160°C for 120 seconds. The mixtures were compacted by a Marshall compacter hammer with 75 blows on each side of the specimen for heavy traffic. The compacted specimens were removed from molds after 24 hours using a specimen extractor. After extraction, each specimen was weighed dry in the air, weighed in water and saturated surface dry weight of the specimens was determined and subjected to a density-voids analysis, and then Marshall stability and flow test were conducted on the cylindrical samples according to ASTM D1559 (ASTM, 2000). The prepared samples were placed in a water bath at 60°C; after 30 ± 5 min of immersion, the Marshall test was conducted. The maximum load at failure and the corresponding deformation (or flow) readings were recorded. Test results were compared to standard specification values for stability and flow.

2.5. Indirect Tensile Strength Test

The Indirect Tensile Strength (ITS) test is used to measure the tensile strength of the bituminous concrete which can be used to assess the fatigue behavior (Dipankar , et al., 2016). The indirect tensile test was developed to determine the tensile properties of cylindrical concrete and asphalt concrete specimens through the application of a compression load along a diametrical plane through two opposite loading heads (Debashish , et al., 2014; Amir & Morteza , 2014). This type of loading produces a relatively uniform stress acting perpendicular to the applied load plane, causing the specimen to fail by splitting along the loaded plane (Amir & Morteza , 2014). The indirect tensile strength tests were conducted at 25°C and 40°C according to the ASTM D6931 standard method. The specimens were immersed in a water tank set at the desired temperature for 30 min, then they were placed in ITS frame and loaded diametrically by Marshal test set up at a rate of 50.8 mm/min until failure (Hasan & Ramin , 2020). ITS provides a measure of the tensile strength of the asphalt mixes. The test is conducted on the conditioned and unconditioned specimens. To calculate the ITS the failure load is measured, according to the maximum load carried by a specimen at failure, the following equation is used.

$$S_t = \frac{2p}{\pi t D} \qquad \text{..... (1)}$$

In which, S_t is the indirect tensile strength in (N/mm^2), P is the maximum applied load for breaking the specimen in N, D is the specimen diameter in mm and t is the thickness of specimen in mm. The indirect Tensile Strength Ratio (TSR) is determined with the following equation:

$$TSR = \left(\frac{S_{cond}}{S_{uncond}}\right) 100 \qquad \text{…….. (2)}$$

where: S_{cond} is the average ITS of the wet specimen and S_{uncond} is the average ITS of the dry specimen.

Water is the worst enemy of asphalt concrete mixtures. The premature failure of a flexible pavement may be caused by the presence of water (Debashish , et al., 2014). From the Marshall Immersion test conducted for mixtures prepared at their optimum asphalt content, the Tensile Strength Ratio (TSR) values are obtained as a ratio of conditioned and unconditioned specimens. This ratio indicates resistance to moisture-induced damage to the bituminous mixture.

3. RESULTS AND DISCUSSION

3.1. Marshall Tests Analysis of asphalt mixture properties

The stability is the maximum load resistance that a test specimen will develop under compression, and the flow value is the total movement or strain occurring in the specimen during the compression test. A total of 30 samples each one of which weighs 1200 grams, were prepared using five different bitumen contents (3.5,4.0, 4.5, 5.0, and 5.5% of total weight) to determine the optimum bitumen content. The results of the Marshall test of specimens prepared with maize cob ash and basaltic stone dust as filler for varying bitumen contents have been presented in Tables 5 and 6 respectively. Marshall properties such as stability, flow, bulk specific gravity, air voids, voids filled with asphalt, and voids in mineral aggregate were determined for each specimen. The results of the Marshall Tests have been presented in Fig. 2 through Fig. 7, in which the variations of Marshall Properties concerning bitumen contents for all the three types of fillers considered in this study are shown. According to (ERA, Pavement Design Manual, 2002) Marshall design criteria for heavy traffic, minimum Marshall Stability must be 7 KN at 600C, flow value must be range between 2 to 4mm, percentage of air voids must be ranged between 3 to 5%, minimum VMA related to 4% air voids and nominal maximum particle size of 19 mm must be 13 and VFB must be ranged between 65 to 75%.

Table 5: Average Marshall Properties of Specimens with 6.0% MCA filler

Bitumen Content	Bulk Specific Gravity (g/cm^3)	Air voids (%)	VMA (%)	VFA (%)	Marshall Stability (KN)	Flow (mm)
3.5	2.336	6.4	14.0	54.3	9.3	3.02
4.0	2.346	5.4	14.1	62.0	11.1	3.12
4.5	2.360	4.1	14.0	70.5	11.4	3.31
5.0	2.358	3.5	14.5	75.8	10.7	3.37
5.5	2.351	3.2	15.2	78.9	9.3	3.44

Table 6: Average Marshall Properties of Specimens with 6.0% BSD filler

Bitumen Content	Bulk Specific Gravity (g/cm^3)	Air voids (%)	VMA (%)	VFA (%)	Marshall Stability (KN)	Flow (mm)
3.5	2.330	6.8	14.2	52.4	8.6	3.03
4.0	2.342	5.6	14.2	60.6	9.4	3.08
4.5	2.355	4.4	14.2	69.4	10.2	3.11
5.0	2.364	3.3	14.3	77.2	10.6	3.30
5.5	2.353	3.0	15.2	80.1	9.4	3.56

Fig. 2 and Fig. 4 show that the Marshall Stability and unit weight for the total mix increases with the increase in the bitumen content up to a maximum and then gradually decreases in both filler types. This may be due to making both types of fillers and asphalt cement combination act as a more viscous binder thus increasing the Marshall stability. Therefore, the maize cob ash filler stiffens the asphalt film and reinforces it. That means a mixture containing maize cob ash filler had good resistance of deformation than basaltic stone dust filler, whereas the voids filled with asphalt (VFA) increased with an increase of bitumen content as shown in Fig. 7. The VFA for the mix with basaltic stone dust is lower than the maize cob ash of the asphalt mix. This was since more effective bitumen content was present in the mix to fill the available voids between the inter-granular spaces. Besides, the percent voids in the mineral aggregate (VMA) decrease to the minimum value then increase with increasing bitumen content as shown in Fig. 6.

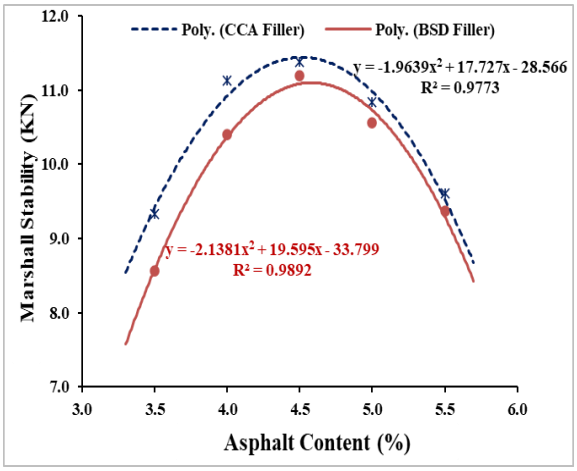

Figure 2: Effect of filler types on Marshall Stability of the mix

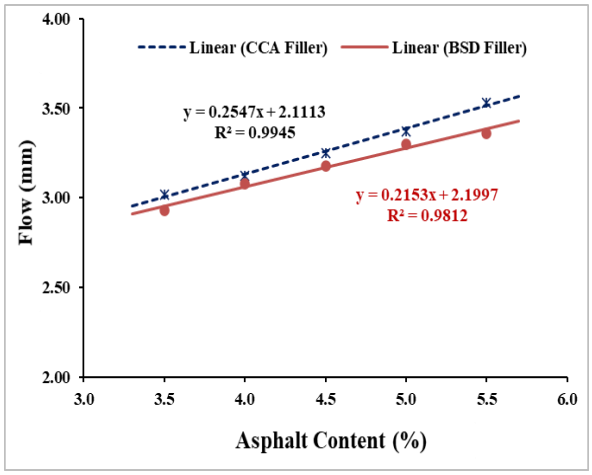

Figure 3: Effect of filler types on flow

As shown in Fig.3 flow value increases with increasing asphalt content. However, the flow value is lowest for mixes with basaltic stone dust as filler compared to maize cob ash. This is because basaltic stone dust makes the mix stiffer compared to maize cob ash fillers.

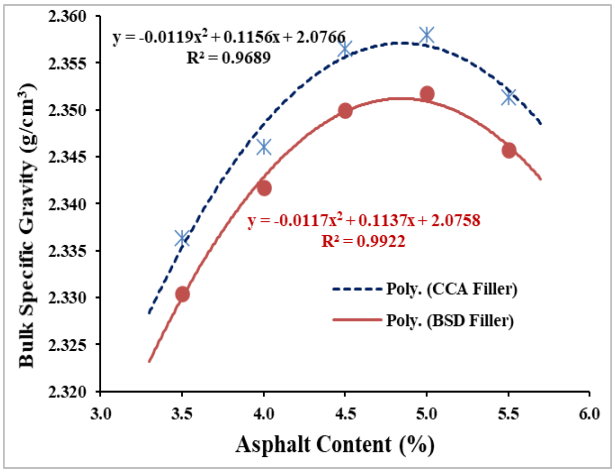

Figure 4: Effect of filler types on unit weight of the mix

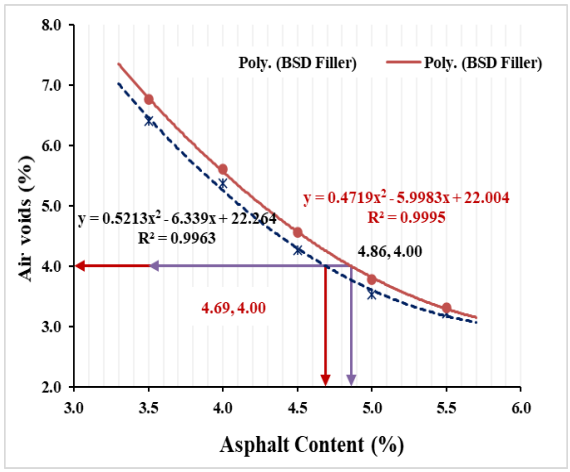

Figure 5: Effect of filler types on the air voids of asphalt mix

Similarly, Fig. 5 shows that the air void decreases with an increase in bitumen content. However, it is to be emphasized that the maize cob ash causes maximum reduction of air voids compared to the basaltic stone dust fillers. This may be since maize cob ash being too fine having the highest surface area fills the voids more effectively.

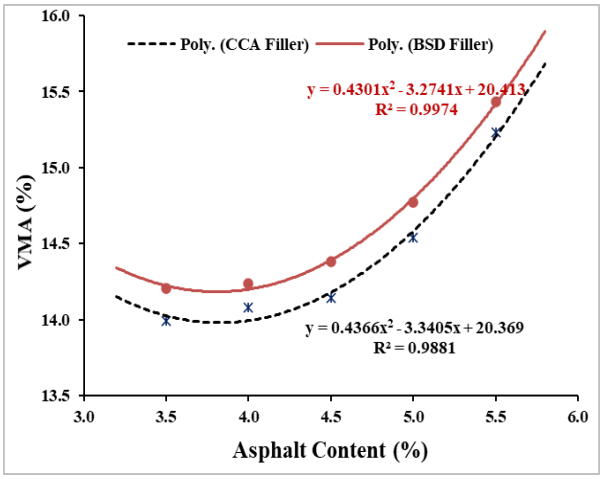

Figure 6: Effect of filler types on VMA of the mix

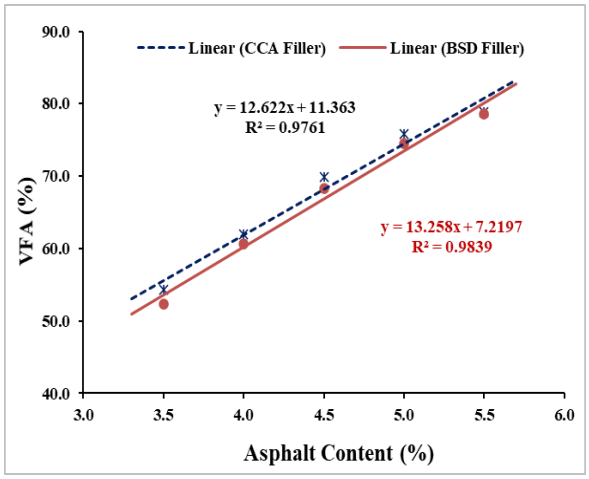

Figure 7: Effect of filler types on VFA of the mix

3.2. Determining the Optimum Bitumen Content

Use of the proper amount of binder is essential to good performance in asphalt concrete mixtures. A too little binder will result in a dry stiff mix that is difficult to place and compact and will be prone to fatigue cracking and other durability problems. Too much binder will be uneconomical since asphalt binder is, by far, the most expensive component of the mixture and will make the mixture prone to rutting and shoving. Typical asphalt binder contents range from 3.0% or less (for lean base course mixtures) to over 5.0% (for surface course mixtures and rich bottom layers), which are designed for exceptional durability and fatigue resistance (ERA, Pavement Design Manual, 2002; Asphalt Institute, 2003). Marshall test was used to examine the specimens of asphalt mixture with bitumen content 3.5, 4.0, 4.5, 5.0, and 5.5% to obtain the optimum bitumen content. The optimum bitumen content is determined by the method of the National Asphalt Pavement Association (NAPA), which suggest preparing the plots of Fig. 2 to Fig. 7. The optimum bitumen content is determined by first finding the bitumen content which corresponds to the median air void content (4 %) of the specification. It is then used to determine the values for Marshall stability, flow, VMA, VFA, and % voids filled for each filler type (Table 7). From the result, the optimum bitumen content is 4.69, and 4.86% at 4 % air voids of MCA and BSD filler respectively as shown in Fig. 5.

Table 7: Marshall Properties with MCA and BSD fillers at optimum bitumen content

Mix Properties	Filler Type		Standard Values (For heavy traffic)
	MCA	BSD	
OBC [%]	4.69	4.86	-
Unit weight [g/cm³]	2.357	2.352	-
Air void [%]	4.0	4.0	3-5
Stability [KN]	11.4	10.9	Min 8
Flow [mm]	3.31	3.25	2-4
VMA [%]	14.3	14.4	Min 13
VFB [%]	70.56	71.65	65 - 75

3.3. Indirect Tensile Strength Test

The test is performed at different temperatures such as 5°C, 10°C, 15°C, 20°C, 25°C, 30°C, 35°C, and 40°C. The test results for the indirect tensile strength test for two types of mixtures obtained in the study are shown in Fig. 8. It has been seen that the indirect tensile strength value generally decreases with an increase in test temperature from 5°C to 40°C. At lower temperatures, the mixes have higher tensile strength. From Fig. 8 it is observed that at a particular temperature the mixture made with maize cob ash as the filler has lower tensile strength as compared to basaltic stone dust fillers, the shape of variation in the case of mix with maize cob ash is relatively gentler, concluding that the temperature susceptibility of mixes improves with the use of maize cob ash.

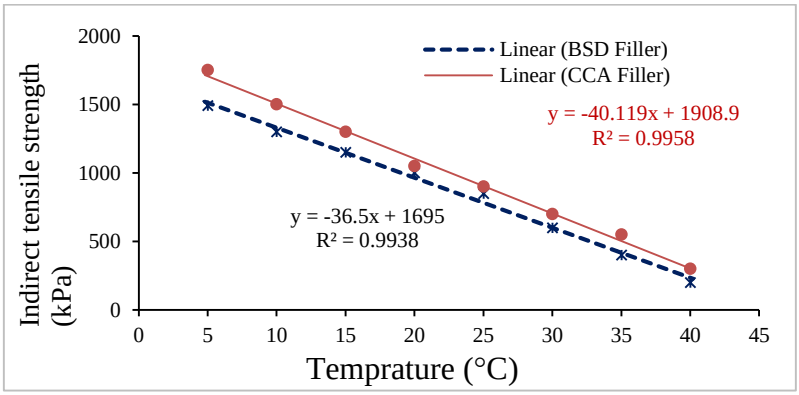

Figure 8: Indirect Tensile Strength of Mixtures with a filler type

Tensile Strength Ratio (TSR) for two types of mixes prepared at their OBCs considered in this study is presented in Table 8. It is noticed that the Indirect Tensile Strength (ITS) is highest when the mix contains maize cob ash and the value is 1.01 N/mm^2 and the corresponding Indirect Tensile Strength Ratio (TSR) is 91.18% which is acceptable for design criteria as per (ERA, Pavement Design Manual, 2002). It has been observed in Fig. 9 that the mixes prepared using basaltic stone dust (BSD) exhibit the lowest Tensile Strength Ratio (TSR) compared to mixes with maize cob ash (MCA) filler. All the tests carried out to determine the moisture susceptibility showed that mixes using maize cob ash filler provide better resistance to moisture effect than mixtures using basaltic stone dust filler.

Table 8: Average of Indirect Tensile Strength Test results

Filler Type	OBC	Indirect Tensile Strength		TSR (%)
		Unconditioned	Conditioned	
MCA Filler	4.69	1.03	0.98	95.15
		1.04	1.01	97.12
		0.97	0.96	98.97
Average		1.01	0.98	97.04
BSD Filler	4.86	0.95	0.93	97.89
		0.93	0.89	95.70
		0.98	0.86	87.76
Average		0.95	0.89	93.71

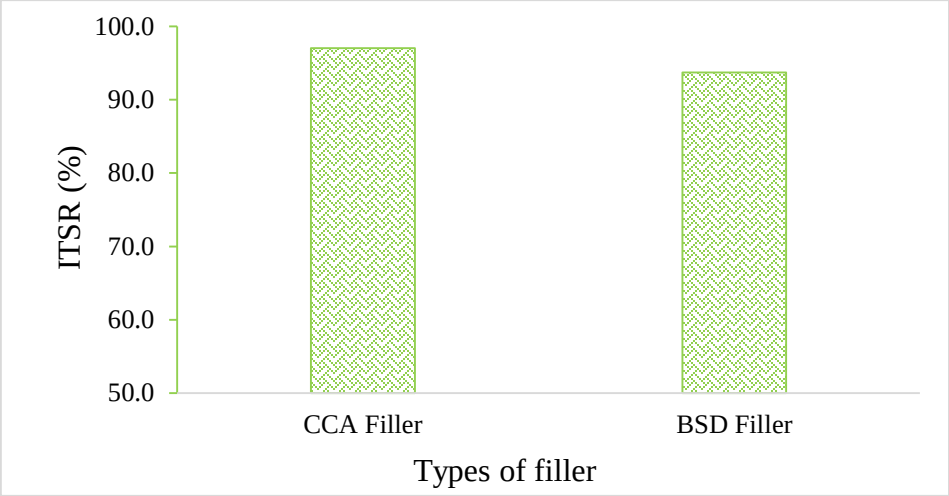

Figure 9: Indirect tensile strength ratio of Mixtures with filler type at OBC

4. CONCLUSION

This study tried to evaluate the influence of maize cob ash as a filler in hot mix asphalt concrete based on Marshall mix design tests. From the results of Marshall Tests and other performance tests conducted to explore the suitability of maize cob ash as filler in hot mix asphalt concrete, the following conclusions have been drawn. The laboratory test result for MCA gives gradation parameters and plastic index, satisfying the specification for use as a filler in hot mix asphalt concrete production. Maximum Marshall stability and unit weight values are observed for the mixes prepared with maize cob ash followed by basaltic stone filler. The optimum bitumen content obtained in the case of basaltic stone dust is slightly higher than maize cob ash. At a particular temperature, the indirect tensile strength of asphalt concrete mixed with maize cob ash as the filler has the highest value than basaltic stone dust. As temperature increases, ITS value in general decreases both filler types. It is observed that the value of ITSR for mixes prepared with maize cob ash as filler offers the highest indirect tensile strength ratio value than basaltic stone dust filler. However, the variations are so small to be considered significant and all the mixes satisfy the minimum ITSR value requirement the limiting value is 80%. It means all the mixes with maize cob ash as filler have very good resistance to moisture-induced damages. Hence, it is generally concluded that the maize cob ash can effectively be used as filler in paving mixes in place of the most commonly used filler such as basaltic stone dust. The use of maize cob ash in paving mixes may give a solution to the maize cob ash utilization and disposal problems and also give the means to make the environment safe and clean.

REFERENCES

Amir, M. & Morteza, R., (2014). Application of coal waste powder as filler in hot mix asphalt. Construction and Building Materials, Volume 66, p. 476–483.

Asmael, N. M., (2010). Effect of Mineral Filler Type and Content on Properties of Asphalt Concrete," vol. 16, no. Journal of Engineering, 16(3), pp. 5352-5362.

Asphalt Institute, (2003). Mix Design Method for Asphalt Concrete and other Hot-Mix Types. Manual series No. 02, Six Edition. Kentucky, USA.

ASTM, (2000). Test method for resistance of plastic flow of bituminous mixtures using Marshall apparatus. Annual Book of ASTM Standards USA.

Debashish, K., Mahabir, P. & Jyoti, P. G., (2014). Influence of Fly-Ash as A Filler in Bituminous Mixes. ARPN Journal of Engineering and Applied Sciences, 9(6), pp. 895-900.

Destaw, K., Emer, T. Q. & Abel, T., (2020). Effect of Partial Replacement of Crushed Stone Dust Filler with Waste Glass Powder in Hot Mix Asphalt Concrete Production. Journal of Xidian University, 14(9), pp. 578-587.

Dipankar, S., Manish, P. & Ashoke, K. S., (2016). Evaluation of the Properties of Bituminous Concrete Prepared from Brick-

Stone Mix Aggregate. Hindawi Publishing Corporation Advances in Materials Science and Engineering, 10(16), pp. 1-7.
ERA, Pavement Design Manual, (2002). Ethipians Road Authority Pavement Design Manual for Flexible pavements. Ethiopia.
Fisseha, W., Emer, T. Q. & Anteneh, G., (2018). Evaluation of the Performance of Brick Dust as a Filler Material for Hot Asphalt Mix Design: A Case Study in Jimma Zone. The International Journal of Engineering and Science (IJES), 7(3), pp. 64-72.
Ghasemi, M. & Marandi, S. M., (2013). Performance improvement of a crumb rubber modified bitumen using recycled glass powder. Journal of Zhejiang University-SCIENCE A (Applied Physics & Engineering), 14(11), pp. 805-814.
Hasan, T. & Ramin, B., (2020). Investigating the properties of asphalt concrete containing recycled brick powder as filler. European Journal of Environmental and Civil Engineering.
Jain, R. K., Kostha, M. K. & Tomar, R., (2013). Effect of Fillers on Bituminous Paving Mixes. International Journal of Engineering Research and Science & Technology, 2(1), p. 137–142.
Mustafa, K. & Serdal, T., (2007). Evaluation of marble waste dust in the mixture of asphaltic concrete. Construction and Building Materials, 21(3), pp. 616-620.
Osuya, D. O. & Mohammed, H., (2017). Evaluation Of Sawdust Ash as A Partial Replacement for Mineral Filler in Asphaltic Concrete. Ife Journal of Science, 19(2), pp. 431-440.
Rahman, A., Ali, S. A., Adhikary, S. K. & Ho, Q. S., (2012). Effect of Fillers on Bituminous Paving Mixes: An Experimental Study. Journal of Engineering Science, 3(1), p. 121–127.
Raja, M. & Tapas. K. R., (2016). Effect of using fly ash as alternative filler in hot mix asphalt. Recent Trends in Engineering and Material Sciences, Volume 8, pp. 307-309.
Rocksana, A. & Kamal, H. M., (2017). Influence of Rice Husk Ash and Slag as Fillers in Asphalt Concrete Mixes. American Journal of Engineering Research (AJER), 6(1), pp. 303-311.
Rocksana, A. & Kamal, H. M., (2017). Influence of Rice Husk Ash and Slag as Fillers in Asphalt Concrete Mixes. American Journal of Engineering Research (AJER), 6(1), pp. 303-311.
Seyed, A. T., Mahyar, A. & Ali. F., (2018). Usage of two biomass ashes as filler in hot mix asphalt. Construction and Building Materials, Volume 170, p. 547–556.
Singh, V. & Sakale, R., (2018). The Effect of Using Waste Plastic and Waste Glass on the Asphalt Pavement Properties. International Journal of Research in Engineering and Technology, 07(02), pp. 2321-7308.
Tomar, R., Jain, R. K. & Kostha, M. K., (2013). Effects of Fillers on Bituminous Paving Mixes. International Journals of Engineering Research, Science and Technology, 2(4), p. 2319 – 5991.
Yildirim, Y., (2007). Polymer modified asphalt binders. Construction and Building Materials, 21(1), p. 66–72.

Syndicate 2:

Smart Materials and Technology

Teleportation of Biosignal to Develop Lung Cancer Telemedicine Platform

Alemayehu Getahun Kumela*, Abebe Belay Gemta, Alemu Kebede Hordofa

Department of Applied Physics, Adama Science and Technology University, P.O.Box 1888, Adama, Ethiopia
**Corresponding author, e-mail: alemayehu.getahun@astu.edu.et*

ABSTRACT

Worldwide investigators have extensively explored telemedicine platform to perform medical activities remotely. However, the current working platform does not exceed diagnostic assistance due to the low sensitivity of the medical equipment and biosignal losses. The new emerging area of quantum information processing called quantum teleportation provides a new opportunity to overcome signal loss and security tolerated in the classical channel. Herein, we propose a unique numerical model to improve the surface sensitivity of the optoplasmonic biosensor for remote-based lung cancer detection and treatment. By applying the finite element method-based simulation technique, the performance of the proposed optoplasmonic biosensor for the detection of various types of lung cancer was outpaced. Then, employing quantum principles, the quantum properties of the resulting sensitive field, transmission fidelity of the teleported biosignals and laser light have been reported. From numerical results, the obtained sensitivities for Calu-1, A427, CK19, EGFR, and 95D lung cancer cells were 10230 nm/RIU, 10265 nm/RIU, 10318 nm/RIU, 10352 nm/RIU, and 10421 nm/RIU, respectively; with 96% transmission fidelity for biosignals and 98% teleportation fidelity for doses of light was also calculated. In conclusion, the proposed telemedicine schemes are expected to solve challenges in realizing faithful lung cancer telemedicine over long distances.

Keywords: *Telemedicine, Quantum Teleportation, Telediagnosis, Lung cancer, Phototherapy*

1. INTRODUCTION

Lung cancer remains the leading cause of cancer-related mortality in men and women (Mederos et al., 2020). Every year, approximately 2.3 million new lung cancer cases and about 1.8 million deaths occurred throughout the world (Li et al., 2022). Recently reported studies suggested, that environmental and industrial pollution, tobacco smoke, and genetic factors are the major causes (Xue et al., 2022). World Health Organization (WHO) categorized lung cancer based on its spread into primary and secondary, to decide which treatment the patient needed. Primary lung cancer occurs due to malignancy in the lung and based on its spread primary lung cancer is further restricted into small-cell lung carcinomas (SCLC) and non-small-cell lung carcinomas (NSCLC). Secondary lung tumors begin in the lungs and spread to other areas by traveling through the bloodstream or lymphatic system (Li and Niu, 2022; Jia et al., 2020; Choe et al., 2019).

For the first time, biosensors were introduced by Clark and Lyons in 1962 for the early detection of different diseases (Metkar and Girigoswami, 2019). Recently, electrochemical, piezoelectric, thermal, and optical biosensors have developed, to transform chemical and biological responses into measurable and processable optical or electrical signals (Esmaeilzadeh et al., 2022; Batool et al., 2022). Optical biosensors (OBs) have been extensively applied to detect, image, and sense chemical and biological substances due to their simplicity of modeling (theoretically, experimentally, and computationally) techniques (Patil et al., 2019). So far, optical resonator, optical fiber, optical waveguide, and surface plasmon polariton models have been introduced to achieve high selectivity, sensitivity, reliability, and robustness (Soler et al., 2020; Butt et al., 2021). In particular, optoplasmonic biosensors (OPBs) have attracted attention and become a more popular field due to their custom-made permittivity and permeability values, and this makes OPBs the best candidate for cancer bio-marker applications (Alqadami et al., 2018; Esfahani Monfared, 2020; Soler et al., 2019).

Several simulations and experimental work have been reported to improve sensor performance and the cost of OPBs (Jia et al., 2020; Patil et al., 2019; Butt et al., 2021). The effect of type or thickness of dielectric materials (SiC, TiO_2,Si_2 O) and metallic nanoparticles (MNPs) (Ag, Au,Al, and Cu) has been investigated with different

geometric structures such as; nanoscale mushrooms, nanocheckerboard, and nanopyramids designs. The results indicated that the MNPs and dielectric aggregates have excellent mechanical stability against repeated binding and are suitable platforms for low-cost and mass production (Nouman et al., 2020). In addition, with further work on incident angle, azimuthal angle, and polarization, high performance, and distinct spectral futures were reported (Bao et al., 2018). Currently, with experimental and simulation work on nanopillars and nanohole designs, the low-cost, high-performance, and angle-sensitive single-band OPBs has introduced (Yang et al., 2019). Since the single-band require sophisticated instrumentation spectroscopy and imaging, a multi-layer structure has been required for cancer biomarker applications, and was investigated in complex design for experimental and simulation work (Pradana et al., 2021; Prasad et al., 2019; Fu et al., 2022). Therefore, it is desirable to design a highly sensitive biosensor with a multi-user platform.

In addition, extensive experimental and theoretical work on the treatment of lung cancer has reported surgery, chemotherapy, and radiation (Chhatre et al., 2021; Sengupta and Balla, 2018; Rudin et al., 2021; Moeller et al., 2018). Chemotherapy is the use of anticancer drugs to kill, shrink, or slow down the growth of cancer cells and is a good treatment option for metastasized prostate cancer (Sengupta and Balla, 2018). Surgery was rarely used because cancer has often spread by the time it has been diagnosed, and difficult to remove tumors close to blood vessels (Rudin et al., 2021). While, due to its minimal evasiveness and relative clinical safety, radiation is the best candidate for lung cancer treatment (Moeller et al., 2018). The recent advancement of radiation technology improves the ability to image, target, and safely, but the substantial cost has far outpaced that of other medical specialties like telemedicine (Haleem et al., 2021)

Telemedicine is the general name for telediagnosis and telecare systems (Silva et al., 2020). Telediagnosis has been performed by using a biopsy needle to extract blood or another sample from the patient's tissue where an abnormal condition has occurred. It is sent to a distant location for further investigation of disease type and level to perform clinical decision-making. Then telecare is performed using an endoscope (Prasad et al., 2021). The endoscope is a long flexible tube with a tiny camera, an ultrasound probe, and a bright light used to perform phototherapy (Garg and Dewan, 2022). Meanwhile, the doses of light depend on the type and level of the cancer cell (Tabish et al., 2020). It requires the development of a stochastic algorithm for the super bright light emitting diode (S-LED) switching to generate a nonuniform irradiation system (NIS) (Gómez-Bombarelli et al., 2016; Brahme, 1987).

However, to perform accurate and effective LED-based telemedicine, a secured channel is the main requirement. By applying the most important theories of time-dependent quantum mechanics to spectroscopy, the study of the interaction of matter with electromagnetic radiation is outpaced (Kosloff, 1988). Quantum mechanically, we will treat spectroscopy as a perturbation induced by the light which acts to couple quantum states of the charged particles in the matter, and their interactions result in standing waves with intermediate spin orientation (Ruggenthaler et al., 2018). This allows us to share information between two infinitely distant particles despite having no conceivable way of communicating; this quantum phenomenon is known as entanglement (Jaeger, 2009). It has potential applications in quantum computing, sensing technology, and secure information transfer like; cryptography, quantum networking, and teleportation (Cacciapuoti et al., 2019; Wang and Alexander, 2020; Awschalom et al., 2021).

In this study, a unique model for optoplasmonic biosensors using laser light, plasmonic particles, and biomolecule interaction was proposed to achieve highly sensitive, specific detection and remote-based treatment of different types of lung cancer. In addition, by applying quantum entanglement, the teleportation of biosignals was assured to perform remote-based diagnosis and laser teletherapy. This work implicates the possibility of using quantum teleportation for effective lung cancer telemedicine.

2. MATERIALS AND METHODS

The study of optical and geometrical properties of plasmonic materials opens up a new approach that enables light confinement to a deep sub-wavelength scale to be applied in nanophotonic devices (Nouman et al., 2020). Those devices experience radiative and absorptive kinds of losses. A search for alternative plasmonic and dielectric material models enables low absorption loss and deep sub-wavelength confinement. The interaction of deep sub-wavelength light with biomolecules results in highly sensitive biosignals (Yang et al., 2019). In our model, we consider the interactions of the sensor region with intense laser light to result in sensitive biosignals for remote-based diagnosis and treatment.

2.1 Design and Performance Analysis of Proposed Biosensor

2.1.1. Design Analysis of Proposed Biosensor

Here we consider the properties of metallic oxide (MO), biomolecules, and the environment for the construction of a proposed biosensor. Crystallinity and aggregation are also considered under MO, and alpha-type Fe_2 O_3 precipitation has been chosen (Zhang et al., 2022a). Besides, under biomolecules; shape, size, sequence, conformation, surface charge, surface charge hydrophobicity, H, and π bond type are considered (Sakulkhu et al., 2015). In addition, under environmental media conditions, pH, ionic strength, polarity, temperature, string, and viscosity are determined (McClements and Gumus, 2016) to construct the proposed biosensor.

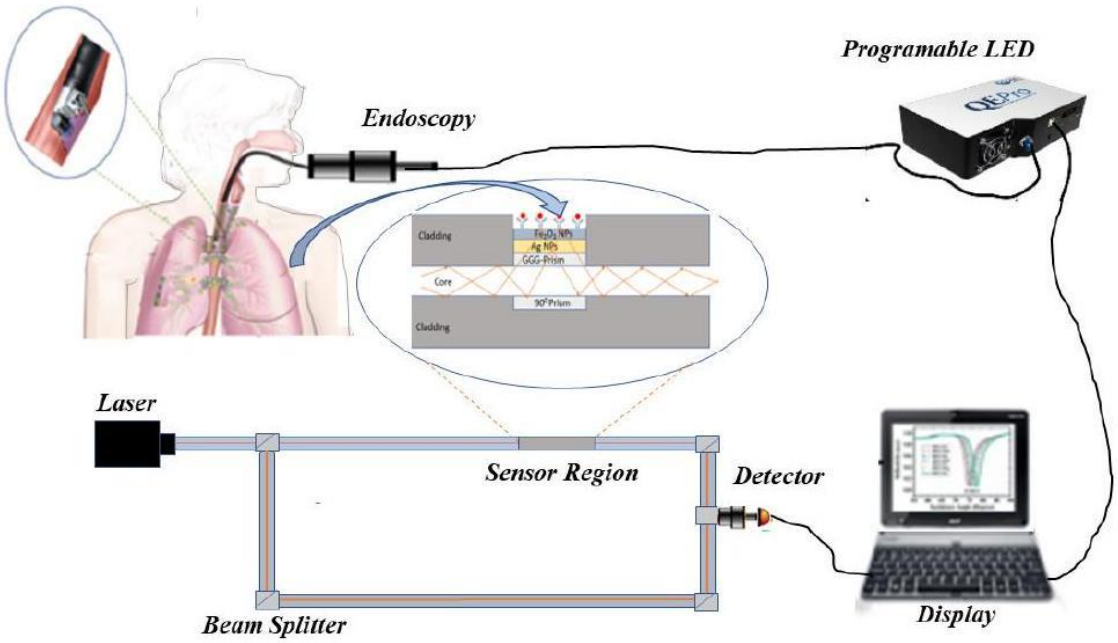

Figure 1: Optical layout of the proposed telemedicine platform

Table 1: Design parameters of proposed sensor structure at visible wavelength

Materials	type	RI	Reference
Biomolecules	EGFR	1.66	Liu et al., 2018
	ck19	1.62	Chiu et al., 2018
	calu-1	1.3	Zhang et al., 2022b
	A427	1.5	Zhang et al., 2022b
	95D	1.7	Zhang et al., 2022b
Dielectric	$\mathrm{Fe_2O_3}$	3.125	Jongen et al., 2000
MNP	Ag	0.156	Kumela et al., 2022
Prism	GGG-Prism	1.97	Matiatou et al., 2021

Coupling the incident electromagnetic field with a metal-dielectric interface, as depicted in Figure.1 sensor region part, results in the collective oscillation of free electrons along metal-dielectric interfaces. It is described by the relative permittivity as a summation of permittivity of metal and dielectric, $(\varepsilon_r(\omega) = \varepsilon_m(\omega) + \varepsilon_d(\omega))$, and each permittivity is given as a summation of the real and imaginary part $\left(\varepsilon_{i=d,m,A}(\omega) = \varepsilon_i'(\omega) + j\varepsilon_i''(\omega)\right)$. Where, ω is the frequency of incident light and the subscript d, m, and A represents; the permittivity of metal, dielectric materials, and biomolecule respectively with j as an imaginary number. Therefore, one can write the relative permittivity of optoplasmonic surface in terms of the classical Lorentz-Drude model using (Huber and Marinero, 1988),

$$\varepsilon_r(\omega) = \sum_{i=d,m}\left[\varepsilon_\infty^i - \frac{\Omega_i^2(\omega_i^{*2}-\omega_i^2)}{(\omega_i^{*2}-\omega_i^2)^2+\gamma_i^2\omega_i^2} + j\frac{\Omega_i^2(\gamma_i\omega_i)}{(\omega_i^{*2}-\omega_i^2)^2+\gamma_i^2\omega_i^2}\right]. \quad \ldots\ldots\ldots\ldots\ldots\ldots\ldots (1)$$

where Ω, ω^* and γ represent the plasma frequency, resonant frequency, and damping factor, respectively, and the refractive index of PMS is also defined with relative permittivity (Jongen et al., 2000).

$$n = \sqrt{\varepsilon_r(\omega)}. \quad \ldots\ldots\ldots\ldots\ldots\ldots\ldots\ldots\ldots\ldots\ldots\ldots\ldots\ldots\ldots\ldots\ldots\ldots\ldots\ldots (2)$$

With this notation, the plasmonic resonance wavelength can be evaluated by (Kumela et al., 2022)

$$k_{sp} = \frac{2\pi}{\lambda}\sqrt{\frac{\varepsilon_d\varepsilon_m}{\varepsilon_d+\varepsilon_m}}. \quad \ldots\ldots\ldots\ldots\ldots\ldots\ldots\ldots\ldots\ldots\ldots\ldots\ldots\ldots\ldots\ldots\ldots\ldots (3)$$

2.1.2. Performance Analysis of the Proposed Biosensor

Inside the sensor region, there is nanosurface and biological molecule (gene) interaction (Yang et al., 2019). With this consideration, the reflectance of laser-dielectric surface (r_{Ld}), dielectric-MNPs (r_{dm}) and plasmonic fieldbiomolecule $\left(\mathrm{r}_{pA}\right)$, interaction takes the form,

$$r_{Ld} = \frac{\varepsilon_m k_p - \varepsilon_p k_m}{\varepsilon_m k_p - \varepsilon_p k_m},$$
$$r_{dm} = \frac{\varepsilon_d k_p - \varepsilon_d k_d}{\varepsilon_d k_m - \varepsilon_m k_d}, \quad \ldots\ldots\ldots\ldots\ldots\ldots\ldots\ldots\ldots\ldots\ldots\ldots\ldots\ldots\ldots\ldots\ldots (7)$$
$$r_{pA} = \frac{\varepsilon_A k_d - \varepsilon_A k_A}{\varepsilon_A k_d - \varepsilon_d k_A}.$$

The reflection coefficient of the incident optical signal of the sensor can be expressed employing Eq. (4) to Eq. (6) as,

$$r_{LmdA} = \frac{r_{dm+r_{LdA}e^{2jk_{mpA}}}}{1+r_{LmdA}e^{2jk_{mdA}}}. \quad \ldots\ldots\ldots\ldots\ldots\ldots\ldots\ldots\ldots\ldots\ldots\ldots\ldots\ldots\ldots\ldots\ldots (8)$$

By applying Eq. (7), the full width at half maximum (FWHM), which can be defined as 50% of the reflectance curve spectral shift can be calculated. In addition, applying the spectral interrogation method into Eq. (7), the sensitivity of proposed OPBs given by,

$$S(\lambda) = \frac{\Delta\lambda}{\Delta n_c}. \quad \ldots\ldots\ldots\ldots\ldots\ldots\ldots\ldots\ldots\ldots\ldots\ldots\ldots\ldots\ldots\ldots\ldots\ldots\ldots\ldots\ldots (9)$$

Where $\Delta\lambda$ represents the change in the refractive index of the resonance peak and Δn_c is the change in the refractive index of biomolecules. Besides, the figure of merit is also given as the ratio of sensitivity to FWHM (Patil et al., 2019).

Furthermore, the resolution of the proposed OPBs expressed using,

$$R = \Delta n_c \frac{\Delta\lambda_{\text{ins}}}{\Delta\lambda}. \quad \ldots\ldots\ldots\ldots\ldots\ldots\ldots\ldots\ldots\ldots\ldots\ldots\ldots\ldots\ldots\ldots\ldots\ldots\ldots\ldots\ldots (10)$$

For, $\Delta\lambda_{\text{ins}}$ is the resolution of instrumental peak wavelength.

2.2. Biosignal Processing for Lung Cancer Telediagnosis

2.2.1. Quantum Features of the Proposed Scheme

Quantum mechanically, we express the interaction of sensor region with laser light using Hamiltonian of the system given in (Kumela et al., 2022),

$$H = H_F + H_{SR} + H_{int}. \quad \ldots\ldots\ldots\ldots\ldots\ldots\ldots\ldots\ldots\ldots\ldots\ldots\ldots\ldots\ldots\ldots\ldots\ldots\ldots\ldots\ldots (11)$$

In which, the Hamiltonian of laser field takes the form,

$$H_F = \hbar\omega\hat{a}^{\dagger}\hat{a}, \quad \ldots\ldots\ldots\ldots\ldots\ldots\ldots\ldots\ldots\ldots\ldots\ldots\ldots\ldots\ldots\ldots\ldots\ldots\ldots\ldots\ldots (12)$$

Besides, the Hamiltonian of the sensor region is expressed as,

$$H_{SR} = \hbar\omega_0 \sum_i \xi_i\left[\hat{b}_i^{\dagger} + \hat{b}_i\right], \quad \ldots\ldots\ldots\ldots\ldots\ldots\ldots\ldots\ldots\ldots\ldots\ldots\ldots\ldots\ldots\ldots\ldots\ldots\ldots\ldots\ldots (13)$$

For i is the parameters of each layer of the sensor region, ω_0 is normalized resonant frequency, $\xi = \frac{Q^2}{8\pi\epsilon M\omega_0 l\times h}$ is coulomb interaction strength, for Q is effective charge, ϵ_0 is vacuum frequency, M is the effective mass of each layer, 1 is the length of each layer, and h is the height of each layer. While, the bosonic operators that must satisfies $[\hat{a}, \hat{a}^{\dagger}] = \sigma_{ii}$ also defined by

$$\hat{b} = \sqrt{\frac{M\omega_0}{2\hbar}}p + i\sqrt{\frac{1}{2\hbar M\omega_o}}q. \quad \ldots\ldots\ldots\ldots\ldots\ldots\ldots\ldots\ldots\ldots \quad (14)$$

Where p and q are the dynamical coordinates and conjugate momentum of each layer respectively.
And the interaction Hamiltonian takes the form,

$$H_{int} = \hbar\sum_i \eta_i\left(\hat{a}_i^{\dagger}\hat{b}_i + \hat{b}_i^{\dagger}\hat{a}_i\right), \quad \ldots\ldots\ldots\ldots\ldots\ldots\ldots\ldots\ldots\ldots \quad (15)$$

in which, $\eta = \omega_0\omega\xi$ is the interaction strength of the sensor region with laser light.

Employing Eq. (11) to Eq. (13) Hamiltonian of system gives,

$$H_s = \omega\sum_i \hat{a}_i^{\dagger}\hat{a}_i + U\sum_i n_i^{+}n_i^{-}. \quad \ldots\ldots\ldots\ldots\ldots\ldots\ldots\ldots\ldots\ldots\ldots\ldots\ldots\ldots \quad (16)$$

Here, $U = \frac{\eta}{\omega_0}$

Laser-sensor region interaction results in different occupations of electrons inside the fiber cable (Al-Azzawi, 2017), this helps to execute biomolecule information. In addition, each occupation of an electron can be expressed by four possible local states of

$$\|u\rangle_i = \|\uparrow\rangle_i, \|\downarrow\rangle_i, \|\uparrow\downarrow\rangle_i, \|\downarrow\uparrow\rangle_i \quad \ldots\ldots\ldots\ldots\ldots\ldots\ldots\ldots\ldots\ldots\ldots\ldots\ldots\ldots \quad (17)$$

. With this notation, the density operator of electron occupation inside fiber cable takes the form,

$$\hat{\rho} = x\,\|\uparrow\uparrow\rangle + y\,\|\downarrow\downarrow\rangle + z\,\|\uparrow\downarrow\rangle\langle\downarrow\uparrow\|. \quad \ldots\ldots\ldots\ldots\ldots\ldots\ldots\ldots\ldots\ldots \quad (18)$$

Where, $z = \langle n^{+}n^{-}\rangle, x = \langle n^{+}\rangle - z$ and $y = \langle n^{-}\rangle - z$.
Applying Von Neumann entropy entanglement given in (Boes et al., 2019), we find,

$$E = -\mathrm{Tr}(\hat{\rho}\log_2\hat{\rho}),$$
$$= -x\log_2 x - y\log_2 y - z\log_2 z. \quad \ldots\ldots\ldots\ldots\ldots\ldots\ldots\ldots\ldots\ldots\ldots\ldots\ldots\ldots \quad (19)$$

The probability of each detection is 1/4, and summing up the two possibilities of detection of further measurement required, the entanglement of the system is re-written as,

$$E = -2z\log_2 z - \left(\frac{1}{4} - 2z\right)\log_2\left(\frac{1}{2} - z\right). \quad \ldots\ldots\ldots\ldots\ldots\ldots\ldots\ldots\ldots\ldots \quad (20)$$

The entanglement described in Eq. (18) can be used in quantum teleportation.

2.2.2. Initialization of Quantum State to Perform Biosignal Teleportation

The discussion made by proposed biosignals based on the concentration of biomolecules is either of cancer detected, no cancer detected, or re-measurement required. Interpretation of such phenomena in the classical computer is impossible. However, there is a possibility to describe such phenomena using quantum parallelism (qubits) that allows us to use 0 and 1 simultaneously using quantum registers of size n (Nowotniak and Kucharski, 2014). Thus, the four possible states are explained in quantum notation as; $|00\rangle$ and $|11\rangle$ represent no cancer and cancer detected, respectively, while $|10\rangle$ and $|01\rangle$ both represent re-measurement required. Hence, the teleportation is performed between two healthcare stations as dispensed in Figure. 1. The quantum state has additional parameters (cosr and sinr) that are used to accelerate information between two distant stations, those stated in other articles as Alice and Bob (Al-Azzawi, 2017). Besides, the generated information can be classified into two ebits that gave as,

$$|+\rangle = \cos r(|00\rangle + |11\rangle),$$
$$|-\rangle = \sin r(|10\rangle + |01\rangle). \quad \ldots\ldots\ldots\ldots\ldots\ldots\ldots\ldots\ldots\ldots \quad (21)$$

In addition, the definition of the acceleration for one qubit in terms of other r is given by $\tan r = \exp\left[-\pi\omega\frac{c}{a}\right]$. In which, the parameters ω represent the frequency of traveling qubits, c is the speed of light and a is the acceleration of qubits with respect to the speed of light. Meanwhile, the acceleration of the quantum state is explained by 8×8 matrix that the nonzero terms explained as follows,

$$\begin{aligned}
\rho^{22} &= \rho^{33} = \rho^{55} = \cos^4 r,\\
\rho^{23} &= \rho^{32} = \rho^{35} = \rho^{52} = \rho^{53} = \cos^3 r,\\
\rho^{28} &= \rho^{38} = \rho^{58} = \rho^{85} = \rho^{82} = \cos^2 r, \qquad \ldots\ldots\ldots (22)\\
\rho^{46} &= \rho^{47} = \rho^{64} = \rho^{67} = \rho^{74} = \rho^{76} = \cos^2 r \sin^2 r,\\
\rho^{77} &= 2\sin^2 r \cos^2 r.
\end{aligned}$$

2.2.3. Performing Teleportation to Assure Lung Cancer Telediagnosis

To perform biosignal teleportation, the first healthcare station (on which the patient sample is collected) combines the teleported state with an accelerated qubit and performs Bell measurement on two ebits. Besides, the second healthcare station (where the spectroscopic instrument detects biosignal) applies the unitary operation to interpret the initially teleported signal.

Moreover, to investigate the effectiveness of teleportation of biosignals we have to calculate the transmission fidelity (TF) of teleported information expressed by (Lewis and Laland, 2012),

$$TF = \mathrm{tr}\left(\rho_{ini}\rho_{fin}\right), \quad \ldots\ldots\ldots\ldots\ldots\ldots\ldots\ldots\ldots\ldots\ldots\ldots\ldots\ldots\ldots\ldots\ldots\ldots \quad (23)$$

Where, ρ_{ini} and ρ_{fin} represent the initial healthcare station's quantum state of coded information and the quantum state teleported to the second health station, respectively. Thus, using Eq. (20) into Eq. (21) we find,

$$TF = 3\cos^4 r \sin^4 r + 2\cos^4 r \sin^2 r + \cos^2 r. \quad \ldots\ldots\ldots\ldots\ldots\ldots\ldots\ldots\ldots\ldots\ldots\ldots\ldots\ldots\ldots\ldots\ldots\ldots \quad (24)$$

2.3. Teleportation of Dose Light for Lung Cancer Telecare

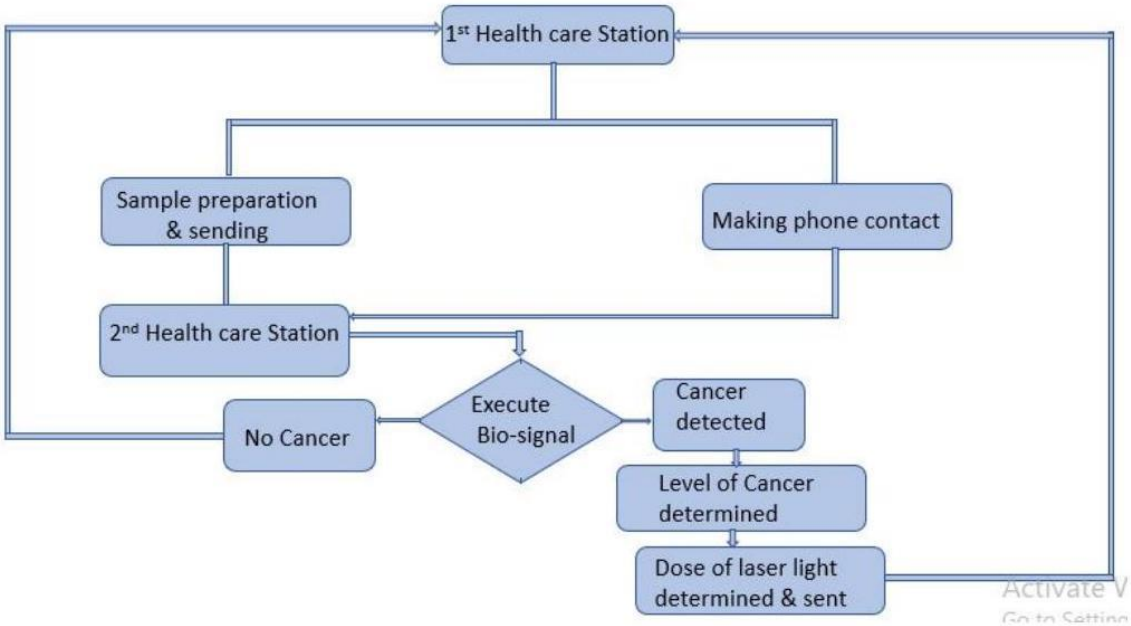

Figure 2: The schematic diagram of the overall process to perform lung cancer telediagnosis and telecare

Before performing teleportation, we have to determine the doses of light according to the patient's level of cancer. Thus, we set up a controller between the teleported signal interpretation and the patient, to perform laser therapy as illustrated in Figure.2. For simplicity, the wavelength-dependent quantum state teleportation with a telecom wavelength can be demonstrated by horizontal and vertical polarisation as

$$|\psi\rangle_{\mathrm{in}} = \cos\frac{r}{2}|H\rangle + e^{i\phi}\sin\frac{r}{2}|V\rangle. \quad \ldots\ldots\ldots\ldots\ldots\ldots\ldots\ldots\ldots\ldots.. (25)$$

In which, ϕ are polarisation states, and H and V are horizontal and vertical polarisation eigenbasis. In addition, the dose of light for teleportation (U(r)) can be introduced into the input state, and as a result, the output state expressed by

$$\begin{aligned} |\psi\rangle_{\mathrm{out}} &= U(r)|\psi\rangle_{\mathrm{in}} \\ &= e^{i\delta\hat{x}_1\hat{x}_2}|\psi\rangle_{in}. \end{aligned} \quad \ldots\ldots\ldots\ldots\ldots\ldots\ldots\ldots\ldots\ldots\ldots\ldots... (26)$$

For $\delta = 1 + \mathrm{tanhr}$, and $\hat{x}_1$ and $\hat{x}_2$ are transformation parameters. While, by tracing the output state, the final output density operator takes the form,

$$\begin{aligned} \rho_{\mathrm{out}} &= \mathrm{Tr}\left(|\psi\rangle_{\mathrm{out\,out}}\langle\psi|\right) \\ &= \int d\rho_{\mathrm{out}}\frac{1}{\delta e^{-r}\sqrt{\pi}}e^{i\delta\hat{x}_1}|\psi\rangle_{\mathrm{inin}}\langle\psi|e^{i\delta\hat{x}_2}. \end{aligned} \quad \ldots\ldots\ldots\ldots\ldots\ldots\ldots (27)$$

Where r is the squeezing parameter.

Finally, we quantify the performance of teleportation employing fidelity expressed in (Huo et al., 2018),

$$F = {}_{\text{in}}\left\langle \psi \left| \rho_{\text{out}} \right| \psi \right\rangle_{\text{in}}, \quad \ldots\ldots\ldots\ldots\ldots\ldots\ldots\ldots\ldots\ldots\ldots\ldots (28)$$

Substituting Eqs. (23) and (25) into Eq. (26), gives,

$$F = 2\delta(\cos^2 r + \cos r(1 + \sin r)). \quad \ldots\ldots\ldots\ldots\ldots\ldots\ldots\ldots (29)$$

3. RESULTS AND DISCUSSION

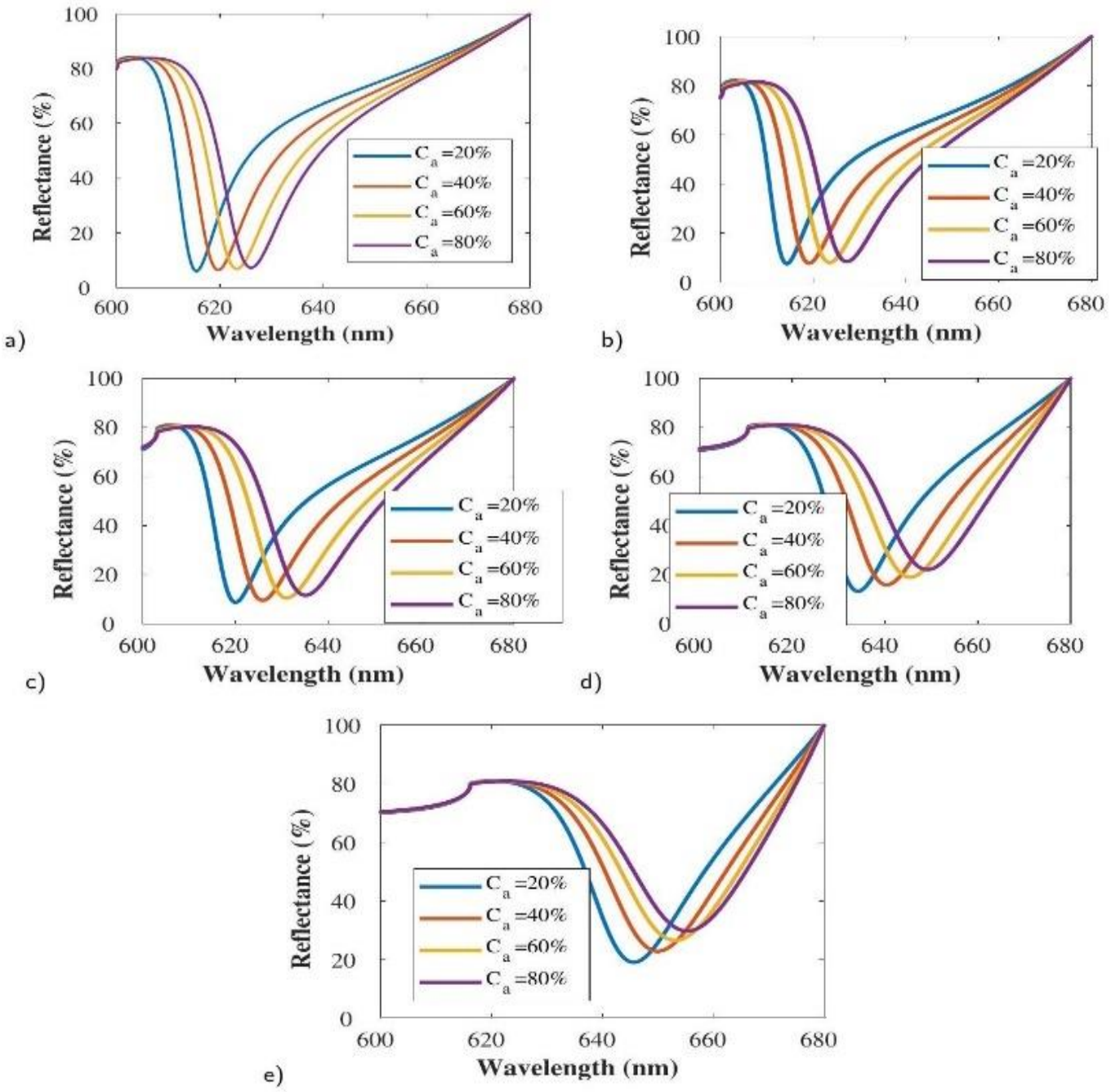

Figure 3: Effect of wavelength, biomolecule type and concentration. For a) Calu-1, b) A427, c) CK19, d) EGFR and e) 95D

The sensitivity and resolution parameters determine the performance of optical biosensors, and the same is dispensed for the proposed OPBs employing frequency modulation. By using the parameters given in Table.1 and the reflectance equation (Eq. 7), the reflectance spectra of different lung cancer cells under different concentrations are demonstrated clearly in Figure.3. Where, Figure.3 a) illustrates the reflectance spectra of the Calu-1 cell, which implies that as the concentration of biomolecules increases, the reflectance also increases, the same is true for Figure.3 b), c) d) and e). In addition, due to the refractive index increment between cancerous cells, the wavelength shifts rightwards with a small increment. This causes a decrease in FOM but increases sensor resolution. In this situation, the cancer cells have a higher refractive index than normal plasma cells, which agrees with other experimental work expressed in (Zhang et al., 2022b; Liu et al., 2018), this helps to differentiate affected and normal cells. In addition, comparing the five considered lung cancer cells, the 95D cell shows maximum detection efficiency hence, it has a high refractive index.

Table 2: The maximum performance of proposed OPBs at 80% concentration of different cancer cells impressed in plasma

Types of cell	S (nm/RIU)	λ_1 (nm)	λ_2 (nm)	FWHM	FOM (RIU^{-1})	R
Calu-1	10230	620	636	16	639.38	2.74
A427	10265	622	639	17	603.82	3.21
Ck19	10318	638	648	20	515.9	3.45
EGFR	10352	640	662	22	470.54	3.59
95D	10421	647	670	23	453.08	3.63

Toward a deeper insight, Table 2 summarizes the evaluation of the sensor performance of proposed OPBs. It clearly shows an increase in pumping frequency increases the sensor sensitivity and resolution. In addition, Figure 4 illustrates the performance of OPBs for the detection of different lung cancer cells. The sensitivity and FOM of the model are calculated under 80% biomolecule concentration. The maximum sensitivity and FOM were recorded to be as high as 10421 nm/RIU and 453.08RIU^(-1) respectively, at a wavelength of 660 nm. By comparing sensitivity and FOM, we can conclude that as sensitivity increases, FOM decreases due to low spectral shift, which causes a small change in FWHM.

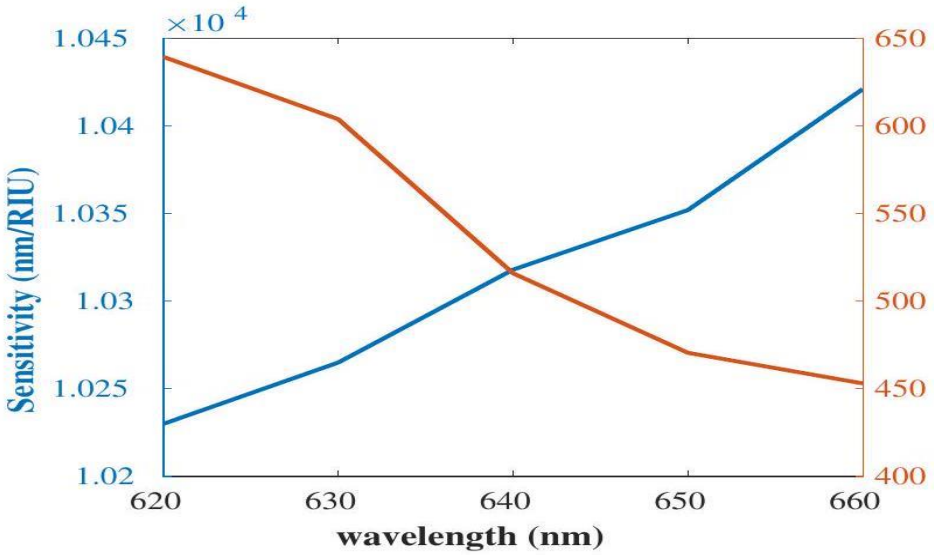

Figure 4: Calculated sensitivity and FOM values versus wavelength.

In Figure.5a, we show the Von Neumann entanglement for a field that carries biosignals, and the result agrees with the work expressed in Lie and Jeong (2019). To investigate the effect of pumping power and accelerating parameters on transmission fidelity, we plot the transmission fidelity versus acceleration power under different pumping modes in Figure.5b. These results show that the transmission fidelity decreases as pumping power increases and the higher transmission fidelity values can be obtained as 96% for 18.5 dB squeezing with 0.4% loss of biosignals. We deduce from this result that the more accelerating power tends to lose biosignals.

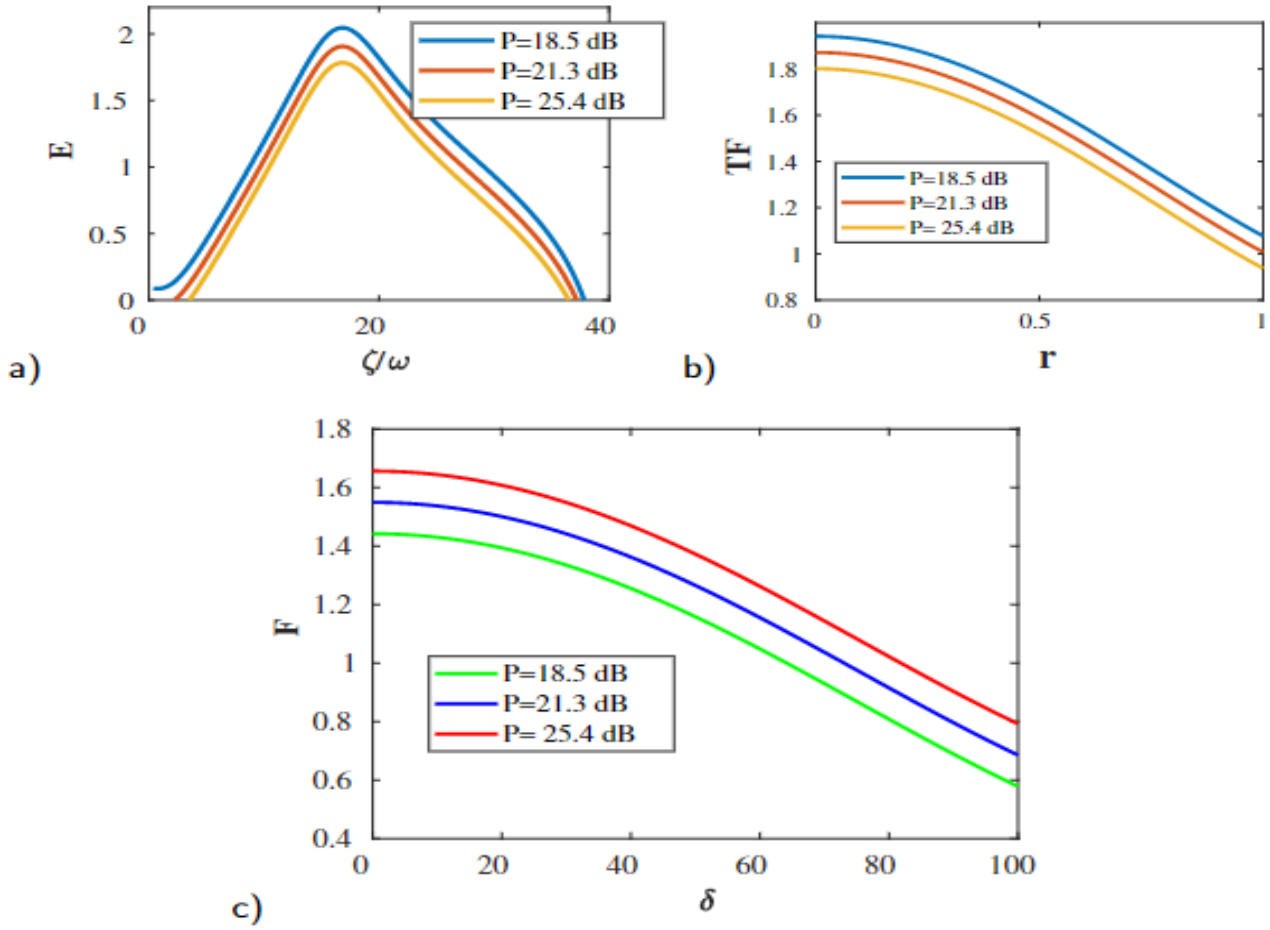

Figure 5: Plot of quantum properties of the proposed system. a) Local entanglement given by the von Neumann entropy E versus $\frac{\zeta}{\omega}$ under different pumping modes. b) Transmission fidelity of biosignal under different pumping power $\left(P = \frac{\pi\omega c}{a}\right)$. c) Teleportation fidelity of doses of light under different pumping power.

Furthermore, in Figure.5c we show a comparison of the teleportation fidelity behavior of the teleported dose of light, which is coded in Eq. (27). It is clear that the fidelities are maximum for higher pumping mode. However, the fidelities begin to decrease gradually until they reach their minimum bounds when the pumping power reaches 60 dB. Therefore, we can conclude that the efficiency of the teleportation of a dose of light increases with pumping power. Finally, the comparison between our proposed biosensor and some recently reported works demonstrates that our proposed biosensor is relatively highly sensitive in terms of wavelength modulation as shown in Table.3.

Table 3: Comparison of the proposed optoplasmonic biosensor with existing plasmonic sensors in the literature

Model Structures	Cancer Type	S (nm/RIU)	FOM (RIU^{-1})	R (RIU)	Reported Year
MIM-disk LSPR	A549	1670		3.5	2018
	Hela	10208.33	340	-	2019
D-shape photonic crystal fber	Basal	17500	430	-	2019
	PC12	10000	375	-	2019
	MCF-7	742.86	-	1.4	2021
photonic crystal fiber	Basal	3150	-	3.2	2021
	PC12	5500	-	1.8	2021
	Jurkat	17143	261.84	5.83	2022
Double gold nanowires	Hela	15833	326.72	6.32	2022
	MCF-7	53571	560.66	1.87	2022
GGG-Prism/Ag/Fe_2O_3/biomolecules	Calu-1	10230	639.38	2.74	2022
	A427	10265	603.82	3.21	2022
	Ck19	10318	515.9	3.45	2022
	95D	10421	453.08	3.63	2022

4. CONCLUSION

In conclusion, we have investigated the reflectance spectrum, RI sensitivity, sensor resolution, and FOM in optoplasmonic biosensors constructed using the frequency interrogation method. A higher RI sensibility, sensor resolution, and FOM are found in a higher concentration of biomolecules and cells with a higher refractive index. In addition, we have investigated the teleportation of resulted biosignals and the dose of light through fiber cable at a telecom wavelength using a controlled quantum teleportation scheme. According to numerical results, the highest sensitivity obtained was 10421 nm/RIU,453.08RIU^(-1) FOM, and 3.63 RIU sensor resolution for 95D cancer cell, and 10230nm/RIU sensitivity, 639.38 RIU ^(-1) FOM, with 2.74 RIU sensor resolution for Calu-1 were achieved. Compared with previously published data and considering the overall sensor performance, our proposed biosensor is a suitable platform for detecting various lung cancer cells. Moreover, introducing quantum principles for biosignal processing and teleporting the dose of light, a high transmission fidelity was recorded. This might bring many extensively promising opportunities in future medical applications for cancer telemedicine applications.

REFERENCES

Al-Azzawi, A., 2017. Fibre Optics: Principles and Advanced Practices. CRC Press.

Alqadami, A.S., Mohammed, B., Bialkowski, K.S., Abbosh, A., 2018. Fabrication and characterization of flexible polymer iron oxide composite substrate for the imaging antennas of wearable head imaging systems. *IEEE Antennas and Wireless Propagation Letters*, 17, 1364-1368.

Awschalom, D., Berggren, K.K., Bernien, H., Bhave, S., Carr, L.D., Davids, P., Economou, S.E., Englund, D., Faraon, A., Fejer, M., et al., 2021. Development of quantum interconnects (quics) for next-generation information technologies. *PRX Quantum* 2, 017002.

Bao, Z.Y., Dai, J., Zhang, Q., Ho, K.H., Li, S., Chan, C.H., Zhang, W., Lei, D.Y., 2018. Geometric modulation of induced plasmonic circular dichroism in nanoparticle assemblies based on backaction and field enhancement. *Nanoscale* 10,19684-19691.

Batool, A., Sherazi, T.A., Naqvi, S.A.R., 2022. Organic-inorganic nanohybrid-based electrochemical biosensors, in: *Hybrid Nanomaterials*. Springer, pp. 151-173.

Boes, P., Eisert, J., Gallego, R., Müller, M.P., Wilming, H., 2019. Von neumann entropy from unitarity. *Physical review letters* 122 , 210402.

Brahme, A., 1987. Design principles and clinical possibilities with a new generation of radiation therapy equipment: a review. *Acta Oncologica*, 26, 403-412.

Butt, M., Khonina, S., Kazanskiy, N., 2021. Plasmonics: a necessity in the field of sensing-a review. Fiber and Integrated Optics 40,14-47.

Cacciapuoti, A.S., Caleffi, M., Tafuri, F., Cataliotti, F.S., Gherardini, S., Bianchi, G., 2019. Quantum internet: networking challenges in distributed quantum computing. IEEE Network 34, 137-143.

Chang, C.Y., Lin, H.T., Lai, M.S., Shieh, T.Y., Peng, C.C., Shih, M.H., Tung, Y.C., 2018. Flexible localized surface plasmon resonance sensor with metal-insulator-metal nanodisks on pdms substrate. Scientific reports 8,1-8.

Chhatre, S., Vachani, A., Allison, R.R., Jayadevappa, R., 2021. Survival outcomes with photodynamic therapy, chemotherapy and radiation in patients with stage iii or stage iv non-small cell lung cancer. Cancers 13,803 .

Chiu, N.F., Lin, T.L., Kuo, C.T., 2018. Highly sensitive carboxyl-graphene oxide-based surface plasmon resonance immunosensor for the detection of lung cancer for cytokeratin 19 biomarker in human plasma. Sensors and Actuators B: Chemical 265, 264-272.

Choe, J., Kim, K.W., Kim, H.J., Kim, D.W., Kim, K.P., Hong, S.M., Ryu, J.S., Tirumani, S.H., Krajewski, K., Ramaiya, N., 2019. What is new in the 2017 world health organization classification and 8th american joint committee on cancer staging system for pancreatic neuroendocrine neoplasms? Korean journal of radiology 20,5-17.

Esfahani Monfared, Y., 2020. Overview of recent advances in the design of plasmonic fiber-optic biosensors. Biosensors 10,77.

Esmaeilzadeh, A.A., Yaseen, M.M., Khudaynazarov, U., Al-Gazally, M.E., Opulencia, M.J.C., Jalil, A.T., et al., 2022. Recent advances on electrochemical and optical biosensing strategies for monitoring of microrna-21: A review. Analytical Methods .

Fu, C., Wang, B., Zhu, X., Xiong, Z., Huang, Y., 2022. Narrowband absorbers based on multi-ridge gratings. Optik 257, 168839.

Garg, A., Dewan, A., 2022. Equipment planning, in: Manual of Hospital Planning and Designing. Springer, pp. 501-527.

Gómez-Bombarelli, R., Aguilera-Iparraguirre, J., Hirzel, T.D., Duvenaud, D., Maclaurin, D., Blood-Forsythe, M.A., Chae, H.S., Einzinger, M., Ha, D.G., Wu, T., et al., 2016. Design of efficient molecular organic light-emitting diodes by a high-throughput virtual screening and experimental approach. Nature materials 15,1120-1127.

Haleem, A., Javaid, M., Singh, R.P., Suman, R., 2021. Telemedicine for healthcare: Capabilities, features, barriers, and applications. Sensors International 2, 100117.

Huber, E., Marinero, E., 1988. Magneto-optical activity of ag at the plasma frequency. Applied Physics A 47, 131-135.

Huo, M., Qin, J., Cheng, J., Yan, Z., Qin, Z., Su, X., Jia, X., Xie, C., Peng, K., 2018. Deterministic quantum teleportation through fiber channels. Science advances 4 , eaas 9401.

Jabin, M.A., Ahmed, K., Rana, M.J., Paul, B.K., Islam, M., Vigneswaran, D., Uddin, M.S., 2019. Surface plasmon resonance based titanium coated biosensor for cancer cell detection. IEEE Photonics Journal 11, 1-10.

Jaeger, G., 2009. Entanglement, information, and the interpretation of quantum mechanics. Springer Science & Business Media.

Jia, M., Yu, S., Yu, J., Li, Y., Gao, H., Sun, P.L., 2020. Comprehensive analysis of spread through air spaces in lung adenocarcinoma and squamous cell carcinoma using the 8th edition ajcc/uicc staging system. BMC cancer 20, 1-11.

Jongen, N., Bowen, P., Lemaître, J., Valmalette, J.C., Hofmann, H., 2000. Precipitation of self-organized copper oxalate polycrystalline particles in the presence of hydroxypropylmethylcellulose (hpmc): control of morphology. Journal of Colloid and Interface Science 226, 189-198.

Kosloff, R., 1988. Time-dependent quantum-mechanical methods for molecular dynamics. The Journal of Physical Chemistry 92, 2087-2100.

Kumela, A.G., Gemta, A.B., Desta, T.A., Kebede, A., 2022. Noble classical and quantum approach to model the optical properties of metallic nanoparticles to enhance the sensitivity of optoplasmonic sensors. RSC Advances 12, 16203-16214. Lewis, H.M., Laland, K.N., 2012. Transmission fidelity is the key to the build-up of cumulative culture. Philosophical Transactions of the Royal Society B: Biological Sciences 367, 2171-2180.

Li, X.P., Zhang, W.D., Li, M.J., Wang, J., Lian, J., Zhou, H.G., 2022. Effectiveness and safety of pd-1 inhibitor monotherapy for elderly patients with advanced non-small cell lung cancer: A real-world exploratory study. Journal of Oncology 2022.

Li, Y., Niu, L., 2022. Identification of the effects of covid-19 on patients with pulmonary fibrosis and lung cancer: a bioinformatics analysis and literature review. Scientific Reports 12,1-17.

Lie, S.H., Jeong, H., 2019. Limitations of teleporting a qubit via a two-mode squeezed state. Photonics Research 7, A7-A13.

Liu, C., Zeng, X., An, Z., Yang, Y., Eisenbaum, M., Gu, X., Jornet, J.M., Dy, G.K., et al., 2018. Sensitive detection of exosomal proteins via a compact surface plasmon resonance biosensor for cancer diagnosis. ACS sensors 3, 1471-1479.

Matiatou, M., Giannios, P., Koutsoumpos, S., Toutouzas, K.G., Zografos, G.C., Moutzouris, K., 2021. Data on the refractive index of freshly-excised human tissues in the visible and near-infrared spectral range. Results in Physics 22, 103833.

McClements, D.J., Gumus, C.E., 2016. Natural emulsifiers - biosurfactants, phospholipids, biopolymers, and colloidal particles: Molecular and physicochemical basis of functional performance. Advances in Colloid and interface Science 234, 3-26.

Mederos, N., Friedlaender, A., Peters, S., Addeo, A., 2020. Gender-specific aspects of epidemiology, molecular genetics and outcome: lung cancer. ESMO open 5, e000796.

Meshginqalam, B., Barvestani, J., 2022. High performance surface plasmon resonance-based photonic crystal fiber biosensor for cancer cells detection. The European Physical Journal Plus 137, 1-10.

Metkar, S.K., Girigoswami, K., 2019. Diagnostic biosensors in medicine-a review. Biocatalysis and agricultural biotechnology 17, 271-283.

Moeller, B., Balagamwala, E.H., Chen, A., Creach, K.M., Giaccone, G., Koshy, M., Zaky, S., Rodrigues, G., 2018. Palliative thoracic radiation therapy for non-small cell lung cancer: 2018 update of an american society for radiation oncology (astro) evidence-based guideline. Practical radiation oncology 8,245-250.

Nouman, W.M., El-Ghany, A., Sallam, S.M., Dawood, A.F.B., Aly, A.H., et al., 2020. Biophotonic sensor for rapid detection of brain lesions using 1 d photonic crystal. Optical and Quantum Electronics 52, 1-14.

Nowotniak, R., Kucharski, J., 2014. Higher-order quantum-inspired genetic algorithms, in: 2014 Federated Conference on Computer Science and Information Systems, IEEE. pp. 465-470.

Patil, P.O., Pandey, G.R., Patil, A.G., Borse, V.B., Deshmukh, P.K., Patil, D.R., Tade, R.S., Nangare, S.N., Khan, Z.G., Patil, A.M., et al., 2019. Graphene-based nanocomposites for sensitivity enhancement of surface plasmon resonance sensor for biological and chemical sensing: A review. Biosensors and Bioelectronics 139, 111324.

Pradana, A., Septiani, N.L.W., Dipojono, H.K., Yuliarto, B., et al., 2021. nanopillar structure in the direction of optical biosensor on-chip integration. Journal of The Electrochemical Society 168, 057505.

Prasad, A., Choi, J., Jia, Z., Park, S., Gartia, M.R., 2019. Nanohole array plasmonic biosensors: Emerging point-of-care applications. Biosensors and Bioelectronics 130, 185-203.

Prasad, M., Ghosh, M., Patki, H.S., Kumar, S., Brar, B., Sindhu, N., Goel, P., Kaushik, S., Mohan, H., Syed, S., et al., 2021. Imaging techniques in veterinary disease diagnosis, in: Advances in Animal Disease Diagnosis. CRC Press, 103-145.

Rudin, C.M., Brambilla, E., Faivre-Finn, C., Sage, J., 2021. Small-cell lung cancer. Nature Reviews Disease Primers 7, 1-20.

Ruggenthaler, M., Tancogne-Dejean, N., Flick, J., Appel, H., Rubio, A., 2018. From a quantum-electrodynamical light-matter description to novel spectroscopies. Nature Reviews Chemistry 2, 1-16.

Sakulkhu, U., Mahmoudi, M., Maurizi, L., Coullerez, G., Hofmann-Amtenbrink, M., Vries, M., Motazacker, M., Rezaee, F., Hofmann, H., 2015. Significance of surface charge and shell material of superparamagnetic iron oxide nanoparticle (spion) based core/shell nanoparticles on the composition of the protein corona. Biomaterials science 3, 265-278.

Sengupta, S., Balla, V.K., 2018. A review on the use of magnetic fields and ultrasound for non-invasive cancer treatment. Journal of advanced research 14,97-111.

Silva, A.B., da Silva, R.M., Ribeiro, G.d.R., Guedes, A.C.C.M., Santos, D.L., Nepomuceno, C.C., Caetano, R., 2020. Three decades of telemedicine in brazil: Mapping the regulatory framework from 1990 to 2018. PLoS one 15 , e0242869.

Soler, M., Estevez, M.C., Cardenosa-Rubio, M., Astua, A., Lechuga, L.M., 2020. How nanophotonic label-free biosensors can contribute to rapid and massive diagnostics of respiratory virus infections: Covid-19 case. ACS sensors 5, 2663-2678.

Soler, M., Huertas, C.S., Lechuga, L.M., 2019. Label-free plasmonic biosensors for point-of-care diagnostics: a review. Expert review of molecular diagnostics 19,71-81.

Tabish, T.A., Dey, P., Mosca, S., Salimi, M., Palombo, F., Matousek, P., Stone, N., 2020. Smart gold nanostructures for light mediated cancer theranostics: combining optical diagnostics with photothermal therapy. Advanced Science 7, 1903441.

Wang, L., Alexander, C.A., 2020. Quantum science and quantum technology: Progress and challenges. Am. J. Electr. Electron. Eng. 8, 43-50.

Xue, Y., Wang, L., Zhang, Y., Zhao, Y., Liu, Y., 2022. Air pollution: A culprit of lung cancer. J. Hazardous Materials, 128937.

Yang, H., Li, S., Yu, H., Zheng, F., Lin, L., Chen, J., Li, Y., Lin, Y., 2019. In situ construction of hollow carbon spheres with n, co, and fe co-doping as electrochemical sensors for simultaneous determination of dihydroxybenzene isomers. Nanoscale 11, 8950-8958.

Yasli, A., 2021. Cancer detection with surface plasmon resonance-based photonic crystal fiber biosensor. Plasmonics 16, 1605-1612.

Zhang, C., Wang, D., Dong, L., Li, K., Zhang, Y., Yang, P., Yi, S., Dai, X., Yin, C., Du, Z., et al., 2022a. Microwave absorption of α-fe2o3@ diatomite composites. International journal of molecular sciences 23, 9362.

Zhang, C., Xue, T., Zhang, J., Liu, L., Xie, J., Wang, G., Yao, J., Zhu, W., Ye, X., 2022b. Terahertz toroidal metasurface biosensor for sensitive distinction of lung cancer cells. Nanophotonics 11, 101-109.

Design and Develop Botnet Detection Method Using Machine Learning Approaches

Gizachew Teshome Habtamu*, Teshome Mulugeta Ababu, Alebachew Destaw Tefera

Department of Computer Science, Dire Dawa University, Dire Dawa, Ethiopia
**Corresponding author, e-mail: gizachewteshome2007@gmail.com*

ABSTRACT

Security threats are developing quickly in parallel with the development of computers and state art technologies. Nowadays, botnet security threats require considerable investigation and attention. Therefore, traditional intrusion detection and deep packet inspection methods are widely used and recommended by scholars but it is no longer adequate to meet the demands of evolving security threats. We looked at machine learning approaches as an alternative method or an additional mechanism to defend against malware, botnets, and other types of network attacks as computing power increases and costs decrease. The aim of this paper was to design and develop botnet detection methods using machine learning approaches such as Random Forest (RF), Gradient Boosting (GB), Decision Tree (DT), and Logistic Regression (LR) to classification task of botnet and normal traffic. CTU-13 datasets were used for offline analysis to assess the performance of the models. First, a detailed data analysis is conducted to generate 22 extracted features from the initial CTU-13 Netflow datasets and based upon the importance score, 6 features were selected. In our experiments, the data were processed using the 60-second duration of the window and using one window. Following that, all of these features are compared to one another in a feature selection process. We used scenario 5 and 11 as training set about 63% of data and scenario 5 as testing set about 37% of data. Then, we develop a botnet detection model using four different machine learning algorithms. As a result of the feature selection strategy and according to the experimental findings RF and GB outperform better for detecting botnets with the f1-score results is 86%, and 83% in all scenarios respectively.

Keywords: *Machine Learning, Botnet, Botnet Detection, Feature Selection, CTU-13*

1. INTRODUCTION

Thousands of computers and users are connected to the Internet via networks as a result of technological advancements over the last few decades. The worldwide network provides access to a wide range of services, resources, and information, making security a critical component. It is critical to recognize that the significant increase in internet usage also increases the likelihood of fraud and other malicious activities in this open environment. As a result of these malicious activities, preventive measures and controls in services are being strengthened, but they are not always effective. Botnet detection systems and methods are necessary supplements to reduce losses and strengthen defenses against malicious activity on systems such as intrusion detection systems (Xing et al., 2021). However, many intrusion detection systems and methods suffer from high false positives when detecting network attacks, and much research is being conducted to try to reduce this high false-positive rate (Goeschel, 2016). We have seen that intrusion detection systems and methods are still regarded as a problem of correctly classifying data and detecting malicious traffic. It can also be seen that any classification scheme is only as good as the data fed into it, and the cleaner the data, the more accurate the results. With this mindset, extracting specific features and using the refined dataset as input for machine learning algorithms will contribute more to determining the normal from botnet traffic, the detection rate, a low false-positive rate, processing speed and efficiency, and memory usage. The primary goal of this paper is to address the issues associated with developing flexible and adaptable botnet detection methods.

Machine learning is a data analytics technology that relies on patterns and inference rather than explicit instructions to carry out particular jobs effectively. Many apps use machine learning to address network and security related problems. It can aid in predicting traffic patterns and identifying network behavior issues (Gizachew Teshome & Asnak Yihunie, 2022). There has been lots of research into the use of machine learning for

botnet detection. The key challenge would be choosing parameters that may produce good quality results when using machine learning to assess NetFlows datasets (Gizachew Teshome, 2022). The following is a description of some popular machine learning techniques.

Decision Tree classification is made based on the mode of the class. A fully developed decision tree will inevitably overfit because it will be unable to handle the unexpected data. The features of the decision tree are chosen, along with the splitting condition and stopping criteria, and then the overgrown branches are pruned (Alauthaman et al., 2018). Random Forest can produce higher accuracy rates. In the study by (Apruzzese & Colajanni, 2018), a brand-new framework for real-time botnet detection is presented. It uses the idea of different trees voting with a majority, it is regarded as an ensemble machine learning algorithm. The aggregate result of each class predicted by each individual tree serves as the basis for the algorithm's output, which is a class prediction. Recent research by (Akash et al., 2022) has investigated Random Forest detection capabilities in security attacks, particularly in IoT attacks, injection attacks, spam filtering, malware detection, and other areas.

The other common machine learning algorithm is Gradient Boosting is an ensemble approach to classification and regression. The process of creating a powerful ensemble classifier is iterative and the objective is to greedily combine weaker models to produce stronger estimators (Vishwakarma, 2020). Logistic Regression is the other classification algorithm that used to detect botnets and essentially a supervised machine learning algorithm in machine learning (Bapat et al., 2018). In recent years, the dynamic and static analyses of malicious software have attracted extensive attention from both academia and industry. An accurate and efficient identification of botnets is the aim of this research. To identify botnets more efficient, feature-based methods of detecting payload data and ML algorithms have been introduced. This class of methods identifies botnets by extracting features from network traffic produced in the connection between the C&C server and the botnet (Wazzan et al., 2021). The following related works are some of botnet detection using different approaches. The detection of botnets communicating over TCP only using CTU-13, which is used for training three different machine learning algorithms (k-NN, Random Forest, and LightGBM) for botnet traffic classification and testing the success of the proposed botnet detection model (Eser et al., 2021). Among the 14 network flow features included in the CTU-13 database, three are deliberately chosen. In contrast to most classification models in the literature that use ip-based approaches, the proposed model can efficiently distinguish botnet traffic from normal traffic with 94.26 percent accuracy using the LightGBM classifier without falling into the overfitting trap. A developed botnet detection TomekRecursion Borderline Synthetic Minority Oversampling Technique generates additional minority samples to achieve class balance, and an improved gradient boosting decision tree algorithm is used to train and establish an abnormal traffic detection model to improve the detection of unbalanced botnet data(Duan et al., 2022). The results of experiments on the ISCX-botnet traffic dataset show that the proposed method achieved better botnet detection performance with 99.10% recall, 99.20% accuracy, 99.1% F1 score, and 99.0% area under the curve. To detect the presence of the botnet in network traffic and the experiments on the CTU13 data set, to detect the presence of a bot, used Decision Trees, Nave Bayes, SVM, and K Nearest Neighbor. In comparison to other algorithms, decision trees provide a 99.9% positive detection rate (Rao et al., 2018).

This research primary goal was to use machine learning approaches to identify malware or botnet activity from a NetFlow dataset. The two objectives are (1) to identify malicious traffic or botnet activity using Netflow dataset. Any Netflow dataset, regardless of size or level of infection, should be accepted by the system and then categorize it as botnet or normal traffic and (2) to compare machine learning botnet detection methods and recommend the suitable one. The general structure of this paper starts with an introduction and related works in Section One, followed by material and methods in Section Two. Section Three, the result and discussion with table and diagram representation. Finally, the conclusion of this research work is described.

2. MATERIAL AND METHODS

2.1 Proposed Botnet Detection System

Based on the characteristics of the machine learning algorithms, a detection method was developed that applies a multilayer model and that performs data collection on the network and applies techniques of machine-learning algorithms in its construction. The new detection method uses classification algorithms to perform the classification of botnet attack and determine whether an instance seen in the network traffic is a botnet or normal.

The proposed method analyzes the behavior patterns of the botnet traffic in real-time, generates packet transmission mappings between hosts, and performs intrusions based on these mappings. The method consists of two layers. In the first layer, there is a machine learning classifier responsible for the collection of botnet traffic data, packet analysis, and classification in two categories: Botnet Traffic and Normal Traffic as defined by CTU-13 dataset. The CTU-13 dataset consists of three botnets ('Virut', 'Sogou', and 'Rbot') (García et al., 2014). A simplified view of the proposed machine learning based botnet detection method is shown in Fig. 1.

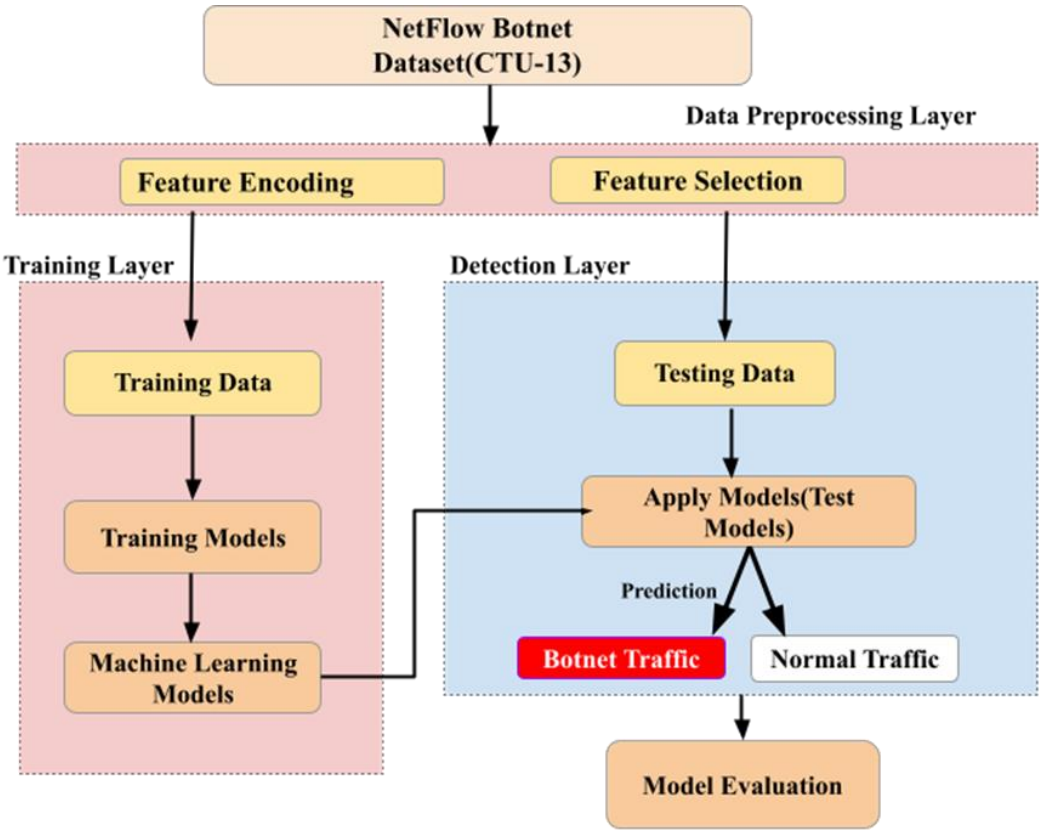

Figure 1: Proposed machine learning based Botnet Detection Method

The developed prototype is based on the idea of machine learning algorithms some of the classification algorithms such as DT, RF, GB, and LR are developed. In the prototype, the input data of CTU-13 consist of 14 variables presented to the classifier and sent to the botnet detector indicated by the classifier according to the analysis of each input pattern. These variables represent relevant characteristics of connections between monitored hosts, such as source and destination address, time connection duration, type of protocol, total bytes, and packets transmitted, among others. The detection method based on machine learning algorithms DT, RF, GB, and LR which is a supervised machine learning technique used for classification analysis (Rezaei, 2020). Python libraries and packages are used for machine learning classification. We train the machine learning algorithms using Scenario-7, and 11 scenarios and testing using Scenario-5.

2.2 Selected Botnet Dataset

Botnet dataset selection is the initial step in this research. By obtaining genuine data traffic from a reputable firm and extracting NetFlows, we are able to accomplish this research objective. Public domain datasets are an alternative strategy in the absence of actual data traffic. For this purpose, we chose a well-known dataset called CTU-13 which is captured by CTU University in 2011. It is widely accessible and has been utilized extensively for numerous previous research papers that are comparable to ours, we picked it over other public datasets. There are 13 scenarios in the CTU-13 dataset out of this we only chose three individual NetFlow dataset: Scenario -5- Virut, Scenario-7- Sogou, and Scenario -11- Rbot because three scenarios contain the most common botnet attacks. The dataset contains IP addresses of malicious and non-malicious hosts are known. The statistical details of the three scenario datasets used in this study are described in Table 1.

Table 1: Dataset description for 5,7 and 11 scenarios

ID	#Packets	#NetFlows	Size	Bot
5	129,833	129,833	17.8 MB	Virut
7	114,078	114,078	17.8 MB	Sogou
11	107,252	107,252	14.6 MB	Rbot

2.3 Feature Extraction and Selection

After choosing a dataset, we then recognize and extract the features from it. Feature extraction and selection is the most important thing to increase the performance of the botnet detection models(Joshi et al., 2020).. The categorical features in NetFlow data must be converted into numerical or boolean values, which would result in an excessively large matrix and memory problems. We have selected a 2-minute period with a 1-minute stride. The bidirectional NetFlow dataset is then preprocessed, and categorical and numerical features that characterize the dataset within the specified time range are extracted. Additionally, to minimize the size of the input training matrix, feature selection approaches are used such as embedded method and correlation matrix with heatmap. The selected features used *Sport, Dport, sTos, dTos, TotBytes, TotPkts* are shown in Fig.2.

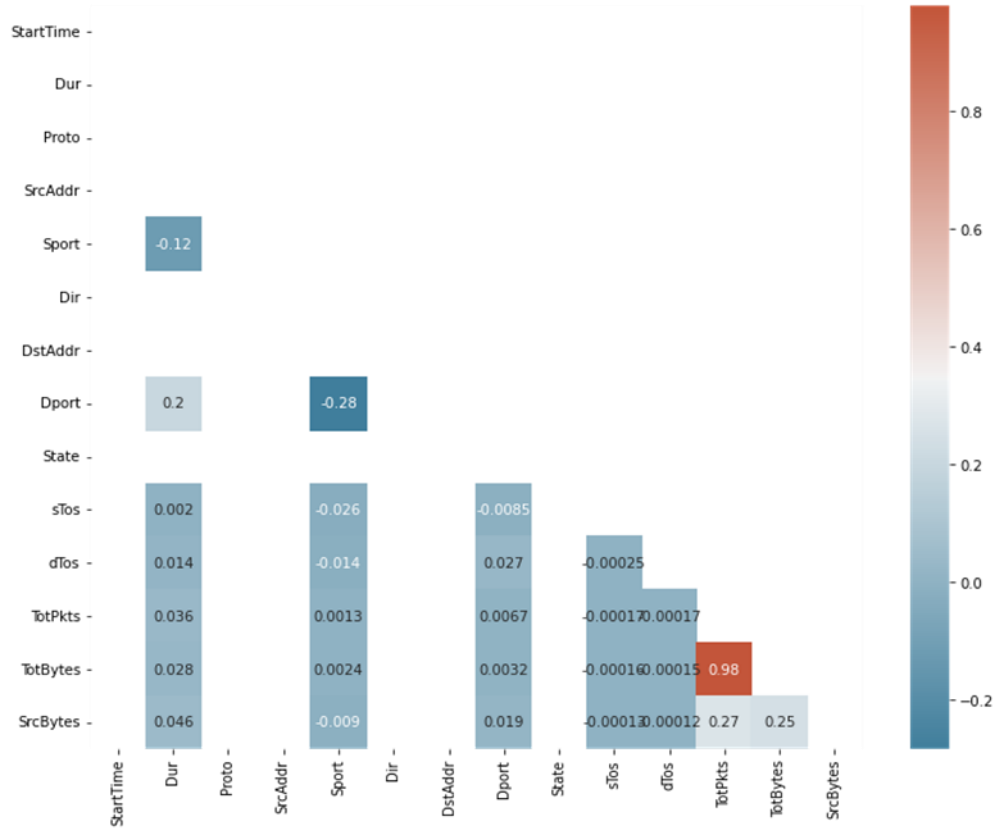

Figure 2: Selected features for botnet detection model

2.4 Training and Testing Data

We chose Scenario-7 and Scenario-11, which consists 63% of the data, as our training datasets, and Scenario-5 as a testing data which consists 37% of the experimental dataset. Six features were extracted from the experimental dataset following the pre-processing step. There are 129,833 NetFlow data from the Virut botnets in Scenario-5 and 221,329 NetFlow records from the Sogou and Rbot botnets in Scenario-7 and 11.

2.5 Model Evaluation

It is necessary to choose evaluation metric criteria to evaluate the effectiveness of the machine learning model to compare the result of four machine learning algorithms. Basically, it is used to count the true positives, true negatives, false positives and false negatives.

- True Positives (TP) are predicted as botnet traffic correctly classified as botnet traffic.
- True Negatives (TN) are predicted normal traffic correctly classified as normal traffic.
- False Positives (FP) are the number of predicted normal traffic falsely marked as botnet traffic samples.
- False Negatives (FN) are the number of predicted botnet traffic samples marked as botnet traffic.
- Recall is defined as the True Positive Rate (TPR) and Precision as the proportion of accurately predicted botnets.

$$\text{Recall} = \frac{\text{TP}}{\text{TP+FN}}$$

$$\text{Precision} = \frac{\text{TP}}{\text{TP+FP}}$$

- F-score is calculating a single number that combines precision and recall to represent the performance of the entire system.

$$F - score = \frac{2 * \text{Recall} * \text{Precision}}{\text{Recall} + \text{Precision}}$$

- Confusion matrix maintains information about actual and predicted classes. The four instances TP, TN, FP, and FN are counted due to the relation between the predicted and actual classes.

Table 2: The Confusion matrix for botnet detection model

		True Label	
		Botnet	**Normal**
Predicted Label	**Botnet**	True Positive (TP)	False Positive (FP)
	Normal	False Negative (FN)	True Negative (TN)

- Area under the ROC curve is plotting the false positive rate versus the true positive rate as the threshold varies over the range of data values gives the Receiver Operating Characteristic (ROC) curve. An improved performance is a data point in the upper left corner. The accuracy of the detection rate increases with the distance between the curve and the top and left borders of the ROC area and better detection rate with lower FPR can be attained with a higher AUC value.

3. RESULTS AND DISCUSSION

The Intel(R) Core (TM) i3-7020U CPU @ 2.30GHz 2.30 GHz processor was used in the experiment on a Lenovo running Windows 10 operating system. Pandas, NumPy, Scikit-Learn (sklearn), and other machine learning libraries were used in the open-source Jupyter Notebook's python environment to develop, train, and evaluate the machine learning model. In this section, we have conducted different experiments and obtained the results for each machine learning classification model used in the experiment. We chose four machine learning model Decision Tree (DT), Random Forest (RF), Gradient Boosting (GB) and Logistic Regression (LR). The result on the CTU-13 dataset shows in three scenarios (5,7 and 11) both in training and testing set and the performance of ML models was evaluated for binary classification (Botnet and Normal).

3.1 Result Comparison

The performance comparison for CTU-13 has been illustrated for both training and testing set in Table 2 in terms of precision, recall, and f1-score.

Table 3: Botnet detection results on training and testing data

Algorithms	**Training Result**			**Testing Result**		
	Precision	***Recall***	***F1-Score***	***Precision***	***Recall***	***F1-Score***
Decision Tree	1.0	1.0	1.0	0.5	0.67	0.57
Random Forest	1.0	1.0	1.0	0.75	1.0	**0.86**
Gradient Boosting	1.0	1.0	1.0	0.83	0.83	**0.83**
Logistic Regression	0.73	0.73	0.73	0.67	0.67	0.67

As shown in Table 3, two machine learning algorithms shown the nearly perfect performance in every metric in the training set and testing set. It is because that the training/testing dataset split and used in the same botnet characteristics. In this experiment, we pre-processed the data by using the 60- second duration of the window and

using one window which can use our botnet detector that provides real-time results at the end of each time window in exchange for specific input data. The testing datasets that consist of only Virut botnet and training dataset we use consist of Rbot and Sogou botnets. The overall performance of Random Forest Classifier and Gradient Boosting algorithms obtained results in the training and testing datasets, with precision, recall and f1 score are 100% on the training set and no false-positive rate except logistic regression algorithms. In the testing set the Random Forest and Gradient Boosting has obtained better results which is f1-score value 86% and 83% respectively.

3.2 Result Analysis of Model Confusion Matrix

As demonstrated in Figs.3 and Fig.4, the confusion matrix results of Random Forest classifier for the unbalanced dataset are true negative or false positive in the confusion matrix. The decision tree and logistic regression had the lowest performance of all the trained models, but the random forest and gradient boosting outperformed it with a slightly higher f-score value by predicting a few true positive values. The analysis of confusion matrix of Random Forest model in classification of botnet and normal traffic data.

Table 4: The classification result of botnet and normal traffic by RF

		True Label	
		Botnet	**Normal**
Predicted Label	**Botnet**	TP = 3009	FP = 12
	Normal	FN = 4	TN = 107050

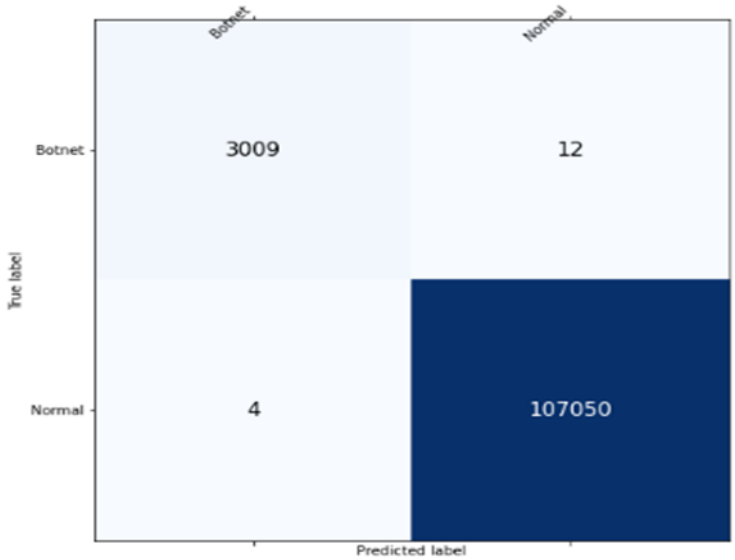

Figure 3: Random Forest Confusion Matrix

Table 5: The classification result of botnet and normal traffic by GB

		True Label	
		Botnet	**Normal**
Predicted Label	**Botnet**	TP = 2904	FP = 117
	Normal	FN = 24	TN = 107030

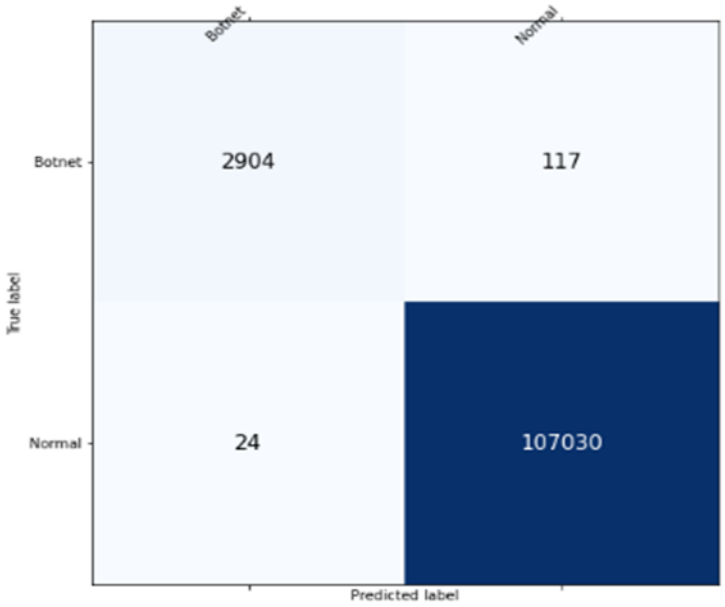

Figure 4: Gradient Boosting Confusion Matrix

3.3 Result Analysis of Model ROC curve

The Random Forest and Gradient Boosting classifiers offer the best AUC values larger than 80%, which denote excellent prediction; the Gradient Boosting classifier is 100% in the training data and 83% on the testing data, as shown in Fig. 5 and Fig. 6, and the areas under the curve for the classifiers used in this experiment. The botnet experiment's AUC values demonstrate that it yields conclusive findings on NetFlow botnet detection.

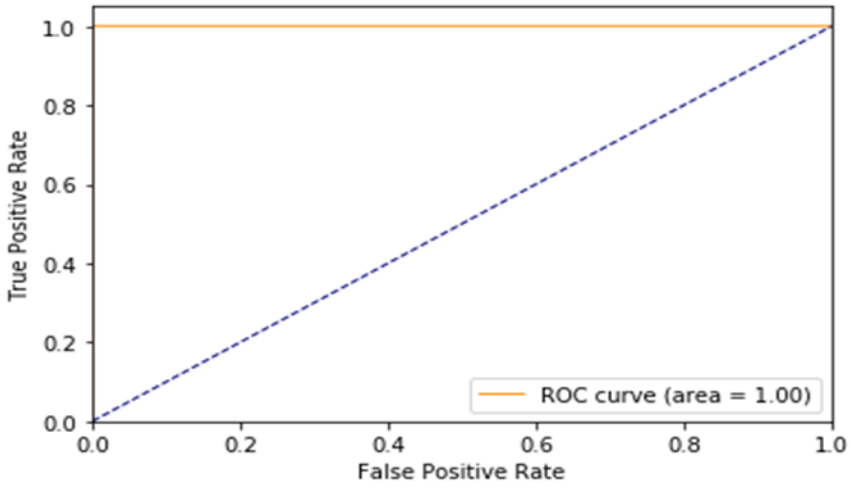

Figure 5: The ROC curves of GB training results on dataset

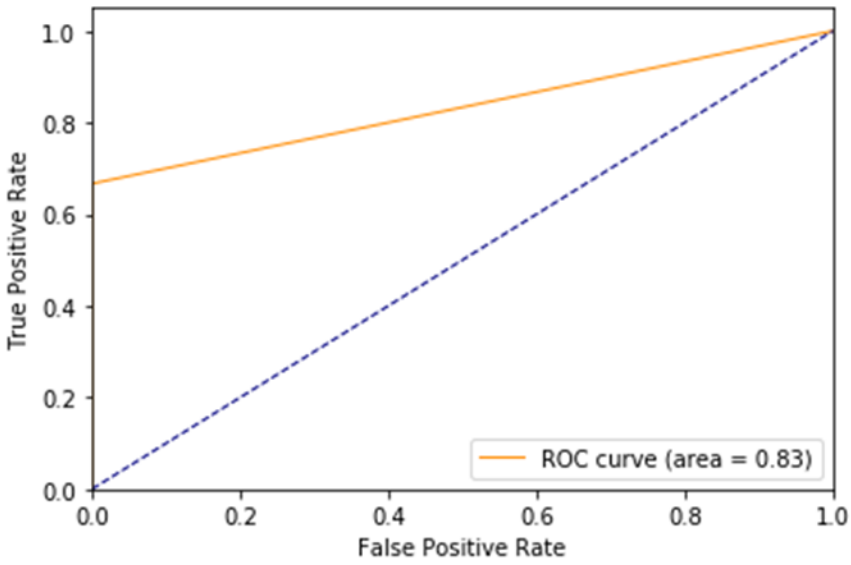

Figure 6: The ROC curves of GB testing results on dataset

4. CONCLUSION

In this paper, the presented method provides more and consistent detection performance in comparison to existing study results. The actual performance of the machine learning classifier tested with feature selection mechanisms. The result showed that Random Forest, and Gradient Boosting are a fast-training method that reduces the false-positive rate, it also provides an excellent generalization performance on machine learning algorithms and establishes a botnet detection model with the best overall performance. The evaluation of the most recent dataset CTU-13 showed that the hierarchical model outperformed different well known and recent machine learning algorithms, giving the highest accuracy for detecting network attacks. Selecting the most important features is better for the detection results. Overall, the proposed method provides the highest detection performance using two machine learning algorithms Random Forest, and Gradient Boosting classifiers. In the future, the current method and approaches are no longer effective in a new scenario of increasing threats and quickly changing botnet behaviors. This challenge requires a more flexible and dynamic approach, that provides quick responses to botnet. For the future, botnet behavior can be detected using unsupervised learning without the label of data.

REFERENCES

Akash, N. S., Rouf, S., Jahan, S., Chowdhury, A., Chakrabarty, A., & Uddin, J. (2022). Botnet Detection in IoT Devices Using Random Forest Classifier with Independent Component Analysis. Journal of Information and Communication Technology, 21(2), 201–232.

Alauthaman, M., Aslam, N., Zhang, L., Alasem, R., & Hossain, M. A. (2018). A P2P Botnet detection scheme based on decision tree and adaptive multilayer neural networks. Neural Computing and Applications, 29(11), 991–1004.

Apruzzese, G., & Colajanni, M. (2018). Evading botnet detectors based on flows and random forest with adversarial samples. NCA 2018 - 2018 IEEE 17th International Symposium on Network Computing and Applications.

Bapat, R., Mandya, A., Liu, X., Abraham, B., Brown, D. E., Kang, H., & Veeraraghavan, M. (2018). Identifying malicious botnet traffic using logistic regression. 2018 Systems and Information Engineering Design Symposium, SIEDS 2018, 266–271

Duan, L., Zhou, J., Wu, Y., & Xu, W. (2022). A novel and highly efficient botnet detection algorithm based on network traffic analysis of smart systems. International Journal of Distributed Sensor Networks, 18(3).

Eser, A. H., Aslan, Z., Gunes, A., & Zontul, M. (2021). Detection of Botnet Communication over Tcp Network Flow Using Machine Learning Algorithms. Ponte International J. of Science and Research, 77(6).

García, S., Grill, M., Stiborek, J., & Zunino, A. (2014). An empirical comparison of botnet detection methods. Computers and Security, 45, 100–123.

Gizachew Teshome (2022). Development of a Method for Detecting Network Attack on Machine Learning Algorithms. SSRN Electronic Journal.

Gizachew Teshome., & Asnak Yihunie. (2022). A Systematic Review of Botnet Detection System using Deep Learning and Machine Learning Approaches. SSRN Electronic Journal.

Goeschel, K. (2016). Reducing false positives in intrusion detection systems using data-mining techniques utilizing support vector machines, decision trees, and naive Bayes for off-line analysis. Undefined, 2016-July.

Joshi, C., Bharti, V., & Ranjan, R. K. (2020). Analysis of Feature Selection Methods for P2P Botnet Detection. Communications in Computer and Information Science, 1244 CCIS, 272–282.

Rao, S., Babu, V., & N., P. (2018). Detecting Bots inside a Host using Network Behavior Analysis. International Journal of Computer Applications, 180(47), 1–4.

Rezaei, A. (2020). Identifying Botnet on IoT by Using Supervised Learning Techniques. Oriental Journal of Computer Science and Technology, 12(4), 185–193.

Vishwakarma, A. R. (2020). Network Traffic Based Botnet Detection Using Machine Learning. Master's Projects.

Wazzan, M., Algazzawi, D., Bamasaq, O., Albeshri, A., & Cheng, L. (2021). Internet of things botnet detection approaches: Analysis and recommendations for future research. Applied Sciences (Switzerland), 11(12).

Xing, Y., Shu, H., Zhao, H., Li, D., & Guo, L. (2021). Survey on Botnet Detection Techniques: Classification, Methods, and Evaluation. Mathematical Problems in Engineering, 2021. 9

RNA-Seq Analysis Reveals Important Factors Involved in Metabolic Adaptation in Transition Cows

Girma Debele Delelesse[1,*], Shengtao G.[2], Ma L.[2], Dengpan B.[2,3]

[1]*Bio and Emerging Technology Institute, P.O. Box 5459, Addis Ababa, Ethiopia.*
[2]*State Key Laboratory of Animal Nutrition, Institute of Animal Science, Chinese Academy of Agricultural Sciences, Beijing, 100193, China.*
[3]*China-Ireland Dairy Science and Technology Center, Director, China*
**Corresponding author, e-mail: getgdd@yahoo.com*

ABSTRACT

The transition period of a dairy cow, mostly defined as the period from week 3 antepartum until 3 week post-partum, is characterized by abrupt changes in physiology, metabolism, and nutrition of the animal. Intensive fetal growth before parturition, morphological and endocrine changes related to mammary gland development, and the tremendous increase in energy and nutrient demand with the onset of lactation are the most substantial challenges the dairy cow has to face during this period. Hence, optimal metabolic adaptation is required to avoid the development of metabolic and infectious diseases. The liver is the key organ controlling and regulating metabolic adaptation. Previous study revealed that liver glucose synthesis, cholesterol metabolism, lipogenesis, and inflammatory response are increased or activated during the transition in dairy cows. However, those works were limited by a low number of animals used or by the use of microarray technology, or both. To overcome such limitations, an RNA sequencing analysis was performed on liver biopsies from 20 Holstein cows. In our results we found 1,475 up regulated and 1,199 down regulated differently expressed genes with a false discovery rate adjusted P-value < 0.01 between pre-partum and post-partum dairy cows. Bioinformatics analysis showed an activation of the metabolism of lipid, glucose and amino acid with increased importance of the mitochondria and a key role of several signaling pathways, chiefly peroxisome proliferators-activated receptor and adipocytokines signaling. Fatty acid oxidation and gluconeogenesis, amino acid utilization to produce glucose, were among the most important functions revealed by the transcriptomic adaptation to lactation in the liver. The analysis also revealed high activation of cell proliferation but inhibition of xenobiotic metabolism, likely due to the liver response to inflammatory like conditions. Our data confirmed the importance of metabolic adaptation to lipid and glucose metabolism in the liver of early postpartum cows.

Keywords: *RNA sequencing, transition cow, metabolic adaptation, liver transcriptome*

1. INTRODUCTION

The transition period of a dairy cow, mostly defined as the period from week 3 antepartum until 3 week post-partum, is characterized by abrupt changes in physiology, metabolism, and nutrition of the animal. Intensive fetal growth before parturition, morphological and endocrine changes related to mammary gland development, and the tremendous increase in energy and nutrient demand with the onset of lactation are the most substantial challenges the dairy cow has to face during this period (Drackley, 1999; Drackley et al., 2005, and Loor et al., 2013). The primary challenge experienced by transition cows is a sudden and large increase in nutrient requirements for milk production that is not satisfied by feed intake, with ensuing negative energy balance (Roche et al., 2017 and Bell, 1995). As a consequence, an array of maternal metabolic adaptations are activated, including increased hepatic gluconeogenesis from endogenous substrates, decreased peripheral glucose utilization, increased fatty acid mobilization from the adipose tissue, and, possibly, increased amino acid mobilization from muscle to meet the nutrient requirements during the transition period (Bell, 1995). However, important metabolic challenges can still weaken the immune system, contributing to increased incidence of diseases, including milk fever, ketosis, retained placenta, metritis, and displaced abomasum (Kremer et al., 1993; Duffield et al., 2002). Thus, physiological

maladaptation during the peripartum negatively affects the net earnings of a dairy enterprise (Esposito et al., 2014; Roche et al., 2017).

The liver is a critical hub for numerous physiological processes, including macronutrient metabolism, blood volume regulation, immune system support, endocrine control of growth signaling pathways, lipid and cholesterol homeostasis, and the breakdown of xenobiotic toxic compounds (Piñeiro-Carrero and Piñeiro, 2004; Trefts et al., 2017). Liver also plays a critical role in the control of glucose homeostasis, especially via gluconeogenesis and storage of glucose via glycogen that is released during fasting conditions (Aschenbach et al., 2010). During prolonged fasting when the animals undergo negative energy balance, the liver also produces a high amount of ketone bodies to supply fuel to other organs (Han et al., 2016; Trefts et al., 2017). Because of the key role of the liver in controlling and regulating the metabolic adaptation during the peripartum (Drackley et al., 2005), several studies have been conducted to investigate liver adaptation to lactation. Those studies revealed that the liver during the adaptation to lactation augments the synthesis of glucose (Reynolds et al., 2003), cholesterol metabolism (Schlegel et al., 2012), and lipogenesis (Qin et al., 2018), and becomes more responsive to stimuli that induce inflammation (Loor et al., 2005). In addition, a recent hepatic transcriptomic study using RNA sequencing (RNAseq; Ha et al., 2017) confirmed that major hepatic changes during the peripartum in dairy cows are related to energy metabolism; in particular, they are related to fatty acid oxidation and metabolism, cholesterol metabolism, and gluconeogenesis.

However, most of the prior studies focused on specific aspects (Schlegel et al., 2012) and did not provide a comprehensive view of the adaptation of the liver to lactation even when high-throughput transcriptomic technologies were used, due to limitation of sensitivity typical of microarrays (Loor et al., 2005; Qin et al., 2018) or inadequate power analysis, as when only 6 cows were used per treatment (Ha et al., 2017). Thus, we found a lingering need for a study to comprehensively investigate the transcriptomic adaptation of the liver of dairy cows during the peripartum. The present study was conducted using RNA-sequencing (RNA-seq) to investigate changes in the liver transcriptome of dairy cows from late pregnancy to early lactation. Therefore the objective of the current study was to perform a comprehensive bioinformatics analysis of the transcriptomic adaptation of the liver using RNA-seq on samples from a large number of peripartum dairy cows.

2. MATERIALS AND METHODS

2.1 Animal and Ethics Statement

This study was approved by the Animal Care and Use Committee of the Institute of Animal Science, Chinese Academy of Agricultural Sciences (No. IAS20180115; Beijing). Use of animals in the present study was in strict accordance with the Directions for Caring for Experimental Animals from the Institute of Animal Science, Chinese Academy of Agricultural Sciences.

2.2 Animal Selection and Experimental Design

Liver tissue samples were collected from dairy cows enrolled in a 2 × 2 factorial design with 2 dietary energy levels and supplemented or without supplementation with rumen-protected lysine during the peripartum (Girma et al., 2019). Liver biopsies were performed in 5 random animals per each group twice, at 7.3 ± 5.1 (mean ± SD) days before parturition (Pre-P) and at 16.4 ± 2.3 d after parturition (PostP). All the cows were in third lactation and entering their fourth lactation, with BCS between 3.25 and 3.5 (1–5 scale). The expected calving date of each cow was considered in selecting cows with similar expected calving dates and previous milk yield.

2.3 Liver Tissue Samples Collection

The liver biopsy procedure was conducted using a Tru-Cut biopsy needle (Baxter Healthcare Corp., Valencia, CA; diameter 4 mm) as previously described (Bu et al., 2017). Briefly, before applying a local anesthetic, the cows received a small dose of xylazine (0.05 mg/kg of BW). Three to four milliliters of lidocaine hydrochloride (2% solution) was injected subcutaneously as a local anesthetic before the incision. A 1.5-cm incision using a sterile scalpel blade was made between the eleventh and twelfth ribs on the right side of the cow. Slight pressure was applied to the incision using sterile gauze, until visual signs of bleeding were absent. Then the liver biopsy was performed, obtaining ~300 mg of liver tissue. Tissue samples were washed with PBS buffer prepared with nuclease-free water and immediately stored in liquid nitrogen. Four or five Michel clips (11 mm; Henry Schein, Melville, NY) were used to close the skin incision after the biopsy. The incision site was sprayed with a topical antiseptic (10% povidone iodine ointment; Taro Pharmaceuticals, Hawthorne, NY). For 7 d after the biopsy, health was monitored by recording rectal temperature and daily feed intake. After the incision was completely healed (~7d), the surgical clips were removed.

2.4 RNA Isolation

TRIzol reagent (Invitrogen, Carlsbad, CA) was used to isolate total RNA from each sample. The NanoPhotometer spectrophotometer (IMPLEN, Westlake Village, CA), the Qubit RNA Assay Kit in Qubit 2.0 Fluorometer (Life Technologies, Carlsbad, CA), and the RNA Nano 6000 Assay Kit of the Bioanalyzer 2100 System (Agilent Technologies, Santa Clara, CA) were used to detect RNA purity, concentration, and integrity of each sample. The optical density OD260/OD280 values were ≥1.9, and RNA integrity number values were ≥8.0.

2.5 Library Preparation and Sequencing

Library preparation and sequencing were performed as previously described (Ren et al., 2016). Before library construction, rRNA was removed using Epicenter Ribo-Zero rRNA Removal Kit (Epicentre Biotechnologies, Madison, WI), and then further cleaned up using ethanol precipitation. Accurate 3-μg RNA per sample was used as input for complementary DNA (cDNA) library construction. Sequencing libraries were generated using the rRNA-depleted RNA following manufacturer's recommendations, using the NEBNext Ultra Directional RNA Library Prep Kit for Illumina (New England Biolabs, Ipswich, MA). The RNA sequencing was performed on an Illumina HiSeq 4000 platform (Illumina, San Diego, CA) at the Novogene Bioinformatics Institute (Beijing, China) according to the manufacturer's instructions. The raw sequence data reported in this paper have been deposited in the Genome Sequence Archive (Wang et al., 2017) in the Beijing Institute of Genomics (BIG) Data Center (National Genomics Data Center Members and Partners, 2020), Chinese Academy of Sciences.

2.6 Quality Analysis, Mapping, and Transcriptome Assembly

Reads containing adapter, poly-N and low-quality reads in the raw data were removed to obtain clean reads. The proportion of bases with a paired base quality score more than 20 and 30 of the clean data and the percentage of base G and C in clean reads were calculated. All downstream analyses were based on clean data with high quality.

2.7 Statistical Analysis

Statistical analysis of sequencing data was performed with the effect of the peripartum assessed using the negative binomial generalized linear model in the DESeq2 package. P-values were adjusted using BenjaminiHochberg method. To obtain more reliable results, a strict threshold of adjusted P-values (Padj) < 0.01 was set as the cut-off to identify differently expressed genes (DEG). Data quality assessment was performed by sample-to-sample distance visualization and principal component analysis using the dist and plotPCA function in DESeq2.

2.8 Bioinformatics Analyses

The dynamic impact approach was used to perform analysis of Kyoto Encyclopedia of Genes and Genomes (KEGG) pathways (Bionaz et al., 2012). The DIA estimates the magnitude of perturbation of a biological pathway by the "impact," and the overall direction of the perturbation is represented by the "flux" (or direction of the impact). Entrez Gene ID of detected transcripts were used as background. The data set including Entrez Gene ID, Padj, expression ratio, and non-corrected P-value was uploaded. Adjusted P-value < 0.01 and unadjusted P-value < 0.01 between the 2 treatments were used as a cut-off. The top 30 impacted pathways were visualized using Path view. The data set of DEG was prepared and uploaded according to the Path view tutorial.

2.9 Enrichment Analysis

Enrichment analysis of DEG using various databases, including KEGG pathways, Gene Ontology biological process, cellular components, and molecular function, was run by Database for Annotation, Visualization and Integrated Discovery (DAVID) version 6.7. For this analysis, the Entrez Gene ID of all transcripts detected were used as background, and 3 separated data sets were analyzed: (1) upregulated DEG (log2 fold change >0, Padj < 0.01) by Post-P versus Pre-P; (2) downregulated DEG (log2 fold change < 0.01) by Post-P versus Pre-P; and (3) both up- and downregulated DEG (Padj < 0.01). Results were downloaded using both functional annotation chart and functional annotation clustering.

2.10 Preparation of the Data Set for Co-Expression Network Construction

Read counts of each gene and each sample were normalized by median normalization using EBSeq version 3.10 in the R package. After normalization, an integer 1 was added to all data to avoid values equal to zero. Then the matrix was transformed to a logarithmic matrix to standardize the variance (Dong et al., 2015). The correlation and correlation significance of every pair of DEG (Padj < 0.01) were calculated using the logarithmic matrix of read counts. The calculation was performed using the R package psych. Pearson was chosen as the correlation method. The resulting table contains gene1 (source gene) and gene2 (target gene), the correlation values of the 2 genes, and the adjusted P-values were generated by the correction calculation. The generated table was filtered based on absolute correlation >0.9 and Padj < 0.01. For convenience, Padj values were converted to logarithmic base 10. To avoid problems with very low P-values, which are reported as 0 by the corr. test function in R, we replaced 0 values with the smallest positive floating-point number interpreted as different from 0 in R configuration. Then, we generated the table containing the statistically significant correlations across the whole data set for every pair of DEG. Those DEG with absolute correlation >0.9 were selected to construct the co-expression network.

2.11 Co-Expression Network Construction and Functional Annotation

The data set including correlation of DEG, degree and betweenness of the nodes, and log2 fold change of DEG were uploaded to Cytoscape version 3.7.2. Gene symbols were set as the node identifiers. The correlation, correlation significance, degree and betweenness, and log2 fold change were mapped to the edge color, edge width, node size, and node fill color, respectively. The co-expression network was clustered by the clusterMaker2. Six major subnetworks (clusters) were generated. The DEG within cluster 3 were, for the most part, upregulated, whereas in clusters 1 and 2, approximately half were upregulated. The functional annotation analysis of the clusters within the clustered network using the ClueGO 2.5.4 application a plug-in of Cytoscape. We selected "GO Biological Process" with evidence code "All" and selected the option "Show only Pathways with p and kept the default value of 0.05. The first 3 subnetworks were successfully annotated with the enrichment significance P-value ≤ 0.05. The visualized results were exported in PDF and transformed to pictures using Adobe Illustrator CC 2019.

3. RESULTS

Principal component analysis revealed a clear separation with no overlap between Post-P and Pre-P samples, indicating that the transcriptome profiles of the liver in Pre-P and Post-P are distinct. Results of hierarchical clustering analysis confirmed a large separation between the samples of the 2 periods. The use of DESeq2 unveiled 2,674 DEG with 1,475 upregulated and 1,199 downregulated.

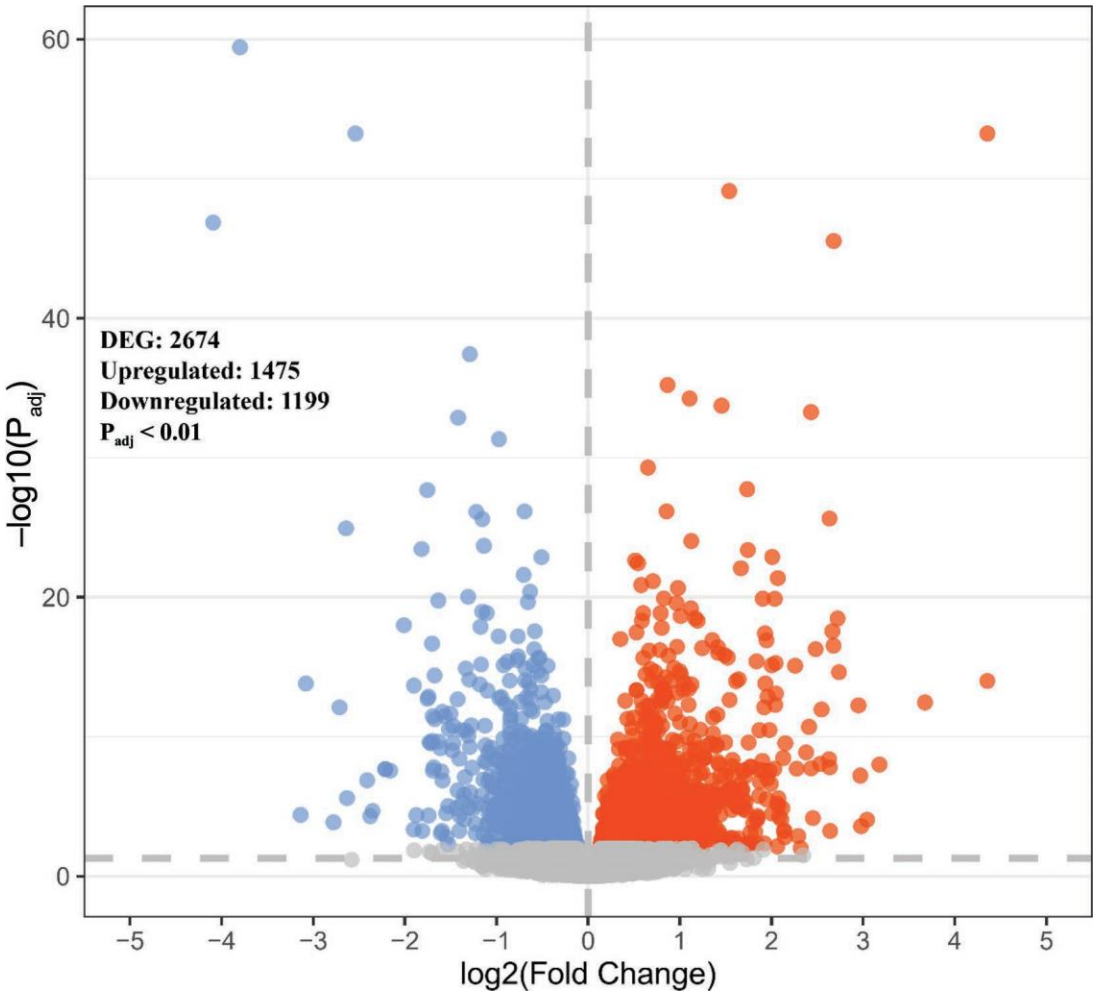

Figure 1: Volcano plot for the differently expressed genes (DEG) of liver tissue of postpartum (Post-P) compared with prepartum (Pre-P). Red points represent upregulated DEG. Blue points represent downregulated DEG. Gray points represent genes that were not significantly upor downregulated. The cut-off used for DEG was adjusted P-value (Padj) < 0.01.

3.1 Dynamic Impact Approach (DIA) Analysis

This analysis revealed overall increased metabolism and cell cycle but inhibited xenobiotic Metabolism. A summary of the KEGG pathways impacted by the transcriptome changes in postpartum versus pre partum in liver tissue of dairy cows as estimated by the DIA, is shown in Figure 2. All the main categories of KEGG pathways were impacted to different extents, and most were activated. The metabolism category, followed by cellular processes, were the most impacted main categories of KEGG pathways. DIA Analysis Reveals Overall Increased Metabolism and Cell Cycle but Inhibited Xenobiotic Metabolism. A summary of the KEGG pathways impacted by the transcriptome changes in Post-P versus Pre-P in liver tissue, as estimated by the DIA, is shown in Figure 2.

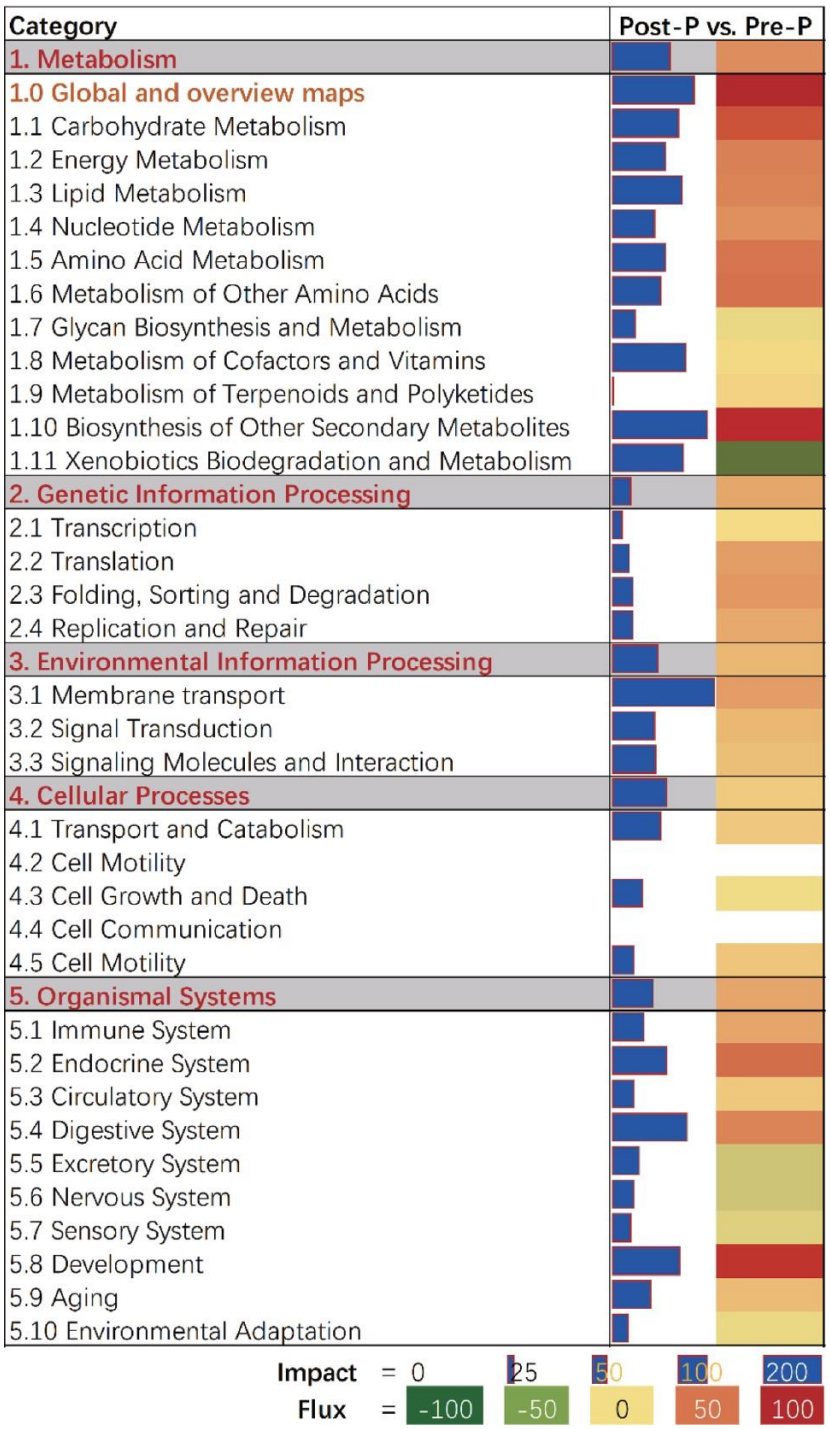

Figure 2: Summary of the main categories and subcategories of Kyoto Encyclopedia of Genes and Genomes pathways as results of the transcriptomic effect on liver tissue of postpartum (Post-P) versus prepartum (Pre-P) dairy cows, as analyzed via the Dynamic Impact Approach. On the right are the bars denoting the overall impact (in blue) and the shade denoting the effect on the pathway (from green = inhibited to red = activated). The darker the color, the greater the activation or inhibition of the pathway become.

All the main categories of KEGG pathways were impacted to different extents, and most were activated. The metabolism category, followed by cellular processes, were the most impacted main categories of KEGG pathways.

Within the main category of metabolism pathways, almost all subcategories of pathways were activated to different extents, except for the subcategory of xenobiotics biodegradation and metabolism, which was inhibited.

The impact and flux of the most impacted pathways in each of the categories of KEGG pathways are shown in Figure 3, and details for all pathways are available in Supplemental File S1 (https://doi.org/10.3168/jds.2020-19101). The importance of metabolic-related pathways is highlighted by the fact that, among the 30 most affected pathways, 16 (>50%) were related to metabolism, followed by organismal systems. Among the metabolic-related pathways, the ones related to carbohydrates, lipid, amino acids, vitamins, and biosynthesis of secondary metabolites were the most impacted and most activated in Post-P compared with Pre-P (Figure 2). Among carbohydrate related pathways, the most impacted and activated were those related to utilization and production of glucose, including the propanoate metabolism pathway, for utilization of propionic acid (Figure 3).

Among the lipid-related pathways highly activated were those related to fatty acid catabolism, along with activation of fatty acid synthesis and production of triglycerides (i.e., glycerolipid metabolism; Figure 3). Highly impacted but inhibited were the steroid hormone biosynthesis and linoleic acid metabolism pathways. All amino acid metabolism–related pathways were activated, with glutathione metabolism as the top activated pathway, followed by pathways associated with the metabolism of Arg, Pro, Cys, Met, and His (Figure 3). Among pathways related to the metabolism of cofactors and vitamins, the riboflavin metabolism pathway was highly activated, whereas other highly impacted pathways in this category were inhibited, such as vitamin B6, retinol, and thiamine metabolism (Figure 3).

Other impacted pathways related to metabolism were caffeine metabolism, highly activated in the liver from Post-P to Pre-P cows, and drug metabolism–cytochrome P450, highly inhibited. Few genetic information processing pathways were highly impacted, all related to the synthesis of proteins, especially in the endoplasmic reticulum that are then exported (Figure 3). Among the pathways associated with cellular processes, peroxisome (highly activated) and phagosome (highly inhibited) were the most important pathways associated with transport and catabolism. The high impact and activation of the cell cycle pathway and inhibition of apoptosis and P53 signaling pathways indicated an increase in cell proliferation in the liver (Figure 3). Several signaling pathways relating to environmental information processing were highly activated, including AMPK, Hippo, ErbB, and Wnt signaling pathways, with the phosphatidylinositol signaling system being inhibited (Figure 3) were highly impacted in the hepatic adaptation to the peripartum. The 3 most impacted and activated signaling pathways were PPAR, adipokines, and glucagon signaling pathways, all part of the organismal systems (Figure 3). Several pathways related to the immune system were activated in the liver for Pre-P, with IL17 and RIG-like receptor being among the most activated, but with important additional activation for toll-like receptor and TNF signaling (Figure 3). Pathways related to the digestive system were, for the most part, inhibited in the liver from Pre-P to Post-P (Figure 2 and Supplemental File S1, https://doi.org/10.3168/jds.2020-19101); however, the digestion and absorption of fat and vitamins were highly activated, but the digestion and absorption of carbohydrates and minerals were overall inhibited (Figure 3).

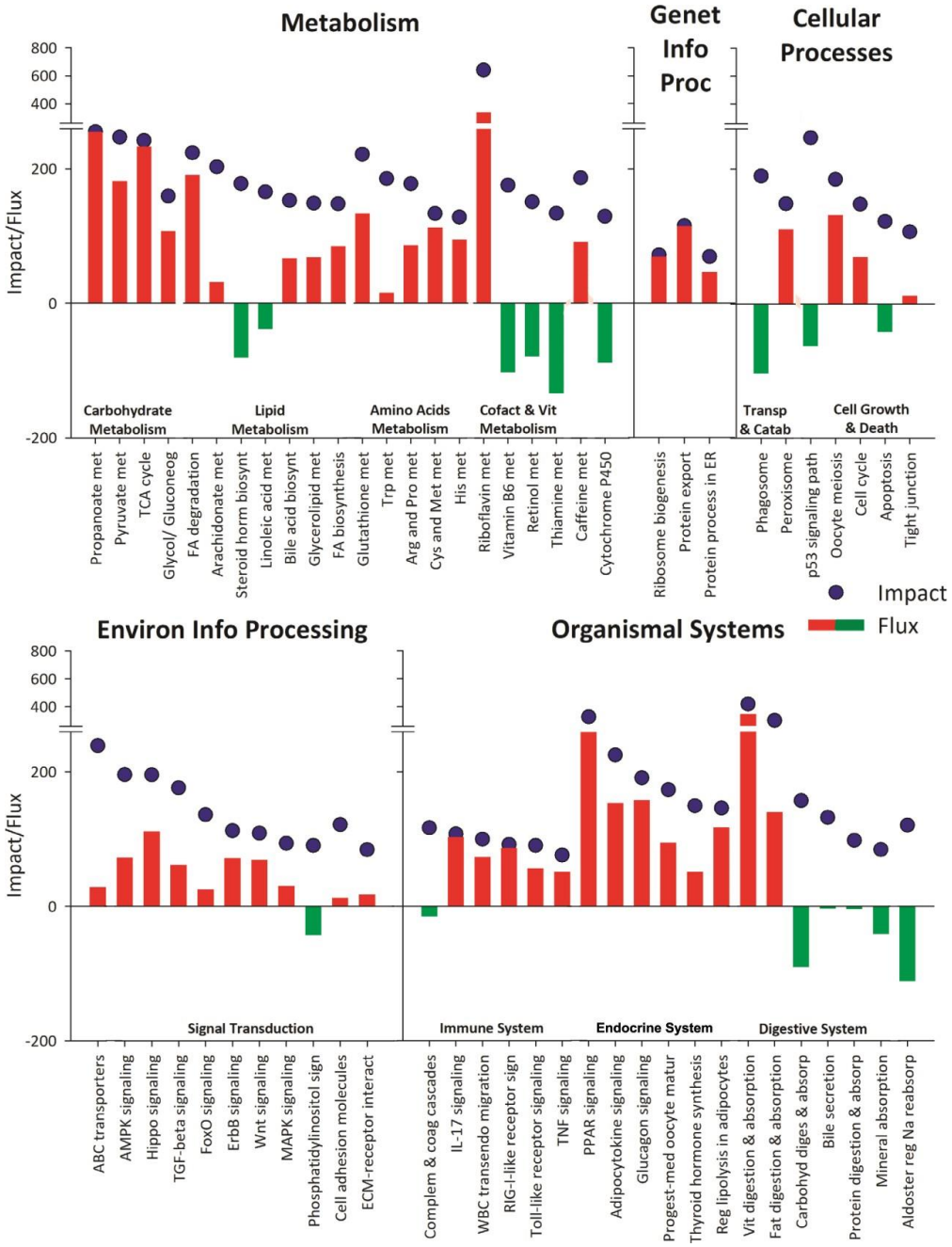

Figure 3: Most impacted pathways in each of the 5 main category of Kyoto Encyclopedia of Genes and Genomes pathways (the category of pathway "Human Disease" is not reported) in the liver of postpartum (Post-P) versus prepartum (Pre-P) pregnancy of dairy cows to 2 wk into lactation, as revealed by Dynamic Impact Approach analysis of RNA sequencing data. In the y-axis is reported the magnitude of the impact and the direction of the impact (or flux; i.e., positive or red = activated, and negative or green = inhibited). Genet Info Proc = genetic information processing; Environ Info Processing = environment information processing; TCA = tricarboxylic acid; FA = fatty acid; cofact = cofactor; vit = vitamin; transp = transportation; catab = catabolism; complem = complementary; coag = coagulation; reg = regulation; absorp = absorption

3.2 Enrichment Analysis Confirms Importance of Metabolism and Cell Division

Most of the enriched terms in DEG between Post-P and Pre-P liver of dairy cows in our study, as revealed by DAVID, were associated with upregulated compared with downregulated DEG (Figure 4 Upregulated DEG were enriched with GO Biological Process associated with the tricarboxylic acid (TCA) cycle and cell division.

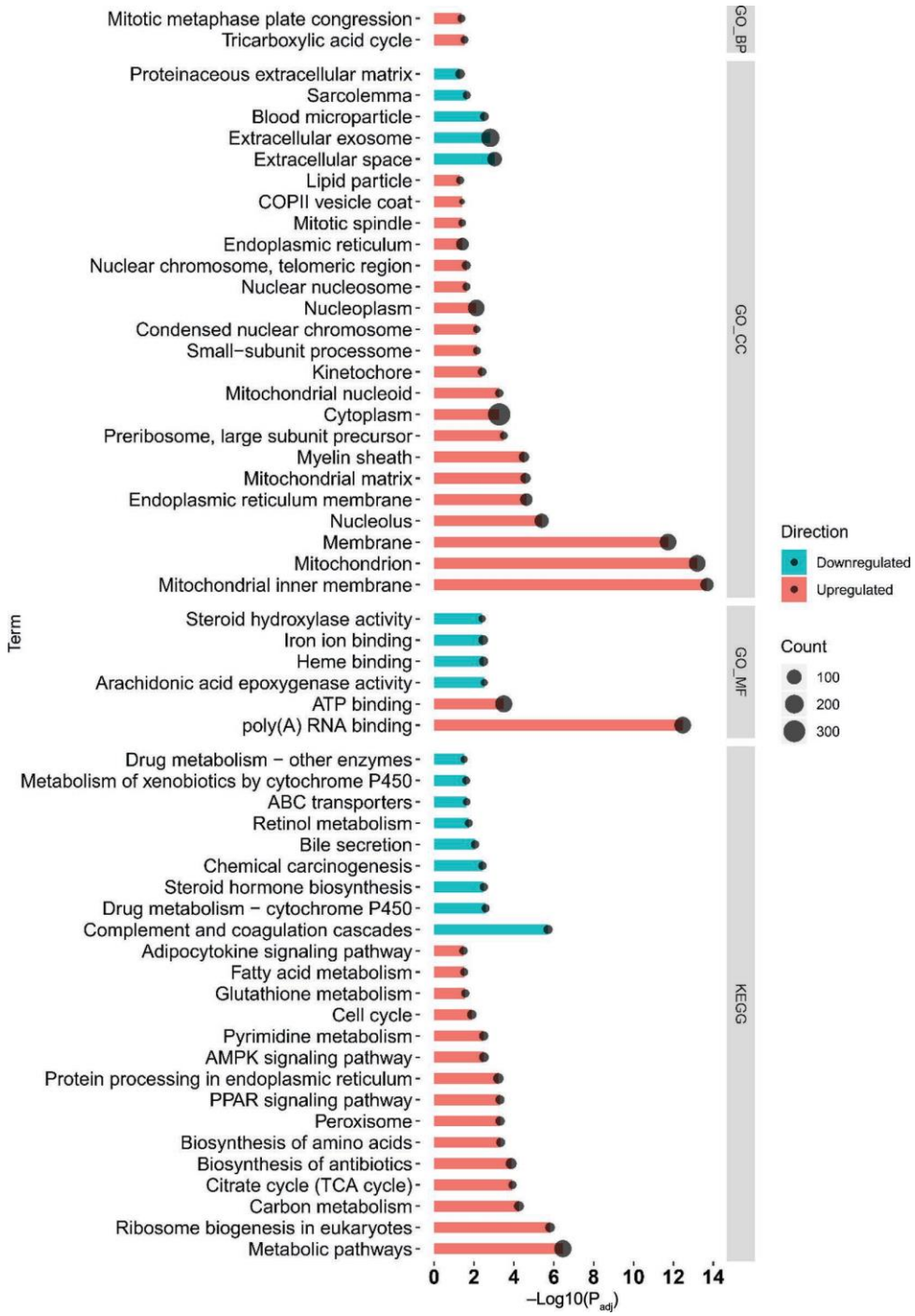

Figure 4: Significantly enriched Gene Ontology (GO; BP = biological process; CC = cellular component; MF = molecular function) and Kyoto Encyclopedia of Genes and Genomes (KEGG) pathways revealed by Database for Annotation, Visualization and Integrated Discovery analysis of the transcripts upregulated (red) or downregulated (blue) in liver tissue of postpartum versus prepartum cows. Vertical axis shows the terms; horizonal axis shows the transformed false discovery rate [−log10 adjusted P-value (Padj)]. TCA = tricarboxylic acid

The most enriched cellular component terms were related to mitochondria and endoplasmic reticulum, whereas, among downregulated DEG, terms related to extracellular space and exosomes were the most enriched. Terms related to transcription and ATP were the most enriched molecular functions among upregulated DEG, and terms related to use of arachidonic acid and steroid were the most enriched among downregulated DEG. Among signaling pathways, DAVID revealed enrichment of AMPK, PPAR, and adipocytokine signaling pathways among upregulated DEG. Drug metabolism, steroid hormone biosynthesis, retinol metabolism, bile secretion, and complement and coagulation cascades were among the most enriched KEGG pathways in downregulated DEG.

Co-Expression Network Analysis Reveals High Coordination Between Cell Division and Metabolism For the first cluster within the co-expression network, 2 major functionally grouped annotation networks were revealed: RNA modification and oxidative phosphorylation. The downregulated DEG in cluster 1 were mainly associated with ensheathment of neurons, activation of GTPase activity, neuroblast proliferation, and pathway-restricted SMAD protein phosphorylation whereas the upregulated DEG were associated mainly with RNA modification, ncRNA processing, oxidative phosphorylation, protein import into mitochondrial matrix, and mitochondrial gene expression. The DEG in the second cluster were mainly enriched with intestinal cholesterol absorption, intestinal lipid absorption, regulation of insulin-like growth factor receptor signaling pathway, and response to insulin. The downregulated DEG of cluster 2 were mainly enriched with positive regulation of protein import in nucleus and cholesterol efflux (whereas upregulated DEG were mainly enriched with fatty acid metabolic process and long-chain fatty acid transport. For the third cluster, which consisted mainly of upregulated DEG, high enrichment of terms associated with cell division (such as mitotic cell cycle process and regulation of chromosome segregation), metabolism (such as positive regulation of ATP metabolic process), and transport (such as intestinal cholesterol absorption) were detected in tightly connected DEG.

4. DISCUSSIONS

The liver is a critical hub for numerous physiological processes. Among these, processing, partitioning, and metabolism of macronutrients are the liver's most critical functions (Nordlie et al., 1999; Trefts et al., 2017). During the peripartum period, the ability of the liver to face increased metabolic challenges is a prerequisite for cows' successful adaptation to lactation without development of health disorders (Graber et al., 2010; Ha et al., 2017). Therefore, several studies have been carried out to improve understanding of the biological changes of the liver during the peripartum, using high-throughput transcriptomic techniques (Loor et al., 2005; Ha et al., 2017; Qin et al., 2018). Prior studies have revealed a relatively mild transcriptomic change of the liver of dairy cows during the peripartum. In the study by Loor et al. (2005), where liver samples from 7 time points from −65 to +49 d relative to parturition were collected from 5 cows, only 62 DEG (~1% of the measured transcripts), using a liberal 0.2 false discovery rate (FDR), were detected. The same data set, analyzed using a more robust statistical approach, uncovered that up to 20% of the measured genes were affected by the peripartum in the liver (Bionaz and Loor, 2012). A work by Qin et al. (2018) detected change of 654 DEG (FDR = 0.05) from −8 to 9 d relative to parturition in 16 Holstein cows (with 2 different diets prepartum) using an Affymetrix array (Affymetrix Inc., Santa Clara, CA), corresponding to 2,500 DEG (15.7% of detected unique genes) appears to confirm that the use of RNAseq, in combination with large numbers of cows, can provide a more in-depth approach to study the adaptation of the liver to lactation.

4.1 Metabolism Is the Major Adaptation of the Liver during the Periparturient Period

The overall activation of metabolism in the liver, as revealed by the transcriptomic analysis in the present study, is in accordance with the major role of the liver in metabolism of macronutrients, both in monogastric animals (Trefts et al., 2017) and in ruminants (Drackley, 1999). Prior transcriptomics data also highlighted metabolism as the predominant functional adaptation of the liver in transition cows (Ha et al., 2017). A cascade of

metabolic adaptive processes follows, including increased hepatic gluconeogenesis and protein synthesis, adipose fat mobilization with increased circulating NEFA, and peripheral mobilization of amino acids that require larger ureagenesis (Bell, 1995). In all of those processes, the liver plays a central role (Drackley et al., 2005). Our data appear to provide further evidence of the physiological adaptation of the liver, as NEFA increased and triglycerides decreased from Pre-P to Post-P. Our data are consistent with prior studies (Davis et al., 2019), including those showing increased gluconeogenesis (Greenfield et al., 2000) and utilization of NEFA via oxidation and re-esterification (Loor et al., 2005) by the liver during the peripartum. In addition, we note that vitamin B6 and thiamine metabolism in liver were decreased in Post-P compared with Pre-P in this study. However, similar results have rarely been revealed by previous studies. Preynat et al. (2010) suggested that liver concentrations of folates and vitamin B12 were increased by their respective supplements via intramuscular injections. Similar results were also revealed by Akins et al. (2013). The results of Graulet et al. (2007) showed that dietary supplements of folic acid and vitamin B12 given from 3 weeks before to 8 weeks after calving increased the plasma and liver concentrations of folates and B12. In the present study, to meet the vitamin requirement of Pre-P cows with low DMI, vitamin B complex content in the close-up cow diet was 2-fold higher than in the fresh cow diet. Thus, the decreased vitamin B6 and thiamine metabolism in the liver of Post-P compared with Pre-P cows can partly be explained by the lower vitamin B consumption by Post-P cows than Pre-P cows. Increased Fatty Acid Metabolism Is Regulated by PPAR and Adipocytokines. Our data clearly indicate a strong increase in expression of genes involved with fatty acid oxidation. As previously argued (Bionaz et al., 2013) and as indicated by the present data, the central player in this adaptation appears to be the PPAR signaling. A detailed visualization of the PPAR signaling KEGG pathways revealed increase in expression of most of the genes in that pathway. However, there are 3 PPAR isotypes, with PPARA as the most abundantly expressed in the liver of dairy cows (Bionaz et al., 2013), which was confirmed in the present data. Contrary to the data from Loor et al. (2005), PPARA was downregulated in our study (1.2-fold, Padj = 0.02), with no change for the other PPAR isotypes. Our data are similar to those from Ha et al. (2017; 1.4-fold downregulated, Padj = 0.001), with no effect on the other 2 PPAR isotypes. Proteome results from Schäff et al. (2012) also indicated an obvious decrease of PPARA and no significant change in abundance of PPARG from prepartum to postpartum. Others have found no change in transcription of PPARA in the liver of peripartum cows (Kessler et al., 2014). The downregulation or lack of change in expression of PPARA, with a higher change in putative downstream target genes, appears to be a contradiction; however, as previously argued (Bionaz et al., 2015), the activity of a transcription factor is not dependent on its transcription. The increased activation of PPAR in the liver of transition cows ispartly explained by increased NEFA, as previously argued (Bionaz et al., 2013) and recently demonstrated in vitro (Busato and Bionaz, 2020). As Figure 5 shows, it appears that more putative downstream targets of PPARD were affected compared with the putative downstream targets of PPARA. Recent data generated in vitro revealed that PPARD responded to NEFA in bovine hepatocytes, but PPARA did not (Busato and Bionaz, 2020). The high importance of PPAR during the transition, as observed in the present manuscript, or during the response to changes in the energy level in the diet (Loor et al., 2007; Bionaz and Loor, 2012; McCabe et al., 2012), further supports the importance of PPAR in the adaptation of the liver to the transition period (Bionaz et al., 2013). The large impact and activation in DIA and enrichment in DAVID of the adipocytokine pathway (Figure 3 and Figure 4), which is consistent with the finding of Ha et al. (2017), suggest an important role of adipose tissue in controlling the adaptation of the liver through the release of adipocytokines such as adiponectin and leptin that, by binding to specific receptors in the liver, can affect PPAR signaling via activation of AMPK signaling (induced in our study, Figure 3 and Figure 4), as observed in monogastric species (Cao, 2014). Thus, in addition to NEFA, adipocytokines released from adipose tissue also appear to play an important regulatory role in the liver of peripartum cows. When NEFA cannot be oxidized to carbon dioxide or transformed to ketone bodies completely, they are reesterified into triglycerides, and fatty liver may develop (Bobe et al., 2004). In the present study,

pathways associated with the synthesis of lipids, including fatty acids and glycerolipids, were induced in Post-P versus Pre-P liver (i.e., fatty acid biosynthesis and glycerolipids metabolism, Figure 3), indicating an increased capacity of the liver to synthesize and accumulate triglycerides. Accumulation of triglycerides in the liver is typical of early-postpartum cows (Drackley, 1999), and our data indicate that this process is regulated at the transcriptomic level, providing support for a previously proposed model (Loor et al., 2005)

4.2 Increase in Early Postpartum Hepatic Proliferation

Regarding the role of lipid metabolism, all the bioinformatics tools used to analyze our data set revealed an important activation of cell proliferation, supported by induction of the cell cycle and inhibition of apoptosis. In addition, the Wnt signaling pathway and ErbB signaling pathway, which are involved in cell growth (Acebron et al., 2014) and proliferation (Marmor et al., 2004), were also induced in Post-P versus Pre-P cows. The hippo signaling pathway, which is the upstream pathway of the Wnt signaling pathway, was also activated in Post-P compared with Pre-P. The hippo signaling pathway negatively regulates cell cycle and cell death by inhibiting the Wnt signaling pathway (Huang et al., 2005; Heallen et al., 2011). Overall, the results of the present study implied an activated cell proliferation in liver during the peripartum, which is consistent with the previously observed 9% increased weight of the liver from 1 week before calving to 3 week postpartum in dairy cows (Reynolds et al., 2004). The higher cell cycle despite a modest increase in liver size might also be due to a response of the liver to increased damage in the early postpartum, as suggested by the previously observed increase of liver enzymes in plasma of early postpartum cows (Shahzad et al., 2014a). This is likely partly due to accumulation of triglycerides (Shahzad et al., 2014a). Carbohydrate Metabolism in the Liver Our data indicated an important transcriptomic adaptation to glucose metabolism in the liver of Pre-P cows. Propanoate metabolism was the most impacted pathways and was highly activated (Figure 3), supporting the observed increase in the capacity of the liver to convert propionate into glucose in early postpartum versus prepartum cows (Drackley et al., 2001). Detailed visualizations of the other most impacted pathways related to glucose metabolism are shown in Figures 6, 7, and 8. From the pathways it is obvious that many energy substrates flowed into the TCA cycle, indicating activation of energy metabolism in the liver. However, the highly impacted and activated TCA cycle might be also associated with the greater utilization of amino acids for gluconeogenesis, due to the insufficient availability of propionate due to insufficient feed intake, as previously reviewed (Drackley et al., 2001). As support, results from our DIA indicated that most amino acid metabolic pathways were induced during Pre-P in the liver of dairy cows (Figure 3). In the present study, we found that the pathways associated with alanine and glutamine metabolism were induced according to DIA but were not among the most impacted; however, amino acid metabolic pathways were not important according to the enrichment tools used. Overall, our data based on DIA suggest a likely increased contribution of amino acid to gluconeogenesis in Post-P versus Pre-P cows. The increasing importance of gluconeogenesis in the liver of peripartum cows in our study is also supported by the upregulation of the genes encoding the key enzymes for this pathway: G6PC, PCK1, and PC (Greenfield et al., 2000; Padj < 0.01. The products of these genes catalyze the reversible interconversion of glucose 1-phosphate (toward glucose synthesis) and glucose 6-phosphate (toward glycolysis). Jin et al. (2018) demonstrated that decreased expression of PGM1 can prevent glycogenesis and leads to more glucose toward glycolysis. Furthermore, several genes related to glucose transport (SLC2A2, SLC2A4, and SLC2A5) were downregulated in the liver during the transition from pregnancy to lactation. Among these transporters, only the transporter coded by SLC2A2 is involved in the release of glucose synthesized by gluconeogenesis in the liver into the blood (Zhao and Keating, 2007). The positive correlation between SLC2A2 and FoxO1 was demonstrated by Kinoshita et al. (2016), but FoxO1 was not detected in the present study. Despite this, the downregulation of the other glucose transporters may suggest that the glucose absorption of liver from blood was decreased in Post-P compared with Pre-P cows. The reason for such observation is unclear; however, it is possible that the liver spared blood glucose for other organs, chiefly the mammary gland.

Overall, our data strongly support an activation of gluconeogenesis in Post-P versus Pre-P cows.

4.3 Increased Protein Synthesis in the Liver and the Inflammatory Response

The liver is a protein synthetic organ that is responsible for 85 to 90% of circulating proteins (Trefts et al., 2017). The bioinformatic analysis of our RNAseq results do not support an overall increase in the induction of protein synthesis in the liver of Post-P versus Pre-P cows (e.g., mTOR pathways were not activated) but clearly support an increase of synthesis of proteins in the endoplasmic reticulum and their export. The major protein synthesized and secreted by the liver is albumin, which is also a negative acute-phase protein. The level of albumin is usually decreased around calving in dairy cows due to inflammatory-like conditions (Bionaz et al., 2007; Bradford et al., 2015). The transcription of albumin, as well as other negative acute phase-proteins such as paraoxonase 1 (coded by the PON1 gene), was downregulated in our experiment indicating a possible response to inflammatory-like conditions. The adaptation of the liver transcriptome from Pre-P to Post-P in our study is also supported by the increased transcription of few positive acute-phase proteins, such as SAA (SAA3) and CRP. Further support is provided by the important impact and induction of several proinflammatory signaling pathways revealed by DIA, including the pathway associated with the proinflammatory IL-17 (Amatya et al., 2017), TNF-A, and toll-like receptors (Aoyama et al., 2010). Activation of several of the same pathways was also detected in a prior experiment where Escherichia coli was infused into the mammary gland of cows, inducing a large inflammation (Moyes et al., 2016). In that experiment, increased protein synthesis in the ER and increase in protein export were also observed. Further support for a mild inflammatory response of the liver is also provided by the inhibition of xenobiotic metabolism in the liver in Post-P compared with Pre-P cows, particularly the P450 system, which is known to be inhibited by inflammation (Morgan, 2009). Co-Expression Network Analysis Co-expression network analysis provides insights into the coordinated transcriptomic response, suggesting common biological functions (Li et al., 2016). This is a systems biology approach for transcriptome data analyses that identifies highly connected genes that may be important to control the expression of other genes (Contreras-López et al., 2018). In the first cluster of the network, the upregulated DEG were enriched with the processes mainly associated with protein synthesis and energy metabolism. Here in, the purpose of the mitochondrial gene expression machinery is to provide the 13 proteins of the oxidative phosphorylation system (Pearce et al., 2017). In addition, the induction of protein import in mitochondrial matrix indicated that more proteins from the cytosol were transported into mitochondria, increasing their number and activity (Endo et al., 2011), including energy metabolism (e.g., oxidative phosphorylation). Modification of RNA, including 5′ cap and 3′ poly (A) tail modifications is known to promote mRNA stability and facilitate nuclear export, translation initiation, and recycling (Roundtree et al., 2017). Increased poly(A) formation and poly(A) tail modifications can be associated with increased functional specialization of the liver but can also increase efficiency of mRNA translation (Shepard et al., 2011). The coupling of oxidative phosphorylation and RNA modification in the same cluster might suggest a coordinated association between production of energy and protein synthesis. It is noteworthy that inhibition of the regulation of insulin receptor signaling pathway and induction of fatty acid metabolic process and long-chain fatty acid transport emerged in the same cluster. Weber et al. (2017) demonstrated that the mRNA abundance of ACADVL and HMGCS1 in the liver of transition cows increased from 5 week prepartum to 3 week postpartum, whereas administration of insulin using euglycemic-hyperinsulinemic clamps decreased the mRNA expression of CPT1A and ACADVL, implying an inhibition of β-oxidation induced by insulin administration (Weber et al., 2017). Interestingly, insulin concentration in blood decreases substantially early postpartum (Graber et al., 2010). In the postprandial state in humans, insulin stimulates de novo lipogenesis and suppresses fatty acid oxidation in the liver (Leavens and Birnbaum, 2011), whereas mice lacking the insulin receptor in hepatocytes have increased fatty acid oxidation and failed to induce de novo lipogenesis in response to a meal (Haas et al., 2012). Thus, our results might suggest that reduced insulin signaling is important to allow fatty acid oxidation in the liver of Post-P cows. Almost all the DEG in cluster 3 were

upregulated and were mainly annotated to the biological process associated with cell proliferation, energy, and lipid metabolism. The induced cell proliferation was also revealed by all the bioinformatics tools we used, including induction of the cell cycle and inhibition of apoptosis. The observed association between induced ATP synthesis and cell cycle process is indicative of the use of energy for the increase in hepatic cell proliferation (Morita et al., 2015).

5. CONCLUSIONS

Our study focused on early-postpartum adaptation using only 2 time points; thus, it is difficult to capture with such a data set the whole dynamic adaptation of the liver to lactation. To capture such adaptation, more time points using the same number of animals should be analyzed. Despite this limitation, our RNAseq analysis performed in a large number of animals revealed a substantial transcriptomic adaptation of the liver early postpartum. The bioinformatic analysis of the data confirmed that the major adaptation of the liver to the early postpartum period in cows is metabolic, chiefly lipid metabolism, with fatty acid oxidation and mitochondria playing a major role. The data confirmed a major role of PPAR and revealed the role of the adipose tissues via adipocytokines in such an adaptation. Our data also confirmed increased gluconeogenesis and cell proliferation, with a possible response to inflammatory-like conditions that may have reduced the capability of the liver to clear xenobiotics. Such data, together with prior findings of a strong response of the liver to energy level in the diet appears to support the management of transition cows focusing on priming the liver metabolically via PPAR to face early-postpartum metabolic challenges.

ACKNOWLEDGMENTS

We are very grateful to Z. K. Zhou, from the Institute of Animal Science of Chinese Academy of Agricultural Sciences (Beijing) for his great contribution to the sequencing data processing. This research was partially supported by the National Key Research and Development Program of China (2018YFD0501600; Beijing), the Scientific Research Project for Major Achievements of the Agricultural Science and Technology Innovation Program (ASTIP; CAAS-ZDXT2019004, ASTIP-IAS071, CAAS-XTCX2016011-01; Beijing), and the Beijing Dairy Industry Innovation Team (BAIC06-2020).

REFERENCES

Acebron, S. P., E. Karaulanov, B. S. Berger, Y. L. Huang, and C. Niehrs. (2014). Mitotic wnt signaling promotes protein stabilization and regulates cell size. Mol. Cell 54:663–674.

Akins, M. S., S. J. Bertics, M. T. Socha, and R. D. Shaver. (2013). Effects of cobalt supplementation and vitamin B12 injections on lactation performance and metabolism of Holstein dairy cows. J. Dairy Sci. 96:1755–1768.

Amatya, N., A. V. Garg, and S. L. Gaffen. (2017). IL-17 signaling: The Yin and the Yang. Trends Immunol. 38:310–322.

Aoyama, T., Y. H. Paik, and E. Seki. (2010). Toll-like receptor signaling and liver fibrosis. Gastroenterol. Res. Pract. 2010:192543.

Aschenbach, J. R., N. B. Kristensen, S. S. Donkin, H. M. Hammon, and G. B. Penner. (2010). Gluconeogenesis in dairy cows: The secret of making sweet milk from sour dough. IUBMB Life 62:869–877.

Bell, A. W. (1995). Regulation of organic nutrient metabolism during transition from late pregnancy to early lactation. J. Anim. Sci. 73:2804–2819.

Biddinger, S. B., A. Hernandez-Ono, C. Rask-Madsen, J. T. Haas, J. O. Alemán, R. Suzuki, E. F. Scapa, C. Agarwal, M. C. Carey, G. Stephanopoulos, D. E. Cohen, G. L. King, H. N. Ginsberg, and C. R. Kahn. (2008). Hepatic insulin resistance is sufficient to produce dyslipidemia and susceptibility to atherosclerosis. Cell Metab. 7:125–134.

Bindea, G., B. Mlecnik, H. Hackl, P. Charoentong, M. Tosolini, A. Kirilovsky, W. H. Fridman, F. Pages, Z. Trajanoski, and J. Galon. (2009). ClueGO: A Cytoscape plug-in to decipher functionally grouped gene ontology and pathway annotation networks. Bioinformatics 25:1091–1093.

Bionaz, M., S. Chen, M. J. Khan, and J. J. Loor. (2013). Functional role of PPARs in ruminants: Potential targets for fine-tuning metabolism during growth and lactation. PPAR Res. 2013:684159.

Bionaz, M., and J. J. Loor. (2012). Ruminant metabolic systems biology: reconstruction and integration of transcriptome dynamics underlying functional responses of tissues to nutrition and physiological state. Gene Regul. Syst. Bio. 6:109–125.

Bionaz, M., J. Osorio, and J. J. Loor. (2015). Triennial Lactation Symposium: Nutrigenomics in dairy cows: Nutrients, transcription factors, and techniques. J. Anim. Sci. 93:5531–5553

Bionaz, M., K. Periasamy, S. L. Rodriguez-Zas, W. L. Hurley, and J. J. Loor. (2012). A novel dynamic impact approach (DIA) for functional analysis of time-course omics studies: Validation using the bovine mammary transcriptome. PLoS One 7:e32455.

Bionaz, M., E. Trevisi, L. Calamari, F. Librandi, A. Ferrari, and G. Bertoni. (2007). Plasma paraoxonase, health, inflammatory conditions, and liver function in transition dairy cows. J. Dairy Sci. 90:1740–1750.

Bobe, G., J. W. Young, and D. C. Beitz. (2004). Invited review: Pathology, etiology, prevention, and treatment of fatty liver in dairy cows. J. Dairy Sci. 87:3105–3124.

Bradford, B. J., K. Yuan, J. K. Farney, L. K. Mamedova, and A. J. Carpenter. (2015). Invited review: Inflammation during the transition to lactation: New adventures with an old flame. J. Dairy Sci. 98:6631–6650.

Bu, D., M. Bionaz, M. Wang, X. Nan, L. Ma, and J. Wang. (2017). Transcriptome difference and potential crosstalk between liver and mammary tissue in mid-lactation primiparous dairy cows. PLoS One 12:e0173082.

Busato, S., and M. Bionaz. (2020). The interplay between non-esterified fatty acids and bovine peroxisome proliferator-activated receptors: Results of a hybrid in vitro approach. J. Anim. Sci. Biotechnol. 11:91.

Cao, H. (2014). Adipocytokines in obesity and metabolic disease. J. Endocrinol. 220:T47–T59.

Contreras-López, O., T. C. Moyano, D. C. Soto, and R. A. Gutiérrez. (2018). Step-by-step construction of gene co-expression networks from high-throughput Arabidopsis RNA sequencing data. Methods Mol. Biol. 1761:275–301.

Dann, H. M., N. B. Litherland, J. P. Underwood, M. Bionaz, A. D'Angelo, J. W. McFadden, and J. K. Drackley. (2006). Diets during far-off and close-up dry periods affect periparturient metabolism and lactation in multiparous cows. J. Dairy Sci. 89:3563–3577.

Davis, A. N., J. E. Rico, W. A. Myers, M. J. Coleman, M. E. Clapham, N. J. Haughey, and J. W. McFadden. (2019). Circulating lowdensity lipoprotein ceramide concentrations increase in Holstein dairy cows transitioning from gestation to lactation. J. Dairy Sci. 102:5634–5646.

Dong, X., A. Yambartsev, S. A. Ramsey, L. D. Thomas, N. Shulzhenko, and A. Morgun. (2015). Reverse enGENEering of regulatory networks from Big Data: A roadmap for biologists. Bioinform. Biol. Insights 9:61–74.

Drackley, J. K., A. D. Beaulieu, and J. P. Elliott. (2001). Responses of milk fat composition to dietary fat or nonstructural carbohydrates in Holstein and Jersey cows. J. Dairy Sci. 84:1231–1237.

Drackley, J. K., H. M. Dann, N. Douglas, N. A. J. Guretzky, N. B. Litherland, J. P. Underwood, and J. J. Loor. (2005). Physiological and pathological adaptations in dairy cows that may increase susceptibility to periparturient diseases and disorders. Ital. J. Anim. Sci. 4:323–344.

Duffield, T., R. Bagg, L. DesCoteaux, E. Bouchard, M. Brodeur, D. DuTremblay, G. Keefe, S. LeBlanc, and P. Dick. (2002). Prepartum monensin for the reduction of energy associated disease in postpartum dairy cows. J. Dairy Sci. 85:397–405.

Endo, T., K. Yamano, and S. Kawano. (2011). Structural insight into the mitochondrial protein import system. Biochim. Biophys. Acta 1808:955–970.

Esposito, G., P. C. Irons, E. C. Webb, and A. Chapwanya. (2014). Interactions between negative energy balance, metabolic diseases, uterine health and immune response in transition dairy cows. Anim. Reprod. Sci. 144:60–71. https://doi.org/10.1016/j.anireprosci.2013 .11.007.

Girma, D. D., L. Ma, F. Wang, Q. R. Jiang, T. R. Callaway, J. K. Drackley, and D. P. Bu. (2019). Effects of close-up dietary energy level and supplementing rumen-protected lysine on energy metabolites and milk production in transition cows. J. Dairy Sci. 102:7059–7072.

Graber, M., S. Kohler, T. Kaufmann, M. G. Doherr, R. M. Bruckmaier, and H. A. van Dorland. (2010). A field study on characteristics and diversity of gene expression in the liver of dairy cows during the transition period. J. Dairy Sci. 93:5200–5215.

Graulet, B., J. J. Matte, A. Desrochers, L. Doepel, M. F. Palin, and C. L. Girard. (2007). Effects of dietary supplements of folic acid and vitamin B12 on metabolism of dairy cows in early lactation. J. Dairy Sci. 90:3442–3455.

Greenfield, R. B., M. J. Cecava, and S. S. Donkin. (2000). Changes in mRNA expression for gluconeogenic enzymes in liver of dairy cattle during the transition to lactation. J. Dairy Sci. 83:1228–1236.

Ha, N. T., C. Drögemüller, C. Reimer, F. Schmitz-Hsu, R. M. Bruckmaier, H. Simianer, and J. J. Gross. (2017). Liver transcriptome analysis reveals important factors involved in the metabolic adaptation of the transition cow. J. Dairy Sci. 100:9311–9323.

Haas, J. T., J. Miao, D. Chanda, Y. Wang, E. Zhao, M. E. Haas, M. Hirschey, B. Vaitheesvaran, R. V. Farese Jr., I. J. Kurland, M. Graham, R. Crooke, F. Foufelle, and S. B. Biddinger. (2012). Hepatic insulin signaling is required for obesity-dependent expression of SREBP-1c mRNA but not for feeding-dependent expression. Cell Metab

Han, H.-S., G. Kang, J. S. Kim, B. H. Choi, and S.-H. Koo. (2016). Regulation of glucose metabolism from a liver-centric perspective. Exp. Mol. Med. 48:e218.

Heallen, T., M. Zhang, J. Wang, M. Bonilla-Claudio, E. Klysik, R. L. Johnson, and J. F. Martin. (2011). Hippo pathway inhibits Wnt signaling to restrain cardiomyocyte proliferation and heart size. Science 332:458–461.

Huang, D. W., B. T. Sherman, and R. A. Lempicki. (2009). Systematic and integrative analysis of large gene lists using DAVID bioinformatics resources. Nat. Protoc. 4:44–57.

Huang, J., S. Wu, J. Barrera, K. Matthews, and D. Pan. (2005). The Hippo signaling pathway coordinately regulates cell proliferation and apoptosis by inactivating Yorkie, the Drosophila Homolog of YAP. Cell 122:421–434.

Jin, G. Z., Y. Zhang, W. M. Cong, X. Wu, X. Wang, S. Wu, S. Wang, W. Zhou, S. Yuan, H. Gao, G. Yu, and W. Yang. (2018). Phosphoglucomutase 1 inhibits hepatocellular carcinoma progression by regulating glucose trafficking. PLoS Biol. 16:e2006483

Kessler, E. C., J. J. Gross, R. M. Bruckmaier, and C. Albrecht. (2014). Cholesterol metabolism, transport, and hepatic regulation in dairy cows during transition and early lactation. J. Dairy Sci. 97:5481– 5490.

Kinoshita, A., L. Locher, R. Tienken, U. Meyer, S. Danicke, J. Rehage, and K. Huber. (2016). Associations between Forkhead box O1 (FoxO1) expression and indicators of hepatic glucose production in transition dairy cows supplemented with dietary nicotinic acid. PLoS One 11:e0146670.

Langmead, B., and S. L. Salzberg. (2012). Fast gapped-read alignment with Bowtie 2. Nat. Methods 9:357–359

Leavens, K. F., and M. J. Birnbaum. (2011). Insulin signaling to hepatic lipid metabolism in health and disease. Crit. Rev. Biochem. Mol. Biol. 46:200–215

Li, L., R. Briskine, R. Schaefer, P. S. Schnable, C. L. Myers, L. E. Flagel, N. M. Springer, and G. J. Muehlbauer. (2016). Co-expression network analysis of duplicate genes in maize (Zea mays L.) reveals no subgenome bias. BMC Genomics 17:875.

Loor, J. J., M. Bionaz, and J. K. Drackley. (2013). Systems physiology in dairy cattle: Nutritional genomics and beyond. Annu. Rev. Anim. Biosci. 1:365–392

Loor, J. J., R. E. Everts, M. Bionaz, H. M. Dann, D. E. Morin, R. Oliveira, S. L. Rodriguez-Zas, J. K. Drackley, and H. A. Lewin. (2007). Nutrition-induced ketosis alters metabolic and signaling gene networks in liver of periparturient dairy cows. Physiol. Genomics 32:105–116

Love, M. I., W. Huber, and S. Anders. (2014). Moderated estimation of fold change and dispersion for RNA-seq data with DESeq2. Genome Biol.

Luo, W., G. Pant, Y. K. Bhavnasi, S. G. Blanchard Jr., and C. Brouwer. (2017). Pathview Web: User friendly pathway visualization and data integration. Nucleic Acids Res. 45(W1):W501–W508.

Marmor, M. D., K. B. Skaria, and Y. Yarden. (2004). Signal transduction and oncogenesis by ErbB/HER receptors. Int. J. Radiat. Oncol. Biol. Phys. 58:903–913.

McCabe, M., S. Waters, D. Morris, D. Kenny, D. Lynn, and C. Creevey. (201)2. RNA-seq analysis of differential gene expression in liver from lactating dairy cows divergent in negative energy balance. BMC Genomics 13:193.

Morgan, E. T. (2009). Impact of infectious and inflammatory disease on cytochrome P450-mediated drug metabolism and pharmacokinetics. Clin. Pharmacol. Ther. 85:434–438.

Morita, M., S.-P. Gravel, L. Hulea, O. Larsson, M. Pollak, J. St-Pierre, and I. Topisirovic. (2015). mTOR coordinates protein synthesis, mitochondrial activity and proliferation. Cell Cycle 14:473–480.

Moyes, K. M., P. Sorensen, and M. Bionaz. (2016). The impact of intramammary Escherichia coli challenge on liver and mammary transcriptome and cross-talk in dairy cows during early lactation using RNAseq. PLoS One 11:e0157480.

National Genomics Data Center Members and Partners. (2020). Database resources of the National Genomics Data Center in 2020. Nucleic Acids Res. 48(D1):D24–D33.

Haute, and M. Minczuk. (2017). Regulation of mammalian mitochondrial gene expression: Recent advances. Trends Biochem. Sci. 42:625–639.

Pertea, M., D. Kim, G. M. Pertea, J. T. Leek, and S. L. Salzberg. (2016). Transcript-level expression analysis of RNA-seq experiments with HISAT, StringTie and Ballgown. Nat. Protoc. 11:1650–1667.

Piñeiro-Carrero, V. M., and E. O. Piñeiro. (2004). Liver. Pediatrics 113(Suppl. 3):1097. Preynat, A., H. Lapierre, M. C. Thivierge, M. F. Palin, N. Cardinault, J. J. Matte, A. Desrochers, and C. L. Girard. (2010). Effects of supplementary folic acid and vitamin B(12) on hepatic metabolism of dairy cows according to methionine supply. J. Dairy Sci. 93:2130–2142.

Qin, N., T. Kokkonen, S. Salin, T. Seppänen-Laakso, J. Taponen, A. Vanhatalo, and K. Elo. (2018). Prepartal high-energy feeding with grass silage-based diets does not disturb the hepatic adaptation of dairy cows during the periparturient period. J. Dairy Sci. 101:8929–8943.

Ren, H., G. Wang, L. Chen, J. Jiang, L. Liu, N. Li, J. Zhao, X. Sun, and P. Zhou. (2016). Genome-wide analysis of long non-coding RNAs at early stage of skin pigmentation in goats (Capra hircus). BMC Genomics 17:67.

Roundtree, I. A., M. E. Evans, T. Pan, and C. He. (2017). Dynamic RNA modifications in gene expression regulation. Cell 169:1187– 1200.

Schäff, C., S. Börner, S. Hacke, U. Kautzsch, D. Albrecht, H. M. Hammon, M. Röntgen, and B. Kuhla. (2012). Increased anaplerosis, TCA cycling, and oxidative phosphorylation in the liver of dairy cows with intensive body fat mobilization during early lactation. J. Proteome Res. 11:5503–5514.

Schlegel, G., R. Ringseis, J. Keller, F. J. Schwarz, and K. Eder. (2012). Changes in the expression of hepatic genes involved in cholesterol homeostasis in dairy cows in the transition period and at different stages of lactation. J. Dairy Sci. 95:3826–3836.

Shepard, P. J., E.-A. Choi, J. Lu, L. A. Flanagan, K. J. Hertel, and Y. Shi. (2011). Complex and dynamic landscape of RNA polyadenylation revealed by PAS-Seq. RNA 17:761–772.

Trefts, E., M. Gannon, and D. H. Wasserman. (2017). The liver. Curr. Biol. 27:R1147–R1151.

Weber, C., C. T. Schäff, U. Kautzsch, S. Börner, S. Erdmann, R. M. Bruckmaier, M. Röntgen, B. Kuhla, and H. M. Hammon. (2017). Variable liver fat concentration as a proxy for body fat mobilization postpartum has minor effects on insulin-induced changes in hepatic gene expression related to energy metabolism in dairy cows. J. Dairy Sci. 100:1507–1520.

Zhao, F. Q., and A. F. Keating. (2007). Functional properties and genomics of glucose transporters. Curr. Genomics 8:113–128.

Evolution of INH Resistance in *Mycobacterium tuberculosis* Strains Inpatients during the Course of Standard Anti-TB Therapy

Ketema Tafess[1,2,*], Gilman Kit-Hang SIU[3]

[1]*Department of Applied Biology, Adama Science and Technology Universty, P.O.Box 1888, Adama, Ethiopia*
[2]*Institute of Pharmaceutical Sciences, Adama Science and Technology University, P.O.Box 1888, Adama, Ethiopia*
[3]*Department of Health Technology and Informatics, the Hong Kong Polytechnic University, Kowloon, Hong Kong SAR, China*
**Corresponding author, e-mail: ttafess@gmail.com*

ABSTRACT

The incidence of isoniazid (INH) resistant Mycobacterium tuberculosis is rising globally. In this study, we aimed to identify the molecular mechanisms of stepwise development of drug resistance in M. tuberculosis strains collected from the same patients during the course treatment. Three M. tuberculosis strains were collected from the same patient before and after 4 months of standardized antituberculosis therapy. Phenotypic drug susceptibility test, MIRU-VNTR, and whole-genome sequencing (WGS) were conducted for strain characterization and identification of mutations associated with INH resistance. The mutated katG were transformed into a katG-deleted M. tuberculosis strain (GA03) to validate the role of novel mutations in INH resistance. Three-dimensional (3D) structures of mutated katG were modeled to predict the impact on INH binding. The pre-treatment isolate (M_11806) was INH susceptible where the two post-treatment strains were resistant. MIRU-VNTR and WGS revealed that all three strains were clonally identical. Genomic analysis identified a missense katG mutation, P232L, and a nonsense katG mutation, Q461Stop, in D1_12327 and D2_12328 strains, respectively. Transformation experiment showed that katG from pre-treatment strain restored the catalase activity in GA03 while katG genes from the post-treatment strains remained catalase-negative and had elevated MIC. 3D protein structure indicated P232L reduce INH-KatG binding affinity and Q461Stop truncate gene transcription.Our results showed that the two katG mutations, P232L and Q461Stop, accounted for the stepwise development of INH resistant clones during standard course of anti-TB therapy. Inclusion of these mutations in the design of molecular assays could increase the diagnostic performance.

Keywords: *M. tuberculosis, Anti-TB, Therapy, INH*

1. INTRODUCTION

Treatment of tuberculosis relies on the combination of several antituberculosis drugs. The current standard short-course 6-month regimen for treatment of drug-susceptible tuberculosis includes 2 months of intensive phase treatment with isoniazid, rifampicin, pyrazinamide, and ethambutol (2HRZE) followed by 4 months of continuation phases with isoniazid and rifampicin (4HR) (Horsburgh *et al*., 2015). The therapy for the MDR-TB strains includes a combination of second-line injectable drugs, fluoroquinolone, and first-line drugs (for which the bacteria remain susceptible) for a minimum of 9 months to over 2 years. Prolonged treatment course always resulted in poor adherence to the regimen, which increases the likelihood of the emergence of drug-resistant *M. tuberculosis* strain (Caminero *et al*., 2013).

Several recent studies have demonstrated heterogeneous bacterial population with drug-resistant conferring mutations within a patient under the course of standard treatment (Liu *et al*., 2015; Sun *et al*., 2012a; Trauner *et al*., 2017). Trauner *et al*. (2017) suggested that the emergence and fixation of drug-resistant conferring mutations depend on the pressure exerted by the drugs. They noted that an accurate dosage of antituberculosis drugs substantially clear the bacteria and limit the emergence of drug-resistant strains. In contrast, when the drugs pressure decline owing to the host-related or programmatic failures, drug-resistant clones would gradually emerge. Strikingly, Liu *et al.* (2015) reported that the microevolution of drug-resistant clones within lung lesions of a patient adversely affects treatment responses reinforcing the above observation. The continued emergence of genetic determinants (canonical or novel genetic alteration) of drug resistance within the patients under standard treatment

is, therefore, becoming a serious concern particularly for isoniazid owing to its complex mechanisms of action and resistance (Torres et al., 2015).

Isoniazid (INH) is one of the most powerful first-line antimycobacterial drugs (Da Silva & Palomino, 2011). INH is a prodrug that requires activation by the bacterial catalase-peroxidase enzyme KatG (encoded by the *katG* gene). Nicotinamide adenine dinucleotide species (NADH/ NAD+) dependent enoyl acyl protein carrier reductase (encoded by *inhA* gene) is the primary target of the activated INH radicals. The inhA is the principal enzyme in the biosynthesis of mycolic acid, the essential cellular structure of *M. tuberculosis* complex. The activated INH combine with NAD forming INH-NAD adduct inhibits the biosynthesis of mycobacterial mycolic acid. The activated drug also has pleiotropic effects on the growing and dormant form of the mycobacteria (Zhang & Yew, 2015). Despite the essential role of INH in the therapy of tuberculosis, the emergence and spreading of INH resistant clinical *M. tuberculosis* strains become the major challenge for the treatment of tuberculosis. The increasing incidence of INH resistance might be attributed to the higher spontaneous mutation rate of *M. tuberculosis* towards INH compared to other drugs (McGrath et al., 2014).

Most of the known INH resistance mechanisms occur through the alteration of genes encoding the activating enzyme or through mutations of other genes that encode the targets of the activated INH. Unlike rifampicin which has well-defined resistance-conferring mutations located in RRDR in more than 95% of the case, resistance mechanism to INH is complex and involves multiple genetic loci (Seifert at al., 2015). Arrays of genetic polymorphisms in genes via mabA-inhA promoter, oxyR-ahpC intergenic region, mshA, nat, ndh, kasA, ahp, inhA and katG have been implicated in INH resistance (Elis et al., 2009; Graham & Vojo, 2006; Jagielski et al., 2014; Mai et al., 2013). The predominant genetic mechanism of INH resistance in clinical *M. tuberculosis* is associated with polymorphisms occurring in *katG* where a single point mutation of S315T in the *katG* account for approximately 60% of INH-resistance while mutations in the regulator and a structural segment of *inhA* contribute for 19% INH resistance (Torres et al., 2015).

Though a wealth of data regarding the emergence and genetic mechanisms of INH resistance has been generated over the last few years, the mechanisms remain elusive with an estimated 15% of INH resistant strains harboring unknown genetic determinants (Hazbon et al., 2006; Projahn et al., 2011). On the other hand, despite the uses of standard combination therapy, there is a rising concern of the emergence of a resistant clone within a patient that exacerbated the global resistance epidemics. These underscore the need to undertake further study to elucidate the mechanisms of the emergence of novel INH resistance within a patient and determine its role through functional genetics.

In this study, three clinical *M. tuberculosis* isolates collected from a patient before and during the course of standard tuberculosis treatment were investigated. As confirmed by pDST, the pre-treatment isolate was susceptible to isoniazid while the other two isolates were INH resistant without known mutation. Mycobacterial Interspersed Repeated Unit-Variable-Number Tandem Repeats (MIRU-VNTR) typing revealed that all three isolates were clonal. Comparative whole-genome sequencings identified two novel mutations in the *katG* gene in two isolates. The functional study of these mutations confirmed the causative role of these mutations.

2. MATERIALS AND METHODS

2.1 Bacterial Strains and Plasmids

M. tuberculosis isolates M_11806, D1_12327, and D2_12328 were collected from a single patient undergoing longitudinal treatment. *E. coli* DH5α harboring *Escherichia coli*-mycobacteria shuttle vector, a pOLYG plasmid with hygromycin resistance marker *(hygR*) and plasmid derivatives used in this study.

2.2 Strain Identification Using Mycobacterial Interspersed Repeated Unit-Variable Number Tandem Repeats

DNA isolation was conducted using the Roche Cobas Amplicor extraction kit (Roche Diagnostics, USA) as previously described (Yam et al., 2004). The PCR amplification of the 24 MIRU-VNTRs was conducted using 24 pairs of primers and the amplification was undertaken using Veriti Thermal cycler. Analysis of the 24 loci MIRU was conducted using MIRU-VNTR plus as previously described (Tafess, Beyen, Girma, Girma, & Siu, 2021).

2.3 Whole Genome Sequence (WGS) and Comparative Genome Analysis

DNA was isolated from isolates grown on LJ media using the phenol-chloroform method as described previously (Benjak et al., 2017). The purity and integrity of the genomic DNA was examined using Qubit HS assay (Thermo Scientific, USA) and 0.8% agarose gel electrophoresis, respectively. The isolated DNA was subjected to library preparation (Qiagen) according to the manufacturer's instructions and sequenced on the Illumina MiSeq platform using 2x150bp version 2 sequencing chemistry (Illumina). To identify the reliable genetic variants conferring INH resistance in the three isolates, variants in the previously reported genomic loci [*katG, furA-katG, mabA-inhA* promoter, *inhA, ahpC, oxyR-ahpC* intergenic, *iniCAB, Rv0340, fabD, kasA, fbpC, srmR, accD6, efpA, fadE24, ndh, Rv1592c, Rv1772, nhoA*] (Ramaswamy et al., 2003) comprising mutations associated with drug resistance were selected and interrogated. Variants were called when the coverage of the specific position was higher than 50X and variant frequency of >20% as previously described (Eldholm et al., 2014)

2.4 Construction of Cloning Plasmid, Transformation and Minimum Inhibitory Concentration (MIC)

E. coli DH5α harboring *Escherichia coli*-mycobacteria shuttle vector, a pOLYG plasmid with hygromycin resistance marker *(hygR*) was streaked on hygromycin-containing Luria-Bertani (LB) agar and a single colony was aseptically transferred to LB broth incubated for a maximum of 16hrs. The plasmid isolation was conducted using a QIAprep spin miniprep kit (QIAGEN). The entire *furA-katG* operon containing the mutations of interests and promoter region was amplified from the three clinical isolates Restriction digestion of the vector backbone and insert DNA, followed by ligation reaction was conducted to produce the cloned plasmids. The cloned plasmids were used to transform the plasmid-free calcium competent *E. coli* DH5α cells. Verification of the insert containing the mutations of interest was conducted by Sanger sequencing as described previously (Siu et al., 2014). Provided the amplicon size of the insert is larger (~ 3000bp), additional forward and reverse primers were also employed during Sanger sequencing to cover the entire segment. The plasmids containing the insert of interest was electroporated into a catalase-negative INH-resistant *M. tuberculosis* strain (GA03) using a gene pulser (Bio-Rad, USA). At each step of cloning and transformation, Sanger sequencing was conducted to confirm the presence of mutations of interest. Determination of MICs for *M. tuberculosis* H37Rv (pansusceptible), GA03 (INH resistant), GA03 harboring pOLYG (without the insert), GA03 harboring pOLYG inserts from M_11806, D1_12327 and D2_12328 were conducted using the standard procedure (Blanco-Ruano et al., 2015)

2.5 Semi-quantitative Catalase Assay

Catalase test for the transformants (GA03) harboring *furA-katG* operon from three strains (M_11806, D1_12327, D2_12328), *M. tuberculosis* H37Rv (positive control), GA03 without the clone (negative control) were conducted as previously described (Siu et al., 2014).

2.6 Modeling of INH Binding in Wild and Mutants katG

Three-dimensional structure of the wild type and mutated katG proteins from three experimental strains was built by protein homology modeling with the crystal structure of the katG protein of *M. tuberculosis* (1SJ2) (Bertrand et al., 2004) using the server SWISS-MODEL with default parameters. The model was further analyzed

using Discovery Studio visualizer (Accelrys), and the Ramachandran plot was examined to ensure that the structure of the model was not in any unfavorable region. INH-heme binding model in the constructed was created by superimposing the katG structure with the drug.

3. RESULTS

3.1 Patient and Sample

The three isolates named M_11806, D1_12327, and D2_12328 were isolated from a single patient undergoing longitudinal treatment at Queen Mary Hospital, The University of Hong Kong. On the first arrival, the patient had the presumptive symptoms of TB and the sputum sample was collected and cultured the mother strain, M_11806, before the initialization of treatment. Phenotypic drug susceptibility test indicated the isolate was susceptible to INH but resistant to RIF, ethambutol, and pyrazinamide. Despite the initiation of standard tuberculosis treatment including INH, unsatisfactory clinical response was observed over the course of four months whereon two separate sputum samples were collected within differences of 4 days. pDST of the two daughter strains, D1_12327 and D2_12328, showed that these isolates were resistant to INH as illustrated in the schematic diagram (Figure 1).

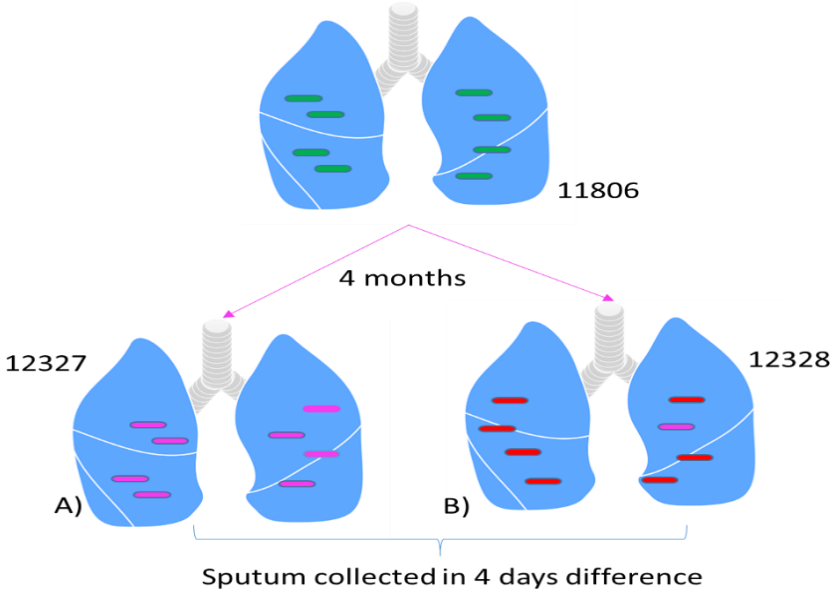

Figure 1: Schematic diagram illustrating the population of the bacteria at different time points in the lung

On the first arrival, the patient had the presumptive symptom of pulmonary tuberculosis, from whom the sputum sample was cultured (M_11806) before the initiation of treatment and the bacilli were susceptible to pDST. Two sputum samples (D1_12327 and D2_12328) were collected four months later and were resistant to INH. The WGS indicated that the pre-treatment (M_11806) had wild type loci (without any mutations all genetic loci known to be associated with INH resistance), while two novel mutations were identified in the post-treatment.

3.2 Strains Characterization

The 24-loci MIRU-VNTR showed that the mother strain and the two daughter strains share the same genetic patterns, suggesting that they originated from the same clonal population and were classified as Beijing lineage. *In silico* spoligotyping and lineage placement from the whole genome sequence data also demonstrated that the three isolates belong to the Beijing family characterized by the absence of spacer 1 to 34. The refined phylogenetic placement using the large sequence polymorphism (LSP) scheme demonstrated the absence of regions of difference (RD)105 and RD207 in three isolates placing it in a member of clade L2 (the ancient Beijing) classification based

on SNP method developed by Coll *et al*.(Coll et al., 2014) indicated that the isolates belong to lineage (L) 2.2.2. substantiating the clonality of these isolates.

3.3 Comparative Genome Analysis and Evolution of INH Resistance-conferring Mutations

Over 6 million of sequence reads were obtained for each isolate with an average read length and depth of coverage of 147.9 and 192X, respectively. The generated reads produce a uniform coverage across the entire genome of the reference genome. After removing polymorphisms in the *pe/ppe* gene families and large sequence polymorphisms (deletions) (markers of the Beijing genotype) and fixing the allelic frequency to ≥ 20X, we found a total of 1621 mutations common to the three isolates when compared to *M. tuberculosis* H37Rv. A total of 4 and 16 single nucleotides polymorphisms were found only in isolates D1_12327 and D2_12328, respectively. As illustrated in Table 1**,** comprehensive comparative analysis of WGS of 19 structural and 2 regulator regions associated with INH resistance was conducted to detect the established and novel genetic alterations conferring INH resistance. Interestingly, comparative genome analysis revealed two novel mutations in *katG* of daughter strains; Pro232Leu substitution (CCG→CTG, chromosomal position 2155417) at an allele frequency of 67% and Gln461Stop termination (CCG→CTG, chromosomal position 2155417) at an allele frequency of 97% in the D1_12327 and D2_12328 strains, respectively. Intriguingly, reads carrying Pro232Leu substitutions (9%) were also detected in the D2_12328 strain IGV; however, Sanger sequencing could only validate Gln461Stop mutation in this strain. In addition to the novel mutations in the post-treatment isolates, the three isolates also carried *katG* R463L (the natural polymorphism) (Van Doorn et al., 2001).

Table 1: Gene/loci evaluated to identify mutations conferring INH resistance

Gene/Loci	Mutation in M_11806 isolates	Mutation in M1_12327	Mutation D2_12328
katG	Arg463Leu	Arg463Leu, **Pro232Leu**	Arg463Leu, **Gln461Stop**
furA-katG	WT	WT	WT
inhA	WT	WT	WT
mabA-inhA	WT	WT	WT
oxyR-ahpC	WT	WT	WT
ahpC	WT	WT	WT
Rv0340	WT	WT	WT
iniA	Ser501Ser	Ser501Ser	Ser501Ser
iniB	WT	WT	WT
iniC	WT	WT	WT
srmR	WT	WT	WT
fabD	WT	WT	WT
kasA	WT	WT	WT
accD6	Asp200Asp; Asp229Gly	Asp200Asp; Asp229Gly	Asp200Asp; Asp229Gly
fbpC	WT	WT	WT
fadE24	WT	WT	WT
efpA	WT	WT	WT
Rv1772	WT	WT	WT
Rv1592c	Ile322Gly	Ile322Gly	Ile322Gly
ndh	WT	WT	WT
nhoA/nat	WT	WT	WT

3.4 Cloning and Transformation of Novel Mutations

The entire *katG* and the promoter region (*furA-katG* operon) were amplified (Figure 2) and Sanger sequenced for the confirmation of the novel mutations. The *furA-katG* operon of the D1_12327 and D2_12328 strains (harboring two novel mutations) and M_11806 strains were cloned into pOLYG and transferred to *E. coli* DH5α for recombinant plasmid amplification. Overall, the transformation experiment generates three new vectors named after the specific inserts.

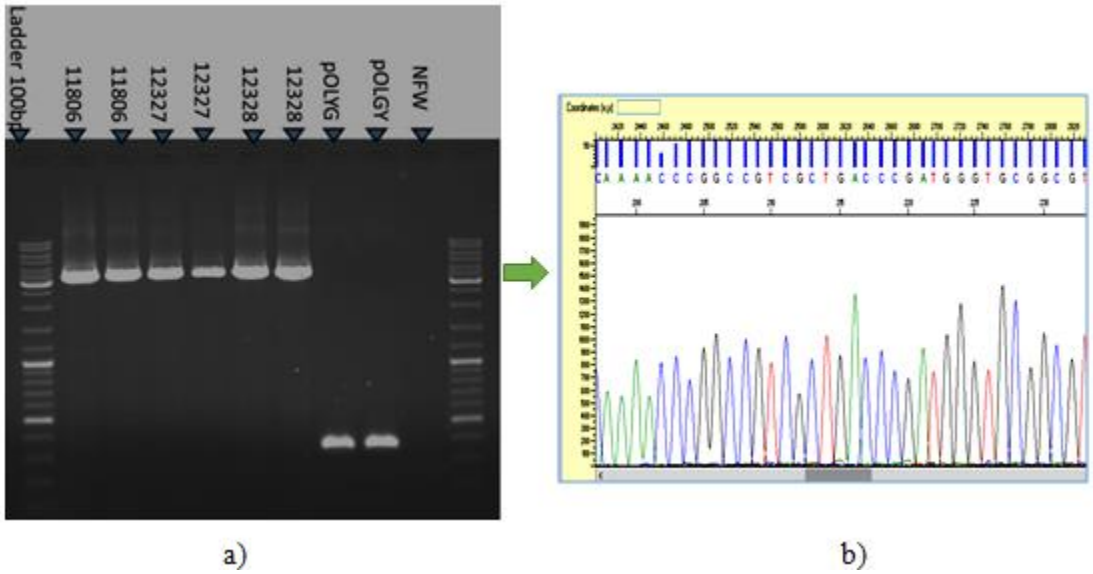

Figure 2: *furA-katG* operon PCR amplicon and Sanger sequence electropherogram for the confirmation of cloned mutations. (a) Gel photo after cloning of *furA-katG* gene into Mycobacterium Tuberculosis (b) Sanger sequence electropherogram of the cloned mutants

3.5 Correlation between Novel Mutations, and INH Resistance and Catalase Activity

The entire *furA-katG* operon with the upstream promoter region of M_11806, D1_12327 and D2_12328 strains were transformed into a *katG*-negative strain, GA03. MICs were determined for *M. tuberculosis* H37Rv, GA03, GA03 harboring vector alone and the GA03 transformants which harboured *furA-katG* operon from M_11806, D1_12327 and D2_12328 strains respectively. MICs of GA03 was greater than 256 µg/ml. Introduction of *furA-katG* operon of M_11806 successfully reduced to MIC to 32 µg/ml, partly restoring the susceptibility to INH. Interestingly, tranformants carrying the constructs pOLYG::*katG* Q461Stop, pOLYG::*katG* P232L remained highly resistant to INH with the MICs of 128µg/ml and 256µg/ml respectively. Further, the impact of these mutations was evaluated by measuring the enzymatic (catalase) activity of GA03 transformants carrying the constructs from mother and daugther isolates. The results showed that complementation of *furA-katG* operon of M_11806 had recovered the catalase activity of GA03. The constructs with novel mutations substantially lost catalase activity with a bubble height of ≤ 3 mm, which was ≥ 8 fold lower than construct carrying pOLYG::M_11806 and *M. tuberculosis* H37Rv. Remarkably, the catalase production was lower for the construct that had termination mutation than with the amino acid substitution.

3.6 Prediction of the Effect of Novel Mutations on INH Binding

A three-dimensional (3D) structure of *katG* (mutant and wild) was modeled with INH and heme in the model for an explanation (Figure 3). The natural polymorphism, R463L in all the three isolates is far away from the active binding site and does not change any structural properties of the protein (same as WT). However, the other two

mutations (Pro232Leu and Gln461Stop) in D1_12327 and D2_12328, respectively results in a considerable difference in the catalytic activity of INH. Interestingly, the proline in wild *katG* at codon 232 is important to the binding of INH/Heme as previously published(Kamachi et al., 2015). The substitution of Leu with Pro in D1_12327 (Pro232Leu) fell in the active site interfering with the binding of the INH to the enzyme and limiting the access of the INH to the iron atom where catalysis takes places. The mutation in D2_12328 (Gln461Stop) results in a truncated protein from 461 residues to 741 residues in the C-terminus (280 total residues) that results in the loss of the enzymatic activity as the protein cannot be folded properly. The deleterious impact of these two novel mutations on the catalase-peroxidase protein was further evaluated using PROVEAN(Choi & Chan, 2015). The PROVEAN score of -9.818 and -10.943 were obtained for Pro232Leu and Gln461Stop, which is considered as deleterious to the function of the catalase-peroxidase enzyme.

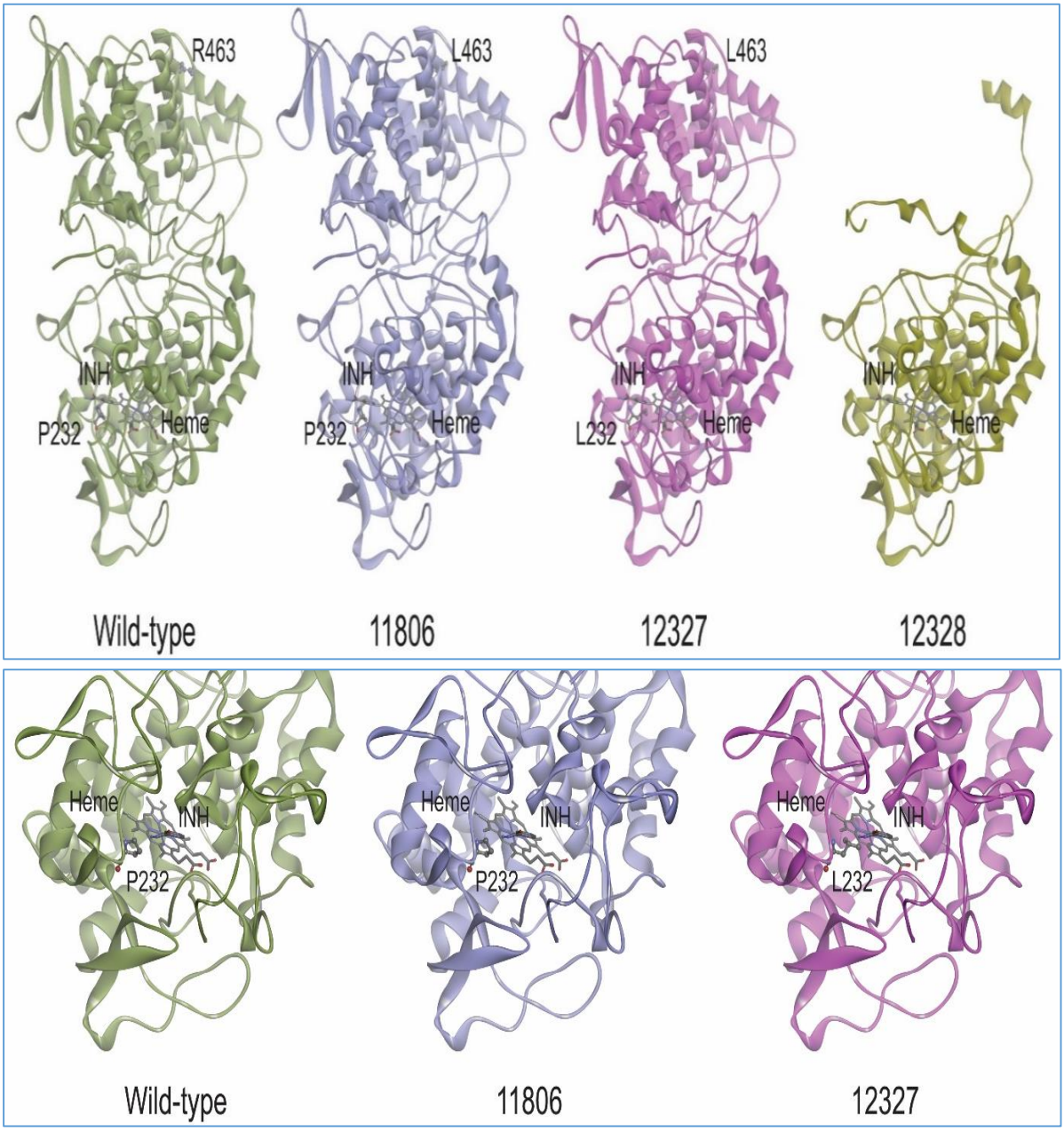

Figure 3: KatG Protein structure of wild and mutant strains

4. DISCUSSION

Isoniazid is the backbone in the standard treatment regimen of tuberculosis. Resistance to INH is frequently associated with diverse ranges of polymorphisms including complete loss of *katG* (Ramaswamy et al., 2003), single amino acid substitution, termination mutations (Bollela et al., 2016), deletions and frameshift insertions in *katG* (Kandler et al., 2018). These mutations have variable effects on *katG* enzymatic activity and the level of resistance to INH (Brossier et al., 2016).

In this study, we described the stepwise development of INH resistance within a patient on the course of standard treatment and demonstrated the causal role of the novel *katG* mutations in post-treatment INH resistant strains. The patient infected with INH susceptible strain. However, poor clinical progress was observed during the treatment course. Two consecutive daughter strains collected at four months during the course of treatment showed that both strains were INH resistant. The standard 24-MIRU-VNTR and WGS data confirmed that the strains were clonally related and belong to the Beijing lineage. We also found little genetic variations across the genome of the three isolates (<15 SNP identified at ≥20% allelic frequency) supporting the clonal relatedness of the three strains. The clonal relatedness of the strains suggests that the post-treatment drug-resistant strains were evolved from the pre-treatment INH susceptible strain in the course of treatment.

Comparative WGS analysis of entire *furA-katG* and *mabA-inhA* genetic regions and the previously reported genetic stretches associated with INH resistance(Ramaswamy et al., 2003) revealed the absence of INH resistance-conferring genetic polymorphisms in all loci but two novel mutations in *katG*, P232L and Q461Stop, in post-treatment strains. *M. tuberculosis* has the natural propensity of spontaneous mutations conferring INH resistance in approximately 1 out of 10^6-10^8 bacterial populations(McGrath et al., 2014). The suboptimal drug pressure either due to patient-related factors or programmatic mismanagement could facilitate the selection of mutant (drug-resistant) clone. *M. tuberculosis* lineage has also been shown affecting the speed of acquisition of genetic variants. Beijing lineage has been shown to be hypermutable compared to other lineages (Merker et al., 2015) which might have increased the chance of the emergence of INH resistance while the patient had been under standard treatment.

The emergence of drug-resistant clones in a single patient has caught substantial attention over the last several decades. Though contrasting results were reported regarding the speed of emergence and fixation of drug-resistant clones *in vivo*, recent studies using highly sensitive WGS technologies have demonstrated the high diversity of mycobacterial strains within a patient (Cohen et al., 2016; Perez-Lago et al., 2014). Studies using serial sputum samples from single or multiple patients under standard treatment regimen showed an emergence and co-existence of several drug-resistant conferring alleles. The fitness cost and level of resistance of particular allele govern the ultimate fixation of these alleles. Mutations that had low fitness cost and conferring high levels of resistance are usually fixed in patients under therapy and subsequently transmitted. Sun *et al*. studied three serial sputum samples collected from a single patient where they identified four INH resistant associated mutations (3 in *katG* and 1 in *inhA*). After 23 months, only one variant with a high resistance level and low fitness cost was fixed (Sun et al., 2012b). A similar study in the RIF and STR associated mutations in sputum collected from the same patient indicated the high drug resistance-conferring and low fitness cost genetic mutations were fixed (Meacci et al., 2005; Sander et al., 2002).

In our study, though we could not generate data supporting the role of two novel mutations in relation to the fitness cost, we demonstrated that both mutations confer high INH resistance through functional genetics. To evaluate the impact of the mutations, a *katG-deleted M. tuberculosis* strain was transformed with mycobacterial vector (pOLYG), carrying the *furA-katG* operon from the two strains. The introduction of mutants *katG* P232L and Q461Stop conferred high INH resistance with MIC of 256 µg/ml and 128 µg/mL, respectively, suggesting that the *katG* genes with these mutations are defective. These MIC results are consistent with a range of 0.19 to 256 µg/ml obtained for single missense mutations of *katG* in the clinical isolates by Ramaswamy *et al*. (2003). Nonetheless, it

worthwhile to mention that Ramaswamy *et al.*(2003) did not conduct the transformation experiment to confirm the causal role of identified substitution. Similar to our results, Kandler *et al*. (2018) and Torres *et al*. (2015) also identified and cloned several novel mutations in the *katG* that increased the MIC of the transformants. The MIC results in our study, however, are higher than those reported in these two studies. This could be related to the difference in the mutations identified and the models H37Rv and *M. smegmatis* used for the functional assay in the respective studies.

Catalase-peroxidase, encoded by *katG* plays a key role in converting the pro-INH to an active form that has pleiotropic effects on the bacilli (Middlebrook, 1954). Potentially, mutations in the coding stretch of the *katG* have an implication in reducing the catalytic activity of the gene product (Ramaswamy et al., 2003). *In vitro* evaluation of catalase activity of the transformants could enable the assessment of the impact of novel mutations in the katG (Ramaswamy et al., 2003). As determined by the catalase activity, our study also revealed that *M. tuberculosis* strain, GA03 harboring mutated *katG* (P232L and Q461Stop) has reduced catalase activity by more than 8 folds than the transformants carrying the gene from the pre-treatment mother strain, suggesting that the mutations resulted in a defective protein. Previous studies have also shown that mutants that are associated with high MIC were all characterized by a drastic reduction in catalase activities (Ando et al., 2010; Brossier et al., 2016).

To consolidate the role of the two novel mutations in the resistance against INH and understand the effect of amino acid substitution and termination, 3D protein-INH binding models were constructed. The P232L substitution is located very close to the INH binding site and could potentially obstruct the binding of INH. As expected, the crystallographic analysis showed that the P232L substitution reduces INH-*KatG* binding affinity affecting the conversion of the prodrug to the active form, the critical step in the mechanism of action of INH. As demonstrated by the MIC study, transformants carrying this mutation were associated with high resistance to INH. Whereas, the termination mutation (Q461Stop) also generates a truncated protein at 461 residues without 280 residues in the C-terminal domain. The Q461Stop mutation truncates gene transcription and limiting the activity of the enzyme causing high-level INH resistance.

In conclusion, our results showed that the two *katG* mutations, P232L and Q461Stop, accounted for the stepwise development of INH resistant clones during standard course of anti-TB therapy. We verified the presence two independent mutations evolved owing to antituberculosis stress from a parental strain and experimentally demonstrated the functional role of both mutations in conferring INH resistance. The inclusion of these mutations in the design of molecular assays increases diagnostic performance.

ACKNOWLEDGMENTS

We would like to express our appreciate to the Department of Microbiology, The Hong Kong University for allowing us their mycobacteriology laboratory to conduct part of this work

REFERENCES

Ando, H., Kondo, Y., Suetake, T., Toyota, E., Kato, S., Mori, T., & Kirikae, T. (2010). Identification of katG mutations associated with high-level isoniazid resistance in Mycobacterium tuberculosis. *Antimicrobial Agents and Chemotherapy, 54*(5), 1793-1799.

Benjak, A., Sala, C., & Hartkoorn, R. C. (2015). Whole-genome sequencing for comparative genomics and de novo genome assembly. *Methods Mol Biol, 1285*, 1-16. doi: 10.1007/978-1-4939-2450-9_1

Bertrand, T., Eady, N. A. J., Jones, J. N., Jesmin, J. M., Nagy, B., Jamart-Grégoire, E. L., . . . Brown, T. (2004). Crystal structure of Mycobacterium tuberculosis catalase-peroxidase. *The Journal of Biological Chemistry, 279*(37), 38991-38999. doi: 10.1074/jbc.M402382200

Blanco-Ruano, D., Roberts, M., Gonzalez-Del-Rio, R., Álvarez, D., José Rebollo, M., Pérez-Herrán, E., & Mendoza, A. (2015). *Antimicrobial Susceptibility Testing for Mycobacterium sp. In: Parish T., Roberts D. (eds) Mycobacteria Protocols. Methods in Molecular Biology* (Vol. 1285). New York: Humana Press.

Bollela, V. R., Namburete, E. I., Feliciano, C. S., Macheque, D., Harrison, L. H., & Caminero, J. (2016). Detection of katG and inhA mutations to guide isoniazid and ethionamide use for drug-resistant tuberculosis. *The International Journal of Tuberculosis and Lung Disease, 20*(8), 1099-1104.

Brossier, F., Boudinet, M., Jarlier, V., Petrella, S., & Sougakoff, W. (2016). Comparative

study of enzymatic activities of new KatG mutants from low-and high-level isoniazid-resistant clinical isolates of Mycobacterium tuberculosis. *Tuberculosis, 100*, 15-24.

Caminero, J., Van Deun, A., & Fujiwara, P. (2013). Guidelines for clinical and operational management of drug-resistant tuberculosis. *International Union Against Tuberculosis and Lung Disease*, 18-19.

Choi, Y., & Chan, A. P. (2015). PROVEAN web server: a tool to predict the functional effect of amino acid substitutions and indels. *Bioinformatics, 31*(16), 2745-2747. doi: 10.1093/bioinformatics/btv195

Cohen, T., Chindelevitch, L., Misra, R., Kempner, M. E., Galea, J., Moodley, P., & Wilson, D. (2016). Within-Host Heterogeneity of Mycobacterium tuberculosis Infection Is Associated With Poor Early Treatment Response: A Prospective Cohort Study. *The Journal of infectious diseases, 213*(11), 1796-1799. doi: 10.1093/infdis/jiw014

Coll, F., McNerney, R., Guerra-Assuncao, J. A., Glynn, J. R., Perdigao, J., Viveiros, M., . . . Clark, T. G. (2014). A robust SNP barcode for typing Mycobacterium tuberculosis complex strains. *Nature Communications, 5*, 4812.

Da Silva, P. E. A., & Palomino, J. C. (2011). Molecular basis and mechanisms of drug resistance in Mycobacterium tuberculosis: classical and new drugs. *Journal of Antimicrobial Chemotherapy, 66*(7), 1417-1430.

Eldholm, V., Norheim, G., von der Lippe, B., Kinander, W., Dahle, U. R., Caugant, D. A., . . . Balloux, F. (2014). Evolution of extensively drug-resistant Mycobacterium tuberculosis from a susceptible ancestor in a single patient. *Genome Biology, 15*(11), 490.

Elis, R. D., Marta, O. R., Márcia, S. S., Liane, S. A., Diana, C. R., Patricia, I. C., . . . etal. (2009). Correlations of mutations in katG, oxyR-ahpC and inhA genes and in vitro susceptibility in Mycobacterium tuberculosis clinical strains segregated by spoligotype families from tuberculosis prevalent countries in South America. *BMC Microbiology, 9*, 39.

Graham, S. T., & Vojo, D. (2006). Mechanisms of action of isoniazid. *Molecular Microbiology, 62*(5), 1220-1227.

Hazbón, M. H., Brimacombe, M., del Valle, M. B., Cavatore, M., Guerrero, M. I., Varma-Basil, M., . . . García-García, L. (2006). Population genetics study of isoniazid resistance mutations and evolution of multidrug-resistant Mycobacterium tuberculosis. *Antimicrobial Agents and Chemotherapy, 50*(8), 2640-2649.

Horsburgh Jr, C. R., Barry III, C. E., & Lange, C. (2015). Treatment of tuberculosis. *New England Journal of Medicine, 373*(22), 2149-2160.

Jagielski, T., Bakuła, Z., Roeske, K., Kamin´ ski, M., Napio´rkowska, A., Augustynowicz-Kopec, E., . . . Bieleck, J. (2014). Detection of mutations associated with isoniazid resistance in multidrug-resistant Mycobacterium tuberculosis clinical isolates. *Journal of Antimicrobial and Chemotherapy, 69*(9), 2369-2375. doi: 10.1093/jac/dku161

Kamachi, S., Hirabayashi, K., Tamoi, M., Shigeoka, S., Tada, T., & Wada, K. (2015). The crystal structure of isoniazid-bound KatG catalase-peroxidase from Synechococcus elongatus PCC7942. *The FEBS journal, 282*(1), 54-64.

Kandler, J. L., Mercante, A. D., Dalton, T. L., Ezewudo, M. N., Cowan, L. S., Burns, S. P., . . . Investigators, G. P. (2018). Validation of novel Mycobacterium tuberculosis isoniazid resistance mutations not detectable by common molecular tests. *Antimicrobial Agents and Chemotherapy, 62*(10), e00974-00918.

Liu, Q., Via, L., Luo, T., Liang, L., Liu, X., Wu, S., . . . Gao, Q. (2015). Within patient microevolution of Mycobacterium tuberculosis correlates with heterogeneous responses to treatment. *Scientific Reports (5*(1), 17507. doi: 10.1038/srep17507

Mai, N., Frank, G., Tran, N. B., Nguyen, T., Nguyen, H. D., Kristin, K., . . . Dick, v. S. (2013). Epidemiology of Isoniazid Resistance Mutations and Their Effect on Tuberculosis Treatment Outcomes. *Antimicrobial Agents and Chemotherapy, 57* (8), 3620-3627.

McGrath, M., Gey van Pittius, N. C., van Helden, P. D., Warren, R. M., & Warner, D. F. (2014). Mutation rate and the emergence of drug resistance in Mycobacterium tuberculosis. *Journal of Antimicrobial Chemotherapy, 69*(2), 292-302. doi: 10.1093/jac/dkt364

Meacci, F., Orru, G., Iona, E., Giannoni, F., Piersimoni, C., Pozzi, G., . . . Oggioni, M. R. (2005). Drug Resistance Evolution of a Mycobacterium tuberculosis Strain from a Noncompliant Patient. *Journal of Clinical Microbiology, 43*(7), 3114. doi: 10.1128/JCM.43.7.3114-3120.2005

Merker, M., Blin, C., Mona, S., Duforet-Frebourg, N., Lecher, S., Willery, E., . . . Wirth, T. (2015). Evolutionary history and global spread of the Mycobacterium tuberculosis Beijing lineage. *Nature Genetics, 47*, 242. doi: 10.1038/ng.3195
https://www.nature.com/articles/ng.3195#supplementary-information

Middlebrook, G. (1954). Isoniazid-resistance and catalase activity of tubercle bacilli: a preliminary report. *American Review of Tuberculosis, 69*(3), 471-472.

Perez-Lago, L., Comas, I., Navarro, Y., Gonzalez-Candelas, F., Herranz, M., Bouza, E., & Garcia-de-Viedma, D. (2014). Whole genome sequencing analysis of intrapatient microevolution in Mycobacterium tuberculosis: potential impact on the inference of tuberculosis transmission.(Report). *Journal of Infectious Diseases*, *209*(1), 98. doi: 10.1093/infdis/jit439

Projahn, M., Köser, C. U., Homolka, S., Summers, D. K., Archer, J. A., & Niemann, S. (2011). Polymorphisms in isoniazid and prothionamide resistance genes of the Mycobacterium tuberculosis complex. *Antimicrobial Agents and Chemotherapy*, *55*(9), 4408-4411.

Rajwani, R., Yam, W. C., Zhang, Y., Kang, Y., Wong, B. K. C., Leung, K. S. S., . . . Siu, G. K. H. (2017). Comparative Whole-Genomic Analysis of an Ancient L2 Lineage Mycobacterium tuberculosis Reveals a Novel Phylogenetic Clade and Common Genetic Determinants of Hypervirulent Strains. *Front Cell Infect Microbiol*, *7*, 539. doi: 10.3389/fcimb.2017.00539

Ramaswamy, S. V., Reich, R., Dou, S.-J., Jasperse, L., Pan, X., Wanger, A., . . . Graviss, E. A. (2003). Single nucleotide polymorphisms in genes associated with isoniazid resistance in Mycobacterium tuberculosis. *Antimicrobial Agents and Chemotherapy*, *47*(4), 1241-1250.

Sander, P., Springer, B., Prammananan, T., Sturmfels, A., Kappler, M., Pletschette, M., & Bottger, E. C. (2002). Fitness Cost of Chromosomal Drug Resistance-Conferring Mutations. *Antimicrobial Agents and Chemotherapy*, *46*(5), 1204. doi: 10.1128/AAC.46.5.1204-1211.2002

Seifert, M., Catanzaro, D., Catanzaro, A., & Rodwell, T. C. (2015). Genetic mutations associated with isoniazid resistance in Mycobacterium tuberculosis: a systematic review. *PloS one*, *10*(3), e0119628.

Siu, G. K. H., Yam, W. C., Zhang, Y., & Kao, R. Y. T. (2014). An Upstream Truncation of the furA-katG Operon Confers High-Level Isoniazid Resistance in a Mycobacterium tuberculosis Clinical Isolate with No Known Resistance-Associated Mutations. *Antimicrobial Agents and Chemotherapy*, *58*(10), 6093-6100. doi: doi:10.1128/AAC.03277-14

Sun, G., Luo, T., Yang, C., Dong, X., Li, J., Zhu, Y., . . . Barry III, C. E. (2012a). Dynamic population changes in Mycobacterium tuberculosis during acquisition and fixation of drug resistance in patients. *The Journal of infectious diseases*, *206*(11), 1724-1733.

Sun, G., Luo, T., Yang, C., Dong, X., Li, J., Zhu, Y., . . . Barry III, C. E. (2012b). Dynamic population changes in Mycobacterium tuberculosis during acquisition and fixation of drug resistance in patients. *Journal of Infectious Diseases*, *206*(11), 1724-1733.

Tafess, K., Beyen, T. K., Girma, S., Girma, A., & Siu, G. (2021). Spatial clustering and genetic diversity of Mycobacterium tuberculosis isolate among pulmonary tuberculosis suspected patients, Arsi Zone, Ethiopia. *BMC Pulmonary Medicine*, *21*(1), 206. doi: 10.1186/s12890-021-01567-7

Torres, J. N., Paul, L. V., Rodwell, T. C., Victor, T. C., Amallraja, A. M., Elghraoui, A., . . . Zadorozhny, V. (2015). Novel katG mutations causing isoniazid resistance in clinical M. tuberculosis isolates. *Emerging Microbes and Infections*, *4*(7), e42.

Trauner, A., Liu, Q., Via, L. E., Liu, X., Ruan, X., Liang, L., . . . Liang, R. (2017). The within-host population dynamics of Mycobacterium tuberculosis vary with treatment efficacy. *Genome Biology*, *18*(1), 71.

Van Doorn, H., Kuijper, E., Van der Ende, A., Welten, A., Van Soolingen, D., De Haas, P., & Dankert, J. (2001). The susceptibility of Mycobacterium tuberculosis to isoniazid and the Arg→ Leu mutation at codon 463 of katG are not associated. *Journal of Clinical Microbiology*, *39*(4), 1591-1594.

Yam, W., Tam, C., Leung, C., Tong, H., Chan, K., Leung, E., . . . Yuen, K. (2004). Direct detection of rifampin-resistant Mycobacterium tuberculosis in respiratory specimens by PCR-DNA sequencing. *Journal of Clinical Microbiology*, *42*(10), 4438-4443.

Zhang, Y., & Yew, W. (2015). Mechanisms of drug resistance in Mycobacterium tuberculosis: update 2015. *The International Journal of Tuberculosis and Lung Disease*, *19*(11), 1276-1289.

Molecular Magnetism Behavior in Triangular Erbium Complex: Two Step of Slow Magnetic Relaxation Exhibited under External Magnetic Field

Mamo Gebrezgiabher[1,2,*], Soren Schlittenhardt[4], Cyril Rajnak[2], Juraj Kuchar[3], Assefa Sergawie[1], Juraj Cernak[3], Mario Ruben[4], Madhu Thomas[1], Roman Boca[2]

[1]*Department of Industrial Chemistry, College of Applied Sciences, Addis Ababa Science and Technology University, Addis Ababa, P.O. Box 16417, Ethiopia*
[2]*Department of Chemistry, Faculty of Natural Sciences, University of SS Cyril and Methodius , 91701, Trnava, Slovakia*
[3]*Department of Inorganic Chemistry, Institute of Chemistry, P.J. Šafárik University in Košice, 041 80, Košice, Slovakia*
[4]*Institute of Nanotechnology, Karlsruhe Institute of Technology, Hermann-von-Helmholtz-Platz 1, 76344, Eggenstein-Leopoldshafen, Germany.*
**Corresponding author, e-mail: mamo.gebrezgiabher@aastu.edu.et*

ABSTRACT

The Triangulo-{Er_3} complex [$Er_3Cl(o\text{-}van)_3(OH)_2(H_2O)_5]Cl_3 \cdot nH_2O$ (n = 9.4; H(o-van) = o-vanillin) was generated by in-situ reaction condition. The isolated Er(III) complex was characterized by elemental analysis and molecular spectroscopy. The results of single crystal X-ray diffraction studies have shown that Er(III) complex is built up of trinuclear $[Er_3Cl(o\text{-}van)_3(OH)_2(H_2O)_5]^{3+}$ complex cations, chloride anions and water solvate molecules. Within the complex cation the three Er(III) central atoms are placed in the apexes of a triangle which are bridged by three $(o\text{-}van)^{2-}$ ligands with additional chelating functions and two μ_3-OH^- ligands. Additionally five aqua and one chlorido ligands complete the octa-coordination of the three Er(III) atoms. AC susceptibility measurements reveal that the compound exhibits slow magnetic relaxation with two relaxation modes. Er Complex exhibits two relaxation modes: the low-frequency mode (LF) below f < 1 Hz, and the high-frequency one (HF) above 100 Hz. On heating, both of them escape. The fitting to a two-set Debye model at B_{DC} = 0.3 T and T = 2.0 K gave the relaxation times τ_{LF} = 1.2(1) s, τ_{HF} = 0.61(4) ms, and the mole fraction of the LF species x_{LF} = 0.73.

Keywords: *Molecular magnetism, o-vanillin, Erbium complex, X-ray structure, slow magnetic relaxation*

1. INTRODUCTION

Single-molecule magnets (SMMs) are usually coordination compounds that exhibit slow relaxation of magnetization in the absence of an external magnetic field at the molecular level [1]. Such slow relaxation is achieved by magnetic anisotropy causing an effective energy barrier (U_{eff}) to spin reversal. Contrary to bulk and molecule-based magnets, a collective long-range of magnetic ordering of magnetic moments is not necessary for SMMs and they are systems that exhibit a slow relaxation of magnetization below a certain blocking temperature, where the barrier blocks the spin reversal [2]. Mechanisms to overcome the barrier include spin-lattice processes (Ram, Orb, Direct) or quantum tunneling of magnetization (QTM) [3]. The first and most studied family of SMMs are the dodecanuclear complexes of manganese with the formula, $[Mn_{12}O_{12}(O_2CMe)_{16}(H_2O)_4]$, shortened as $\{Mn_{12}\}$[4]. This interdisciplinary field of molecular magnetism has undergone revolutionary changes since the early 1990s when it was discovered that the 3-dimensional manganese coordination cluster, $[Mn_{12}O_{12}(O_2CMe)_{16}(H_2O)_4]$ behaved as a tiny single-domain magnet comparatively at a very low temperature [5–7]. This discovery has given birth to a "hot" area of 'Single-Molecule Magnetism'. After the discovery of the dodecanuclear manganese cluster as an SMM [8], a plethora of SMMs were made of homometallic [9–13] and heterometallic [14–21] transition metals and have been reported. It was believed that high spin, strongly coupled 3d transition metal complexes were initially considered to be the most potential complexes for the development of SMMs.

Data storage at the molecular level was a matter of interest to scientists for the last several years. Their efforts to this interest have made some achievements in the magnetic properties and a better understanding of various SMMs.

In comparing the success of different SMMs, the bigger the magnitude of the anisotropy barrier, the more prominent the SMM properties are at higher temperatures [22]. Therefore, SMM-based technology can only be practically implemented when those two major problems are being addressed. The expected properties of SMMs are nowadays accessible only using liquid helium cooling, as a result of which, either the operating temperatures need to rise significantly or applications arising out of these materials should be significant. On the other hand, addressing individual molecules of SMMs on surfaces has been explored only in a few cases [23]. Hence, one of the imposing challenges in this field is to design and synthesize well-organized SMMs which can operate at ambient temperatures perspective of practical use, or that exhibit property that goes beyond the limits achievable by the domain of classical magnets.

It has been confirmed in recent years that the f-block elements can also be used in constructing molecular-based magnetic materials, based on the interaction between the electron density of the 4f ions and the crystal field environments in which it is placed and lanthanides-based SMMs entered the field in 2003 with the report on the slow relaxation of magnetization in the Phthalocyanine Double-Decker $LnPc_2$ complexes [24] and many lanthanide SMMs were reported then after [19–21,23,25–34]. The coordination chemistry of Ln(III) ions has attracted the interest of many researchers for their ability to form clusters (polynuclear) with unprecedented and nanosized structures [35]. Despite their weak exchange interaction due to the efficient shielding of the unpaired electrons in the 4f orbitals, lanthanide-based SMMs got special attention in molecular magnetism on account of their large spin state and high magnetic anisotropy [36]. The effective energy anisotropic barrier for magnetization reversal arises from the intrinsic electronic sub-level structure of the Stark components depending on the subtle variation of several parameters such as Kramers/non-Kramers character of the Ln(III) center, its oblate/prolate 4f-electron density, the geometry of the complex, the symmetry of the coordination sphere, and donor atoms strength [23,32,37,38].

2. MATERIALS AND METHODS

2.1 Synthesis of Trinuclear-Er (III) Complex

The Complex was prepared by the addition of a metahnolic solution $ErCl_3 \cdot 6H_2O$ (1.0 mmol, 0.381 g) in 15 mL dropwise to a stirring solution of *o*-vanillin (1 mmol, 0.152g), 2-aminomethyl pyridine (1 mmol, 0.108 mL) in the presence of triethylamine (1 mmol, 0.101 mL) in methanol (50 mL) (**Scheme 1**). The resultant reaction mixture was refluxed for 4 h in an oil bath. The yellow solution obtained on reflux was cooled to room temperature and filtered. Vapor diffusion of diethyl ether to the filtered yellow solution yielded X-ray quality yellow block crystals. The complex was collected by filtration and washed with cold MeOH and dried in air and vacuum to yield, 160 mg/35%. Elemental analysis (Calculated/Found): Anal.Calcd for Er complex, $C_{24}H_{33}O_{25.47}Cl_4Er_3$ (Mr = 1372.613 g/mol). Yield, 160 mg / 35%, Anal.Calcd for Er complex, $C_{24}H_{33}O_{25.47}Cl_4Er_3$ (Mr = 1372.613 g/mol): C, 20.98%, H, 2.4%. Found: C, 21.19%, H, 2.35%.

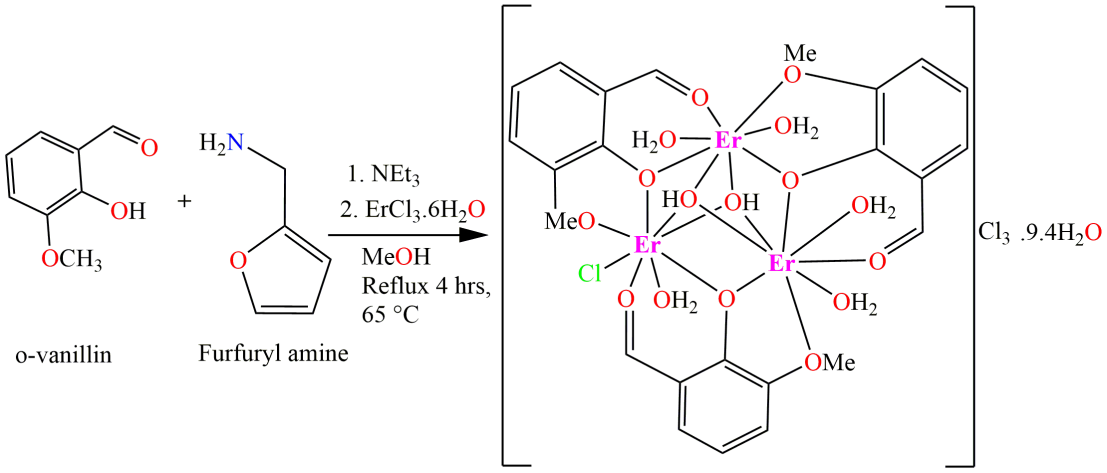

Scheme 1: Schematic representation for the *in-situ* synthesis of trinuclear Er(III) complex

2.2 Characterization Techniques

The isolated complex was characterized by elemental analyses (CHN), single crystal X-ray diffractometer and molecular spectroscopic. The magnetic property of the cluster was studied by DC and AC-SQUID magnetometers.

2.3 X-ray Crystallography Analysis of the Complex

The crystal structure analysis of the complexes was done at 119.97 K, on an Agilent dual wavelength SuperNova with monochromated Cu-Kα (λ = 1.54178 Å) or Mo-Kα (λ = 0.70926 Å) radiation. CrysAlisPro was used for data processing and data collection [39]. The structure was solved using intrinsic phasing with SHELXT [40] and refined using Olex2 program [41] using all data by full matrix least-squares procedures with SHELXL [42]. Multi-scan absorption correction was used SCALE3 ABSPACK. The hydrogen atoms were included in the calculated positions with an isotropic displacement of parameters 1.2 times the isotropic equivalent of their carrier atoms. For Er complex no sensible disorder model could be found for a large number of solvent molecules present in the structure. Hence, the SQUEEZE [43] function of PLATON [44] was applied.

2.4 FT-IR Spectroscopic Analysis of the Metal Complexes

The FTIR spectra were measured in the region of 400 – 4000 cm^{-1} at room temperature (Shimadzu IR Affinity^{-1}, Quest holder). The metal cluster was grounded and mixed finely with KBr. A KBr-disc of the sample, 1 cm in diameter, was obtained by applying hydraulic pressure under a vacuum.

2.5 Elemental Analysis (C, H, and N) of the Metal Complexes

Elemental analysis for C, H, and N was carried out on a Flash 2000 CHNSO apparatus (Thermo Scientific). To ensure the purity of the sample and for further analysis, the amounts of carbon, hydrogen, and nitrogen in the samples were quantitatively analyzed and compared to the theoretically calculated values.

2.6 Magnetic Measurements of the metal Complex

Magnetic susceptibility data were collected at temperatures between 2–300 K using a Quantum Design MPMS-XL SQUID magnetometer at an external field of 0.1 T. The samples were grounded and fixed in a gelatine capsule using small amounts of eicosane to avoid any movement of the sample. The data obtained were corrected for the diamagnetic contributions of the sample, the eicosane, the gelatine capsule, and the sample holder. The diamagnetic contribution for the samples was calculated using Pascal's constants [45]. All measurements were performed on dry polycrystalline samples to see the temperature dependent measurement of magnetic susceptibility.

3. RESULTS AND DISCUSSION

3.1 Structural Description of Trinuclear-Er(III) Complex

The Er trinuclear complex was isolated by reacting hydrated Erbium chloride with 2-hydroxy-3-methoxybenzaldehyde (*o*-vanillin) and 2-(aminomethyl)pyridine in the presence of triethylamine in the methanolic medium under *in-situ* conditions. Instead of the expected formation of a complex with a Schiff base type ligand, a triangular complex based only on a deprotonated *o*-vanillin ligand was separated from the reaction mixture. This is in line with our synthetic experience that the topology of *o*-vanillin is mostly favoring the triangular architecture even if *o*-vanillin is mixed with a variety of aromatic or heterocyclic primary amines during *in-situ* synthesis [46]. In the IR spectrum of Er complex, the peaks at 1631 cm^{-1}, 1355 cm^{-1}, 1221 cm^{-1}, and 1468 cm^{-1} are corresponding to aldehydic carbonyl (C=O), ring phenolic oxygen (C-O), methoxy and aromatic ring stretching vibrations, respectively [47]. It has been observed that on complexation, the vibrational stretching frequencies of the complexes are shifted to a lower region compared to the ligand [48]. The broad band around 3261 cm^{-1} is assigned to the O–H bridging OH vibration. Also, the vibration around 432 cm^{-1} is identified as Er–O stretching vibration [47].

Single crystal X-Ray study confirms that the asymmetric part of the crystal structure of Er complex contains one trinuclear $[Er_3Cl(o\text{-}van)_3(OH)_2(H_2O)_5]^{3+}$ complex cation, three chloride anions, and water solvate molecules. According to the crystal structure of Er complex (Figure 1, left), the *o*-vanillin (HL1, Scheme 2 a) adopts coordination/bridging modes of μ-1, μ-2, μ-1 respectively after deprotonating (L^-, Scheme 2b) for Er1, Er2 and/or Er3 respectively. The ligand is acting in chelating and bridging fashion forming the core structure in the molecular structure of Er complex (Figure 1, left). Therefore, the structure of Er complex consisting of the three Er(III) ions (Er1, Er2 and Er3) ions, is bridged by the three deprotonated phenolate oxygen atoms, leading to the formation of an Er_3O_5 motif (Figure 1, right).

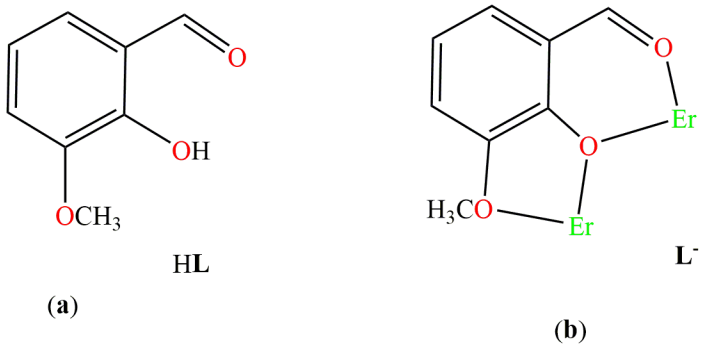

Scheme 2: Ligands used (H**L**) and their coordination modes in complex (μ-1, μ-2, μ-1), respectively.

An analogous triangular arrangement of Er(III) atoms was already observed in the triangular Er(III) motif with the 5-bromo derivate of *o-van*, *o-van*Br, and methanol as ligands as well as solvate molecules, namely $[Er_3Cl_3(o\text{-}vanBr)_3(OH)_2(CH_3OH)_3]Cl{\cdot}3CH_3OH$ [49]. It should be noted that in this complex the donor sets of the Er(III) central atoms differ from that observed in Er complex. As to the other lanthanide elements, such triangular arrangement was reported for Dy(III) $[Dy_3Cl(o\text{-}van)_3(OH)_2(H_2O)_5]Cl_3{\cdot}9H_2O$ [46] and Yb(III) $[Yb_3Cl(o\text{-}van)_3(OH)_2(H_2O)_5]Cl_3{\cdot}4H_2O$ [50]. The Er(III) complex is similar to previously reported Gd(III) [51] and Dy(III) triangles in terms of their bond distances and bond angles [46].

Within the $[Er_3(o\text{-}van)_3(OH)_2Cl(H_2O)_5]^{3+}$ complex cation, two aqua ligands are coordinated to Er(2) and Er(3) atoms (Figure 1, left) above and below the plane of the triangle, while for Er(1) atom, the terminal ligands are formed by a single aqua ligand above and a chlorido ligand below the plane of the triangle (Figure 1, left). In addition to this, there are two μ_3-hydroxo bridges above and below the plane capping the

Er_3 triangular arrangement from both sides of the triangle (Figure 1, left). In the $\{Er_3O_5\}$ core, as indicated in Figure 1, right, three Er(III) centers are held together by multiple monoatomic o-bridges. The respective distances between the Er(III) atoms are 3.5091(6), 3.4779(6) and 3.5052(5) Å for Er(1)···Er(2), Er(2)···Er(3) and Er(1)···Er(3) contacts, respectively. The Er···Er distances (Table 1) are very close to those found in the analogous complex $[Er_3Cl_3(o\text{-}vanBr)_3(OH)_2(CH_3OH)_3]Cl{\cdot}3CH_3OH$ (3.4845(7), 3.4895(9) and 3.5219(7) Å) [49] and comparable to previously reported Dy···Dy, Gd···Gd and Yb···Yb distances for the same type *o*-vanillin based triangular complexes [46,50,51].

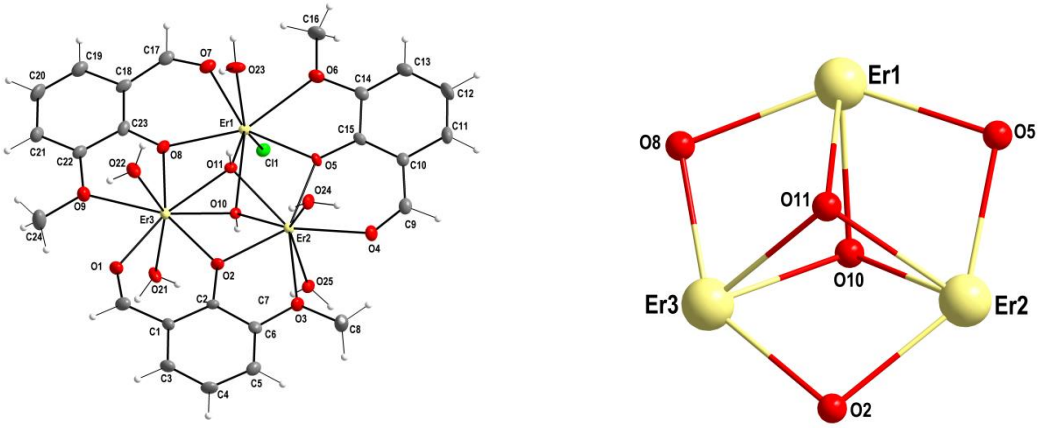

Figure 1: Left**:** Thermal ellipsoid plot of the complex cation in Er complex along with atoms numbering scheme. The thermal ellipsoids are drawn at 30% probability level; right: Trinuclear core structure of Er complex formed by Er(III) atoms and bridging O atoms. Hydrogen atoms are omitted for clarity

All Er centers in the triangular array are octa-coordinated with O_7Cl, O_8 and O_8 donor sets for Er1, Er2, and Er3 atoms, respectively. Calculations using the SHAPE procedure [52] indicate that the coordination polyhedra of all three Er central atoms correspond to triangular dodecahedra (Figure 2). The minimum deviation from an ideal mode is triangular dodecahedra (D_2d) with shape values of 0.909, 0.540, and 0.921 for Er1, Er2, and Er3, respectively (Table 1). The same polyhedra for Er(III) central atoms are present in the analogous $[Er_3Cl_3(o\text{-}vanBr)_3(OH)_2(CH_3OH)_3]Cl{\cdot}3CH_3OH$ complex [49] and somewhat similar coordination modes have been observed for the Gd and Dy analogues from the previous reports [46,51].

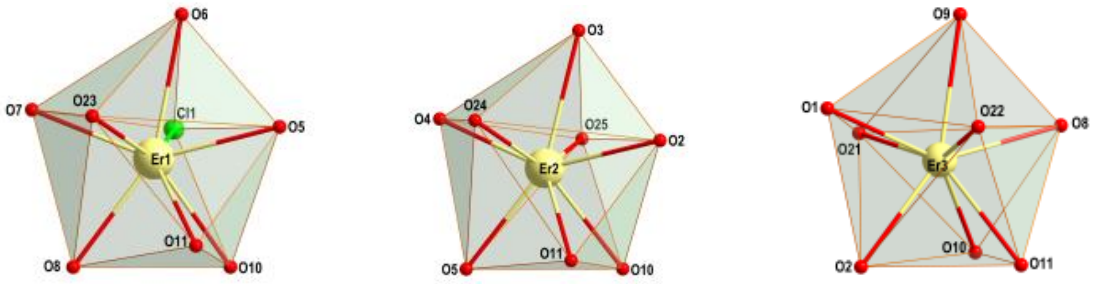

Figure 2: View of the coordination polyhedra of the respective Er(III) atoms in Er complex

The observed Er-O distances in Er complex are in the range 2.284(3) - 2.509(3) Å while the Er-Cl bond exhibits a value of 2.661(1) Å (Table 1). These values have well correspondes to the ranges of 2.283(4) – 2.525(4) Å and 2.6406(17)-2.6714(17) Å for Er-O and Er-Cl bond distances, respectively, in the analogous Er(III) complex $[Er_3Cl_3(o\text{-}vanBr)_3(OH)_2(CH_3OH)_3]Cl{\cdot}3CH_3OH$ [49].

Table 1: Selected bond distances (Å) and bond angles (°) for Er complex

O11- Er3	2.328(3) Å	O11-Er2	2.341(3) Å
O10- Er3	2.360(3) Å	O24- Er2	2.361(3) Å
O2-Er3	2.284(3) Å	O4-Er2	2.292(4) Å
O21- Er3	2.330(3) Å	O10-Er2	2.336(3) Å
O1- Er3	2.324(3) Å	O2- Er2	2.314(3) Å
O9-Er3	2.500(4) Å	O25- Er2	2.316(3) Å
O22- Er3	2.319(4) Å	O3- Er2	2.512(4) Å
O8- Er3	2.298(3) Å	Er3--Er2	3.4779(7) Å
O6- Er1	2.509(3) Å	Er1--Er3	3.5052(5) Å
O5- Er1	2.295(3) Å	Er2--Er1	3.5091(7) Å
O23- Er1	2.329(3) Å	Er2-O2-Er3	98.3(1)°
O7-Er1	2.339(4) Å	Er2-O10-Er3	95.5(1)°
O8- Er1	2.313(3) Å	Er2-O11-Er3	96.3(1)°
O11- Er1	2.394(3) Å	Er3-O11-Er1	95.8(1)°
O10- Er1	2.335(3) Å	Er2-O11-Er1	95.6(1)°
Cl1- Er1	2.661(1) Å	Er2-O5-Er1	99.6(1)°
O5- Er2	2.298(3) Å	Er3-O8-Er1	98.9(1)°

The positive charge of the complex cation in Er complex is counter balanced with the negative charge of three chloride anions. These chloride anions along with the chlorido ligand are involved in the formation of a hydrogen bonding network which results in a three-dimensional supramolecular structure of complex 4 (Figure 3, Table 2).

Table 2: Possible bond distances (Å) and bond angles (°) in the hydrogen bonds of Er complex

D-H···A	D-H	H···A	D···A	DHA
O10–H10O···Cl2^{i}	0.84	2.47	3.268(3)	161
O11–H11O···Cl3	0.84	2.48	3.274(3)	158
O21–H21A···Cl2^{ii}	0.83	2.25	3.041(4)	159
O21–H21B···Cl2^{i}	0.84	2.38	3.212(4)	170
O22–H22A···Cl3	0.84	2.40	3.175(4)	154
O22–-H22B···O35A	0.84	1.84	2.669(8)	168
O23–H23A···Cl3^{iii}	0.84	2.26	3.100(4)	176
O23–H23B···Cl3	0.84	2.33	3.157(4)	166
O24–H24A···Cl1^{iv}	0.84	2.32	3.161(3)	177
O24–H24B···O34	0.84	1.88	2.724(7)	175
O25–H25A···Cl2^{i}	0.84	2.305	3.126(3)	165
O25–H25B···Cl4B^{i}	0.84	2.34	3.173(5)	171
O25–H25B···O31^{i}	0.84	1.78	2.609(9)	169

Symmetry codes: i: 1-x, -1/2+y, 1/2-z; ii: -1/2+x, 1-y, z; iii: 1-x, 1-y, 1-z; iv: 1/2+x, 1-y, z.

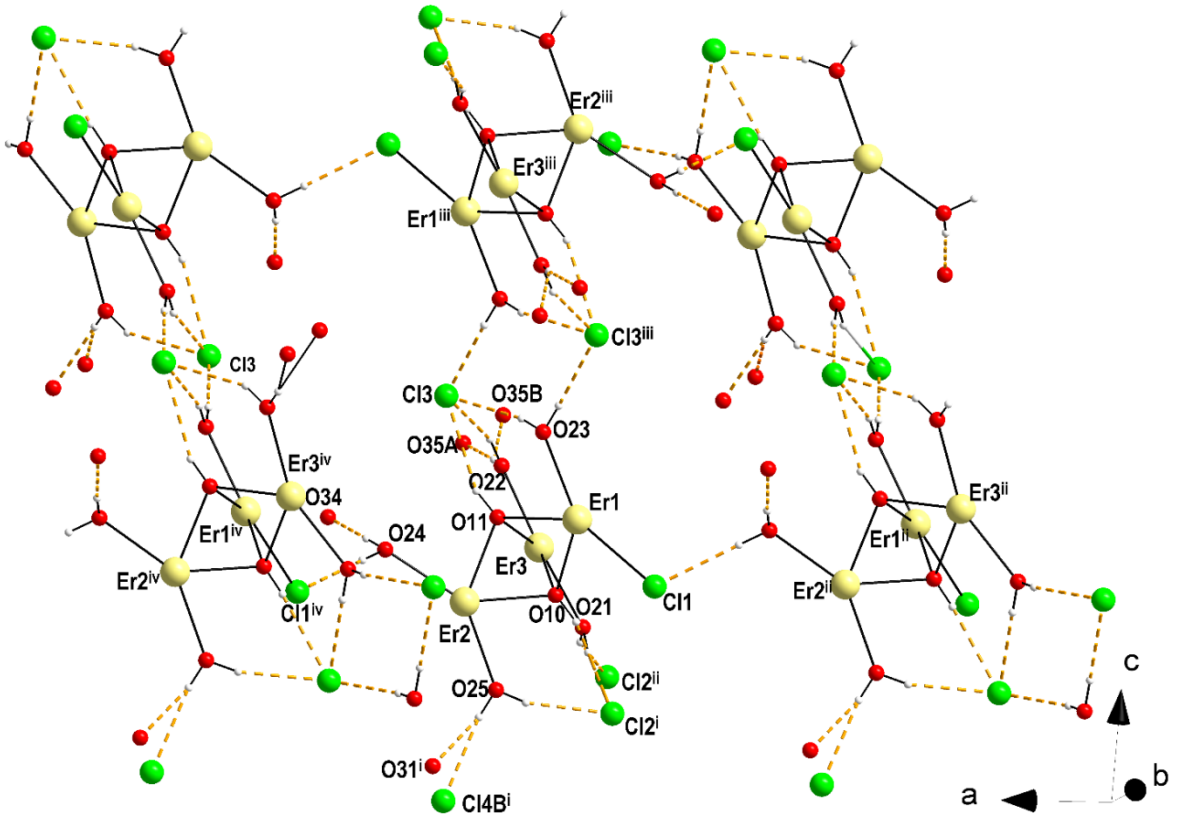

Figure 3: View on hydrogen bonding system in Er complex formed by O-H···O and O-H···Cl hydrogen bonds. Symmetry codes: i: 1-x, y-0.5, 0.5-z; ii: x-0.5, 1-y, z; iii: 1-x, 1-y, 1-z; iv: 0.5+x, 1-y, z.

Within the polymeric hydrogen bonded system, a chain-like arrangement of triangular complex cations can be distinguished (Figure 4). The chloride counter ions Cl2 and Cl3 link the triangular units by hydrogen bonds with the two bonded aqua ligands (O21 and O23) (Table 2) and these hydrogen bonds are reinforced by hydrogen bonds formed by capping hydroxide ligands (O10 and O11). Within this chain-like arrangement exists the shortest intermolecular distance of 8.104 Å between two Er(III) atoms, namely the one Er1···Er1^{iii} (iii: 1-x, 1-y, 1-z).

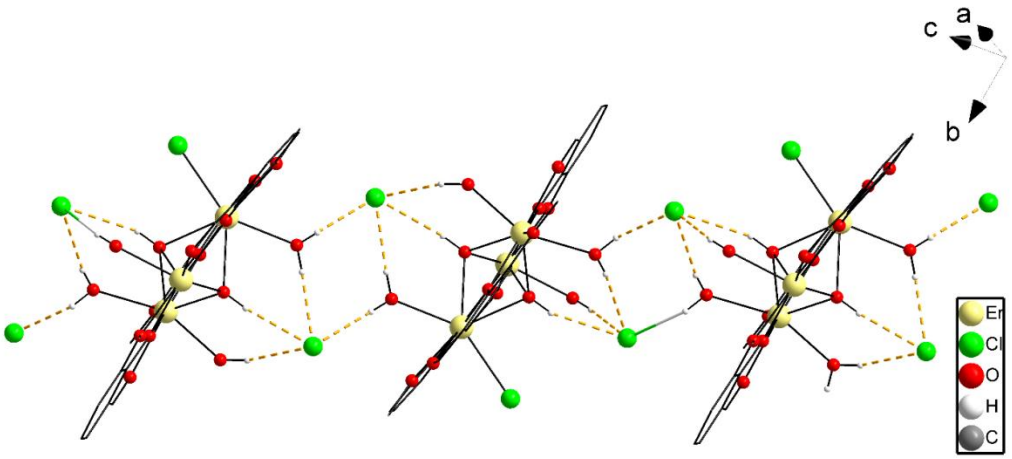

Figure 4: View on the chain-like arrangement of trinuclear {Er_3} entities linked by hydrogen bonds of the O-H···Cl type in Er complex. Only hydrogen atoms involved in the propagation of chains are shown.

For each of the triangular pairs along the chain, a phenyl ring from a unit in the neighboring chain interleaves giving a side-on phenyl carbon C(13)-Cl(4B) distance of 3.51 Å. This phenyl is also between two other phenyl groups on a neighboring chain at ca. 3.84 Å. Hence, considering plane 1 (1-x, -1/2 + y, 3/2 - z), the angle of π-π interaction is 12.890° with a centroid-centroid distance of 3.811 Å and a distance shift of 1.150 Å. When we look along plane **2** (3/2-x, +y, 1-z), the π-π interaction angle is around 12.690° with a centroid-centroid distance of 3.876 Å having a distance shift of 0.696 Å. No interaction is found along plane 3. It is observed that the π-π interaction has resulted in a trimeric structure which is comparable with Dy_3 triangular report by Powell *et al.* [28].

3.2 Magnetic Properties of Trinuclear-Er(III)(A) Er Complex

3.2.1 DC magnetic data for Er complex

The ground electronic state (multiplet) of an Er(III) centre is $^4I_{15/2}$ with g_J = 6/5. Three Er(III) centres produce $N = 16^3 = 4096$ magnetic states and M = 192 zero field states with equal energy. When only the isotropic exchange is considered, the total molecular angular momentum (J) is a good quantum number and the large-dimensional interaction matrix can be factored in to low-dimensional blocks. Namely, for the molecular values J_{min} = 1/2 to $J_{max} = 3\cdot(15/2) = 45/2$ the dimensions of blocks are 2, 4, 6, 8, 10, 12, 14, 16, 15, 14, 13, 12, 11, 10, 9, 8, 7, 6, 5, 4, 3, 2, and 1. This means that the block of the maximum dimensionality is a matrix 16 × 16 that can easily be diagonalized in order to get energy levels. Each block can be filled by exploiting the apparatus of the irreducible tensor operators as described elsewhere [53]. Then the eigenvalues enter the partition function and the magnetization and the magnetic susceptibility are calculated using statistical thermodynamics. A requirement for such a procedure is a uniform set of g-factors that is fulfilled in the present case.

The temperature dependence of the magnetic susceptibility was converted to the dimensionless product function $\chi T/C_0$ where $C_0 = N_A\mu_0\mu_B^2/k_B$ = 4.714 × 10^{-6} m^3 mol^{-1} [SI] is the reduced Curie constant containing only the fundamental physical constants in their usual meaning (**Figure 5, left**).

The product function at room temperature adopts a value of $\chi T/C_0$ = 84.4 and on cooling it decreases to a value of 51.4 at T = 2.0 K with the theoretically expected value for three uncoupled Er(III) centres possessing the maximum J = 15/2 is 3·30.6 = 91.8 [53]. The observed lower value is a consequence of the exchange coupling of an antiferromagnetic nature [54] and irregular energy spectrum as explained below.

The magnetization (**Figure 5, right**) per formula unit $M_1 = M_{mol}/(N_A\mu_B)$ does not saturate at T = 2.0 K and B = 7.0 T to the maximum values for J_{max} = 45/2. Also, this is a fingerprint of the irregular energy spectrum.

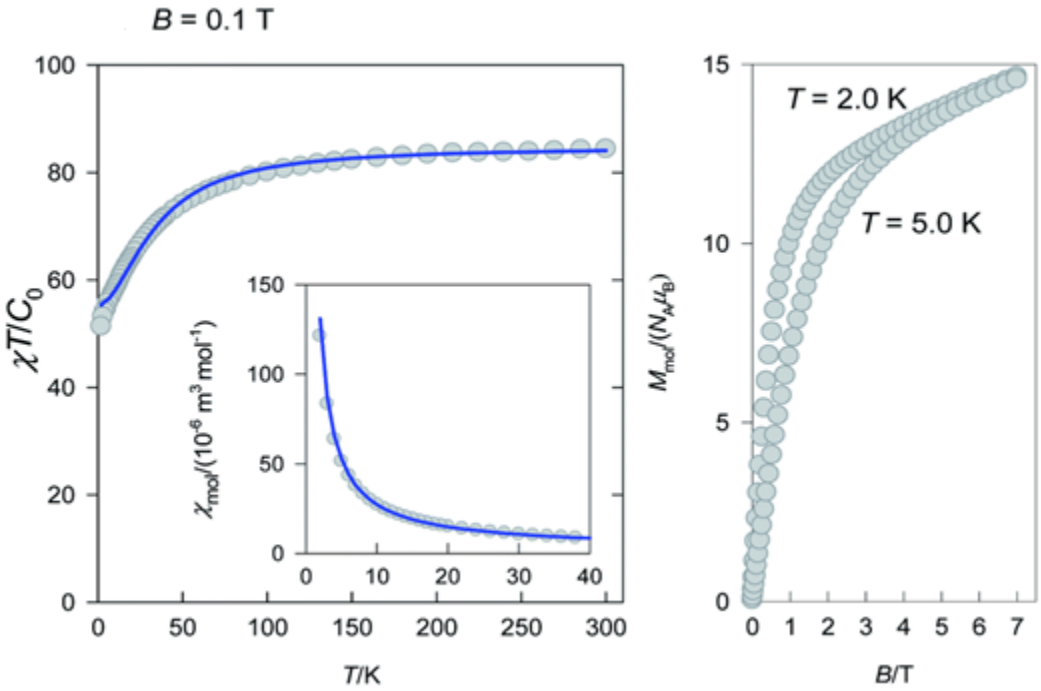

Figure 5: Magnetic data for Er complex (inset – molar magnetic susceptibility) (left) and Magnetization curve (right). Solid lines – fitted.

Before fitting the magnetic data there is a need to be emphasized that a trinuclear-{Er_3} complex refers to the isosceles triangle (C_{2v}) since the Er-Er distances are 3.505, 3.509, and 3.478 Å so that instead of a single exchange coupling constant two different (J twice, and J') need be considered. The simple exchange coupling model with the isotropic exchange Hamiltonian (equation 1).

$$\hat{H} = -J[(\vec{J}_1 \cdot \vec{J}_2) + (\vec{J}_1 \cdot \vec{J}_3)] - J'(\vec{J}_2 \cdot \vec{J}_3) + \mu_B B g_{eff}(\hat{J}_{1z} + \hat{J}_{2z} + \hat{J}_{3z}) \qquad \textbf{(Eq 1)}$$

gave the following set of magnetic parameters: J/hc = 0.48 cm^{-1}, J'/hc = –1.00 cm^{-1}, and g_{eff} = 1.15; the discrepancy factor of the fit is R = 0.054. The calculated susceptibility is drawn in Figure 5 as a solid line.

The zero-field energy levels (M = 192) are displayed in Figure 6 showing that the ground molecular state is J = 21/2. This explains the observed value of the product function and maximum M_1. A further improvement of the model would be based on the g-factor asymmetry, zero-field splitting, asymmetric exchange and/or antisymmetric exchange. Then, however, the blocking of the interaction matrix with N = 4096 states is not beneficial since there would be the off-diagonal matrix elements mixing the blocks of the different angular momentum [53].

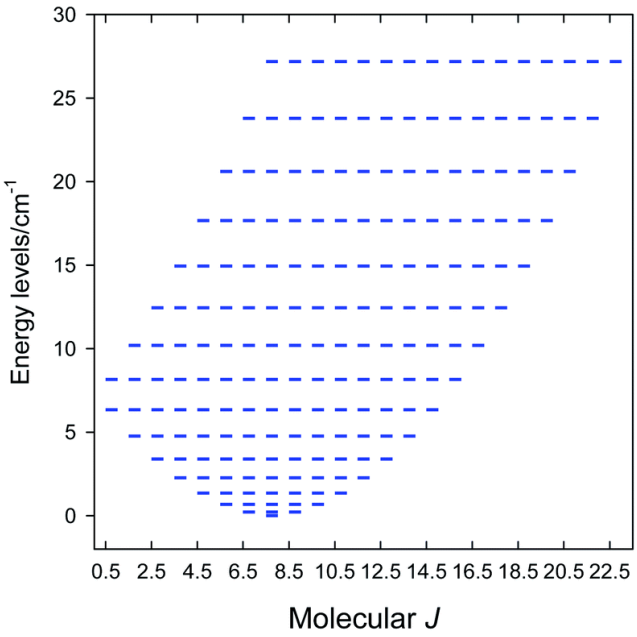

Figure 6: Calculated energy spectrum of Er complex. Ground state J = 21/2

3.2.2 AC magnetic data for Er complex

The AC susceptibility data were taken with the same hardware as DC ones at the different temperature-frequency-DC field regimes; B_{AC} = 0.35 mT. The AC susceptibility components are displayed in Figure 7 for a set of trial frequencies at different external fields B_{DC} = 0 – 0.5 T and T = 2.0 K. In the absence of the external field, the out-of-phase susceptibility *(χ″)* is silent. With increasing applied field it increases and culminates around B_{DC} = 0.3 T for the lowest frequencies. However, the maximum alters with the frequency of the AC field. It can be concluded that Er complex exhibits a field supported slow magnetic relaxation.

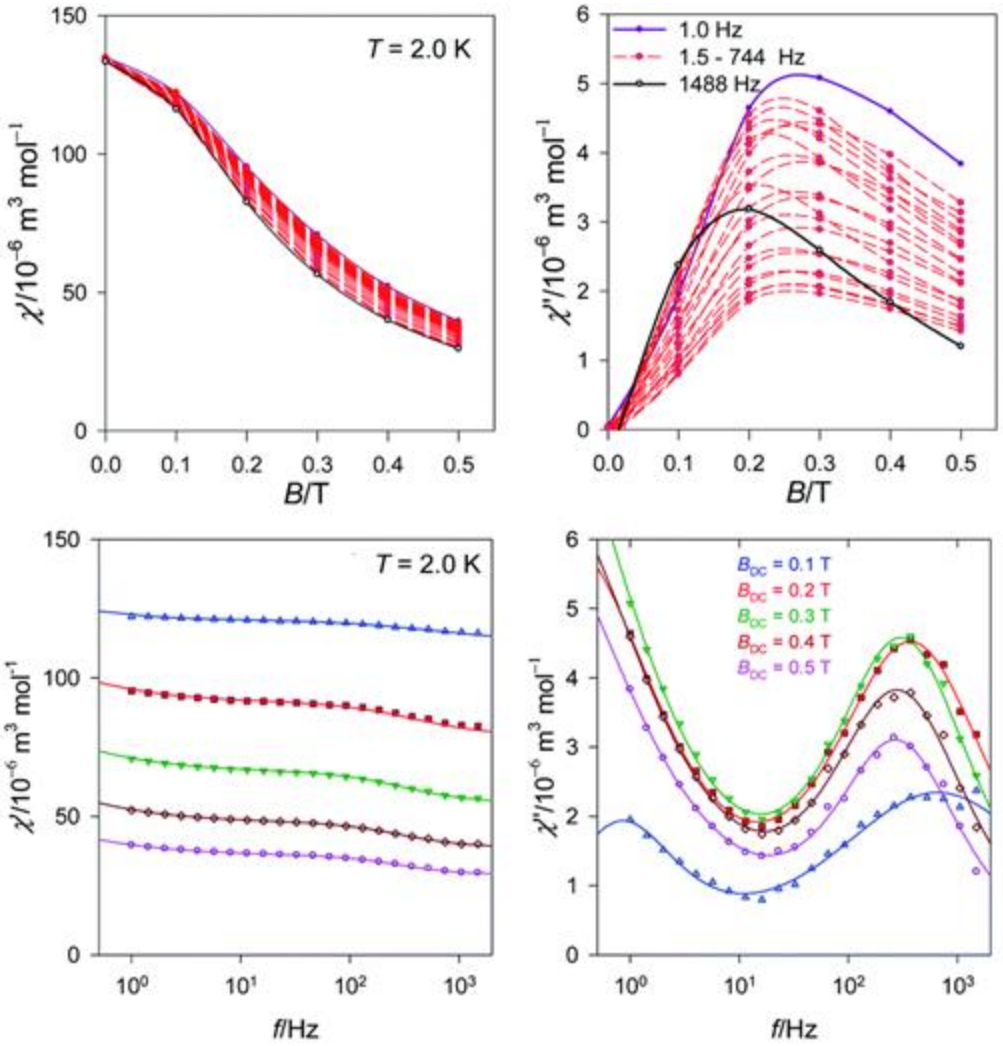

Figure 7: Field dependence (top) and frequency dependence (bottom) of the AC susceptibility components for Er complex at T = 2.0 K.

The second scan refers to a selected external field B_{DC} = 0.3 T and the variable is the frequency between f = 0.1 and 1500 Hz for temperature rising from T = 2.0 – 4.5 K in steps of 0.25 K (Figure 8).

Complex Er complex exhibits two relaxation modes: the low-frequency mode (LF) below f < 1 Hz, and the high-frequency one (HF) above 100 Hz. On heating, both of them escape. The fitting to a two-set Debye model [55] at B_{DC} = 0.3 T and T = 2.0 K gave the relaxation times τ_{LF} = 1.2(1) s, τ_{HF} = 0.61(4) ms, and the mole fraction of the LF species x_{LF} = 0.73. The relaxation time over the magic border of 1s is rare [56]. The adiabatic susceptibility $\chi_{\square}$ = 53 × 10^{-6} m^3 mol^{-1} [SI units] is also large.

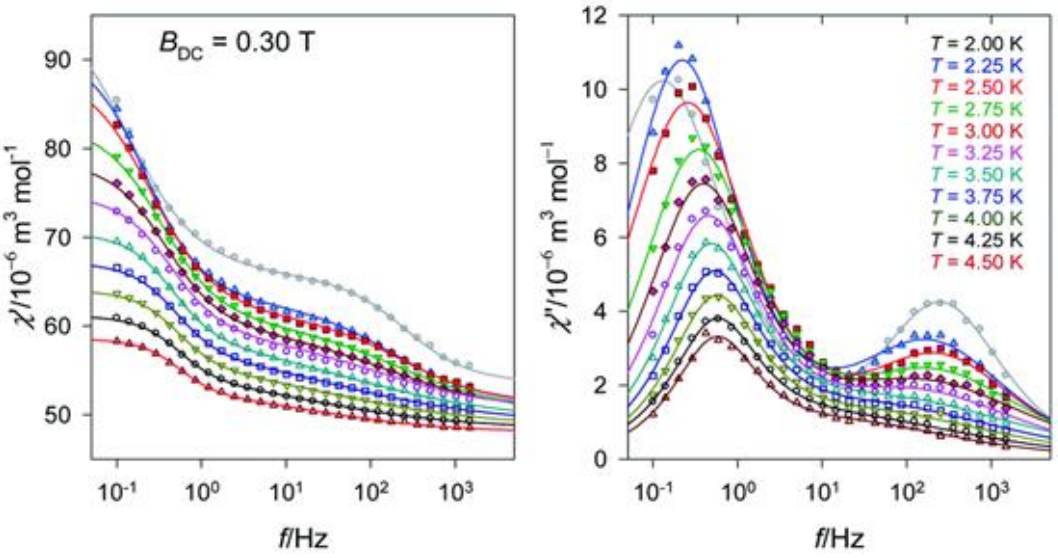

Figure 8: Frequency dependence of the AC susceptibility components for a set of temperatures for Er complex . Lines – fitted.

The Argand diagram is presented in Figure 9 shows two overlapped arcs.

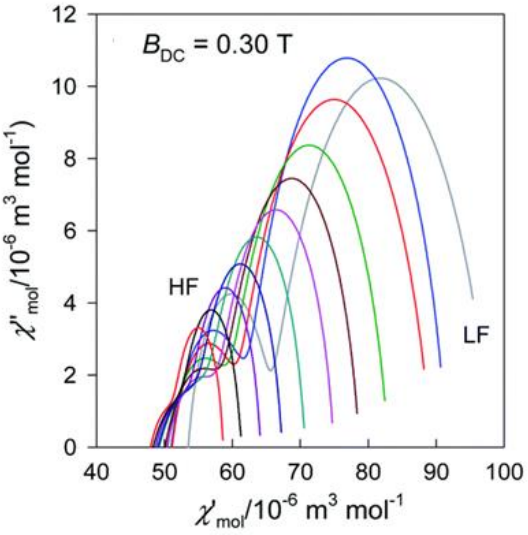

Figure 9: Argand diagram for Er complex. Lines are fitted. Colour codes from **Figure 8**.

On heating the high-temperature mode exhibits a reciprocating thermal behavior [57,58]; the relaxation time decreases in contrast to the usual thermal development. At B_{DC} = 0.3 T and T = 4.0 K; the relaxation times are τ_{LF} = 0.30(1) s, τ_{HF} = 4.5(16) ms, and the mole fraction of the LF species x_{LF} = 0.54.

The Arrhenius-like plot $\ln\tau$ *vs.* T^{-1} for the relaxation time and its $\ln\tau$ *vs.* $\ln T$ counterpart are drawn in Figure 10 (left). The reciprocating thermal behavior is well visible as a prolongation of the relaxation time on heating between T = 2.0 – 4.0 K.

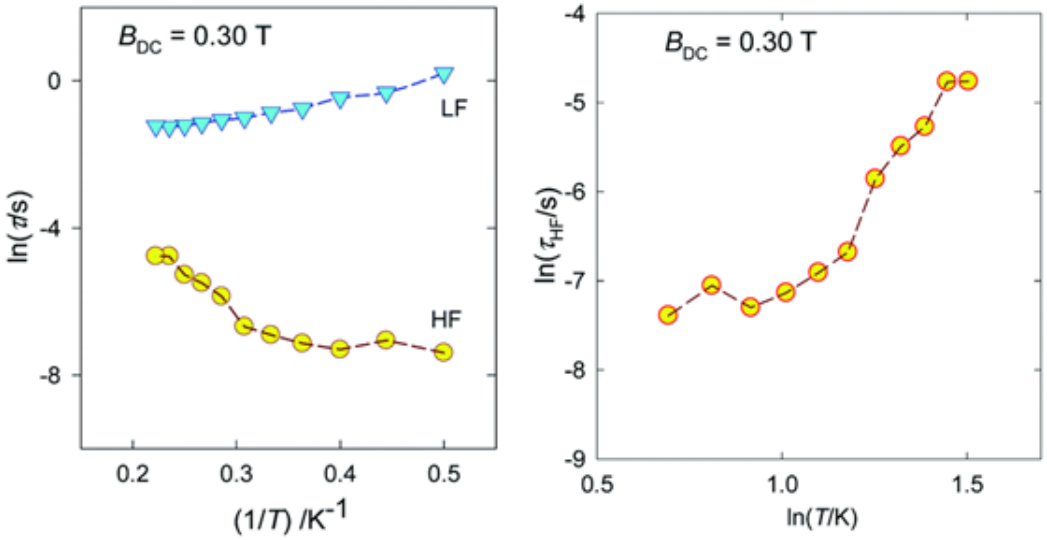

Figure 10: Various representations of the relaxation time *vs*. temperature for Er complex. Lines are a guide for eyes

The magnetic properties of Er complex were compared with the reported triangles made up of the same type of ligand [46,51] and this behavior is different from the Dy_3 system reported by Powell *et al* [46] and the Gd_3 species presented by Costes *et.al*. [51].

4. CONCLUSION

In summarizing, a novel triangular {Er_3} complex has been synthesized and characterized by single crystal X-ray diffraction studies and elemental analysis. In the *triangulo*-{Er_3} species, for the Er2 and Er3 centers two aqua ligands are coordinated below and above the plane of the triangle, while for Er1 the coordination site is occupied by one aqua ligand above and one chlorido ligand below the plane. In addition, two μ_3-hydroxo bridges link the Er centers generating a coordination number of eight to all the three central atoms. Magnetic measurements reveal two maxima in χ'' that are indicative of a two-set relaxation process. In the present compound a distinct anisotropic center is created to Er1 compared to Er2 and Er3 due to the change in the coordination centers creating significant magnetic disparities between them. This creates ample of opportunity to vary the coordination mode and thus tune the SMM properties.

REFERENCES

1. Gatteschi, D.; Sessoli, R.; Villain, J. *Molecular Nanomagnets*; Oxford University Press: Oxford, UK, 2006.
2. Ritter, S.K. Single-molecule magnets evolve. *Chem. Eng. News* **2004**, *82*, 29–32.
3. Layfield, R.A.; Murugesu, M. *Lanthanides and Actinides in Molecular Magnetism*; John Wiley & Sons: Hoboken, NJ, USA, 2015.
4. Kahn, O. *Molecular Magnetism*; VCH Pubilishers: New York, 1993.
5. Caneschi, A.; Gatteschi, D.; Sessoli, R.; Barra, A.L.; Brunel, L.C.; Guillot, M. Alternating Current Susceptibility, High Field Magnetization, and Millimeter Band EPR Evidence for a Ground S = 10 State in [$Mn_{12}O_{12}(CH_3COO)_{16}(H_20)_4$)].2$CH_3COOH$.4$H_20$. *J. Am. Chem. Soc.* **1991**, *113*, 5873–5874.
6. Bagai, R.; Christou, G. The Drosophila of single-molecule magnetism :[$Mn_{12}O_{12}(O_2CR)_{16}(H_2O)_4$]. *Chem. Soc. Rev.* **2009**, *38*, 1011–1026.
7. Gao, S. *Molecular Nanomagnets and Related Phenomena, Structure and Bonding*; Springer: Springer-Verlag Berlin Heidelberg, 2015; ISBN 9783662457221.
8. Sessoli, R.; Gatteschi, D.; Caneschi, A.; Novak, M.A. Magnetic bistability in a metal-ion cluster. *Nature* **1993**, *365*, 141–143.
9. Langley, S.K.; Chilton, N.F.; Moubaraki, B.; Murray, K.S. Structure and magnetic exchange in heterometallic 3d – 3d transition metal triethanolamine clusters. *Dalt. Trans.* **2012**, *41*, 1033–1046.

10. Abbasi, P.; Quinn, K.; Alexandropoulos, D.I.; Damjanovi, M.; Escuer, A.; Mayans, J.; Pilkington, M.; Stamatatos, T.C. Transition Metal Single-Molecule Magnets : A { Mn_{31} } Nano-sized Cluster with a Large Energy Barrier of ~ 60 K and Magnetic Hysteresis at ~ 5 K Transition Metal Single-Molecule Magnets : A { Mn_{31} } Nano-sized Cluster with a Large Energy Barrier of ~ 60 K. *J. Am. Chem. Soc.* **2017**, *139*, 15644–15647.
11. Ako, A.M.; Hewitt, I.J.; Mereacre, V.; Clérac, R.; Wernsdorfer, W.; Anson, C.E.; Powell, A.K. A ferromagnetically coupled Mn19 aggregate with a record S = 83/2 ground spin state. *Angew. Chemie - Int. Ed.* **2006**, *45*, 4926–4929.
12. Gavrilenko, K.S.; Cador, O.; Bernot, K.; Rosa, P.; Sessoli, R.; Golhen, S.; Pavlishchuk, V. V; Ouahab, L. Delicate Crystal Structure Changes Govern the Magnetic Properties of 1D Coordination Polymers Based on 3d Metal Carboxylates. *Chem. Eur. J.* **2008**, *14*, 2034–2043.
13. Kawamura, A.; Filatov, A.S.; Anderson, J.S.; Jeon, I. Slow Magnetic Relaxation of Co(II) Single Chains Embedded within Metal–Organic Superstructures. *Inorg. Chem.* **2019**, *58*, 3764–3773.
14. Wu, G.; Clérac, R.; Wernsdorfer, W.; Qiu, S.; Anson, C.E.; Hewitt, I.J.; Powell, A.K. The " Building-Block " Assembly of a [Ni 12 Mn 6] Aggregate. *Eur. J. Inorg. Chem.* **2006**, *2006*, 1927–1930.
15. Portolés-Gil, N.; Gómez-Coca, S.; Vallcorba, O.; Marbán, G.; Aliaga-Alcalde, N.; López-Periago, A.; Ayllón, J.A.; Domingo, C. Single molecule magnets of cobalt and zinc homo- and heterometallic coordination polymers prepared by a one-step synthetic procedure. *RSC Adv.* **2020**, *10*, 45090–45104.
16. Cle´rac, R.; Miyasaka, H.; Yamashita, M.; Coulon, C. Evidence for Single-Chain Magnet Behavior in a Mn III - Ni II Chain Designed with High Spin Magnetic Units : A Route to High Temperature Metastable Magnets. *J. Am. Chem. Soc.* **2002**, *124*, 12837–12844.
17. Oshio, H.; Nihei, M.; Koizumi, S.; Shiga, T.; Nojiri, H.; Nakano, M.; Shirakawa, N.; Akatsu, M. A Heterometal Single-Molecule Magnet of [Mn^{III}_2 $Ni^{II}_2Cl_2$ $(salpa)_2$]. *J. Am. Chem. Soc.* **2005**, *127*, 4568–4569.
18. Mereacre, V.; Ako, A.M.; Clérac, R.; Wernsdorfer, W.; Hewitt, I.J.; Anson, C.E.; Powell, A.K. Heterometallic [Mn_5-Ln_4] single-molecule magnets with high anisotropy barriers. *Chem. - A Eur. J.* **2008**, *14*, 3577–3584.
19. Dolai, M.; Ali, M.; Rajnák, C.; Titiš, J.; Boča, R. Slow magnetic relaxation in Cu(II)-Eu(III) and Cu(II)-La(III) complexes. *New J. Chem.* **2019**, *43*, 12698–12701.
20. Hazra, S.; Titiš, J.; Valigura, D.; Boča, R.; Mohanta, S. Bis-phenoxido and bis-acetato bridged heteronuclear {$Co^{III}Dy^{III}$} single molecule magnets with two slow relaxation branches. *Dalt. Trans.* **2016**, *45*, 7510–7520.
21. Vráblová, A.; Tomás, M.; Falvello, L.R.; Dlháň, Ľ.; Titiš, J.; Černák, J.; Boča, R. Slow magnetic relaxation in Ni-Ln (Ln = Ce, Gd, Dy) dinuclear complexes. *Dalt. Trans.* **2019**, *48*, 13943–13952.
22. Carolina R. Ganivet; Ballesteros, B.; Torre, G. de la; Clemente-Juan, J.M.; Coronado, E.; Torres, T. Influence of Peripheral Substitution on the Magnetic Behavior of Single-Ion Magnets Based on Homo- and Heteroleptic TbIII Bis(phthalocyaninate). *Chem. Eur. J.* **2013**, *19*, 1457–1465.
23. Woodruff, D.N.; Winpenny, R.E.P.; Layfield, R.A. Lanthanide Single-Molecule Magnets. *Chem. Rev.* **2013**, *113*, 5110–5148.
24. Ishikawa, N.; Sugita, M.; Ishikawa, T.; Koshihara, S.; Kaizu, Y. Lanthanide Double-Decker Complexes Functioning as Magnets at the Single-Molecular Level. *J. Am. Chem. Soc.* **2003**, *125*, 8694–8695.
25. Dreiser, J. Molecular lanthanide single-ion magnets: From bulk to submonolayers. *J. Phys. Condens. Matter* **2015**, *27*, 1–20.
26. Lin, S.Y.; Tang, J. Versatile tetranuclear dysprosium single-molecule magnets. *Polyhedron* **2014**, *83*, 185–196.
27. Boča, R.; Stolárová, M.; Falvello, L.R.; Tomás, M.; Titiš, J.; Černák, J. Slow magnetic relaxations in a ladder-type Dy(III) complex and its dinuclear analogue. *Dalt. Trans.* **2017**, *46*, 5344–5351.
28. Tang, J.; Hewitt, I.; Madhu, N.T.; Chastanet, G.; Wernsdorfer, W.; Anson, C.E.; Benelli, C.; Sessoli, R.; Powell, A.K. Dysprosium Triangles Showing Single-Molecule Magnet Behavior of Thermally Excited Spin States. *Angew.Chem. Int.Ed.* **2006**, *45*, 1729–1733.
29. Zhang, P.; Zhang, L.; Tang, J. Lanthanide single molecule magnets: Progress and perspective. *Dalt. Trans.* **2015**, *44*, 3923–3929.
30. Luzon, J.; Sessoli, R. Lanthanides in molecular magnetism: so fascinating, so challenging. *Dalt. Trans.* **2012**, *41*, 13556–13567.
31. Sorace, L.; Benelli, C.; Gatteschi, D. Lanthanides in molecular magnetism: old tools in a new field. *Chem. Soc. Rev.* **2011**, *40*, 3092–3104.
32. Liddle, S.T.; Slageren, J. van Improving f-element single molecule magnets. *Chem. Soc. Rev.* **2015**, 6655–6669.
33. Habib, F.; Murugesu, M. Lessons learned from dinuclear lanthanide nano-magnets. *Chem. Soc. Rev.* **2013**, *42*, 3278–3288.
34. Pinkowicz, D.; Southerland, H.I.; Avendan, C.; Prosvirin, A.; Sanders, C.; Wernsdorfer, W.; Pedersen, K.S.; Dreiser, J.; Cle, R.; Nehrkorn, J.; et al. Cyanide Single-Molecule Magnets Exhibiting Solvent Dependent Reversible "On" and "Off " Exchange Bias Behavior. *J. Am. Chem. Soc.* **2015**, *45*, 14406–14422.
35. Peng, J.B.; Kong, X.J.; Zhang, Q.C.; Orendáč, M.; Prokleška, J.; Ren, Y.P.; Long, L.S.; Zheng, Z.; Zheng, L.S. Beauty,

symmetry, and magnetocaloric effect-four-shell keplerates with 104 lanthanide atoms. *J. Am. Chem. Soc.* **2014**, *136*, 17938–17941.
36. Vincent, R.; Klyatskaya, S.; Ruben, M.; Wernsdorfer, W.; Balestro, F. Electronic read-out of a single nuclear spin using a molecular spin transistor. *Nature* **2012**, *488*, 357–360.
37. Liu, J.L.; Chen, Y.C.; Tong, M.L. Symmetry strategies for high performance lanthanide-based single-molecule magnets. *Chem. Soc. Rev.* **2018**, *47*, 2431–2453.
38. Guo, Y.N.; Xu, G.F.; Guo, Y.; Tang, J. Relaxation dynamics of dysprosium(iii) single molecule magnets. *Dalt. Trans.* **2011**, *40*, 9953–9963.
39. CrysAlisPro 1.171.41.93a, R. *Oxford Diffraction*; Oxford Diffraction Ltd: England, 2020.
40. Sheldrick, G.M. SHELXT - Integrated space-group and crystal-structure determination. *Acta Crystallogr. Sect. A Found. Crystallogr.* **2015**, *71*, 3–8.
41. Dolomanov, O. V.; Bourhis, L.J.; Gildea, R.J.; Howard, J.A.K.; Puschmann, H. OLEX2: A complete structure solution, refinement and analysis program. *J. Appl. Crystallogr.* **2009**, *42*, 339–341.
42. Sheldrick, G.M. Crystal structure refinement with SHELXL. *Acta Crystallogr. Sect. C Struct. Chem.* **2015**, *71*, 3–8.
43. Van Der Sluis, P.; Spek, A.L. BYPASS: an Effective Method for the Refinement of Crystal Structures Containing Disordered Solvent Regions. *Acta Crystallogr. Sect. A* **1990**, *46*, 194–201.
44. Spek, A.L. Single-crystal structure validation with the program PLATON. *J. Appl. Crystallogr.* **2003**, *36*, 7–13.
45. Boudreaux, E.A.; Mulay, L.N. Theory and Applications of Molecular Paramagaetism. *John Wiley , New York* **1976**, 510.
46. Tang, J.; Hewitt, I.; Madhu, N.T.; Chastanet, G.; Wernsdorfer, W.; Anson, C.E.; Benelli, C.; Sessoli, R.; Powell, A.K. Dysprosium triangles showing single molecule magnet behavior of thermally excited spin states. *Angew.Chem. Int.Ed.* **2006**, *45*, 1729–1733.
47. Kazuo Nakamoto *Infrared and Raman Spectra of Inorganic and Coordination Compounds Part A : Theory and Applications in Inorganic Chemistry*; John Wiley & Sons, Inc., Hoboken, New Jersey: New Jersey, 2008; ISBN 9780471743392.
48. Rodríguez, M.R.; Del Plá, J.; Piro, O.E.; Echeverría, G.A.; Espino, G.; Pis-Diez, R.; Parajón-Costa, B.S.; González-Baró, A.C. Structure, tautomerism, spectroscopic and DFT study of o-vanillin derived Schiff bases containing thiophene ring. *J. Mol. Struct.* **2018**, *1165*, 381–390.
49. Yang, X.; Jones, R.A.; Wiester, M.J. A nanoscale slipped sandwich of Tb_{10}-stabilization of a benzaldehyde methyl hemiacetyl. *Dalt. Trans.* **2004**, *3*, 1787–1788.
50. Zou, X.; Yan, P.; Zhang, J.; Zhang, F.; Hou, G.; Li, G. NIR luminescence and catalysis of multifarious salen type ytterbium complexes modulated by anions. *Dalt. Trans.* **2013**, *42*, 13190–13199.
51. Costes, J.P.; Dahan, F.; Nicodème, F. A trinuclear gadolinium complex: Structure and magnetic properties. *Inorg. Chem.* **2001**, *40*, 5285–5287.
52. M. Llunell, D. Casanova, J. Cirera, P.A. and S.A. SHAPE - Program for the Stereochemical Analysis of Molecular Fragments by Means of Continuous Shape Measures and Associated Tools version 2.1 2013.
53. Boča, R. *A Handbook of Magnetochemical Formulae*; Elsevier: Amsterdam, 2012; ISBN 978-0-12-416014-9.
54. Ishikawa, N.; Sugita, M.; Ishikawa, T.; Koshihara, S.Y.; Kaizu, Y. Lanthanide double-decker complexes functioning as magnets at the single-molecular level. *J. Am. Chem. Soc.* **2003**, *125*, 8694–8695.
55. Boča, R.; Rajnák, C. Unexpected behavior of single ion magnets. *Coord. Chem. Rev.* **2021**, *430*, 1–14.
56. Boča, R.; Rajnák, C.; Moncol, J.; Titiš, J.; Valigura, D. Breaking the Magic Border of One Second for Slow Magnetic Relaxation of Cobalt-Based Single Ion Magnets. *Inorg. Chem.* **2018**, *57*, 14314–14321.
57. Rajnák, C.; Boča, R. Reciprocating thermal behavior in the family of single ion magnets. *Coord. Chem. Rev.* **2021**, *436*, 1–12.
58. Rajnák, C.; Titiš, J.; Boča, R. Reciprocating thermal behavior in multichannel relaxation of cobalt(II) based single ion magnets. *Magnetochemistry* **2021**, *7*, 1–76.

Novel Metal Complexes of Aminoquinoline Derivative for Drug Design: Experimental and Computational Studies

Tadewos Damena[1,*], Mamaru Bitew[2], Digafie Zeleke[3], Tegene Desalegn[2], Taye B. Demissie[4]

[1]*Department of Chemistry, Wachemo University, P.O. Box 667, Hossana, Ethiopia*
[2]*Department of Applied Chemistry, Adama Science and Technology University, P.O. Box 1888, Adama, Ethiopia*
[3]*Department of Chemistry, Salale University, P.O. Box 245, Fitche, Ethiopia*
[4]*Department of Chemistry, University of Botswana, Notwane Rd, P/bag UB 00704 Gaborone, Botswana,*
**Corresponding author, e-mail: tad.dam.keb2010@gmail.com*

ABSTRACT

Interest is increasingly focused on the use of transition metal complexes as biochemical, medical, pharmaceutical, anticancer, and antibacterial agents. In this work, five (5) novel transition metal complexes of Zn(II), Cu(II), Co(II), Ni(II), and V(IV) were prepared from (E)-2-(((2-((2-hydroxyethyl)amino)quinolin-3-yl)methylene)amino)ethanol. The compounds were characterized with physicochemical and spectroscopic methods. The analyses were supported with DFT and TD-DFT calculations. The structural features, the crystallite size, and elemental composition of the metal complexes were deduced from FTIR, Mass spectroscopy, powder XRD, thermogravimetric analysis and EDX studies. In vitro antibacterial activity analysis of the complexes were studied with disc diffusion and agar dilution methods, and the Zn(II), Cu(II), Co(II), and Ni(II) complexes, with mean inhibition zones of 18.85 0.34, 20.65 0.18, 18.62 0.19, and 15.64 0.22 mm diameters at 300 g/mL, respectively, showed good activities against Pseudomonas aeruginosa respectively. The complexes were also evaluated for their antioxidant properties and showed higher antioxidant activities. All the Zn(II), Cu(II) and Co(II) complexes exhibited better antioxidant activities with IC_{50} values of 8.62, 4.70 and 9.20 µg/mL, respectively. Overall, the newly synthesized Zn(II), Cu(II), Co(II), and Ni(II) complexes have biological activities, with the Cu(II) complexes having much better activity than other complexes and these result were found to be in good agreement with binding mode against E. coli DNA gyrase B.

Keywords: *Metal complexes; heterocyclic ligand, biological activities, computational studies*

1. INTRODUCTION

Metal ions are known to combine with many drugs and/or organic ligands to form complexes of enhanced bioactivity compared to free ligands (Hamdani and Amane, 2019). Results of researches over the past decades have witnessed that metal complexes of (chromium, cobalt, copper, iron, nickel, vanadium and zinc) have been applied in the various biological applications, including, antimicrobial and antioxidant (Kargar et al., 2021). In this aspect, the search for natural products with potential biologically active ligands have confirmed that quinoline derivative such as 2-chloro-8-methylquinoline-3-carbaldehyde, and 2-chloroquinoline-3-carbaldehyde are pharmacologically active compounds that cure different communicable and non-communicable diseases (Aly et al., 2020). It has been used as chelating agent due to its N-donor ligands in the synthesis of coordination compounds or complexes (Nainwal et al., 2019) that have attracted attention of bioinorganic, pharmaceutical and medicinal chemists. The issue of metal-based therapy has witnessed increasing focus with respect to efficient strategies in the design of repository, slow-release or long-acting drugs (Raja et al., 2012). In order to develop a clinically useful metallo-pharmaceutics, the study of coordination compounds focusing on their long-term toxicity including side effects, clear evidence of target compounds for the *in vivo* as well as *in vitro* pharmacological action and their pharmacokinetic property are very crucial (Patel et al., 2017).

Now a days, zinc based complexes have shown anti-inflammatory (Koleša-Dobravc et al., 2018), antimicrobial, antioxidant activities (Nagesh, Mahendra Raj, and Mruthyunjayaswamy 2015). There also exist reports about structures, magnetic properties, antidiabetic, anti-inflammatory and catalytic activities of oxovanadium complexes, but the study of their antimicrobial activity is relatively rare (Sehimi et al., 2019). Other studies have indicated that

Cu(II) complexes containing heterocyclic ligand exhibited antimicrobial and antioxidant behavior (Raja et al., 2013). Various studies reported that Co(II) complexes of heterocyclic ligand were known for their antioxidant, antimicrobial and antiviral effect (Li et al., 2020). Bioinorganic chemists were interested to study Ni(II) complexes due to antibacterial (Skyrianou et al., 2009), antifungal (Alomar et al., 2013) and antioxidant (Betanzos-Lara et al,. 2012) activities. However, the structural and biological properties of metal complexes with imine and N-heterocyclic ring containing ligands, **L** = (E)-2-(((2-((2-hydroxyethyl)amino)quinolin-3-yl)methylene)amino) ethanol, is rare and need to be further investigation. Hence, in this study we reported the synthesis of, Zn(II), Cu(II), Co(II), Ni(II) and V(IV) complexes from metal salts with the mentioned ligands. Furthermore, *in silico* analysis (DFT, molecular docking and Absorption, Distribution, Metabolism, and Excretion (ADME)) had been performed to determine the 3D structure of the complexes, correlate experimental results with theoretical value and to predict drug likeness of the targeted metal complexes (Belkhir-Talbi et al., 2021).

2. MATERIALS AND METHODS

2.1. Chemicals and Reagents

The chemicals and reagents used for this study were acetic anhydride 99.8%, acetic acid glacial 99.5%, aniline 99%, zinc dust 95%, N, N- dimethyl formamide 99%, phosphorus oxychloride 98%, methanol 99.5%, Triethylamine 99%, cobalt chloride hexahydrate 98%, copper nitrate trihydrate 98%, nickel nitrate hexahydrate 98%, zinc chloride 98%, vanadyl sulphate 96%, silver nitrate 99.9%, L-Ascorbic acid 99%, Dimethyl sulphoxide 99% and 2, 2-diphenyl-1-picrylhydrazyl (DPPH). All these chemical and reagents were purchased from Loba chemie PVT. LtD (Mumbai, India) and all chemical reagents, including salts and solvents, were of analytical grade and used without further purification.

2.2. Synthesis of Ligand

The ligand (**L**) was prepared based on the previous reported procedure (Digafie et al., 2021), accordingly, 2-chloroquinoline-3-carbaldehyde (2.5 g, 0.013 mol) was added to 10 mL 2- aminoethan-1-ol in a 250 mL round-bottom flask and heated to 90 – 95 °C for 2 h in oil bath. The completion of the reaction was monitored with TLC. The resulting mixture was cooled to room temperature and added to 200 mL cold ice water. The precipitate was separated by suction filtration and washed with 400 mL ice cold water.

2.3. Synthesis of Transition Metal Complexes

Under constant stirring, a drop of triethylamine was added to 10 mL methanolic solution of **L** (0.5 g, 1.93 mmol) in 250 mL two neck round bottom flasks. After 30 min of stirring, methanollic solutions (10 mL) of $ZnCl_2$ (0.13 g, 0.96 mmol), $Cu(NO_3)_2 \cdot 3H_2O$ (0.232 g, 0.96 mmol), $CoCl_2.6H_2O$ (0.228 g, 0.9 mmol), $Ni(NO_3)_2.6H_2O$ (0.279 g, 0.96 mmol) and $VOSO_4$ (0.16 g, 0.96 mmol were added dropwise to the solution of the ligand under constant stirring in separate flasks and the resulting yellowish white, deep green, brownish red, reddish pink, and deep green colour solution was refluxed for 3h at 80 ^oC respectively (Li et al., 2020; Ramachandran et al., 2013, 2018; Sutradhar et al., 2013). The reaction processes were monitored using TLC. After the completion, the reactions were allowed to cool to room temperature and section filtered off, washed with ice cold methanol, and dried at room temperature.

2.4. Biological Activity

2.4.1. Antibacterial and Antioxidant Activity of the Complexes

Antibacterial activity of the free ligand and its complexes were examined using paper disc diffusion technique in which two Gram-positive bacteria (*Staphylococcus aureus*, ATCC25923, and *Streptococcus pyogenes*, ATCC19615 and two Gram-negative bacteria (*Escherichia coli*, ATCC 25922, and *Pseudomonas aeruginosa*,

ATCC 27853) were used to examine their activity (Digafie et al., 2021). The bacterial activities of the synthesized complexes were also confirmed by calculating percent activity index (AI), (El-Gammal et al. 2021) equation 1.

$$\%\ Activity\ index\ (AI) = \frac{Mean\ inhibition\ zone\ \ of\ compounds}{Mean\ \ inhibition\ zone\ of\ standard} \times\ 100 - - - (1)$$

The minimum inhibitory concentration (MIC) were determined by agar dilution method (Abu-Dief et al., 2021; Al-Hazmi et al., 2020). Bacterial suspension was prepared by inoculated nutrient broth with a loopful of the bacterial culture from the slant and incubated at 37 ± 1°C for 24 h. A few mL of the bacterial suspensions (24-h broth cultures) of each strain was added to 20 mL fresh broth until the final inoculum concentration is closely approximates to 5×10^5 CFU/mL (colony-forming unit per millilitre) and a two-fold serial dilution method was followed(Atta-ur-Rahman et al. 2001; Azam et al. 2021; Chen et al. 2020; Wiegand, Hilpert, and Hancock 2008). The complexes were dissolved in water separately to a concentration of 2.5 mg/mL solution. A 0.2 mL solution of the complex was added to 1.8 mL of the seeded broth to form the first dilution in each case (250 µg/mL concentration). Then, ten various dilutions were prepared for each complex by diluting 1 mL of this dilution with further 1 mL of the seeded broth to produce the second dilution. The process was repeated until the tenth dilution generating different concentration. After incubation for 24 h at 37 ± 1°C, the last tube with no visible growth of the microorganism was taken to represent the minimum inhibitory concentration (MIC) of the complexes in each strain. All experiments were performed in triplicate and the mean of the triplicates were reported (Azam et al., 2021; Chen et al., 2020).

Antioxidant studies of the free ligands and their transition metal complexes were performed using a 2,2-diphenyl-1-picrylhydrazyl (DPPH) assay (Digafie et al., 2021). All the activities were performed in triplicate and the average absorbance was taken for calculating the percentage of inhibition using equation 2.

$$\mathrm{DPPH}_{\mathrm{Inhibition\ (\%)}} = \left[\frac{(\mathrm{A_C} - \mathrm{A_S})}{\mathrm{A_C}}\right] \mathrm{X}\ 100\% - - - - - - - - - - - - - - - - (2)$$

where A_C is the absorbance of the 2, 2-diphenyl-1-picrylhydrazyl (DPPH) solution without the samples, and A_S is the absorbance of the titled complex compounds with DPPH solution.

3. RESULTS AND DISCUSSION

3.1. Synthesis of Ligands and Their Transition Metal Complexes

The preparation of ligand and its all metal complexes were performed following established procedure. The complexes (**1 – 5**) were then synthesized in 1:1 metal: Ligand [**M: H_3L**] ratio with metal salts of zinc chloride, copper nitrate trihydrate, cobalt chloride hexahydrate, nickel nitrate hexahydrate and vanadyl sulphate.

3.1.1. Ligand (H_3L)

Representation for the synthesis and proposed mechanisms of **H_3L** is presented in scheme 1.

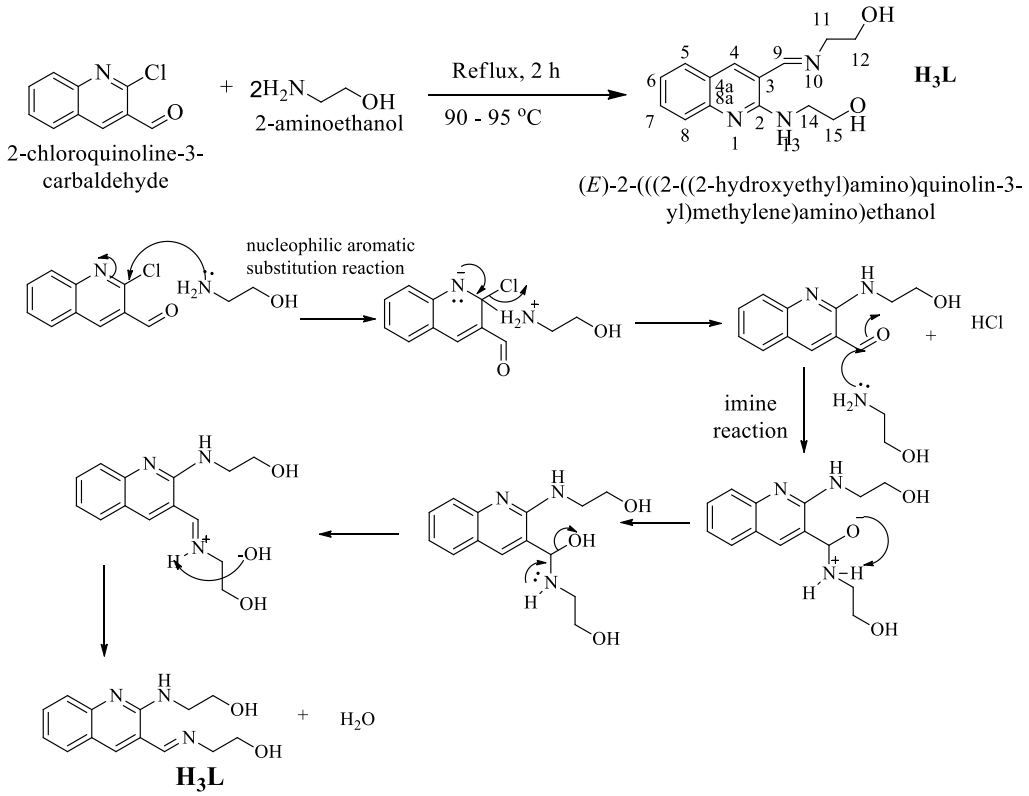

Scheme 1: Proposed synthesis and reaction mechanisms of **H_3L**

Table 1: Physicochemical properties of ligands and their transition metal complexes

Compounds	Colour	Yield (%)	Melting point (°C)	Conductivity ($\Omega^{-1}mol^{-1}$ cm^2.25 °C)
$C_{14}H_{17}N_3O_2$ **(H_3L)**	Yellow	(2.91 g) 86	80 – 85	-
$[Zn(H_2L)Cl]$ **(1)**	Light yellow	(0.25 g) 63	225 – 230	7.21
$[Cu(H_2L)(H_2O)(NO_3)]$ **(2)**	Deep green	(0.24 g) 62	195 – 200	18.57
$[Co(H_2L)Cl)(H_2O)_2]$ **(3)**	Brownish purple	(0.25 g) 63	215 – 220	8.47
$[Ni(H_2L)(NO_3)].2H_2O$ **(4)**	Reddish brown	(0.26 g) 66	115 –120	15.07
$[V(O)(H_2L)(H_2O)(SO_4)]$ **(5)**	Deep green	(0.19 g) 59	205 – 210	13.20

Note: [$C_{14}H_{17}N_3O_2$ (Ligand = **H_3L**], [**H_2L**=deprotonated ligand]

3.1.2 Complex 1

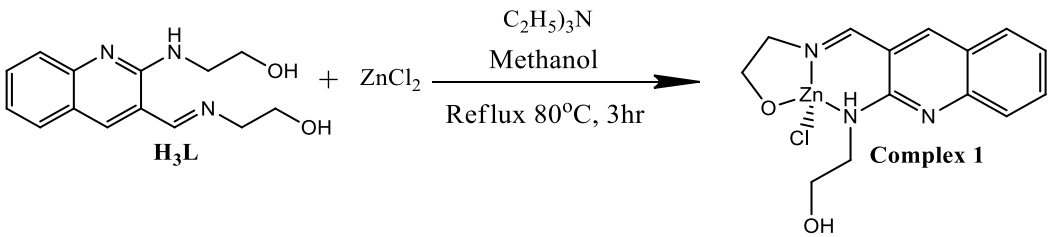

Scheme 2: Proposed chemical reaction of complex **1**

3.1.3 Complex 2

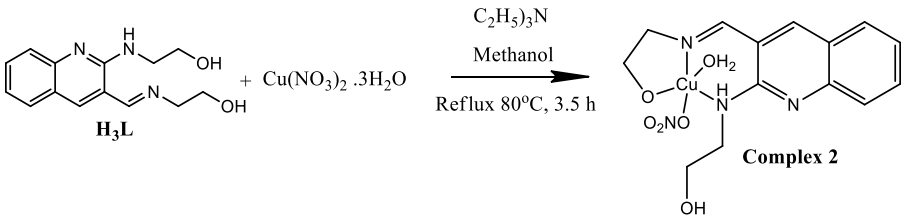

Scheme 3: Proposed chemical reaction of complex **2**

3.1.4 Complex 3

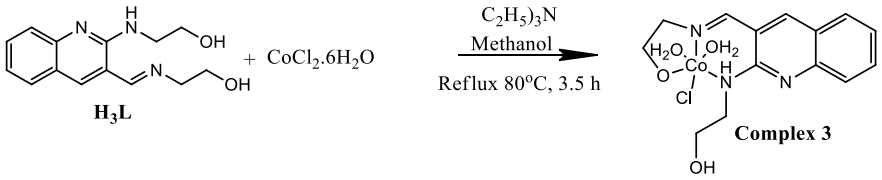

Scheme 4: Proposed chemical reaction of complex **3**

3.1.5 Complex 4

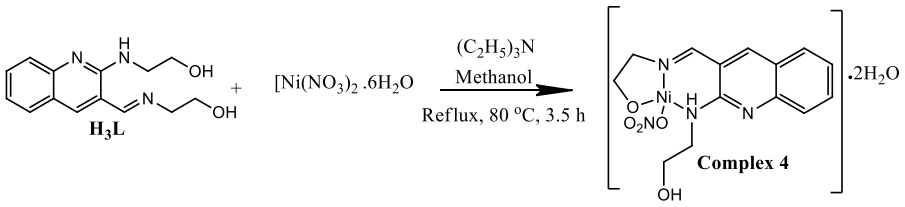

Scheme 5: Proposed chemical reaction of complex **4**

3.1.6 Complex 5

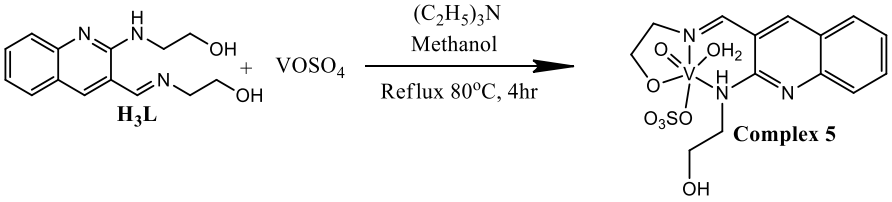

Scheme 6: Proposed chemical reaction of complex **5**

3.2. Characterization of compounds

The synthesised compounds were characterized with Uv-Vis, FTIR, PXRD, NMR, TGA, MS and SEM-EDX.

3.2.1. UV- Visible Spectroscopy

The Cu(II), Co(II), V(IV) and Ni(II) complexes' characteristic spectra were observed in the ranges of 231–293 nm and 302–304 nm that would be assigned to the π→π* and n→π* transitions, respectively. Additionally, the broad band observed at 406, 427, 408 and 401 nm, for Cu(II), Co(II), V(IV), and Ni(II) respectively, were observed. These red shifts from free ligand are mainly due to the ligand to metal charge transfer (LMCT). Moreover, as it can be seen from the insets of the absorption plots presented in Fig. 1, there is a very weak d→d transition around 480 nm in the case of the Ni(II) complex. In addition, to shed more light on the absorption spectra

of the ligand and its complexes, we used TD-B3LYP to calculate the absorption spectra. Comparison of the experimental electronic spectra with TD – DFT calculations has been carried out and it was found that the experimental results are in very good agreement with the calculated results as Fig. 2. This further confirms the successful syntheses of the intended complexes.

3.2.2. FTIR Spectroscopy

The IR spectrum of **H_3L** shows a stretching band at 1639 cm^{-1} for ν(C=N) imine group, but this band shifted towards different frequency in the spectral of all metal complexes (**1** – **5**) to the range (1647 – 1688 cm^{-1}) indicating the participation of nitrogen atom of imine group ν(C=N), in coordinate covalent bonds (Table 2), in line with the reported studies (Digafie et al., 2021). In other case FTIR stretching frequency of **H_3L** at 3368cm^{-1} ν(O-H) is decreased in case of all complexes, this also shows the deprotonation of hydroxyl group and participation of oxygen in dative bond formation. In addition FTIR stretching frequency of ligand at 3275 cm^{-1} ν(N-H) is diminished in case of all the synthesised metal complexes, which indicate that participation of nitrogen of amine group to complex formation (Chiriac et al., 2008).

Weak and broad band stretching frequency which ranged from (3687 – 3000) cm^{-1}, is clearly emerged which could be assigned as stretching vibration of water molecules as water of coordination for Cu(II), Co(II), V(IV) and as lattice water for Ni(II) respectively. In addition new stretching vibration band of the spectral are displayed at 524 cm^{-1} ν(Zn-O), 460 cm^{-1} ν(Zn-N) bonds, 626 cm^{-1} ν(Cu-O), 474 cm^{-1} ν(Cu-N) bonds, 546 cm^{-1} ν(Co-O), 466 cm^{-1} ν(Co-N) bonds, 534 cm^{-1} ν(Ni-O), 462 cm^{-1} ν(Ni-N), bonds and the bending bond at 604 cm^{-1} δ(V-O), 459 cm^{-1} δ(V-N), for, Zn(II), Cu(II), Co(II), Ni(II) and V(IV) complexes respectively (Table 2).

The stretching band at 977 cm^{-1} is special for ν(V=O), for the V(IV) complex which is in line with reported studies (Zhu et al., 2019). In addition, the presence of nitrate in both Cu(II) and Ni(II) complexes were signalled by the strong and broad band IR peaks at 1380 cm^{-1} and 1351 cm^{-1}, (Ali et al., 2019) respectively, which gave good indication for the participation of nitrate in complexation reaction (El-Sonbati et al., 2020), and weak bending vibration of δ(O-H) was clearly observed in the range of 1200–1450 cm^{-1} in case of all metal complexes confirming the appearance of free bending hydroxyl (O-H) group in good agreement with the reported studies (Zhu et al., 2019).

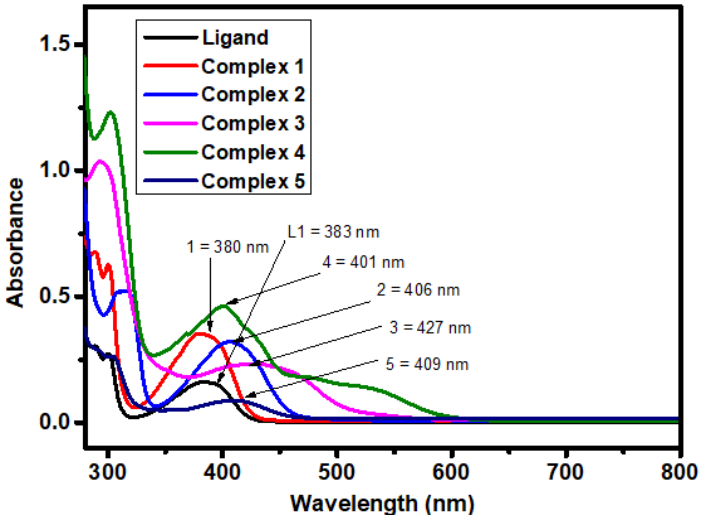

Figure 1: UV-Vis spectra of **H_3L** and its metal complexes

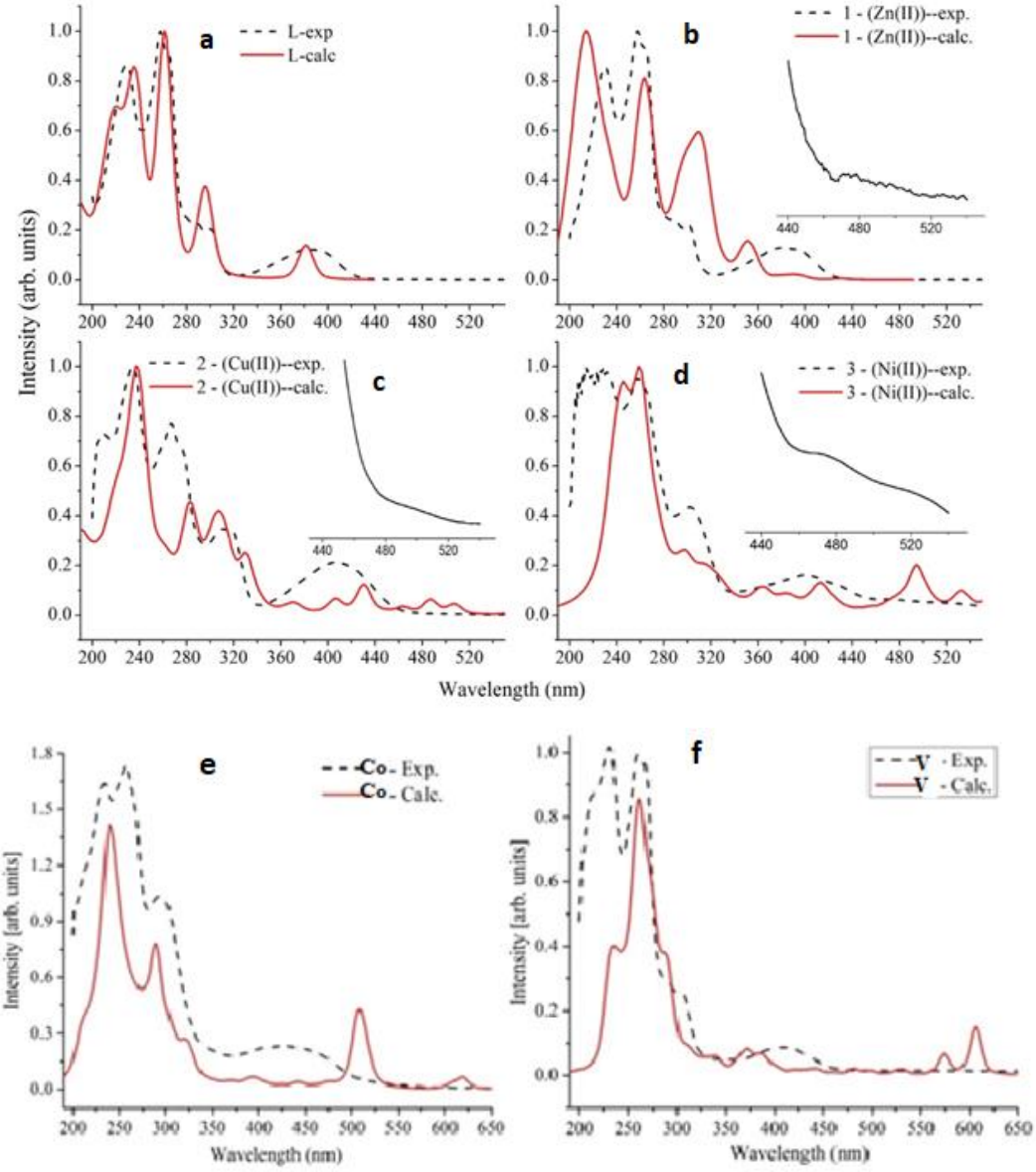

Figure 2: Comparison of the experimental absorption wavelengths with calculated results of the **H_3L** and (**1 – 5**). Insets are experimental plots for the range between 440 and 540 nm.

The DFT calculated IR frequencies and TD-DFT calculated absorption spectra were also in good agreement with the corresponding experimental results (Table 2 and Fig. 2), which further confirmed the successful synthesis of the targeted complexes.

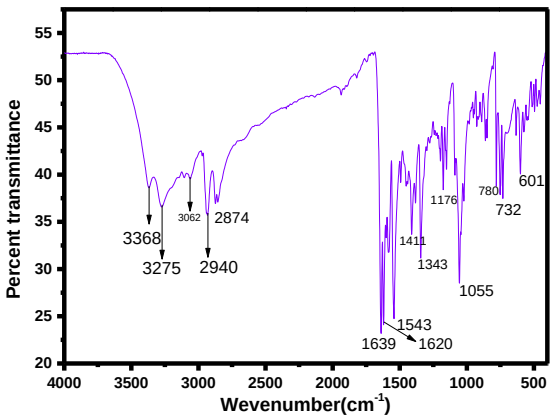

Figure 3: FT-IR spectra of free ligand (**H_3L**)

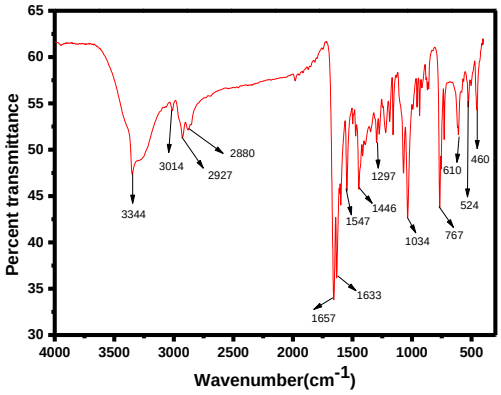

Figure 4: FT-IR spectrum of complex **1**

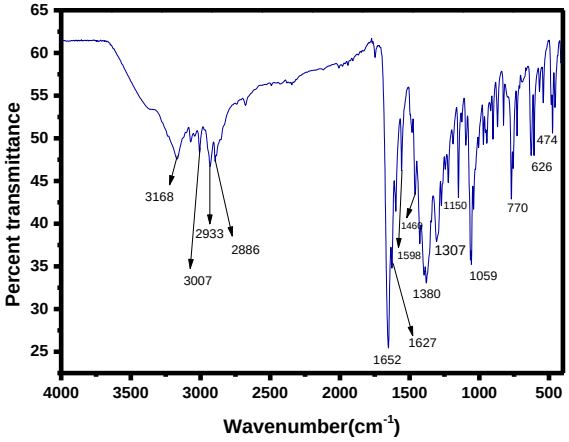

Figure 5: FT-IR spectrum of complex **2**

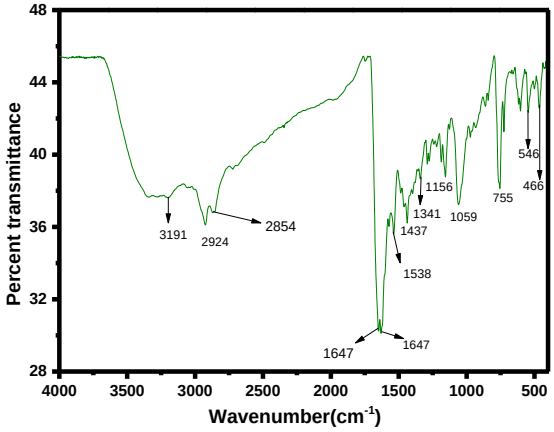

Figure 6: FT-IR s spectrum of complex **3**

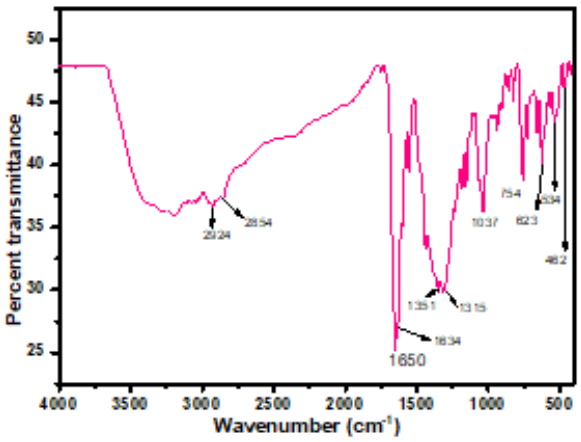

Figure 7: FT-IR spectrum of complex **4**

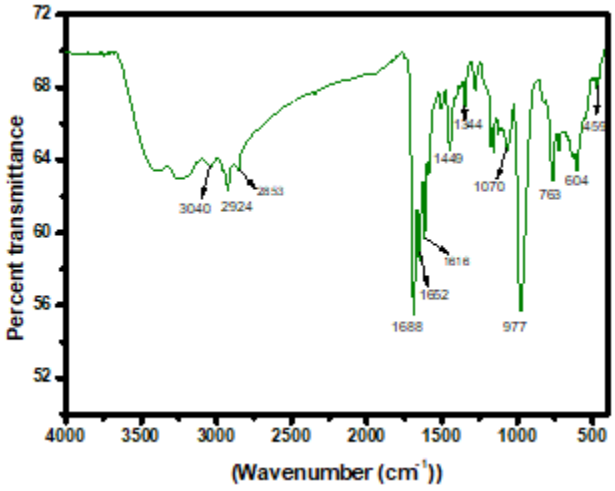

Figure 8: FT-IR spectrum of complex **5**

Table 2: Selected FTIR vibrations and band assignments for the **H_3L** and its complexes (**1** – **5)**. Experimental results are without parenthesis whereas the B3LYP-GD3/6-311++G**/LanL2DZ calculated results are presented in parenthesis.

	ν(O-H)	ν(N-H)	Im. ν(C=N)	Ql. ν(C=N)	δ(O-H)	ν(NO_3)[c]	ν(V=O)	ν(M-O)	ν(M-N)
H_3L	3368[m] (3564)	3275 [m] (3359)	1639[s] (1579)	1620[s] (1532)	1411 [m] (1323)	-	-	-	-
1	3349 [w] (3575)	3294 [w] (3374) [w]	1657[s] (1680)	1633[s] (1608)	1446 [m] (1362)	-	-	524 [m] (490)	460[m] (464)
2	3664-3334 (3734, 3713[b])	3168 [w] (3374)	1652[s] (1661)	1627[s] (1586)	1460 [m] (1426),	1380[s] (1381)		626 [m] (703)	474[m] (467)
3	3687[b,w] (3652)	3346 [w]	1647[s] (1642)	1630[s] (1538)	1437[m] (1508)			546[w] (486)	466[w] (382)
4	3673-3373 [b] (3736, 3574 [b])	3197[w] (3088)	1650[s] (1669)	1634[s] (1593)	1439 [m] (1421)	1351[s] (1457)		534 [m] (750, 563)	462 (503, 470)
5	3668[b,w] (3675)	3282[w]	1688[s] (1610)	1652[s] (1540)	1449[m] (1395)		977[s] (1070)	604[b.m] (619)	459[w] (502)

S= strong m = mediam, b = broad, w= weak

3.2.3. X-ray Diffraction Analysis of complexes (1-10)

The powder X-ray diffraction (PXRD) patterns of the synthesised all metal complexes (**1 – 5**) were recorded using 80 mg of dried powdered samples and the patterns of the complexes (**1 – 5)** have showed polycrystalline like characteristic peaks Fig. 9, because the complexes showed many diffraction peaks which are in line with previously reported studies (El-Sonbati et al. 2019). It is important to note that the average crystallite size (D) can be calculated from the XRD pattern according to Debye–Scherrer equation (Sumalatha et al., 2021).

$$D = \frac{K\lambda}{\beta \cos\theta} \quad \text{---------- (3)}$$

The equation uses the reference peak width at angle θ, where λ is the wavelength of X-ray radiation (1.5406 Å), K is Scherrer constant (0.9) and β is the width at half maximum of the reference diffraction peak measured in radians. Accordingly, the average crystallite sizes of complexes **1 – 5,** are 28, 34, 22, 37 and 8 nm, respectively, which is in line with previously reported studies (Ramachandran et al., 2018; Sumalatha et al., 2021).

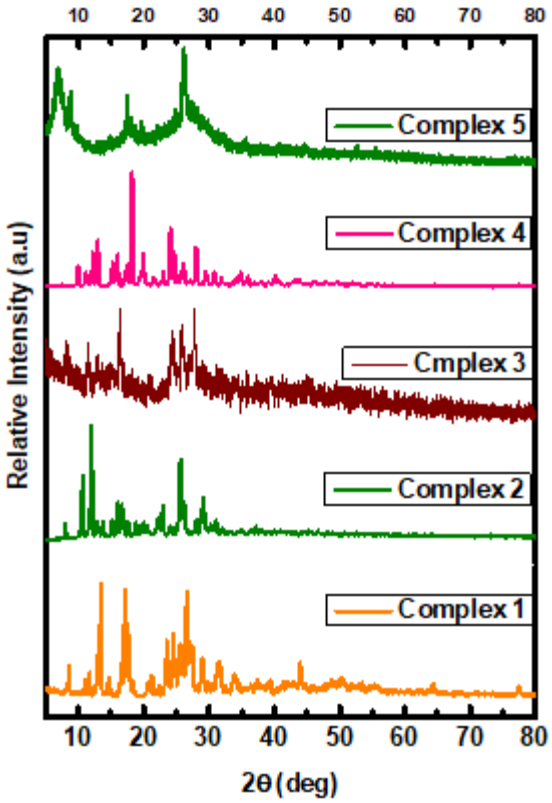

Figure 9: Powder XRD spectra of complexes **1 – 5**

3.2.4. SEM – EDX analysis

In EDX spectrum complex **1** shows five characteristic signals which correspond to carbon, oxygen, nitrogen, Chlorine and zinc atoms and confirms the formation of CHZnNOCl compound. Similarly, in EDX complex **2** spectrum shows four characteristic signals which correspond to carbon, oxygen, nitrogen and copper atoms and it clearly confirms the formation of CHCuNO complex. The EDX spectrum of complex **3** shows five characteristic signals which correspond to carbon, oxygen, nitrogen, chlorine and cobalt atoms and are signalled the formation of CHCoNOCl compound, in EDX spectrum the complex **4** shows four characteristic signals which correspond to carbon, oxygen, nitrogen, and nickel atoms. The characteristic peak confirms the formation of CHNiNO compound and the EDX spectrum of complex **5** shows five characteristic signals which correspond to carbon, oxygen, nitrogen, sulphur and vanadium atoms and indicated the formation of CHVSNO compound which is in line with the previous reported studies (El-Sonbati et al. 2019).

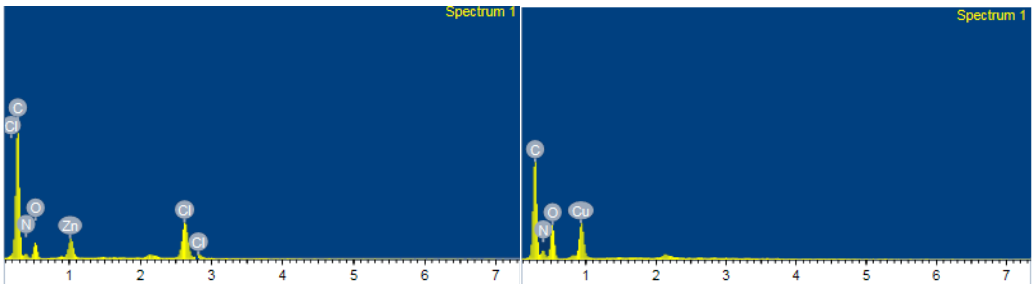

(a) (b)

Figure 2: EDX spectra of: (a) complex **1** and (b) complex **2**

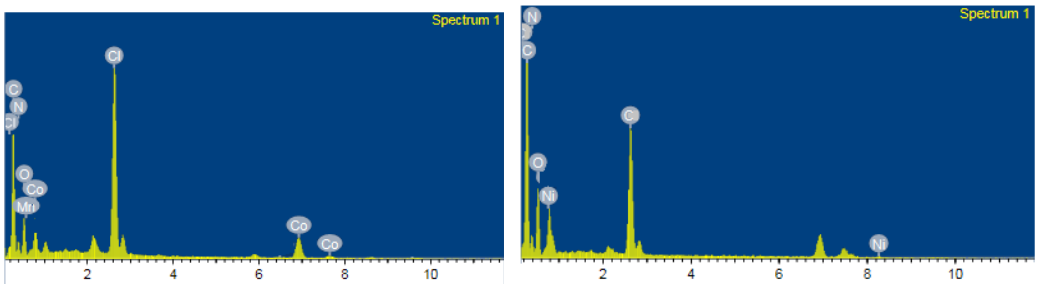

(a) (b)

Figure 11: EDX spectra of: (a) complex **3** and (d) complex **4**

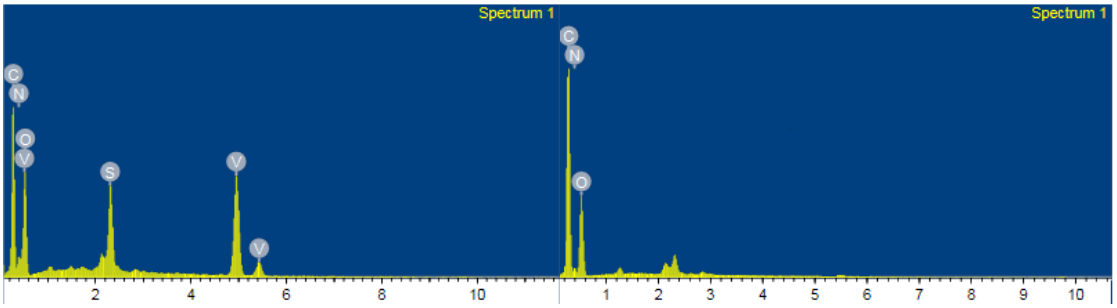

(a) (b)

Figure 12: EDX spectra of: (a) complex **5** and (b) Ligand

Finally, in EDX spectrum the free **H_3L** shows three characteristic signals which correspond to C (carbon), O (oxygen), and N (nitrogen) atoms, which clearly confirms the formation of CHNO compound (Fig.12b). Generally, the EDX spectra showed the ligand and all its metal complexes are presented without impurity in which the analysis indicated that the experimental percentage composition of atom is in agreement with the expected (theoretical) values.

3.2.5. Mass Spectra of Transition Metal Complexes

The mass spectra of the transition metal complexes (**1** – **5**) are characterized using LC-MS. Accordingly, the mass spectrum of complex **1** exhibits a parent molecular ion peak at *m/z* = 392.90 (Found = 392.98) which corresponds to the formula of [$C_{14}H_{15}Cl_2N_3O_2Zn$] (M.Wt.= 393.57 g/mol). The complex **2** exhibits a parent molecular ion peak at *m/z* = 400.08 (Found = 400.04) which corresponds to the formula of [$C_{14}H_{17}CuN_4O_6$] (M.Wt= 400.85 g/mol) and the mass spectrum of complex **3** exhibits a parent molecular ion peak at *m/z* = 404.05 (Found= 404.00) which is similar to the formula of [$C_{14}H_{17}Cl_2CoN_3O_3$] (M.Wt= 405.14 g/mol). Complex **4** exhibits a parent molecular ion peak at *m/z* = 413.09 (Found = 413.06) which is similar to the formula of [$C_{14}H_{19}N_4NiO_7$] (M.Wt= 414.02 g/ mol). Complex **5** exhibits a parent molecular ion peak at *m/z* = 438.11 (Found = 438.02) which related to the formula of [$C_{14}H_{17}N_3O_8SV$] (M.Wt = 438.31 g/mol).

3.2.6. Thermogravimetric Analysis

Thermogravimetric analyses (TGA) of metal complexes were recorded under N_2-atmosphere (20 ml/min) using 8 mg dried sample. In this analysis, heating rate was controlled at 10 $^oC\ min^{-1}$ under nitrogen atmosphere and the weight loss is measured at temperature ranges from 25 to 800 ^oC. Accordingly, thermogravimetric analysis (TGA) diagram of complex **1** [$C_{14}H_{16}ClN_3O_2Zn$] showed three decomposition steps with the residue corresponds to zinc oxide (ZnO) about 22.52% (calcd = 22.66%) in agreement with reported studies.

The TGA diagram of complex **2**, [$C_{14}H_{18}CuN_4O_6$], indicates three decomposition steps with leaving residue copper (II) oxide (CuO), representing 18.91 % (calcd. = 19.80 %) of the complex and the actual weight loss is 81.09 % ;very close to the calculated one 80.33 %, in line with reported studies (Ambala and Lincoln 2020; Badwaik et al., 2009; Zordok and Sadeek 2018). The thermal decomposition of complex **3**, [$C_{14}H_{20}ClCoN_3O_4$] exhibits three degradation steps with the weight of the residue corresponds to the respective metal oxide (CoO) about 19.42% (calcd = 19.03%). The thermal decomposition of complex **4,** [$C_{14}H_{20}N_4NiO_7$] exhibits four degradation steps with leaving residue of organic compound moieties and nickel oxide (NiO) representing 29.24% (calcd. = 27.22%) of the total complex. From the data, the actual mass loss from these steps is 70.06 % which is very close to the calculated value of 69.91% in line with the previous studies (Ambala and Lincoln 2020; Zordok and Sadeek 2018). Similarly, the thermal decomposition of complex **5**, [$C_{14}H_{18}N_3O_8SV$] exhibits three degradation steps with leaving residue of VO_2 representing 31.56% (calcd. = 32.52%) of the total complex. From the data, the actual mass loss from these steps is 68.44 % which is close to the calculated value of 69.23% in agreement with reported studies (Ambala and Lincoln 2020).

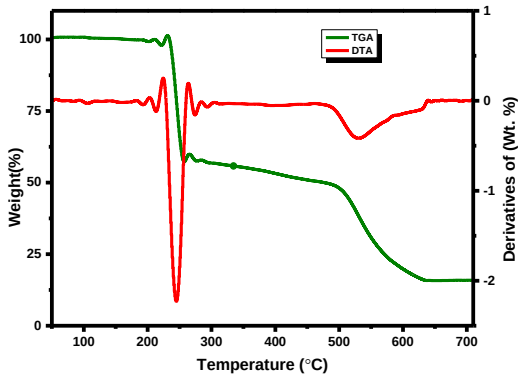

Figure 13: TGA and DTA curve of complex **2**

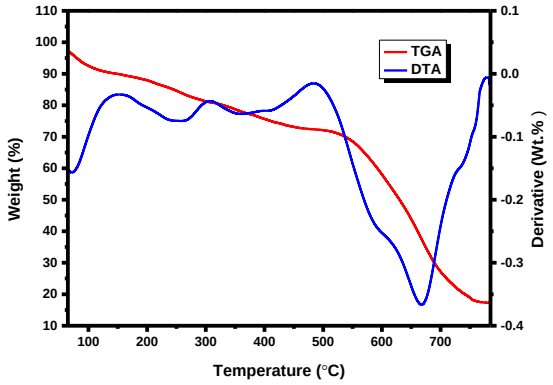

Figure 14: TGA and DTA curve of complex **3**

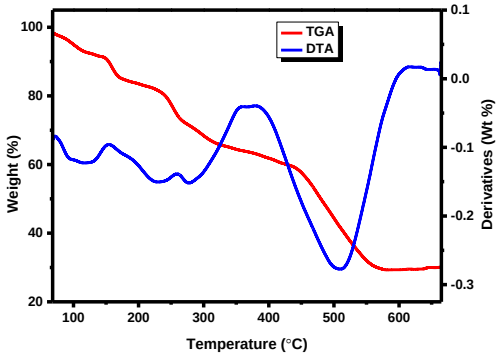

Figure 15: TGA and DTA curve of complex **4**

3.2.7. Molar Conductance

The molar conductance of the synthesised ligands and their metal complexes was recorded in triplicate using concentration of 1mM in methanol at room temperature. The molar conductance of metal complex (**1** – **5**) was ranged from 7 to 19 ($\Omega^{-1}mol^{-1}cm^2$ 25 ^oC) (Table 1). These indicate that the conductivity of the synthesized metal complexes is relatively low; hence the non-electrolytic nature of the complexes and which are very low to account for their electrolytic behaviour. Generally, molar conductance of complexes (**1** – **5**) are very low, this is because

there is no primary valance in the complexes, in other word the complexes consists lower electrolytes which results in non-electrolytic nature of the complexes (Ismael et al., 2020). This is mainly due to the fact that the metal cations received electrons from the ligand to make the net charge balance of the complexes to be zero in line with the previous reported studies (Mandewale et al,. 2019).

The molar conductance also used in the investigation of the geometrical structures of the complexes (El-Sonbati et al., 2020). According to the non-electrolytic nature of the metal complexes specifically metal complexes **1** and **3,** the chloride ion is coordinated to metal ion to satisfy the valence of the coordination sphere hence, the presences of chloride ions inside the coordination sphere of the specified complexes were confirmed by reaction with silver nitrate ($AgNO_3$) solution whereas, there is no precipitate formation during the experiment. Therefore, the formed Zn(II) and Co(II) complex would be formulated as $[Zn(H_2L)Cl]$ and $[Co(H_2L)(H_2O)_2Cl]$ in line with the reported studies (Ismael et al., 2020; Mandewale et al., 2019).

3.3. Biological Application

3.3. 1. Antibacterial Activity of Ligand and Its Metal Complexes

In vitro antimicrobial activity of the compounds was tested against four human pathogenic bacteria two Gram negative *(Escherichia coli* (*E. coli*) and *Pseudomonas aeruginosa)* and two Gram positive bacteria (*Staphylococcus aureus* and *Streptococcus pyogenes)*. The zone of inhibition values of the studied compounds had shown their potential antimicrobial activity when compared to the ligand (Fig. 16).

All the synthesized complexes were proven to have a range of activity against two or more bacterial strains, with the mean zones of inhibition for complexes 1 through 5 ranging from the lowest (7.32 0.90 mm at 150 g/mL) to the highest (20.65 0.18 mm at 300 g/mL). When compared to the positive control. The first four of these complexes, with mean inhibition zones of 18.85 0.34, 20.65 0.18, 18.62 0.19, and 15.64 0.22 mm diameters at 300 g/mL, respectively, showed good activities against *Pseudomonas aeruginosa*. Complexes **1** – **3** have medium to high bacterial activities with the mean inhibition zones ranged from 10.62 ± 0.36 to 20.65 ± 0.18 mm at both concentration 150 and 300 μg/ for all bacterial strain (*E.coli*, *P. aeruginosa*, *S. pyogenes* and *S. aureus*). Among these complex **2** has comparable antibacterial activities with positive standard that has maximum mean inhibition zones of 20.65 ± 0.18 with positive control at the same concentration (300 μg/mL) respectively. Complex **4** has low to medium mean inhibition zones range from 8 ± 0.13 to 15.64 ± 0.22 mm diameter at both 150 and 300 μg/mL for gram negative (*E.coli, P. aeruginosa)* and gram positive *(S. aureus)*, but has no antibacterial activity for gram positive bacteria specifically *Streptococcus pyogenes*. Complex **5** has low antibacterial activities with mean inhibition zone of 7 ± 0.31 to 8 ± 0.52 for gram positive bacteria *(S. aureus*) and 7.32 ± 0.90 to 9.52 ± 0.49 for gram negative bacteria (*E.coli*) at both 150 and 300μg/mL concentration, while has no effect on both bacteria called *P. aeruginosa, S. pyogenes.* The free ligand has very low mean inhibition zone of 6.22 ± 0.14 to 7 ± 0.11 range for *E.coli*, *P. aeruginosa* and *S. pyogenes* while has no antibacterial activity effect for gram positive bacteria *S. aureus*, this indicate that free ligand has lower antibacterial activity than its metal complexes (Fig. 16).

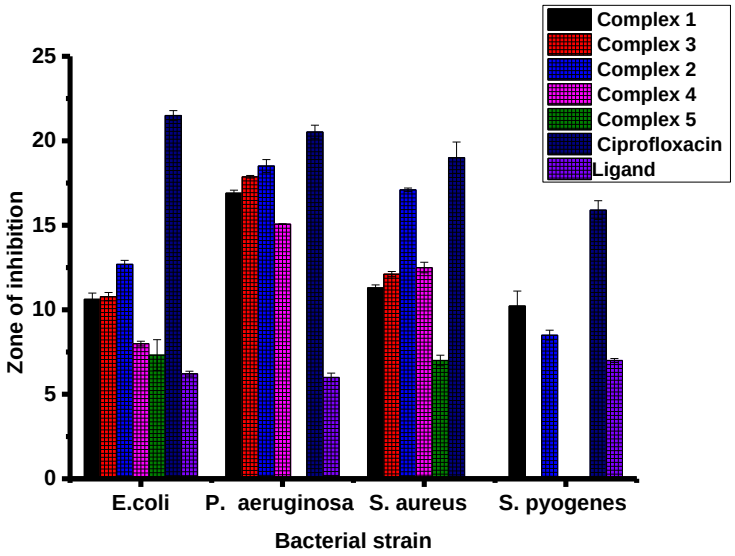

Figure 16: Mean inhibition zone of antibacterial activity of complexes **(1** – **5) (**n = 3. Error bars indicate st. dev.)

Furthermore, results shown in Table 3 indicated better antibacterial activity for complex **2** against *P. aeruginosa*, *S. aureus* and *S. pyogenes* with MIC values of 0.98, 3.91, and 62.5 (µg/ml) respectively. The complex showed significant antibacterial activity against *P. aeruginosa* in comparison to other bacterial strains and have smaller MIC values against this bacteria in which complex **2** is stronger than other complexes in all the four bacterial strains. However, in all cases, the MIC is somewhat larger than that of positive control.

Table 3: Minimum inhibitory concentration (MIC in µg/mL) of the complexes

Complexes	Bacterial strains			
	E. coli	*P. aeruginosa*	*S. aureus*	*S. pyogenes*
1	125.0	1.95	15.63	>250
2	125.0	0.98	3.91	62.5
3	125.0	1.95	15.63	62.5
4	125.0	1.95	15.63	62.5
Ciprofloxacin	<0.49	<0.49	0.98	31.25

From the complexes obtained from the two ligands, Cu(II) complexes showed the highest percent activity index against all the examined bacterial strains. This is may be due to borderline Lewis acid nature of Cu (II) ion. It helps Cu(II) to easily bind with similar biomolecules such as protein and enzyme by "hard soft acid-base (HSAB)" Principle hence copper complexes showed good binding activity with both G. negative and G. positive (*Pseudomonas aeruginosa and S. aureus)* bacterial due to H- bonding interaction with amino acid like arginine having both acid and base end (section 3.5.3). In addition to this, copper(II) coordination compounds can be highly effective in treating microbial infections due to the redox activity of copper ions which interacted with the bacterial chromosome, which led to a decrease in bacterial reproduction (Krasnovskaya et al., 2020).

Moreover, all the complexes showed higher antibacterial activity than the precursor ligand which might be due to chelation of the metal with the ligand that promoted the ability of the complexes to penetrate the cell membrane of the bacterial strains (Indira et al., 2019).

3.3.2. Antioxidant Activity of the Ligand and Its Metal Complexes

The antioxidant activities of the free ligand and its metal complexes were conducted in terms of their proton donating ability with UV-Visible absorbance using DPPH assay. Accordingly, compounds that have antioxidant activity may reduce the absorbance of DPPH at 517 nm, which is resulted in changes in color of DPPH in the reaction process (Fig. 17) in line with previous study (Sumalatha et al. 2021).

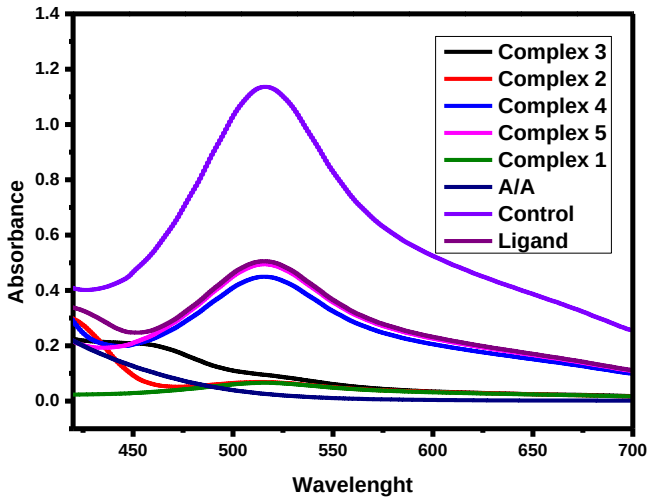

Figure 17: Absorbance spectra of DPPH and with 115 µg/ml of complexes (**1** – **5)**

The data shows that the entire synthesised complex (**1** – **5**) showed antioxidant activities, while complex **1** and **2** shown better antioxidant activity with half maximal inhibitory concentration (IC_{50}) values of 8.62, 4.70, 9.20, 27.56, 34.79 and 35.36 µg/mL for complexes **1**– **5** and the $\mathbf{H_3L}$, respectively **(**Fig. 18). From IC_{50} values, complexes **1** and **2** have comparable activities. This has direct correlation with the good antioxidant properties (Belkhir-Talbi et al. 2021).

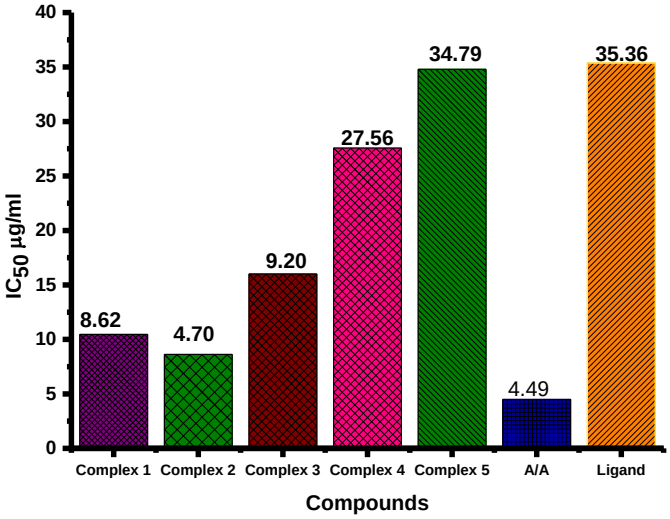

Figure 18: Half maximal inhibitory concentration of $\mathbf{H_3L}$ and its complexes (**1** – **5)**

3.4. *In silico* Analysis of Ligand and its Metal Complexes

3.4.1. Drug-likeness and ADME predictions

The ligand and its complexes (**1** – **5**) have molecular weights ranging from 259.30 to 440.32 g/mol. The iLogP value of the ligand was found to be 2.22 and that of all the metal complexes showed similar iLogP value of zero compared to ciprofloxacin (2.24). The low value of iLogP for the metal complexes indicates good water solubility of the metal complexes relative to the ligand and the control (Balajee et al. 2016). This is in agreement with the experimental solubility values. The number of hydrogen bond donors of all the compounds range from 2 to 3 (≤ 5), whereas, the number of hydrogen bond acceptors range from 4 to 8 (≤ 10). The predicted physicochemical properties for drug likeness screening showed that the synthesized compounds (**H_3L** and complexes **1** – **5**) fulfil drug-like molecular nature in agreement with previous reported studies(Lipinski et al. 2012). Moreover, the topological polar surface area (TPSA) ranges from 66.74 to 142 $Å^2$ for the synthesized compounds. It has been reported that compounds with TPSA of 140 $Å^2$ and above would be poorly absorbed (< 10% fractional absorption) and those with a TPSA 60 $Å^2$ would be well absorbed (> 90%) (Belkhir-Talbi et al., 2021). Therefore, from the TPSA data of the synthesized compounds, it is possible to deduce that the ligand and its complexes (**1** – **5**) have very good intestinal absorption (Daina et al. 2017; Lipinski et al. 2012). Skin permeability (logKp) value of the free ligand and its metal complexes were found within the range of -7.1 to -8.29 cms^{-1}, deducing that all compounds have low skin permeability in agreement with reported studies(Daina et al., 2017; Lipinski et al. 2012). Similarly, the synthesized compounds were predicted as a substrate of P-glycoprotein (P-gp) which is a transporter and biological barrier and responsible for the ADME of drugs (Daina et al., 2017). This inferred that the compounds have no tendency to interact to other drugs fingered by the transporter and hence no drug-drug interactions. The inhibition of CYPs leads to toxicity end points (Khojasteh et al., 2011). The high gastrointestinal absorption (GI) together with their fewer tendencies to inhibit cytochrome P450 family enzymes of the liver (CYPs) gives the compounds theoretically safe from toxicity point of view.

4.4.2. Quantum Chemical Analysis

Transitional metals and their complexes have been investigated by computational chemistry. The band gap energy (E_g) is correlated with various biological aspects like antibacterial, antioxidant and DNA binding activities (Ismael et al. 2020). It has been reported that the band gap energy between the E_{HOMO} and E_{LUMO} is an important stability descriptor (Balajee et al. 2016). A large band gap energy is associated with stable systems, whereas small band gap energy is associated with little stable systems making more reactive compound (Balajee et al. 2016). A decrease in the band gap energy upon coordination may be associated with the presence of LMCT (Ismael et al., 2020). The energy gap ($E_g = E_{LUMO} - E_{HOMO}$) for possible electron transition were calculated to be 3.834, 4.002, 3.272, 3.684, 3.669 and 3.991 eV for the **H_3L** and its complexes **1 – 5** respectively.

The chemical reactivity of the complexes increases with decrease in the energy gap (ΔE) values. In other ways, the complexation between the metal ions and the ligand has reduced the HOMO–LUMO energy gap (Fig. 19 and 20), which can be considered as an indication for better biological activities (Ali et al. 2019; Ismael et al. 2020). Accordingly, from the band gap analyses, the metal complexes were predicted to have better biological activities than the free ligand, in good agreement with the experimental biological activities.

Table 4: The HOMO, LUMO, energy gap (*Eg*), chemical potential (*μ),* hardness (η), softness (*σ*), electrophilicity (ω), nucleophilicity index (Nu) of the ligands and complexes

Cpds.	HOMO	LUMO	Eg(eV)	μ	η	σ	ω	Nu
H_3L	-5.960	-2.126	3.834	4.043	1.917	0.261	4.264	0.235
1	-6.364	-2.362	4.002	4.363	2.001	0.250	4.756	0.210
2	-6.571	-3.299	3.272	4.935	1.636	0.306	7.445	0.134
3	-6.219	-2.536	3.684	4.378	1.842	0.921	5.202	0.192
4	-6.303	-2.634	3.669	4.468	1.834	0.273	5.441	0.184
5	-7.158	-3.167	3.991	5.163	1.996	0.998	6.678	0.150

The biological activity of the complexes toward appropriate molecules can be discussed with the hard–soft–acid–base (HSAB) principle, which states that soft acids prefer to bind with soft bases and hard acids prefer to bind with hard bases (Ismael et al. 2020). Hence, the biological activity of a compound increases with increasing softness and decreasing hardness. Accordingly, the biological structures of enzymes, which are commonly soft, prefer to bind with soft complexes. The order of chemical hardness (η) it is possible to suggesting that complex **1** is more stable. This is in agreement with the TGA analysis. In other way, chemical potential (μ) measures tendency of an electron to escape from equilibrium, and the chemical reactivity of a compound increases with decreasing chemical potential. Chemical potential (μ) is also directly proportional with the Gibbs free energy and related to spontaneity.

The electrophilicity index implies the ability of the complexes to accept electrons, while nucleophilicity index displays the ability to donate electrons (Ismael et al. 2020). In this aspect, complex 2 has stronger electron accepting potential than the remaining complexes while the free ligand is more electron donor, based on their electrophilicity index and nucleophilicity index value, respectively (Table 4). This activity is in line with antioxidant properties of complex 2.

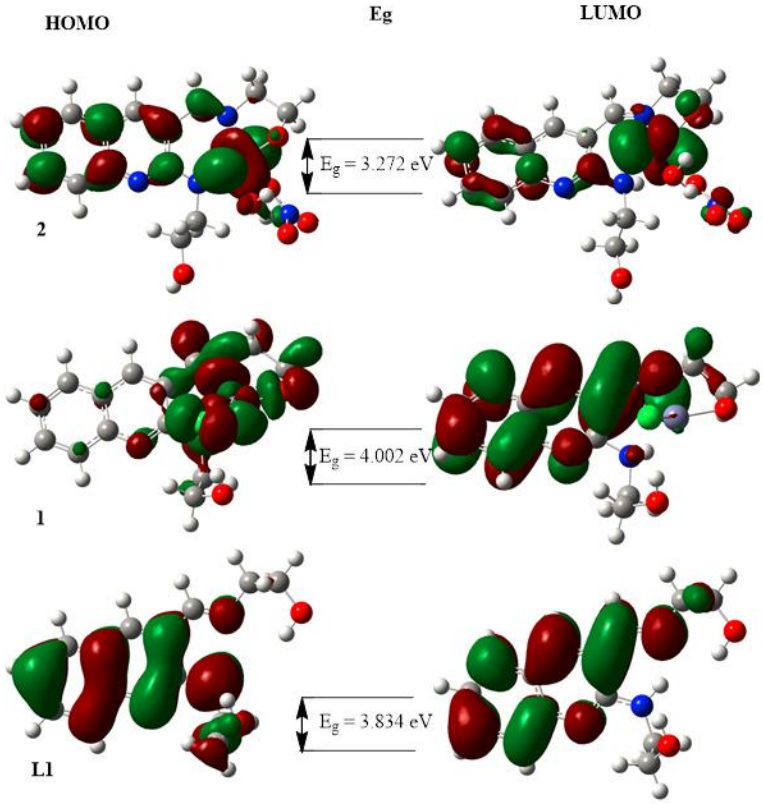

Figure 19: The HOMO and LUMO of **H_3L, 1** and **2** (DFT/ B3LYP/6-311++Gdp)

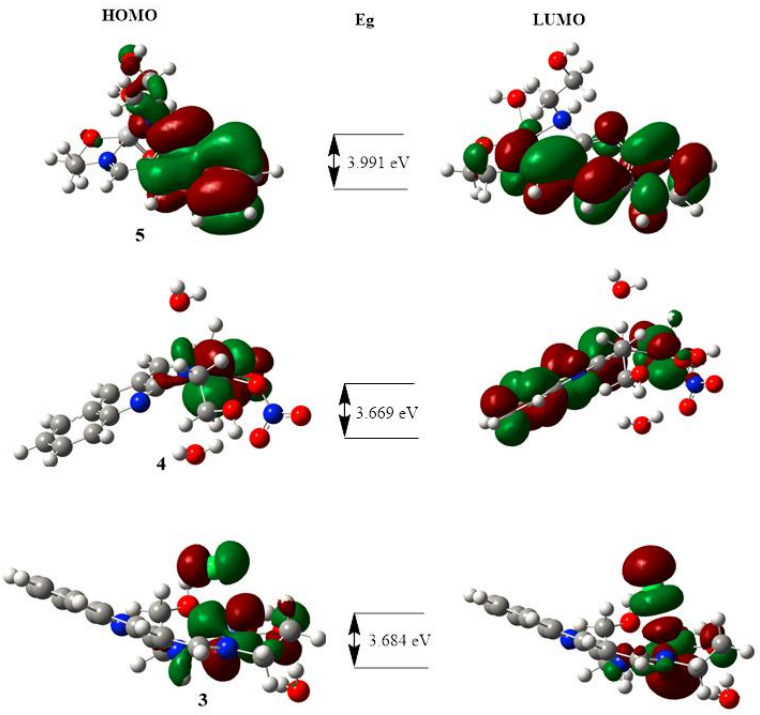

Figure 3: The HOMO and LUMO of **3, 4** and **5** (DFT/ B3LYP/6-311++Gdp)

3.4.3. Molecular Docking Analysis

Bioactive molecules inhibit either the reproduction of pathogenic bacteria or kill them by acting on some essential components of bacterial strains. DNA gyrase is one of the essential enzymes which induce negative supercoils into bacterial DNA. In this aspect, the fluoroquinolones are among DNA gyrase-targeted drugs (Collin, Karkare, and Maxwell 2011). Some bacteria also secrete a variety of toxic substances, including exotoxin A (ETA), phospholipases, and several proteases. *P. aeruginosa* is opportunistic pathogenic bacteria which activate the expression of LasR gene required for transcription of the genes for elastase (LasA and LasB) protease, associated with virlence (Suneby, Herndon, and Schneider 2017). Therefore, the molecular docking of the complexes were docked against DNA gyrase of *E. coli* and LasR of *P. aeruginosa* to investigate their mode of action and the results were compared with the *in vitro* antibacterial activities. We studied the molecular interaction between the synthesized ligand and its complexes against the *E.coli* DNA gyrase (PDB ID 6F86) to understand the mechanism of action. Autodock 4.2 was used to explore the protein-ligand interactions between complexes and *E.coli* DNA gyrase (PDB ID 6F86) (Fig. 21 – 23). The compounds interacted with the key amino acids by forming hydrogen bond with Asp-73, Gly-77, Thr-165, and hydrophobic interaction with Ile-78, Ile-94, Glu-50, and Pro-79 within the active site. The results clearly show that the free hydroxyl chain in the complexes was interacted with the amino acids within the active sites of the protein. The *in vitro* antimicrobial analysis results are matching with the molecular docking analysis.

The metal complexes have shown significant interactions within the active site of the LasR. DNA protein with the key amino acids, Tyr-47, Trp-60, Asp-73, Tyr-64, Leu-36, Trp-88, Arg-61, Thr-75, Cys-79, and Ala-127. All the investigated compounds showed moderate to equivalent binding scores compared to the clinical drug ciprofloxacin. The overall *in silico* docking analysis indicated that the Cu (II) complex interacted with the LasR.DNA residues of Tyr-47 (H-bond), Trp-60, Asp-73, Tyr-64, Leu-36, Arg-61, Thr-75, and Ala-127 with binding energies of -8.2 kcal/mol. Similar docking activity trends were observed for both *E. coli* DNA gyrase B and *P. aeruginosa* LasR, in very good agreement with the *in vitro* bacterial activities.

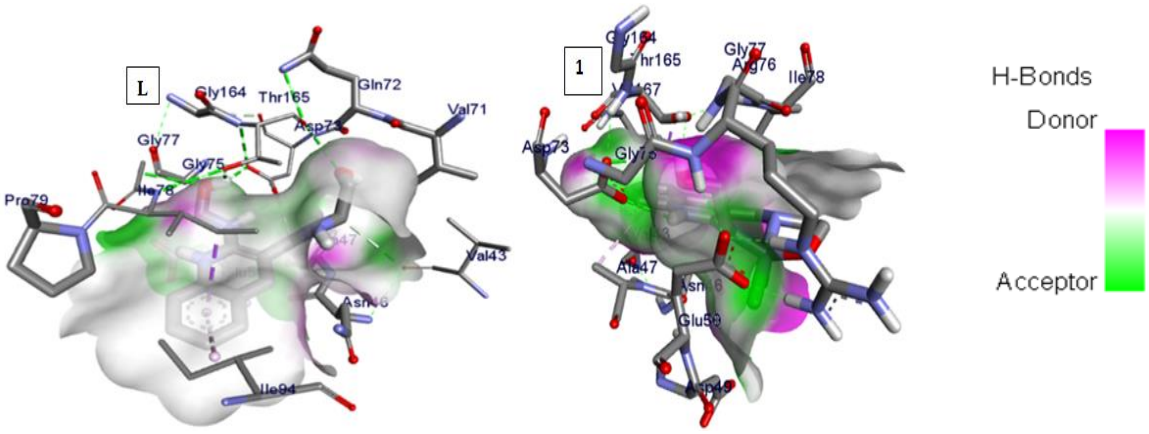

Figure 21: The interactions of **H_2L** and **1** against *E.Coli* DNA gyrase (PDB ID: 6F86)

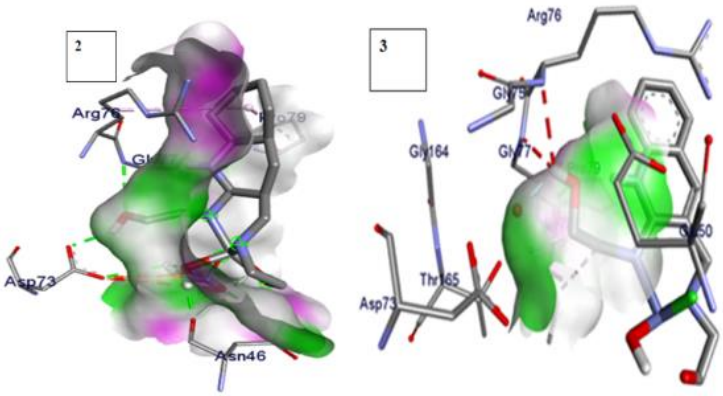

Figure 22: The interactions of **2** and **3** against *E.Coli* DNA gyrase (PDB ID: 6F86)

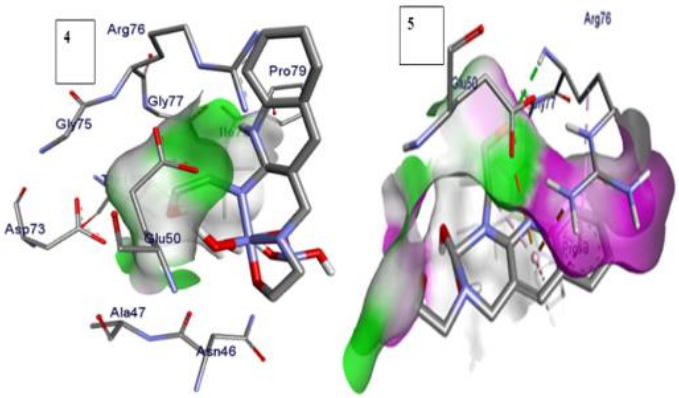

Figure 23: The interactions of **4** and **5** against *E.Coli* DNA gyrase (PDB ID: 6F86)

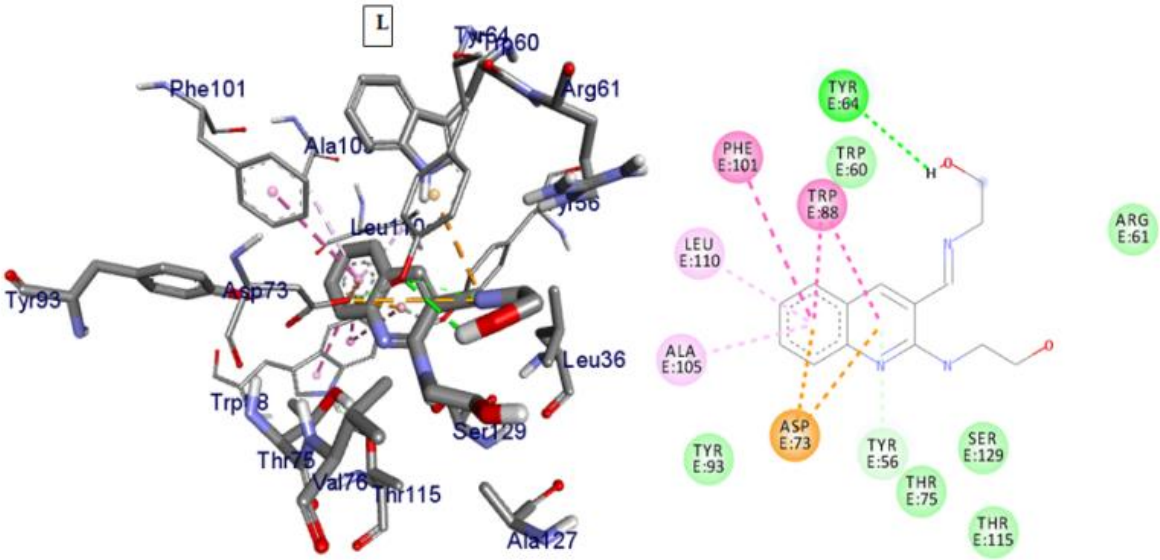

Figure 24: The interactions of **H_3L** against *P. aeruginosa* LasR.DNA (PDB: 2UV0)

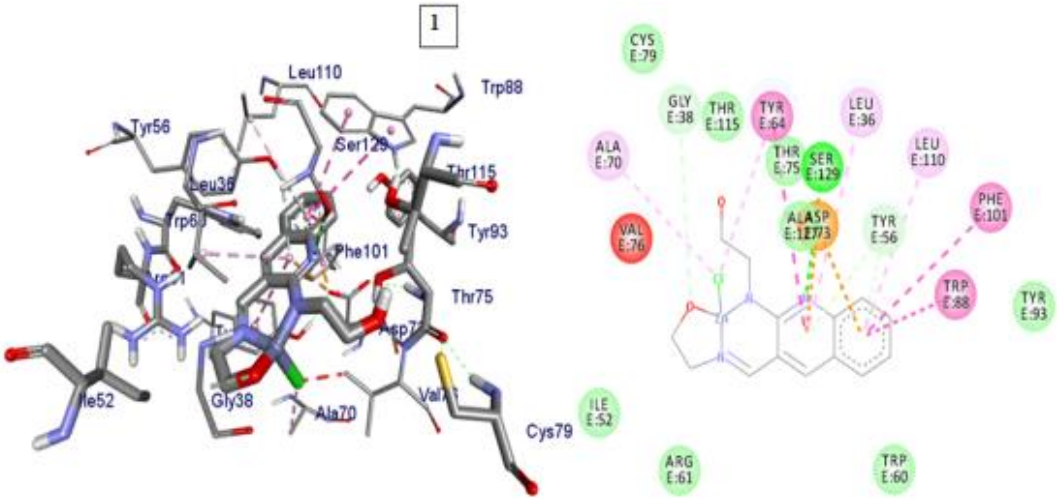

Figure 25: The interactions of **1** against *P. aeruginosa* LasR.DNA (PDB: 2UV0)

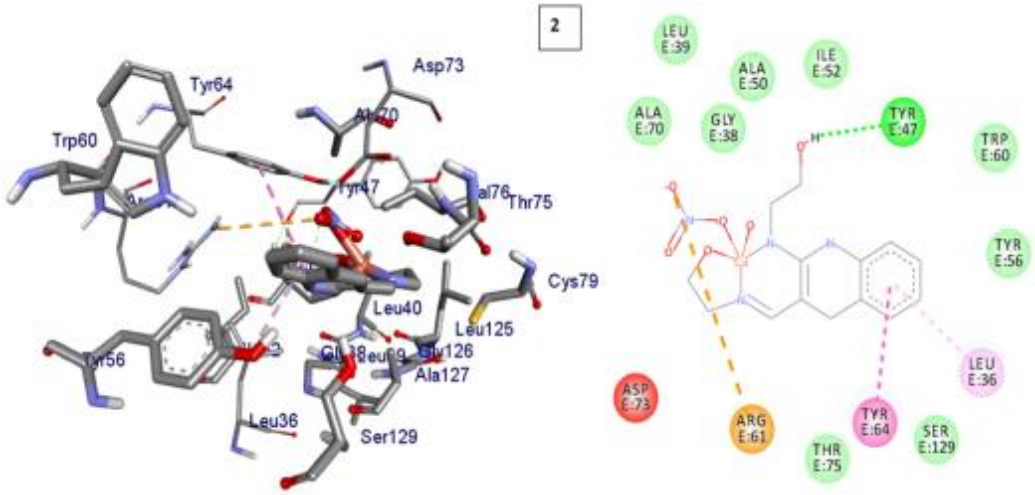

Figure 26: The interactions of **2** against *P. aeruginosa* LasR.DNA (PDB: 2UV0).

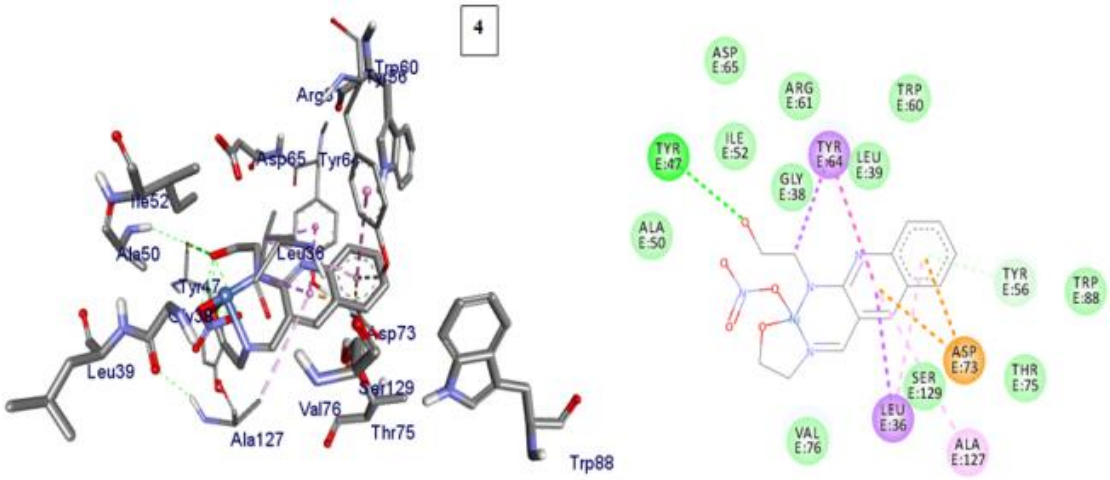

Figure 27: The interactions of **4** against *P. aeruginosa* LasR.DNA (PDB: 2UV0)

4. CONCLUSIONS

Quinoline derivatives have been a successful scaffold to develop bioactive molecules. In the present work, novel Zn(II), Cu(II), Co(II), Ni(II) and V(IV) complexes were successfully synthesized from a tridentate ONN atoms donor ligand. The compounds were characterized by physicochemical and spectroscopic methods. The analysis was supported by DFT and TD-DFT calculations. From both experimental (EDX, MS and TGA) and DFT analysis, the **H_3L** acts as an ONN donor tridentate chelating agent. The analyses also indicated that the complex **1** has a distorted tetrahedral geometrical structure, on the other hand, the complex **2** showed distorted square pyramidal geometry similarly, complex **3** showed octahedral, while that of complex **4** has square planar geometry and complex **5,** showed octahedral structure. The stability of the metal complexes of **H_3L** are ($K_{Zn(II)} = 2.3 \times 10^6$, $K_{Cu(II)} = 2.9 \times 10^6$, $K_{Co(II)} = 1.10 \times 10^8$, $K_{Ni(II)} = 3.8 \times 10^5$ and $K_{V(IV)} = 7.6 \times 10^5$). All metal complexes are stable at the specified temperatures, and the thermodynamic parameters indicated that the reactions are spontaneous with exothermic nature of metal-ligand interactions. All the **1 – 4** complexes exhibited good activities with *P. aeruginosa* (18.85 ± 0.34, 20.65 ± 0.18, 18.62 ± 0.19 and 15.64 ± 0.22 mm diameter, respectively) compared to ligand. Complex **2** showed higher percent activity index (*AI* = 62, 90%), than all Zn(II) (*AI* = 54, 82%), Co (*AI* = 54, 81%) and Ni(II) (*AI* = 41, 68%) complexes against both *E. coli* and *P. aeruginosa*, respectively. The complexes **1, 2** exhibited higher values of antioxidant activities (IC_{50} = 8.62, 4.70. From the *in silico (*drug likeness and molecular docking) analysis all complexes (**1 – 5**) fulfil Lipinski's rule of five. Overall, the newly synthesized Zn(II), Cu(II), Co(II), and Ni(II) complexes have biological activities, whereas the Cu(II) complex showed much better activity than other complexes. The results of binding mode of these compounds against *E. coli* DNA gyrase B were in good agreement with the *in vitro* biological activity results. The higher antibacterial activity of Cu(II) complex against Gram-negative bacteria makes the complex potential alternative drug for treating diseases caused by Gram-negative bacteria after passing cytotoxicity testing. In other ways the compounds that can scavenge DPPH radicals might exhibit anticancer, antiaging, anti-inflammatory activities. Hence our complexes have pronounced DPPH radical scavenging activities, they may have the anticancer and antidiabetic related activities and the door is open for any interested researchers.

ACKNOWLEDGEMENTS

The authors would like to acknowledge ASTU, Wachemo University and University of Botswana for the research facilities. Computational resources were supplied by the project "e-Infrastruktura CZ" (e-INFRA CZ ID:90140) supported by the Ministry of Education, Youth and Sports of the Czech Republic.

REFERENCES

Abu-Dief, Ahmed M., Nashwa M. El-Metwaly, Seraj Omar Alzahrani, Fatmah Alkhatib, Matokah M. Abualnaja, Tarek El-Dabea, and Mahmoud Abd El Aleem Ali Ali El-Remaily. 2021. "Synthesis and Characterization of Fe(III), Pd(II) and Cu(II)-Thiazole Complexes; DFT, Pharmacophore Modeling, in-Vitro Assay and DNA Binding Studies." *Journal of Molecular Liquids* 326:1–15.

Al-Hazmi, Gamil A. A., Khlood S. Abou-Melha, Nashwa M. El-Metwaly, Ismail Althagafi, Fathy Shaaban, and Rania Zaky. 2020. "Green Synthesis Approach for Fe (III), Cu (II), Zn (II) and Ni (II)-Schiff Base Complexes, Spectral, Conformational, MOE-Docking and Biological Studies." *Applied Organometallic Chemistry* 34(3):1–15.

Ali, Ibrahim A. I., Sahar S. A. El-Sakka, Mohamed H. A. Soliman, and Omayma E. A. Mohamed. 2019. "In Silico, In Vitro and Docking Applications for Some Novel Complexes Derived from New Quinoline Derivatives." *Journal of Molecular Structure* 1196:8–32.

Alomar, Kusaï, Anne Landreau, Magali Allain, Gilles Bouet, and Gérald Larcher. 2013. "Synthesis, Structure and Antifungal Activity of Thiophene-2,3- Dicarboxaldehyde Bis(Thiosemicarbazone) and Nickel(II), Copper(II) and Cadmium(II) Complexes: Unsymmetrical Coordination Mode of Nickel Complex." *Journal of Inorganic Biochemistry* 126:76–83.

Aly, Ashraf A., Mohamed Ramadan, Gamal El Din A. Abuo-Rahma, Yaseen A. M. M. Elshaier, Mohammed A. I. Elbastawesy, Alan B. Brown, and Stefan Bräse. 2020. "Quinolones as Prospective Drugs: Their Syntheses and Biological Applications." *Advances in Heterocyclic Chemistry* 1–50.

Ambala, Anilkumar, and Ch Abraham Lincoln. 2020. "Synthesis, Characterization, Antimicrobial Activity and DNA Cleavage Study of (E)-2-(((2-(P-Tolyloxy)Quinolin-3-Yl)Methylene)Amino)Benzenethiol Schiff Base Metal Complexes." *Chemical Data Collections* 27:1–6.

Atta-ur-Rahman, M. Iqbal Choudhary, William J. Thomson, Arena Pharmaceuticals, San Diego, and USA. 2001. *Bioassay Techniques for Drug Development*.

Azam, Mohammad, Saikh Mohammad Wabaidur, Mahboob Alam, Agata Trzesowska-Kruszynska, Rafal Kruszynski, Saud I. Al-Resayes, Fahad Fahhad Alqahtani, Mohammad Rizwan Khan, and Rajendra. 2021. "Design, Structural Investigations and Antimicrobial Activity of Pyrazole Nucleating Copper and Zinc Complexes." *Polyhedron* 195:1–10.

Badwaik, V. B., R. D. Deshmukh, and A. S. Aswar. 2009. "Transition Metal Complexes of a Schiff Base: Synthesis, Characterization, and Antibacterial Studies." *Journal of Coordination Chemistry* 62(12):2037–47.

Balajee, R., V. Srinivasadesikan, M. Sakthivadivel, and P. Gunasekaran. 2016. "In Silico Screening, Alanine Mutation, and DFT Approaches for Identification of NS2B/NS3 Protease Inhibitors." *Biochemistry Research International* 2016:1–13.

Belkhir-Talbi, Drifa, Naima Ghemmit-Doulache, Souhila Terrachet-Bouaziz, Malika Makhloufi-Chebli, Amal Rabahi, Lhassane Ismaili, and Artur M. S. Silva. 2021. "Transition-Metal Complexes of N,N′-Di(4-Bromophenyl)-4-Hydroxycoumarin-3-Carboximidamide: Synthesis, Characterization, Biological Activities, ADMET and Drug-Likeness Analysis." *Inorganic Chemistry Communications* 127(March):1–12.

Betanzos-Lara, Soledad, Celedonio Gómez-Ruiz, Lidia R. Barrón-Sosa, Isabel Gracia-Mora, Marcos Flores-Álamo, and Noráh Barba-Behrens. 2012. "Cytotoxic Copper(II), Cobalt(II), Zinc(II), and Nickel(II) Coordination Compounds of Clotrimazole." *Journal of Inorganic Biochemistry* 114:82–93.

Chen, Shao Chun, Jing Wei Liu, Xing Zhong Wu, Wenling Cao, Feng Wang, Jin Mei Huang, Yan Han, Xiao Yu Zhu, Bang Yong Zhu, Quan Gan, Xiao Zheng Tang, Xing Shen, Xiao Lin Qin, Yu Qi Yu, He Ping Zheng, and Yue Ping Yin. 2020. "Comparison of Microdilution Method with Agar Dilution Method for Antibiotic Susceptibility Test of Neisseria Gonorrhoeae." *Infection and Drug Resistance* 13:1775–80.

Chiriac, H., A. E. Moga, and C. Gherasim. 2008. "Synthesis and Characterization of Co and Ni Magnetic Nanoparticles." *Journal of Optoelectronics and Advanced Materials* 10(3):654–58.

Collin, Frédéric, Shantanu Karkare, and Anthony Maxwell. 2011. "Exploiting Bacterial DNA Gyrase as a Drug Target: Current State and Perspectives." *Applied Microbiology and Biotechnology* 92(3):479–97.

Daina, Antoine, Olivier Michielin, and Vincent Zoete. 2017. "SwissADME: A Free Web Tool to Evaluate Pharmacokinetics, Drug-Likeness and Medicinal Chemistry Friendliness of Small Molecules." *Scientific Reports* 7(October 2016):1–13.

Digafie, Zeleke, Yadessa Melaku, Zerihun Belay, and Rajalakshmanan Eswaramoorthy. 2021. "Synthesis , Molecular Docking Analysis , and Evaluation of Antibacterial and Antioxidant Properties of Stilbenes and Pinacol of Quinolines." *Advances in Pharmacological and Pharmaceutical Sciences* 2021:1–17.

El-Gammal, Ola A., Farid Sh Mohamed, Ghada N. Rezk, and Ashraf A. El-Bindary. 2021. "Synthesis, Characterization, Catalytic, DNA Binding and Antibacterial Activities of Co(II), Ni(II) and Cu(II) Complexes with New Schiff Base Ligand." *Journal of Molecular Liquids* 326:1–17.

El-Sonbati, A. Z., M. A. Diab, G. G. Mohamed, and M. A. Saad. 2019. "Polymer Complexes. LXXVII. Synthesis, Characterization, Spectroscopic Studies and Immune Response in Cattle of Quinoline Polymer Complexes." *Applied Organometallic Chemistry* 33(8):1–13.

El-Sonbati, A. Z., M. A. Diab, Sh M. Morgan, M. I. Abou-Dobara, and A. A. El-Ghettany. 2020. "Synthesis, Characterization,

Theoretical and Molecular Docking Studies of Mixed-Ligand Complexes of Cu(II), Ni(II), Co(II), Mn(II), Cr(III), UO2(II) and Cd(II)." *Journal of Molecular Structure* 1200(2020):1–17.

El-Sonbati, Adel Z., Mostafa A. Diab, Ahmed M. Eldesoky, Shaimaa M. Morgan, and Omnia L. Salem. 2019. "Polymer Complexes. LXXVI. Synthesis, Characterization, CT-DNA Binding, Molecular Docking and Thermal Studies of Sulfoxine Polymer Complexes." *Appl. Organomet. Chem.* 33(5):1–22.

Hamdani, H. EL, and M. EL Amane. 2019. "Preparation, Spectral, Antimicrobial Properties and Anticancer Molecular Docking Studies of New Metal Complexes [M(Caffeine) 4] (PF 6) 2; M = Fe(II), Co(II), Mn(II), Cd(II), Zn(II), Cu(II), Ni(II)." *Journal of Molecular Structure* 1184:262–70.

Indira, S., G. Vinoth, M. Bharathi, and K. Shanmuga Bharathi. 2019. "Synthesis, Spectral, Electrochemical, in-Vitro Antimicrobial and Antioxidant Activities of Bisphenolic Mannich Base and 8-Hydroxyquinoline Based Mixed Ligands and Their Transition Metal Complexes." *Journal of Molecular Structure* 1198:1–8.

Ismael, Mohamed, Abdel Mawgoud M. Abdel-Mawgoud, Mostafa K. Rabia, and Aly Abdou. 2020. "Design and Synthesis of Three Fe(III) Mixed-Ligand Complexes: Exploration of Their Biological and Phenoxazinone Synthase-like Activities." *Inorg. Chim. Acta* 505(December 2019):1–11.

Kargar, Hadi, Amir Adabi Ardakani, Muhammad Nawaz Tahir, Muhammad Ashfaq, and Khurram Shahzad Munawar. 2021. "Synthesis, Spectral Characterization, Crystal Structure and Antibacterial Activity of Nickel(II), Copper(II) and Zinc(II) Complexes Containing ONNO Donor Schiff Base Ligands." *Journal of Molecular Structure* 1233:1–12.

Khojasteh, Siamak Cyrus, Harvey Wong, and Cornelis E. C. A. Hop. 2011. *Drug Metabolism and Pharmacokinetics Quick Guide*.

Koleša-Dobravc, Tanja, Keiichi Maejima, Yutaka Yoshikawa, Anton Meden, Hiroyuki Yasui, and Franc Perdih. 2018. "Bis(Picolinato) Complexes of Vanadium and Zinc as Potential Antidiabetic Agents: Synthesis, Structural Elucidation and: In Vitro Insulin-Mimetic Activity Study." *New Journal of Chemistry* 42(5):3619–32.

Krasnovskaya, Olga, Alexey Naumov, Dmitry Guk, Peter Gorelkin, Alexander Erofeev, Elena Beloglazkina, and Alexander Majouga. 2020. "Copper Coordination Compounds as Biologically Active Agents." *Int.J. of Molecular Sciences* 21(11).

Li, Yun, Yueqin Li, Xiaohui Liu, Yong Yang, Dong Lin, and Qinwei Gao. 2020. "The Synthesis, Characterization, DNA/Protein Interaction, Molecular Docking and Catecholase Activity of Two Co(II) Complexes Constructed from the Aroylhydrazone Ligand." *Journal of Molecular Structure* 1202:1–15.

Lipinski, Christopher A., Franco Lombardo, Beryl W. Dominy, and Paul J. Feeney. 2012. "Experimental and Computational Approaches to Estimate Solubility and Permeability in Drug Discovery and Development Settings." *Advanced Drug Delivery Reviews* 64(SUPPL.):4–17.

Mandewale, Mustapha C., Santosh Kokate, Bapu Thorat, Sudhir Sawant, and Ramesh Yamgar. 2019. "Zinc Complexes of Hydrazone Derivatives Bearing 3,4-Dihydroquinolin-2(1H)-One Nucleus as New Anti-Tubercular Agents." *Arabian Journal of Chemistry* 12(8):4479–89.

Nagesh, G. Y., K. Mahendra Raj, and B. H. M. Mruthyunjayaswamy. 2015. "Synthesis, Characterization, Thermal Study and Biological Evaluation of Cu(II), Co(II), Ni(II) and Zn(II) Complexes of Schiff Base Ligand Containing Thiazole Moiety." *Journal of Molecular Structure* 1079:423–32.

Nainwal, Lalit Mohan, Sharba Tasneem, Wasim Akhtar, Garima Verma, Mohammed Faraz Khan, Suhel Parvez, Mohammad Shaquiquzzaman, Mymoona Akhter, and Mohammad Mumtaz Alam. 2019. "Green Recipes to Quinoline: A Review." *European Journal of Medicinal Chemistry* 164:121–70.

Patel, R. N., Yogendra Pratap, and Yogendra Singh. 2017. "New Oxidovanadium(V) Complexes with NNO Donor Schiff Bases: Synthesis, Crystal Structures and Electrochemical Studies." *Polyhedron* 133:102–9.

Ramachandran, Eswaran, Valentina Gandin, Roberta Bertani, Paolo Sgarbossa, Karuppannan Natarajan, Nattamai S. P. Bhuvanesh, Alfonso Venzo, Alfonso Zoleo, Antonella Glisenti, Alessandro Dolmella, Alberto Albinati, and Cristina Marzano. 2018. "Synthesis, Characterization and Cytotoxic Activity of Novel Copper(II) Complexes with Aroylhydrazone Derivatives of 2-Oxo-1,2-Dihydrobenzo[h]Quinoline-3-Carbaldehyde." *Journal of Inorganic Biochemistry* 182(September 2017):18–28.

Ramachandran, Eswaran, Duraisamy Senthil Raja, Nattamai S. P. Bhuvanesh, and Karuppannan Natarajan. 2013. "Synthesis, Characterization and in Vitro Pharmacological Evaluation of New Water Soluble Ni(II) Complexes of 4N-Substituted Thiosemicarbazones of 2-Oxo-1,2-Dihydroquinoline-3-Carbaldehyde." *European J. of Medicinal Chem.* 64(3):179–89.

Sehimi, Hiba, Badiaa Essghaier, Elisa Barea, Najla Sadfi-Zouaoui, and Mohamed Faouzi Zid. 2019. "Synthesis, Structural Study, Magnetic Susceptibility and Antimicrobial Activity of the First (μ-Oxo)-Bis(Oxalato)-Vanadium(IV) 1D Coordination Polymer." *Journal of Molecular Structure* 1175:865–73.

Senthil Raja, Duraisamy, Nattamai S. P. Bhuvanesh, and Karuppannan Natarajan. 2012. "Synthesis, Crystal Structure and Pharmacological Evaluation of Two New Cu(II) Complexes of 2-Oxo-1,2-Dihydroquinoline-3-Carbaldehyde (Benzoyl) Hydrazone: A Comparative Investigation." *European Journal of Medicinal Chemistry* 47(1):73–85.

Senthil Raja, Duraisamy, Eswaran Ramachandran, Nattamai S. P. Bhuvanesh, and Karuppannan Natarajan. 2013. "Synthesis,

Structure and in Vitro Pharmacological Evaluation of a Novel 2-Oxo-1,2-Dihydroquinoline-3-Carbaldehyde (2′-Methylbenzoyl) Hydrazone Bridged Copper(II) Coordination Polymer." *European Journal of Medicinal Chemistry* 64:148–59.

Skyrianou, Kalliopi C., Eleni K. Efthimiadou, Vassilis Psycharis, Aris Terzis, Dimitris P. Kessissoglou, and George Psomas. 2009. "Nickel-Quinolones Interaction. Part 1 - Nickel(II) Complexes with the Antibacterial Drug Sparfloxacin: Structure and Biological Properties." *Journal of Inorganic Biochemistry* 103(12):1617–25.

Sumalatha, V., Sreenu Daravath, Aveli Rambabu, Gali Ramesh, and Shivaraj. 2021. "Antioxidant, Antimicrobial, DNA Binding and Cleavage Studies of Novel Co(II), Ni(II) and Cu(II) Complexes of N, O Donor Schiff Bases: Synthesis and Spectral Characterization." *Journal of Molecular Structure* 1229:1–14.

Suneby, Emma G., Leslie R. Herndon, and Tanya L. Schneider. 2017. "Pseudomonas Aeruginosa LasR·DNA Binding Is Directly Inhibited by Quorum Sensing Antagonists." *ACS Infectious Diseases* 3(3):183–89.

Sutradhar, Manas, Tannistha Roy Barman, Saktiprosad Ghosh, and Michael G. B. Drew. 2013. "Synthesis and Characterization of Mixed-Ligand Complexes Using a Precursor Mononuclear Oxidovanadium(V) Complex Derived from a Tridentate Salicylhydrazone Oxime Ligand." *Journal of Molecular Structure* 1037:276–82.

Wiegand, Irith, Kai Hilpert, and Robert E. W. Hancock. 2008. "Agar and Broth Dilution Methods to Determine the Minimal Inhibitory Concentration (MIC) of Antimicrobial Substances." *Nature Protocols* 3(2):163–75.

Zhu, Shuang-Shuang, Xin Dong, and Zhao-Hui Zhou. 2019. "Mixed Ligand Oxidovanadium(IV) Complexes: Synthesis, Spectral, Structural Characterization and Catalytic Degradations of Methyl Orange." *Inorganica Chimica Acta* 486(October 2018):395–400.

Zordok, W. A., and S. A. Sadeek. 2018. "Synthesis, Spectroscopic Characterization, Biological Studies and DFT Calculations on Some Transition Metal Complexes of NO Donor Ligand." *Journal of Molecular Structure* 1158:205–20.

Nanomaterials Based Electronic Thermometer Design and Development

Almaw Ayele Aniley*

School of Electrical and Computer Engineering, Debre Markos University, Debre Markos, Ethiopia
**Corresponding author, e-mail: lingerayele@gmail.com*

ABSTRACT

Temperature is defined as the measure of the average kinetic energy of the particles in materials. It is a fundamental quantity which affects any object and process including industrial processes, electrical systems' components, life and health of living things, agricultural soil, bridges, highways, buildings, dams, environment, etc. So, it should be properly quantified and controlled using highly accurate, precise, environmentally friendly, in-situ, low-power and inexpensive thermometers. There are many kinds of thermometers with the disadvantages of high-power requirement, possession of poison sensing materials, high cost, inaccurate and imprecise. Here, we discuss the development of nanoceramic nickel manganate ($NiMn_2O_4$) thermistor powder based digital electronic thermometer probe. The nanomaterial was synthesized using acetates of Nickel (Ni) and Manganese (Mn) as precursor materials by using the solution route technique. The fabricated powder was characterized using field emission scanning electronic microscopy (FeSEM) and energy dispersive spectroscopy (EDS) for its morphology and composition respectively. Powder x-ray diffraction (XRD) was also used to determine the crystal structure and crystallite size of the sample. The sample is unformed in morphology, spinel in structure, 24 nm in average crystallite size and composed of Ni, Mn and O_2 in the proper ratio. About 0.35 gm of the powder was filled and pressed well in 2 mm diameter and 2 cm long cylindrical tube to fabricate and characterize the thermistor-based thermometer. The resulting thermistor was characterized and calibrated using the Stein and Hart and the β-coefficient thermistor models. The embedded system for the thermometer was developed using atmega328 microprocessor-based microcontroller, a simple voltage divider electric circuit, stainless steel cylindrical tube and 3D printed package. The system was programmed using Arduino programming integrated development environment (Arduino IDE). The features of resulting thermometer are 4-digit precision, 0 ℃-70 ℃ range of temperature measurement, 5 V DC power supply requirement, contains environmentally friendly chemicals and is highly accurate. It can be used primarily in agriculture. It can also be used in industry, medicine, automobile, environment, food processing, home automation, etc. Additionally, it can be the element of sensor nodes in wireless sensor networks (WSNs) and Internet of Things (IoT) technology in automation.

Keywords: *Thermometer probe, nanoceramic, NiMn2O4, Digital*

1. INTRODUCTION

A thermometer is an instrument used to measure temperature. It is used in industry, medicine(Husain et al., 2014; Ota et al., 2017; Sun et al., 2018), agriculture (Aniley et al., 2017, 2019a, 2019b; Kumar et al., 2019), home automation (David et al. 2015; Hamed and Hamed 2015; Reza et al., 2018), food processing, environment, and research (Goswami and Kumar, 2018; Priyadarshi, 2015; Sahu et al., 2015). World metrological organization (WMO) defines temperature as a physical quantity characterizing the mean random motion of molecules in a physical object (IAEA, 2008). Temperature can also be defined as the measure of how much warm or cold an object is. In general, temperature affects both living and non-living things in any ecosystem. For example, in the soil and soil ecosystem (Zuk-Golaszewska et al., 2003) temperature affects photosynthesis (Arai-Sanoh et al., 2010; Cai and Dang, 2002; Shah and Paulsen, 2003), respiration (Wang, 2004), transpiration (Boselli et al., 1998; Cox and Boersma, 1967; Clements and Martin, 1931; Gardner and Ehlig, 1963; Pallas et al., 1967), the water potential of the soil (Caron and Boudreau, 2006; de Jong and Best 1979) soil translocation (Ge et al. 2015; Luan et al. 2014; Onwuka 2018; Trust and Phytologist, 2012), and microbial activities (Davidson and Janssens, 2006; Mew, 1977). Hence, it reduces crop product in terms of quantity and quality in agriculture (Valente *et al.*, 2006). Generally, it therefore affects the physio-chemical processes that are taken place on the earth.

Figure 1 depicts the different types of temperature measuring devices for different applications. The details of most of these devices are available in the original works like (Kedzierski, 1993; Fluke Corporation, 2006; Gruner, 2003; Aniley et al., 2017; Kumar et al., 2019). But, in this paper, only thermistors are going to be explained because of their own advantages discussed below over the others.

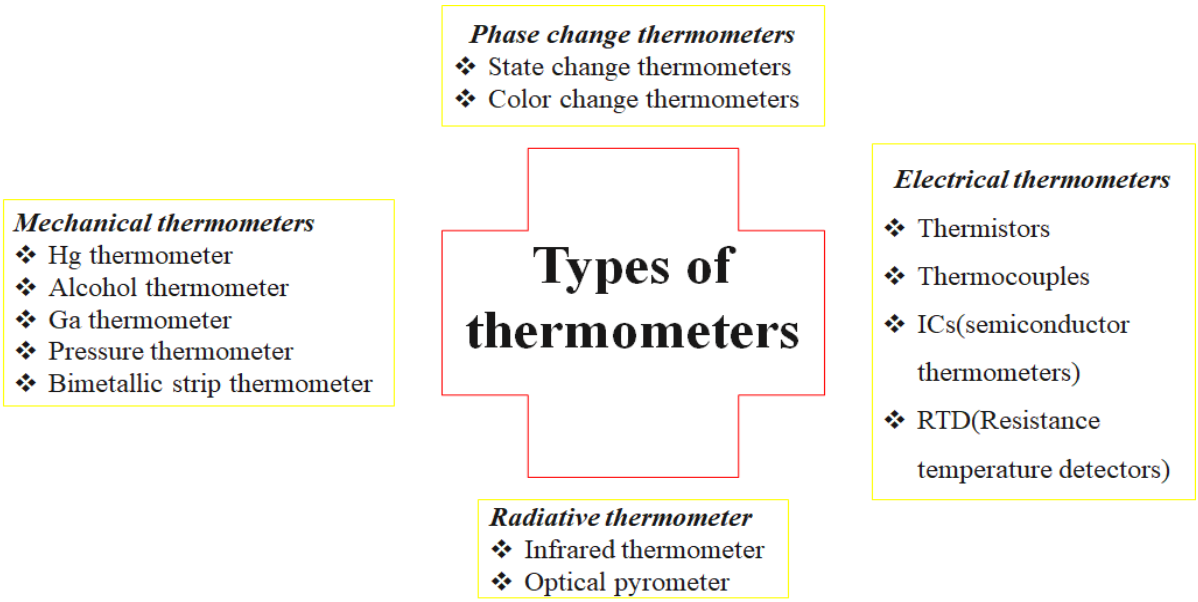

Figure 1: Classification of the available thermometers

The word thermistor is obtained from the two words thermal and resistor, as a **therm**ally sensitive res**istor** (Fraden, 2004, Jagtap et al., 2010). Based on the resistance temperature characteristics, thermistors can be classified as positive temperature coefficient resistance (PTCR) thermistors and negative temperature coefficient resistance (NTCR) thermistors. In PTCR thermistors as the temperature increases, the resistance also increases. But in the case of NTC thermistors the opposite event occurs. The first evidence for the NTCR behaviour was registered on 21 February 1833, by the English philosopher Michael Faraday, who observed the resistance of silver sulphide, Ag_2S, decreasing with increasing temperature (Fraden, 2010). Thermistors can also be classified as low temperature (-323-423K) and high temperature (423-1173K) thermistors depending on the range of temperature they can measure. Low-temperature thermistors can be synthesized from mixed oxides of Mn, Ni, and Co. The principal advantages of using thermistors in measuring temperatures are having a large change of resistance with temperature i.e.,10 times higher than that of metals; availability in a wide range of resistances; no need of reference junction; little affection by the usual chemical and physical conditions of the environment (can be fully secured); small and mechanically rugged.

Thermistors can be fabricated as pellets, discs, rods and thick films. For example, Jungho Ryu et al. fabricated NTC thermistor thick films of $NiMn_2O_4$ on the glass substrate by Aerosol Deposition (AD) at room temperature (RT) (Fluke Corporation, 2006). One big disadvantage of thick film thermistors is the presence of lead (Pb) as an adhesive material which is extremely toxic for life (Jagtap *et al.*, 2010). In addition, film fabrication techniques are complex and expensive.

In this work, synthesis and characterization of $NiMn_2O_4$ nanoceramic powder based and lead (Pb) free digital electronic thermometer probe fabrication, calibration and testing are implemented using simple and an economical method.

Thermistors are being used for many different areas of applications in every day to day activity of the society. To mention a few, they can be used as temperature sensors, inrush current limiters, self-resetting over-current protectors and self-regulating heating elements etc.

2. MATERIALS AND METHODS

2.1 Theory

There are two models for NTC thermistors, the Stein and Hart model and the β-coefficient models (Gregg Lavenuta, 2018). These models are given in equation (1) and equation (2) respectively.

$$\frac{1}{T(K)} = A + B.\ln(R) + C.(\ln(R))^3 \quad \ldots\ldots\ldots (1)$$

$$\frac{1}{T(K)} = \frac{1}{T_0(K)} + \frac{1}{\beta}\ln(\frac{R}{R_0}) \ldots\ldots\ldots\ldots\ldots\ldots\ldots (2)$$

Where, $T(k)$ is the temperature in degree Kelvin:A, B, and C are constants; R is the resistance of the thermistor in Ω; $T_o(K)$ is reference temperature; R_o is the resistance of the thermistor at a reference temperature. The constants can be obtained simultaneously from any three temperature and resistance measurement data of the given thermistor. Software applications such as srs thermistor calculator can be used to calculate the coefficients by providing the three resistance of the thermistor and the corresponding temperatures (Coefficient and Rt, 2012). It is also very simple to calculate the coefficients and the constants using paper and pencil method. A simple MATLAB code can also be written to solve any simultaneous equations in general.

From equation (2), β can be simplified and given in equation (3) to calculate β.

$$\beta = \frac{\ln(\frac{R}{R_0})}{\frac{1}{T(K)} - \frac{1}{T_0(K)}} \ldots\ldots\ldots\ldots\ldots\ldots\ldots\ldots\ldots\ldots (3)$$

2.2 Experiments

2.2.1 Synthesis of NIMN2O4 Nanoceramic Thermistor Powder

The $NiMn_2O_4$ nanoceramic powder was synthesized by a modified wet chemical method called solution route. The 0.002 Kgs. of tetra-hydrated nickel acetate and 0.00394 Kgs of tetra-hydrated manganese acetate powders were dissolved in 0.02 litre of distilled water each in separate beakers. Each solution was kept in a magnetic stirrer on a hot plate at a temperature of 310K for 1800 seconds. Then, we mixed the two solutions and kept the mixture in a hot plate for more than 1800 seconds. In addition, 0.0007 Kgs of oxalic acid was dissolved in 0.0l litre of distilled water in a separate beaker at room temperature. The second solution was added to the previous solution under vigorous stirring condition that facilitates the chemical reaction and gel formation process. Then, stirring was stopped and the resulting solution was kept at 343K on a hot plate until very thick solution was found. Next, the thick solution was dried in a muffle furnace at 373K for 600 seconds. Finally, the resulting powder was grounded using pestle and mortar which was then calcined in a muffle furnace at 1223K for 12600-14400 seconds. The synthesis setup, the resulting sample powder and the calcination process are shown in Figure(a, b & c) respectively.

Figure 2: Experimental setup (a) sample powder (b) and calcination(c)

FeSEM/EDS and powder XRD are used to characterize the surface morphology and average crystallite size, composition, and crystal structure of the resulting nanoceramic powder respectively.

2.2.2 Fabrication and Calibration of the Thermistor

Characterization and calibration setup is also shown in Figure **4** 4. For characterization and calibration, we have used LM35 temperature sensor self-interfaced with Atmega328 microprocessor-based microcontroller, homemade FTO coated glass heater, digital multimeter and computer loaded with the required software. The calibration experiment was conducted to relate the resistance and the temperature of the resulting thermistor. The experimental results were used for calculating thermistor-based thermometer modelling parameters. We have used the two thermistor modelling techniques, the Stein and Hart and the β-coefficient models. The thermistor modelling parameters are coefficients (A, B and C), the room temperature resistance (R_0), the room temperature (T_0) and β-coefficient or material constant.

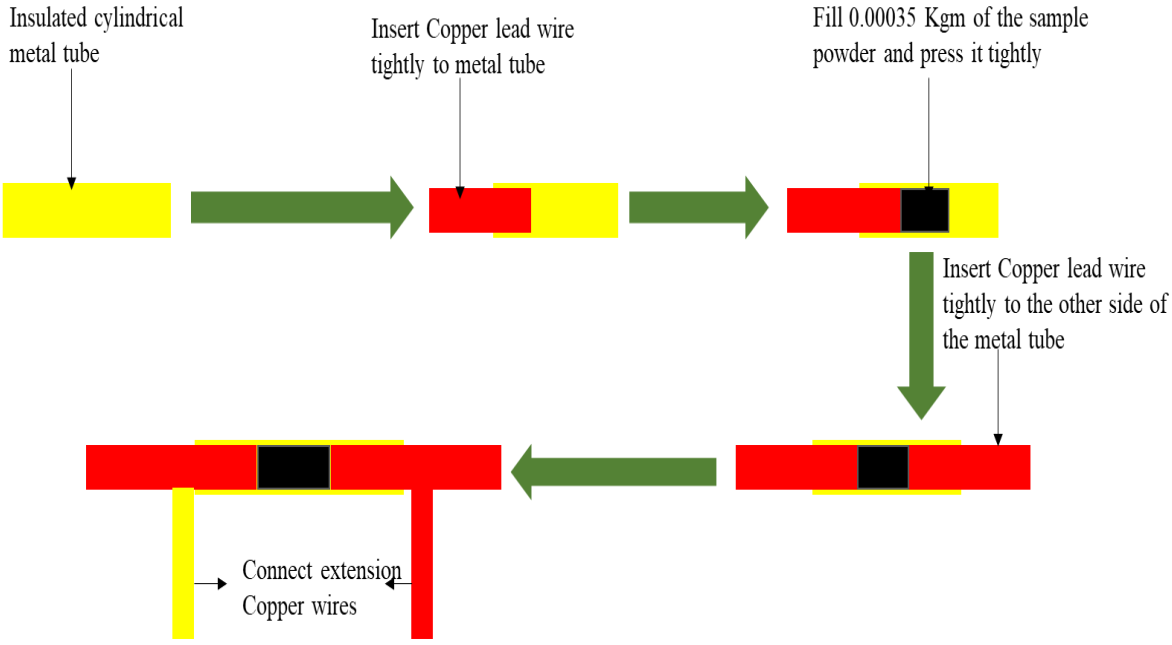

Figure 3: Fabrication process of the thermistor

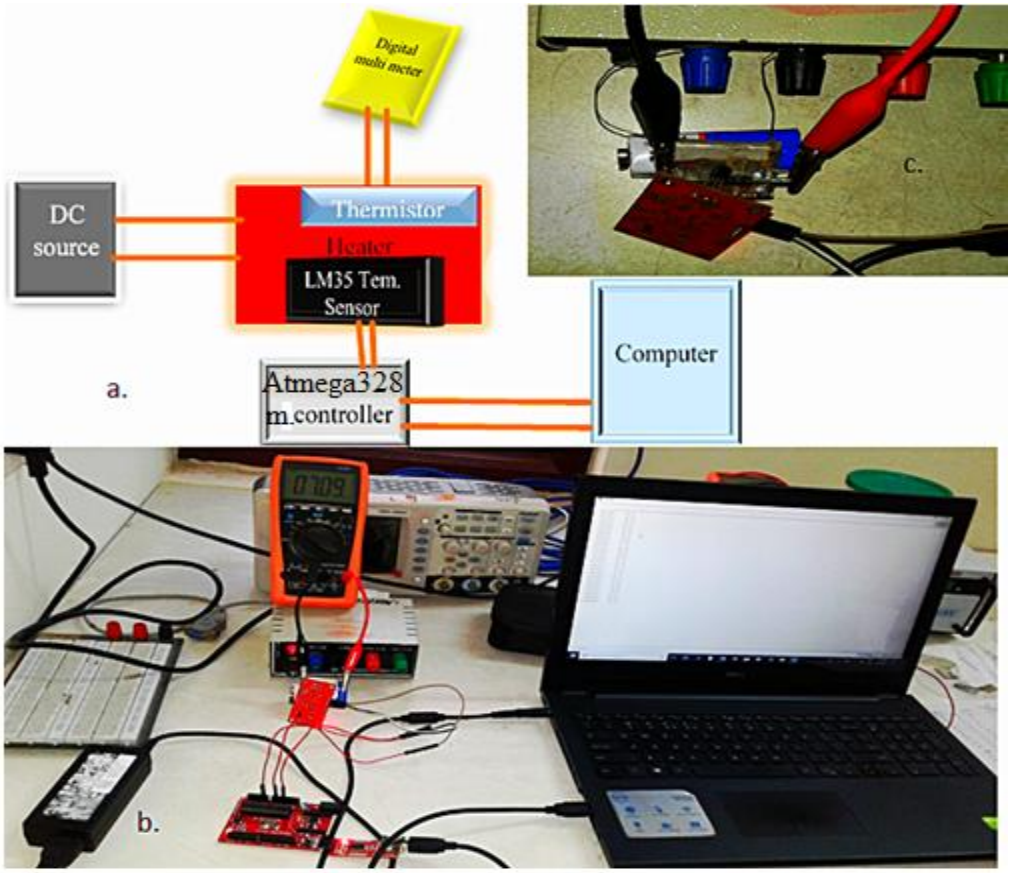

Figure 4: Characterization and calibration setup for the thermistor: (a) in block diagram; (b) physical characterization setup; (c) component interconnection

3. RESULTS AND DISCUSSION

3.1 $NIMN_2O_4$ Nanoceramic Thermistor Powder

The calcined powder was characterized using FeSEM/EDS for its morphology and particle size and composition respectively. The FeSEM result shows that the crystalline morphology of the ceramic powder and the size as is shown in Figure b whereas, the EDS result confirms that the powder contains Ni, Mn, and O_2 in appropriate proportion as shown in Figure a.

The X-ray powder diffraction (XRPD) analysis was conducted in a Rigaku X-ray diffractometer using Bragg–Brentano geometry in the continuous mode with speed of 0.00883/second. Cu Ka radiation was used and the tube operated at 40000V and 0.025A current. The X-ray diffraction patterns were taken in the range of 10–80º in order to cover the most intense peaks of the $NiMn_2O_4$ phase. The crystallite size of the powder was determined using the Scherrer formula as given in equation (4).

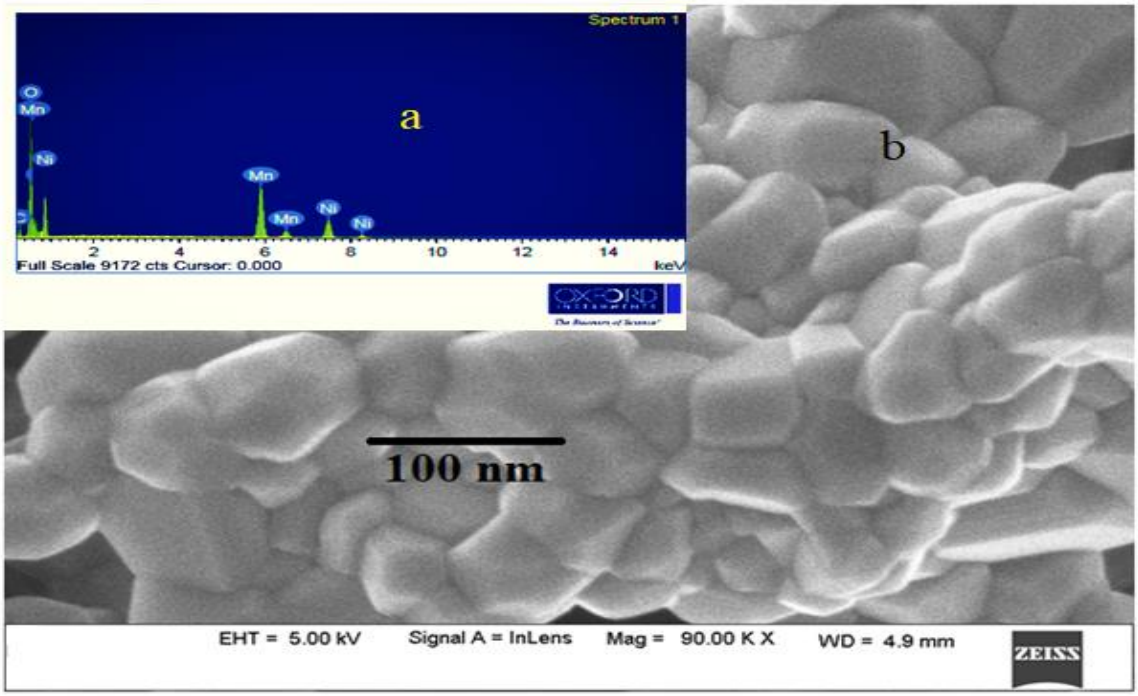

Figure 5: FeSEM/EDS characterization result of the sample, (a) EDS result and (b) FeSEM result

$$D = \frac{0.9\lambda}{\beta Cos(\theta)} \quad \text{..... (4)}$$

Where λ is the x-ray wavelength of CuKα source 0.154059x10^{-9}m, θ is the Bragg's angle and β is the full width at half maximum (FWHM) of the diffraction peak in radians.

The average crystallite size of the nine peaks became about 34x10^{-9}m whereas, the minimum size was about 29x10^{-9}m which was observed at the seventh peak and the maximum size was about 38x10^{-9}m observed in the first peak as shown in Figure . These results are also consistent within the range of the previous work (Almeida et al., 2008). The XRD result also confirms the existence of a spinel structure of the resulting nanoceramic powder.

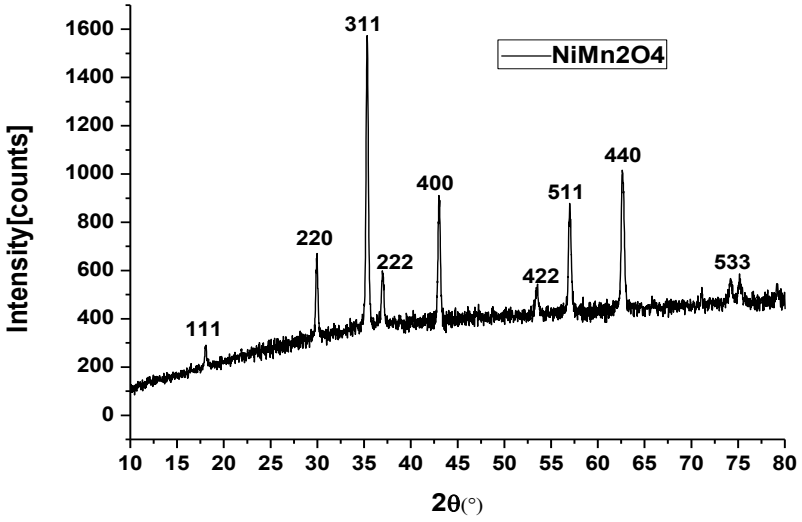

Figure 6: XRD result of the sample powder

3.2 Thermistor Calibration Results

The Stein and Hart and the β-coefficient models have been analyzed and given in equations (5) and (6) respectively.

$$\frac{1}{T(K)} = -0.006489926 + 0.0010145764\ln(R) - 0.000001598861\,(\ln(R))^3 \quad \text{..... (5)}$$

Where A = -0.006489926, B = 0.0010145764 and C = -0.00000158861

The coefficients were calculated using MATLAB and srs software applications.

$$\frac{1}{T(K)} = \frac{1}{298.15K} + \frac{1}{6332.36K}\ln\left(\frac{R}{123.3646K\Omega}\right) \quad \text{..... (6)}$$

Where, R_0 = 1233646Ω, β = 6332.36K and T_0=298.15K.

The two thermistor models are compared and they became compatible. Therefore, the mathematical models are representatives of the practically measured thermistor characteristics.

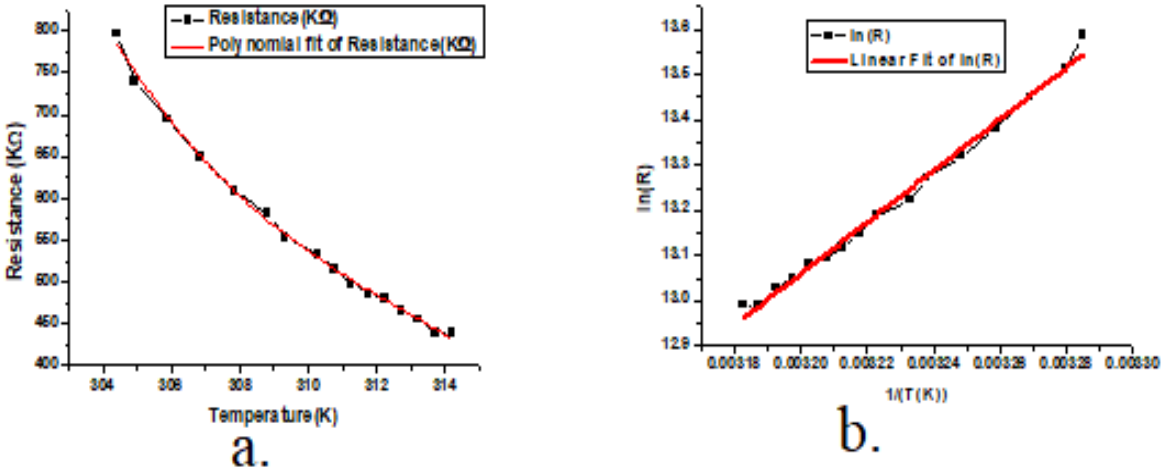

Figure 7: Temperature versus resistance characterization and calibration results of the thermistor, (a) polynomial fit and (b) linear fit

Figure (a) shows the existence of a very good fit between a third order polynomial and the resulting tested values of the thermistor. Figure (b) also confirmed the existence of a good linear fit of the thermistor model which assured the same characteristic. Therefore, the mathematical models are representatives of the practically measured thermistor characteristics. This thermometer can be used to measure temperature up to 70 °C.

3.3 Embedded System Development Results

The embedded system consists of both hardware and software. The hardware design is expressed by the block diagram as shown in Figure while the algorithm for the software design is represented by the flow chart as shown in Figure .

The fabricated thermistor, Atmega328, stainless steel tube, 16X2 LCD display, and 8cmx8cmx4cm 3-D printed plastic box for packaging, and 5V DC power supply hardware incorporated with Arduino programming software were used for the embedded system development. The 15cm long, 7mm inner diameter and 8mm outer diameter stainless steel tube was used as a probe (Figure) to hold the thermistor. Stainless steel tube has two main functions, protecting the sensor from rust and other damages, and easily inserted during installation and testing in the field.

Since the microcontrollers cannot read resistance and temperature directly, the resistance should be converted into microcontroller readable physical quantities i.e., current or voltage signals. Therefore, the thermistor resistance variation should be converted into a voltage signal. To do so, a 1.02MΩ resistor is connected in series with the thermistor as a voltage divider. The detailed circuitry for the prototype of the system is shown in Figure . The complete circuit for the thermistor, on the other hand, is shown in Figure . The voltage V_o supplied to the microcontroller's one of the analogue terminals is given in equation(7)(web-1).

$$V_o = \frac{V_2.R_{thermistor}}{R_{thermistor}+R} \quad \ldots\ldots\ldots\ldots\ldots\ldots\ldots (7)$$

The microcontroller displays a value which is given by the following formula (equation 8):

$$ADC = \frac{1023V_0}{V_{ref}} \quad \ldots\ldots\ldots\ldots\ldots\ldots\ldots\ldots (8)$$

If we substitute V_o from equation (7), we will get the following expression (equation 9).

$$ADC = 1023 \left(\frac{V_2.R_{thermistor}}{R_{thermistor}+R}\right) \Big/ V_{ref} \quad \ldots\ldots\ldots (9)$$

If V_{ref}=V_2=5V, then equation (9) becomes (equation 10):

$$ADC = 1023 \frac{R_{thermistor}}{R_{thermistor}+R} \quad \ldots\ldots\ldots\ldots\ldots (10)$$

From equation (10), R_thermistor becomes (equation (11)):

$$R_{thermistor} = \frac{R}{\left(\frac{1023}{ADC}-1\right)} \quad \ldots\ldots\ldots\ldots\ldots\ldots (11)$$

$R_{thermistor}$ will be substituted in the thermistor models to calculate the temperature. The final output of the microcontroller is temperature. The temperature is displayed on the 16X2 LCD display or serial monitor of the computer. The assembled and embedded system is shown in Figure .

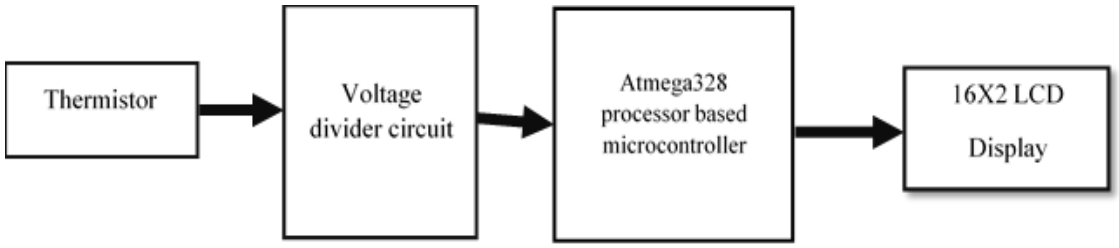

Figure 8: Design of the embedded system in block diagram

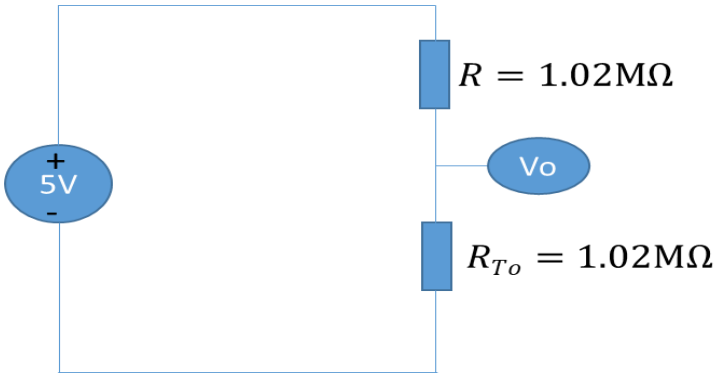

Figure 9: Voltage divider circuit for the microcontroller input

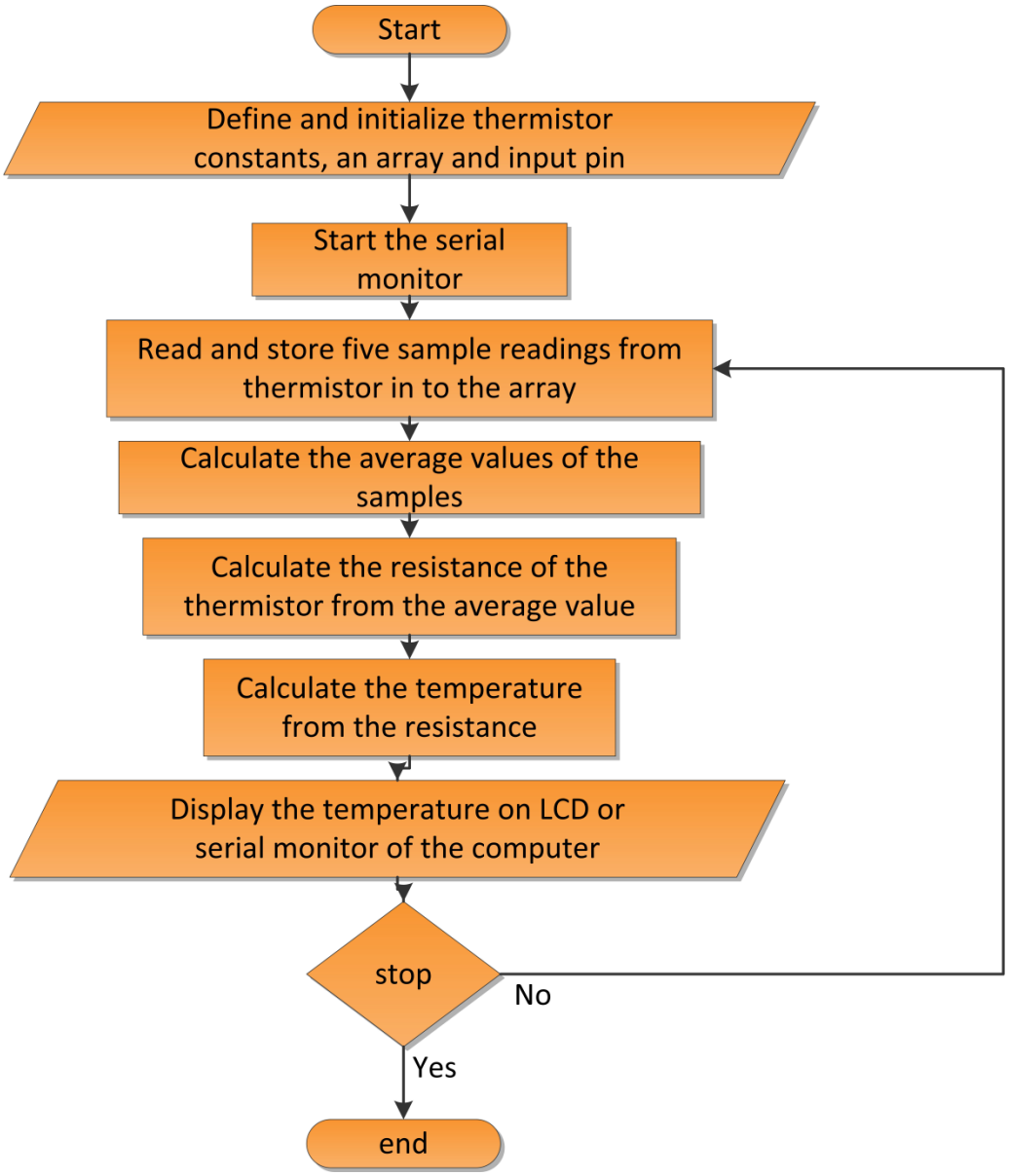

Figure 10: Design of the software part of the embedded system in the flowchart

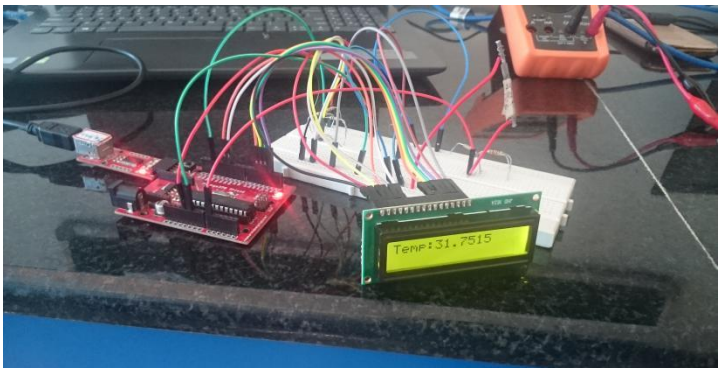

Figure 11: Prototype of the embedded system

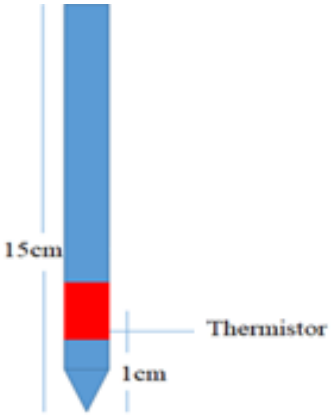

Figure 12: Designed thermometer probe

Figure 13: Fabricated embedded system

3.4 Testing the Thermometer

The fabricated thermometer has been tested by taking soil samples and by adding water at different temperatures as shown in Figure . LM35 IC temperature sensor and the fabricated thermometer are compared by measuring the environment temperature. The readings are almost the same except small variations after the decimal point of the reading, i.e. the maximum error read from the results is 0.033K. The result shows that the fabricated thermometer is working properly and became the most promising one especially in terms of cheaper cost, easy preparation, easy operation, durability and better accuracy.

Figure 14: Application of the fabricated thermometer in real-time soil temperature monitoring in agriculture

4. CONCLUSION

Thermometer from NTC nanoceramic thermistor powders can be prepared easily using an inexpensive method and simple procedure. The procedures are synthesizing nanoceramic powders, characterizing the powders, preparing the thermistor, characterizing and calibrating the thermistor, developing the embedded system and finally testing the thermometer. The unique features of this thermometer are four-digit precision temperature measurement and no requirement of any pellet making or film-making process. The other advantage of this device is that it is free from lead, a poison chemical. In the future, this thermometer can be modified and to be used in medical applications, ambient temperature measurement applications and other critical temperature measurement application areas.

5. REFERENCES

Almaw Ayele Aniley, Naveen Kumar S.K, and Akshaya Kumar A (2017) 'Soil temperature Sensors in Agriculture and the role of Nanomaterials in Temperature Sensors Preparation', *IJEMS*, 7(2), pp. 363–372.

Almaw Ayele Aniley Naveen Kumar S K Akshaya Kumar A Renny Edwin Fernandez, Shekhar Bhansali (2019) 'Thin Film Dual Probe Heat Pulse (DPHP) Micro Heater Network for Soil Moisture Content Estimation in Smart Agriculture', *Journal of The Electrochemical Society*, 166(2), pp. B63–B67. doi: 10.1149/2.0511902jes.

Almaw Ayele Aniley Naveen Kumar S K Akshaya Kumar A Renny Edwin Fernandez, S. B. (2019) 'Fabrication, Characterization and Comparison of Nanocrystalline NiMn2O4 and NiZn0.2Mn1.8O4 NTCR Ceramic Thermistor Powders', *Journal of Nanoscience and Technology*, 5(1), pp. 603–606.

Almeida, J. M. A. *et al.* (2008) 'Synthesis and characterization of NiMn 2 O 4 nanoparticles using gelatin as organic precursor', *Journal of Magnetism and Magnetic Materials*, 320, pp. 304–307. doi: 10.1016/j.jmmm.2008.02.062.

Arai-Sanoh, Y. *et al.* (2010) 'Effects of Soil Temperature on Growth and Root Function in Rice', *Plant Production Science*, 13(3), pp. 235–242. doi: 10.1626/pps.13.235.

Boselli, M., Di Vaio, C. and Pica, B. (1998) 'Effect of soil moisture and transpiration on mineral content in leaves and berries of Cabernet sauvignon grapevine', *Journal of Plant Nutrition*, 21(6), pp. 1163–1178. doi: 10.1080/01904169809365475.

Cai, T. and Dang, Q. L. (2002) 'Effects of soil temperature on parameters of a coupled photosynthesis-stomatal conductance model', *Tree physiology*, 22(12), pp. 819–828. doi: 10.1093/treephys/22.12.819.

Caron, J. and Boudreau, J. (2006) 'Soil water potential detector', (May), p. 6.

Clements F. E. and Martin E. V. (1931) 'effect of soil temperature on transpiration in helianthus annuus', *clements and martin: soil temperature and transpiration*, (2), pp. 619–630.

Coefficient, N. T. and Rt, W. (2012) 'Calibrate Steinhart-Hart Coefficients for Thermistors', (408), pp. 1–3.

Cox, L. M. and Boersma, L. (1967) 'Transpiration as a function of soil temperature and soil water stress.', *Plant physiology*, 42(4), pp. 550–556. doi: 10.1104/pp.42.4.550.

David, N. *et al.* (2015) 'Design-of-a-Home-Automation-System-Using-Arduino.docx', (June).

Davidson, E. A. and Janssens, I. A. (2006) 'Review: Temperature sensitivity of soil carbon decomposition and feedbacks to climate change', *Nature*, 440, pp. 165–173. doi: 10.1038/nature04514.

Fluke Corporation (2006) 'Infrared thermometer user manual', *Science (New York, N.Y.)*, p. 483.

Gardner, W. R. and Ehlig, C. F. (1963) 'The influence of soil water on transpiration by plants', *Journal of Geophysical Research*, 68(20), pp. 5719–5724. doi: 10.1029/JZ068i020p05719.

Ge, L. *et al.* (2015) 'Effects of different warming patterns on the translocations of cadmium and copper in a soil–rice seedling system', *Environmental Science and Pollution Research*, 22(20), pp. 15835–15843. doi: 10.1007/s11356-015-4760-8.

Goswami, R. and Kumar, R. (2018) 'Design fabrication and satic calibration of thermocouple and thin film gauges', *IOP Conference Series: Materials Science and Engineering*, 377(1). doi: 10.1088/1757-899X/377/1/012207.

Hamed, B. and Hamed, B. (2015) 'Design & Implementation of Smart House Control Using LabVIEW Design & Implementation of Smart House Control Using LabVIEW', (October).

https://learn.adafruit.com/thermistor/using-a-thermistor (no date).

Husain, M. D., Kennon, R. and Dias, T. (2014) 'Design and fabrication of Temperature Sensing Fabric', *Journal of Industrial Textiles*, 44(3), pp. 398–417. doi: 10.1177/1528083713495249.

IAEA (2008) *Field estimation of soil water content: A practical guide to methods, instrumentation and sensor technology*, *Atomic Energy*. Vienna.

Jacob Fraden (2004) *Handbook of Modern Sensors:PHYSICS, DESIGNS, and APPLICATIONS*. 3rd edn. Calfornia: Springer.

Jacob Fraden (2010) *Handbook of Modern Sensors:Physics, Designs, and Applications*. 4th edn. London: Springer.

Jagtap, S. *et al.* (2010) 'Low temperature synthesis and characterization of NTC powder and its "lead free" thick film thermistors', *Microelectronic Engineering*. Elsevier B.V., 87(2), pp. 104–107. doi: 10.1016/j.mee.2009.05.026.

Kedzierski, M. a. (1993) 'Principles and methods of temperature measurement', *Experimental Thermal and Fluid Science*, 6(1), p. 106. doi: 10.1016/0894-1777(93)90045-K.

Klaus-Dieter Gruner (2003) 'Principles of Non-contact Temperature Measurement', *Raytek Corporation*.

Luan, J. *et al.* (2014) 'Different effects of warming and cooling on the decomposition of soil organic matter in warm–temperate oak forests: a reciprocal translocation experiment', *Biogeochemistry*, 121(3), pp. 551–564.

Mew, T. W. (1977) 'Effect of Soil Temperature on Resistance of Tomato Cultivars to Bacterial Wilt', *Phytopathology*, 77, p. 909. doi: 10.1094/Phyto-67-909.

Naveen Kumar S K, Akshaya Kumar A, Almaw Ayele Aniley, Renny Edwin Fernandez, and S. B. (2019) 'Hydrothermal Growth of Zinc Oxide (ZnO) Nanorods (NRs), Structural, and Chemical Composition Studies for pH Measurement Sensor Applications Naveen Kumar S K', in *ECS Transactions*, pp. 437–447.

Naveen Kumar S K, Almaw Ayele Aniley, Akshaya Kumar A, Renny Edwin Fernandez, Shekhar Bhansali (2019) 'Nanoceramic NiMn 2 O 4 Powder-Based Resistance Thermometer for Soil Temperature Measurement Application in Agriculture Naveen Kumar S.K', in *ECS Transactions*, pp. 455–470.

Onwuka, B. (2018) 'Effects of Soil Temperature on Some Soil Properties and Plant Growth', *Advances in Plants & Agriculture Research*, 8(1). doi: 10.15406/apar.2018.08.00288.

Ota, H. *et al.* (2017) '3D printed "earable" smart devices for real-time detection of core body temperature', *ACS Sensors*, 2(7), pp. 990–997. doi: 10.1021/acssensors.7b00247.

Pallas, J. E. *et al.* (1967) 'Photosynthesis, Transpiration, Leaf Temperature, and Stomatal Activity of Cotton Plants under Varying Water Potentials.', *Plant physiology*, 42(1), pp. 76–88. doi: 10.1104/pp.42.1.76.

Priyadarshi, A. (2015) 'Design and Fabrication of Plate Thermometer for the Measurement of Incident Radiation Heat Flux on a Surface', *International Journal of Science and Research (IJSR)*, 4(8), pp. 1460–1465.

R. DE JONG and K. F. BEST (1979) 'The Effect of Soil Water Potential, Temperature and Seeding Depth on Seedling Emergence of Wheat', *Can. J. Soll Sci.*, 59, pp. 259–264.

Reza, M. S., Mamun, S. and Mossadded, M. M. (2018) 'Design and Development of a GSM-based Smart Home Automation System: A Low Cost Approach', *Preprints*, (November), pp. 1–5. doi: 201811.0472.v1.

Sahu, S. *et al.* (2015) 'Design and fabrication of a data logger for atmospheric pressure, temperature and relative humidity for gas-filled detector development', (July).

Shah, N. H. and Paulsen, G. M. (2003) 'Interaction of drought and high temperature on photosynthesis and grain-filling of wheat', *Plant and Soil*, 257(1), pp. 219–226. doi: 10.1023/A:1026237816578.

Sun, Y. *et al.* (2018) 'Fabrication of composite microneedle array electrode for temperature and bio-signal monitoring', *Sensors*, 18(4), pp. 1–12. doi: 10.3390/s18041193.

Trust, N. P. and Phytologist, N. (2012) 'Effect of temperature on wood decay and translocation of soil-derived phosphorus in mycelial cord systems', *New Phytologist*, 129(2), pp. 289–297. doi: 10.1111/j.1469-8137.1995.tb04299.x.

Valente, A. *et al.* (2006) 'Multi-functional probe for small-scale simultaneous measurements of soil thermal properties, water content, and electrical conductivity', *Sensors and Actuators, A: Physical*, 132(1 SPEC. ISS.), pp. 70–77. doi: 10.1016/j.sna.2006.05.010.

WANG, G. (2004) 'Experimental study on soil respiration of temperate grassland in China', *Chinese Science Bulletin*, 49(6), p. 642. doi: 10.1360/03wd0241.

Zuk-Golaszewska, K., Upadhyaya, M. K. and Golaszewski, J. (2003) 'The effect of UV-B radiation on plant growth and development', *Plant, Soil and Environment*, 49(3), pp. 135–140. doi: 10.1080/02648725.1990.10647868.

Defect-Rich Ultrathin NiCoFeOx Nanosheets for Efficient Oxygen Evolution Catalysts

Lemma Teshome Tufa[1,2,*], Birhanu Bayissa Gicha[3], Jaebeom Lee[2]

[1]Department of Chemistry, School of Natural Sciences, Adama Science and Technology University, Adama, Ethiopia
[2]Research Institute of Materials Chemistry, Chungnam National University, South Korea
[3]Environmental Science Program, Haramaya University, Ethiopia
**Corresponding author, e-mail: lemmat2003@yahoo.com*

ABSTRACT

The hydrogen fuel cell has surged to the top of the priority list as part of broader efforts to decarbonize and expand clean energy economies. Because of its exceptional performance for alkaline oxygen evolution reactions (OERs), layered NiCoFe-hydroxide is considered a promising trifunctional water-splitting catalyst. We present an electrochemical synthesis strategy and green exfoliation strategy to synthesize boundary defect-rich ultrathin transition metal hydroxide nanosheet networks by ultrasonic etching of NiCoFeOx LDHs. The resultant ultrathin NiCoFeOx LDHs nanoarray is an effective trimetalic-based oxygen evolution catalyst. Through varying the green etching technique, the defect-rich, ultrathin materials can be tailored for different chemical compositions. This ultrathin nanostructure enables a number of synergistic effects and beneficial functions, including easy access to water, electron transport, rapid oxygen release, enhanced stability in alkaline medium electrolytes, and overpotential of 210 mV at a current density of 10 mA cm^{-1}. Our work demonstrates the ability of novel synthesis routes to produce highly efficient nanomaterials for water splitting.

Keywords: NiCoFeOx LDHs, ultrathin nanosheets, Oxygen Vacancy, Oxygen Evolution Reaction

1. INTRODUCTION

The development of ultrathin two-dimensional (2D) nanostructures have attracted considerable scientific research interest due to their graphene like laminar structures, as well as unique electronic structures, numerous active site, and high surface area characteristics (Tan et al., 2017; Wu et al., 2021). In particular, earth abundant transition metal layered double hydroxide (LDH) transition catalysts have been prioritized due to their electron arrangement in e_g orbits and ability to catalyze the transition of $[M^{n+}\text{-}OH_{ad}]/[Mn^{+1}\text{-}O_{ad}]$ (Liang et al., 2020; Zhang et al., 2020). Furthermore, their exposed metallic centers serve as coordinatives to reduce the energy barrier to the electrochemical reactions, and to increase the ability of electrolytes to capture ions, thereby improving the kinetics of electrochemical reactions (Che et al., 2019). In order to improve the electrocatalytic performance of non-noble metal-based composite, various strategies are applied, including phase and morphology control,(Li et al., 2015) defect engineering (Jin et al., 2019) heteroatoms doping (Reddy et al., 2020) and surface strain (Luo et al., 2019). Most of the transition metal LDHs have layered nanostructures (including the host layer metal ions and interlayer anions), which provide flexible in chemical composition and structural adjustment(Yi et al., 2021). However, LDHs are stacked with many layers and have a limited number of active sites. Therefore, it is vital to tailor the structure and morphology of 2D materials precisely. Typically, LDHs can be exfoliated into unilamellar nanosheets with a molecular-level thickness of about 1 nm versus a 2D lateral size of about 0.1 to 1.0 mm (Kuai et al., 2019) .

Several studies have proved that engineering defects can be used to control the electronic structure and surface properties of electrocatalysts for improved catalytic activity(Chen et al., 2020). Defect engineering through exfoliation is considered a promising approach to increase the intrinsic activity of electrocatalysts on an atomic level. The common exfoliation techniques such as chemical exfoliation,(Qin et al., 2019) mechanical exfoliation,(Li et al., 2013) chemical vapor deposition (CVD),(Komsa & Krasheninnikov, 2012) and intercalation exfoliation(Ambrosi, Sofer, & Pumera, 2015) have limitation in using multiple synthesis steps, uncontrollable distributions of components, low yield with no scalability, high cost, and require inert environment. There is still a

challenge to fabricate ultrathin 2D metal LDH hybrid nanostructures easily and with the required level of electrochemical performance, production rate, reproducibility, and tenability. Furthermore, other factors such as thickness and roughness can affect the efficacy of the chemical intercalation and exfoliation processes, as well as the quality and crystallinity of the exfoliated 2D transmission metal nanosheets (NSs).

Electrochemical route is a promising exfoliation method, as it is performed under mild condition with controllable and large scale fabrication, simple manufacturing process and low cost (Zhu et al., 2022) . An electric current behaves as an appealing driving force to carry foreign molecules or ions in bulk materials, thus expanding their interlayer spacing(Yang et al., 2016). For instant, Wells *et al*. fabricated a high-performance semiconducting 2D NSs from layered transition metal dichalcogenide powder through gentle exfoliation method involving bulk MoS_2 powder (pressed into pellets) and an electrochemical intercalation involving quaternary alkyl ammonium (Wells et al., 2022). This method is simple and allows large-scale preparation to be easily achieved.

In addition to engineering the electronic structure and surface properties of electrocatalyst, the intrinsic properties of the catalysts play crucial role in accelerating the electrochemical activities(Lemma et al., 2021). Fe, Co, Ni, Mn, and Mo oxides and hydroxides, and their composites, are promising catalysts for various electrochemical reactions, and vacancies in the compounds can serve as active sites for the electrochemical reactions(Tong et al., 2020; Zhu et al., 2020). The electrocatalytic performances of Ni-based in OER can be realized by electrically conductive Ni-Fe LDH based NSs and their derivatives. Kuai *et al*. synthesized Ni−Fe LDH via an alcohol intercalation method with 100% exposed active sites for catalyzing OER with a thickness of ∼1.2 nm (Kuai et al., 2019). At low OER potentials, all metal ions in ultrathin LDH can undergo complete oxidation into the tetravalent state, which facilitates the lattice-oxygen-involved OER in a decoupled proton/electron decoupled mode without any interference from "bulk" inactive species.

Here we create thin layer NSs enriched with defect, in which the bulk $NiCoFeO_x$ LDH NSs synthesized by electrochemical method with stacked surfaces restricting exposure of catalytically active sites exfoliated into single layers using an electrochemical etching technique. We show that the $NiCoFeO_x$ LDH NSs prepared exhibited high OER performance demonstrating that our technique is suitable for exfoliating a range of bimetallic transition metal bimetallic LDH NSs including $NiCoO_x$, $NiFeO_x$, and others.

2. MATERIAL AND METHODS

2.1 Materials

Cobalt (II) nitrate hexahydrate ($Co(NO_3)_2{\cdot}6H_2O$), Nickel (II) nitrate hexahydrate ($Ni(NO_3)_2{\cdot}6H_2O$), Iron (III) nitrate nonahydrate ($Fe(NO_3)_3{\cdot}9H_2O$), and hydrochloric acid (HCl) were purchased from Sigma Aldrich Chemicals (Seoul, South Korea) and used without further purification. Ultrapure water used through this experiment was prepared by Milli-Q grade (>18.2 $m\Omega\ cm^{-1}$).

2.2 Electrodeposition and Exfoliation of NiCoFeOx_P LDH NSs Electrocatalysts

The NiCoFe oxy(hydroxide) nanosheets were prepared by a one-step electrodeposition method. Prior to electrodeposition, Ni foam (20 mm length x 10 mm width x 1.6 mm thickness) was cleaned with 2 M HCl for 10 minutes to remove the oxide layer, then washed with ethanol and water and dried under a stream of nitrogen gas. The electrochemical deposition process was carried out under three electrode system, which employed platinum wire auxiliary electrode, A Ag/AgCl wire (placed in saturated KCl solution that was periodically refreshed to counteract the contamination from electrolytes) was used as the reference electrode, and Ni foam working electrode. In typical processes, a voltage of -1.0 V was applied for 300 s in the electrolyte containing of 1 mM $Fe(NO_3)_3{\cdot}9H_2O$, 1 mM $Ni(NO_3)_2{\cdot}6H_2O$, and 1 mM $Co(NO_3)_2{\cdot}6H_2O$. The bulk NiCoFeOx NS was initiated by applying a low positive bias of +2 V prior to CV cycles. The exfoliation process was performed by running CV of different cycles (NiCoFeOx_EC).

2.3 Electrochemical Measurement

All electrochemical measurements were performed on a potentiostat at ambient environment (25° ± 1°C, 1 atm). Electrochemical tests of cyclic voltammetry (CV), linear sweep voltammetry (LSV), chronopotentiometry (CP), chronoamperometry (CA), and electrochemical impedance spectroscopy (EIS) were measured using three electrodes setup in nitrogen-saturated 1 M NaOH solution at 25ºC. The potential of the Ag/AgCl reference electrode was converted to a RHE scale following the equation E (RHE) = E (Ag/AgCl) + 0.059 pH V. LSV were measured at scan rate of 5 mV s^{-1} in the potential range of 1.0 to 2.0 V vs. RHE. RuO_2 ink was prepared by dispersing 10 mg of commercial RuO_2 powder into solution of 950 µL ethanol + 50 µL Nafion, and then coated onto Ni foam with a mass loading of about 0.7 mg cm^{-2} and dried in vacuum oven at 60°C. EIS measurements were performed from 1 × 10^5 Hz to 0.1 Hz at a potential of 1.30 V vs. RHE. Typically, the OER measurement was conducted in 1 M NaOH in an H-type cell with the cathode (Pt foil) and the anode ($NiCoFeO_x$–EC) NSs and the anodic chamber contained a Ag/AgCl reference electrode) separated by a membrane. Before electrocatalysis, the anodic chamber was purged with N_2 gas for 1 h. The headspace of the chamber containing working electrode is 20.0 mL. To meausure the amount of O_2 evolved, a constant current of 10 mA was applied for 60 min. The O_2 gas generated was determined by taking 500 μL of the gas sample in the chamber containing working electrode to gas chromatography mass spectroscopy (GCMS) and measured in 5 min time interval.

2.4 Material characterization

Electron microscopic images were captured using a field emission scanning electron microscope (FE-SEM S-4700; Hitachi, Tokyo, Japan) and transmission electron microscope (TEM, JEM-2100F, JEOL Ltd., Tokyo, Japan). Transmission electron microscopy (TEM) and scanning transmission electron microscopy (STEM) were at Korea Advanced Institute of Science and Technology University (KAIST) based on a JEOL 2100F transmission electron microscope operating at 200 kV accelerate voltage. X-ray diffraction analyses (XRD, PANalytical X'Pert PRO) were utilized. Cyclic voltammetry, linear sweep voltammetry, chronoamperometry, and electrochemical impedance spectroscopy (EIS) were carried out by means of an Iviumstat electrochemical interface (Eindhoven, Netherlands). Atomic Force Microscopy (Park system, XE7, Seongnam, Korea) characterization was conducted under a scanning-assisted mode. The gaseous products of OER were analyzed by gas chromatography mass spectroscopy (GCMS, Shimadzu GCMS-QP2010). Chemical compositions were analyzed by an X-ray photoelectron spectroscopy (XPS, Thermo (K-alpha+)) with Mg as excitation source.

3. RESULTS AND DISCUSSION

3.1 Fabrication and Characterization of $NiCoFeO_x$ LDH NSs

Fabrication approaches of ultrathin $NiCoFeO_x$_EC LDH NSs are schematically presented in **Scheme 1**. In brief, the pristine $NiCoFeO_x$ LDH ($NiCoFeO_x$_P) NSs were synthesized via electrodeposition from a solution containing 1 mM $Fe(NO_3)_3{\cdot}9H_2O$, 1 mM $Ni(NO_3)_2{\cdot}6H_2O$, 1 mM $Co(NO_3)_2{\cdot}6H_2O$ supported on conductive 3D Ni foam. The $NiCoFeO_x$_P LDH NSs was deposited by reduction of $Ni^{2+}(aq)$, $Co^{2+}(aq)$, and $Fe^{3+}(aq)$ as well as generation of OH^- by reducing of NO_3^- (**Eq. 1-3**) (Ma et al., 2019; Ni et al., 2021; Yarger, Steinmiller, & Choi, 2008). An oxidized or reduced product can continuously be deposited on a working electrode or counter electrode by tuning the cell potential. Working electrode potential is monitored using a reference electrode. Cell potential and deposition current are two important parameters affecting the reaction's course, both of which can be controlled as a function of time(Yan et al., 2020).

$$NO_3^- + H_2O + 2e^- \rightarrow NO_2^- + 2OH^- \quad (1)$$

$$Fe^{2+} \rightarrow Fe^{3+} + e^- \quad (2)$$

$$Ni^{2+} + 2Co^{2+} + xFe^{3+} + (6+2x)OH^{-} \rightarrow (3+X)\left[Ni_{\frac{1}{3+x}}Co_{\frac{2}{3+x}}Fe_{\frac{x}{3+x}}(OH)_2\right]^{x+} \quad (3)$$

After raising and drying the Ni foam (NF) coated with $NiCoFeO_x$_P NSs were immersed in solution containing 1 M NaOH and exfoliated by running cyclic voltammetry (CV) of different cycles (denoted as $NiCoFeO_x$_EC).

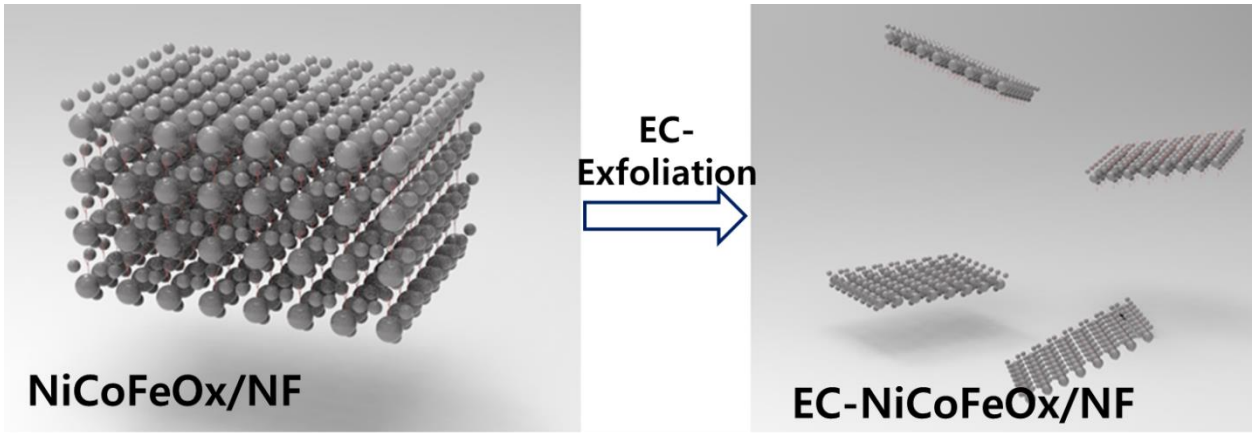

Scheme 1: Schematic presentation of EC exfoliation of $NiCoFeO_x$_P LDH NSs

The surface micromorphology of the fabricated NSs were characterized by field emission scanning electron microscopy (FESEM) and transmission electron microscopy (TEM). The FESEM image clearly shows that the as-prepared $NiCoFeO_x$_P LDH have an interconnected uniformity grown on NF with nanosheet structure morphology with micro size and these NSs have a smooth surface with a lateral size of tenth nanometers (Fig. 1A). Product sizes and morphologies can be controlled by controlling electrodeposition parameters (*e.g.* current, potential, time, pH, additives, and temperature). The SEM cross-sectional thickness measurement of the electrochemically fabricated $NiCoFeO_x$ NSs was 688 nm. The number of atomic layers in each NS was investigated using high-angle annular dark field (HAADF) scanning TEM (STEM), a technique sensitive to thickness of thin samples(LeBeau, Findlay, Allen, & Stemmer, 2012). The HAADF STEM image in Fig. 1B shows the stacked NSs of the bulk material. Traditional exfoliating techniques could be effective in terms of efficiency and control over morphology. However, during exfoliation, the change causes loss in electrochemical activity(Voiry et al., 2013). So, a facile electrochemical technique was chosen to maintain the intrinsic materials' properties and catalytic activity. The FESEM and HAADF STEM of electrochemically exfoliated $NiCoFeO_x$_EC LDH NSs are shown in Fig. 1C, respectively. The exfoliated NSs are retained their original bulk LDHs along (00n) planes without a change of the basic structure of the layer. The presence of monolayers was further verified by atomic force microscopy. The thickness of the exfoliated NS was ~2 nm, which is consistent with the HRTEM observation. Notably, unlike the previous observations with NS exfoliated by ultrasonication,(Yu & Sivula, 2017; Zheng & Lee, 2022) EC exfoliation method produces a majority of monolayer sheets over the entire observed area range of the NS (Gicha et al., 2021; Zhang et al., 2020).

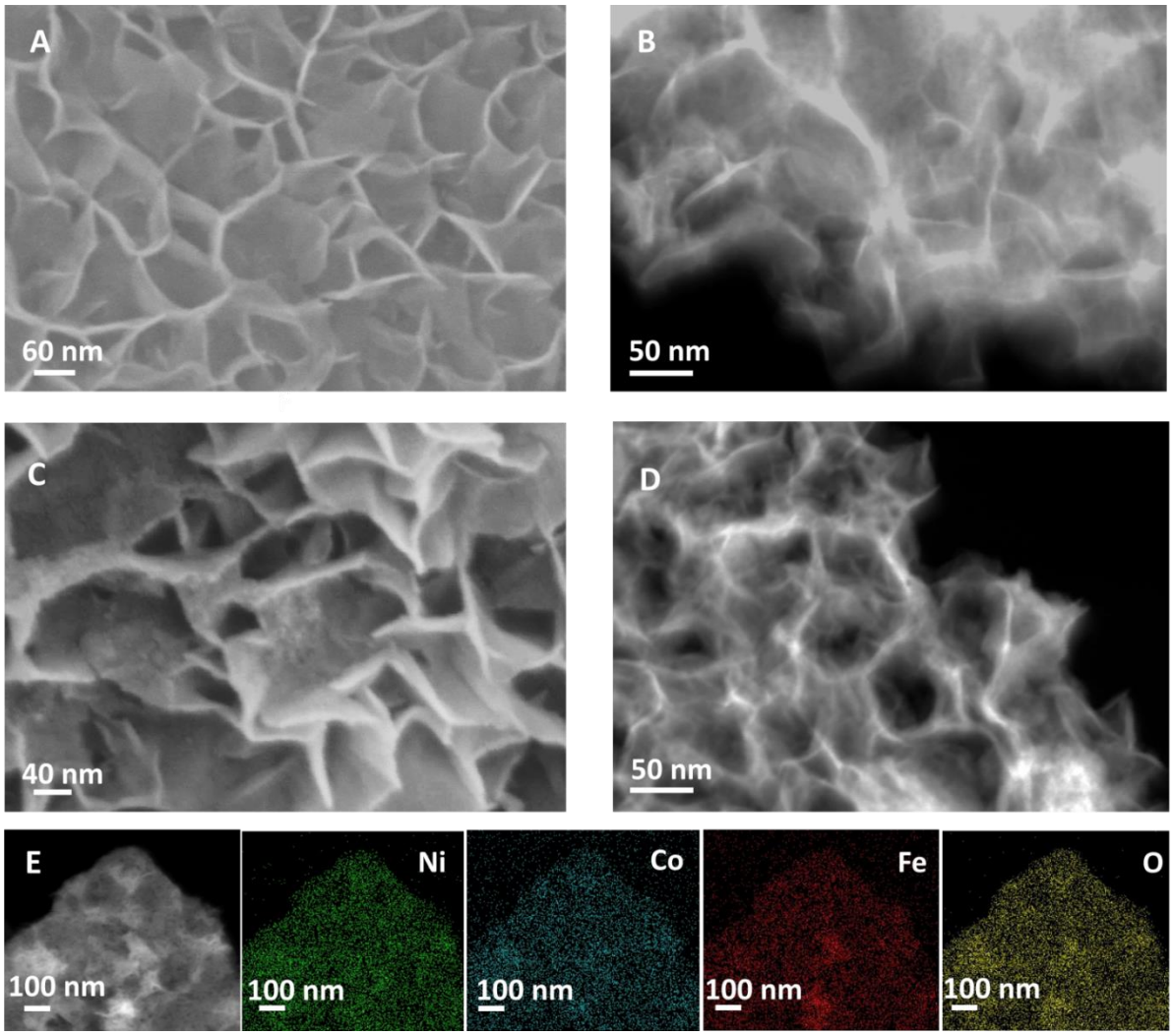

Figure 1: Characterization of the NiCoFeOx NSs: (A) FESEM images and (B) STEM image of NiCoFeOx_P LDH NSs, (C) the SEM and (D) STEM images of NiCoFeOx_EC LDH NS, (E) STEM-EDX elemental mapping of Ni, Co,Fe, and O.

A consistent relationship has been observed between NS lateral size and the number of atomic layers (thickness) in the previous descriptions of the exfoliation using various synthesis approaches. In monolayers, the dimensions are the smallest, but larger dimensions are only possible using NSs prepared by liquid exfoliation, mechanical cleavage, CVD growth, and wet chemical synthesis (Gong et al., 2018; Jung et al., 2015; Xi et al., 2016; J. Zheng et al., 2014). This has been explicitly discussed for the NSs produced by ultra-sonication, plasma treatment, chemical etching, and it is likely linked to the anisotropic mechanical properties of the layered TMDs (stemming from the layered crystal structure). In stark contrast, our EC exfoliation method can produce very thin NSs (mono-bi-trilayers) with different thicknesses, with relatively mild fabrication conditions (room temperature (25 ºC), short reaction time), surfactant free, and high electrochemical performance (Fig. 2a).

A low magnification TEM image of exfoliated $NiCoFeO_x$ LDHs NS (Fig. 2A) revealed translucent, flat, and ultrathin NSs. The uniformity of the contrast means that the thicknesses of the NSs are basically the same and a few multilayers are observed. Intense signal of Ni, Co, Fe, and O can be clearly observed from its energy dispersive X-ray spectroscopy (EDS) spectrum (Fig. 1E), indicating the elemental composition. The elemental ratio obtained from the EDS analysis gives the chemical formula of NiCoFeOx (Fig. 1E). X-ray diffraction spectroscopy and

Raman spectroscopy techniques probed the chemical composition of the surface coating (Wang et al., 2011). XRD measurements are further employed to characterize the composition and crystal structures of the NSs. Due to the ultrathin nature of the surface coating NSs, we were unable to differentiate the signal of the surface coating NSs from that of NF (Fig. 2A). Alternatively, we prepared a powder sample of NiCoFeOx_EC LDH NSs on Fluorine doped tin oxide (FTO) glass slide. All XRD peak patterns can be indexed to Ni with slight shifts, indicating the crystalline nature of the material (Fig. 2A). The peaks of 43.0°, 50.3°, and 75.8° correspond to (111), (200), and (220) crystal planes, respectively, corresponding with the pattern of NiCo-LDHs (Wu et al., 2016).

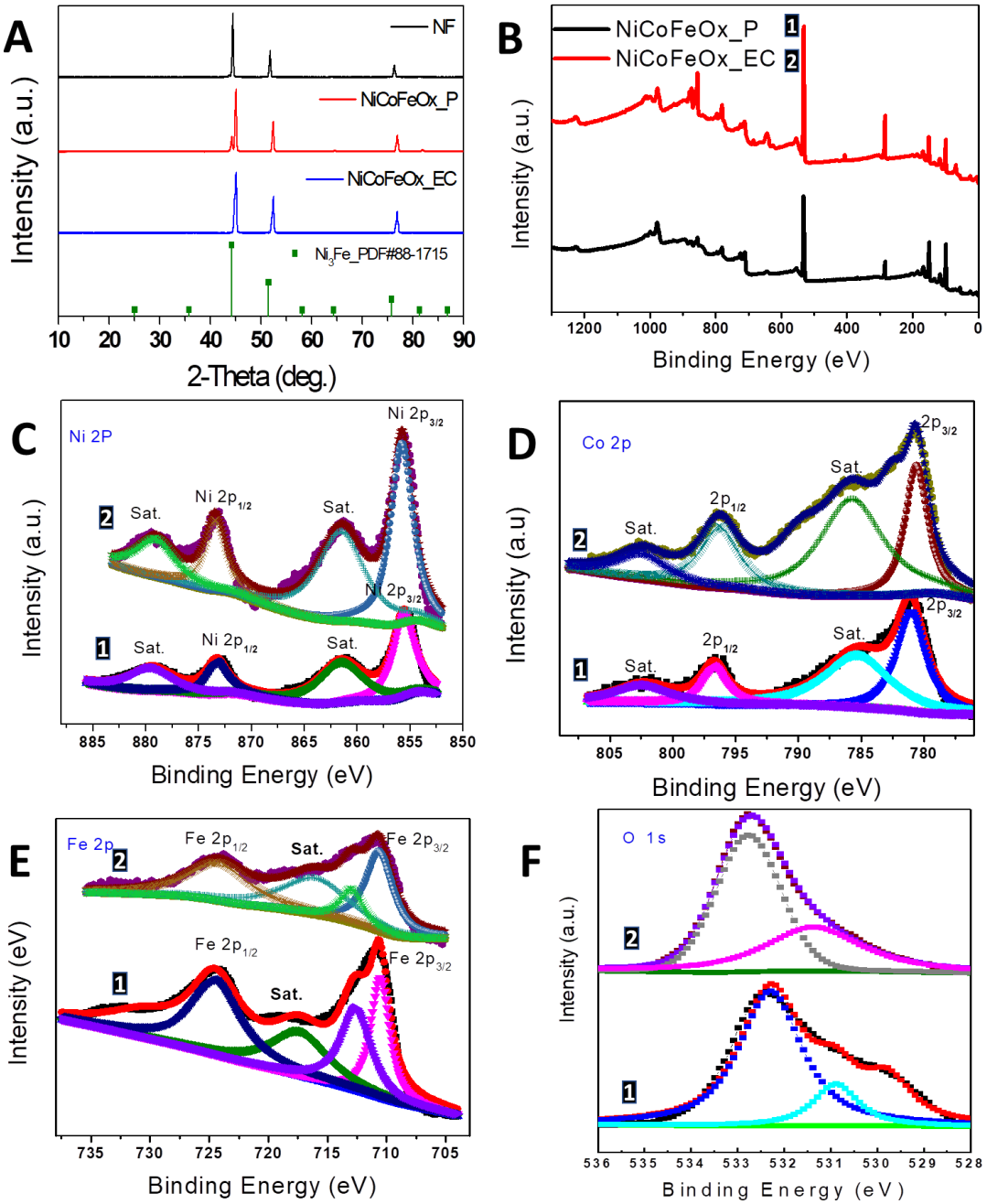

Figure 2: Spectroscopy Characterization: (A) XRD patterns of NiCoFeOx_EC LDH NSs (B) XPS spectra of NiCoFeOx_P and NiCoFeOx_EC LDH NSs, High-resolution XPS spectra of (C) Ni (D) Co (E) Fe and (F) O of as-prepared sample.

X-ray photoelectron spectroscopy (XPS) was then employed to investigate the chemical composition of the multi-elements catalysts and few layers NiCoFe LDH NSs. Fig. 2B shows that the surface of NiCoFeOx_P and NiCoFeOx_EC LDH NSs are composed of Ni, Co, Fe, and O. As can be observed in the high resolution Ni 2p spectrum (Fig. 2C), the two main peaks at 873.1 and 855.6 eV can be ascribed to $2p_{3/2}$ and $2p_{1/2}$ of Ni^{2+}.(Zhang et al., 2021) The peaks at 796.6 and 781.1 eV in the Co 2p spectrum (Fig. 2D) indicate that Co exists in the form of a high-spin Co^{2+} state(Tan et al., 1991). The three main peaks at 711.4, 715.8 and 724.9 eV correspond to $2p_{3/2}$, satellite and $2p_{1/2}$ of Fe^{3+}, respectively (Fig. 2E) (Grosvenor et al., 2004). The O 1s deconvolution spectrum (Fig. 2F) resulted in three peaks representing the metal–oxygen bonds (M−O, 531.38 eV), metal-surface hydroxyl bond and surface adsorbed water ((M−OH and H_2O, 532.6 eV) and intercalated anions ($M-NO_3^-$, 532.78 eV)(Fan et al., 2018).

3.2 Electrocatalytic OER Performance

The electrocatalytic performances of NiCoFe LDH NSs toward OER were evaluated using three-electrode setup in 1 M NaOH. A rational strategy for controlling NiCoFeOx_P LDH NSs catalytic activity was first devised by optimizing its deposition time. The NiCoFeOx_P LDH NSs catalyst showed optimum performance for OER at 300 s deposition time, which is probably due to a balance between the decreased conductivity and increased in active sites for the electrocatalysts with increased deposition time (GolrokháAmin, 2017). So, this deposition duration were used to prepare other of NiCoFeOx_P LDH NSs catalysts in the following studies. SEM, TEM, Raman spectroscopy, and XPS characterizations additionally validate the successful synthesis and exfoliation of NiCoFeOx_EC LDH NSs. Oxygen-deficient sites can be clearly observed from O 1s XPS. Electron spin resonance (ESR) spectra were collected to identify the oxygen vacancy locations on the Ni foam electrode. Cyclic voltammetry (CV) was used to evaluate the electrochemical behavior of NiCoFeOx_EC LDH NSs in 0.1 M and 1 M NaOH. The pair of redox peaks located around 1.38 and 1.28 V *vs.* RHE for oxidation and reduction, respectively, is related to the redox reaction between FeCo:$Ni(OH)_2$ and FeCo:NiOOH, and their current relates to the number of electrochemically active Ni, CO, Fe sites. As a result of the electro-oxidation reaction between FeCo:$Ni(OH)_2$ and FeCoNiOOH, multiple phase transitions were observed, such as FeCo:α-$Ni(OH)_2$ and FeCo:β-$Ni(OH)_2$ formations, as well as the reversible cycles between them and FeCo:γ-NiOOH and β- FeCo:NiOOH (Chavhan et al., 2017; Jin et al., 2018) (Eq. 4), which play pivotal active species for the catalytic OER (Chen et al., 2016).

$$Ni(OH)_2 + OH^- \rightleftharpoons NiO(OH) + H_2O + e^- \quad (4)$$

The linear scan voltammetry (LSV) was performed in 1.0 M NaOH at the scan rate of 5 mV s^{-1} to study the OER catalytic activity. LSV curves of the NF, RuO_2, pristine NiCoFeOx_P, and NiCoFeOx_EC LDH NSs are shown in Fig. 3A. At a potential of 1.53 V *vs* RHE, NiCoFeOx_EC NSs gave a current density of 67.40 mA cm^{-2} for the OER, which is much higher than that of NiCoFeOx_P LDH NSs (21.09 mA cm^{-2}), RuO_2 (8.53 mA cm^{-2}), and NF (0.71 mA cm^{-2}). We then compared the electrochemical water oxidation properties of the two samples, with commercial RuO_2 as a reference. Ultrathin LDH presents much higher performance than bulk LDH and RuO_2 in 1 M NaOH (Fig. 3A). The unique 2D layered structure of NiFe LDHs has the advantages of interlayer anion tunability, resulting in enhanced intrinsic activity (Dang et al., 2018). The OER performance of the different electrocatalysts were further tested in terms of their Tafel slopes (Fig. 3B). The NiCoFeOx_EC LDH NSs showed a lower Tafel slope (30 mV dec^{-1}) compared to pristine NiCoFeOx_P (42 mV dec^{-1}), RuO_2 (46 mV dec^{-1}), and NF (102 mV dec^{-1}), which indicates significantly improved kinetics for OER.

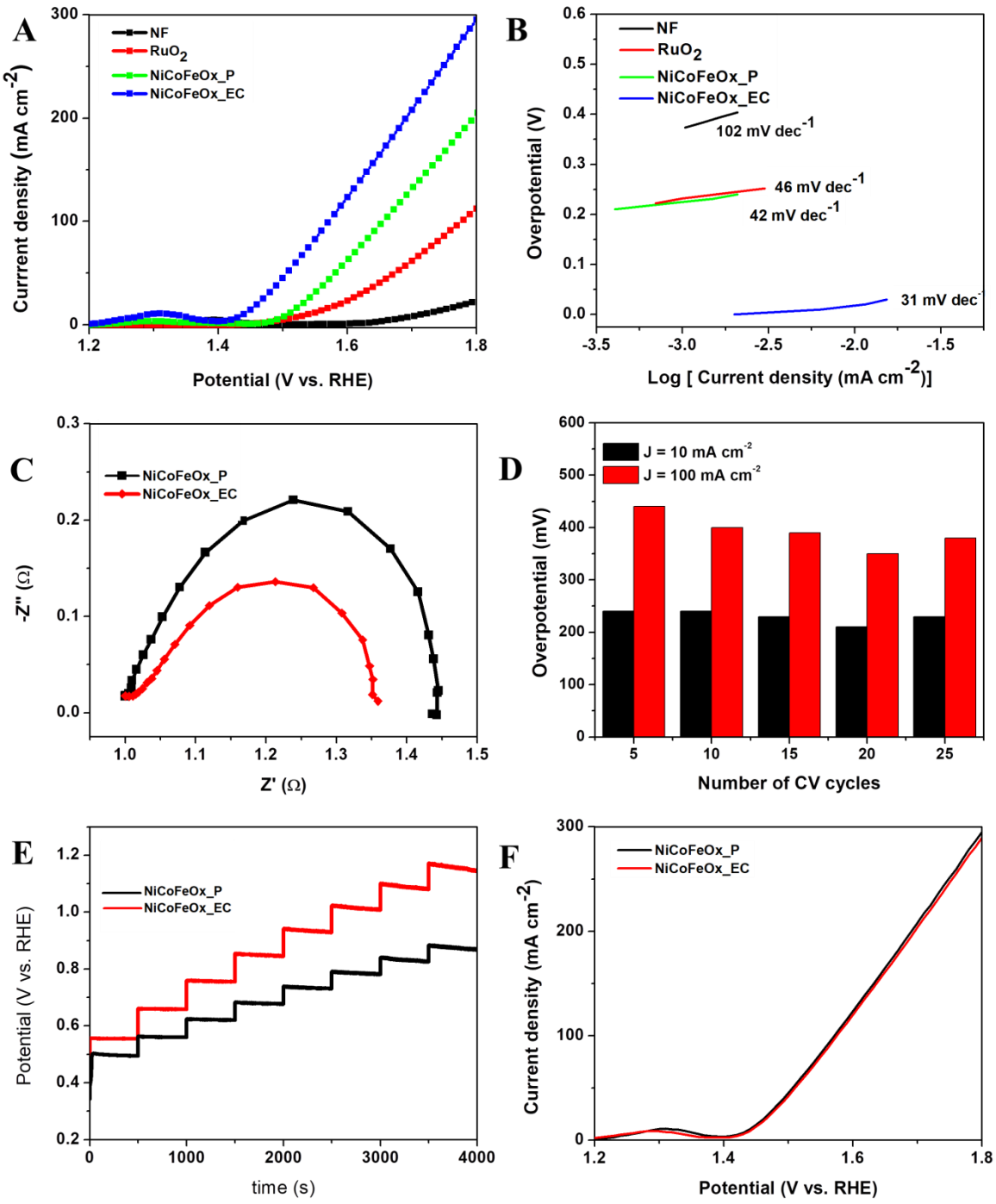

Figure 3: OER activities and electrochemical properties of green exfoliated electrodes in 1 M NaOH solution: (A) OER polarization curves of NF, RuO_2, NiCoFeOx_P - LDH NSs, NiCoFeOx_EC - LDH NSs at a scan rate of 5 mV S-1 and the corresponding (B) Tafel slopes, (C) EIS of NiCoFeOx_P - LDH NSs and NiCoFeOx_EC - LDH NSs, (D) overpotential vs. number of cycles (E) multistep chronopotentiometric curves with the current density started at 50 mA cm^{-2} and finished at 400 mA cm^{-2}, with an increment of 50 mA cm^{-2} every 500 s for of NiCoFeOx_P LDH NSs and NiCoFeOx_EC LDH NSs, (F) LSV curves before and after long stability test measured 1 M NaOH solutions at 5 mV s^{-1}.

To further study the effect of exfoliation on the intrinsic property of the materials such as charge transport and conductivity, electrochemical impedance spectroscopy (EIS) was measured. These factors will both have a large influence on the onset potential and propagation of OER catalytic activity.(Masud, Swesi, Liyanage, & Nath, 2016) On the other hand, the electron transfer resistance (R_{et}) will also affect the electron transfer within the catalyst film, thereby influencing the overall catalytic activity(Lemma Teshome Tufa et al., 2018). From the EIS data, R_{et} of the NiCoFeOx_EC LDH NSs is smaller than the pristine NiCoFeOx_P LDH NSs (Fig. 3C). The superior OER performance of the NiCoFeOx_EC NSs LDH array was therefore attributed primarily to its intrinsic activity, as indicated by the smaller onset potential (Fig. 3A) and low overpotential at current density of 10 and 100 mA cm^{-2} (Fig. 3D). The superior activity of the NiCoFeOx_EC - LDH NSs array was further confirmed when compared with the other reported catalysts, outperforming all reported NiFe and NiCo based nanostructures and most of the state-of-the-art counterparts. The ultrathin NS electrode also accelerated electrochemical reactions through electrode infiltration, ion transport, and gas release. An increase of 50 mA cm^{-2} per 500 s in multistep chronopotentiometric curves in 1.0 M KOH indicates a fast response of the potential to changes in current from 50 to 400 mA cm^{-2} (Fig. 3E). Besides the high activity, the NiCoFeOx_EC LDH NSs array also shows good stability. Fig. 3F shows the performance durability of the NiCoFeOx_EC LDH NSs array, in which the current density was 96.74 % retained after being evaluated at 100 mA cm^{-2} for 72 h. The ultrathin 2D nanostructure of the NiCoFeOx_EC LDH NSs after the stability test is still retained and the tiny NSs with abundant edges exposed can still be clearly observed. The SEM could still be maintained the structure of NiCoFeOx_EC LDH NSs, indicating that only a surface layer of NiCoFeOx_EC changed into NiFeOOH during OER.

This exfoliation "nanosheets" architecture not only provides enlarged surface area with more active sites for the redox reactions, but also possesses open porous structure that can facilitate the fast mass transport and electrolyte penetration; therefore, endowing the electrodes with high electrocatalytic performance. Therefore, the exploration of the optimized size of the conductive substrate, the concentration of the metal salts and the voltage and the time of the electrochemical deposition are required when using the electrochemical deposition method.

The electrochemical surface area (ESCA) was estimated from the double-layer capacitance (C_{dl}) of the films. The C_{dl} was determined by a simple CV method conducted in a potential window of (0.8–0.9 V *vs*. RHE) at various scan rates of 2, 4, 6, 8, and 10 mV s^{-1}. Then capacitive current ($j_{anodic} - j_{cathodic}$) at 0.85 V *vs*. RHE was plotted against various scan rates, while the slope obtained was divided by two to acquire the C_{dl} value, which represents ECSA. The NiCoFeOx_EC – LDH NSs demonstrated a higher value of C_{dl} (7.28 mF cm^{-2}) than NiCoFeOx_P – LDH NSs C_{dl} (2.37 mF cm^{-2}), implying that more active sites on the surface of NiCoFeOx_EC LDH NSs were activated to execute the OER performance. In addition, to prove that all the current is due to water oxidation, the theoretical and experimental O_2 evolved by NiCoFeOx_EC - LDH NSs electrode at a constant current of 10 mA were determined.

4. CONCLUSION

The unique morphological characteristics coupled with metallic nature, as well as synergistic effect between Ni, Co and Fe, led to the optimal electronic structure and moderate hydrogen adsorption energy, contributing to the significant enhancement OER performances. The NiCoFeOx_EC LDH NSs catalyst demonstrated superior OER activity and robust stability in all the basic media with relatively low overpotentials of 210 mV to afford 10 mA cm^{-2} current density. The current strategy opens new insights to design efficient electrocatalysts to further improve both activity and stability for OER.

ACKNOWLEDGMENTS

This research was supported by Brain Pool program funded by the Ministry of Science and ICT through the National Research Foundation of Korea (NRF-2021H1D3A2A01099457, 2022H1D3A2A01093556).

REFERENCES

Ambrosi, A., Sofer, Z., & Pumera, M. (2015). Lithium intercalation compound dramatically influences the electrochemical properties of exfoliated MoS2. *Small*, *11*(5), 605-612.

Chavhan, S. D., Hansson, R., Ericsson, L. K., Beyer, P., Hofmann, A., Brütting, W., . . . Moons, E. (2017). Low temperature processed NiOx hole transport layers for efficient polymer solar cells. *Organic Electronics*, *44*, 59-66.

Che, Q., Li, Q., Tan, Y., Chen, X., Xu, X., & Chen, Y. (2019). One-step controllable synthesis of amorphous (Ni-Fe) Sx/NiFe (OH) y hollow microtube/sphere films as superior bifunctional electrocatalysts for quasi-industrial water splitting at large-current-density. *Applied Catalysis B: Environmental*, *246*, 337-348.

Chen, G., Wan, H., Ma, W., Zhang, N., Cao, Y., Liu, X., . . . Ma, R. (2020). Layered metal hydroxides and their derivatives: Controllable synthesis, chemical exfoliation, & electrocatalytic applications. *Adv. energy materials*, *10*(11), 1902535.

Chen, L., Dong, X., Wang, Y., & Xia, Y. (2016). Separating hydrogen and oxygen evolution in alkaline water electrolysis using nickel hydroxide. *Nature communications*, *7*(1), 1-8.

Dang, L., Liang, H., Zhuo, J., Lamb, B. K., Sheng, H., Yang, Y., & Jin, S. (2018). Direct synthesis and anion exchange of noncarbonate-intercalated NiFe-layered double hydroxides and the influence on electrocatalysis. *Chemistry of Materials*, *30*(13), 4321-4330.

Fan, Y., Wu, Y., Clavel, G., Raza, M. H., Amsalem, P., Koch, N., & Pinna, N. (2018). Optimization of the activity of Ni-based nanostructures for the oxygen evolution reaction. *ACS Applied Energy Materials*, *1*(9), 4554-4563.

Gicha, B. B., Tufa, L. T., Choi, Y., & Lee, J. (2021). Amorphous Ni1–x Fe x Oxyhydroxide Nanosheets with Integrated Bulk and Surface Iron for a High and Stable Oxygen Evolution Reaction. *ACS Applied Energy Materials*, *4*(7), 6833-6841.

GolrokháAmin, B. (2017). CoNi 2 Se 4 as an efficient bifunctional electrocatalyst for overall water splitting. *Chemical Communications*, *53*(39), 5412-5415.

Gong, Y., Yuan, H., Wu, C.-L., Tang, P., Yang, S.-Z., Yang, A., . . . Brongersma, M. L. (2018). Spatially controlled doping of two-dimensional SnS2 through intercalation for electronics. *Nature nanotechnology*, *13*(4), 294-299.

Grosvenor, A., Kobe, B., Biesinger, M., & McIntyre, N. (2004). Investigation of multiplet splitting of Fe 2p XPS spectra and bonding in iron compounds. *Surface and Interface Analysis: An International Journal devoted to the development and application of techniques for the analysis of surfaces, interfaces and thin films*, *36*(12), 1564-1574.

Jin, W., Chen, J., Liu, B., Hu, J., Wu, Z., Cai, W., & Fu, G. (2019). Oxygen Vacancy–Rich In-Doped CoO/CoP Heterostructure as an Effective Air Cathode for Rechargeable Zn–Air Batteries. *Small*, *15*(46), 1904210.

Jin, Y., Huang, S., Yue, X., Du, H., & Shen, P. K. (2018). Mo-and Fe-modified Ni (OH) 2/NiOOH nanosheets as highly active and stable electrocatalysts for oxygen evolution reaction. *ACS Catalysis*, *8*(3), 2359-2363.

Jung, W., Lee, S., Yoo, D., Jeong, S., Miro, P., Kuc, A., . . . Cheon, J. (2015). Colloidal synthesis of single-layer MSe2 (M= Mo, W) nanosheets via anisotropic solution-phase growth approach. *Journal of the American Chemical Society*, *137*(23), 7266-7269.

Komsa, H.-P., & Krasheninnikov, A. V. (2012). Two-dimensional transition metal dichalcogenide alloys: stability and electronic properties. *The Journal of Physical Chemistry Letters*, *3*(23), 3652-3656.

Kuai, C., Zhang, Y., Wu, D., Sokaras, D., Mu, L., Spence, S., . . . Du, X.-W. (2019). Fully oxidized Ni–Fe layered double hydroxide with 100% exposed active sites for catalyzing oxygen evolution reaction. *ACS Catalysis*, *9*(7), 6027-6032.

LeBeau, J., Findlay, S., Allen, L. J., & Stemmer, S. (2012). *Quantitative STEM: Experimental Methods and Applications.* Paper presented at the Journal of Physics: Conference Series.

Li, C., Han, X., Cheng, F., Hu, Y., Chen, C., & Chen, J. (2015). Phase and composition controllable synthesis of cobalt manganese spinel nanoparticles towards efficient oxygen electrocatalysis. *Nature communications*, *6*(1), 1-8.

Li, H., Lu, G., Wang, Y., Yin, Z., Cong, C., He, Q., . . . Zhang, H. (2013). Mechanical exfoliation and characterization of single-and few-layer nanosheets of WSe2, TaS2, and TaSe2. *Small*, *9*(11), 1974-1981.

Liang, C., Zou, P., Nairan, A., Zhang, Y., Liu, J., Liu, K., . . . Yang, C. (2020). Exceptional performance of hierarchical Ni–Fe oxyhydroxide@ NiFe alloy nanowire array electrocatalysts for large current density water splitting. *Energy & Environmental Science*, *13*(1), 86-95.

Luo, M., Zhao, Z., Zhang, Y., Sun, Y., Xing, Y., Lv, F., . . . Qin, Y. (2019). PdMo bimetallene for oxygen reduction catalysis. *Nature*, *574*(7776), 81-85.

Ma, Y., Wang, K., Liu, D., Yang, X., Wu, H., Xiao, C., & Ding, S. (2019). Surface dual-oxidation induced metallic copper doping into NiFe electrodes for electrocatalytic water oxidation. *J. of Materials Chemistry A*, *7*(40), 22889-22897.

Masud, J., Swesi, A. T., Liyanage, W. P., & Nath, M. (2016). Cobalt selenide nanostructures: an efficient bifunctional catalyst with high current density at low coverage. *ACS applied materials & interfaces*, *8*(27), 17292-17302.

Ni, C.-S., Liu, S.-F., Lee, J.-F., Pao, C.-W., Chen, J.-L., Chen, H.-Y., & Huang, J.-H. (2021). Binder-free NiCoFe layered double hydroxide nanosheets for flexible energy storage devices with high-rate-retention characteristics. *Electrochimica Acta*, *384*, 138415.

Qin, M., Li, S., Zhao, Y., Lao, C. Y., Zhang, Z., Liu, L., . . . Liu, Z. (2019). Unprecedented synthesis of holey 2D layered double hydroxide nanomesh for enhanced oxygen evolution. *Advanced Energy Materials*, *9*(1), 1803060.

Reddy, C. V., Reddy, K. R., Shetti, N. P., Shim, J., Aminabhavi, T. M., & Dionysiou, D. D. (2020). Hetero-nanostructured metal oxide-based hybrid photocatalysts for enhanced photoelectrochemical water splitting–a review. *International journal of hydrogen energy*, *45*(36), 18331-18347.

Tan, B. J., Klabunde, K. J., & Sherwood, P. M. (1991). XPS studies of solvated metal atom dispersed (SMAD) catalysts. Evidence for layered cobalt-manganese particles on alumina and silica. *J. of the American Chemical Society*, *113*(3), 855-861.

Tan, C., Cao, X., Wu, X.-J., He, Q., Yang, J., Zhang, X., . . . Nam, G.-H. (2017). Recent advances in ultrathin two-dimensional nanomaterials. *Chemical reviews*, *117*(9), 6225-6331.

Tong, Y., Guo, H., Liu, D., Yan, X., Su, P., Liang, J., . . . Dou, S. X. (2020). Vacancy engineering of iron-doped W18O49 nanoreactors for low-barrier electrochemical nitrogen reduction. *Angewandte Chemie*, *132*(19), 7426-7431.

Tufa, L. T., Gicha, B. B., Wu, H., & Lee, J. (2021). Fe-Based Mesoporous Nanostructures for Electrochemical Conversion and Storage of Energy. *Batteries & Supercaps*, *4*(3), 429-444.

Tufa, L. T., Oh, S., Kim, J., Jeong, K.-J., Park, T. J., Kim & Lee, J. (2018). Electrochemical immunosensor using nanotriplex of graphene quantum dots, Fe3O4, and Ag nanoparticles for tuberculosis. *Electrochimica Acta*, *290*, 369-377.

Voiry, D., Salehi, M., Silva, R., Fujita, T., Chen, M., Asefa, T., . . . Chhowalla, M. (2013). Conducting MoS2 nanosheets as catalysts for hydrogen evolution reaction. *Nano letters*, *13*(12), 6222-6227.

Wang, G., Ling, Y., Wheeler, D. A., George, K. E., Horsley, K., Heske, C., . . . Li, Y. (2011). Facile synthesis of highly photoactive α-Fe2O3-based films for water oxidation. *Nano Letters*, *11*(8), 3503-3509.

Wells, R. A., Zhang, M., Chen, T.-H., Boureau, V., Caretti, M., … Radenovic, A. (2022). High Performance Semiconducting Nanosheets via a Scalable Powder-Based Electrochemical Exfoliation Technique. *ACS nano*, *16*(4), 5719-5730.

Wu, J., Ren, Z., Du, S., Kong, L., Liu, B., Xi, W., … Fu, H. (2016). A highly active oxygen evolution electrocatalyst: Ultrathin CoNi double hydroxide/CoO nanosheets synthesized via interface-directed assembly. *Nano Research*, *9*(3), 713-725.

Wu, X., Zhang, H., Zhang, J., & Lou, X. W. (2021). Recent Advances on Transition Metal Dichalcogenides for Electrochemical Energy Conversion. *Advanced Materials*, *33*(38), 2008376.

Xi, X., Wang, Z., Zhao, W., Park, J.-H., Law, K. T., Berger, H., . . . Mak, K. F. (2016). Ising pairing in superconducting NbSe2 atomic layers. *Nature Physics*, *12*(2), 139-143.

Yan, Z., Liu, H., Hao, Z., Yu, M., Chen, X., & Chen, J. (2020). Electrodeposition of (hydro) oxides for an oxygen evolution electrode. *Chemical Science*, *11*(39), 10614-10625.

Yang, S., Lohe, M. R., Müllen, K., & Feng, X. (2016). New-generation graphene from electrochemical approaches: production and applications. *Advanced Materials*, *28*(29), 6213-6221.

Yarger, M. S., Steinmiller, E. M., & Choi, K.-S. (2008). Electrochemical synthesis of Zn− Al layered double hydroxide (LDH) films. *Inorganic chemistry*, *47*(13), 5859-5865.

Yi, H., Liu, S., Lai, C., Zeng, G., Li, M., Liu, X., . . . Li, L. (2021). Recent Advance of Transition-Metal-Based Layered Double Hydroxide Nanosheets: Synthesis, Properties, Modification, and Electrocatalytic Applications. *Advanced Energy Materials*, *11*(14), 2002863.

Yu, X., & Sivula, K. (2017). Photogenerated charge harvesting and recombination in photocathodes of solvent-exfoliated WSe2. *Chemistry of Materials*, *29*(16), 6863-6875.

Zhang, M., Liu, Y., Liu, B., Chen, Z., Xu, H., & Yan, K. (2020). Trimetallic NiCoFe-layered double hydroxides nanosheets efficient for oxygen evolution and highly selective oxidation of biomass-derived 5-hydroxymethylfurfural. *ACS Catalysis*, *10*(9), 5179-5189.

Zhang, W.-D., Hu, Q.-T., Wang, L.-L., Gao, J., Zhu, H.-Y., Yan, X., & Gu, Z.-G. (2021). In-situ generated Ni-MOF/LDH heterostructures with abundant phase interfaces for enhanced oxygen evolution reaction. *Applied Catalysis B: Environmental*, *286*, 119906.

Zhang, W.-D., Yu, H., Li, T., Hu, Q.-T., Gong, Y., Zhang, D.-Y., . . . Yan, X. (2020). Hierarchical trimetallic layered double hydroxide nanosheets derived from 2D metal-organic frameworks for enhanced oxygen evolution reaction. *Applied Catalysis B: Environmental*, *264*, 118532.

Zheng, J., Zhang, H., Dong, S., Liu, Y., Tai Nai, C., Suk Shin, H., . . . Ping Loh, K. (2014). High yield exfoliation of two-dimensional chalcogenides using sodium naphthalenide. *Nature communications*, *5*(1), 1-7.

Zheng, W., & Lee, L. Y. S. (2022). Beyond sonication: Advanced exfoliation methods for scalable production of 2D materials. *Matter*.

Zhu, K., Shi, F., Zhu, X., & Yang, W. (2020). The roles of oxygen vacancies in electrocatalytic oxygen evolution reaction. *Nano Energy*, *73*, 104761.

Zhu, X., Su, Z., Wu, C., Cong, H., Ai, X., Yang, H., & Qian, J. (2022). Exfoliation of MoS2 Nanosheets Enabled by a Redox-Potential-Matched Chemical Lithiation Reaction. *Nano Letters*, *22*(7), 2956-2963.

Syndicate 3:

Environment and Natural Resources

HSSFCW Efficiency and Microbial Dynamics in Treating UASBR Brewery Effluent

Ermias Alayu[1,*], Seyoum Leta[2]

[1]*Department of Environmental Science, College of Agricultural Sciences, Wachemo University, P.O. Box 667, Hosanna, Ethiopia*
[2]*Center for Environmental Science, College of Natural and Computational Science, Addis Ababa University , P.O.Box 1176, Addis Ababa, Ethiopi*
**Corresponding author, e-mail: ermias.alayu@gmail.com*

ABSTRACT

Brewery effluent has a high concentration of organics, suspended solids and nutrients that can significantly degrade the quality of aquatic habitats. Some breweries in Ethiopia have used a UASBR (Up-flow Anaerobic Sludge Blanket Reactor) technology to treat their wastewaters, but the final treated effluent doesn't achieve the national discharge limit and needs subsequent polishing. The goal of this study was to assess the treatment efficiency and bacterial community profile of a two-stage pilot-scale HSSFCW (horizontal subsurface flow constructed wetland) used for UASBR effluent polishing. The HSSFCW system was integrated with the existing UASBR and its effectiveness was evaluated for the main brewery pollutants. Colometric and 16S rRNA metagenomic sequencing techniques were used to evaluate the HSSFCW wastewater quality and macrophytes nutrient accumulation potential; and microbial community dynamics, respectively. The HSSFCW's water quality index (WQI) was also calculated. The results revealed that the two-stage HSSFCW achieved an overall abatement efficiencies of 92%COD, 89%TSS, 92.9%NH_4^+ – N, 83.6%TN, 79.5% PO_4^{3-}, and 74.4%TP. These enhanced removals of main brewery pollutants are due to the combined effect of macrophytes, clay media and different microbial communities. The two-stage HSSFCW macrophytes nutrient absorption potential was 708.7 $gTPm^{-2}$and 1290 $gTNm^{-2}$. The dominant microbial community species in the first cell were Clavibacter michiganensis, Dokdonella immobilis, and Longilinea arvoryzae; whereas, Syntrophorhabdus aromaticivorans, Aminiphilus circumscriptus, Thermovirga lienii, Longilinea arvoryzae, Methanothrix soehngenii, and Desulfoglaeba alkanexedens were the most prevalent species in the second cell. In general, further polishing of the UASBR effluent with two-stage HSSFCW has shifted the WQI from a good to excellent water quality rating, and meets the discharge cap of all examined parameters. Hence, post – treatment of UASBR treated brewery effluent using two-stage HSSFCW system is promising.

Keywords: *Brewery wastewater, constructed wetland, water quality index, microbial community dynamics, nutrient removals*

1. INTRODUCTION

In Ethiopia, agro-industries such as breweries are seen as a multi-national business complex and have played a significant economic role. However, their untreated or partially treated effluent discharge poses a severe threat to the environment and public health (Temesgen Oljira et al., 2018). Todays, up-flow anaerobic sludge blanket reactor (UASBR) is thought to be a sustainable solution for the treatment of organic matter-rich wastewaters and create value-added products like biogas and organic fertilizer. Some brewery industries in Ethiopia have employed this technology (Kebena Bulla, 2014). But, the final treated effluents would not meet the required discharge standards for residual carbon, nutrients, and other contaminants; it cannot be viewed as offering a "full" environmental solution (Yasar and Tabinda, 2009). This has given an impetus for further polishing in order to safeguard the environment and public health. Among the many alternatives, constructed wetland (CW) systems have become more economical, effective and ecologically sound polishing options (Vymazal, 2007; Vymazal and Kropfelova, 2008). The HSSFCW is frequently used for the removal of suspended solids, organic matter, and nitrogen from primary and secondary-treated wastewaters worldwide including Ethiopia (Zeb et al., 2013; Adey Feleke et al., 2014). However, the treatment of high strength food processing wastewaters using this polishing stage is difficult to produce high-quality effluent (Vymazal, 2005).

Use of a variety of macrophyte-planted HSSFCW system is recommended for improved elimination of pollutants by raising the microbial activity, and nutrient uptakes (Cheng et al., 2010). Individual performance efficiency assessment of *C. alternifolius* and *T. latifolia* exhibited good removal efficiency of organic matter and nutrients from wastewater (Ciria et al., 2005; Sa'at et al., 2017). However, their combined treatment efficiency was not studied until yet. Besides, bacterial communities in the CW bioreactor contributed enhanced pollutants reductions through oxidation and nitrification-denitrification processes (Vymazal, 2005; Kadlec and Wallace, 2009). Some few studies investigated the microbial community dynamics' and their relationships to the removal of organic matter, phosphate, and nitrogen in single stage HSSFCW systems (Adey Feleke et al., 2014). However, the type and operational circumstances of the CW system and the physicochemical composition of wastewater might affect microbial taxonomic and functional diversity (Wang et al., 2016). Similarly, no research has been done on the microbial dynamics of a two-stage HSSFCW system planted with *C. alternifolius* and *T. latifolia* for treating UASBR brewery effluent. As a result, this study was carried out to assess the effectiveness (removal efficiency and water quality index (WQI)) and the microbial community dynamics in a two-stage HSSFCW system.

2. MATERIALS AND METHODS

2.1 Experimental Location

A two-stage pilot-scale HSSFCW system was connected with the existing UASBR brewery effluent treatment plant in Kombolcha town, Northern Ethiopia, located at 11º04´42.43´´N 39º43´34.45´´ E and 1833 m above sea level, an area with annual average minimum and maximum temperatures varying between 6.1–15.2ºC and 24.7–30.4ºC, respectively, and mean annual rainfall of 255.7 mm.

2.2 Experimental Design and Setup of the Two-stage HSSFCW

The experimental setup is represented in Fig. 1(a) by the current UASBR treatment plant (I), distribution tank (II), two-stage HSSFCW system (III), and collection tank (IV). A first-order plug flow model equation (1) was used to calculate the size of the HSSFCW area (UN-HABITAT, 2008).

$$As = Qd(\ln C_i - \ln C_e)/K_{BOD} \quad \ldots(1)$$

Accordingly, each series-connected pilot-scale HSSFCW cell was sized using the daily hydraulic flow rate, Q_d (0.698 m^3d^{-1}), inlet BOD concentration (223.9114 mgL^{-1}), outlet BOD concentration (60 mgL^{-1}), and BOD rate constant (KBOD). The K_{BOD} is fluctuating between 0.07 and 0.1 md^{-1}. But many nations utilized 0.08 md^{-1} (Vymazal and Kropfelova, 2008). Therefore, each HSSFCW cell had a diameter of 7.56 m 1.52 m (Length x Width) and a depth of 0.45 m. Each cell's actual aspect ratio (L/W) was 5:1, which is in line with the suggested value of 5:1 (Kadlec and Wallace 2009). An equation (2) was used to compute the theoretical HRT (day):

$$\text{HRT (day)} = \frac{LWDP}{Qd} \quad \ldots(2)$$

The interior of the HSSFCW body's was insulated to prevent seepage. Inside the HSSFCW, the output pipe was mounted 0.35 m above the floor and connected to the collection tank using T-shaped tubing. Each HSSFCW cell was filled with a 15–25 mm-sized local clay rock media with an effective media porosity of 0.27 and a mineral composition of 76.36%SiO_2, 13.69%Al_2O_3, 4.24% Fe_2O_3, 1.52% CaO, <0.1% MgO. Two readily available macrophytes were taken from the Borkena River and identified at the National Herbarium of Addis Ababa University. In August 2018, the macrophytes were then planted in each HSSFCW cells. The plantation order is shown in Fig. 1(b), *C. alternifolius* came first because of its high pH resistance, high productivity, relatively strong root system, ease of adaptation to changes in organic load, salinity tolerance, and high nutrient absorption capacity (Bilgin *et al.*, 2014). *T. latifolia* came second because of its short root length (Bonanno and Cirelli, 2017), less

salinity tolerance, and ability to reduce nutrient (Mollard *et al.*, 2013). In addition, the ability of these macrophytes to maintain adequate porosity in order to allow good hydraulic conductivity, and low evapotranspiration rates (Leto *et al.*, 2013) were considered as a selection criteria. Diluted brewery effluent to clean pipe water (75:25) was used to acclimatize the macrophytes. The two-stage HSSFCW cell was operated for a year (January 2019 to December 2019) at 4 days HRT, by pumping a daily hydraulic flow rate of 0.7 m^3d^{-1} after optimization.

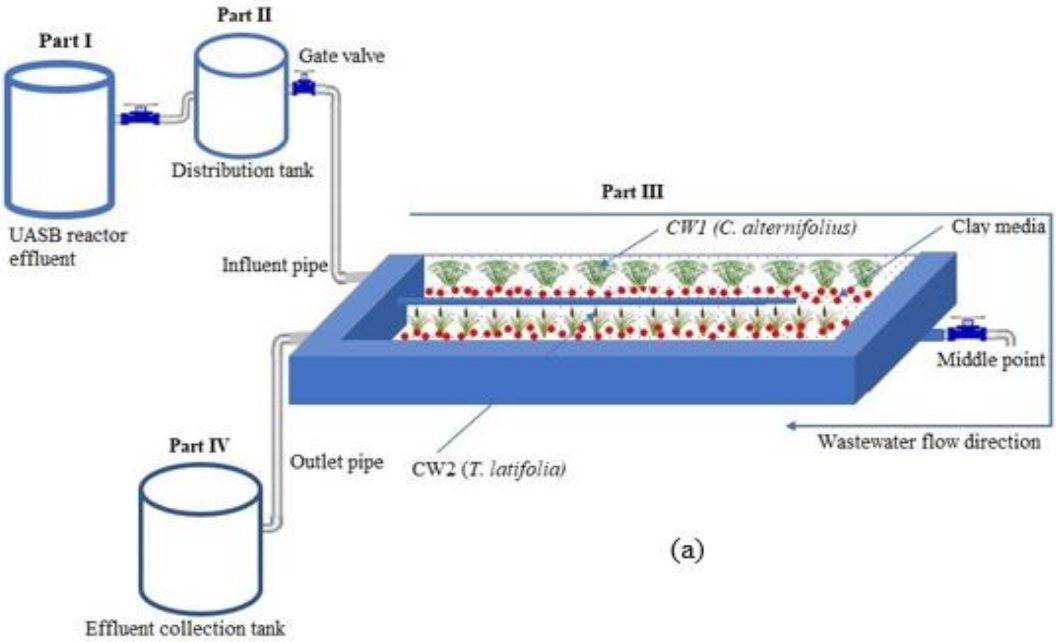

(b)

Figure 1: *(*a) Schematic design of the *t*wo-stage HSSFCW cell experimental setup, and (b) field view of the cell after plantation

2.3 Wastewater, Macrophytes and Biofilm Sampling and Analysis

2.3.1 Wastewater Sampling and Analysis

Wastewater samples were collected three times a month for one year from the inlet of CW1, the middle point of the two macrophytes, and the outlet of CW2 (Fig. 1(a)) and then transferred to the lab for immediate examination. A handheld IntelliCALTM pH/temperature digital probe (HACH® HD30d Flexi, Loveland, USA), conductivity meter (OAKTON®, Vernon Hills, IL, USA), and DO meter (YSI 550A, Yellow Springs, OH, USA) were used to measure pH, temperature, EC, and DO in-situ. TSS, COD, TN, NH_4^+- N, TP, and PO_4^{3-} were measured ex situ, using the gravimetric method (SKU Carbolite CD Drying Oven, Germany), closed reflux (HACH, SKUDR900, Germany), Nessler (HACH, SKUDR900, Germany), Molybdovanadate with Acid Persulfate Digestion, and

PhosVer 3® methods, respectively (APHA, 1998). Equation (3) was used to calculate the pollutant removal efficiency (RE) (Juang and Chen, 2007):

$$RE\ (\%) = \frac{C_i - C_e}{C_i} \times 100 \ldots(3)$$

For analysis of the WQI of the UASBR and two-stage HSSFCW treatment plant effluents, the EEPA (2003) discharge guideline and one-year effluent record data of temperature, pH, TSS, COD, TN, NH_4^+ – N, and TP were used. The WQI was calculated using the CCME guideline conceptual framework (Betis et al., 2020) indicated in equation (4):

$$WQI=100 - \left(\frac{\sqrt{F_1+F_2+F_3}}{1.732}\right) \ldots(4)$$

Where, F_1 is the percentage of treated effluent parameters, which does not meet or failed the discharge standard limits at least once relative to the total number of parameters measured:

$$F_1= \frac{\text{Number of failed paramters}}{\text{Total number of parameters}} \times 100 \ldots (5)$$

F_2 is the percentage of all measurement parameters that do not meet their discharge standard limits or failed tests:

$$F_2= \frac{\text{Number of failed tests}}{\text{Total number of tests}} \times 100 \ldots (6)$$

F_3 is the normalized sum of the excursions (NSE); calculated by summing the individual test extrusions dividing by the total number of tests (both meeting and not meeting the objectives).

$$F_3= \frac{NSE}{0.01NSE + 0.01} \ldots(7)$$

The NSE is calculated using:

$$NSE= \frac{\sum_{i=1}^{n} \text{extrusions}}{\text{Total number of tests}} \ldots(8)$$

But, extrusions are determined using:

$$\text{extrusion}_i= \left(\frac{\text{Failed test}_i}{\text{Objective}_j}\right) -1 \ldots(9)$$

1.732 is a factor that is used to normalize the result to a value between 0 and 100. WQI values were classified into five categories following CCME as Excellent: 95≤WQI≤100; Good: 80≤WQI≤94; Fair: 65≤WQI≤79; Marginal: 45≤WQI≤64; and Poor: 0≤WQI≤44 (Betis et al., 2020).

2.3.2 HSSFCW Macrophytes Sampling and Analysis

Aboveground biomasses (AGB) of *C. alternifolius* and *T. latifolia* were collected from the two-stage HSSFCW cells for every three months during the year, and transported in plastic bags to the lab for analysis of their dry weight and nutrient content. Macrophytes AGB were baked for 24 hours at 105°C and weighed. The AGB pieces were finely ground to a size of around 2 mm. TN was examined using UV-Vis spectroscopy and the potassium-persulfate digestion technique (APHA, 1998). TP was measured by digesting a 0.5 g powdered sample in aquaregia for 2h at 90°C on a hot plate and determined using Inductively Coupled Plasma (ICP - OES, Arcos spectrophotometer, Germany). Equation (10) was used to determine the nutrient accumulation (N) in the macrophytes AGB.

$$N\ (gm^{-2}) = DM_{macrophyte} x\ C_{macrophyte} \ldots(10)$$

Where C is the concentration of TN ($gN\ kg^{-1}$) or TP ($gPkg^{-1}$) in the macrophytes and DM is the dry weight biomass of macrophytes (kgm^{-2}).

2.3.3 HSSFCW Biofilm Sampling and Analysis

HSSFCW biofilm sampling: Composite biofilm samples were collected from each HSSFCW cell. Then, following their shipping guidelines, raw samples were sent to Admera Health LLC (South Plainfield, NJ, USA) within a week through DHL. **DNA extraction:** according to the manufacturer's instructions, biofilm samples were extracted from a 0.4 g of sample using the NucleoSpin Soil Kit (Macherey-Nagel, Allentown, PA, USA). The quality of the extracted genomic DNA was determined by the Tapestation genomic DNA Assay and its quantity was determined using a Qubit 2.0 DNA HS Assay from ThermoFisher in Massachusetts (Agilent Technologies, California, USA). **PCR amplification and Library preparation of the 16S rRNA gene:** the FloracheckTM panel was used to perform PCR amplification of the 16S at the V3-V4 hyper variable regions of the extracted DNA (Admera Health LLC, South Plainfield, NJ, USA). The 16S V3-V4 (341–806) region was covered by multiplex primers, and the primers were chosen and designed to provide thorough taxonomic coverage before spike-ins were eliminated. According to the manufacturer's instructions, the PCR reactions were conducted under the required conditions. Additionally, the Tapestation DNA Assay was used to verify the PCR products (Amplicon), and the QuantStudio ® 5 System's APA SYBR® FAST qPCR was used to determine their quantity (Applied Biosystems, California, USA). Following quality control on the 16S barcoded libraries, Illumina MiSeq V2 Standard (Illumina, CA, USA) was used to sequence the amplicons using a read length of 250 PE for 0.1 M pair end (PE) reads per sample. **Sequence data analysis**: the NCBI sequence read repository was used for sequencing data storage. With the help of USEARCH and UCLUST algorithms, taxonomy assignment, abundance estimation, and diversity studies were performed on the raw sequence reads to produce high quality (HQ) reads (Edgar, 2016). Adaptor sequences, failed reads, Barcodes, sequences containing ambiguous reads (N), unknown nucleotides, and low quality sequences were trimmed to produce high quality clean PE reads. USEARCH pipeline was used to combine the high-quality or clean PE data into single end (SE) readings. The clean sequences were checked for chimeras using UCHIME. The operational taxonomic unit (OTU) clustering, chimera filtering, read mapping to OTUs, and production of OTU table were carried out using UPARSE workflow at 97% sequence similarity level (Nguyen *et al*., 2016). The taxonomy of the query sequences was predicted using the SINTAX algorithm (Edgar, 2016).

2.4 Data Analysis

The krona Tool (PhyloSift Markers) was used to analyze the bacterial composition of each HSSFCW cell. To comprehend the relationship between pollutant removals and microbial populations, principal components analysis (PCA) was carried out using Origin® Pro 2017 software. The mean and standard deviation data were used to express the results. Graphs and tables were used to display the results.

3. RESULTS AND DISCUSSION

3.1. Pollutant Reduction in the Pilot Scale HSSFCW System

3.1.1 Properties of In-situ Measured Parameters

The two-stage HSSFCW influent's average pH value was 7.6±0.3. However, polishing with CW1 cell, its value increased to 7.7±0.3, and further polishing with CW2 cell decreased it to 7.6±0.2 (Table 1). These pH values were fall within the ideal pH range of 6.5 - 8.5 (Vymazal, 2007). As a result, they cannot affect both microbial activity and macrophyte growth in the two-stage HSSFCW cells. The two-stage HSSFCW influent had also an average temperature of 32.7±1.6^{o}C, which again meet the ideal temperature range of 19 - 34^{o}C that enhances the

development and activity of microorganisms as well as the growth of macrophytes (Zamora *et al.*, 2019). Treatment with CW1 cell lowered to 25±2.2°C, and additional treatment with CW2 cell decreased to 20.1±0.6°C (Table 1) might be due to its contact with the wetland components. The two-stage HSSFCW influent's DO concentration was 0.4±0.1 mgL^{-1}. However, treatment with CW1 cell increased to 3.5±0.6 mgL^{-1}, and further polishing with CW2 cell significantly decreased to 2.3±0.6 mgL^{-1} (Table 1). The higher DO level in CW1 might be associated with *C. alternifolius* adequate aeration because of its extensive lacunar systems, which facilitate convective air delivery from the atmosphere to the rhizosphere (La Bella *et al.*, 2016; Rehman *et al.*, 2017). Whereas, the decreased DO level in the CW2 cell may be due to the shorter root growth of *T. latifolia* (Bonanno and Cirelli, 2017).

Table 6: Average influent and effluent concentrations and percentage removal efficiencies of main brewery pollutants in two-stage HSSFCW system

Parameters	Influent concentration	CW1 effluent concentration	CW2 effluent concentration	CW1 RE	CW2 RE	CW1 + CW2 RE
Temp. (°C)	32.7±1.6	25±2.2	20.1±0.8	-	-	-
pH	7.6±0.3	7.7±0.4	7.6±0.2	-	-	-
DO (mgL^{-1})	0.41±0.15	3.54±0.62	2.31±0.56	-	-	-
TSS (mgL^{-1})	211.23±42.75	68.17±25.93	24.31±13.29	68.53±6.79	20.51±2.68	89.66±3.53
COD (mgL^{-1})	386.44±112.18	103.85±46.2	32.71±16.97	74.23±5.35	17.81±3.04	92.03±2.6
TN (mgL^{-1})	51.1±22.4	23.18±11.91	8.94±5.41	55.68±3.38	27.94±2.76	83.63±3.3
NH_4^+-N (mgL^{-1})	35.29±16.54	12.09±7.79	2.92±1.47	68.55±8.86	24.33±6.52	92.88±2.84
TP (mgL^{-1})	28.97±7.7	17.34±6.33	7.58±4.76	41.1±7.03	33.3±9.7	74.43±13.3
PO_4^{3-} (mgL^{-1})	21.07±6.9	11±4.31	4.43±2.95	48.14±7.48	31.33±6.78	79.47±11.32

3.1.2 Suspended Solids, Organic Matter and Nutrient Removals

As indicated in Table 1, post – treatment of the UASBR treated brewery effluent with CW1 cell reduced its influent TSS and COD concentrations significantly with an average removal efficiency of 68.53±6.79% TSS and 74.23±5.35% COD (Table 1). Further treatment with CW2 cell able to achieved an overall abatement efficiencies of 89%TSS and 92%COD with enhanced TSS and COD concentration reductions that met the EEPA standard limits of < 50 $mgTSSL^{-1}$ and 250 mg $CODL^{-1}$. The current two-stage HSSFCW system achieved better abatement efficiency as compared to another two-stage HSSFCW system planted with *P. australis* and *P. stratiotes* for polishing of the UASBR treated mixture of sewage and swine wastewater at HRT of 13.5 days; achieved 79.4%TSS and 75.9%COD removals (Cheng et al., 2010). These promising removals are associated with macrophytes' roots and presence of diversified microbial communities, which filter more suspended solids and breaks down organic matters (Lloréns et al., 2020; Wijaya et al., 2016). The two-stage HSSFCW system also showed encouraging removal efficiency for TN and NH_4^+– N throughout the HSSFCW cells. As shown in Table 1, the concentrations of TN and NH_4^+– N significantly decreased across each treatment stages. Overall, the entire system achieved encouraging TN and NH_4^+– N abatement efficiencies (Table 1) and concentration reductions below the respective national discharge standard limits of 40 $mgTNL^{-1}$ and 20 $mgNH_4^+$– NL^{-1}. This outcome was similar to Da Motta Marques et al. (2001), who reported 90.4%TN and 95% NH_4^+ - N removal efficiencies at 1.5 days HRT using a HSSFCW cells planted with *Z. bonorriensis* and *T. subalata* during the polishing of the UASBR treated municipal wastewater. This promising result achievement might be due to the crucial role of *C. alternifolius* in reliable oxygen transport and improved nitrification (La Bella et al., 2016), as well as higher denitrification efficiency of *T. latifolia* (Fahlgren, 2017), because of its short root growth (Bonanno and Cirelli, 2017).

The two-stage HSSFCW polishing also revealed encouraged removal efficiency for TP and PO_4^{3-} (Table 1). Significant reductions in TP and PO_4^{3-} concentrations were observed after influent polishing with a CW1 cell with average removal efficiency of 41.1±7.03% and 48.14±7.48%, respectively (Table 1). Further polishing with CW2

cells decreased TP and PO_4^{3-} effluent significantly with corresponding average removal efficiencies of 33.3±9.7% and 31.33±6.78% (Table 1), and thus the complete system able to achieve the phosphorous concentration in compliance with the national EEPA discharge standard limit value of 5 mgL^{-1}. The overall system removal efficiency explored in this study (Table 1) was lower than Da Motta Marques et al. (2001) findings, who reported 93.3% of phosphorous removal at 1.5 days HRT using HSSFCW units planted with *Z. bonorriensis* and *T. subalata* during polishing of UASBR treated municipal wastewater; and higher than Cheng et al. (2010), who reported 75.1%TP removal using a two-stage HSSFCW system planted with *P. australis* and *P. stratiotes* during polishing of the UASBR treated mixture of sewage and swine wastewater at HRT of 13.5 days. This encouraging reduction may be attributable to the clay media's active adsorption, macrophytes and microbial uptakes. In general, the WQI evaluation revealed that the WQI of a UASBR effluent was varied from 91.6 to 92.9. But, further treatment with a two-stage HSSFCW system improved its WQI to the range of 95.8 to 100. Comparing to the CCME water quality rating guidelines (Betis et al., 2020), the present study WQI of the UASBR effluent is classified into a Good water quality class, while the two-stage HSSFCW effluent is classified into an Excellent water quality class.

3.2. Nutrient Uptakes by Macrophytes

The *C. alternifolius* and *T. latifolia* dry weight biomass was 8.64±4.32 kgm^{-2} and 12.09±6.04 kgm^{-2}, respectively (Fig. 2a). The above-ground biomass of *C. alternifolius* and *T. latifolia* contained 23.26±1.16 $gTNkg^{-1}$ and 25.61±1.28 $gTNkg^{-1}$, respectively. While the TP concentrations in these macrophytes was respectively 11.97±5.985 gkg^{-1} and 16.45±8.22 gkg^{-1} (Fig. 2b). The TN accumulation of *C. alternifolius* and *T. latifolia* was 260.55± 13.03 gm^{-2} and 388.6± 19.43 gm^{-2}, respectively. The TP accumulation potential for *C. alternifolius* and *T. latifolia* was 129.93±6.5 gm^{-2} and 231.8±11.59 gm^{-2}, respectively (Fig. 2c). Overall, both macrophytes absorbed 649.15 $gTNm^{-2}$ and 361.73 $gTPm^{-2}$, contributed a significant role in the reduction nutrients. Overall in Fig. 3cdef, there was a significant correlations between dry weight biomass and nutrient concentrations for both TN and TP: dry weight biomass and TN concentration (R^2 = 0.96, r = 0.98 for *C. alternifolius*; R^2 = 0.99, r = 0.99 for *T. latifolia*); dry weight biomass and TN accumulation (R^2 = 0.96, r = 0.98 for *C. alternifolius*; R^2 = 0.98, r = 0.99 for *T. latifolia*); and dry weight biomass and TP accumulation (R^2 = 0.92, r = 0.96 for *C. alternifolius*; R^2 = 0.98, r = 0.99 for *T. latifolia*).

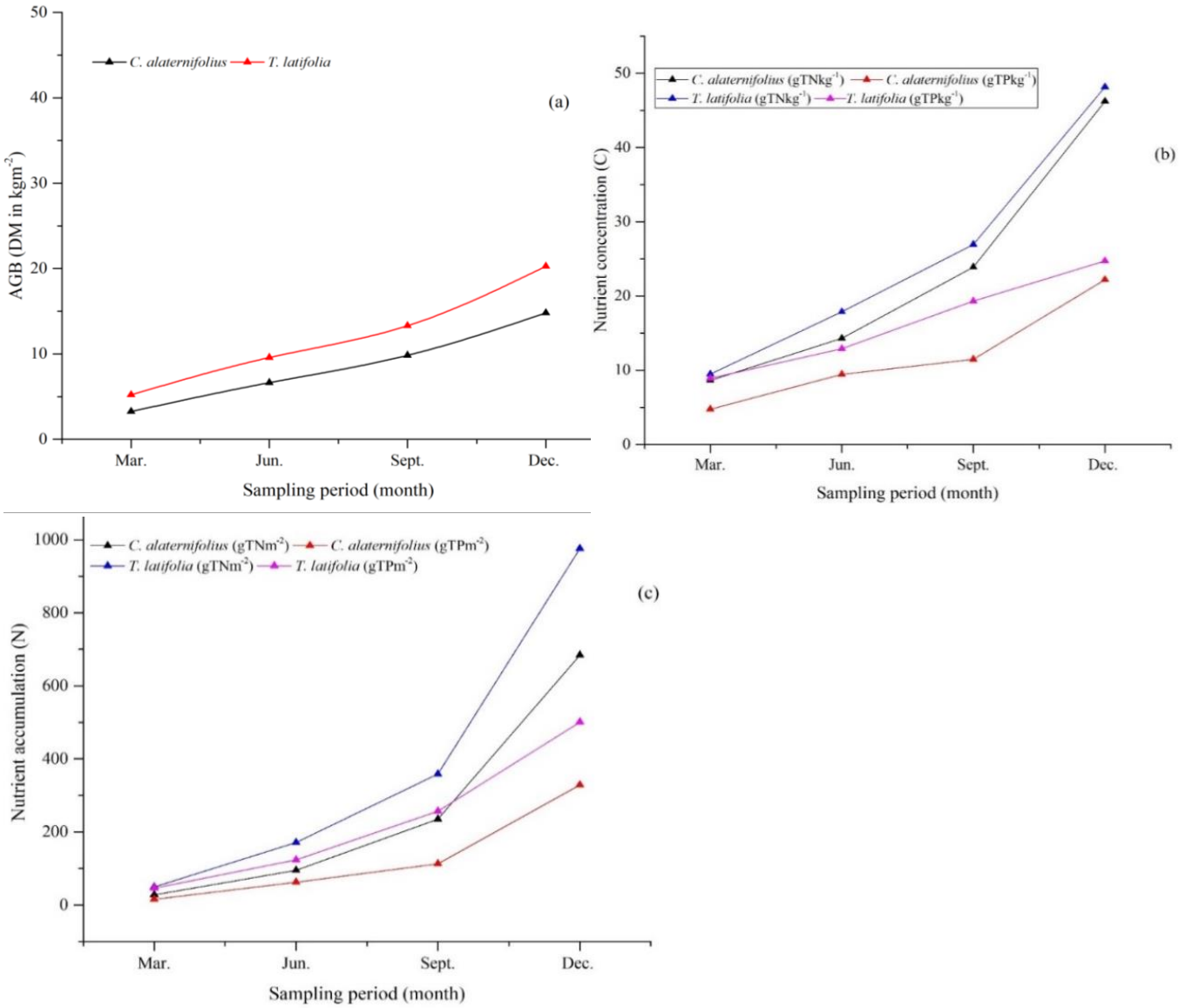

Figure 2: *C. alternifolius* and *T. latifolia* (a) aboveground biomass, (b) nutrient concentration, and (c) Nutrient accumulation

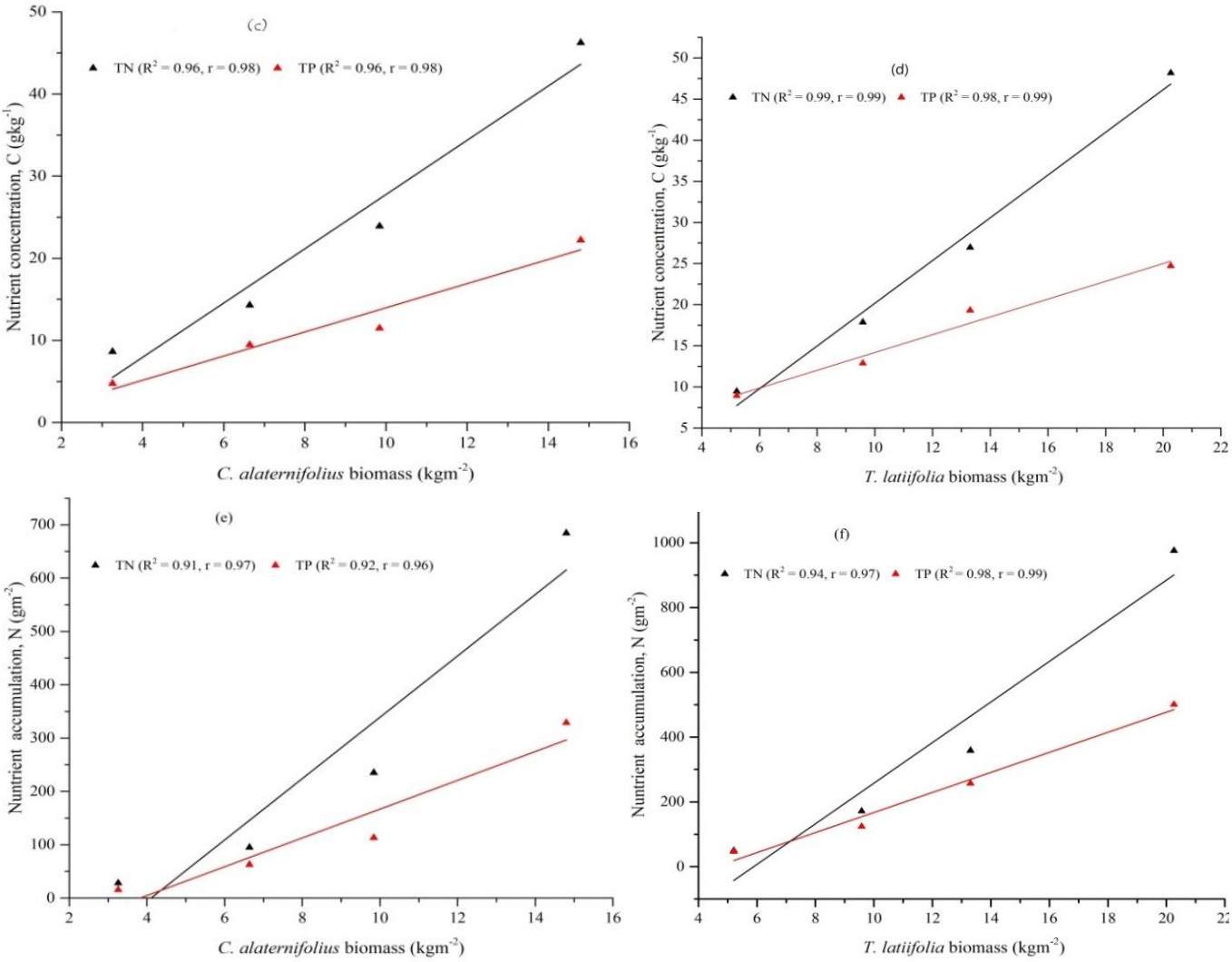

Figure 3: Correlation of (c) *C. aternifolius* DM with C, (d) *T. latifolia* DM with C, (e) *C. aternifolius* DM with N, and (f) *T. latifolia* DM with N

3.3 Microbial Community Dynamics in the Two-stage HSSFCW System

3.3.1 Microbial Community Taxonomic Richness

The 16S rRNA sequencing of biofilm samples produced 51, 929 and 53, 096 high-quality sequences with a total of 105,035 reads for CW1 and CW2 cells, respectively. Following further processing at 97% sequence similarity level, these sequence reads were divided into 517 OTUs (Table 2). The Shannon's diversity index of the CW1 cell was 5.13, while that of the CW2 cell was 4.83. These values were found in the range of 4.9 to 5.3, which have been observed in series-connected HSSFCW systems treating tannery effluent (Adey Feleke *et al*., 2014). On the other hand, these values exceeded the Shannon index range of the CW system, which is 2.25 to 3.55 (Garrido *et al*., 2014). This demonstrates that the rhizosphere of macrophytes offers several habitats for microorganisms.

Table 2: Alpha diversity indexes in the two-stage HSSFCW cells

HSSFCW stages	Reads	OTUs	Shannon index	Richness
CW1	51,939	517	5.13	324
CW2	53,096	517	4.83	310

3.3.2 Microbial Community Composition

Most of the sequences obtained in this investigation were bacteria (i.e., 96% for CW1 and 87.85% for CW2). But, some archaea communities were found in CW1 and CW2 cells having abundances of 4% and 12.15%, respectively. The archaea communities predominated in the CW2 cell may be related to the cell's predominately anaerobic zone favored by *T. latifolia's* short roots. The bacterial communities' presence in a CW bioreactor is beneficial for removing pollutants via various biological processes (Adrados *et al.*, 2014). Table 3 displays the species-level taxonomic classification of the microbial communities. Among the major identified species, *Novosphingobium arabidopsis*, *Rhodopseudomonas palustris*, *Aquabacterium limnoticum*, *Pseudoxanthomonas kaohsiungensis*, and *Nitratireductor aquimarinus* species were widely spread in the CW1 cell, and can perform enhanced nitrification - denitrification, and ammonia removal. Furthermore, higher abundance of *Micropruina glycogenica* and *Phreatobacter oligotrophus* were found in the CW1 cell, and plays a key role in phosphorous removal. The majority of these species are vital to the process of treating wastewater. For example, *Methanothrix soehngenii* breaks down organic chemicals into CH_4 and CO_2 (Huser et al., 1982) and *Xenophilus azovorans* (Blümel et al., 2001) break down xenobiotic compounds. *Syntrophorhabdus aromaticivorans* (do Nascimento et al., 2021) and *Dokdonella immobilis* (Chen et al., 2019) are used for the degradation of aromatic hydrocarbons and metabolize phenols. *Aminiphilus circumscriptus* is also an amino acid degrading bacteria (Diaz et al., 2007). While *Arcobacter suis* is used for nitrification and organic matter breakdown (Diaz et al., 2007). Lin et al. (2014) were employed *Novosphingobium arabidopsis* for nitrate reduction activities, and found it was successfully remove nutrients and organic debris (Dan et al., 2020), *Rhodopseudomonas palustris* utilized carbon sources and increased ammonium removal (Huang et al., 2018), while *Dokdonella immobilis* showed effective nitrate reduction efficiency (Liu et al., 2013). *Aquabacterium limnoticum* removes both organic matter and nutrients (Chen et al., 2012). *Nitratireductor aquimarinus* (Jang et al., 2011), and *Pseudoxanthomonas kaohsiungensis* (Chang et al., 2005) are used for nitrate conversion to dinitrogen. On the other hand, a higher abundance of *Methanothrix soehngenii*, *Aminiphilus circumscriptus*, *Desulfoglaeba alkanexedens*, *Syntrophorhabdus aromaticivorans*, *Dokdonella immobilis*, and *Arcobacter suis* species in the CW2 cell contributing further organic matter and nutrient removals left over the CW1 cell.

3.4 PCA of HSSFCW Effluent Pollutants and Microbial Community Species

The PCA analysis (Fig. 4) indicates that the COD and TSS removals are mostly associated many of the microbial species like *Xenophilus_azovorans*, *Longilinea arvoryzae*, *Brevundimonas nasdae*, *Rhodopseudomonas palustris*, *Ferruginibacter_alkalilentus*, *Syntrophorhabdus aromaticivorans*, *Rhodobacter blasticus Novosphingobium arabidopsis*, *Rhodopseudomonas palustris*, *Aquabacterium limnoticum*, *Pseudoxanthomonas kaohsiungensis*, *Dokdonella immobilis* and *Arcobacter suis* in CW1. Whereas, the nutrient removals were achieved in the CW2 with the presence *Methanobacterium_aarhusense*, *Syntrophorhabdus_aromaticivorans*, *Aminiphilus circumscriptus*, *Methanothrix_soehngenii*, *Novosphingobium arabidopsis*, *Nitratireductor aquimarinus*, *Methanothrix soehngenii*, *Arcobacter_suis*, *Desulfovirga_adipica*, and *Desulfoglaeba alkanexedens* microbial species. Similarly, Faulwetter et al. (2009) reported that the removal of a particular pollutant is typically correlated with a specific microbial functional group.

Table 2. Relative abundance of major species in the two-stage HSSFCW system

Family	Genus	Species	Species accession ID	% of species in the total microbial community CW1	% of species in the total microbial community CW2
Synergistaceae	*Aminiphilus*	*Aminiphilus_circumscriptus*	290732	0.15	2.8
Burkholderiales_incertae_sedis	*Aquabacterium*	*Aquabacterium_limnoticum*	708634	1.95	0.65
Iamiaceae	*Aquihabitans*	*Aquihabitans_daechungensis*	1052257	1.55	0.35
Campylobacteraceae	*Arcobacter*	*Arcobacter_suis*	1278212	0	1.2
Caulobacteraceae	*Brevundimonas*	*Brevundimonas_nasdae*	708634	1	0.4
Xanthomonadaceae	*Chiqvivirga*	*Chiqvivirga_flava*	659595	1.15	0.25
Microbacteriaceae	*Clavibacter*	*Clavibacter_michiganensis_subsp.*	33013	3.6	1.6
Microbacteriaceae	*Cryobacterium*	*Cryobacterium_mesophilum*	433647	1.55	0.65
Microbacteriaceae	*Curtobacterium*	*Curtobacterium_citreum*	2036	1.35	0.45
Syntrophobacteraceae	*Desulfoglaeba*	*Desulfoglaeba alkanexedens*	361111	2.25	10.6
Syntrophobacteraceae	*Desulfovirga*	*Desulfovirga_adipica*	149712	0.35	1.15
Xanthomonadaceae	*Dokdonella*	*Dokdonella_immobilis*	323415	1.3	2
Chitinophagaceae	*Ferruginibacter*	*Ferruginibacter_alkalilentus*	563170	1.95	1
Anaerolineaceae	*Longilinea*	*Longilinea_arvoryzae*	360412	9.15	5.9
Methanobacteriaceae	*Methanobacterium*	*Methanobacterium_aarhusense*	256826	1.15	2
Methanotrichaceae	*Methanothrix*	*Methanothrix_soehngenii*	2223	1.2	8.65
Propionibacteriaceae	*Micropruina*	*Micropruina_glycogenica*	75385	1.05	0.2
Phyllobacteriaceae	*Nitratireductor*	*Nitratireductor_aquimarimus*	889300	1.2	0.4
Sphingomonadaceae	*Novosphingobium*	*Novosphingobium_arabidopsis*	1305696	1.15	0.45
Porphyromonadaceae	*Petrimonas*	*Petrimonas_sulfuriphila*	285070	1	0.95
Rhizobiales_incertae_sedis	*Phreatobacter*	*Phreatobacter_oligotrophus*	1122261	1.55	0.55
Xanthomonadaceae	*Pseudoxanthomonas*	*Pseudoxanthomonas_kaohsiungensis*	283923	1.4	0.95
Rhodobacteraceae	*Rhodobacter*	*Rhodobacter_blasticus*	1075	1.45	0.65
Bradyrhizobiaceae	*Rhodopseudomonas*	*Rhodopseudomonas palustris*	1513892	1.75	1.05
Sphingomonadaceae	*Sandaracinobacter*	*Sandaracinobacter_sibiricus*	56359	1.1	0.2
Syntrophorhabdaceae	*Syntrophorhabdus*	*Syntrophorhabdus_aromaticivorans*	328301	0.8	2.85
Synergistaceae	*Thermovirga*	*Thermovirga_lienii*	336261	1.75	3.4
Comamonadaceae	*Xenophilus*	*Xenophilus_azovorans*	151755	1.65	0.7

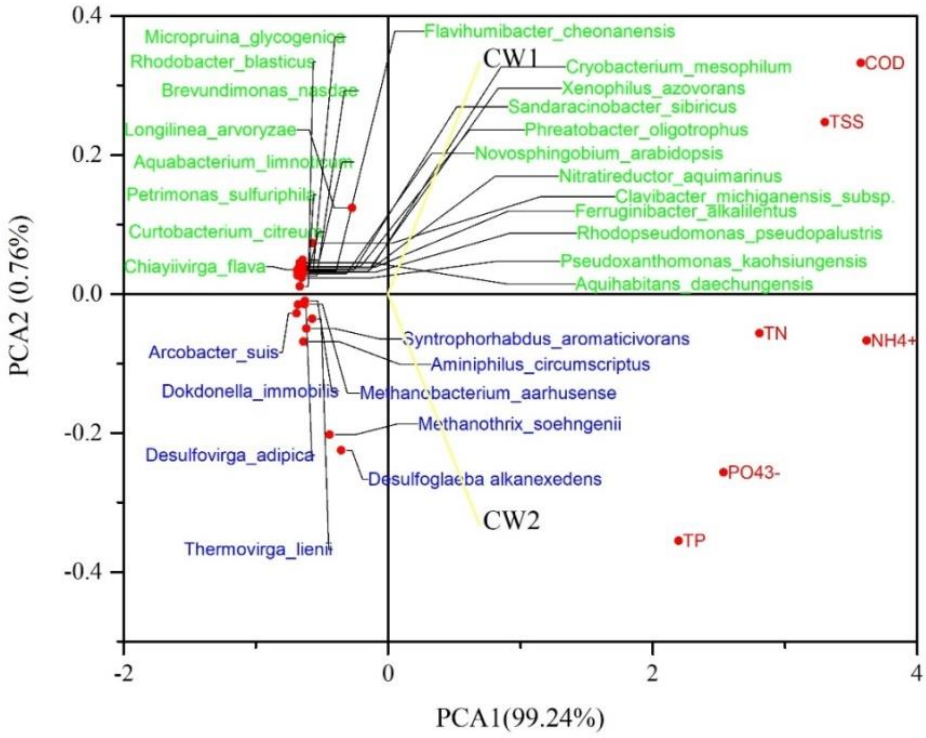

Figure 4: PCA of CW effluent pollutants and microbial community species

4. CONCLUSION

A system with a combination of macrophytes in the series connected two-stage HSSFCW system has been found suitable for the post-treatment of anaerobically treated brewery effluent. This system showed enhanced pollutant removal efficiencies of TSS, COD, TN, NH_4^+ – N, TP, and PO_4^{3-}, and meets the tolerable national discharge limits. The nutrient accumulation potential of *C. alternifolus* and *T. latifolia* were promising across the two – stage HSSFCW cells with respective cumulative nutrient accumulation. The microbial community dynamics assessment in the two-stage HSSFCW cell showed high and diversified microorganisms, which have a distinct role in the removal of organic matter and nutrients in the HSSFCW cells. Overall, the two-stage HSSFCW system planted with *C. alternifolius* followed by *T. latifolia* is recommended for the post-treatment of UASBR treated brewery effluent.

ACKNOWLEDGMENTS

The authors thank Kombolcha brewery factory for providing necessary equipment and laboratory facilities; Addis Ababa University for its financial support.

REFERENCES

Adey Feleke Desta, Fassil Assefa, Seyoum Leta, Stomeo, F., Wamalwa, M., Njahira, M., and Djikeng, A. (2014): Microbial Community Structure and Diversity in an Integrated System of Anaerobic-Aerobic Reactors and a Constructed Wetland for the Treatment of Tannery Wastewater in Modjo , Ethiopia. PLOS ONE, *9*(12): 1–22.

Adrados, B. Á. R. A., Sánchez, O. L. G. A., Arias, C. A., Becares, E. L. O. Y., Garrido, L. A. U. R. A., Mas, J. O. R. D. I. ... and Morató, J. O. R. D. I. (2014): Microbial communities from different types of natural wastewater treatment systems: vertical and horizontal flow constructed wetlands and biofilters. Water research, *55*:304-312.

APHA (1998): Standard methods for the examination of water and wastewater. American Public Health Association. *Inc., Washington, DC*.

Betis, H., St-Hilaire, A., Fortin, C., Duchesne, S. (2020): Development of a water quality index for watercourses downstream of harvested peatlands. *Water Quality Research Journal*, 119–131.

Blümel, S., Busse, H. J., Stolz, A., and Kämpfer, P. (2001): Xenophilus azovorans gen. nov., sp. nov., a soil bacterium that is able to degrade azo dyes of the Orange II type. International journal of systematic and evolutionary microbiology, 51(5):1831-1837.

Bilgin, M., Simsek, I., Tulun, S. (2014) : Treatment of domestic wastewater using a lab-scale activated sludge/vertical flow subsurface constructed wetlands by using Cyperus alternifolius. *Ecological Engineering*, 70:362 - 365.

Bonanno, G., Cirelli, G.L. (2017): Comparative analysis of element concentrations and translocation in three wetland congener plants: Typha domingensis, Typha latifolia, and Typha angustifolia. Ecotoxicology and Environmental Safety, *143:*92-101.

Kebena Bulla (2014): Treatment and Biogas Production Performances Efficiency of St. George Brewery Full Scale Waste Water Treatment System (MSc Thesis]. Addis Ababa (ET): Addis Ababa University).

Cao, Q., Wang, H., Chen, X., Wang, R., & Liu, J. (2017): *C*omposition and distribution of microbial communities in natural river wetlands and corresponding constructed wetlands. Ecological Engineering, *98:40–48.*

Ciria, M. P., Solano, M. L., Soriano. P. (2005): Role of Macrophyte Typha latifolia in a Constructed Wetland for Wastewater Treatment and Assessment of Its Potential as a Biomass Fuel. Biosystems Engineering, *92*(4):535–544.

Chang, J. S., Chou, C. L., Lin, G. H., Sheu, S. Y., and Chen, W. M. (2007): Pseudoxanthomonas kaohsiungensis, sp. nov., a novel bacterium isolated from oil-polluted site produces extracellular surface activity. Systematic and applied microbiology, *28*(2):137-144.

Chen, X., Lang, X. L., Xu, A. L., Song, Z. W., Yang, J., and Guo, M. Y. (2019): Seasonal variability in the microbial community and pathogens in wastewater final effluents. Water, *11*(12):2586.

Chen, W. M., Cho, N. T., Yang, S. H., Arun, A. B., Young, C. C., and Sheu, S. Y. (2012): Aquabacterium limnoticum sp. nov., isolated from a freshwater spring. *I*nternational journal of systematic and evolutionary microbiology, *62*(3):698-704.

Cheng L., Lee H., Lin J., Chou M. (2010): Treatment of Mixture of Sewage and Partially Treated Swine Wastewater by a Combination of UASB and Constructed Wetlands. Practice periodical of hazardous, toxic, and radioactive waste management, *14*:234–239.

Dan, N. H., Rene, E. R., and Le Luu, T. (2020): Removal of nutrients from anaerobically digested swine wastewater using an intermittent cycle extended aeration system. Frontiers in microbiology, 11.

Da Motta Marques, D. M. L., Leite, G. R., Giovannini, S. G. T. (2001): Performance of two macrophyte species in experimental wetlands receiving variable loads of anaerobically treated municipal wastewater. Water Science and Technology, 44(11–12):311–316.

Diaz, C., Baena, S., Fardeau, M. L., and Patel, B. K. C. (2007): Aminiphilus circumscriptus gen. nov., sp. nov., an anaerobic amino-acid-degrading bacterium from an upflow anaerobic sludge reactor. International journal of systematic and evolutionary microbiology, *57*(8): 1914-1918.

do Nascimento, J. G. D. S., Silva, E. V. A., Dos Santos, A. B., da Silva, M. E. R., and Firmino, P. I. M. (2021): Microaeration improves the removal/biotransformation of organic micropollutants in anaerobic wastewater treatment systems. Environmental Research, *198*: 111 - 313.

Edgar, R. C. (2016): SINTAX: a simple non-Bayesian taxonomy classifier for 16S and ITS sequences. *biorxiv*, 074161.

Ethiopian Environmental Protection Authority, EEPA. (2003): Provisional standards for industrial pollution control in Ethiopia, Prepared under the ecologically sustainable development (ESID) project–US. ETH/99/068/Ehiopia, EPA/UNIDO, Addis Ababa.

Fahlgren, D. (2017): *G*enetic variation in common cattail (Typha latifolia) in southern Sweden. Swedish University of Agricultural Sciences.

Faulwetter, J. L., Gagnon, V., Sundberg, C., Chazarenc, F., Burr, M. D., Brisson, J. ... and Stein, O. R. (2009): Microbial processes influencing performance of treatment wetlands: a review. Ecological engineering, 35(6):987-1004.

Garrido, L., Sánchez, O., Ferrera, I., Tomàs, N., and Mas, J. (2014): Dynamics of microbial diversity profiles in waters of different qualities. Approximation to an ecological quality indicator. Science of the total environment, *468*:1154-1161.

Huang, X., Ni, J., Yang, C., Feng, M., Li, Z., and Xie, D. (2018): Efficient ammonium removal by bacteria rhodopseudomonas isolated from natural landscape water: China case study. Water, *10*(8):1107.

Huser, B. A., Wuhrmann, K., and Zehnder, A. J. (1982): Methanothrix soehngenii gen. nov. sp. nov., a new acetotrophic non-hydrogen-oxidizing methane bacterium. Archives of Microbiology, *132*(1):1-9.

Jang, G. I., Hwang, C. Y., and Cho, B. C. (2011): Nitratireductor aquimarinus sp. nov., isolated from a culture of the diatom Skeletonema costatum, and emended description of the genus Nitratireductor. International journal of systematic and evolutionary microbiology, *61*(11): 2676-2681.

Juang, D. F., & Chen, P. C. (2007): Treatment of polluted river water by a new constructed wetland. International Journal of Environmental Science and Technology, *4*(4):481–488.

Kadlec, R. H., and Wallace, S. D. (2009): Treatment wetlands, 2nd edn. CRC Press, Boca Raton.

Kantawanichkul, S., Kladprasert, S., Brix, H. (2009): Treatment of high-strength wastewater in tropical vertical flow

constructed wetlands planted with Typha angustifolia and Cyperus involucratus. Ecological engineering, *35*:238-247.

Leto, C., Tuttolomondo, T., La Bella, S.L., Leone, R., Licata, M. (2013): Effects of plant species in a horizontal subsurface flow constructed wetland – phytoremediation of treated urban wastewater with Cyperus alternifolius L . and Typha latifolia L . in the West of Sicily (Italy). Ecological Engineering, *61*:282–291.

La Bella, S., Tuttolomondo, T., Leto, C., Bonsangue, G., Leone, R., Virga, G., Licata, M. (2016): Pollutant removal efficiency of a pilot-scale Horizontal Subsurface Flow in Sicily (Italy) planted with Cyperus alternifolius L. and Typha latifolia L. and reuse of treated wastewater for irrigation of Arundo donax L. for pellet production—Results of two-year tests under Mediterranean climatic conditions. Desalination and water treatment, 57(48-49):22743-22763.

Lin, S. Y., Hameed, A., Liu, Y. C., Hsu, Y. H., Lai, W. A., Huang, H. I., and Young, C. C. (2014): Novosphingobium arabidopsis sp. nov., a DDT-resistant bacterium isolated from the rhizosphere of Arabidopsis thaliana. International journal of systematic and evolutionary microbiology, 64(2):594-598.

Liu, Y., Jin, J. H., Liu, H. C., and Liu, Z. P. (2013): Dokdonella immobilis sp. nov., isolated from a batch reactor for the treatment of triphenylmethane dye effluent. International journal of systematic and evolutionary microbiology, *63*(4):1557-1561.

Lloréns, M., Pérez-Marín, A. B., Aguilar, M. I., Ortuño, J. F., Meseguer, V. F. (2020): Oxygen Consumption in Two Subsurface Wastewater Infiltration Systems under Continuous Operation Mode. Water, *12*:3007.

Mollard. F. P. O., Roy, M., Foote, A. L. (2013): Typha latifolia plant performance and stand biomass in wetlands affected by surface oil sands mining. Ecological Engineering, *58*:26–34.

Nguyen, N. P., Warnow, T., Pop, M., and White, B. (2016): A perspective on 16S rRNA operational taxonomic unit clustering using sequence similarity. NPJ biofilms and microbiomes, *2*(1):1-8.

Platzer, C. (1999): Design recommendations for subsurface flow constructed wetlands for nitrification and denitrification. *Water Science and Technology*, *40:*257-263.

Rehman, F., Pervez, A., Khattak, B. N., Ahmad, R. (2017): Constructed wetlands: perspectives of the oxygen released in the rhizosphere of macrophytes. CLEAN–Soil, Air, Water, *45*(1).

Sa'at, S.K.M., Zaman, N.Q., Yusoff, S.M., Ismail, H.A. (2017): Investigation of the potential of Cyperus alternifolius in the phytoremediation of palm oil mill effluent. In AIP Conference Proceedings, 1892(1):040009. AIP Publishing LLC.

UN-HABITAT (2008): Constructed Wetlands Manual. UN-HABITAT, Water for Asian Cities Programme Nepal, Kathmandu.

Vymazal, J. (2005): Horizontal subsurface flow and hybrid constructed wetlands systems for wastewater treatment. Ecological Engineering, 25:478 – 490.

Vymazal, J. (2007): Removal of nutrients in various types of constructed wetlands. Science of the Total Environment, 380:48 – 65.

Vymazal, J., Kropfelova, L. (2008): Wastewater Treatment in Constructed wetlands with horizontal sub – surface flow. Springer: Dordrecht, the Netherlands.

Wijaya, D.S., Hidayat, T., Sumiarsa, D., Kurnaeni, B., Kurniadi, D. (2016): A Review on Sub-Surface Flow Constructed Wetlands In Tropical And Sub-Tropical Countries. Open Science Journal, 1(2):1–11.

Wang, X., Hu, M., Xia, Y., Wen, X., and Ding, K. (2012): Pyrosequencing analysis of bacterial diversity in 14 wastewater treatment systems in China. Applied and environmental microbiology, *78*(19): 7042-7047.

Wang, S., Liu, J., Yi, N. K., Lu, L. J., and Huang, X. F. (2016): Impact of plant species on spatial distribution of metabolic potential and functional diversity of microbial communities in a constructed wetland treating aquaculture wastewater. Ecological Engineering, *94*:564-573.

Yasar, A., Tabinda, A. B. (2010): Anaerobic treatment of industrial wastewater by UASB reactor integrated with chemical oxidation processes; an overview. Pol. J. Environ. Stud., 19(5):1051-1061.

Zamora, S., Marín-Muñíz, J. L., Nakase-Rodríguez, C., Fernández-Lambert, G., Sandoval, L. (2019): Wastewater Treatment by Constructed Wetland Eco-Technology: Influence of Mineral and Plastic Materials as Filter Media and Tropical Ornamental Plants, Water, 11(11):2344.

Zeb, B. S., Mahmood, Q., Jadoon, S., Pervez, A., Irshad, M., Bilal, M., Bhatti, Z. A. (2013): Combined industrial wastewater treatment in anaerobic bioreactor post-treated in constructed wetland. BioMed research international, *2013*.

Local Microalgae Potential for Wastewater Remediation, Lipid and Bioethanol Production

Zenebe Yirgu[1,*], Seyoum Leta[2], Ahmed Hussen[2], Mohammed Mazharuddin Khan[2]

[1]*Department of Environmental Science, Wolaita Sodo University, Wolaita, Ethiopia*
[2]*Center for Environmental Science, Addis Ababa University, Addis Ababa, Ethiopia*
**Corresponding author, e-mail: zeneyw944@gmail.com*

ABSTRACT

Microalgae are recently considered promising resources to couple wastewater remediation with biofuel production due to their ability to utilize nutrients in wastewater and being rich in lipids and carbohydrates. The objective of this study was to evaluate the potential of local microalgae, Scenedesmus sp. for coupling agro-industrial wastewater remediation with lipid and bioethanol production. The local microalga, Scenedesmus sp. was isolated and grown in brewery wastewater for biomass production and remediation processes. Lipids were extracted from microalgal biomass with pretreatment methods, such as microwave, autoclave, osmotic stress, oven heating, and acid digestion. Bioethanol was produced after reducing sugar extraction in the microwave using the hydrolytic agents (HCl, H_2SO_4, NaOH, and KOH) with the optimization of the most effective hydrolytic agent using response surface methodology (RSM). Scenedesmus sp. achieved a removal efficiency of 78%, 94.6%, 99.98%, and 69% for COD (chemical oxygen demand), TN (total nitrogen), NH_4^+-N, and TP (total phosphorus), respectively. The highest lipid content obtained was 24.27% using microwave, followed by HCl digestion (19.43%), autoclaved (17.57%), osmotic shock (16.73%), and oven heating (15.53%). The maximum reducing sugar was found to be 146.78 mg/g using the hydrolytic agent HCl. This value was increased by 19.6% after RSM optimization under the optimum conditions of an acid concentration of 1.68 N, microwave power of 1200 W, temperature of 145 ℃ and extraction time of 19 min. The maximum bioethanol yield of 0.44 g/g reducing sugar was obtained at 24 h of fermentation time with a fermentation efficiency of 88.15%. This study demonstrated that the local microalgae have great potential for wastewater remediation with lipid and bioethanol production, and thus they could be used as feedstock for biofuel production after growing in wastewater.

Keywords: *Bioethanol, Nutrient removal, Lipid, Reducing sugar, Fermentation*

1. INTRODUCTION

Energy security issues and greenhouse gas emissions due to the utilization of fossil fuels have led to the development of alternative energies. Biofuels are perceived as viable alternative energy sources due to their potential to be renewable, sustainable, and environment-friendly (Cheng & He, 2014). They are categorized into different generations based on the types of feedstocks used. The first-generation biofuels are derived from edible feedstocks like corn, soybeans, and sugarcane, while the second-generation biofuels are obtained from non-edible feedstocks such as jatropha and waste. However, the first-generation biofuels have an issue like "food versus energy," and the second-generation biofuels face difficulties in overcoming technological barriers, showing that these two sources are unsustainable (Ashokkumar et al., 2017; Noraini et al., 2014). The third-generation biofuels, which are derived from microalgae and macroalgae, have attracted enormous attention due to their capability to overcome the issues in the above-mentioned two generations of biofuels (Mubarak et al., 2015).

Moreover, microalgae are able to remediate wastewater by removing nutrients and other pollutants. Microalgae such as *Chlorella* and *Scenedesmus* species are well adapted to grow in various wastewaters. Moreover, they can accumulate a considerable amount of lipids and carbohydrates in their biomass (Sivaramakrishnan & Incharoensakdi, 2018). For example, Mercado et al. (2020) cultivated *Scenedesmus* sp. in dairy wastewater and obtained a maximum content of 51% lipids and 27% carbohydrates with a removal of 88.4% total nitrogen (TN) and 97.1% total phosphorus (TP). Diniz et al. (2017) found a maximum of 19.5% carbohydrates and 12.5% lipids with the removal of 70% TN and 90% TP from *Scenedesmus* sp. grown in municipal wastewater. Hence,

microalgal biomass obtained after wastewater treatment has a great potential to produce lipids and carbohydrates and, subsequently, biofuels.

Biofuel production from microalgal biomass needs pretreatment for lipid and carbohydrate extraction because these biochemical products are typically encapsulated within the microalgal cellular structures. Several pretreatment methods, such as autoclave, microwave, ultrasonic oven heating, homogenization, sonication, bead-beating, and osmotic stress, have been employed for lipid and carbohydrate extractions so far (Lee et al., 2010; Miranda et al., 2012; Halim et al., 2012). For examples, Yu et al. (2020) and Chandra et al. (2020) employed microwave and autoclave pretreatments for carbohydrate extraction and consequently, bioethanol production, respectively. Moreover, Lee et al., (2010) and Guldhe et al. (2014) used various pretreatments, including microwaves for lipid extraction and both obtained the highest lipid content using microwave pretreatment.

Several previous studies have produced bioethanol and lipid from microalgae grown in synthetic medium (Chandra et al., 2020; Guldhe et al., 2014; Miranda et al., 2012; Lee et al., 2010), which adds an extra cost for biofuel production. However, there are a few studies that have been used to couple wastewater remediation with bioethanol or lipid production (Onay, 2018; Li et al., 2011). In addition, there is a lack of concrete and reliable data on microalgae utilization in Ethiopia. Therefore, the objective of this study was to evaluate the potential of local microalgae, *Scenedesmus* sp., for coupling wastewater remediation with lipid and bioethanol production, Furthermore, response surface methodology (RSM)-based optimization of reducing sugar extraction was performed for bioethanol production.

2. MATERIAL AND METHODS

2.1. Microalgae and Wastewater

The local microalga, *Scenedesmus* sp., was isolated and identified from lake water (Ziway Lake) based on the standard methods. The agro-industrial wastewater was collected from the St. George brewery industry, Addis Ababa, after an up-flow anaerobic sludge blanket (UASB) reactor. The *Scenedesmus* sp. was then cultured in a 2 L conical flask used as a photobioreactor with a light intensity of 5000 lux and a photoperiod of a 12:12 light-dark cycle at room temperature (21 ± 3.0) on anaerobically digested (AD) brewery effluent. A Time switcher (SUL 180h) was used to keep the photoperiod of the culture. Aeration was supplied by an aerator (SB-648, China) with a 0.45 µm air filter to provide atmospheric CO_2 and to mix the culture. The growth characteristics and the change in nutrient concentrations were investigated over the cultivation period. At the end of cultivation, the biomass was harvested using a centrifuge and washed with distilled water. The biomass was then dried in an oven at 60 ℃ and prepared for lipid and reducing sugar extraction and then bioethanol production.

2.2. Pretreatment Methods for Lipid Extraction

The microalgal biomass pretreatment for lipid extraction was carried out using an autoclave (Models: DIXONS and ST3028), a microwave (Models: Milestone SK-10 and SK-12, Italy), oven heating (Model: GX65B), osmotic shock, and acid digestion in a water bath (Model: DK-98-II). Dry microalgal biomass of 500 mg was blended with 30 mL of distilled water and pretreated using: (i) an autoclave at 121 ℃ for 15 min, (ii) a microwave at 1000 W and 100 ℃ for 10 min, and (iii) oven heating at 120 ℃ for 15 min (Yu et al., 2015). 500 mg of dry microalgal biomass was also suspended in 30 mL of (i) 10% NaCl for osmotic stress pretreatment for 48 h, and (ii) 3 N HCl for acid digestion at 80 ℃ in a water bath. Lipid extraction without pretreatment was also performed to compare the magnitude of lipid production due to pretreatment methods. After pretreatment, lipids were extracted using the modified procedures of the Bligh and Dyer (1959) method.

2.3. Pretreatment and Optimization for Reducing Sugar Extraction

A dried and pulverized microalgal biomass of 5% (w/v) was mixed separately with 3 N HCl, H_2SO_4, NaOH, and KOH as well as H_2O and then subjected to microwave pretreatment at 1000 W and 120 ℃ for 15 min. The concentration of the acids and alkalis was selected according to Miranda et al. (2012). After pretreatment, the supernatant was separated using centrifugation and analyzed for reducing sugar content. After obtaining the most effective hydrolytic agent, optimization of the main parameters, such as concentration, microwave power, temperature, and extraction time, was employed using the RSM approach. MINITAB software (version 18) was used to design the experiment and to develop the model using the central composite design (CCD) of RSM with an alpha (α) value equal to 1. The suitability of the developed model for predicting the optimal reducing sugar yield was confirmed by performing a triplicate experiment at optimum conditions.

Table 1: Independent variables and their levels in the response surface design

Independent variables	Unit	Symbol	Levels		
			Low (-1)	Center (0)	High (1)
HCl concentration	N	A	0.1	2.55	5
Microwave power	W	B	800	1000	1200
Temperature	℃	C	80	120	180
Extraction Time	min	D	5	17.5	30

2.4. Bioethanol Production

Following the optimum conditions achieved, bioethanol was produced from hydrolysates of microalgal biomass obtained under optimum conditions. The fermentation process was performed with *Saccharomyces cerevisiae* (commercial baker's yeast). The yeast was first activated and prepared using Luria Broth (LB) medium, according to Harun et al. (2010). Fermentation was performed with a 50 mL working volume in 125 mL conical flasks, containing the microalgal hydrolysate extracted at optimum conditions. The microalgal hydrolysate was mixed with fermentation nutrients, with a composition of 0.1 g ammonium chloride (NH_4Cl), 0.2 g potassium dihydrogen phosphate (KH_2PO_4), and 0.5 g yeast extracted (Yu et al., 2020). The mixture was first adjusted to a pH of 5 (Mahzabin et al., 2019) and then sterilized at 121 ℃ for 20 min in an autoclave. 10% of pre-cultured *Saccharomyces cerevisiae* yeast was added under aseptic conditions in the flasks to inoculate the sterilized hydrolysate solution (Thu et al., 2009). The flasks containing hydrolysate solution were placed on a shaker incubator (ZHWY-103B, China) at 150 rpm and 30 ℃ for three days. Bioethanol was determined after distillation within an interval of 24 h.

2.5. Analytical Methods and Calculations

2.5.1. Biomass Production

Microalgal growth and biomass concentration were monitored by measuring optical density at 680 nm using a JENWAY spectrophotometer (model 6705) during the experiment. The biomass concentration was calculated as a dry weight using the standard method for total suspended solids (APHA, 1999). The correlation between the dry weight (DW, g/L) and the corresponding optical density (OD) was obtained as DW = 0.95 (OD) – 0.037, with an R^2 value of 0.992.

2.5.2. Nutrient Removal

Chemical oxygen demand (COD), nitrogen, and phosphorus nutrients in a brewery effluent and microalgal culture were determined after filtration using a 0.45 µm syringe filter. COD and TN were analyzed following the Hack DR 2400 spectrophotometer manual (Hach, 2002). TP was determined by the ascorbic acid method after

persulfate digestion, and NH_4^+-N was determined using the phenate method (APHA, 1999). The removal efficiency was calculated using Equation (1) (Renuka et al., 2013).

$$R_f = \frac{C_o - C}{C_o} \times 100 \quad (1)$$

where R_f is removal efficiency and C_o and C are concentrations before and after microalgae cultivation

2.5.3. Lipid Determination

After each pretreatment, a chloroform and methanol mixture (1:2 v/v) was used to extract lipids according to the modified procedures of the Bligh and Dyer (1959) method. Briefly, the pretreated microalgal biomass was mixed with 30 mL of chloroform and methanol (1:2 v/v). After shaking for 5 minutes, the final solvent ratio of chloroform/methanol/water was adjusted to 1:2:1.8. The chloroform layer containing lipids was washed with 1% NaCl to separate it from the methanol aqueous layer. The organic layer was placed in a pre-weighed glass beaker, and the solvent was evaporated in a 60 °C oven. Finally, the total lipid contents were measured gravimetrically. The total lipid content (LC) was calculated according to Equation (2) (Pandey et al., 2019).

$$LC\ (\%) = \frac{Weight\ of\ extracted\ lipid}{Weight\ of\ microalgal\ biomass} \text{ x } 100 \quad (2)$$

2.5.4. Reducing sugar Determination

The procedures of the DNS method with minor modifications were used to determine reducing sugar content (Miller, 1959). Briefly, an equal amount of hydrolysate of microalgal biomass and DNS reagent (1 mL each) was mixed in capped test tubes and heated in boiling water (95 ℃). 8 mL of distilled water was added to the test tubes after they are cooled using running tap water to room temperature. The calibration curve was constructed using D-glucose as the standard, ranging from 0.1 mg/mL to 0.3 mg/mL with $R^2 = 0.9951$ in the test range. The amounts of reducing sugar were determined according to the absorbance read at 540 nm using a UV/Vis spectrophotometer (JENWAY). The yield of reducing sugar (mg/g) was estimated using Equation (3) (Manmai et al., 2020).

$$\text{Reducing sugar} = \frac{Reducing\ sugar\ content\ (\frac{mg}{g})}{microalgal\ biomass\ (g)} \quad (3)$$

2.5.5. Bioethanol Determination

Following the distillation of the fermented sample, the bioethanol concentration was estimated according to the procedures provided by Crowell & Ough (1979) using the potassium dichromate method. Briefly, the distilled sample of bioethanol (2 mL) and the acidic potassium dichromate reagent (10 mL) were mixed in a test tube and then heated in a water bath for 2 h at 60 ℃. After cooling the test tube, the bioethanol concentration was determined on the basis of absorbance measured at 600 nm using a UV/Vis spectrophotometer. A calibration curve was prepared using absolute ethanol solution as the standard (Williams & Darwin Reese, 1950), ranging from 1 mg/mL to 3 mg/mL providing an R^2 of 0.997. The bioethanol yield kinetics, including bioethanol yield (based on microalgal biomass), bioethanol yield (based on reducing sugar), bioethanol productivity, and fermentation efficiency, were calculated using Equations. (4), (5), (6), and (7), respectively (Manmai et al., 2020).

$$\text{Bioethanol yield (\%)} = \frac{Bioethanol\ obtained\ in\ fermentation\ (g)}{Microalgal\ biomass\ (g)} \text{ x } 100 \quad (4)$$

$$\text{Bioethanol yield (\%)} = \frac{Bioethanol\ obtained\ in\ fermentation\ (\frac{g}{L})}{Reducing\ sugar\ in\ \ LEMB\ (\frac{g}{L})} \quad (5)$$

$$\text{Bioethanol productivity (g/L/h)} = \frac{\text{Bioethanol obtained in fermentation } (\frac{g}{L})}{\text{Fermentation time (h)}} \quad (6)$$

$$\text{Fermentation efficiency (\%)} = \frac{bioethanol\ obtained\ in\ fermentation\ (\frac{g}{L})}{0.51 \times reducing\ sugar\ in\ hydrolysate\ (\frac{g}{L})} \text{ x } 100 \quad (7)$$

2.6. Statistical Analysis

All experiments in this study were performed in triplicate, except for the fermentation process (duplicate), and findings were presented as the mean ± standard deviation. A one-way ANOVA with the Tukey post-doc test was employed to compare lipid contents among pretreatment methods and reducing sugar yields among hydrolytic agents using R-software. The differences were significant when $P < 0.05$. In RSM, the experimental results were analyzed using a MINITAB software version 18. A mathematical model was developed to determine the functional relationship between independent variables and sugar yield. The statistical significance of the developed quadratic model and the model terms were evaluated by analysis of variance (ANOVA). Surface plots were created to estimate the relationship between the independent variables and the response (reducing sugar yield).

3. RESULTS AND DISCUSSION

3.1. Biomass Yield and Nutrient Removals

The AD brewery effluent used for *Scenedesmus* sp. cultivation had a concentration of 399.58 ± 29.14 mg/L COD, 41.52 ± 4.73 mg/L NH_4^+-N, 53.42 ± 6.2 mg/L TN, and 50.00 ± 2.64 mg/L TP. The concentration of these nutrients is above the permissible discharge limits of brewery effluent, which are 250, 40, 20, and 10 mg/L for COD, TN, NH_4^+-N, and TP, respectively. Therefore, the discharge of this effluent without the appropriate treatment method may cause the deterioration of the receiving water bodies. As a result, microalgae are proposed as an effective method for the treatment of this type of effluent. The nutrient concentrations found in this study are higher in COD but lower in TN than those reported by Darpito et al. (2014), who used AD brewery effluent for microalgae cultivation.

The potentials of local *Scenedesmus* sp. for biomass production and wastewater remediation were investigated by measuring dry weight and COD, TN, NH_4^+-N, and TP removals, respectively. Fig. 1 (a and b) shows the biomass production with nitrogen and phosphorus nutrients or COD removal over the cultivation time. The biomass production increased throughout the cultivation period and reached a maximum value of 1.05 ± 0.11 g/L on the 18th day. This result was comparable to those reported by Ferreira et al., (2017) using *Scenedesmus* sp., but lower than those reported by Darpito et al. (2014) using *Chlorella sp.* in AD brewery effluent. The concentrations of TN, NH_4^+-N, and TP gradually decreased until the end of the cultivation period and eventually reached a maximum removal efficiency of 94.6%, 99.98%, and 69%, respectively.

The concentration of COD was gradually decreasing until day 6. However, after the sixth day, the COD concentration fluctuated, sometimes increasing and sometimes decreasing until the end of the cultivation. This is due to the utilization and release of COD during the cultivation time (Wang et al., 2012; Wang et al., 2010). However, the removal efficiency of COD reached 78% at the end of cultivation. Darpito et al. (2014) reported a similar removal efficiency in TN and COD but a higher removal efficiency in TP. Furthermore, Ferreira et al. (2017) obtained a lower removal efficiency of NH_4^+-N, TN, and TP than this study. The result obtained in this

study shows that agro-industrial wastewater, like AD brewery effluent, is used for sustainable biomass production from microalgae with nutrient removal for biofuel production.

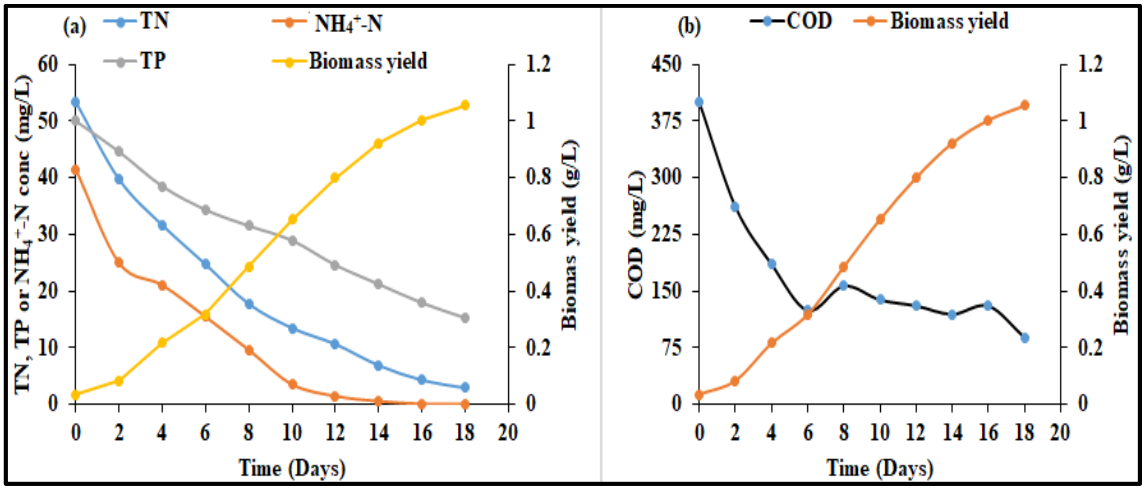

Figure 1: Biomass yield with (a) nutrients or (b) COD concentration variation over the cultivation time

3.2. Lipid Extraction

The microalgal biomass obtained after growing in AD brewery effluent was used to extract lipids with and without pretreatment methods. Fig. 2 shows the contents of total lipids obtained after different pretreatment methods (autoclave, microwave, osmotic stress, oven heating, and acid digestion in a water bath). All the pretreatments performed in this study were able to disrupt the cells of *Scenedesmus* sp., but their lipid yields differed. The maximum and minimum lipid contents were extracted from *Scenedesmus* sp. cells using microwave and osmotic stress, respectively. The statistical analysis showed that there are no significant differences ($P > 0.05$) among autoclave, osmotic, and HCl digestion. However, microwave pretreatment was significantly different ($P < 0.05$) from the other pretreatments. The highest lipid content obtained was 24.27% using microwave pretreatment, which was followed by HCl digestion (19.43%), autoclaved (17.57%), osmotic shock (16.73%), and oven heating (15.53 mg/g). The total lipids achieved without pretreatment (14.79 ± 1.02%) are significantly different ($P < 0.05$) from the other pretreatments (except oven heating) evaluated in this study. As a result, pretreatment is an option to maximize the lipid content of microalgal biomass obtained after wastewater treatment, and it should be performed before further processing.

Results from this study are in compliance with previous studies by Lee et al. (2010) and Guldhe et al. *(*2014), where microwave pretreatment has been shown to extract the highest content of lipids from *Scenedesmus* sp. as compared to autoclave, sonication, or osmotic shock. Moreover, Patrícya *et al.* (2014) reported a higher lipid content extraction from mixed cultures using microwave pretreatment as compared to autoclave pretreatment. However, Yu *et al.* (2015) investigated different pretreatments, including autoclave, microwave, acid digestion, and sonication, for lipid extraction from *Chlorella sorokiniana*, and reported acid digestion provided the highest lipid content of the other pretreatments.

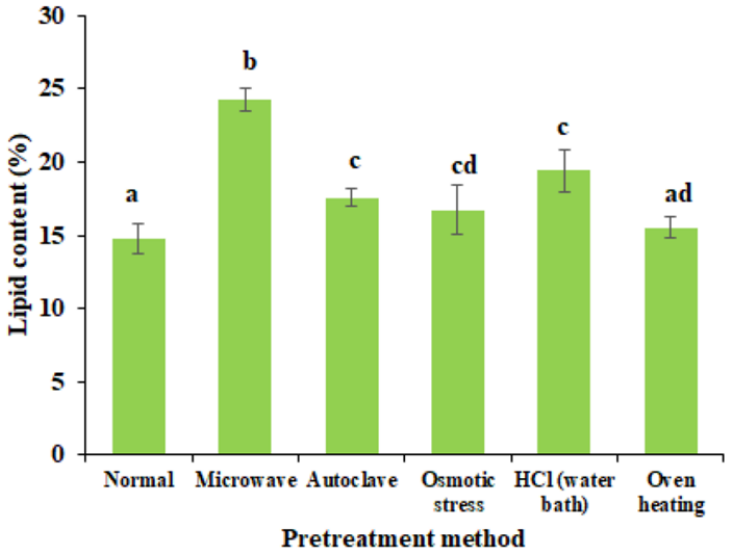

Figure 2: Lipid production from local Scenedesmus sp. using different pretreatment ($P < 0.05$ for different letters)

3.3. Selection of Hydrolytic Agent for Reducing Sugar Extraction

Microalgal biomass pretreatment with different hydrolytic agents (H_2O, HCl, H_2SO_4, NaOH, and KOH) in microwave was investigated to identify the most effective hydrolytic agent for reducing sugar extraction. Fig. 3 shows the reducing sugar yield using different hydrolytic agents in microwave pretreatment. The highest reducing sugar yield was obtained using HCl, whereas the lowest reducing sugar yield was achieved using H_2O. Therefore, an acid (HCl) was selected for the optimization of reducing sugar extraction from microalgal biomass.

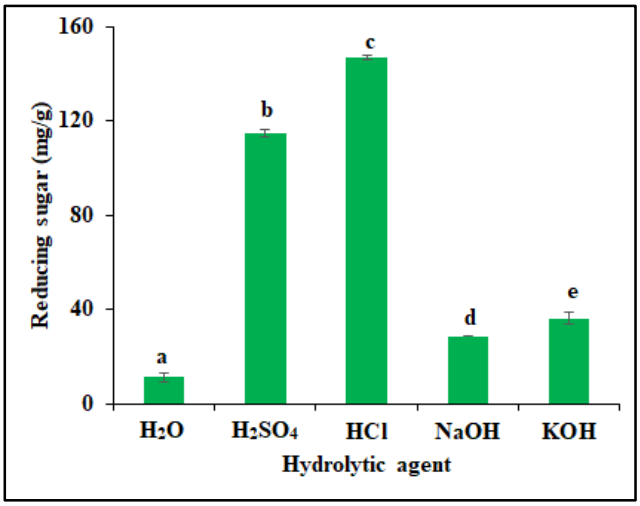

Figure 3: Effect of microwave pretreatment using acids and alkalis on total carbohydrate production ($P < 0.05$ for different letters)

Moreover, the alkaline pretreatment method rendered a lower reducing sugar yield than the acid pretreatment method. Hernández et al. (2015) and Shokrkar et al. (2017) reported that alkaline pretreatment releases less reducing sugar than acid pretreatment from *Scenedesmus* and mixed microalgae in autoclave pretreatment. However, Kassim & Bhattacharya (2016) and Harun et al. (2011) found a higher reducing sugar yield using alkaline pretreatment from *Chlorella* sp. and *Chlorococcum infusionum* using autoclave and oven heating pretreatments, respectively. The findings in this study showed that the extraction of microalgal reducing sugar using

microwaves is dependent on the types of hydrolytic agents. Acid hydrolytic agents are more favorable than alkaline hydrolytic agents for reducing sugar extraction from microalgae in the microwave.

The reducing sugar content obtained in this study was higher than that obtained by Hernández et al. (2015) and Kassim & Bhattacharya (2016), who found a maximum of 88 mg/g from *Scenedesmus almeriensis* and *Chlorella* sp. using acid and alkaline pretreatments, respectively. The variation in reducing sugar yield among different studies is due to the fact that the accumulation of carbohydrates in the cells of microalgae depends on the growth medium, microalgae species types, and growth conditions (such as temperature, pH, light intensity, and photoperiod) (Ho et al., 2013). Most previous studies utilized synthetic medium as a growth medium, which increases the cost of bioethanol production; however, this study used wastewater. As a result, the reducing sugar yield obtained in this study is promising for producing bioethanol using cost-cutting strategies.

3.4. Optimization of Reducing Sugar Extraction

3.4.1. Regression Model Development

The main factors of microwave pretreatment were statistically optimized with RSM in this study. The optimization of reducing sugar extraction was employed after selecting HCl as an effective hydrolytic agent for microwave pretreatment. Table 2 shows the actual and predicted responses to reducing sugar yield obtained from microalgal biomass. A quadratic model (Eq. (8)) was generated through a multiple nonlinear regression analysis of the experimental data to predict the reducing sugar yield.

$$Y = -264 + 41.82\,A + 0.026\,B + 4.528\,C + 0.09\,D - 2.258\,A^2 - 0.000006\,B^2 - 0.02005\,C^2 - 0.0357\,D^2 - 0.03033AB + 0.0184AC - 0.0230AD + 0.000933BC + 0.000295BD + 0.00664CD \quad (8)$$

where Y denotes the predicted responses and A, B, C, and D denote the coded values of the test variables concentration, microwave power, temperature, and extraction time, respectively. AB, AC, AC, BC, BD, and CD are the interaction terms, and A^2, B^2, C^2, and D^2 are the quadratic terms. The coefficients with a positive sign indicate that the increasing of these parameters causes an increase in reducing sugar extraction, whereas the coefficients with a negative sign indicate that the increasing of these parameters cause a decrease in reducing sugar yield.

Table 2: Experimental design, actual and predicted values of reducing sugar yield.

Std Order	Run	Coded value				Actual Value				Reducing Sugar (mg/g)	
		A	B	C	D	A	B	C	D	Actual value	Predicted value
29	1	0	0	0	0	2.55	1000	130	17.5	158.62	157.23
23	2	0	0	0	-1	2.55	1000	130	5.00	152.85	152.43
4	3	1	1	-1	-1	5.00	1200	80	5.00	65.920	63.060
22	4	0	0	1	0	2.55	1000	180	17.5	125.67	127.56
31	5	0	0	0	0	2.55	1000	130	17.5	167.12	157.22
2	6	1	-1	-1	-1	5.00	800	80	5.00	78.640	87.810
24	7	0	0	0	1	2.55	1000	130	30.0	145.22	150.83
10	8	1	-1	-1	1	5.00	800	80	30.0	76.486	75.030
12	9	1	1	-1	1	5.00	1200	80	30.0	60.280	53.230
27	10	0	0	0	0	2.55	1000	130	17.5	157.24	157.22
1	11	-1	-1	-1	-1	0.10	800	80	5.00	59.250	51.560
3	12	-1	1	-1	-1	0.10	1200	80	5.00	85.020	86.250
14	13	1	-1	1	1	5.00	800	180	30.0	112.39	110.14
6	14	1	-1	1	-1	5.00	800	180	5.0	111.26	106.33
18	15	1	0	0	0	5.00	1000	130	17.5	144.81	148.48
20	16	0	1	0	0	2.55	1200	130	17.5	162.18	169.52
5	17	-1	-1	1	-1	0.10	800	180	5.00	55.028	61.060
19	18	0	-1	0	0	2.55	800	130	17.5	146.57	144.42
30	19	0	0	0	0	2.55	1000	130	17.5	167.12	157.22
17	20	-1	0	0	0	0.10	1000	130	17.5	137.32	138.85
8	21	1	1	1	-1	5.00	1200	180	5.00	120.60	118.89
11	22	-1	1	-1	1	0.10	1200	80	30.0	74.595	79.240
15	23	-1	1	1	1	0.10	1200	180	30.0	152.83	142.64
13	24	-1	-1	1	1	0.10	800	180	30.0	65.110	67.690
26	25	0	0	0	0	2.55	1000	130	17.5	150.23	157.22
21	26	0	0	-1	0	2.55	1000	80	17.5	83.305	86.600
16	27	1	1	1	1	5.00	1200	180	30.0	118.24	125.65
7	28	-1	1	1	-1	0.10	1200	180	5.00	131.89	133.06
9	29	-1	-1	-1	1	0.10	800	80	30.0	40.900	41.590
28	30	0	0	0	0	2.55	1000	130	17.5	157.13	157.22
25	31	0	0	0	0	2.55	1000	130	17.5	158.62	157.22

3.4.2. Statistical Analysis

Table 3 displays the ANOVA for the data generated by Eq. (8). The model's F-value (78.36) and p-value (0.000) indicated that the model was significant. All linear terms except extraction time had significant effects on reducing sugar extraction. The p-value for lack of fit was 0.26, indicating that the lack of fit was not significant in comparison to the pure error and that the model fit was satisfactory. The larger value of R^2 (0.98) showed the high reliability of the model in predicting of reducing sugar production. The high value of adjusted R^2 (0.97) showed a reasonable agreement between the observed and predicted values of the reducing sugar yields. The values of R^2 and adjusted R^2 are close to 1, indicating a high degree of correlation between the observed and predicted values of

reducing sugar yields. The low value of the coefficient of variance (2.37%) indicated a high degree of precision and good reliability of the experimental data. Therefore, the developed model was adequate for predicting reducing sugar yield in the range of experimental variables. The adequacy of the developed model was also evaluated through diagnostic plots such as predicted versus actual and normal probability plots (Alexander et al., 2020). Fig. 4a shows the plot of the predicted value versus the actual value of reducing sugar yield, which showed that values lie reasonably close to a straight line, indicating that the predicted values obtained from the developed model adequately agreed with the experimental values. The normal probability plot of the residuals is displayed in Fig. 4b, which demonstrated that the errors were normally distributed across a straight line. This indicates that the residuals for reducing sugar yield fit a normal distribution.

Table 3: ANOVA of the developed model for reducing sugar yield

Source	DF	Adj SS	Adj MS	F-Value	P-Value
Model	14	48381.1	3455.80	66.46	0.000
Linear	4	10814.1	2703.53	51.99	0.000
A	1	417.5	417.47	8.03	0.012
B	1	2835.0	2835.02	54.52	0.000
C	1	7550.1	7550.08	145.19	0.000
D	1	11.6	11.56	0.22	0.644
Square	4	32267.9	8066.97	155.14	0.000
A^2	1	476.8	476.82	9.17	0.008
B^2	1	0.2	0.15	0.00	0.958
C^2	1	6522.7	6522.72	125.44	0.000
D^2	1	80.9	80.91	1.56	0.230
2-Way Interaction	6	5299.1	883.19	16.98	0.000
A*B	1	3534.0	3533.96	67.96	0.000
A*C	1	81.2	81.23	1.56	0.229
A*D	1	7.9	7.94	0.15	0.701
B*C	1	1392.0	1392.01	26.77	0.000
B*D	1	8.7	8.72	0.17	0.688
C*D	1	275.3	275.29	5.29	0.035
Error	16	832.0	52.00		
Lack-of-Fit	10	617.7	61.77	1.73	0.260
Pure Error	6	214.3	35.72		
Total	30	49213.1			

R^2= 0.983, R^2 (Adjust) = 0.968, R^2 (Predicted)= 0.904, CV = 2.37%

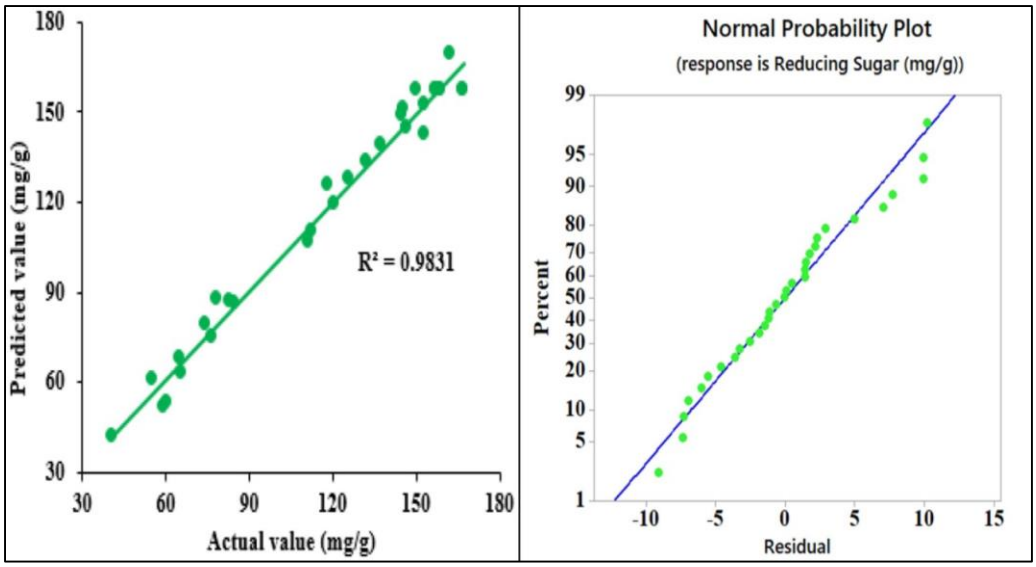

Figure 4: Diagnostic plot (a) predicted values versus actual values of reducing sugar yield and (b) normal plot of residuals

3.4.3. Combined Effect of Process Variables

The three-dimension surface plot was drawn to visualize the mutual interaction between independent variables and to determine the optimum levels of each variable for reducing sugar yield. Fig. 5 (a-f) shows the three-dimension surface plot as a function of two independent variables, while the other two independent variables have been kept constant (at fixed values).

The highest reducing sugar yield obtained was 173.9 mg/g by the interactive effect of microwave power (1200 W) and temperature at the optimum values of 1200 W and 145 ℃, respectively (Fig. 5d), while the lowest reducing sugar yield of 156.2 mg/g was obtained by the interaction of HCl concentration (3.0) and temperature (140.6 ℃) (Fig. 5b). The other interactions, such as acid concentration and microwave power (Fig. 5a), acid concentration and extraction time (Fig. 5c), microwave power and extraction time (Fig. 5e), and temperature and extraction time (Fig. 5f), released a maximum reducing sugar of 171.2, 157.7, 169.5, and 159.3 mg/g with optimum values of 1.64 N & 1200 W, 3.0 N & 16.4 min, 1200 W & 17.4 min, and 140.2 ℃ & 17.6 min, respectively.

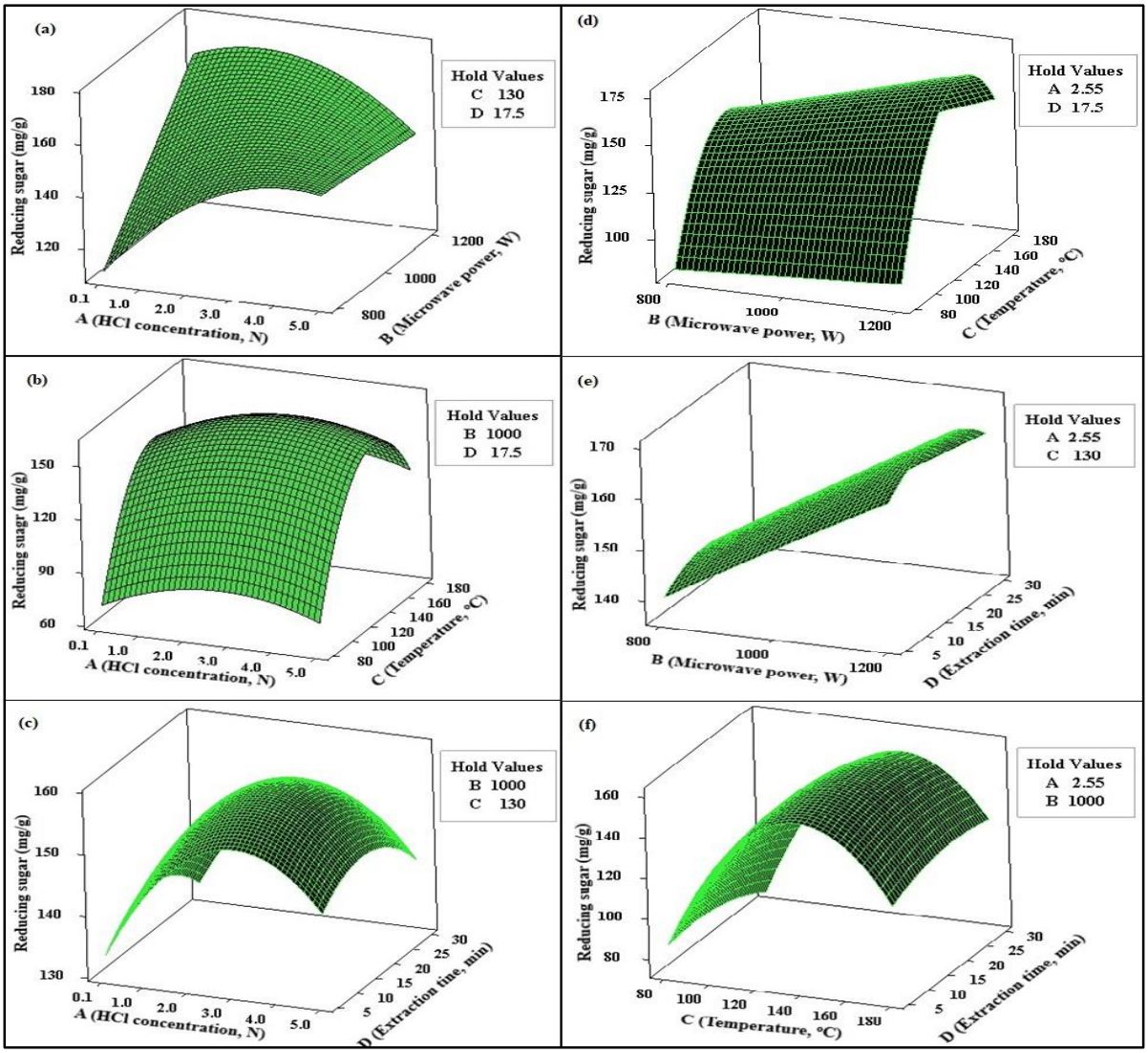

Figure 5: Surface plot showing the combined effect of variables on reducing sugar (a) acid concentration versus microwave power, (b) acid concentration versus temperature, (c) acid concentration versus extraction time, (d) microwave power versus temperature, (e) microwave power versus extraction time, and (f) temperature versus extraction time

3.4.4. Validation of Optimized Reducing Sugar Extraction Conditions

The predicted reducing yield obtained at optimum conditions was 175.5 mg/g. The acid concentration, microwave power, temperature, and extraction time are optimally 1.68 N, 1200 W, 144.65, and 18.89, respectively. The predicted reducing sugar yield was validated by carrying out experiments in triplicate at optimal conditions. Accordingly, the actual result obtained was 172.5 mg/g, which is in good agreement with the predicted value. Thus, the model was appropriate and adequate to describe the microwave-assisted reducing sugar extraction from microalgal biomass.

3.5. Bioethanol Production

The optimum conditions obtained were used to extract reducing sugar from microalgal biomass for bioethanol production. The bioethanol was produced using a commercial baker's yeast, *Saccharomyces cerevisiae*. The

microalgal hydrolysate used for the fermentation process had a concentration of 178.99 ± 0.92 mg/g reducing sugar. Fig. 6 shows the bioethanol production profiles from Scenedesmus sp. within 72 h of fermentation time in this study. As shown in Fig. 6, the concentration of reducing sugar was drastically decreased from its initial concentration to 74.43 ± 0.69 mg/g within 24 h, then it decreased slowly until the end of fermentation. Conversely, the concentration of bioethanol was increased from 0 to 24 h, after which there is no significant change in the concentration. Therefore, the maximum bioethanol yield was obtained after a 24-hour fermentation period. Table 4 shows the kinetic parameters of bioethanol production over the 72 h fermentation time. The results showed that 24 h is the best fermented time for bioethanol production, as displayed by the highest bioethanol concentration (g/L), bioethanol yield (g/g microalgal biomass), bioethanol yield (g/g reducing sugar), bioethanol productivity (g/L/h), and fermentation efficiency (%) of 4.02 ± 0.04 g/L, 0.44 ± 0.00 g/g, 0.17 ± 0.00 (g/L/d), and 88.2 ± 0.45 (%), respectively.

The bioethanol yield obtained in this study was similar to that obtained the study by Sivaramakrishnan & Incharoensakdi (2018), who produced bioethanol using autoclave pretreatment from *Scenedesmus* sp. grown on BG11. However, it was slightly lower than the results obtained by Guo et al. (2013) and Chandra et al. (2020), who produced bioethanol from *Scenedesmus abundans* and *Scenedesmus acuminatus* grown on BG 11 medium, respectively. The maximum bioethanol productivity obtained by Chandra et al. (2020) is comparable with this study. Unlike this study, most of the previous studies used a synthetic medium for microalgae growth. However, this study used brewery effluent as a growth medium; therefore, the result of this study is more attractive when compared to the bioethanol obtained in other studies.

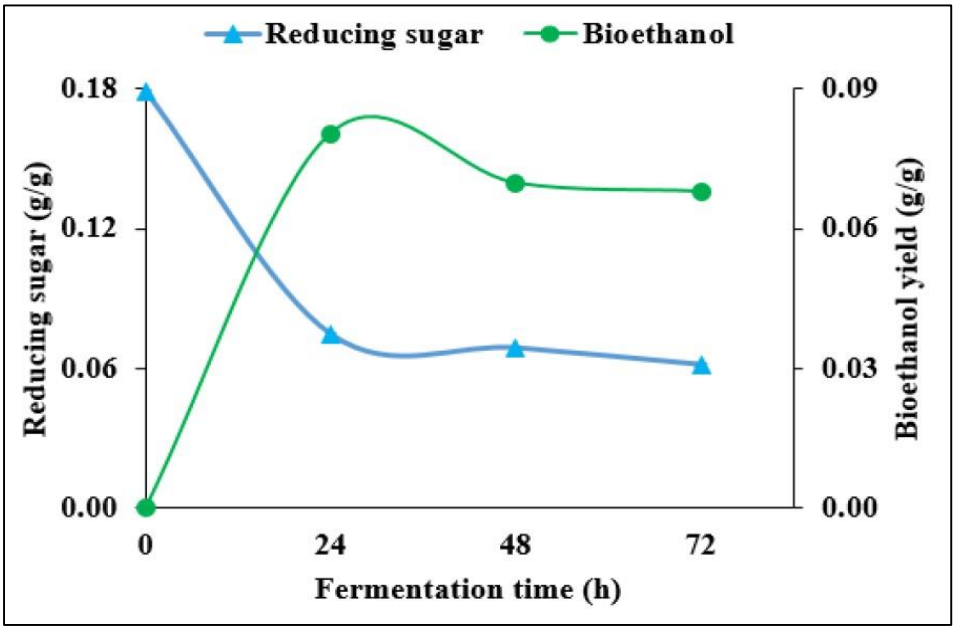

Figure 6: Changes in bioethanol and reducing sugar concentration during fermentation period

Table 4: Kinetic parameters of bioethanol production during 72 h fermentation time

Fermentation time (h)	Bioethanol conc. (g/L)	bioethanol yield (g/g biomass)	bioethanol yield (g/g reducing sugar)	Bioethanol productivity (mg/L/d)	Fermentation efficiency
0	0.00 ± 0.00	0.00 ± 0.00	0.000 ± 0.000	0.00 ± 0.00	0.00 ± 0.00
24	4.02 ± 0.04	0.08 ± 0.00	0.44 ± 0.00	0.17 ± 0.00	88.2 ± 0.45
48	3.49 ± 0.06	0.07 ± 0.00	0.39 ± 0.00	0.07 ± 0.00	76.8 ± 1.20
72	3.40 ± 0.07	0.06 ± 0.00	0.38 ± 0.01	0.05 ± 0.00	74.8 ± 1.60

4. CONCLUSION

This study demonstrated that the local microalga, *Scenedesmus* sp., has a potential to remediate wastewater and produce biomass that can be converted into biofuels like bioethanol. *Scenedesmus* sp. effectively removed nitrogen nutrients (> 90%) from AD brewery effluent when compared to the phosphorus nutrients. The highest lipid content was found to be 24.27% using microwave pretreatment. The hydrolytic agent, HCl, is more effective for reducing sugar extraction in microwave. The reducing sugar yield increased by 19.57% after RSM optimization. The RSM optimization results showed that the developed mode was significant, and its predictions are in line with experimental results. The bioethanol yield obtained was 0.44 g/g reducing sugar at 24 h of fermentation time. Based on the findings of this study, it can be suggested that local microalgae provide a promising result for lipid and bioethanol production after growing on wastewater. Pilot-scale microalgal cultivation should be carried out to evaluate large-scale biomass production for lipids, carbohydrates, and biofuel (bioethanol and biodiesel) production.

REFERENCES

APHA. (1999). Standard Methods for the Examination of Water and Wastewater (20th ed.). Washington, D.C., USA.

Ashokkumar, V., Razman, M., Salam, Z., Sivakumar, P., Tung, C., Elumalai, S., Suresh, V., & Nasir, F. (2017). Production of liquid biofuels (biodiesel and bioethanol) from brown marine macroalgae Padina tetrastromatica. Energy Conversion and Management, 135;351–361. https://doi.org/10.1016/j.enconman.2016.12.054

Bligh, E. G., & Dyer, W. J. (1959). A Rapid Method of Total Lipid Extraction and Purification. Canadian Journal of Biochemistry and Physiology, 37.

Chandra, N., Shukla, P., & Mallick, N. (2020). Role of cultural variables in augmenting carbohydrate accumulation in the green microalga *Scenedesmus acuminatus* for bioethanol production. Biocatalysis and Agricultural Biotechnolog, 26, 1–11.

Chellamboli, C., & Perumalsamy, M. (2014). Application of response surface methodology for optimization of growth and lipids in *Scenedesmus abundans* using batch culture system. RSC Advances, 4:22129–22140.

Cheng, D., & He, Q. (2014). Assessment of environmental stresses for enhanced microalgal biofuel production –an overview. Frontiers in Energy Research, 2(26):1–8. https://doi.org/10.3389/fenrg.2014.00026

Crowell, E. A., & Ough, C. S. (1979). A Modified Procedure for Alcohol Determination By Dichromate Oxidation. Am J Enol Vitic, 30(1):61–63.

Darpito, C., Shin, W.-S., Jeon, S., Lee, H., Nam, K., Kwwon, J.-H., & Yang, J.-W. (2014). Cultivation of *Chlorella protothecoides* in anaerobically treated brewery wastewater for cost-effective biodiesel production. Bioprocess Biosyst Eng, 38(3). https://doi.org/10.1007/s00449-014-1292-4

Diniz, G. S., Silva, A. F., Araújo, O. Q. F., & Chaloub, R. M. (2017). The potential of microalgal biomass production for biotechnological purposes using wastewater resources. J Appl Phycol, 29:821–832.

Ferreira, A., Ribeiro, B., Marques, P. A. S. S., Ferreira, A. F., Paula, A., Pinheiro, H. M., Reis, A., & Gouveia, L. (2017). *Scenedesmus obliquus* mediated brewery wastewater remediation and CO2 biofixation for green energy purposes. Journal of Cleaner Production, 165:1316–1327. https://doi.org/10.1016/j.jclepro.2017.07.232

Guldhe, A., Singh, B., Rawat, I., & Bux, F. (2014). Synthesis of biodiesel from *Scenedesmus* sp. by microwave and ultrasound assisted in situ transesterification using tungstated zirconia as a solid acid catalyst. Chemical Engineering Research and Design, 92(8):1503–1511. https://doi.org/10.1016/j.cherd.2014.05.012

Guo, H., Daroch, M., Liu, L., Qiu, G., Geng, S., & Wang, G. (2013). Biochemical features and bioethanol production of microalgae from coastal waters of Pearl River Delta. Bioresource Technology, 127:422–428.

Hach. (2002). Model DR / 2400 Spectrophotometer. Hach Company, U.S.A.

Halim, R., Harun, R., Danquah, M. K., & Webley, P. A. (2012). Microalgal cell disruption for biofuel development. Applied Energy, 91:116–121. https://doi.org/10.1016/j.apenergy.2011.08.048

Harun, R., Danquah, K., & Forde, G. M. (2010). Microalgal biomass as a fermentation feedstock for bioethanol production. J Chem Technol Biotechnol 20, 85, 199–203. https://doi.org/10.1002/jctb.2287

Harun, R., Jason, W. S. Y., Cherrington, T., & Danquah, M. K. (2011). Exploring alkaline pre-treatment of microalgal biomass for bioethanol production. Applied Energy, 88:3464–3467. https://doi.org/10.1016/j.apenergy.2010.10.048

Hernández, D., Riaño, B., Coca, M., & García-González, M. C. (2015). Saccharification of carbohydrates in microalgal biomass by physical , chemical and enzymatic pre-treatments as a previous step for bioethanol production. Chemical Engineering Journal, 262:939–945. https://doi.org/10.1016/j.cej.2014.10.049

Ho, S., Huang, S., Chen, C., Hasunuma, T., & Kondo, A. (2013). Characterization and optimization of carbohydrate production

from an indigenous microalga *Chlorella vulgaris* FSP-E. Bioresource Technology, 135:157–165.
Kassim, M. A., & Bhattacharya, S. (2016). Dilute alkaline pretreatment for reducing sugar production from Tetraselmis suecica and *Chlorella* sp. biomass. Process Biochemistry, 51:1757–1766.
Lee, J., Yoo, C., Jun, S., Ahn, C., & Oh, H. (2010). Comparison of several methods for effective lipid extraction from microalgae. Bioresource Technology, 101:S75–S77. https://doi.org/10.1016/j.biortech.2009.03.058
Li, Y., Zhou, W., Hu, B., Min, M., Chen, P., & Ruan, R. R. (2011). Integration of algae cultivation as biodiesel production feedstock with municipal wastewater treatment : Strains screening and significance evaluation of environmental factors. Bioresource Technology, 102:10861–10867. https://doi.org/10.1016/j.biortech.2011.09.064
Mahzabin, Q., Zhang, B., Wang, L., & Shahbazi, A. (2019). A combined pretreatment , fermentation and ethanol-assisted liquefaction process for production of biofuel from Chlorella sp . Fuel, 257: 1–8. https://doi.org/10.1016/j.fuel.2019.116026
Manmai, N., Unpaprom, Y., & Ramaraj, R. (2020). Bioethanol production from sunflower stalk : application of chemical and biological pretreatments by response surface methodology (RSM). Biomass Conv. Bioref. https://doi.org/10.1007/s13399-020-00602-7
Maran, J. P., Mekala, V., & Manikandan, S. (2013). Modeling and optimization of ultrasound-assisted extraction of polysaccharide from *Cucurbita moschata*. Carbohydrate Polymers, 92(2):2018–2026.
Mercado, I., Xavier, Á., Verduga, M., & Cruz, A. (2020). *Scenedesmus* sp. Cultivated in the Wastewater of the Dairy Industry. Processes, 8(1458):1–19.
Miller, G. L. (1959). Use of Dinitrosalicylic Acid Reagent for Determination of Reducing Sugar Use. Analytical Chemistry, 31(3):426–428.
Miranda, J. R., Passarinho, P. C., & Gouveia, L. (2012). Bioethanol production from *Scenedesmus obliquus* sugars : the influence of photobioreactors and culture conditions on biomass production. Appl Microbiol Biotechnol, 96:555–564.
Mubarak, M., Shaija, A., & Suchithra, T. V. (2015). A review on the extraction of lipid from microalgae for biodiesel production. Algal Research, 7:117–123. https://doi.org/10.1016/j.algal.2014.10.008
Noraini, M. Y., Chyuan, H., Jan, M., & Chong, W. T. (2014). A review on potential enzymatic reaction for biofuel production from algae. Renewable and Sustainable Energy Reviews, 39:24–34. https://doi.org/10.1016/j.rser.2014.07.089
Onay, M. (2018). Bioethanol production from *Nannochloropsis gaditana* in municipal wastewater. Energy Procedia, 153:253–257. https://doi.org/10.1016/j.egypro.2018.10.032
Pandey, A., Srivastava, S., & Kumar, S. (2019). Sequential optimization of essential nutrients addition in simulated dairy effluent for improved *Scenedesmus* sp ASK22 growth , lipid production and nutrients removal. 128.
Patrícya, A. F. de S. S., Costa, M. C., Lopes, A. C., Neto, E. F. A., Leitão, R. C., Mota, C. R., & Santos, A. B. dos. (2014). Comparison of pretreatment methods for total lipids extraction from mixed microalgae. Renewable Energy, 63:762–766.
Renuka, N., Sood, A., & Ratha, S. K. (2013). Evaluation of microalgal consortia for treatment of primary treated sewage effluent and biomass production. J Appl Phycol, 25:1529–1537. https://doi.org/10.1007/s10811-013-9982-x
Shokrkar, H., Ebrahimi, S., & Zamani, M. (2017). Bioethanol production from acidic and enzymatic hydrolysates of mixed microalgae culture. Fuel, 200:380–386. https://doi.org/10.1016/j.fuel.2017.03.090
Sivaramakrishnan, R., & Incharoensakdi, A. (2018). Utilization of microalgae feedstock for concomitant production of bioethanol and biodiesel. Fuel 217, 458–466. https://doi.org/10.1016/j.fuel.2017.12.119
Thu, M., Choi, S. P., Lee, J., Lee, J. H., & Sim, S. J. (2009). Hydrothermal Acid Pretreatment of *Chlamydomonas reinhardtii* Biomass for Ethanol Production. J. Microbiol. Biotechnol, 19(2):161–166. https://doi.org/10.4014/jmb.0810.578
Wang, B., Lan, C. Q., & Horsman, M. (2012). Closed photobioreactors for production of microalgal biomasses. Biotechnology Advances, 30(4):904–912. https://doi.org/10.1016/j.biotechadv.2012.01.019
Wang, L., Min, M., Li, Y., Chen, P., Chen, Y., Liu, Y., Wang, Y., Roger, & Ruan. (2010). Cultivation of Green Algae Chlorella sp . in Different Wastewaters from Municipal Wastewater Treatment Plant. Appl Biochem Biotechnol, 162, 1174–1186. https://doi.org/10.1007/s12010-009-8866-7
Williams, M. B., & Darwin Reese, H. (1950). Colorimetric Determination of Ethyl Alcohol. Analytical Chemistry, 22(12):1556–1561. https://doi.org/10.1021/ac60048a025
Yu, K. L., Chen, W.-H., Sheen, H.-K., Chang, J.-S., Linh, C.-S., Ong, H. C., Show, P. L., & Ling, T. C. (2020). Bioethanol production from acid pretreated microalgal hydrolysate using microwave-assisted heating wet torrefaction. Fuel, 279: 118435. https://doi.org/10.1016/j.fuel.2020.118435
Yu, X., Dong, T., Zheng, Y., Miao, C., & Chen, S. (2015). Investigations on cell disruption of oleaginous microorganisms: Hydrochloric acid digestion is an effective method for lipid extraction. Eur. J. Lipid Sci. Technol, 117:730–737.

Landslide Factor Optimization for Landslide Susceptibility Modeling

Wubalem Azemeraw[1,*], Getahun Belete[1], Hailemariam Yohannes[2], Mesele Alemu[1], Tesfaw Gashaw[1], Dawit Zerihun[1], Goshe Endalkachew[2]

[1]*Department of Geology, College of Natural and Computational Science, University of Gondar, Ethiopiar*
[2]*School of Civil, Hydraulic and Water Resource Engineering, The Institution of Technology, University of Gondar, Ethiopia*
**Corresponding author, e-mail: azmeraw.wubalem@uog.edu.et*

ABSTRACT

This study assessed the suitability of the area under the receiver operating characteristics curve (AUC) to select the best landslide factors in landslide susceptibility modeling. For this purpose, twelve landslide factors and 712 landslides were collected from literature, detailed fieldwork, and Google Earth Imagery analysis. These landslides were divided into two categories: 498 (70%) training landslide datasets for modeling and 214 (30%) landslide datasets for model validation. A spatial database was built for landslide factors, and landslide inventory, then the relationship between past landslides and landslide factors was performed using the frequency ratio (FR) method and ArcGIS 10.3. Landslide factor optimization was performed using the AUC method, then six landslide factors whose AUC value > 0.5 were determined. But the rest landslide factors provided an AUC value of <0.5. Then the weighted 12 and 6 landslide factors separately were summed using a raster calculator and produced landslide susceptibility indexes (LSIs). The natural break classification method was used to divide the LSIs into five categories: very low, low, moderate, high, and very high susceptibility zones. The areas under the curve (AUC) were determined after the receiver operating characteristic (ROC) curves were produced. The results showed that the FR model provided an AUC value of 66.41% of prediction for 12 factors before optimization. The optimized FR model has a success rate of 78.1%, and a predictive rate of 73.5%. The results showed that the AUC value before factor optimization is less than the AUC value after factor optimization as well as the model's classifying and predicting capacity increases. This result showed that landslide factors can influence the performance and predictability of landslide susceptibility mapping methods. As a result, landslide factors optimization is a critical task prior to landslide susceptibility mapping. This optimized FR model can be used by researchers and decision-makers in regional land use planning and landslide hazard reduction strategies.

Keywords: *landslides, optimization, GIS, frequency ratio, Ethiopia*

1. INTRODUCTION

Understanding the severity of the landslide problem and its process is critical for determining the conditioning and triggering factors, as well as identifying high susceptibility/hazard/risk zones for predicting, assessing, and mitigating the impacts and losses associated with these landslides. As a result, one of the most effective and conclusive techniques is to develop a landslide susceptibility model (Nohani et al. 2019). Landslide inventory and susceptibility mapping are some of the ways used to reduce loss or damage due to landslide incidence. The aim of landslide inventory and susceptibility mapping is to identify the spatial distribution of existing landslides and future landslide-prone areas, respectively (Pourghasemi et al. 2012). The landslide susceptibility mapping can be performed based on the relationship between geo-environmental parameters and past landslide events.

The quality of the landslide susceptibility map can be affected by the quality of landslide factors and landslide sizes besides landslide susceptibility mapping approaches. Therefore, landslide factor selection and landslide size analysis are very important tasks in landslide susceptibility mapping. Researchers have selected landslide factors based on the geo-environmental condition and landslide type analysis (Dou et al. 2015). However, the researchers selected the landslide factors randomly in the domain of hydrological, geological, geomorphological, climate, and anthropological conditions. Lee and Talib (2005) stated that landslide factor optimization can improve the performance and prediction accuracy of landslide susceptibility models (LSM). Therefore, landslide factor optimization or reduction should be performed based on their significance before the LSM is built. This helps to

eliminate the factors that showed a very low relationship to landslide occurrence. This can improve the quality of LSM by reducing noise and uncertainty in the modeling process (Lee and Talib 2005; Dou et al. 2015). Pradhan and lee (2010) developed a landslide susceptibility model considering four, seven, and eleven factors. They found that seven landslide factors that have large prediction weight gave the best accuracy in the landslide susceptibility model. But they did not set or specified the threshold weight for factor selection. Dou et al (2015) have used the certainty factor (CF) to screen causative factors and they found that six landslide factors gave a high-quality landslide susceptibility map compared to the model generated before landslide factor optimization. But the CF approach in factor selection is a time-consuming procedure. To reduce the number of landslide factors in the modeling process and improve the quality of the landslide susceptibility model, landslide factor optimization is critical. As a result, we are inspired to work on landslide factor optimization. In this study, we choose the area under the receiver operating characteristics curve (AUC) to select the suitable landslide factors in landslide susceptibility modeling. The study's originality comes from the fact that, for the first time, landslide factor optimization using AUC and rigorous landslide susceptibility approaches, such as statistical methods, was done in the study area to produce a landslide susceptibility model.

The main goal of this study is determining the most influential factors in causing landslides in the study area using the area under the curve (AUC) of receiver operating characteristics (ROC). The result will motivate researchers to perform landslide factors suitability analysis before landslide susceptibility mapping.

2. MATERIALS AND METHODS

2.1 Study Area and Geological Setting

The study area is located in the highlands of Ethiopia in which, landslides occurred after heavy and prolonged rainfall. It is characterized by a plateau, deep gorge, and rugged topography. The lowest elevation is 1,470 m and the maximum elevation is 3, 807 m. The study area receives heavy and prolonged rainfall from July to September and low rainfall from November to June. The maximum, and the minimum mean annual rainfall are 169 and 79 mm, respectively. The study area is characterized by a dendritic drainage pattern, which emanates from the plateau and drains into low-lying lands (Fig.1). Geologically, the study area belongs to the tertiary and quaternary formation. The tertiary formations are grouped into different lithological units considering their age and composition. These are lower lava flows (TV1), middle basalt flows (TV2), bedded tuff (TV3), upper basalt with trachyte (TV4), plateau basalt with pyroclasts (TV45), wuchale formation (Twf), gishen maryam volcanic(Tgv), wegel tena rhyolite-ignimbrite association (Twri), densa rhyolite-basalt association (Tdrb), kulmesk formation or alajae formation (Tkb), wurgesa basalt or aiba basalt (Twrb), weldiya basalt or ashengi formation (Twb), and quaternary sediments including alluvial-eluvial mixed sediments (Qae) and eluvial sediments (Qe) (Fig. 2).

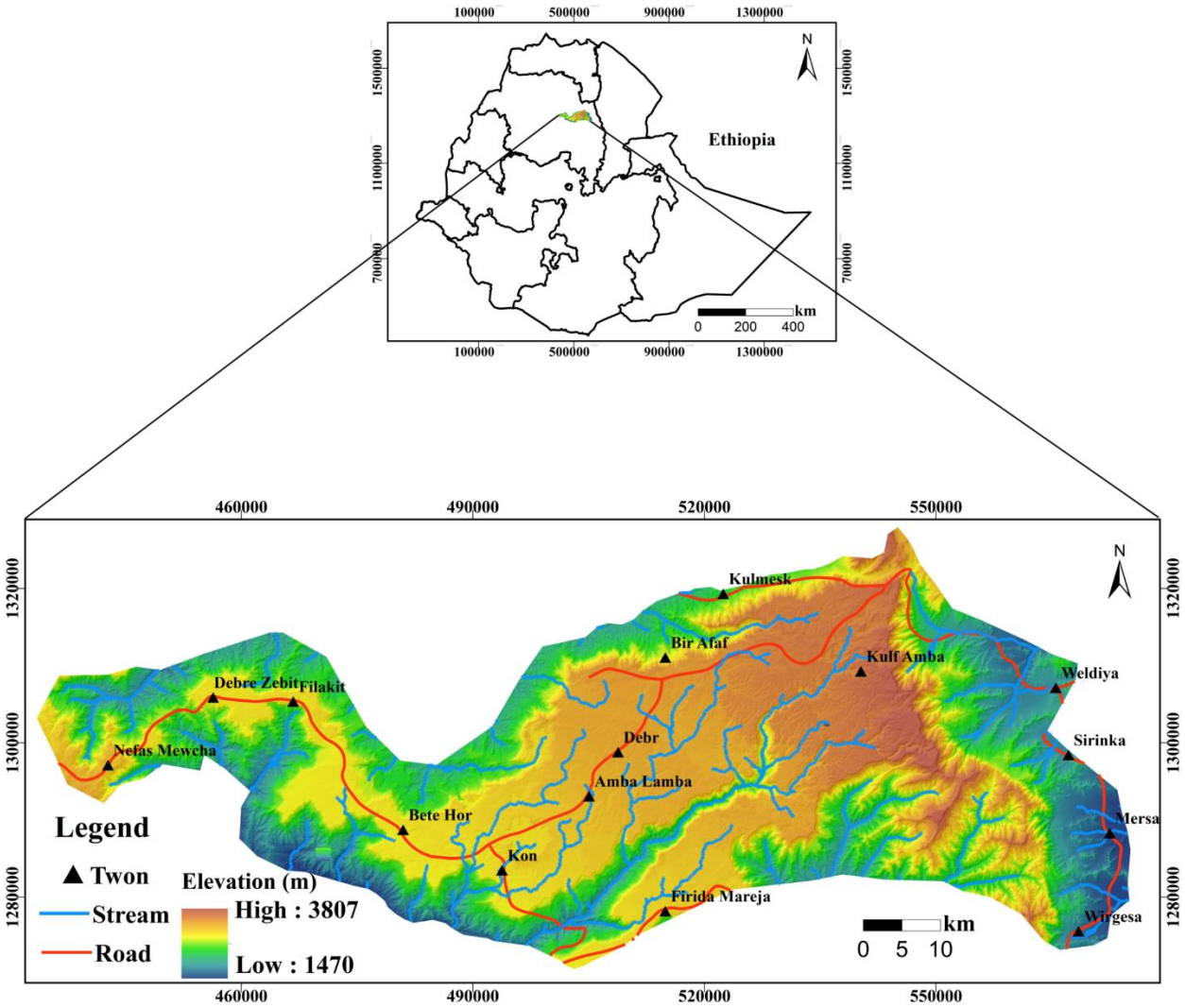

Figure 1: Location map of the study area

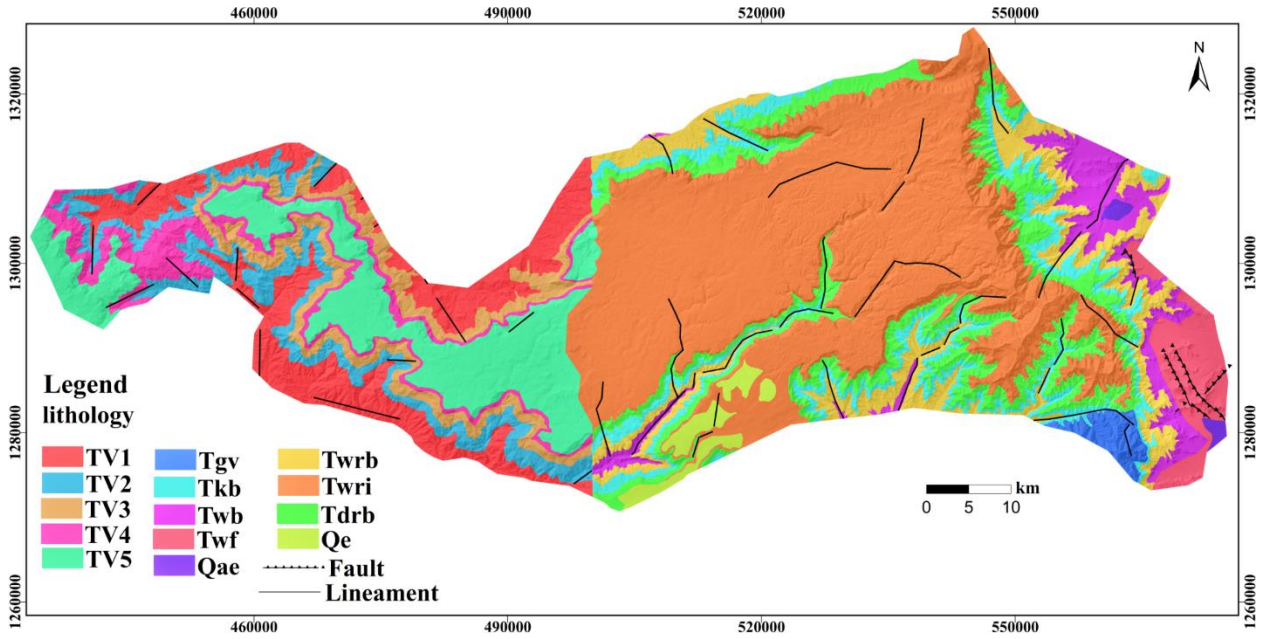

Figure 2: Geological map of the study area (digitized after Institute of Ethiopia Geological survey, 2010 and 2013)

2.2 Data Sources

In this study, landslide factors, and landslide inventory data were used in landslide susceptibility mapping. The landslide factor data were collected from different sources and fieldwork (Table 1). The landslide inventories were collected using google earth imagery analysis and fieldwork.

Table 7: Input data type and source

Data type	Spatial resolution	Variable	Sources
DEM	12.5 m	Slope angle, aspect, curvature, distance to drainage, drainage density, relief, and elevation map	NASA earth data: https://search.asf.alaska.edu
Geological map	1:250,000	Lithology and lineaments	Institute of Ethiopian Geological Survey (IEGS)
Google earth image		Landslide inventory	NASA/google earth
Rainfall	---	Annual and monthly mean rainfall	Ethiopian National Meteorological Agency (NMA) 1989-2019 years
Soil map	1:250,000	Soil type	Amhara national regional state investment office and Food and agriculture organization (FAO)

2.3 Methodological Summary

After the data were collected, four geodatabases were built to make easy statistical analysis under the ArcGIS environment. These databases contain landslide inventory layer (training and testing/validation landslide datasets), landslide conditioning and triggering factors, landslide susceptibility model for frequency ratio (FR), and index of entropy (IOE) methods. The scale of the data source of landslide conditioning and triggering factors can affect the quality of landslide susceptibility models. Therefore, we transformed all the components to a raster format with a spatial resolution of 12.5 m, which corresponds to the DEM resolution to be appropriate for the diversity of the data source and differences in scales. After the projection systems were converted into Adindan UTM Zone 37N, the

spatial relationship between landslide conditioning and triggering factors, and training landslide datasets were performed using the combined method in spatial analysis of ArcGIS. Then landslide pixels in each landslide factor class were extracted. After determining the weight of individual factors and classes using FR and IOE method, the weighted landslide factors are changed into raster using the lookup tool. And then, four landslide susceptibility indexes (LSIs) were developed before and after landslide conditioning and triggering factors optimization. The LSIs were classified into five susceptibility classes of very low, low, moderate, high, and very high using the natural break classification method. The generated models were evaluated by the ROC curve using real statistics software. Generally, the research approach, which was applied in this study, is summarized in Fig. 3.

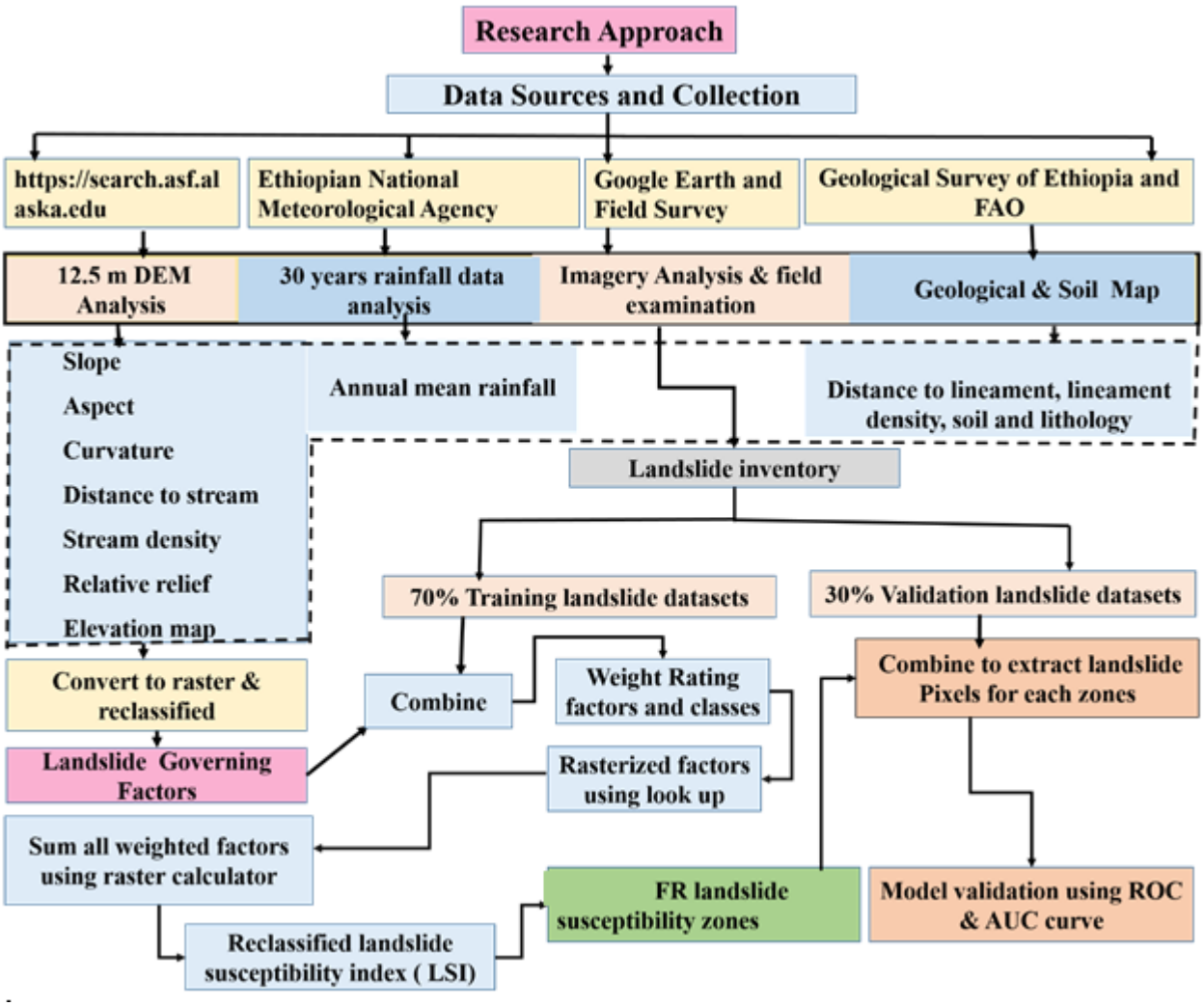

Figure 3: General research approach flow chart

2.4 Landslide Inventory Mapping

The first and most important step in understanding landslides and their impact on landform evolution as well as the most beneficial form of landslide study representation is to prepare a landslide inventory map (Ubaidulloev et al. 2021). A landslide inventory map can consist of geographical location, zone of depletion, zone of accumulation, scarps, depth, type, magnitude, frequency, activity, and date of landslide incidence (Guzzetti et al. 2005; Wubalem and Meten 2020; Wubalem 2021b). Landslide inventories can be used to keep track of previous landslides, which is

useful for landslide susceptibility, hazard, and risk mapping as well as to reduce landslide incidence (Lazzari et al. 2017; Valeria et al. 2019).

Therefore, the preparation of a quality landslide inventory map is very important to determine the spatiotemporal susceptibility, hazard, and risk of landslide incidences in a given terrain. The methods that are used to map landslide inventory are generally grouped into two broad categories such as traditional and innovative methods (Guzzetti et al. 2012; Di Martire et al. 2016; Ubaidulloev et al. 2021). Traditional methods include geomorphological field investigations, analysis of historically recorded landslides, and desk study interpreting aerial stereoscopic photos. The advancement of remote sensing technologies, satellite image accuracy, and GIS applications have considerably increased the capacity of remotely landslide investigation as well as improved the quality of landslide inventory mapping; these approaches are considered innovative methodologies (Guzzetti et al. 2012; Di Martire et al. 2016; Ubaidulloev et al. 2021). The aerial photograph is a very important method to map very large and deep-seated landslides, but it is not good for mapping very small landslides (Ubaidulloev et al. 2021). google earth is used to map large, medium, and small size regional landslides (Ubaidulloev et al. 2021). Many researchers have used google earth for landslide inventory mapping (Meten et al. 2015; Mersha and Meten 2020; Wubalem and Meten 2020; Wubalem 2020; Getachew and Meten 2021; Ubaidulloev et al. 2021; Wubalem 2021a). Google earth imagery is a very simple method to identify landslide boundary even landslide types as well as to collect time-series landslide inventory using time series slides for all ranges of landslide sizes, but it requires a high internet connection and time. Fieldwork is the most important method to evaluate the type, failure mechanism, displaced material, future landslide, damage, and potential triggering and conditioning factors. However, it is difficult in areas that are not easily accessible, and expensive to cover a large area.

Therefore, it is recommendable to use both google earth imagery, and fieldwork to have well distributed and quality landslide inventory map. In this study, detailed fieldwork and google earth imagery analysis were used. The polygon-based inventory was chosen for this study because it includes not only landslide initiation places but also run-out areas, such as valleys that have been affected by debris flows (Shano et al. 2021). A total of 712 landslides were mapped and digitized using google earth imagery and based on field survey. The maximum landslide area is 1,021, 963.8 m^2, and the minimum area is 65.44 m^2. The mapped landslide covered 11, 119, 248.6 m^2 of the entire area. As shown in Fig. 4**,** the size of 73% of landslides in the study area is less than 200, 000 m^2, but the remaining 27% of landslides size range from 200,000 to 1,021,963.8 m^2. The landslides in this study were classified into 70% as training datasets, and 30% as testing landslide datasets keeping their spatial distribution using a subset in the ArcGIS tool (Fig. 5). As indicated from the result, landslides in the study area are concentrated in places closer to rivers, lineaments, weak rock units, and steep slopes. The dominant landslide types in the study area are rotational slide, transitional slide, debris flow, and rock fall. The transitional, rotational, and debris flow landslides covered 22.46%, 11.23%, and 36.72% of the total landslide area, respectively whereas rock fall and unknown landslides together covered about 29.55% of the total landslide area.

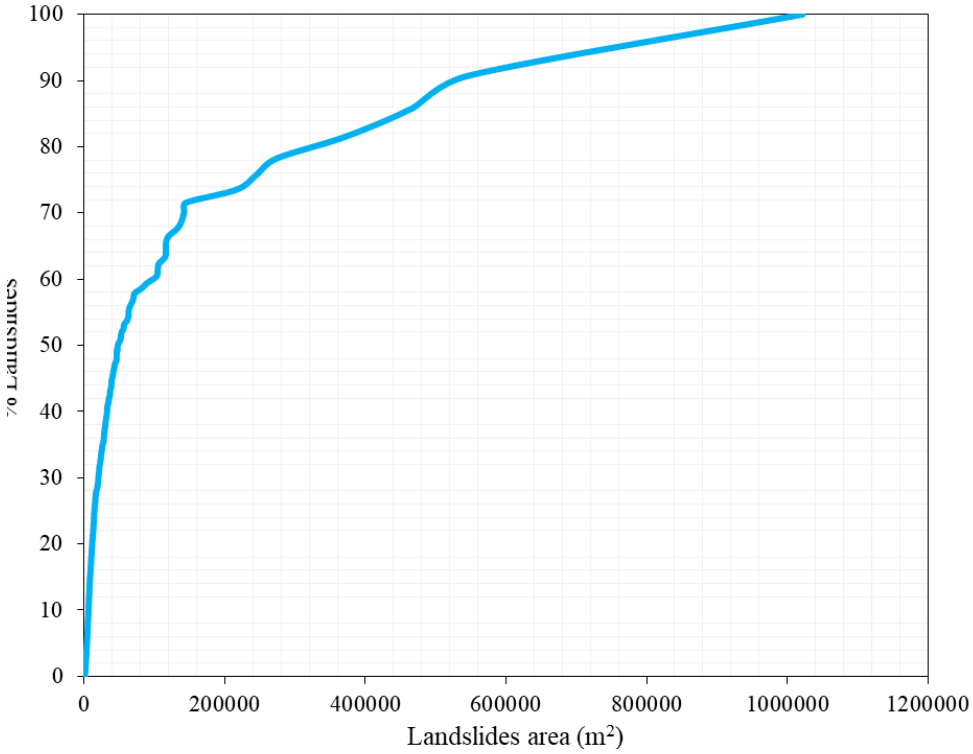

Figure 4: Landslide area

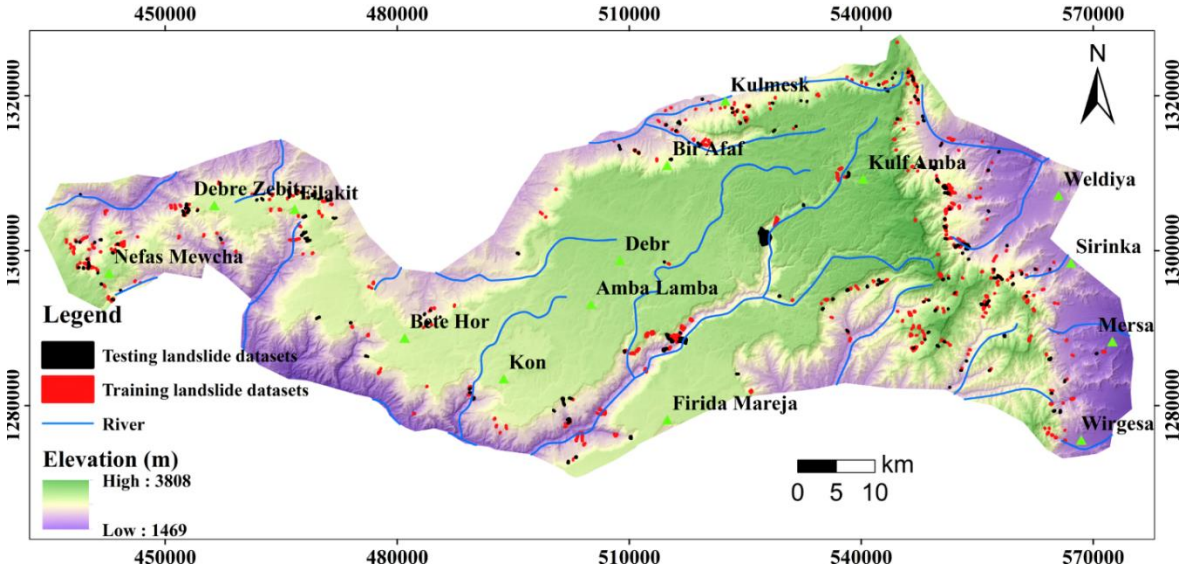

Figure 5: Landslide inventory map (WGS 1984 UTM Zone 37N): red polygons are training landslide datasets and black polygons are testing landslide datasets.

2.5 Landslide Conditioning and Triggering Factors

The evaluation of landslide conditioning and triggering factors is a critical effort in hazard minimization (Wubalem 2021b). Landslides can occur when shear stress exceeds the shear strength of the slope material (Wubalem 2021b). The factors that cause landslides have been divided into those that contribute to an increase in shear stress and those that contribute to a decrease in shear strength; however, water is another factor that

contributes to both an increase in shear stress and a decrease in shear strength of slope material (Wubalem 2021b). The combination of geomorphological, hydrological, and geological factors can influence the incidence of landslides, therefore, selecting the appropriate conditioning and triggering factors is a critical stage in landslide susceptibility modeling. Based on an investigation of the geo-environmental conditions, landslide inventory data, and the underlying geo-morphometric circumstances, twelve landslide conditioning and triggering factors were selected. These twelve variables were chosen from their corresponding spatial databases. The Lithology, slope degree, aspect, curvature, soil type, relief, distance to lineament, lineament density, river density, distance to river, elevation, and mean annual rainfall are the variables to be considered (Fig. 6 f, j, b, a, k, g, d, e, i, c, h, and l)). These parameters were further divided into subcategories using the natural break classification method (Fig. 6). The interval for all landslide factor classification is not uniform because they are classified based on their statistical significance. The researchers grouped landslide factors into geologic, climatic, geomorphic, and hydrologic factors.

2.5.1 Geological Factors

The geologic factors include lithology, soil type, and geological structures/lineaments. The effects of lithology on landslide occurrence are highly dependent on the composition, stratigraphy, degree of weathering, and the presence of a geological discontinuity. Lithology can control not only landslide probability but also it can control landslide distribution, failure mechanism, type of failure, size, and damage of landslide (Anbalagan 1992; Zhang et al. 2017). The lithology of the study area was digitized from the geological map of Weldiya to Wegel Tena area and the Debre Tabor area, at the scale of 1:250,000 (digitized after the Institute of Ethiopian Geological survey 2010 and 2013). The lithology of the study area is classified into fourteen lithological units (Fig. 6 f). These are lower lava flows (TV1), middle basalt flows (TV2), bedded tuff (TV3), upper basalt with trachyte (TV4), plateau basalt with pyroclasts (TV45), wuchale formation (Twf), gishen maryam volcanic(Tgv), wegel tena rhyolite-ignimbrite association (Twri), densa rhyolite-basalt association (Tdrb), kulmesk formation or alajae formation (Tkb), wurgesa basalt or aiba basalt (Twrb), weldiya basalt or ashengi formation (Twb), and quaternary sediments including alluvial-eluvial mixed sediments (Qae) and eluvial sediments (Qe).

The geological structure is the second geologic factor that can control the stability of the slope, which may be faults, joints, and lineaments. The geological structure can decrease the strength of slope material when it serves as a conduit for the passage of fluids. The invisible structure of the rock basement is revealed by lineament, which can be recognized as a line of landscape (Yusof et al. 2011). Along the junction of a fracture plane or the surface expression of a fault, these discontinuities in rocks commonly result in linear or curvilinear morphological characteristics (Yusof et al. 2011). Many experts have highlighted structural weakness due to the presence of lineaments as a source of slope displacement (Yusof et al. 2011; Meten et al. 2015; Wubalem and Meten 2020; Getachew and Meten 2021). Lineament density and distance to lineament were developed from the available geological structures using ArcGIS 10.3. As the density of lineaments increase, the strength of the material decreases which initiate slope movement. Distance to lineament and density were prepared using Euclidean distance and line density, respectively. Distance to lineament was classified into five classes using natural break classification method: <500 m, 500-1000 m, 1000-1,500 m, 1,500-2,000 m and >2,000 m (Fig. 6 d). Lineament density was classified into five classes using the natural break classification method: <12 km^{-1}, 12-37 km^{-1}, 37-66 km^{-1}, 66-103 km^{-1}, and 103-186 km^{-1} (Fig. 6 e).

The Soil type of the study area is classified into a subclass of lithic leptosol, eutric cambisol, eutric leptosol, and eutric vertisols (Fig. 6 k). The presence of shallow-depth soils on steep slopes has the greatest impact on landslide probability (Sharma et al. 2012).

2.5.2 Geomorphic Factors

Geomorphic factors such as slope angle, aspect, curvature, elevation, and relief were used in this study to map landslide susceptibility. The geomorphic factors are classified into subclasses to determine the internal effects of factors on landslide probability. For example, slope angle is classified into five classes <9°, 9-18°, 18-29°, 29-41°, and >41° (Fig. 6 j). The steepness of the slope determines not only the stress distribution inside the slope mass but also the depth of the weathering layer and surface runoff (Regmi et al. 2014; Wang et al. 2016; Wubalem and Meten 2020). The amount of runoff and the extent of soil erosion is influenced by the slope's degree and height. A steep slope increases the velocity of running water whereas there is a greater erosive power. As a result, the slope material that supports the slope will be eliminated exacerbating the problem of slope instability. As usual, as the slope angle increase, landslide probability increases up to a certain point, then decrease, but it is not always true in practical due to a set of constraints (Jaafari et al. 2014; Wubalem and Meten 2020; Wubalem 2020; Wubalem 2021a). For example, when the slope material is a massive rock, the landslide will not occur, but if the steep slope is covered by very loose soil or highly weathered rock units, then a landslide will occur. This will disprove the theoretical concept, that landslide probability will increase as the slope angle increase. Therefore, other phenomena should consider besides slope angle for landslide probability assessment. In this study, a slope map was developed from 12.5m DEM resolution and classified into five classes using the natural break classification method (Fig. 6 j). Weather conditions, land cover, and solar radiation intensity vary by slope direction (slope aspect). Aspect affects the slope's exposure to solar radiation, wind effect, and rainfall (Regmi et al. 2014; Meten et al. 2015; Wang et al. 2016; Wubalem and Meten 2020). The aspect map was developed from 12.5 m DEM resolution. Using the natural break method, the aspect map was classified into ten subclasses flat, northeast, north, southwest, east, west, north, northwest, southeast, and east (Fig. 6 b).

As stated by Vijith and Madhu (2008), slope curvature is a critical characteristic that influences the slope's surface and subsurface hydrological regime as well as the effects of gravity. The rate of change in slope degree or aspect is known as general curvature. The general curvature map can be used to characterize slope morphology. Flat, concave, and convex slope curvature are the three types of slope curvature classes. As stated by Meten et al (2015), a negative value denotes a valley, a positive value denotes a hill slope, and zero/ approaches zero value refers to a flat land area. The curvature condition regulates the hydraulic condition as well as gravity's impact on slope stability (Meten et al. 2015; Wubalem and Meten 2020). The slope's concavity had a major impact on landslide occurrence. It is advantageous for water storage when the slope shape is bowl-shaped. The water from the pound will be percolated into the ground and generate pore water pressure, which can increase stress in the soil. Convex slopes facilitate landslide incidence due to gravity's effect (Jaafari et al. 2014). The curvature was classified into subclass -31- - 1, -1 – 0.7, and 0.7- 34 (Fig. 6 a).

The elevation is a common landslide conditioning component in the development of the landslide susceptibility model (Conoscenti et al. 2015; Trigila et al. 2015; Chen et al. 2018). The differences in landforms across distinct geomorphic units are reflected in the elevation variations (Liu and Duan 2018). Elevation can control landslide probability by differing rainfall patterns and human activity. The elevation values in the study area were classified into five classes (Fig. 6 l). These are 1,469-2,014 m, 2,014-2,373 m, 2,373-2,735 m, 2,735-3,126 m, and >3,126 m (Fig. 6 h). Another way to express the sloping terrain is relative relief. It is the difference in slope height between the highest and lowest points. A landslide can occur in a high relative relief zone (Das and Lepcha 2019). The grid approach and the IDW technique were applied to prepare the relative relief map. The relative relief was classified into subclasses using the natural classification method. These are 1,316-1,443 m, 1,443-1,604 m, 1,604-1,788 m, 1,788-1,948 m, and 1,948-2,169 m (Fig. 6 g).

2.5.3 Hydrologic Factors

Hydrologic factors can control the stability of slope mass which include distance to river, river density, and groundwater depth. For example, distance to rivers and density can control slope toe erosion, soil sediments, and moisture content. The important factor that influences the likelihood of a landslide is the distance from the rivers. This can exacerbate other factors such as groundwater level changes and slope toe erosion (Wang et al. 2016; Wubalem and Meten, 2020). Aside from that, the drainage system is influenced by the degree of surface incision and reflects the state of the surface material. A denser stream network indicates loose slope materials. Rivers can erode the toes of slopes or saturate the lower half of a slope material unit. When slope materials become saturated, it can raise the water levels. As the level of groundwater rises, the effects of pore water pressure will increase on the stability of the slope materials (Wang et al. 2016). In general, the frequency of landslides reduces as the distance from rivers increases (Youssef et al., 2015; Wang et al. 2016; Wubalem and Meten 2020; Wubalem 2021a). In this study, the distance to the river was prepared using Euclidean distance. Distance to drainage was classified into five classes using the natural break classification method. These are <783 m, 783-1,664 m, 1,664-2,643 m, 2,643-3,981 m, and >3,981 m (Fig. 6 c).

The length of a stream per unit area of a river basin is known as drainage density (Onda 1993). Landslides are common in locations where the soil layer is too thin and the drainage density is excessive (Onda 1993). The river density was classified into <0.5 km^{-1}, 0.5-1.5 km^{-1}, 1.5-2.5 km^{-1}, 2.5-3.4 km^{-1}, 3.4-4.5 km^{-1}, 4.5-6.1 km^{-1}, and >6.1 km^{-1} (Fig. 6 i).

2.5.4 Climatic Factors

Rainfall is one of the most critical landslides triggering factors (Kirsto et al. 2017). Landslides can occur when shear stress in the slope exceeds the shear strength of the slope material because of a change in rainfall pattern in a particular region (Kirsto et al. 2017; Wubalem and Meten 2020). The degree of saturation of soils or rocks will raise when rainwater infiltrates into the slope through soil or rock pores. As the groundwater level raise, pore water pressure and soil moisture content will increase. Thus, effective stress and shear strength in soil grains will decrease. The surface tension between particles and the intermolecular attraction between soil particles will decrease as the moisture content of the soil mass increases. As a result, the soil takes on the characteristics of a fluid. This is creating a slope material more vulnerable to failure. Slope failure has mostly occurred in the research region during the middle, end, and early months of July, August, and September, when there has been heavy and prolonged rainfall. The annual mean rainfall of the study area was classified into 79-102 mm, 102-113 mm, 1013-126 mm, 126-144 mm, and 144-169 mm (Fig. 6 l).

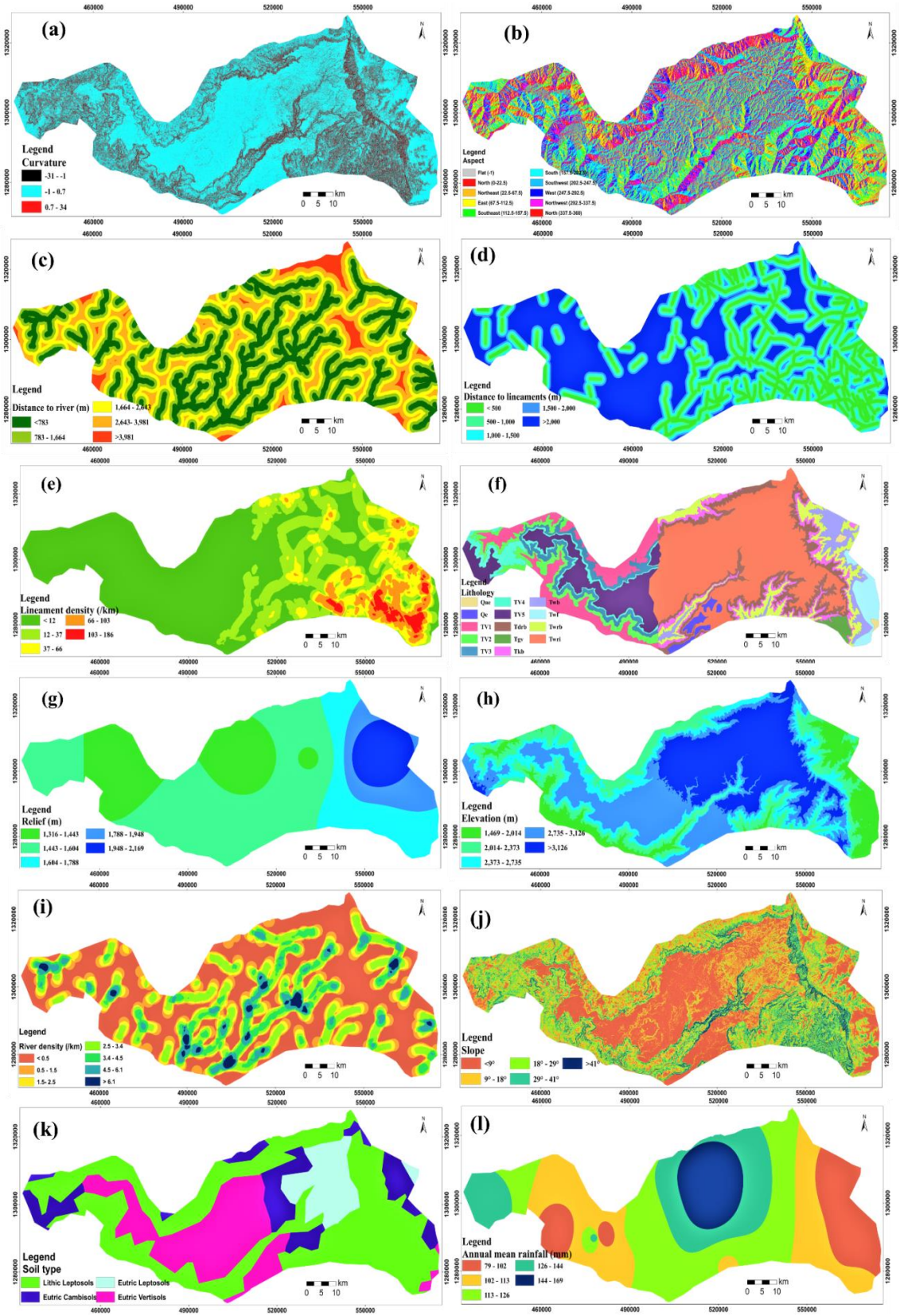

Figure 6: Landslide factor maps: (a) curvature, (b) aspect, (c) distance to river, h) distance to lineament, (d) lineament density, (f) lithology, (g) relief, and (h) elevation, (i) river density, (j) slope angle, (k) soil type, and (l) annual mean rainfall

2.6 Landslide Factor Optimization

In landslide susceptibility mapping, the quality of the models highly depends on the quality, and type of landslide factors as well as quality landslide inventory data. Therefore, factor selection is one of the most important steps. In this study, the area under the curve (AUC) was applied to select the most important landslide factors. Landslide factors combined with landslide raster to extract landslide pixels in each landslide factor using ArcGIS. As stated by Yesilnacar and Topal (2005), the AUC value can be calculated under the area of ROC and varies from 0.5 to 1, with the closer the value to one, the better the model's accuracy. When the AUC is greater than 0.5, the landslide factor has positive relation, but if AUC < 0.5 the factor has a negative relationship with landslide occurrence. As result, only six landslide factors (relief, lithology, slope, stream density, rainfall, and curvature) provide an AUC value > 0.5. To determine the effects of all landslide factors on landslide susceptibility mapping, landslide susceptibility models were produced for twelve, and six landslide factors.

2.7 Landslide Susceptibility Mapping Methods

2.7.1 Introduction

The advancement of technology/computers and geographic information systems (GIS) have resulted in the development of various landslide susceptibility modeling approaches, which depend on expert experience, and statistical analysis. They are grouped into semi-quantitative (analytical hierarchy process (AHP)), qualitative (landslide inventory/heuristic, and geomorphology analysis), and quantitative methods (deterministic/probabilistic/numeric, machine learning, and statistical) (Wubalem 2020). Based on the literature, all methods are capable to produce accurate landslide susceptibility maps except few differences. Therefore, based on input data, the purpose of study, scale, simplicity, quick ability, and the capability to produce reliable results, FR bivariate statistical method is selected to produce a landslide susceptibility map in this study. FR is one of the routinely used probability methods in landslide susceptibility mapping (Meten et al. 2015; Wang et al. 2016; Nohani et al. 2019; Silalahi et al. 2019; Mersha and Meten 2020; Wubalem 2020). The advantage of the FR method is, that it is very simple, quick, and used to evaluate the effects of each factor class. The frequency ratio model is applicable based on the assumption that future landslides will occur under identical conditions to previous ones (Lee and Pradhan 2007; Najafi and Pourghasemi 2014). The drawback of the FR approach is that it requires previous landslides. However, because previous landslides are known in this work, there is no constraint to using FR in landslide susceptibility modeling.

2.7.2 Frequency Ratio (FR)

The frequency ratio method is simple, has a rapid calculation procedure, and provides reliable results (Jaafari et al. 2014; Regmi et al. 2014; Meten et al. 2015; Wang et al. 2016; Wubalem et al. 2021; Wubalem 2021a). The FR is used to calculate the relationship between landslides with landslide factor classes. FR value is the ratio of the area of landslide in a factor class to an area of a factor class (Jaafari et al. 2014; Regmi et al. 2014; Meten et al. 2015; Wang et al. 2016; Wubalem 2021a). FR method has the following limitations: (1) it requires preexisting landslide data (2) it cannot evaluate the effects of landslide factors rather than landslide factor class on landslide probability (Meten et al. 2015; Wubalem et al. 2022). The FR value for all landslide factor classes was calculated using equation (Eq.) 1. The results of FR values are summarized in Table 2. FR value equal to 1 represents the average number of landslides. A FR value less than one suggests a less likelihood of landslide occurrence, whereas a value more than one indicates a higher likelihood of landslide occurrence (Kayastha et al. 2013b; Jaafari et al. 2014; Wang et al. 2016; Wubalem 2021a). After calculating the FR value, the landslide susceptibility index (LSI) of the study area was generated by combining all causative factors using a raster calculator in the ArcGIS tool as shown in equation (Eq.) 2.

$$FR = \frac{S}{Y} = \frac{\frac{Nlspix}{Ntlspix} * 100}{\frac{Ncpix}{Ntcpix} * 100} \qquad \text{Eq. 1}$$

Where FR is frequency ratio, Nlspix is a landslide pixel/area in a landslide factor class, Ntlspix is the total area of a landslide in the whole study area (S), Ncpix is an area of the category within the study area, and Ntcpix is the total pixel area within the whole study area (Y).

$$LSI = \sum_{i=1}^{n} FR_i X_i \qquad Eq. 2$$

LSI is the landslide susceptibility index, n is the number of landslide factors, X_i is the landslide factor, and FR_i is the frequency ratio of each landslide factor type or class. FR is the frequency ratio value of each factor class.

2.8 Model Validation Method

Landslide susceptibility modeling without model performance evaluation and prediction makes no sense for disaster mitigation efforts (Wubalem 2020). Therefore, after the landslide susceptibility model is generated, validation of the results is the most important step in the landslide susceptibility modeling. Although many landslide susceptibility model validation methods are available, the receiver operating characteristics curve (ROC) and area under the curve (AUC) are the most commonly used effective methods (Meten et al. 2015; Mersha and Meten 2020; Wubalem and Meten 2020; Getachew and Meten 2021; Wubalem 2021b). In this study, ROC, and AUC methods were used to validate maps that were generated using FR and IOE statistical methods. ROC is a graphical representation of a binary classifier system's performance while the discrimination threshold is changed (Al-Abadi et al. 2016). The ROC is constructed by plotting the trade-off between false-positive rates (also known as sensitivity) on the X-axis and true positive rates (also known as 1- specificity) on the Y-axis at various threshold values. The area under the curve (AUC) describes a forecast system's capacity to properly predict the occurrence or non-occurrence of predetermined landslides (Devkota et al. 2013; Al-Abadi et al. 2016). The landslide susceptibility maps were reclassified into 100 classes and ordered the value in descending order. Then the landslide pixels for each model class were extracted using GIS through the combine tool. The true positive rate (TPR) and false-positive rate (FPR) values were calculated using real statistics software as shown in equations (Eq.) 3 and 4. Then the ROC is drawn using the fraction value of true positives out of positives vs the fraction of false positives out of negatives (Devkota et al. 2013; Jaafari et al. 2014). The landslide susceptibility maps' prediction accuracy and model performance were quantified using the area under the curve (AUC) based on true and false-positive rates (Yesilnacar and Topal 2005; Devkota et al. 2013; Jaafari et al. 2014; Wubalem 2021a).

After the ROC curve is drawn, the AUC value was calculated under the area of ROC and varies from 0.5 to 1 (Yesilnacar and Topal 2005), with the closer the value to one, the better the model's accuracy. Where Xi and Yi are specificity and sensitivity, respectively, n is classes for a landslide susceptibility index, n+1 thresholds are defined so that the value of the first threshold (i=1) is lower than the minimum susceptibility observed in the most stable class, and the value of the last threshold (i = n+1) is higher than the maximum susceptibility in the most sensitive class. Each threshold forms a confusion matrix in which four types of pixels are defined: false positive (FP), true positive (TP), false negative (FN), and true negative (TN) pixels. FN and TP pixels are landslides within the classes above and below the value of the threshold, respectively. TN and FP pixels, on the other hand, are the stable pixels inside the classes below and above the threshold value, respectively. Based on the numbers of these pixels for each threshold, two statistics are calculated, namely TPR (true positive rate) and FPR (false positive rate) as shown in Eq. 3 and 4. According to Vakhshoori and Zare (2018), the TPR and FPR form points (1,1) on the curve for the first threshold (i=1) and the point of (0,0) for the last threshold (i=n+1). After the ROC curve was plotted AUC of the IOE and FR models were calculated using Eq. 5 based on the TPR and FPR values from the ROC curve.

$$\text{Specifity (FPR)} = \left(\frac{\text{False positive}}{\text{False positive} + \text{True negative}}\right) \quad \text{Eq. 3}$$

$$\text{Sensitivity (TPR)} = \left(\frac{\text{True positive}}{\text{True positive} + \text{False negative}}\right) \quad \text{Eq. 4}$$

$$\text{AUC} = \sum_{i=1}^{n+1} \frac{1}{2} \sqrt{(X_i - X_{i+1})2\ (Y_i + Y_{i+1})} \quad \text{Eq.5}$$

3. RESULTS AND DISCUSSION

3.1 Relationship between Factor Classes and Landslide Probability

The spatial relationship between sets of landslide factors and landslide occurrence was performed using FR method under the GIS environment. Landslide factor optimization analysis was performed using AUC from the ROC curve considering 0.5 as a cutting point. As result, six landslide factors provided an AUC value > 0.5. Besides, landslide susceptibility maps were produced using allthe landslide factors, and factors whose AUC value > 0.5. This was helpful to determine the effects of a number of landslide factors on landslide susceptibility map quality. The quality of the landslide susceptibility map decreases when the landslide factors whose AUC value <0.5 includes in landslide susceptibility mapping. The capacity of statistical methods in producing a quality landslide susceptibility map also decreases when the landslide factors whose AUC value <0.5 includes in landslide susceptibility mapping. The results are summarized in Tables 2, 3, and 4.

3.1.1 Frequency Ratio Model

To evaluate the effects of classes in each thematic layer, the thematic maps are reclassified into subclasses and combined with training landslide datasets using ArcGIS software. Then the FR values were determined from the ratio of the percent of landslide pixels in a class to the percent of class pixels. Lithology in this study has 14 rock units or classes, among these classes, four lithologic units show a great effect on landslide occurrence. Such as highly weathered upper basalt interbedded with pyroclastic mix rhyolite unit (TV4, FR=1.36), densa rhyolite-basalt intercalation (Tdrb, FR=3.6), kulmesk basalt or alajae formation (Tkb, FR=2.49), and wurgesa basalt or aiba basalt formation (Twrb, FR=1.97). This is due to the presence of shallow soil deposits, high degree of weathering, steep slope, and they are closer to rivers/streams. 65.6% of past landslides occurred in the lithological units of TV4, Tkb, Twrb, and Tdrb. Landslide density is high in the lineament density class of 12-37 km^{-1} (FR=2.27), and 37-66 km^{-1} (FR=1.11). 60.5% of past landslides occurred in lineament density classes of 12-37, and 37-66 km^{-1}.

The frequency ratio results show that as the distance to the geological lineaments decreases, the landslide density increase, which is due to the low strength of slope materials, the presence of springs, and highly fragmented slope materials. This result is similar to the work of Wang et al (2016), Wubalem and Meten (2020), and Wubalem (2020). Distances to lineament class <500 m (FR=1.93) and 500-1000 m (FR=1.32) showed a strong relation with landslide occurrence. In these classes, 68% of past landslide incidences occurred. Soil can control the infiltration of water and the development of pore water pressure that can reduce the effective stress. The depth, erosion-resistant, size, shape, and pore distribution of the soil matrix have an impact on slope stability, and specific soil features can help to determine landslide frequency (Rossi and Reichenbach 2016; Silalah et al. 2019). Water infiltration, the velocity and rate of interflow/base flow, and the ability of the soil to hold water are all influenced by the physical properties of soil masses.

Soils containing smaller (finer texture) particles such as clay and silt have a higher surface area and can hold more water, especially in unsaturated circumstances than coarse-textured soils (Lepore et al. 2011). In the relation between soil type and landslide occurrence probability, the lithic leptosol (FR=1.39), and eutric leptosol (FR=1.34)

classes received high FR values. 85.9% of past landslides occurred in the soil type class of lithic leptosol, and eutric leptosol soils (Table 2 and Fig. 7). This is due to the presence of unconsolidated soil properties with a very shallow depth profile. From the FR analysis, the first class of distances to streams <783 m (FR=2.1) indicated a strong correlation with landslide probability. The closer to the rivers, the higher will be erosive power and erosion rate, which can remove slope-toe support. This can decrease shear strength, but increase driving forces, then the slope material strength will be shifted from equilibrium to in equilibrium conditions. As indicated in Table 2, as the distance to the river increases, the landslide density decreases, which is similar to the work of Jaafari et al (2014), Wang et al (2016), Anis et al (2019), Wubalem and Meten (2020), Wubalem (2020), Shano et al (2021), and Wubalem (2021a). In these classes of distance to rivers, 60.8% of past landslides occurred. As a result, a high density of landslides in the study area occurred closer to the rivers. The highest FR value (3.05) for river density is class 3.4-4.5 km^{-1}, followed by >6.1, 2.5-3.4, and 4.5-6.1 km^{-1} (Table 2). 54.4% of past landslides occurred in the river density class of 2.5-3.4, 3.4-4.5, 4.5-6.1, and >6.1 km^{-1}. In this study, only three slope angle classes showed a strong correlation with landslide probability. Landslides are more common in slope classes of 18°-19°, 29°-41°, and >41° (Table 2). The slope class >41° (FR=4.02) has the greatest FR value, followed by 29°-41° (FR=1.83) and 18°-19° (FR=1.3) (Table 2). Of the past landslides, 69.9% of landslides have occurred in the slope classes of 18°-19°, 29°-41°, and >41°.

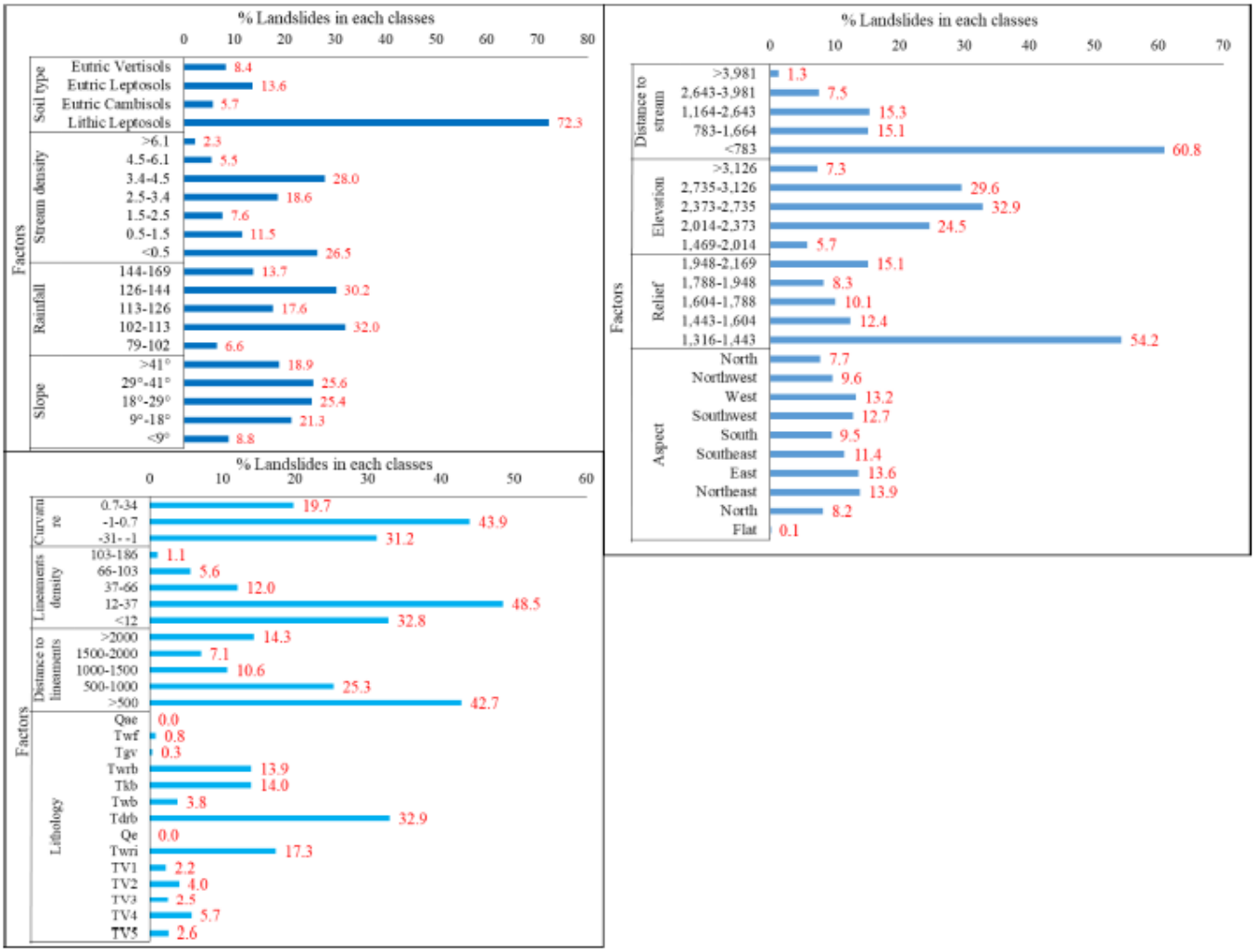

Figure 6: Landslide percent in each landslide factor class

As shown in Table 2, as the slope angle increases, the FR value increases, but as the slope angle decreases, the FR value decreases. Because as the slope angle decreases the shear stress in slope materials decreases, which is related to low slope gradients, but as the slope angle increases stress increases (Wang et al. 2016; Anis et al. 2019). This finding may not always be true because landslides can occur on a gentle slope (Jaafari et al. 2014; Wubalem and Meten 2020). Landslides can occur on a gentle slope when the slope is modified by natural or manmade activity, but they cannot occur on a steep slope if the slope materials are massive rock mass or the slope is not covered by unconsolidated soils (Jaafari et al. 2014; Regmi et al. 2014; Wubalem and Meten 2020). As stated by Pradhan (2011), Jaafari et al (2014), Meten et al (2015), Wubalem and Meten (2020), Shano et al (2021), Wubalem (2021a), the slope aspect is one of the critical landslide factors for landslide probability that affects the exposure of slope materials for wind, rainfall, and sunlight as well as moisture content and weathering. 69.3% of past landslides occurred in the north, east, west, southwest, and northeast facing slopes. Curvature is an important parameter in landslide susceptibility mapping as it can cause landslides due to pore water pressure and gravity effects. The curvature has three classes of flat, convex, and concave slope shapes. The frequency ratio values of general curvature suggest that the first class of -31--1 has the largest influence on initiating landslides, with FR value of 1.45. In the -31--1 class, 50.9% of past landslides occurred. This is due to the concave slope allowing rain to be accumulated and develop water pressures that can initiate landslide incidence (Jaafari et al. 2014; Riaz et al. 2018; Wubalem and Meten 2020; Shano et al. 2021; Wubalem 2021a). As indicated in Table 2, the convex and flat portion of curvature shows a negative relationship with landslide occurrence. The elevation is another important landslide factor in the study area, which affects human activity, rainfall distribution, vegetation cover, soil deposit, and temperature. Landslide density become high at the elevation class of 2,373 to 2,735 meters, followed by 2,014-2, 373 and 2,735-3,126 meters. At these elevation ranges, the FR value of the elevation is greater than one and 87% of past landslides occurred in these ranges (Table 2, and Fig. 7).

Landslide occurrence is high at medium elevation ranges, but not at the lower or the higher elevation because of massive rocks and plateau topographic nature (Pourghasemi et al. 2012; Zare et al. 2013; Anis et al. 2019). The FR value was greater than one for relief classes of 1,316-1,443 m (FR=1.15), 1,788-1,948 m (FR=1.1), and 1,948-2,169 m (FR=2.83), indicating a high chance of landslide occurrence. 77.6% of past landslides occurred in the relief class of 1,316-1,443 m, 1,788-1,948 m, and 1,948-2,169 m. Rainfall is one of the most important landslides triggering factors because it raises the pore pressure and soil moisture conditions on slope materials, causing resisting forces to decrease while driving forces increase. Rainfall's impacts on landslides are highly dependent on slope material condition, slope angle, and land use/land cover conditions (Silalah et al. 2019). In the annual mean rainfall classes of 102-113 (FR=1.31), 126-144 (FR=1.55), and 144-169 (FR=1.28) mm/year, the FR value is high. 75.9% of past landslides occurred in these classes. The result shows that moderate and high annual mean rainfall classes have a strong relationship to landslide probability because rainfall can increase moisture content, develop pore pressure (decrease shear strength), and lubricate slope material contact which facilitates slope materials movement (Yalcin 2007; Anis et al. 2019).

The landslide susceptibility index (LSI) values of twelve factors were determined using ArcGIS 10.3 software in this study. The range of values is from 5 to 26. The relative sensitivity to landslide occurrence is represented by the landslide susceptibility index value. The higher the LSI values, the higher the landslide probability in the region (Jaafari et al. 2014; Wang et al. 2016). Using the natural break classification method, the index values were then divided into five categories very low, low, moderate, high, and very high (Fig. 8). Very low, low, moderate, high, and very high landslide susceptibility zones account for 23.7%, 30.7%, 23%, 16%, and 6.6% of the total area, respectively (Table 3). Meanwhile, Table 3 shows that very low and low susceptibility zones account for 2.28% and 12.51% of the total training landslides as well as 2.38% and 12.7% of testing landslides, respectively. The landslides in the moderate, high, and very high susceptible zones account for 17.36%, 19.61%, and 48.24% of the total training landslides as well as 18.36%, 20.76%, and 45.8% of testing landslides. 67.85% and 66.56% of the

total training and testing landslides in the research region occur in the high and very high landslide susceptibility zones. The high and very high landslide susceptibility classifications are primarily found in ridges, steep slopes, and along rivers in the southeast, east, west, and northeast.

Landslide susceptibility maps with five susceptibility zones were also produced after factor optimization (Fig. 9). After factor optimizations, the area coverage of the very low (26.1%) and low (32.8%) FR landslide susceptibility zones increased, but the area coverage of the moderate (21.3%), high (15.1%), and very high (4.8%) landslide susceptibility zones decreased (Table 4). Due to the presence of noise and uncertainty, including improper causal factors in landslide susceptibility modeling may result in incorrect classification of susceptibility zones (Lee and Talib 2005; Dou et al. 2015).

Table 2: FR values of the landslide-conditioning factors

Factor	Class	Pixel	% CA	TLSP	%TLSP	FR
Slope	<9°	10273447	37.60	4331	8.82	0.23
	9°-18°	6609504	24.19	10458	21.29	0.88
	18°-29°	5336329	19.53	12462	25.37	1.30
	29°-41°	3820080	13.98	12575	25.60	1.83
	>41°	1286563	4.71	9301	18.93	4.02
Rainfall (mm)	79-102	4276063	15.65	3224	6.56	0.42
	102-113	6680033	24.45	15700	31.96	1.31
	113-126	8123895	29.73	8655	17.62	0.59
	126-144	5318045	19.46	14819	30.16	1.55
	144-169	2926130	10.71	6729	13.70	1.28
Stream density (km^{-1})	<0.5	11323662	41.44	13022	26.51	0.64
	0.5-1.5	3605352	13.19	5655	11.51	0.87
	1.5-2.5	3598201	13.17	3755	7.64	0.58
	2.5-3.4	4410095	16.14	9126	18.58	1.15
	3.4-4.5	2509074	9.18	13747	27.98	3.05
	4.5-6.1	1410216	5.16	2703	5.50	1.07
	>6.1	469323	1.72	1119	2.28	1.33
Soil type	LL	14245731	52.14	35516	72.29	1.39
	EC	3715865	13.60	2803	5.71	0.42
	EL	2784149	10.19	6698	13.63	1.34
	EV	6578207	24.07	4110	8.37	0.35
Lithology	TV5	2912135	10.66	1255	2.55	0.24
	TV4	1153109	4.22	2817	5.73	1.36
	TV3	1298553	4.75	1213	2.47	0.52
	TV2	1397314	5.11	1986	4.04	0.79
	TV1	2413474	8.83	1091	2.22	0.25
	Twri	9802362	35.87	8490	17.28	0.48
	Qe	141172	0.52	0	0.00	0.00
	Tdrb	2499270	9.15	16176	32.93	3.60
	Twb	1128245	4.13	1859	3.78	0.92
	Tkb	1532210	5.61	6859	13.96	2.49
	Twrb	1930491	7.06	6823	13.89	1.97
	Tgv	265928	0.97	171	0.35	0.36
	Twf	772321	2.83	387	0.79	0.28
	Qae	78842	0.29	0	0.00	0.00

Distance to lineaments (m)	<500	6046805	22.13	20996	42.74	1.93
	500-1000	5248116	19.21	12415	25.27	1.32
	1000-1500	3882733	14.21	5216	10.62	0.75
	1500-2000	2861238	10.47	3464	7.05	0.67
	>2000	9285274	33.98	7036	14.32	0.42
Lineaments density (km^{-1})	<12	16302230	59.66	16099	32.77	0.55
	12-37	5833383	21.35	23847	48.54	2.27
	37-66	2962900	10.84	5904	12.02	1.11
	66-103	1667946	6.10	2756	5.61	0.92
	103-186	557707	2.04	521	1.06	0.52
Curvature	-31- (-1)	5885724	21.54	16153	31.15	1.45
	-1-0.7	15590983	57.06	22751	43.88	0.77
	0.7-34	5849216	21.41	10223	19.72	0.92
Aspect	Flat	262762	0.96	33	0.07	0.07
	North	1806578	6.61	4025	8.19	1.24
	Northeast	2958579	10.83	6817	13.88	1.28
	East	3080921	11.27	6698	13.63	1.21
	Southeast	3861166	14.13	5623	11.45	0.81
	South	3690102	13.50	4652	9.47	0.70
	Southwest	3473790	12.71	6258	12.74	1.00
	West	3155870	11.55	6490	13.21	1.14
	Northwest	3525270	12.90	4726	9.62	0.75
	North	1510885	5.53	3805	7.75	1.40
Relief (m)	1,316-1,443	12907188	47.24	26633	54.21	1.15
	1,443-1,604	6672782	24.42	6082	12.38	0.51
	1,604-1,788	4240235	15.52	4955	10.09	0.65
	1,788-1,948	2050293	7.50	4054	8.25	1.10
	1,948-2,169	1453668	5.32	7403	15.07	2.83
Elevation (m)	1,469-2,014	3096218	11.33	2811	5.72	0.50
	2,014-2,373	4977996	18.22	12057	24.54	1.35
	2,373-2,735	4695938	17.18	16143	32.86	1.91
	2,735-3,126	7260832	26.57	14531	29.58	1.11
	>3,126	7294939	26.70	3585	7.30	0.27
Distance to stream (m)	<783	7909714	28.95	31529	60.81	2.10
	783-1,664	7978672	29.20	7845	15.13	0.52
	1,164-2,643	6679435	24.44	7941	15.32	0.63
	2,643-3,981	3741273	13.69	3882	7.49	0.55
	>3,981	1016829	3.72	651	1.26	0.34

Table 3: Landslide susceptibility class area coverage for FR before factor optimization

Methods	LSI range	Class	Pixels	%Area	Km^2	ha	TRLSP	%TRLSP	TLSP	%TLSP
FR	5-9	Very low	36536	23.7	57.1	570.9	1118	2.28	516	2.38
	9-11	Low	47410	30.7	74.1	740.8	6145	12.51	2755	12.70
	11-14	Moderate	35445	23.0	55.4	553.8	8529	17.36	3982	18.36
	14-17	High	24782	16.1	38.7	387.2	9634	19.61	4504	20.76
	17-26	Very high	10201	6.6	15.9	159.4	23701	48.24	9934	45.80

Note: LSI is landslide susceptibility index, TRLSP is training landslide pixels, TLSP is testing landslide pixels

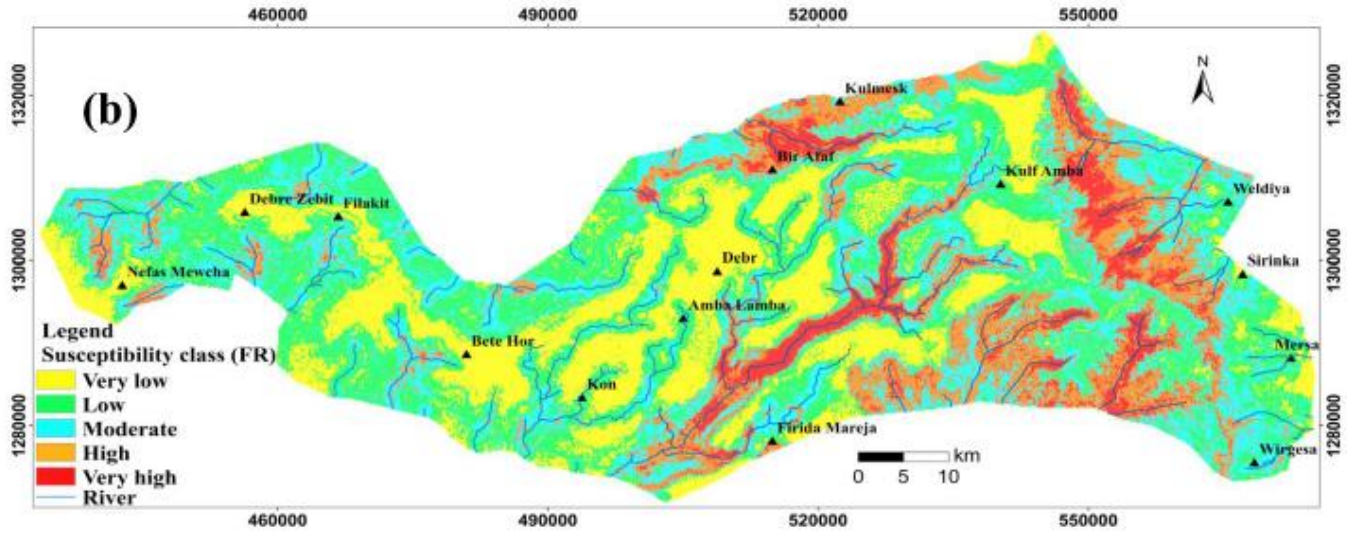

Figure 9: Landslide susceptibility map before factor optimization using frequency ratio

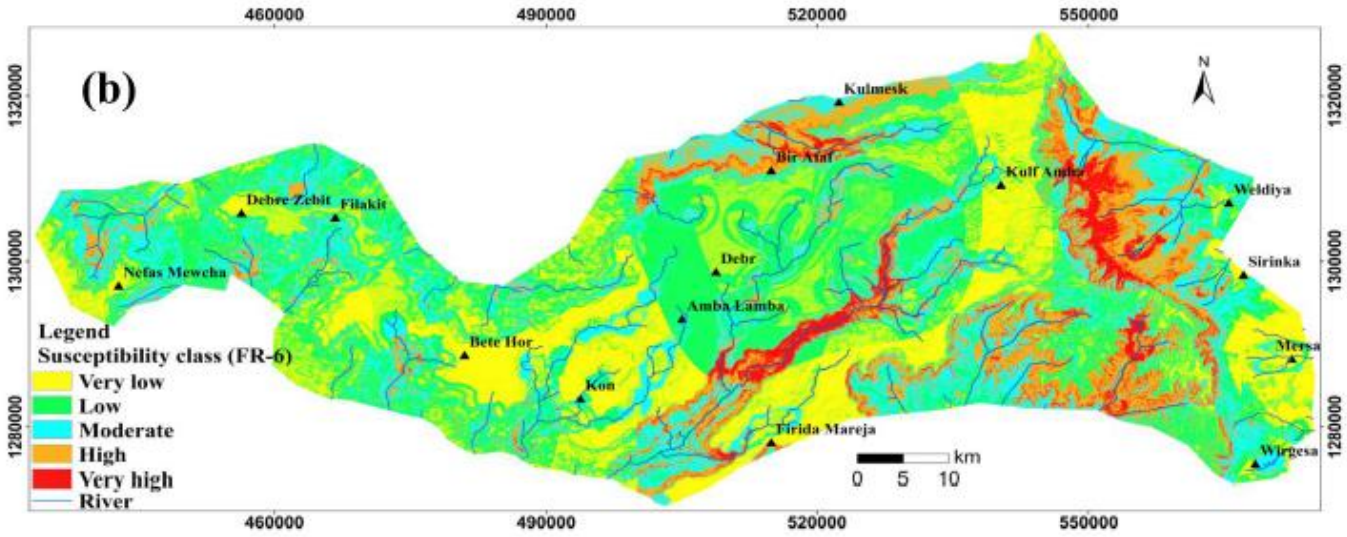

Figure 10: Landslide susceptibility map after factor optimization using frequency ratio

3.1.2 Model Validation and Factor Optimization

To evaluate and compare the models' performance and accuracy, the researchers used the well-known ROC, and area under the curve (AUC) methods. The success rate evaluation and the prediction rate evaluation are the two primary steps in AUC's model evaluation. The success rate was calculated using training data, and the prediction rates were calculated using a set of validation data. The outcomes of the success rate showed the model's fitness for the training data. Compare to the predictive rate, the success rate method is useless in determining the model's predictive capacity (Nahoni et al. 2019). We developed landslide susceptibility models for all 12 landslide factors as well as optimized landslide factors. To validate the models generated before and after factor optimization, the receiver operating characteristics curve (ROC) was prepared from training and a testing landslide dataset, respectively (Pradhan 2011b; Xu et al. 2013). The ROC (success rate) indicates how effectively the model and controlling variables predicted the landslide (Xu et al. 2013; Meten et al. 2015). Fig. 11 depicts the FR model's ROC (success and prediction rate curves), which were produced before factors optimization. According to the ROC

(success rate curves), the first 10% of the region of the susceptibility classes can explain approximately 39% and 38% of all used landslides (out of 498 landslides), respectively. Similarly, the ROC (prediction rate curves) showed that the first 10% of the region of the susceptibility classes can account for 38.5% of all used landslides (out of 214 landslides). To evaluate how much the methods produced accurate models, area under the receiver characteristics curve (AUC) was calculated using real statistics from the ROC curve. Based on the AUC value, the success rate value or training accuracy of the susceptibility maps was 69% and AUC prediction rate value is 66.41%. This shows FR model successfully estimated future landslide occurrence.

Factor optimization was performed using the AUC method to determine the most effective landslide factors in landslide susceptibility mapping, considering a 0.5 AUC value as a lower boundary. The result has shown that only six landslide factors have AUC values greater than 0.5. Based on the optimized AUC values, the relief, lithology, slope, river density, rainfall, and curvature are the most effective landslide factors in which their AUC values are greater than 0.5. The remaining landslide factors provide AUC values less than 0.5. In the FR landslide susceptibility model, the AUC value of the success rate curve (78.1%) using six factors is higher than that of 69% using all twelve factors as shown in Fig. 11 and 12. At the same time, the prediction rate has similar results as the success rate curve, it is observed that six landslide factors give the highest accuracy than that of all the twelve factors. From the analysis, the models' AUC values of ROC (success rate and predictive rate) increase as the factors whose AUC value was less than 0.5 were excluded in the model generation. In this finding, we concluded that before landslide susceptibility mapping, landslide factor optimization should be performed to determine the most effective landslide factors and to minimize the number of landslide factors in landslide susceptibility mapping. Furthermore, considering the AUC value, the performance and predictive ability of the FR method increased after landslide factor optimization (Fig. 12). From this result, we concluded that landslide factors can affect the quality of landslide susceptibility maps using different mapping methods. Besides, the areas covered by high and very susceptibility classes decrease as the number of landslide factors decreases in modeling (Table 3 and 4). This finding shows that a number of landslide factors can affect the quality of the landslide susceptibility model. Therefore, landslide factor evaluation should be performed before landslide susceptibility model generation.

The two primary aims of this work are landslide factor optimization and landslide susceptibility mapping using statistical methods in the Nefas-Mewcha to Weldiya road corridor. The most crucial element in producing a high-quality landslide susceptibility model is knowledge of the landslide causative factors in a given environment. Several studies in the past (Meten et al. 2015; Wubalem and Meten et al. 2020; Nega and Meten 2021; Shano et al. 2021) have manually identified landslide factors however this was subjective. To be clear, there are no standard rules on how to identify and select the number of landslide causative factors. As a result, a number of researchers have used a variety of different causal factors to produce the landslide susceptibility map. In the literature, it has been reported that 12-15 landslide factors are employed to construct the landslide susceptibility model (Wang et al. 2016). However, based on the availability and accessibility of information, 6–15 factors were most frequently used (Meten et al. 2015; Wubalem and Meten 2020; Wubalem 2021b). As a result, based on an understanding of the triggering mechanism, it is feasible to limit the number of factors. For example, in landslides caused by rainfall, the triggering factors are not related to the earthquake, but rather to rainfall duration and intensity. In such instances, it is common knowledge that the superfluous factors in the analysis can be readily omitted. When the triggering mechanism is unknown, and the landslide inventory database produce from several images taken over time, the screening out process necessitates the use of statistical or computational models.

Based on the certainty value, Dou et al. (2015) have screened six factors out of 15 for landslide susceptibility mapping in Niigata, Japan. In this method, first, it needs to calculate the certainty value for each landslide factor class and then the certainty value for induvial landslide factors, which is tedious work. Besides, the CF method has no specified threshold weight to select landslide factors. Multivariate models' prediction performance is limited by similar statistical equations based on correlation or association indexes. Costanzo et al. (2012) on the other hand,

determined the factors based on the ranks associated with the factor's predicted contribution to a multivariable model's prediction capability. When the majority of the variables are statistically significant, approaches to using logistic regression on the forward selection of variables will fail. For the same reason, the stepwise logistic regression model was not considered in this study because the statistical tests revealed that the majority of the variables are significant. Furthermore, in landslide susceptibility assessment, the stepwise logistic regression model requires both landslide and non-landslide pixels to be calculated. Because the proposed AUC method only employed landslide pixels in the computation, it was able to overcome these constraints. Furthermore, the proposed method is a simple method that allows the causative factors to be rated based on their AUC values, which range from 0.5 to 1. AUC values > 0.5 are thought to have a substantial influence on the occurrence of landslides, and vice versa. The identification of the most determinant factors using an AUC-based factor screening procedure, we feel, is a crucial step in landslide susceptibility mapping. From AUC results, six landslide-causative factors whose AUC values > 0.5 are: relief, lithology, slope, river density, rainfall, and curvature, all of which have a strong relationship with the occurrence of landslides. Moreover, the results of landslide susceptibility models generated from six factors were also validated by the ROC (success rate and prediction rate) curves. It is found that the landslide susceptibility map produced from the six factors has higher accuracy than that of the original twelve factors. The results demonstrated that a larger number of causative factors do not necessarily give a better landslide predictability map. This is most likely due to data duplication or spatial self-correlation with the research area.

Table 4: Landslide susceptibility class area after factor optimization (FR)

Methods	LSI Range	Class	Pixels (m)	%A rea	Area (km^2)	Area (ha)
FR for 6 factors whose AUC value > 0.5	2.7-4.6	Very low	7094619	26.1	11085.3	110853.4
	4.6-5.9	Low	8923750	32.8	13943.4	139433.6
	5.9-7.5	Moderate	5784218	21.3	9037.8	90378.4
	7.5-9.6	High	4115088	15.1	6429.8	64298.3
	9.6-15.5	Very high	1300256	4.8	2031.7	20316.5

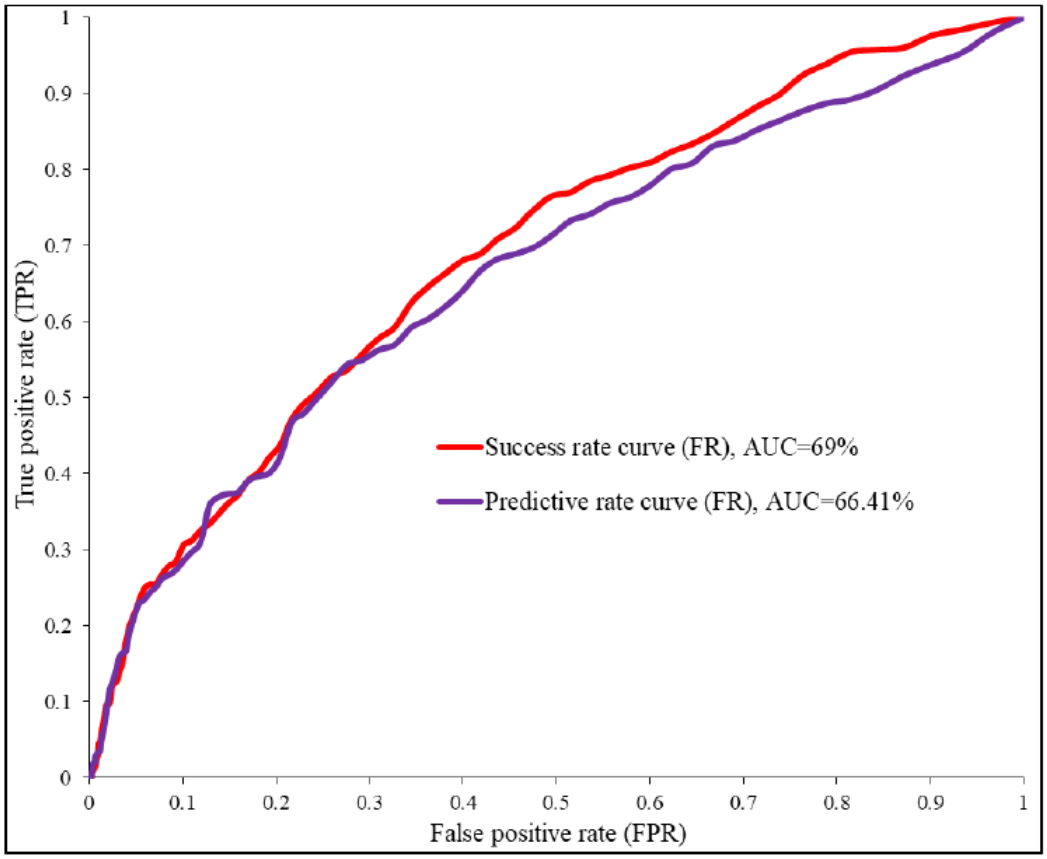

Figure 11: Receiver-operating characteristics curve (ROC) (Prediction and Success rate curves (before optimization)

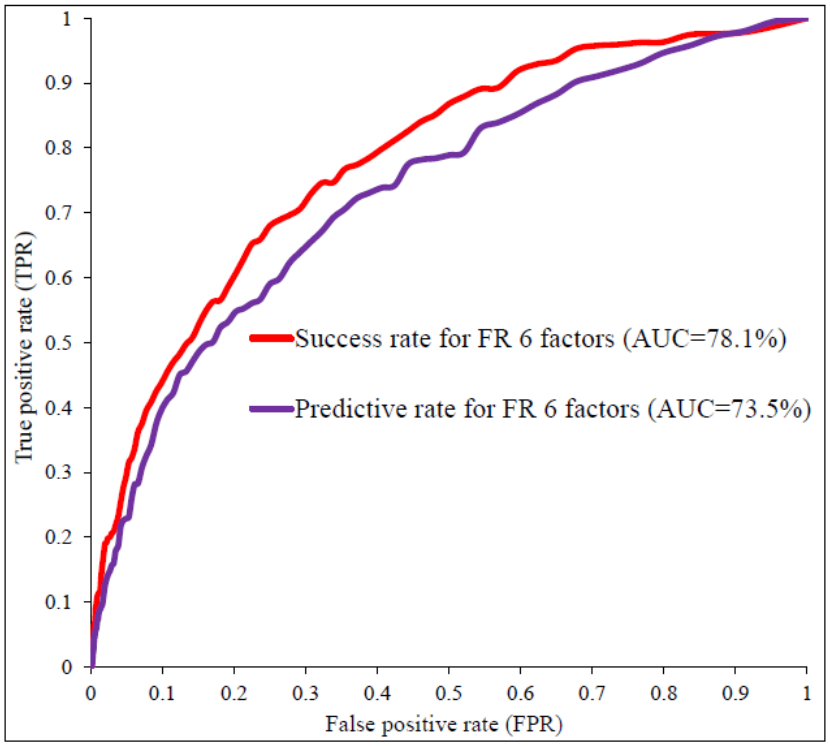

Figure 12: Receiver operating characteristics curve after optimization for 6 landslide factors

4. CONCLUSION

Detail fieldwork and Google Earth Imagery analysis were conducted to prepare a landslide inventory map. As a result, rotational, transitional, debris flow, and rockfall types of landslides and 712 landslides were identified. The result of landslide inventory from detailed fieldwork and Google Earth Imagery analysis showed that most of the preexisting landslides are concentrated along streams, closer to lineaments, steep slopes, and weak rock unit formations. Landslide susceptibility maps of the study area were developed from the spatial relationship between 498 training landslide datasets and 12 landslide factors using FR methods, which were classified into five susceptibility classes very low, low, moderate, high, and very high. The very low and low susceptibility zones are relatively safe for infrastructure and agricultural development compared to the moderate, high, and very susceptibility zones, which require critical measurements to reduce loss of life and properties. The models produced without factors optimization were evaluated using the AUC value of the ROC curve. The result showed that the FR model has a success rate AUC value of 69% and a predictive rate AUC value of 66.41%. The landslide susceptibility models were also produced after landslide factor optimization, and they are validated using the AUC of the ROC curve. The result showed that the FR model has a success rate value of 78.1% (six factors), and a predictive rate value of 73.5% (six factors). The result shows that the AUC values are increasing as the number of landslide factors decreases from twelve to six (relief, lithology, slope, stream density, rainfall, and curvature). This finding helps to conclude that landslide factors can affect the performance and predictability of the landslide susceptibility mapping methods. Therefore, before landslide susceptibility mapping, landslide factors optimization is a very important task. Based on the AUC value of the models generated after factor optimization, the FR method produced a little bit best susceptibility map, which can be used by researchers, and a land-use planner for regional land use planning, environmental protection, and landslide mitigation purposes.

ACKNOWLEDGMENTS

We would like to express our gratitude to the University of Gonder for its financial support and geological equipment, as well as to the National Meteorological Agency and the Ethiopian Geological Survey for their valuable data.

REFERENCES

Abadi, Al-A.M., Temmeme, Al A.A., Ghanimy, Al. M.A (2016): A GIS-based combining of frequency ratio and index of entropy approaches for mapping groundwater availability zones at Badra–Al Al-Gharbi–Teeb areas, Iraq. Sustain. Water Resour. Manag, 2: 265–283 (2016).

Anbalagan, R. (1992): Landslide hazard evaluation and zonation mapping in mountainous terrain. Eng Geol, 32: 269-277.

Anis, Z., Gallala, W., Vakhshoori, V., Habib, S., and Gaied, ME. (2019): GIS-based landslide susceptibility mapping using bivariate statistical methods in North-western Tunisia. Open Geosci, 11:708–726.

Chen, W., Shahabi, H., Shirzadi, A., et al (2018): Novel hybrid artificial intelligence approach of bivariate statistical-methods-based kernel logistic regression classifier for landslide susceptibility modeling. Bull Eng Geol Environ, 1–23.

Chen, Z., Wang, J. (2007): Landslide hazard mapping using a logistic regression model in Mackenzie Valley, Canada. Nat Hazards, 42:75–89.

Conoscenti, C., Ciaccio, M., Caraballo-Arias, N., et al (2015): Assessment of susceptibility to earth-flow landslide using logistic regression and multivariate adaptive regression splines: A case of the Belice River basin (western Sicily, Italy). Geomorphol, 242: 49–64.

Costanzo, D., Rotigliano, E., Irigaray, C., Jiménez-Perálvarez, JD., Chacón, J. (2012): Factors selection in landslide susceptibility modelling on large scale following the gis matrix method: application to the river Beirobasin (Spain). Nat Hazards Earth Syst Sci., 12: 327–340.

Das, G., Lepcha, K. (2019): Application of logistic regression (LR) and frequency ratio (FR) models for landslide susceptibility mapping in Relli Khola river basin of Darjeeling Himalaya India. SN Appl Sci, 1:1453.

Devkota, KC., Regmi, AD., Pourghasemi, HR., et al (2013): Landslide susceptibility mapping using certainty factor, index of entropy and logistic regression models in GIS and their comparison at Mugling Narayanghat road section in Nepal Himalaya. Nat Hazards, 65:135–165.

Di Martire, D., Novellino, A., Ramondini, M., Calcaterra, D. (2016): A-differential synthetic aperture radar interferometry analysis of a deep-seated gravitational slope deformation occurring at Bisaccia (Italy). SciTotal Environ, 550: 556–573.

Dou, J., Dieu, T.B., Ali, P. Y., Kun, J., Xuan, S., Inge, R., Huan, X., Zhongfan, Z. (2015) Optimization of Causative Factors for Landslide Susceptibility Evaluation Using Remote Sensing and GIS Data in Parts of Niigata, Japan. PLOS 1-29.

Getachew, N., Meten, M. (2021): Weights of evidence modeling for landslide susceptibility mapping of Kabi-Gebro locality, Gundomeskel area, Central Ethiopia. Geoenviron Disasters, 8 (6):1-22.

Guzzetti, F., Cardinali, M., Reichenbach, P., Cipolla, F., Sebastiani, C., Galli, M. (2004): Landslides triggered by the 23 November 2000 rainfall event in the Imperia Province, Western Liguria. Italy. Eng. Geol., 73(2):229-245.

Guzzetti, F., Mondini, AC., Cardinali, M., et al. (2012): Landslide inventory maps: new tools for an old problem. Earth Sci Rev, 112:42–66. https://doi.org/ 10.1016/j.earscirev.2012.02.001

Guzzetti, F., Reichenbach, P., Cardinali, M., Galli, M., Ardizzone, F. (2005): Landslide hazard assessment in the Staffora basin, northern Italian Apennines. Geomorphology

Jaafari, A., Najafi, A., Pourghasemi, HR., Rezaeian, J., Sattarian, A. (2014): GIS-based frequency ratio and index of entropy models for landslide susceptibility assessment in the Caspian Forest, northern Iran. Int J Environ Sci Technol, 11(4):909–926. https://doi.org/ 10.1007/s13762-013-0464-0

Kayastha, P., Dhital, M.R., & De Smedt, F. (2013): Application of the analytical hierarchy process (AHP) for landslide susceptibility mapping: a case study from the Tinau watershed, west Nepal. Comput Geosci, 52: 398-408.

Kayastha, P., Dhital, MR., De Smedt, F. (2013b): Evaluation of the consistency of landslide susceptibility mapping: a case study from the Kankai watershed in east Nepal. Landslides, 10:785–799.

Lazzari, M., Gioia, D., (2017): UAV images and historical aerial photos for geomorphological analysis and hillslope evolution of the Uggiano medieval archaeological site (Basilicata, Southern Italy). Geomatics Nat Hazards Risk, 8:104–119.

Lee, S., Talib, JA. (2005): Probabilistic landslide susceptibility and factor effect analysis. Environ Geol, 47: 982–990.

Lee, S., and Pradhan, B. (2007): Landslide Hazard Mapping at Selangor, Malaysia Using Frequency Ratio and Logistic Regression Models. Landslides, 4: 33-41.

Mersha, T., Meten, M. (2020): GIS-based landslide susceptibility mapping and assessment using bivariate statistical methods in Simada area, northwestern Ethiopia. Geoenviron Disasters, 7:20.

Meten, M., Bhandary, NP., Yatabe, R. (2015): GIS-based frequency ratio and logistic regression modeling for landslide susceptibility mapping of Debre Sina area in central Ethiopia. J Mountain Sci, 12(6): 1355 – 1372.

Najafi, A., Jaafari, A., Pourghasemi, H., Rezaeian, R., J., Sattarian, A. (2014): GIS-based frequency ratio and index of entropy models for landslide susceptibility assessment in the Caspian forest, northern Iran. Int. J. Environ. Sci. Technol., 11:909–926.

Nohani, E., Moharrami, M., Sharafi, S., Khosravi, K., Pradhan, B., Pham, BT., Melesse, M.A. (2019): Landslide susceptibility mapping using different GIS-based bivariate models. Water, 11(7):1402.

Onda, Y. (1993): Underlying rock type controls of hydrological processes and shallow landslide occurrence. Sedim Probl Strateg Monit Predict Control, 217:47–55.

Pourghasemi, H.R., Majid, M., Biswajeet, P. (2012): Landslide susceptibility mapping using index of entropy and conditional probability models in GIS: Safarood Basin, Iran. CATENA, 97: 71-84.

Pradhan, B. (2011b): Use of GIS-based fuzzy logic relations and its cross-application to produce landslide susceptibility maps in three test areas in Malaysia. Environ Earth Sci, 63:329–349.

Pradhan, B., Mansor, S., Pirasteh, S., Buchroithner, M. (2011): Landslide hazard and risk analyses at a landslide-prone catchment area using the statistical-based geospatial model. Int J Remote Sens, 32(14):4075–4087.

Regmi, AD., Yoshida, K., Pourghasemi, HR., Dhital, MR., Pradhan, B. (2014): Landslide susceptibility mapping along Bhalubang-Shiwapur area of mid-western Nepal using frequency ratio and conditional probability models. J Mountain Sci, 11(5): 1266-1285.

Riaz, MT., Basharat, M., Hameed, N., Shafique, M., Luo, J. (2018): A data-driven approach to landslide-susceptibility mapping in mountainous terrain: a case study from the Northwest Himalayas. NatHazards Rev, 19:05018007.

Rossi, M., Reichenbach, P. (2016): LAND-SE: a software for statistically-based landslide susceptibility zonation, version 1.0. Geosci Model Dev, 9:3533–3543.

Shano, L., Tarun, K.R., Matebie, M. (2021): Landslide susceptibility mapping using frequency ratio model: the case of Gamo highland, South Ethiopia. Arabian J Geosci, 14:623.

Sharma, LP., Patel, N., Debnath, P., Ghose, MK. (2012): Assessing landslide vulnerability from soil characteristics a GIS-based analysis. Arabian J Geosci, 5(4):789–796.

Silalahi, E.S.P., Yukni, A., Fahrul, H. (2019): Landslide susceptibility assessment using frequency ratio model in Bogor, West Java, Indonesia Florence. Geosci Lett, 6 (10):1-17.

Trigila, A., Iadanza, C., Esposito, C., Scarascia-Mugnozza, G. (2015): Comparison of logistic regression and random forests techniques for shallow landslide susceptibility assessment in Giampilieri (Ne Sicily, Italy). Geomorphol, 249: 119–136.

Ubaidulloev, A., Kaiheng, H., Rustamov, M., Kurbanova, M. (2021): Landslide Inventory along a National Highway Corridor in the Hissar-Allay Mountains, Central Tajikistan. GeoHazards, 2:212–227.

Wang, HB., Wu, SR., Shi, JS., Li, B. (2013): Qualitative hazard and risk assessment of landslides: a practical framework for a case study in China. Nat Hazards, 69:1281–1294.

Wang, Q., Li, W., Chen, W., Bai, H. (2015): GIS-based assessment of landslide susceptibility using certainty factor and index of entropy models for the Qianyang County of Baoji city, China. J Earth Syst Sci, 124:1399–1415.

Wang, Q., Wenping, L., Shishun, Y., Yanli, W., Yabing, P. (2016): GIS-based frequency ratio and index of entropy models to landslide susceptibility mapping (Daguan, China). Environ Earth Sci, 75:780.

Wubalem, A. (2020): Modeling of Landslide susceptibility in a part of Abay Basin, northwestern Ethiopia. Open Geosci, 12(1): 1440-1467.

Wubalem, A. (2021a): Landslide susceptibility mapping using statistical methods in Uatzau catchment area, northwestern Ethiopia. Geoenviron Disasters, 8 (1):1-21.

Wubalem, A. (2021b): Landslide Inventory, Susceptibility, Hazard and Risk Mapping. Intechopen 1-32.

Wubalem, A., Meten, M. (2020): Landslide susceptibility mapping using information value and logistic regression models in Goncha Siso Eneses area, northwestern Ethiopia. SN Appl Sci, 2 (807) 1-19.

Wubalem, A., Tesfaw, G., Dawit, Z., Getahun, B., Mekuria, T., Muralitharan, J. (2021): Comparison of statistical and analytical hierarchy process methods on flood susceptibility mapping: in a case study of Tana sub-basin in northwestern Ethiopia. Open Geosci, 13(1):1668-1688.

Xu, C., Xu, X., Dai, F., et al. (2013): Application of an incomplete landslide inventory, logistic regression model and its validation for landslide susceptibility mapping related to May 12, 2008, Wenchuan earthquake of China. Nat Hazards, 68:883–900

Yalcin, A., (2007): The effects of clay on landslides: A case study. Appl Clay Sci, 38(1-2):77-85.

Yesilnacar, E., Topal, T. (2005): Landslide susceptibility mapping: A comparison of logistic regression and neural networks method in a medium scale study, Hendek region (Turkey). EngGeol, 79:251-266.

Yusof, N., M. F. Ramli, S. Pirasteh & H. Z. M. Shafri (2011): Landslides and lineament mapping along the Simpang Pulai to Kg Raja highway, Malaysia. Int J Remote Sens, 32(14): 4089-4105.

Zare, M,. Pourghasemi, HR., Vafakhah, M., Pradhan, B. (2013): Landslide susceptibility mapping at Vaz Watershed (Iran) using an artificial neural network model: a comparison between multilayer perceptron (MLP) and radial basic function (RBF) algorithms. Arabian J of Geosci, 6:2873-88.

Zhang,YS., Javed, I., Yao, Y. (2017): Landslide susceptibility mapping using an integrated model of information value and logistic regression methods in the Bailongjiang watershed, Gansu province, China. J Mountain Sci, 14: 249 – 268.

Roles of Formal and Customary Institutions in Environmental Resource Governance and Sustainability along Ethiopia-Kenya Borderlands: Do Complement or Compete?

Girma Defere[1,*], MessayMulugeta[2], Teferi Tolera[3]

[1]*Department of Governance and Development Studies, Jimma University, Jimma, Ethiopia*
[2]*College of Development Studies, Addis Ababa University, Addis Ababa, Ethiopia*
[3]*Department of Rural Development and Agricultural Extension, Jimma University, Jimma, Ethiopia*
**Corresponding author, e-mail: girma.defere@ju.edu.et*

ABSTRACT

This study has attempted to examine the roles of state and indigenous institutions in environmental resource governance along the Ethiopia-Kenya border. The study mainly used a qualitative approach to discuss the research objectives. Interviews, Focus group discussions and schedule interview were used as instruments of data collection. The results demonstrate that the customary institution survived and served for generations in defending the rangeland environment from tragic destruction which enabled the pastoralists to go beyond borders to get the ecological benefits of mobility as an adaptive strategy during drought and violent conflict conditions. Now, unlike before, indigenous institutions' role is declining from time to time due to lack of recognition and exploitation by the state apparatus for its expediency. The study indicates strong synergy should be established between the formal and customary institutions to ensure better environmental resource governance to enhance sustainability. Also mainstreaming traditional institutions in environmental conservation, and climate change is advisable.

Keywords: *Ethiopia-Kenya borderlands, institutions (formal vs customary), environmental resource governance, sustainability, Moyale corridor*

1. INTRODUCTION

The most commonly cited definition for an institution is the one stated by North (1991) defined it as a body of humanly made checks that builds political, economic and social interactions. Institutions cover both formal and informal rules that make up the constitutions, laws and property rights. And the informal ones refer to sanction, taboos, customs, traditions, and codes of conduct. Machlis et al. (1995) defined institution as a collective solution to a prevailing societal problem. Lukes (1986) in Watson (2001) elaborated institutions as constraining and enabling factors with regard to limiting and making possible various forms of social action and organization. Institutions decide who makes use of which resources accordingly individuals, groups' and organizations do not get equal resource use benefit. This meant that institutional codes determine resource use. Institutions can be formal (state-organized peasants' associations and services cooperatives and state legislature). Informal that includes kin networks, local cultural administrative structures (Watson 2001). Institutions involve social structure but having social structures cannot be an indicator of institutions because social structures include sets of relations that may not be organized in discourse, for example, he mentioned that it is possible to classify demographic structure either in human or animal species without comprehending demography (Hodgson 2006). Hodgson (2006) further elaborated rules as a socially transferred and customary normative sanction which covers norms of behavior and social conventions containing legal rules that members of a certain community share tacit or explicit knowledge of these rules.

Environmental governance refers to interventions so as to bring the desirable level changes in environment related issues these include: incentives, knowledge, institutions, decision making, and behaviors, and governance covers various actors not only government but also communities, NGOs, and business groups (Lemos and Agrawal 2006). It also refers to rules, regulations, incentives, knowledge, institutions, decision making and behavior to defend environmental resources from degradation to ensure environmental sustainability (IUCN 2013; Savage and Osborne 2020). It can be understood as interventions which bring the desirable level changes in environment

related issues such as incentives, knowledge, institutions, decision making and behaviors, and governance, covering various actors not only government but also communities, NGOs, and business groups (Lemos and Agrawal 2006).

According to Ostrom (1990), environmental governance covers: (i) exclusion of unauthorized users (ii) regulating of authorized resource uses and distribution of their benefits (iii) provisioning and the recovery of its costs (iv) monitoring (v) enforcement (vi) conflict resolution, and (vii) collective choice

Ensuring better governance of environmental resources is a base for establishing climate resilient livelihoods and economies of Africa's drylands (Tari and Pattison 2014). That is why in many developing countries today there is the call for decentralized environmental resource governance to enhance efficiency, local compliance, and democratic participation in natural resource management (Hohbein et al. 2021).For the effectiveness of environmental resource governance the engagement of local and indigenous people and international support should be compatible with the interests and needs of the concerned people (Brondizio and Le Tourneau 2016). Fernandez-Gimenez and LeFebre (2006) identified three issues that may influence sustainability: (i) the structure and function of ecosystems, (ii) resource management practices, and (iii) management institutions. According to them, common practices among pastoral communities elsewhere include herds' mobility mainly to get access to water and/or pasture, splitting herds by species, collecting dung for fuel or fertilizer, maintaining multiple species and grazing crops. In light of this, institutions regulate and govern people's interaction with the natural environment and other human beings by promoting sustainable resource utilization and discouraging unsustainable practices.

In Ethiopia and Kenya there is political decentralization of power to empower the local governments while Kenya as per the 2010 constitution promoted decentralization and Ethiopia established a federal structure along Ethno-linguistic lines whereby political power constitutionally share between the federal government and regions. How far the customary institution embedded in the socio-culture of the society and formal state institutions do function together to defend rangeland resources from depletion is the concern of this study.

Against this backdrop, this study has assessed the roles of formal and customary institutions in environmental resource governance and sustainability along the Ethiopia-Kenya border (Borana zone of Moyale Ethiopia and Marsabit County) of Moyale Kenya.

2. THEORETICAL ISSUES

2.1 Theoretical Frameworks to Analyze the Study

This part of the study presents the theoretical issues related to environmental resource governance and identified 3 ways of thought: tragedy of the commons, institutionalism school and critical institutionalism.

2.1.1 Garret Hardin-the Tragedy of the Commons

Hardin, an American ecologist, published his work in science in 1968 and to refer to the tragedy of the commons suggesting that sustainably managing natural resources; property rights of the commons resources should be either state regulated or privatized (Hardin 1968). Hardin argued that for either privatization or centralized state control of rangelands would ensure sustainability of environmental resources. Otherwise, open access to rangelands would culminate in the tragedy of the commons. By this, he meant that, when environmental resources are open for all users, there is a possibility that one would take maximum advantage or benefit that could hurt all other users. Cox (1985) criticized the tragedy of the commons and refers to common grazing lands of medieval and post-medieval England which contrast with the modem concept of the common grazing land that was not available to the general public but rather only to certain individuals who inherited it or were granted the right to use it. The use of commons resource, even by these people, was not unregulated. In the same vein, Basurto and Ostrom (2009) in the article *the Core Challenges of Moving beyond Garrett Hardin* stated that Hardin had predicted some common pool resources. They mentioned that the major problem of Hardin's view was considering the tragedy as a universal phenomenon,

while in fact, overharvesting frequently occurs when resource users are totally anonymous, do not have a foundation of trust and reciprocity, cannot communicate, and have no established rules.

By the same token, Hanna et al. (1995) contended Hardin's environmental problems solution is either to privatize or state to own of environmental resources otherwise there is room for a tragedy of the commons by mentioning that private owners may opt for better cash earning on their environmental resources such as land. In the same way, in the state owning, state bodies might dictate to use the resources for short term benefits that meaning that, in both cases (private and state ownership), there is ground for a tragedy to happen.

As per this theory, African pastoralists might suffer from overgrazing, land degradation and bush encroachment. This theory failed to take into consideration the fact that African pastoralists are known for pastoral herd dynamics, pastoral mobility over a wide and changing system of boundaries, the change of natural pastures, customary rules to govern rangelands resources, seasonal growth of cycles and the existence of various social, cultural, political and economic rules governing pastoral communities (African Union 2010). Similarly, IIED and SOS Sahel (2010), and Schlee (2013) argued that there is no evidence that proves the tragedy of the commons in African arid and semi-arid areas where pastoralism, is the major source of livelihood. Given this fact, the tragedy of the commons theory cannot help in analyzing this study.

2.1.2 Elinor Ostrom's Institutionalism Thought

Ostorm's institutional thesis emerged to respond to the limitations of the dominant theory of Garrett Hardin's tragedy of the commons that calls for either state control or privatization of commons property as a remedy to deter environmental resources from depletion. In her field work in various parts of the world, Ostrom documented how communities develop ways to govern the commons to realize commons sustainability for the present and coming generations. In this regard, a noticeable example was her field research in a Swiss village where farmers share communal meadows to graze their cows without facing any problem of overgrazing and unlike the anticipation of Hardin's tragedy of the commons.

For Ostrom, the reason for the tragedy of the commons not occurring was because of a common agreement among members of the village. She documented other similar effective cases of the commons governing in her studies in Kenya, Guatemala, Nepal, Turkey, and Los Angeles (USA). Ostrom listed eight (8) institutional governing principles labeled as design principles to combat commons related problems; a design principle, according to her, is defined as an important factor or condition that helps to account for the success of institutions in sustaining the Common Pool Resources (CPR). These are: clearly defined boundaries, congruence between appropriation/provision rules and local conditions, collective-choice arrangements, monitoring, graduated sanctions, conflict-resolution mechanisms, minimal recognition of rights to organize, and nested enterprises. These are stated as follows:

1. Establishing defined boundaries: this meant that individuals who have rights to withdraw resource units from the CPR must be clearly defined in the CPR itself.
2. Conformity between provision rules to govern the common pool resources and local realities
3. Ensuring that most members of the commons affected by the operational rules can participate in amending the governing principles.
4. Devising a mechanism to monitor the behavior of members of common pool resources.
5. Imposing sanctions those who disrupt the operational in order to correct them for their acts.
6. Conflict handling mechanisms-this contains offering accessible, low-cost means to resolve disputes.
7. Guarantee that those affected by the rules can partake in amending the rules so as not to be defied by government authorities.
8. To establish a responsibility to oversee the common resources in a nested level from the lowermost to the whole unified system (Ostrom 1990).

Despite multicollinearity issues raised in Ostrom's design principles (Cox et al. 2010); her institutionalism theory remained influential in natural resource governance and sustainability literature.Ostrom and her associates further discussed that, if people are enabled to sit down in a round table discussion and discuss their common concern on resource utilization, they can develop trust and reciprocity. Accordingly, they could address the concern of overharvesting and work jointly for a common cause (Ostrom et al. 1992 as cited in Basurto and Ostrom 2009). In addition, Basurto and Ostrom (2009) cited numerous works pertinent to the usage of Common Pool Resources such as inshore of fisheries, forests, irrigation systems, and pastures by establishing a diversity of norms and rules that have helped them to address problems related to overharvesting.

Araral (2014) commented that Ostrom's institutional approach is relevant for small-scale, locally governed commons while Hardin's thesis is valid for large scale or national open access resources. Verrax (2019) by citing Costanza et al. (2000) responded to Araral's comment on Ostrom's design principles failed to identify whether it fits well to small or large scale open access resources, was answered by Ostrom and her colleagues that different design rules should be pursued for small and large scale systems. As per the cross-border African pastoralists, since they have shared values, institutions and culture that attempt to govern their socio-economic and environmental issues; this theory is more relevant to analyze the present study.

2.1.3 The Critical Institutionalism School of Thought

Critical institutionalism is an emerging thought that provided for alternative approach to the mainstream of institutionalism that proposes institutions for governing the commons are either created or amended through procedures of careful discussion by individual members to govern the commons (Feeny et al. 1990; Schlager and Ostrom 1992; Pomeroy and Berkes 1997; Ostrom 1999; Dietz et al. 2002 cited in Whaley 2018).

Cleaver, the author of alternative institutionalism approach, considered including the mechanism by which institutions role to be intertwined in people's day-to-day practices, and amid changing that happens naturally as a result of interactions. Institutional bricolage refers to customs whereby people act intentionally and unintentionally together to form an institutional approach as a result of socio-cultural practices to respond to their prevailing conditions. Consequently, the institution that emerges is an amalgamation of modern and traditional, formal and informal (Cleaver 2001). Institutional *bricolage* covers principles, customs, norms and relations of meaning and authority that subsequently enables people to adjust the existing practices with the devised new ones, where novel ideas or practices could usually connected to create acceptable ways of taking activities (Cleaver 2012). This theory also helps to analyze this study as the existence different institutions will require collaboration for the governance of the commons.

2.2 Gap in the Literature

Watson (2001), Dejene and Zerihun (2020) and Bassi (1999) have studied the roles of the indigenous institutions in natural resource governance. However, there is little evidence regarding the indigenous institutions mode of operation with the state institutions and their current status in the borderlands of Ethiopia and Kenya that this study has attempted to demonstrate.

3. MATERIALS AND METHODS

3.1 Description of the Study Area

Kenya and Ethiopia share a large permeable border straddling a length of 861 kilometers that traverses Marsabit, Mandera, Turkana and Wajir Counties from the Kenyan state side, and Borana, Dawa and Omo zones from the Ethiopian state side. On the Kenyan side, Marsabit County shares a longer border with Ethiopia about a 500 kilometer stretch with Borana zone of Oromia region (Asfaw 2019; Shikuku et al 2020). The Borana, Gabra, and Garri, among others, live on border areas of Ethiopia and Kenya. They also share the same identity that makes it

challenging to divide them into a clear-cut territorial or administrative constituency, particularly as these groups of people have lived together for many years. As the livelihood of these people is mainly based on livestock keeping, during dry seasons, these communities move with their livestock within the region as well as across the Ethiopia-Kenya border as pastoralists often do not consider official and international boundaries (Asfaw 2019; Pavanello 2009; Tesfaye 2015).

In Southern Ethiopia, the Moyale area is found in both Oromia and Somali regional state governments. This study will focus on the Oromia part of Moyale that is part of a Borana zone. As per the Oromia region 2007 national census report Moyale district has a total population of 31, 162 of which male makes up 16, 129 and female 15,033. In this report, the urban Moyale population is not reported (CSA 2007). Afan Oromo and Somali languages are the predominantly spoken ones. Afan Oromo is the district working language as the study area is the one in Oromia regional state. The livelihood of the people in the area is mainly based on pastoralism that involves trading of live animals such as cattle, goats, camel and sheep and livestock products such as milk and milk products and hides and skins including other items such as tea, salt, vegetables, species and chat (OSSREA 1999). The climate is characterized by arid and semi-arid climate with recurrent drought. The drought is due to lack of adequate rainfall and limited availability of perennial fresh water bodies.

The district is a warm semi-arid lowland that receives 50% of annual rainfall during the rainy season (Ganna) that covers from March to May and short rainy season (Hagaya) from September to November. The long dry season (Bona) follows from December to February, and the short dry season (Adolessa) takes place from June to August. The Kenyan–Moyale is located in the Marsabit district of north-Kenya has a total population of 103, 799 with a household size 6.2 as per the 2009 Kenyan population census (Marsabit District Secondary Data Review 2013). The population grows at 2.8 % annually. The poverty incidence is at 83.2%. The area is food insecure and depends on humanitarian assistance. Moreover, the area has no adequate water for livestock, crop and industrial use. The rainfall in the area is inadequate and unreliable. The ground water resources are low and saline because the basement rock system (Environmental and Social Impact Assessment Project Report of Marsabit County 2021). The area is arid and semi-arid (ASALS) is dependent on limited and highly variable rainfall. Pastoralism makes up a significant portion of the population's livelihood (Schrepter 2014). The region receives rain twice in a year: the long rains (akiporo) covers between March to May/June that accounts nearly 70% of total annual rainfall and the short rains (akecheres) begin from October to November/December (USAID 2019). Given the area is lowland the temperature varying from 10.0 to 30.2 degree celsius. It receives low rainfall with high evapotranspiration rates that affects crop and pasture productivity as results the population are highly vulnerable to drought (Aliow et al 2017). The agro-ecology of Moyale of Ethiopia is lowland and the topography is mainly plain. The vegetation coverage of the area is more of thorny bush scrub, acacia species and bush land (Isa et al 2015).

3.2 Research Approach and Design

This study used mainly a qualitative approach to investigate the issue under study. Interview and FGD extensive used as data collection methods. Also a schedule interview method employed to examine the cross-border pastoralists' perception and attitudes towards indigenous vs formal institutions, and the roles the two institutions play on defending rangelands from degradation and the current status of poverty in the community.

Key informant research participants were purposively selected on the basis of their knowledge and the positions in the field of pastoral affairs from state and non-state actors. Community elders were solicited through snowball sampling. Accordingly seventeen key informants were selected purposively because of their rich and lived experience on pastoral affairs. Also the pastoral people were randomly contacted for in-depth interview. Data were collected mainly in 2021 for six months. Institutions covered by key informant interview include: Ethiopian peace ministry, Kenya Pastoralist Community Initiative Development and Assistance (PACIDA), Oromia Pastoral Association, World Vision Kenya, Care International Borana field office, UNDP-Nairobi office, Oromia Pastoralist

Development Commission, Kenyan Community Initiative Facilitation Assistance (CFIA Kenya), Community Initiatives Facilitations and Assistance (CIFA), Borana University located in Pastoral area in Ethiopia, Kenya Government body on pastoral affairs, Borana Zone rangeland expert, Moyale district natural resource management department, Oromia Pastoral Development Commission, Kenyan Pastoral Initiative Development, Community Initiative Facilitation, indigenous institution, community representatives, researchers and cross-border pastoralists.

The Focus Group Discussion data was collected from the local authorities, development workers and pastoralists of the three *gandas (i.e the lowest administrative unit)* in Ethiopia–Moyale namely: *Maddo*, *Bakkola* and *Argane*. And, three locations from Kenyan-Moyale areas such as *Oda*, *Somare* and *Butiye* encompassed in the FGD. Participants of FGD were from six to eight members in each study area and one FGD per study area was conducted including development workers from Moyale local government. Accordingly, a total of seven FGDs were conducted. Most of the interviews and FGDs were conducted in the local language (Afan Oromo). Some of the interviewees were conducted in English with concerned people from Kenya. While secondary data was generated mainly through a review of literature and reports relevant to the issue under study.

3.3 Data Analysis

The qualitative data obtained through key informant interviews and focused groups were analyzed using thematic analysis approach. This involved first, organizing and preparing the data for analysis which involves completing the field notes taken during the interviews, focus group discussions (FGD) and field observations. Then, coding all the data that means organizing the data, this procedure involved during data collection, segmenting sentences into categories and labeling other categories this helps to identify the main theme of the responses obtained from various participants. Then after the themes were described and interpreted the meaning of the themes or descriptions to state the results or findings of the research. In this regard, when different informants give contradictory versions of information, the study is interpreted in a way that most informants have reflected also by triangulating with the results of focus group discussion and with what happening in the ground. The data obtained from schedule interview was analyzed using descriptive statistics and interpreted in triangulation with the qualitative data.

4. RESULTS AND DISCUSSIONS

4.1 Roles of Customary Institution

The pastoralists stranded along the Ethiopia-Kenya border area use various indigenous or customary institutional mechanisms to govern environmental resources such as grazing land, water and rangeland at large. Environmental resources in principle are owned and utilized on a communal basis. According to pastoralists research informants in the interview, in recent time's privatization of these resources has started to be a phenomenon. Gada institution which is the custodian of the indigenous people has specific rules to govern the resources. According to research participants in the interview, the following are the most known indigenous institutions: *koraedaa*, *koradheedhaa*, and *koradheebuu* are the major ones.Koraedaa means the assembly for the wells. This institution is responsible for the well services.

Koradheedhaa is an institution responsible for grazing that is responsible for managing access to water ponds. Also Aba Ella-according to this institution a well has an owner. According to this institution, the man who first excavated the well has the first rights to use it. This institution is responsible for water from wells to be properly utilized.

What if a conflict arises on resource use is there a way for the state apparatus to intervene? Or is there a way for someone to apply to the state apparatus? Then what happens? Among the pastoralists there are various methods utilized to use natural resources:

Kaloo refers to a communal pasture among the cross-border pastoralists. Research respondents stated that there is a way for the state to intervene or to take the case to a state institution; however, a state institution is not as effective as a traditional institution to resolve disputes and bring back normalization.

Among the Borana people, the *Jaarsaamadda* takes responsibility related to permanent deep wells. *Abba herrega* is the one who takes for daily utilization of drinking water and regulating mismanagement of water resources. He is responsible to punish as per the institution those who violate the rules of the rangeland management.

Jaarsaa dheeda is responsible for managing the grazing land including livestock mobility. The results of the interview showed that both indigenous and formal institutions have a role in promoting environmental conservation activities. Both institutions are promoting environmentalism. According to pastoral research informants the practice of the pastoralists in environmental resource conservation is not strong. These days because of poverty the pastoral people have compromised their indigenous system of environmental resource conservation during hard seasons they engage in deforestation for fuel and charcoal selling. Furthermore, most research informants expressed that even if the indigenous institution has been able to manage the pastoral mode of life the role of this institution in environmental resources conservation is degraded from time to time even because of lack of offering recognition to this institution and the government exploits this institution for its own purpose. They also discussed that the state institution is weakening the traditional institution by intervening in the role of traditional institutions to manipulate it. Pastoral research participants regarding the role of the indigenous institution in the beyond border mobility in the interview said that:

> the pastoralists use cross-border environmental resources as per the customary rules, not as they like it is as per the customary rule. Those who dig the water for instance use it on a reciprocal basis; they have their own grazing calendar and system to get access to environmental resources and use it. The pastoralists have good knowledge of the environment, and every four to eight years the *Abba Gada* (the highest decision making body of the indigenous people and institution) formulate environmental resource laws. They have also good knowledge of waste management with regard to water resource use management.

4.2 Cross-border People's Attitude and Perceptions towards Institutions

Most of the research informants from both Ethiopia and Kenyan indicated that customary rules have not gotten attention even if they are highly regarded and adhered to by the people. Customary rules are not incorporated in modern education to support the pastoral people's mode of life which is highly associated with environmental resource use, governance and sustainability. Research informants expressed that customary rules are more effective compared to state laws in environmental resource governance. According to our research informant, the indigenous people are aware of trees where to be planted and what type of trees that fits to the soil type and ecology which is not well known among the formal institution owners. Also in terms of resource competition induced conflicts, the customary rules are more effective than the formal institution.

Most of the research informants who participated in the interview and FGD explained the importance of both institutions with respect to rangeland management, mainly the indigenous institution has a wider acceptance among the people that traditional institution has a strong support from the people has paramount importance although these days its role is declining. One of the research participants in the interview stated that the customary institution sometimes is seen emphasizing on specific areas where the *Gada* assemblies are practiced while the formal state institution covers a wider area.

In the FGD participants expressed that those customary rules and fined 50 birr for someone who violates the grazing rules to feed his cow. In Kenya, if someone violates the customary rules he/she will be punished by 5000 to 20000 shilling depending on the level of violation. Also if someone uses a water pond without permission he will

be forced to prepare one water pond. And if someone cuts a tree, he will plant two trees. This finding shares similarity with Dejene and Zerihun (2020) that showed that if a Borana person in southern Ethiopia breaks the rules of the rangeland he would be fined from 1 to 5 cattle depending on the nature of the violation he committed. In addition, for those who do not take part in maintaining deep wells and pond water the person or the community will be denied access to the resource service.

Research informants from Kenya and Ethiopia dealing with pastoral affairs indicated that the mixture of customary and current systems have caused confusion in the local people who are caught between customary and new government systems.For the question how do the cross-border people view the role of government institutions with regard to environmental resource Governance and Sustainability? One of our research respondents in the interview expressed that:

> there are mixed reactions, some of the communities feel that government institutions are very supportive while others give more credit to the indigenous ones. The bottom-line on this squarely falls on the issue of trust and how pastoral communities interact with government institutions, these institutions have clearly defined mandate to deliver on and you know sometimes governments operate in more complex and dynamic ways that the pastoral communities cannot fully understand. The other research respondent stated that the pastoral communities in general face difficulties of conforming to state institutions as the latter is often at odds with values and practices of pastoral communities. This applies to cross-border pastoral communities who find themselves stranded between two or more states.

The research informant further stated that pastoral groups living across the borders are either pushed from their high potential areas in the name of development/modernization, agriculture and sedentarization policies by the governments. In less potential areas, pastoral groups are not provided and supported by the desired services since pastoral groups are regarded as backward and not willing to change. Also research informants in the interview discussed that neither the *Gada* system nor the state institution deterred land privatization of natural resources such as grazing land which is not supported by both institutions.

In this regard, research participants were asked about their perception regarding the roles of state institutions in environmental resource governance and sustainability if the roles have increased, decreased or as it is, accordingly, from Ethiopian Moyale-5 respondents have replied increased, while 281 respondents have replied decreased (Table 1). This shows that the role of state institutions in defending rangelands is weak. Likewise, 37, 235 and 14 respondents from Kenya Moyale answered increased, decreased and no change in the status (Table 1).

Table 1: Perceptions on the roles of state institution

No.	Location	Perception indicators					
		Increased		Decreased		No change	
		Frequency	percentile	Frequency	percentile	Frequency	percentile
1	Ethiopian - Moyale	5	1.75	281	98.25	0	0
2	Kenyan-Moyale	37	13	235	82	14	5

Regarding the roles of indigenous or customary institutions, research participants from Ethiopian Moyale have answered fully decreased. While the Kenya respondents 40 respondents (14%) increased while 245 respondents (86%) have decreased (Table 2). In both study locations, the results of the study regarding the roles of institutions are low.

Table 2: Perceptions on the roles of customary institution

Location	Perception indicators					
	Increased		Decreased		No change	
	Frequency	percentile	Frequency	percentile	Frequency	percentile
Ethiopian -Moyale	0	0	286	100	0	0
Kenyan-Moyale	40	14	245	86	0	0

In respect to trans-boundary movement and resource use the customary institutions served the cross-border pastoralists to cross-international boundaries whenever there was a lengthy drought and violent conflict. And most of the cross-border mobility is informed ahead of mobility by each clan where to move and for how long are agreed upon by all members of the group.Whenever resource conflict occurs, it is redressed through the council of elders of all the Boranas and the *Gada* systems (see also PPF, IIRR and DF 2010). Research participants in the interview from Kenya and Ethiopia discussed that the pastoral communities prefer customary institutions than the formal institutions to govern their natural resources, resolve their conflicts and ensure their peaceful coexistence. Nevertheless, according to them the formal state institution has influenced the customary institution's role in natural resource governance. They further expressed "if utilized the role of indigenous institutions in natural resource governance is pretty high but the significance of this institution is undermined by state institution". Failure to document and disseminate the indigenous knowledge practices costs two things: it distorts thisknowledge that means cannot meaningfully pass to the next generation and development policies cannot yield the desired results without inculcating this wisdom as this institution is established on long time experience.

Kenyan pastoral research informants said that lands are often grabbed by the high and mighty privatizing land and pushing pastoral groups to the marginal areas exacerbating their vulnerability and poverty. In this respect, research respondents were asked to state their perception regarding the current conditions of poverty, all research participants (100%) from the Ethiopian-Moyale side responded that the level of poverty in pastoral areas has increased. Also the majority (89.1%) of the research participants from Kenyan-Moyale side responded that the level of poverty increased, only 29 respondents(10.2%) decreased and 2 respondents (0.7%) responded that there was no change in the status of the community's poverty (see Table 3).

Table 3: Perceptions on the current conditions of community's poverty

Location	Perception indicators					
	Increased		Decreased		No change	
	Frequency	percentile	Frequency	percentile	Frequency	percentile
Ethiopian -Moyale	286	100	0	0	0	0
Kenyan-Moyale	254	89.1	29	10.2	2	0.7

5. CONCLUSION AND WAYS FORWARD

The contention between indigenous and modern knowledge system mainly centers on whether indigenous knowledge is sound enough to be considered in addressing various human problems involving health, agriculture, peace and security building, governance and so forth. Indigenous knowledge is embedded in society's social, cultural and moral life. This study found that the indigenous institution survived and served the rangeland environment for generations and saved it from tragic destruction. But, now unlike the old times, indigenous institutions' role is declining from time to time due to lack of recognition and exploitation by the state for its expediency. Indigenous practices should be further explored through research and documented and utilized in educational institutions which also be supported by offering adequate recognition and consulting it development policy making should be forwarded to use this knowledge in an integrated way with modern.

But, there is a gap in each knowing system. If they are utilized complementarity in an institutionalized approach they can contribute a lot to the existing fund of world knowledge and enhance the existing practices in natural resource management, resource allocation, adaptation and conflict management on sustainable manner, as Alexander et al (2019) in coastal-marine research areas of Canada has come up with a finding that confirms the integration of multiple types of knowledge as vital to support evidence regarding policy advice, decision making and environmental management. Likewise Castleden et al (2017) revealed that, these days, it has become increasingly apparent to see that Western knowledge and technology are not addressing water issues and water-related challenges.

Pastoralist communities living on the Ethiopia-Kenya border have long adopted a wide range of activities to protect their livelihoods and cope with recurrent droughts. These include, among others, cross-border resource management, sharing natural resources through seasonal cross-border mobility, setting-aside dry season grazing reserve, and other acts that promote reciprocity. Enforcement and compliance with rangeland management rules by cross-border respective traditional institutions that govern and manage resource use authorization may be a mere formality or a complicated procedure depending on the circumstances.

They in general face difficulties of conforming to state institutions as the latter is often at odds with values and practices of pastoral communities. This applies to cross-border pastoral communities who find themselves stranded between two or more states. Why the Ostorm's theory isvalid among the cross-border pastoralists but not Garrett Hardin? For generations the pastoralists have developed and used institutions to govern and use rangeland environmental resources. The *Gada* system which is a source for laws, rules and regulations to govern and access environmental resources and settle conflicts that arise among the people on various causes has served as the guardian of the peoples' onus so the indigenous institution saved the rangeland resources from the tragedy of the commons. This does not mean however that the indigenous institution is as strong now as it used to be before. There are overlapping hierarchies between the two institutions (indigenous and state institutions) this has created confusion. Hence, as explained by Cleaver (2012) author of critical institutional theory, promoting adjustment of the existing practices by the newly devised new ones could help to amalgamate the roles of the institutions in a complementary way rather than competitive so as to create acceptable ways of rangeland resource management. Similarly it helps to entertain the complexity of institution entwined in people's day to day life their historical formation and informal, traditional and modern organization and the power relations among them that allows to amend the existing practices and invent the new ones that means it creates adapted configuration of rules, practices, norms and relationships among them (Cleaver and De Knoning 2015).Therefore, integrating the two institutions is vital in the process of crafting environmental laws and policies to serve the people at large that may help to replace existing practices by the better ones that fit more to the prevailing situation.

Governments should work in collaboration with the indigenous institution to ensure environmental resource governance and sustainability. Likewise, in conflict management, customary institutions play significant roles compared to the formal state institution by incorporating modern scientific knowledge with indigenous knowledge and practices to use rangeland resources on a sustainable basis. Hence, concerned governmental and non-governmental bodies should support the proper documentation and dissemination of indigenous natural resource and conflict management practices in a way to contribute to the existingdevelopment policy or project interventions to manage common pool resources otherwise as the old Africa saying "when an old man dies, a library burns to the ground".

Encouraging and strengthening the use of indigenous knowledge study for university teaching, research and community service activities so as to create a venue for dialogue, debate and knowledge and experience sharing, potentially to use in public policy making. Acknowledging and strengthening traditional governance institutions in environmental conservation, climate change and sustainability. Therefore, indigenous institutions with its rules and regulations should receive recognition by the states and legally implement them.

ACKNOWLEDGEMENTS

We are grateful to the many participants in the study from state and non-state actors including individuals, research institutes and indigenous people in the Moyale part of Ethiopia and Kenya. Thanks to Robdu, Messay Eshetu, and FugichaDenge for facilitating and assisting us in the data collection process. We also would like to thank ZEIT-Stiftung Ebelin und GerdBucerius for the PhD scholarship ward fund to the corresponding author.

REFERENCES

Africa Union (2010) Policy Framework for Pastoralism in Africa: Securing, Protecting and Improving the Lives, Livelihoods and Rights of Pastoralist Communities.Addis Ababa, Ethiopia.

Alexander, SM,Provencher, JF, Henri, DA (2019) Bridging Indigenous and Science-based Knowledge in Coastal-Marine research, monitoring, and management in Canada: A systematic map protocol.*Environ Evid (2019) 8:5* doi.org/10.1186/s13750-0190159-1.

Aliow, I.M., Samuel, S. and Aluoch, D.W. (2017) Changes in Drought Trends and Effectiveness of Social Safety-Nets on Post-Drought Recovery of Households in Moyale Sub-County, Kenya. *Int. J. of Agriculture Innovations and Research, 6(3).*

Amsale K.T (2010) Climate change to conflict? Lessons from Southern Ethiopia and Northern Kenya.Fafo 2010.

Araral, E. (2014). "Ostrom, Hardin and the Commons: A Critical Appreciation and a Revisionist View."*Environmental Science & Policy* 36 (February): 11–23.

Asfaw K. (2019), Strategy to Prevent Violent Conflicts and Fragility in the Cross-Border Areas of Ethiopia and Kenya.*Journal of Social and Political Sciences, Vol.2, No.2, 413-428.*

Bassi, M. (1999) The Complexity of a Pastoral African Polity: An Introduction to the Council "organization of the Borana-Oromo. JES XXXII, Vol.2, December 1999.

Basurto, X & E. Ostrom, E. (2009) The Core Challenges of Moving Beyond Garrett Hardin. Journal of Natural Resources Policy Research. Vol. 1, No. 3, 255–259, July 2009.

Brondizio, E.S and Le Tourneau, F-M (2016) *Science* Vol. 352, Issue 6291, pp. 1272-1273.

Bisson, L., Cottyn, I., Bruijne, K.de, and Molenaar, F. (2021) The root causes of the problem of natural resource governance. Clingendael Institute.

Byers, BA, Cunliffe, RN, Hudak, AT (2001) Linking the conservation of culture and nature: A case study of sacred forests in Zimbabwe. *Human Ecology 29 (2):187-218.*

Castleden, H. E., Martin, D., Cunsolo, A., Harper, S., Hart, C., Sylvestre, P., Stefanelli, R., Day, L., Lauridsen, K. (2017).Implementing Indigenous and Western Knowledge Systems (Part 2): "You Have to Take a Backseat" and Abandon the Arrogance of Expertise.*The International Indigenous Policy Journal* 8(4).

Cleaver, F. and DeKnoning, J. (2015) Furthering Critical Institutionalism. International *J. of the Commons*.Vol.9, no.1, 1-18.

Cleaver, F. (2012) *Development through Bricolage: Rethinking Institutions for Natural Resource Management.* London: Routledge.

Cox, M., G. Arnold, and S. Villamayor T. (2010). A review of design principles for community-based natural resource management. *Ecology and Society 15(4): 38.*

CSA (2007) Ethiopia Housing census.

DejeneA.andZerihun D. (2020) Indigenous Environmental Knowledge of Borana pastoralists. *Grassroots Journal of Natural Resources, 3(4):110-131.*

Dyer, N., Omondi, S., and Wantsusi,M. (2008) Securing Pastoralism in East and West Africa: Protecting and Promoting Livestock Mobility.Karamojong Cluster Desk Review: Livestock mobility in northeast Uganda, northwest Kenya, Southwest Ethiopia and Southern Sudan.

FAO (2019) "Cross-border coordination of livestock movements and sharing of natural resources among pastoralist communities in the Greater Karamoja Cluster".

Feeny, D., Berkes, F., Mccay, B.J., Acheson, J.M. (1990) The Tragedy of the Commons: Twenty-Two Years Later. *Human Ecology 18(1)1*: 1-19.

Fernandez-Gimenez, E.M and Le Febre, S. (2006) Mobility in Pastoral systems: Dynamic flux or downward trend? *International Journal of Sustainable Development and World Ecology*, vol. 13(2006), 1-22.

Gegeo, W D (1998) Indigenous Knowledge and Empowerment: Rural Development Examined from Within. The contemporary Pacific.fall 1998.

Green, J.F, Lesley (2008), indigenous knowledge and science: Reframing the Debate on Knowledge Diversity.*Journal of the World Archaeological Congress*.

Hanna, S., Folke, C. and Maler, K-G (1995) "Property Rights and Environmental Resources". In Hanna, S. and Munasinghe, M. (eds.) Property Rights and the Environment Social and Ecological issues, The Beijer International Institute of Ecological Economics and The World Bank.

Hardin, G. (1968) "The Tragedy of Commons." Science, New Series, 162, no.3859 (December 1968):1243-1248.

Hellan, J. (2000) Institutional erosion in the drylands: The case of the Borana pastoralists. In Leif Manger and Abdel Ghaffar M. Ahmed (eds.): Pastoralists and environment: Experiences from the greater Horn of Africa. Proceedings of the regional workshops on African drylands, Addis Ababa and Jinja. Addis Ababa: OSSREA pp. 19-49.

Hodgson, G.M. (2006) What Are Institutions?*Journal of Economic Issues, 40:1, 1-25*.

Hohbein, R.R., Nibbelink, N. & Cooper, R.J. Impacts of Decentralized Environmental Governance on Andean Bear Conservation in Colombia. Environmental Management 68, 882–899 (2021).

Homann, S. and Rischkowsky, B. (2005) Integrating the Indigenous Knowledge of Borana Pastoralists into Rangeland Management Strategies in Southern Ethiopia, No. 81, June 2005.

International Institute for Environment and Development (IIED) and SOS Sahel (2010) Modern and Mobile: the future of Livestock production in Africa's dry lands.

Isa A., Nuraddis I. and Yosef D. (2015) Prevalence of Camel Trypanosomosis and Its Associated Risk Factors in Moyale District, Borena Zone, Southern Ethiopia. *Bulletin of Animal Health and Production in Africa. Vol.63 No.3*, Sep. 2015.

IUCN (2013) "International Union for the Conservation of Nature". Available onhttps://www.iucn.org

Kamara, A.B., Swallow,B. and Kirk, M. (2004) Policies, Interventions and Institutional Change in Pastoral Resource Management in Borana, Southern Ethiopia. *Development Policy Review,22(4): 381-403.*

Lemos, M.C & Agrawal, A. (2006) Environmental Governance. *Annu.Rev.Environ*. 297-325. Univ. of Michigan, Ann Arbor.

Machlis, G. E., J. E. Force, and W. R. Burch Jr. 1997. The human ecosystem part I: the human ecosystem as an organizing concept in ecosystem management. Society and Natural Resources 10 (4):347-367.

Maweu, M.J (2011) "Indigenous Ecological Knowledge and Modern Western Ecological Knowledge: Complementary, not Contradictory ". Thought and Practice*: A J. of the Philosophical Association of Kenya (PAK). .3(.2):35- 47.*

Marsabit Secondary Data Review - Kira (December 2013) Marsabit, Kenya.

Ministry of Agriculture, Oromia Bureau of Agriculture, Oromia Pastoral Area Development Commission, Somali Livestock, Crop and Rural Development Bureau (2015) Rural Resilience Enhancement Project. In The Federal Democratic Republic of Ethiopia, Technical Manuals for Resilience Enhancement in Pastoral Areas. Japan International Cooperation Agency (Jica)/Sanyu Consultants Inc.

Morelli, J. (2011) Environmental Sustainability: A Definition for Environmental Professionals. *Journal of Environmental Sustainability: Vol. 1: Iss. 1, Article* 2.

North, D.C (1991) Institutions. *Journal of Economic Perspectives*.vol.5.no.1.97-112.

Ostrom, E. (2010) Governing the Commons: the evolution of institutions for collective action. Cambridge University press.

OSSREA (1999) Cross-Border Livestock Trade and Food Security in the Southern and Southeastern Ethiopia Borderlands. Development Research Report Series, no. 1. Addis Ababa: Ethiopia.

Ostrom, E. (1990) *Governing the Commons: The Evolution of Institutions for Collective Action.*New York. Cambridge University press.

Pavanello, S. (2009) "Pastoralists' Vulnerability in the Horn of Africa: Exploring Political Marginalization Donors' Policies, and Cross-Border Issues". Humanitarian Policy Group (HPG) Overseas Development Institute London, UK.

Paavola, J. (2007) Institutions and environmental governance: A reconceptualisation. Ecological Economics 63 (2007) 93-103. Sustainability research institute. School of Earth and Environment, Leeds, United Kingdom.

PFE, IIRR and DF (2010) Pastoralism and Land: Land tenure, Administration and Use in Pastoral Areas of Ethiopia.

Savage, J.N. and Osborner, P.E. (2020) The Challenges of Establishing Marine Protected Areas In South East Asia.In*Marine Protected Areas.*

Schlager, E. and Ostorm, E. (1992) Property-Rights Regimes and Natural Resources: A Conceptual Analysis. Land Economics. 68(3): 249-62.

Schlee, G. (2013) Territorializing ethnicity: the imposition of a model of statehood on pastoralists in northern Kenya and southern Ethiopia. *Ethnic and Racial Studies*. Vol. 36, No. 5.

Steelman, T.A. (2010) Implementing Innovation. Fostering Enduring change in Environmental and Natural Resource Governance. Georgetown University press, Washington, DC.

Tari, D.and Pattison, J. (2014)Evolving Customary Institutions in the Drylands: An opportunity for devolved natural resource governance in Kenya? Issue Paper. International Institute for Environment and Development (IIED).

Tesfaye M. (2015) "Inter-Communal Conflicts in Moyale: Drivers, Dynamics and their Impact on Micro-Regionalization", Ph.D. Dissertation, Addis Ababa University.

Verrax, F. (2019) ElinorOstrom or the Revolution of the Commons. In T. Hoerber and A. Anquetil (eds.). *Economic Theory and Globalization.*

Watson, E. (2001) Inter-institutional Alliances and Conflicts in Natural Resource Management. Preliminary Research Findings from Borana, Oromia, Ethiopia.Marena research project, working paper no.4.

Whaley, L. (2018) The Critical Institutional Analysis and Development (CIAD) Framework. *International Journal of the Commons, Vol.12, no.2, pp. 137–161.*

Potential Groundwater Recharge Zones within Dinder River Basin, Ethiopia

Teka Afera Halefom*, Dar Imran Ahmad

Department of Hydraulic and Water Resources Engineering, Faculty of Technology, Debre Tabor University, Ethiopia
**Corresponding author, e-mail: aferahalefom@gmail.com*

ABSTRACT

Analyzing and understanding the determinant factors is a pre-requisite for groundwater management of Dinder River basin, Ethiopia. Eleven determinant factors (thematic maps) of groundwater potential recharge; namely, geology, lineament density, distance to lineament, soil type, soil texture, hydrological soil groups, slope gradient, drainage density, curvature and landuse, were generated and evaluated. Each thematic map was reclassified into five and a suitable groundwater potential recharge value was assigned to each class depending on its influence to groundwater potential recharge. All the determinant factors were given suitable weightages using multi-criterion decision analysis and overlaid in GIS domain. The final result showed "Very high", "High", "Moderate", "Low" and "Very low" groundwater potential recharge zones (GWpRZ) with areal extents of 4127.20 km^2 (27.92%), 4043.71 km^2 (27.35%), 4220.78 km^2 (28.55%), 1880.85 km^2 (12.72%) and 510.74 km^2 (3.45%), respectively. The influence of topography and geology on GWpRZ was analyzed well in this paper.

Keywords: *Dinder basin, Geology, GIS, Groundwater potential, Topography*

1. INTRODUCTION

In recent years many hydrological investigations has been done by analyzing various thematic maps (geology, lineaments, landuse, soil, slope) in GIS domain (Senanayake et al., 2016; Kumar 2016; Sener et al., 2018). Many studies have used geospatial technology to study the groundwater potential areas of their region of interest (Sener et al., 2018; Jhariya 2019; Kesana and Dinesh., 2019). Some studies have applied probabilistic models such as multi-criteria decision analysis and weights-of evidence modeling for groundwater potential mapping (Rajat and Garg 2015; Fenta et al., 2015; Swetha et al., 2017).

Groundwater occurrence depends mainly on geological settings and topographic formations along with the climatic conditions (Tamiru 2006; Garg 2007). Due to multifaceted geological history, the aquifers in Ethiopia are the most complex as well as compartmentalized (Chowdhury et al., 2003).In countries like North Ethiopia where rainfall is either scarce or unevenly distributed; geospatial technology offers an efficient means for delineation of groundwater potential zones. Bereket (2017) studied the groundwater potential areas in Rift Valley Lakes Basin, Weito Sub Basin, Ethiopia using remote sensing and GIS. Tesfa et al., (2018) studied the groundwater potential areas in Tigray region, Ethiopia by analyzing various thematic parameters (like geology, slope, landuse etc.) in GIS environment. There are studies documented on the evaluation of the groundwater water potential of the Blue Nile basin, Ethiopia (Abiy et al., 2015; Tesfa and Girum, 2019) using remote sensing and GIS. An attempt has been made in this paper to demarcate the groundwater potential recharge areas (GWpRZ) using GIS coupled with Analytical Hierarchy Process (AHP) of Saaty (1980). The main objectives of this paper included (1) identifying the spatial distribution of groundwater potential zones in Dinder Basin, Ethiopia using geographic information system, and (2) analyzing the influence of elevation and geology towards groundwater potential zones.

2. MATERIALS AND METHODS

2.1. Study Area

Dinder River basin (Fig. 1) is the lower sub-basin of Upper Blue Nile basin (also called Abay basin), Ethiopia. The Dinder basin is located towards Northwest of the Abay basin and its centroid coordinates are 35° 47' 16.372" E and 11° 44' 39.734" N. The areal extent of Dinder basin is 14890.55 km2 with the perimeter of 607.27 km. Dinder basin has a varied topography with elevation ranging from 466 to 2752 meters above mean sea level. According to

Hurst et al., (1959) Dinder River derives its water from the runoff of the Ethiopian highlands 30 km west of Lake Tana. Dinder River basin is characterized by complex hydrology, with varying geology, topography, vegetation and soil (Hassaballh et al., 2016). Coluvium and alluvial deposits dominates the study area with faults dominating the east and southeast of the study area.

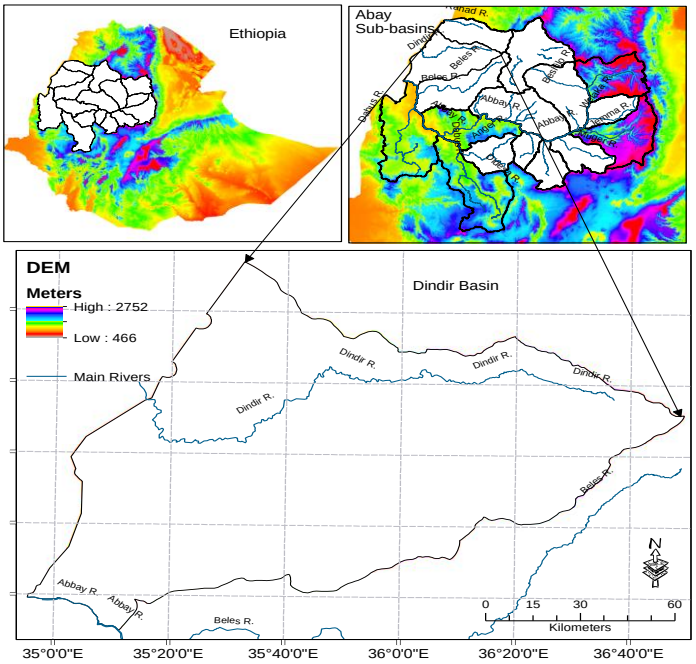

Figure 1: Location map of the study area with elevation

2.2. Study Design

The Advanced Space-borne Thermal Emission and Reflection Radiometer-Digital Elevation Model (ASTERDEM) with 30-m resolution (Hirano et al., 2003) is used to extract elevation, drainage network, slope gradient and curvature by using appropriate algorithms and following sets of topographical functions, as described in ArcGIS (ESRI 2009). Soil (30×30m resolution) was collected from ministry of water, irrigation, and electricity of Ethiopia. Geology map (at a scale of 1:250,000) was collected from the geological survey of Ethiopia. Landuse image (30×30m resolution) was downloaded from USGS Earth Explorer website for January 2018. The drainage-density and fault density layers were estimated using the in the ArcGIS software (Nair et al., 2017). The overall methodology employed here involves five main steps. The first step deals with the generation of spatial distribution maps of determinant factors pertaining to groundwater potential recharge. The second involves preprocessing these thematic layers to ensure uniform projection (projection: UTM Zone 37N, datum: WGS84) and resolution, assigning groundwater potential recharge values of various classes in each thematic map and computing weights for thematic layers using AHP proposed by Saaty (1980). The third step involves integration of all the weighted thematic layers in using weighted index overlay analysis method in method GIS domain. The fourth step categorizes the outcome into five classes viz., Very good, Good, Moderate, Poor and Very poor GWpRZ. The final step analyses the behavior and influence of various parameters on GWpRZ (Fig. 2).

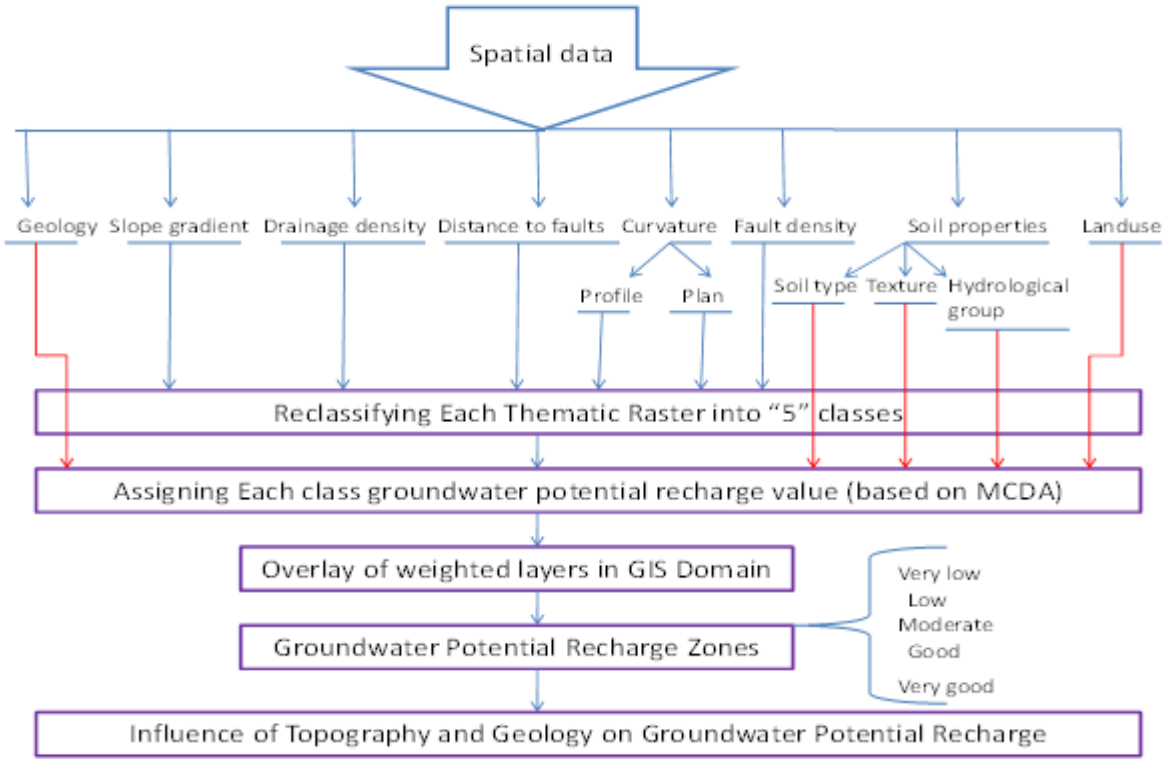

Figure 2: Overview of methodology employed

2.3 Determinant factors

Eleven determinant factors were identified and analysed; viz., geology, lineament density, distance to lineament, soil type, soil texture, hydrological soil groups, slope gradient, drainage density, curvature and land use. Each factor/thematic map was reclassified into five classes. The relative importance of individual class within the same map and thematic maps were computed based on Saaty's AHP (Saaty 1980). Areal extent of each class has been estimated using "Zonal statistics" tool in GIS domain.

3. RESULTS

3.1. Geology

According to Yeh et al., (2016), spatial occurrence of groundwater in any topography is dependent on the geological settings. Kieffer et al., (2004) divide the stratigraphy of Ethiopian flood basalts as follows: (a) Ashengie: the basal basalt sequence characterized by deep weathering and low groundwater potential, (b) Aiba-Alaji-Termaber sequences: the upper basalt sequence characterized by low degree of weathering; good permeability , Aiba formation contains intercalations of rhyolitic formations; (c) Shield volcanics: characterized by rhyolites and trachytes; shield diameters range from 50 to 100 km and (d) Quaternary basalts: characterized by very high groundwater potential with dual porosity nature. The flood basalts have been divided traditionally into four stratigraphic units all diachronous: from bottom to top, Ashangie (Eocene), Aiba (32-25), Alaji (32-15 Ma) and Termaber (30-13) according to Mohr and Zanettin (1988).

The major geological units in the study area are Coluvium deposits (32.42%), Ashangi Basalts (30.99%), Alluvium deposits (14.71%) and other geological units together cover 21.88% of the study area. Coluvium was found mainly towards the west of the study area; Ashangi Basalts dominates the east and Alluvium spreads towards the north of the study area. Based on the hydraulic properties of the geological units (hydraulic conductivity,

transmissivity and expert knowledge) geological units are ranked as Alluvium> Coluvium> Amba Aiba basalts> Termaber basalts>Adigrate sandstone> Syntectonic granodiorites & diorites> Post-tectonic granites> Syntectonic granites> Ashangi basalts> Tsaliet & Tambien Group clastics> Alcalitrachyte sand-subordinate basalts> Undifferentiated lower complex> Tambien Group marbles>Adola group. The relative groundwater potential recharge value of each class was determined and presented in Fig. 3 and Table 1.

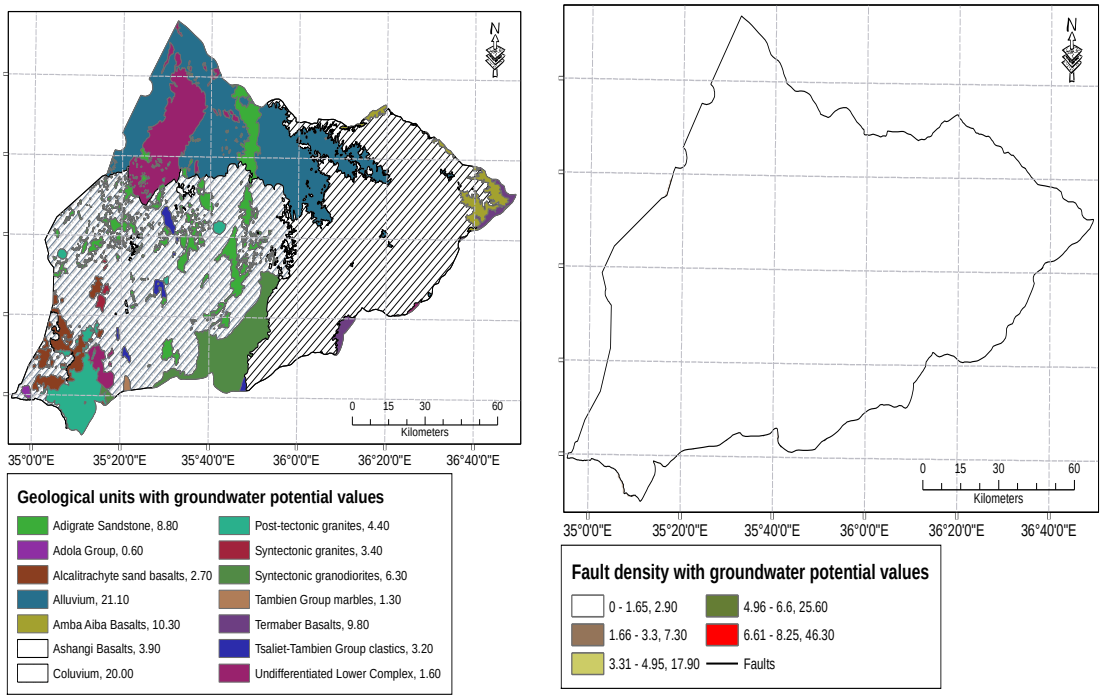

(a) (b)

Figure 3: (a) Geological units and (b) Fault density, with groundwater potential recharge values

3.2 Fault Density and Distance to the Fault

According to Pradhan et al., (2013), the surface expression of fractures is reflected by lineaments/faults. These faults enhance the infiltration rate of rainfall and surface runoff (Devi et al., 2001). Faults have been observed mainly in the west of the study area. According to Yeh et al., (2016) faults usually denote a permeable zone. Several studies have confirmed that groundwater potential increases with higher fault density (Fashae et al., 2014). Groundwater potential is inversely proportional to fault distance. Therefore, fault density map and distance to fault map have been generated in GIS domain. The fault density varies from 0-17.9 (km/km2). The fault density map and distance to fault map was reclassified into five classes in equal-interval classification in GIS domain. The relative groundwater recharge potential recharge value of each class of fault density and distance to fault is presented respectively in Fig. 3b and Fig. 4a and Table 1.

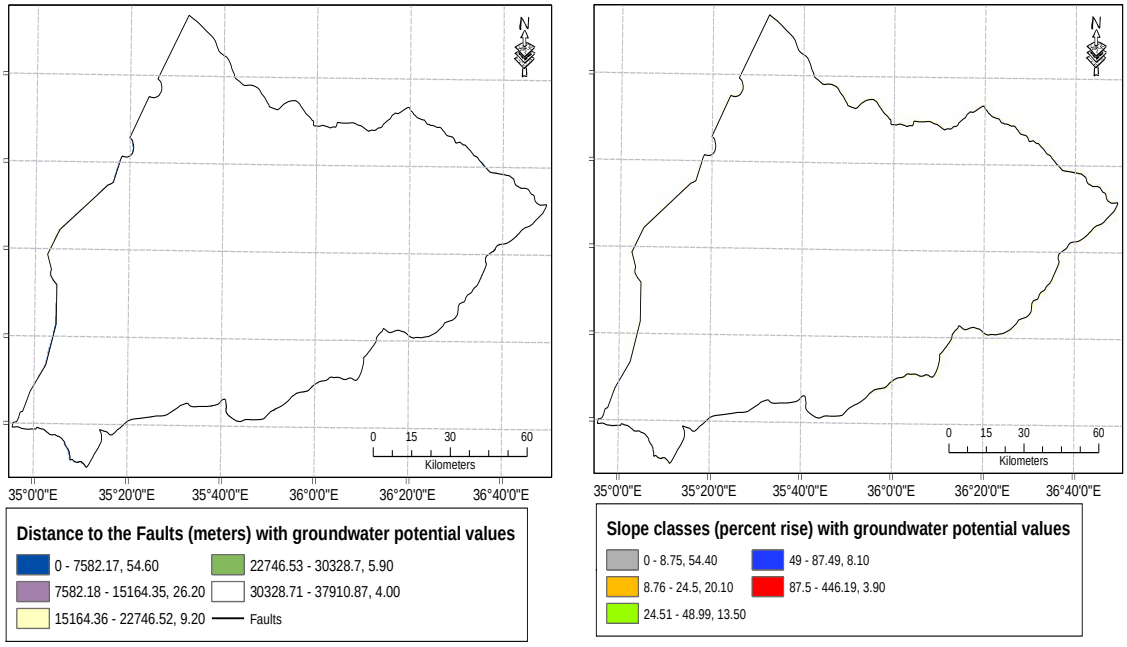

(a) (b)

Figure 4: (a) Distance to fault (in meters) and (b) Slope gradient (percent rise), with groundwater potential recharge values

3.3 Slope Gradient

According to (Naghibi et al., 2016) slope gradient influences the rate of infiltration and surface runoff. Identification of slope is a key parameter to understand groundwater conditions (Al Saud 2010). Steep slope gradient promote surface runoff and hence comparatively less infiltration due to less concentration time (Fashae et al., 2014), whereas gentle slope areas facilitate infiltration and groundwater recharge due to more concentration time for rainfall to infiltrate. Slope gradient of the study area varies from 0- 446.19 (percent rise) and was reclassified into five classes in equal-interval classification in GIS environment. The reclassified slope map of the study area shows 45.98% flat (0 - 8.75 percent rise), 38.98 % gentle (8.76 - 24.5 percent rise), 10.56% steep (24.51 - 48.99 percent rise), 3.68% very steep (49 - 87.49 percent rise) and 0.79% extremely steep (87.5 - 446.19 percent rise). Fig. 4b and Table 1 depicts the slope classes of the study area along with their relative groundwater potential recharge values.

3.4 Soil Type, Soil Texture and Hydrological Soil Group

The infiltration capacity and the groundwater recharge of any region is mainly determined by the type of soil (Savita 2018). The study area is dominated by humic nitisols (5335.83 km2, 35.80%) followed by eutric vertisols (3351.67 km2, 22.55%), chromic luvisols (2649.23 km2, 17.82%) and haplic luvisols (1364.90 km2, 9.18%). Other soils (haplic acrisols, haplic nitisols, eutric cambisols, eutric fluvisols, eutric leptosols and haplic alisols) contribute 14.65% of the study area. The spatial distribution of soil type in the study area along with their groundwater potential recharge value is showing in Fig. 5a and their areal extents are shown in Table 1.

So far soil texture of the study area is concerned, it was found that loam dominates the study area with its area extent of 10761.00 km2 (72.51%) followed by clay, sandy loam, loamy sand and clay loam with their areal extents of 3387.60 km2 (22.83%), 581.43 km2 (3.92%), 84.02 km2 (0.57%), 25.93 km2 (0.17%) respectively. The relative groundwater potential recharge value of soil texture along with their areal extent is shown in Fig. 5b and Table 1.

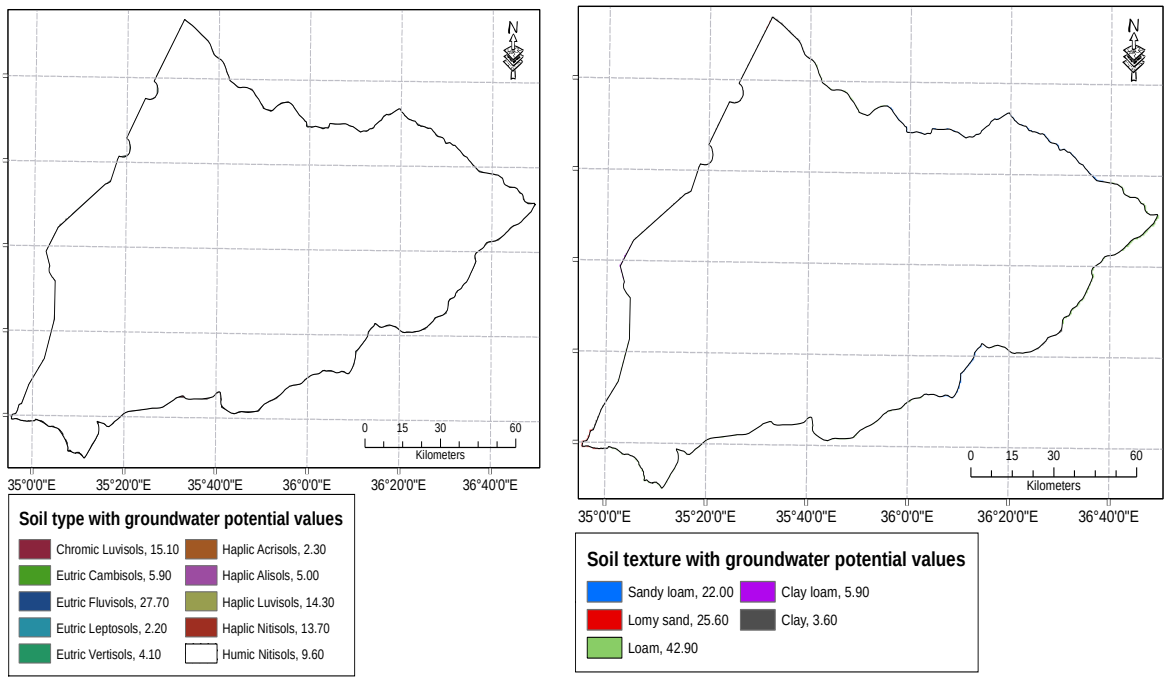

(a) (b)

Figure 5: (a) Soil types and (b) soil texture, with groundwater potential recharge values

Hydrologically soil group "B" dominates the study area (10773.03 km^2, 72.48%), followed by "D" (3418.27 km^2, 23.0%) and "A" (672.22 km^2, 4.52%). The groundwater potential recharge values and their coverage are shown in Fig. 6a and Table 1.

3.5 Landuse

According to Yeh et al., (2016) the information about soil moisture, infiltration and groundwater prospects can be determined by the type of landuse existing in an area. Woodland (7576.99 km2, 50.95%) dominates the study area followed by shrubland (5190.60 km2, 34.91%), cultivation (1216.10 km2, 8.18%) and grassland (686.19 km2, 4.61%), bareland (96.82 km2, 0.65%), natural forest (48.41 km2, 0.33%), highland bamboo (18.84 km2, 0.13%), wetland (19.17 km2, 0.13) and water body (17.22 km2, 0.12%). The relative groundwater potential values are shown in Fig. 6b and Table 1.

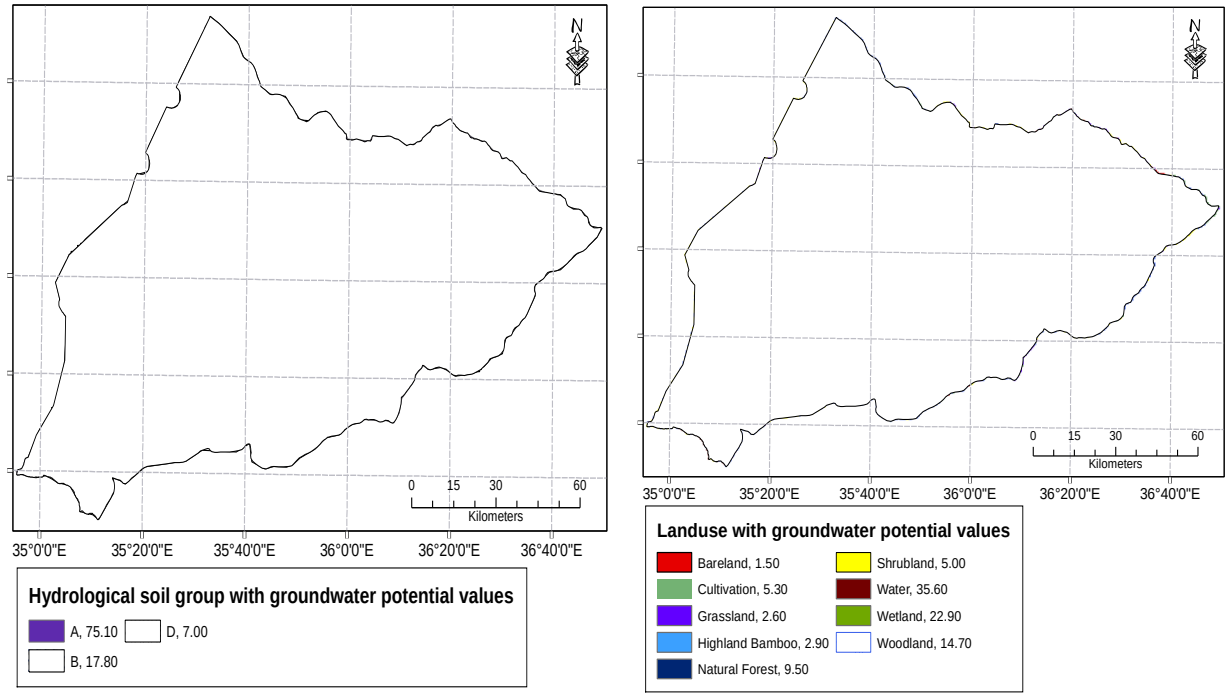

(a) (b)

Figure 6: (a) Hydrological soil groups and (b) land use with groundwater potential recharge values

3.6 Drainage Density and Curvature

Permeability of any terrain is inversely proportional to drainage density. Groundwater potential, availability and its contamination is inferred by drainage density (Ganapuram et al., 2009). Drainage density is the sum of all the streams in a given basin divided by the area of the basin (Yeh et al. 2016). An area with high drainage density reflects low infiltration and poor groundwater potential (Prasad et al., 2008; Fashae et al., 2014). Drainage density of the study area varies from 0.04- 5.26 km/km2. The relative groundwater potential recharge values have been given to different drainage density classes (Fig. 7a) and their areal extent has been shown in Table 1.

Profile curvature represents the morphology of the topography in the direction of maximum slope gradient. Profile curvature value varies from negative, through zero to positive. Positive curvature values represent upwardly concave and negative values, which indicate upwardly convex, and a value zero, which indicates the flat surfaces. Groundwater potential is high on concave surfaces when compared with convex surfaces as concave slope retains more water for a longer period of rainfall (Manap et al., 2014). Profile curvature of the study area ranges from -34.40 to +33.47. The relative groundwater potential recharge of profile curvature along with their areal extent is shown in Fig. 7b and Table 1.

Plan curvature represents the morphology of the terrain in a direction of 90^0 angles to the slope gradient in which the positive, negative and zero values represent the convexity (divergence of flow) and concavity (convergence of flow) and flat nature of the topography respectively. Here convex topography curvature has been given the highest groundwater potential values. The relative groundwater potential recharge value along with their coverage is shown in Fig. 8a and Table 1.

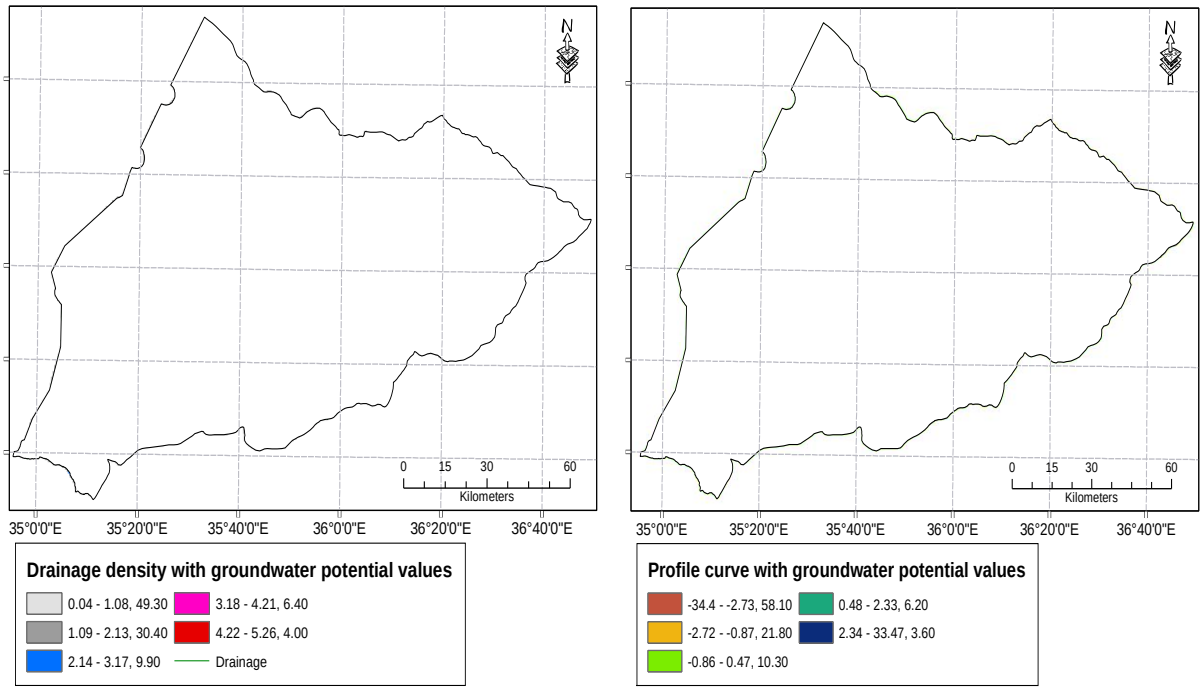

(a) (b)

Figure 7: (a) Drainage density (km/km^2) and (b) Profile curvature, with groundwater potential recharge values

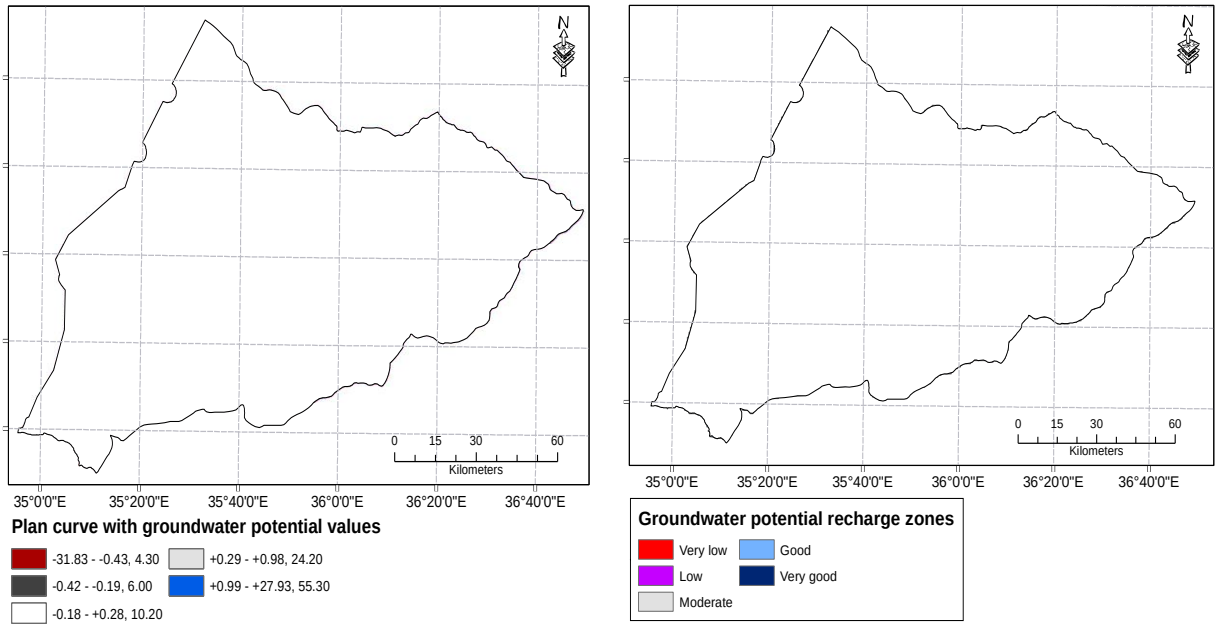

(a) (b)

Figure 8: (a) Planform curvature with groundwater potential recharge values and (b) Groundwater potential recharge zones

Table 1: Themes, Classes, areal extent, groundwater potential recharge value and weight

Theme	Class	Area (km^2)	Percentage	Potential value	Weight
Geology	Termaber Basalts	98.2	0.66	9.8	11
	Alluvium	2184.38	14.71	21.1	
	Adigrate Sandstone	793.73	5.34	8.8	
	Undifferentiated Lower Complex	798.31	5.38	1.6	
	Amba Aiba Basalts	180.92	1.22	10.3	
	Ashangi Basalts	4602.02	30.99	3.9	
	Coluvium	4813.81	32.42	20	
	Posttectonic granites	394.57	2.66	4.4	
	Tsaliet & Tambien Group clastics	71.58	0.48	3.2	
	Syntectonic granites	24.51	0.17	3.4	
	Syntectonic granodiorites & diorites	611.58	4.12	6.3	
	Alcalitrachyte sandsubordinate basalts	253.61	1.71	2.7	
	Tambien Group marbles	10.84	0.07	1.3	
	Adola Group	12.11	0.08	1.2	
Fault density (km/km^2)	0 - 1.65	8429.71	64.22	2.90	10
	1.66 - 3.3	1827.05	13.92	7.30	
	3.31 - 4.95	1358.09	10.35	17.90	
	4.96 - 6.6	970.36	7.39	25.60	
	6.61 - 8.25	541.33	4.12	46.30	
Distance to fault (m)	0 - 7,582.17	7694.87	58.62	54.60	9
	7,582.18 - 15,164.35	2654.22	20.22	26.20	
	15,164.36 - 22,746.52	1612.35	12.28	9.20	
	22,746.53 - 30,328.7	901.29	6.87	5.90	
	30,328.71 - 37,910.87	263.81	2.01	4.00	8
Slope (Percent rise)	0 - 8.75	6839.14	45.98	54.40	
	8.76 - 24.5	5797.66	38.98	20.10	
	24.51 - 48.99	1571.23	10.56	13.50	
	49 - 87.49	547.68	3.68	8.10	
	49 - 87.49	118.24	0.79	3.90	
Soil type	Haplic Acrisols	26.32	0.18	2.30	7
	Haplic Nitisols	33.79	0.23	13.70	
	Eutric Cambisols	6.50	0.04	5.90	
	Eutric Fluvisols	84.80	0.57	27.70	
	Eutric Leptosols	587.42	3.95	2.20	
	Eutric Vertisols	3351.67	22.55	4.10	
	Haplic Luvisols	1364.90	9.18	14.30	
	Humic Nitisols	5335.83	35.90	9.60	
	Chromic Luvisols	2649.23	17.82	15.10	
	Haplic Alisols	1423.06	9.57	5.00	

Soil texture	Loamy sand	84.02	0.57	25.60	6
	Sandy loam	581.43	3.92	22.00	
	loam	10761.00	72.51	42.90	
	Clay	3387.60	22.83	3.60	
	Clay loam	25.93	0.17	5.90	
Hydrological soils	D	3418.27	23.00	75.10	5
	A	672.22	4.52	17.80	
	B	10773.03	72.48	7.00	
Landuse	Shrubland	5190.60	34.91	5.00	4
	Woodland	7576.99	50.95	14.70	
	Cultivation	1216.10	8.18	5.30	
	Grassland	686.19	4.61	2.60	
	Natural Forest	48.41	0.33	9.50	
	Bareland	96.82	0.65	1.50	
	Highland Bamboo	18.84	0.13	2.90	
	Water	17.22	0.12	35.60	
	Wetland	19.17	0.13	22.90	
Drainage density (km/km^2)	0.04 - 1.08	1018.00	6.87	49.30	3
	1.09 - 2.13	9676.87	65.27	30.40	
	2.14 - 3.17	3746.45	25.27	9.90	
	3.18 - 4.21	321.46	2.17	6.40	
	4.22 - 5.26	62.15	0.42	4.00	
Profile curve	-34.4- -2.73	353.20	2.37	58.10	2
	-2.72- -0.87	2267.41	15.24	21.80	
	-0.86- 0.47	7128.13	47.92	10.30	
	0.48- 2.33	4621.18	31.07	6.20	
	2.34- 33.47	504.03	3.39	3.60	
Plan curve	-31.83- -0.43	2645.92	17.79	4.30	1
	-0.42- -0.19	1320.08	8.88	6.00	
	-0.18- 0.28	6657.36	44.76	10.20	
	0.29- 0.98	2683.73	18.04	24.20	
	0.99- 27.93	1566.86	10.53	55.30	

3.7 Groundwater Potential Recharge Zones

Each thematic layer was converted into raster file and appropriate groundwater potential recharge values were given values using AHP (Saaty 1980) in a GIS environment. The final output shows the spatial distribution of GWpRZ of the study area (Fig. 8b). The output of the overlay was further reclassified into five classes, viz., "Very good", "Good", "Moderate", "Poor" and "Very poor" GWpRZ.

4. DISCUSSION

Areas with very low, low, moderate, high and very high GWpRZ were demarcated. After careful analyzing the influence of all the factors on GWpRZ , it was found that mainly the topography and the geology were highly influencing the groundwater potential. Areas with very low, low, moderate, high and very high GWpRZ cover 510.74 km2 (3.45%), 1880.85 km2 (12.72%), 4220.78 km2 (28.55%), 4043.71 km2 (27.35%) and 4127.20 km2

(27.92%) of the study area respectively (Table 2). Lower topography facilitates the water storage than at higher topography (Godebo 2005). While comparing the groundwater potential theme with the slope gradient theme, it is evident that most of the areas with very low and low groundwater potential are located on topographic highs while areas with medium to very high potential are located on topographic lows. The areal extent of "very high groundwater potential is 4127.20 km2, out of which 96% (3977.75 km2) is found at a gentle slope gradient between 0 - 8.75 (percent rise) (Table 3). This is because, the gentler the slope, the higher the concentration time and hence infiltration too. Whereas areas with steepest slopes are seen to have low GWP (Figure) in agreement with earlier workers (Chuma et al., 2013; Fashae et al., 2014).

According to Bouwer (1978), sedimentary rocks are known to have a far higher permeability and porosity in comparison to crystalline rocks. However, fracturing (lineaments and faults) can greatly increase the secondary porosity and permeability when prospecting for groundwater in such terrains (Gupta 2003). A hydrogeological investigation of the study area reveals that areas underlain by alluvial and coluvial deposits have the highest groundwater potential (Fig. 1 Table 4). The total areal extent of very high groundwater potential is 4127.205 km2, out of which coluvium deposits were found to cover 2815.908 km2 (68%), followed by alluvial deposits (1271 km2, 30.79%), syntectonic-granodiorites anddiorites (19.17 km2, 0.17%), adigrate sandstone (10.17 km2, 0.24%) and amba-aiba basalts (4.55 km2, 0.11%). Very high groundwater potential were found to be null in undifferentiated lower complex, tambian group marbles, adola group and ashangi basalts. Very low groundwater potential was mostly encountered in ashangai basalts, followed by post-tectonic granites, alcalitrachyte-sandsubordinate_basalts, undifferentiated lower complex, amba-aiba basalts and termaber basalts. Ashangai basalts were found to dominate the areas covered by moderate groundwater potential.

The areas underlain by lineaments were also found to have high to very high groundwater potential in consonance with several workers (eg. Chuma et al., 2013; Fashae et al., 2014). The influence of topography on the groundwater recharge zones as shown in Table 3 and Fig. 9 (black circles on the left shows the areas of very low groundwater potential recharge; whereas the respective circles on the right show the areas of topographic highs). In addition to this, the impacts of geology on the groundwater recharge zones shows in table 4 and Fig. 10 (Red circles on the left shows the areas of very high groundwater potential recharge; whereas the respective circles on the right show the respective geological units).

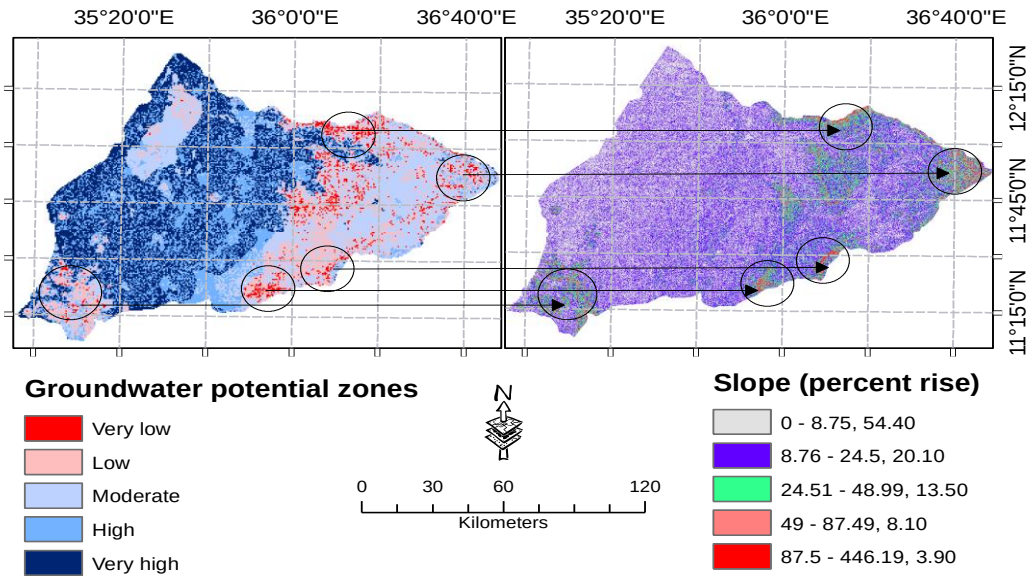

Figure 9: Influence of topography on groundwater potential recharge

Table 2: Groundwater potential recharge zones class and their areal extent in Dinder basin, Ethiopia

Groundwater potential recharge zones class	Area (km^2)	Percentage
Very low	510.74	3.45
Low	1880.85	12.72
Moderate	4220.78	28.55
High	4043.71	27.35
Very high	4127.20	27.92

Table 3: Influence of slope on groundwater potential recharge zones in Dinder basin, Ethiopia

	Groundwater potential recharge zones*				
Slope	Very low	Low	Moderate	Good	Very good
0 - 8.75	0.32	20.47	1811.32	1019.86	3977.75
8.76 - 24.5	1.62	658.57	2031.60	2913.70	149.13
24.51 - 48.99	106.24	1018.89	323.60	110.14	0.32
49 - 87.49	315.15	156.60	54.26	0.00	0.00
49 - 87.49	87.40	26.32	0.00	0.00	0.00

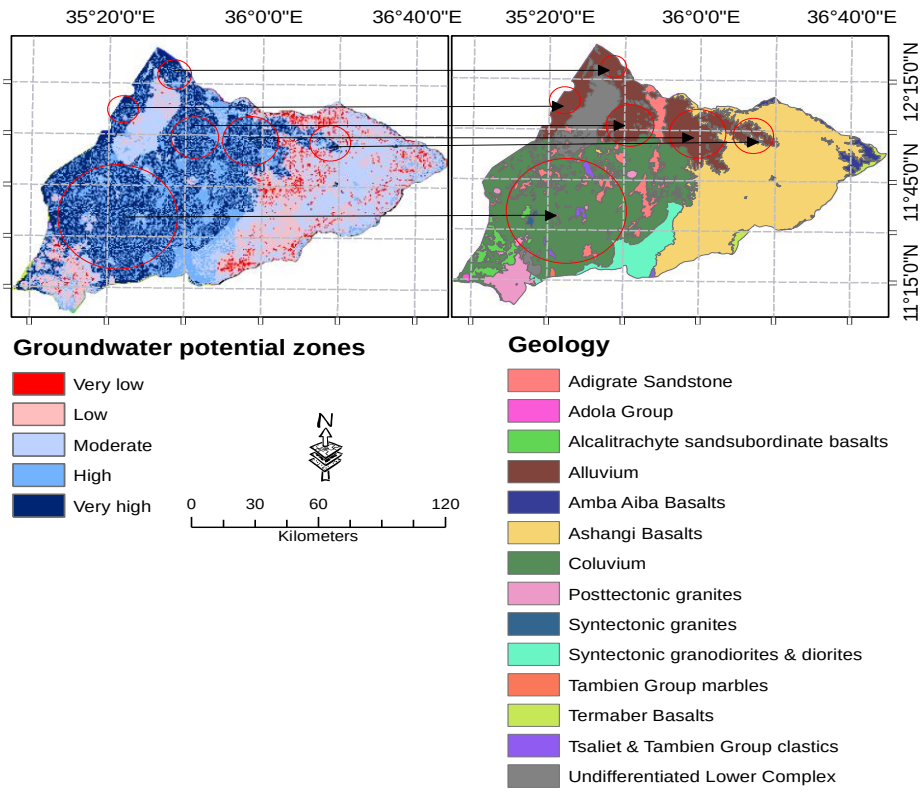

Figure 10: Influence of geology on groundwater potential recharge

Table 4: Influence of geology on groundwater potential recharge zones in Dinder basin, Ethiopia

Groundwater potential Recharge zones	Tb	Al	Ads	Ulc	Aib	Asb	Col	PosG	Ttgc	Sg	Sgd	Agsb	Tgm	Adb
Very low	2.27	0.00	0.32	7.47	3.25	459.73	0.00	21.77	0.00	0.00	0.32	15.27	0.00	0.32
Low	16.9	4.55	2.60	125.1	37.7	1389.3	3.57	163.4	4.87	7.15	10.40	102.7	6.50	6.17
Moderate	45.2	99.42	109.2	658.6	94.9	2665.2	68.88	146.2	38.0	13.3	190.1	82.52	4.55	4.87
High	23.1	789.83	670.6	9.75	40.0	83.50	1894.2	64.66	32.2	4.55	382.7	48.09	0.00	0.65
Very high	6.50	1271.0	10.07	0.00	4.55	0.00	2815.9	0.00	0.00	0.00	19.17	0.00	0.00	0.00

Tb: Termaber basalts; Al: Aluvial deposits; Ads: Adigrate sandstone; Ulc: Undifferentiated lower complex; Aib: Amba-aiba basalts; Asb: Ashangai basalts; Col: Coluvium deposits; PosG: Post-tectonic granites; Ttgc: Tsaliet & Tambien Group clastics; Sg: Syntectonic granites; Sgd: Syntectonic granodiorites & diorites; Agsb: Alcalitrachyte sand-subordinate basalts; Tgm: Tambien Group marbles; Adb: Adola group (All values are estimated in km^2)

5. CONCLUSIONS AND RECOMMENDATIONS

Eleven thematic maps were identified and analyzed based on their influence on groundwater occurrence namely: geology, lineament density, distance to lineament, soil type, soil texture, hydrological soil groups, slope gradient, drainage density, curvature and landuse. Multicriterion decision analysis was employed to determine the groundwater potential value of each class in a thematic map. All the eleven thematic maps were overlaid in GIS domain. Five groundwater zones were delineated. These include zones of: very low and low potential coinciding with high topographic areas with steep slopes (>50% of slope); moderate potential coinciding with lower relief (25-50% of slope) characterized by ashangai basalts; high and very high potential coinciding with flat to gentle topography (0-25% of slope) characterized by coluvial and alluvial deposits mainly. This study shows the large spatial variability of groundwater potential across the Dinder basin due to variability in the geology, soil and land use/cover in the study area. This study testifies the efficiency of spatial analyst tool coupled with multi-criteria decision analysis method in delineation of groundwater potential zones and can be successfully used elsewhere with appropriate modification.

REFERENCES

Abiy, A.Z., Demissie, S.S., MacAlister, C., Dessu, S.B., Melesse, A.M. (2016). Groundwater Recharge and Contribution to the Tana Sub-basin, Upper Blue Nile Basin, Ethiopia. In: Melesse, A., Abtew, W. (eds) Landscape Dynamics, Soils and Hydrological Processes in Varied Climates. *Springer Geography*. Springer, Cham.

Bereket B.B. (2017). Groundwater Potential Mapping using Remote Sensing and GIS in Rift Valley Lakes Basin, Weito Sub Basin, Ethiopia. *International Journal of Scientific & Engineering Research* (8): 42–50.

Bouwer H. (1978). *Groundwater Hydrology*. McGraw-Hill, New York. 480.

Chowdhury A., Jha M.K., Machiwal D. (2003). Application of remote sensing and GIS in groundwater studies: an overview. Proceedings of the international conference on water & environment. Proceedings of Int. Conference on Water & Environment (WE-2003), December 2003, M.P., India, pp 39–50.

Chuma C., Orimoogunje O.I.O., Hlatywayo D.J., Akinyede J.O. (2013). Application of remote sensing and geographical information system in determining the groundwater potential in the crystalline basement of Bulawayo Metropolitan area, Zimbabwe. *Adv. Remote Sens*. 2(2): 149-161.

Devi P.S., Srinivasulu S., Raju K.K. (2001). Hydrogeomorphological and groundwater prospects of the Pageru river basin by using remote sensing data. *Environ. Geol*. 40(9): 1088–1094.

Fashae O.A., Tijani M.N., Talabi A.O., Adedeji O.I. (2014). Delineation of groundwater potential zones in the crystalline basement terrain of SWNigeria: an integrated GIS and remote sensing approach. *Appl. Water Sci*. (4): 19–38.

Fenta, A.A., Kifle, A., Gebreyohannes, T., Hailu G. (2015). Spatial analysis of groundwater potential using remote sensing and GIS-based multi-criteria evaluation in Raya Valley, northern Ethiopia. *Hydrogeol J*. 23, 195–206.

Ganapuram S., Vijaya Kumar G.T., Murali Krishna I.V., Kahya E., Cuneyd Demirel M. (2009). Mapping of groundwater potential zones in the Musi basin using remote sensing data and GIS. *Adv. Engg. Software* 40(1):506–518.

Garg (2007). Weathered, fractured and sediment are the main source of ground water and identified zone in India.

Godebo T.R. (2005). *Application of remote sensing and GIS for geological investigation and groundwater potential zone identification, southeastern Ethiopian Plateau, Bale Mountains and the Surrounding Areas*. Unpublished M. Sc. Thesis. Addis Ababa University, Ethiopia.

Gupta R.P. (2003*). Remote Sensing Geology*. 2nd ed. Springer, Berlin, Germany, pp. 460-477.

Hirano A., Welch R., Lang H. (2003). Mapping from ASTER stereo image data: DEM validation and accuracy assessment. *ISPRS J. Photogramm Remote Sens*. 57(5):356–370.

Hurst H., Black R., Simaika Y. (1959). The Nile Basin, vol. IX. The hydrology of the Blue Nile and Atbara and the Main Nile to Aswan, with reference to some Projects, Ministry of Public Works, Physical Department, Cairo, Egypt.

Jhariya D.C. (2019). Groundwater prospect mapping using remote sensing, GIS and resistivity survey techniques in Chhokra Nala Raipur district, Chhattisgarh, India. *Journal of Water Supply: Research and Technology—AQUA, 68(7):595-606.*

Kesana S.T., Dinesh S. (2019. Identification of Groundwater Potential Zones using Remote Sensing and GIS, Case Study: Mangalagiri Mandal. *International Journal of Recent Technology and Engineering (IJRTE)* (7): 860-864.

Kieffer B., Arndt N., Lapierre H. (2004). Flood and shield basalts from Ethiopia: Magmas from the African Superswell. *J Petrol.* (45):793–834.

Kumar P., Herath S., Avtar R., Takeuchi K. (2016). Mapping of groundwater potential zones in Killinochi area, SriLanka, using GIS and remote sensing techniques. *Sustainable Water Resource Management*, 2(4): 419.

Kumar T., Gautam A.K. (2014). Appraising the accuracy of GIS-based Multi-criteria decision-making technique for delineation of Groundwater potential zones. *Water Resources Management* 28(13): 4449–4466.

Manap M.A., Nampak, Pradhan B., Lee S.S., Ramli M.F. (2014). Application of probabilistic-based frequency ratio model in groundwater potential mapping using remote sensing data and GIS. *Arab. J. Geosci*. 7(2): 711–724.

Mohr P, Zanettin B. (1988). The Ethiopian flood basalt province. In: Macdougall J.D. (ed) Continental flood basalts. Kluwer Academic, Dordrecht.

Naghibi A., Pourghasemi H.R. (2015). A comparative assessment between three machine learning models and their performance comparison by bivariate and multivariate statistical methods for groundwater potential mapping in Iran. *Water Resour. Manage*. 29 (14): 5217–5236.

Nair H.C., Padmala D., Joseph A., Vinod P.G. (2017). Delineation of groundwater potential zones in river basins using geospatial tools—an example from southern Western Ghats, Kerala, India. *J. Geovisual. Spat. Anal.* 1(1–2): 5.

Pradhan B. (2013). A comparative study on the predictive ability of the decision tree, support vector machine and neuro-fuzzy models in landslide susceptibility mapping using GIS. *Comput. Geosci.* 51: 350–365.

Prasad R.K., Mondal N.C., Banerjee P., Nandakuma, M.V., Singh V.S. (2008) Deciphering potential groundwater zone in hardrock through the application of GIS. *Environ. Geol.* (55): 467–475.

Rajat A., Garg P.K. (2015). Remote Sensing and GIS Based Groundwater Potential & Recharge Zones Mapping Using Multi-Criteria Decision Making Technique. *Water Resour Manage*, 30:243–260.

Savita R., Mittal H.K., Satishkumar U., Singh P.K., Yadav K.K. (2018). Delineation of Groundwater Potential Zones using Remote Sensing and GIS Techniques in Kanakanala Reservoir Subwatershed , Karnataka, India. *Int. J. Curr. Microbiol. App. Sci.* 7(1): 273-288.

Senanayake I.P., Dissanayake D.M., Mayadunna B.B., Weerasekera W.L. (2016). An approach to delineate groundwater recharge potential sites in Ambalantota, Sri Lanka using GIS techniques. *Geoscience Frontier*, 7(1): 115–124.

Sener E., Sener S., Davraz A. (2018) Groundwater potential mapping by combining fuzzy-analytic hierarchy process and GIS in Beys¸ehir Lake Basin, Turkey. *Arabian Journal of Geosciences*, 11(8): 187.

Swetha T.V., Girish G., Thrivikramji K.P., Jesiya N.P. (2017). Geospatial and MCDM tool mix for identification of potential groundwater prospects in a tropical river basin, Kerala. *Environ. Earth Sci*., 76(428).

Tamiru A (2006): Groundwater occurance in Ethiopia, Addis Ababa.

Tesfa G., Ebissa G., Imran A., Mithas A.D., Afera H.T., Asirat T.T., Assefa F., Ermias S.B. (2018). Groundwater resources evaluation using geospatial technology. *Environmental Geosciences* 25(1): 25-35.

Tesfa G.A., Girum G.D. (2019). Groundwater potential assessment using GIS and remote sensing: A case study of Guna tana landscape, upper blue Nile Basin, Ethiopia. *Journal of Hydrology: Regional Studies, 100610.*

Yeh H.F., Cheng Y.S., Lin H.I., Lee C.H. (2016). Mapping groundwater recharge potential zone using a GIS approach in Hualian River, Taiwan. *Sustain. Environ. Res.* (26): 33–43.

Assessing the Impact of Land Use/Land Cover Change on the Hydrology of Gidabo River Sub-basin, Ethiopian Rift Valley Lakes Basin

Henok Mekonnen Aragaw[1,*], Surendra Kumar Mishra[2], Manmohan Kumar Goel[3]

[1]*Department of Water Resources and Irrigation Engineering, College of Engineering and Technology, Dilla University, Dilla, P.O.Box 419, Ethiopia,*
[2]*Department of Water Resources Development and Management, Indian Institute of Technology Roorkee, Roorkee 247667, Uttarakhand, India,*
[3]*Groundwater Hydrology Division, National Institute of Hydrology, Roorkee 247667, Uttarakhand, India*
**Corresponding author, E-mail: henok_mekonen@du.edu.et*

ABSTRACT

Land use/land cover (LULC) changes greatly affect the basin hydrology. Their lump-sum effect on various components of hydrologic cycle has been generally evaluated and reported in literature, except for a few studies which dealt with individual LULC changes. This study is a step forward in this direction to evaluate the hydrological response of individual LULC changes on different components of hydrological cycle of the Gidabo River sub-basin, Rift Valley Basin, Ethiopia during the period 1988-2018 using the Soil and Water Assessment Tool (SWAT) and Partial Least Squares Regression (PLSR) models. The hydrological evaluation revealed that LULC changes resulted in an increase in annual mean surface runoff by 23.6 mm during the period 1988-2018 while the annual mean baseflow, lateral flow, percolation and evapotranspiration (ET) were found to decrease by 9.1, 4.2, 10.2, and 12.2 mm, respectively. The changes in hydrological elements were much pronounced at sub-basin levels, which were mainly associated with uneven spatial LULC alterations. PLSR analysis detected that expansion of cultivated and urban areas and contraction of forest evergreen, agroforestry, and grassland are the main contributors to the upsurge in surface runoff and decline in baseflow and percolation. Likewise, cultivated land affected the lateral flow and ET negatively in contrast to the agroforestry and grassland, which influenced these hydrologic components positively. The change in LULC is expected to continue in near-future in the Gidabo River sub-basin and it will be crucial to examine its impact on future basin hydrology for planning water management strategies.

Keywords: *Gidabo River sub-basin; LULC change; hydrological component; SWAT model; PLSR model*

1. INTRODUCTION

Water is one of the most important natural resources on which all living things thrive. It goes through system of circulation among ocean, atmosphere, and land, known as the hydrologic cycle (Chow *et al*. 1988). The changing land use/land cover (LULC) and climate affect various components of the hydrologic cycle and consequently, the water resources in a river basin (Zhang *et al.* 2016). LULC changes influence the hydrologic processes (Gebremicael *et al.* 2019) such as interception rates, soil moisture storage, evapotranspiration (ET) loss, infiltration and groundwater recharge leading to modifications in basin water resources (Gebremicael *et al.* 2013, Ayele *et al.* 2017, Gashaw *et al.* 2018). These changes amend vegetation cover and surface roughness affecting the timing and magnitude of surface runoff and groundwater recharge, leading to modifications in streamflow and magnitude/frequency of floods (Zhang *et al.* 2016). As an example, conversion or amendment of forest into urban and agricultural area results in higher surface runoff and reduced groundwater recharge (Baker and Miller 2013, Gyamfi *et al.* 2016).

Hydrological models are generally used to evaluate the effects of LULC changes on hydrological processes. These models simulate the spatial as well as temporal responses of various LULC changes on the hydrological components in a river basin (Zhou *et al.* 2013, Gashaw *et al.* 2018, Yan *et al.* 2018, Garg *et al.* 2019, Liyew *et al.* 2019b). Using the hydrological models, a number of researches have evaluated the hydrological response to environmental changes at the watershed level. However, at different spatial and temporal scales, the predominant

factors and the degree to which LULC changes influence the hydrological conditions often vary. Spatially, the impact of LULC changes on hydrology is commonly more evident at a sub-basin scale (Wagner *et al.* 2013, Schilling *et al.* 2014, Marhaento *et al.* 2017) while their impact on the water budget elements is relatively small at a larger basin level due to compensating effects (Schilling *et al.* 2014, Shawul *et al.* 2019). For water resources managers, the information about how and by how much, the LULC changes will influence the water availability at sub-basin level is more relevant for planning appropriate mitigation measures (Marhaento *et al.* 2017). As such, research is required at the sub-basin level to better realize the responses of LULC changes on the hydrological conditions.

In addition to quantifying the impacts of gross LULC changes on hydrological components using a hydrologic model, it is also important to scrutinize the effect and contribution of each LULC change on different hydrological components of a catchment (Shi *et al.* 2013, Yan *et al.* 2013, Gashaw *et al.* 2018, Gebremicael *et al.* 2019, Shawul *et al.* 2019). The Partial Least Squares Regression (PLSR) model, is an advanced multivariate statistical method that is useful to investigate the interaction of individual LULC classes (independent variable) with different hydrological components (dependent variables) (Carrascal *et al.* 2009, Fang *et al.* 2015, Shawul *et al.* 2019). PLSR approach is a useful tool to ascertain whether the observed change in LULC is large enough to cause the change in hydrological processes and it can be applied to zoom into the LULC class responsible for the change in hydrological elements (Gebremicael *et al.* 2019). Further, this technique is suitable for solving the multicollinearity problems, an issue which arises when at least two predictors (independent variables) in the model are correlated (Abdi 2010, Shi *et al.* 2013).

In Ethiopia, anthropogenic activities have affected the water resources availability in river basins (Ayele *et al.* 2017, Liyew *et al.* 2019b). Intensive grazing, deforestation, and extraordinary cultivating practices are some key alterations in the catchments which modified the hydrological processes (Legesse *et al.* 2003, Ayele *et al.* 2017) and devastating not only the highland areas due to enhanced erosion and reduction in crop yield (Setegn *et al.* 2009, Liyew *et al*. 2019a) but also in the water channels and storages because of sedimentation (Setegn *et al.* 2009). Several studies reported the effects of LULC changes on hydrology in Ethiopia (e.g. Legesse *et al.* 2003, Gebremicael *et al.* 2013, Gashaw *et al.* 2018, Liyew *et al.* 2019b). Gashaw *et al.* (2018) reported the enhanced cultivated and built-up areas at the cost of forest, shrub land, and grassland during 1985 - 2015 in Andassa watershed, Blue Nile Basin, Ethiopia. As a result, surface runoff and water yield were amplified while lateral flow, groundwater flow, and ET diminished. Gebremicael *et al.* (2013) also studied the trend analysis of runoff and sediment fluxes in the Upper Blue Nile Basin by combination of the statistical test and hydrological model and the results revealed that the rainfall over the basin did not change significantly during 1970–2005 though surface runoff increase which due to landuse changes in the basin.

As only a few studies have been attempted to ascribe the LULC changes to hydrological components using coupled hydrologic and PLSR models (Gebremicael *et al.* 2019, Shawul *et al.* 2019), the primary objective of this study is to quantify the contribution of changes in individual LULC classes to changes in components of water balance by using the combination of hydrologic model (Soil and Water Assessment Tool) and PLSR model. The Gidabo watershed, Rift Valley Basin, Ethiopia has been selected for the study which is one of the most profitable areas in the basin and suffers from human-induced resource degradation because of the increased cultivated land and unregulated LULC alterations along with the booming population growth. The impact of such LULC changes on hydrological components are poorly studied in this basin and such information can be vital for developing sustainable water resources management plans for the basin.

2. MATEDRIALS AND METHODS

2.1 Description of the Study Area

The Gidabo watershed (Figure 1) is located in the Abaya-Chamo sub-basin of the Rift Valley Basin in Ethiopia.

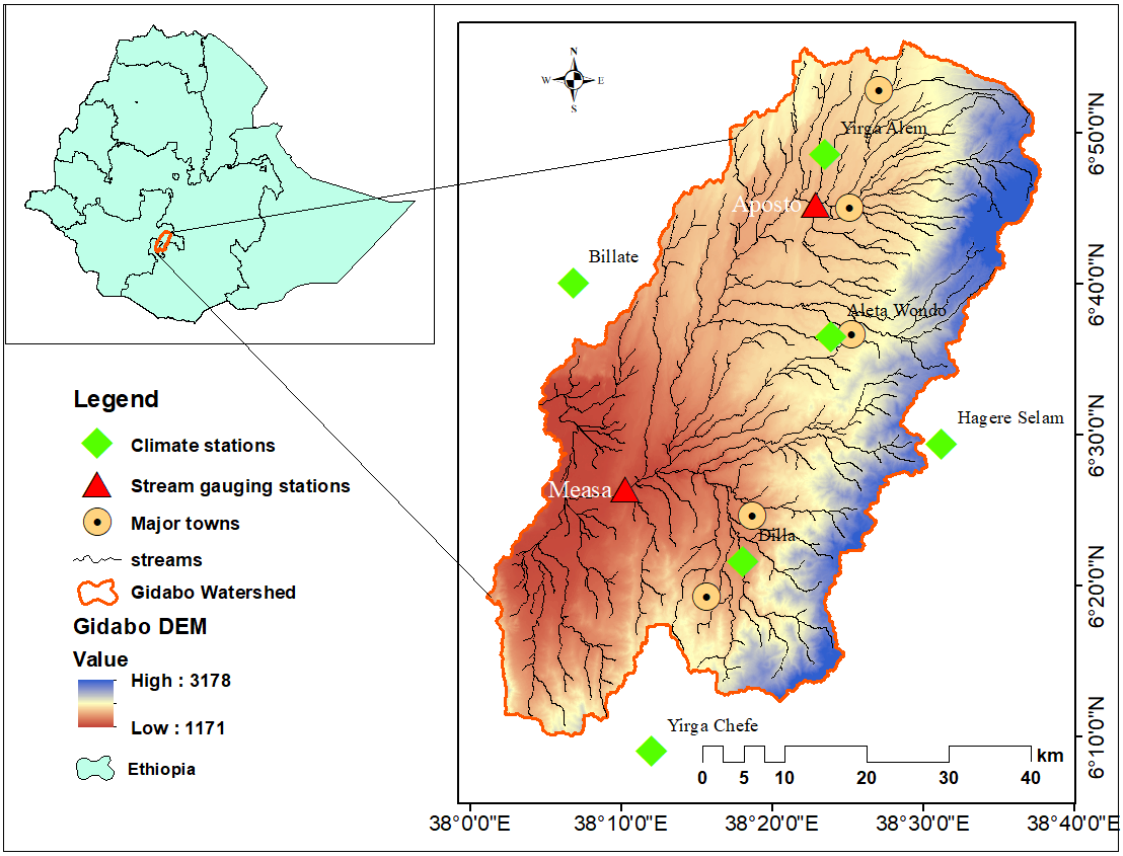

Figure 1: Location map of the study area - Gidabo watershed, stream gauging stations, climate stations and streams

The River Gidabo twists through forested and agricultural land of escarpment and rift floor, finally ending into Lake Abaya, the biggest lake in the Rift Valley (Mechal *et al.* 2015). The river is around 120 km long, with an estimated catchment area of 3097 km^2. The topographical area begins from the north-eastern piles of Soka Sonicha and lies in the range of 6.11° to 6.58° N latitude and 38.0° to 38.38° E longitude. In particular, the basin lies in Sidama and Gedeo Zones of the Southern Nation Nationalities and People of Regional State (SNNPRS) and the Borena Zone of Oromiya Regional State. The altitude of the basin ranges from 3178 m at the most elevated point to 1171 m at the outlet. The pattern of rainfall in the area has four seasons, namely the high rainy season (April and May), moderate rainy season (September to October), low rainy season (July and August), and dry rainy season (November to February) (Belihu *et al.* 2018). The mean annual rainfall in the basin is 1385 mm and the average monthly temperature varies from 11 ºC to 25 ºC.

2.2 Data Availability

The dataset required for the SWAT model setup includes a Digital Elevation Model (DEM), soil map, LULC map, and the climate data. The Shuttle Radar Topographic Mission (SRTM) DEM (30 m spatial resolution) was downloaded from United States Geological Survey (USGS) Earth Explorer (https://earthexplorer.usgs.gov) and was used for watershed discretization, sub-watershed formation, slope classification, and extraction of the stream network. Images from Landsat satellite (Table 1) have been downloaded from USGS Earth Explorer (https://earthexplorer.usgs.gov). The satellite images have been taken during the dry season (January–February) and carefully chosen based on the data availability and cloud conditions in the catchment. Ground truth points in the study area, used for classification and accuracy evaluation, have been gathered from field surveys, Google Earth, countrywide LULC maps, and literature.

Table 1: Explanations of satellite images used in this study

Satellite	Sensor	Path/Row	Resolution (m)	Acquisition date
Landsat 5	TM Multispectral	168/55/56	30	28/02/1988
Landsat 7	ETM+ Multispectral	168/55/56	30	05/02/2000
Landsat 8	Operational Land Imager (OLI)	168/55/56	30	29/01/2018

The soil map was collected from the Ministry of Agriculture, Ethiopia while the soil properties was derived from latest irrigation design and feasibility study report (WWDSE 2007) in the basin and the harmonized World Soil Database (http://www.fao.org/soils-portal/soil-survey/soil-maps-and-databases/harmonized-world-soil-database-v12/en/).

The daily precipitation, maximum and minimum daily temperature data of eight stations from 1987-2018 were obtained from the National Meteorological Services Agency of Ethiopia. After analyzing the data, six rainfall stations and five temperature stations have been selected. The observed daily streamflows of two gauging sites have been obtained from the Ministry of Water, Irrigation, and Electricity of Ethiopia for model calibration and validation. Finally, all the input data for the study basin have been processed for input to the SWAT model.

2.3 Methodology Adopted

2.3.1 Image Classification and LULC Change Detection

For LULC change detection, Landsat images have been first pre-processed for their enhanced quality and features' visibility (Liyew *et al.* 2019a). The maximum likelihood technique (Gashaw *et al.* 2017, Liyew *et al.* 2019a) has been used for supervised classification, and the majority filter has been employed for post-processing. Ground truth points of 191 locations have been utilized for accuracy assessment for the images of 2018. However, for the images of 1988 and 2000, 149 and 155 reference data, obtained from Google Earth, have been used. Overall accuracy and Kappa statistics, derived from the error matrix, have been used to evaluate the accuracy. ERDAS 2018 and ArcGIS 10.5 have been used for image classification and mapping. The LULC maps for the years 1988, 2000, and 2018 are shown in Figure 2. The rate of change of the classified LULC maps (Gashaw *et al.* 2017, Liyew *et al*. 2019a) has been estimated as follows:

$$Rate\ of\ \ change\,(km^2/year) = \frac{A-B}{Z} \qquad (1)$$

where A is the area of LULC (km^2) at time-2, B is the area of LULC (km^2) at time-1; Z is the time interval between A and B years.

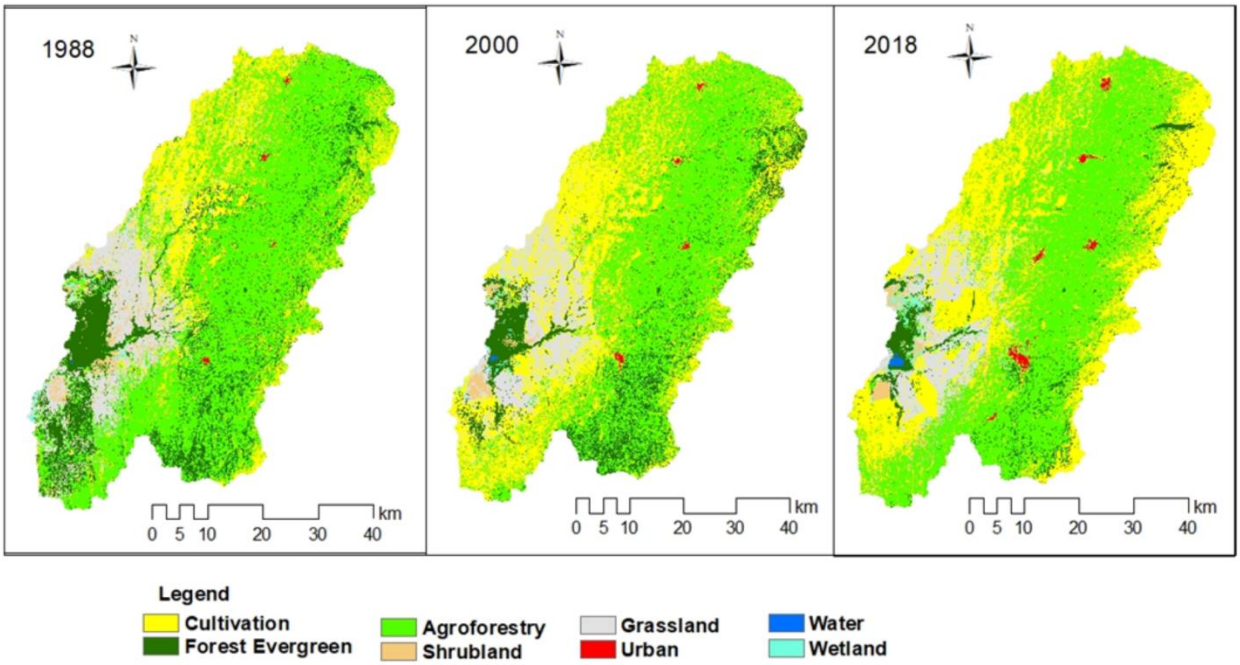

Figure 2: LULC maps of the study area in the years 1988, 2000, and 2018

2.3.2 Description of the SWAT Model

SWAT is a semi-distributed physically-based simulation model that can predict the effect of climate and anthropogenic alterations on the hydrological systems in watersheds with varying soils, land use, and management conditions over long periods (Arnold *et al.* 1998). The SWAT divides the basin into groups of similar soils, slopes, and land covers, which provide similar hydrological responses, called hydrological response units (HRUs) (Neitsch *et al.* 2011). The model simulates the land phase processes of the hydrological components based on the following water balance equation (Arnold *et al.* 1998):

$$SW_t = SW_0 + \sum_{i=1}^{t}(R_d - Q_s - E_a - W_s - Q_g) \qquad (2)$$

where SW_t is the final soil water content (mm), SW_o is the initial soil water content i (mm), t is the time (days), R_d is the amount of precipitation on day i (mm), Q_s is the amount of surface runoff on day i (mm), E_a is the amount of evapotranspiration on day i (mm), W_s is the amount of percolation and bypass flow exiting the soil profile bottom on day i (mm), and Q_g is the amount of return flow on day i (mm). Details of the model are available at (http://swatmodel.tamu.edu/).

2.3.3 Setup and calibration of SWAT Model

The SWAT Version 2012 (Neitsch *et al.* 2011) has been used to evaluate the impacts of LULC changes on the hydrology of Gidabo watershed. The model has been setup for the study watershed using the available hydro-meteorological and spatial data. The study area is delineated in SWAT using SRTM DEM (30 m spatial resolution) with a minimum threshold drainage area of 6000 ha. Subsequently, the basin is divided into 45 sub-basins. A soil database that includes soil physical properties was prepared and imported to SWAT databases. The LULC map, soil map, and slope map have been imported and overlaid and linked with the SWAT databases to define HRUs. The slope of the basin is divided into three classes by considering the multi-slope option. As a threshold, 10% of land use, 10% of soil, and 10% of slope have been used to discretize the 45 sub-basins into 409 HRUs derived from LULC, soil, and slope maps. Finally, the precipitation and weather data have been overlaid before writing and

finalizing all input files. Then, the Soil Conservation Service (SCS) Curve Number (CN) (USDA-SCS 1972) method has been selected to simulate surface runoff, Penman-Monteith (Monteith 1965) method for potential evapotranspiration, and the kinematic storage method for predicting the lateral flow. Details of model setup are available elsewhere (http://swatmodel.tamu.edu/).

After obtaining and processing the input data, the model is evaluated through calibration and validation (Abbaspour *et al.* 2017). Before calibration, the most sensitive parameters of the model for the present setup have been identified by using global sensitivity analysis available in SWAT CUP (Abbaspour *et al.* 2017) and the t-stat and p-value (Abbaspour *et al.* 2007, Gashaw *et al.* 2018) have been used for their significance. Sequential Uncertainty Fitting (SUFI – 2) algorithm has been used for calibration and validation. In line with the suggestion of Niraula *et al.* (2015) and Ayele *et al.* (2017) for spatial evaluation, the model has been calibrated using monthly flow data available for the period 1990-2005 and 1997-2003 at the Aposto and Measa gauging sites, respectively. Subsequently, the model has been validated using the flow data for the period 2006-2014 (at the Aposto gauging site) and 2004-2007 (at the Measa gauging site). The LULC map of the year 2000 has been used for calibration as well as validation. Various performance evaluation criteria, such as Nash-Sutcliffe Efficiency (NSE), Coefficient of Determination (R^2), and percentage bias (PBIAS) have been used to evaluate the performance (Moriasi *et al.* 2007) which are described below:

$$NSE = 1 - \frac{\sum(Q_o - R_s)^2}{\sum(Q_o - Q_a)^2} \qquad (3)$$

$$R^2 = \left\{ \frac{\sum(Q_o - Q_a)(R_s - R_a)}{\left[\sum(Q_o - Q_a)^2\right]^{0.5} [\sum(R_s - R_a)^2]^{0.5}} \right\} \qquad (4)$$

$$PBIAS = \left[\frac{\sum Q_o - R_s}{\sum Q_o}\right] \times 100 \qquad (5)$$

where R_s is the simulated flow, R_a is the mean simulated flow, Q_o is the observed flow, and Q_a is the mean observed flow. All flow values are in m^3/s.

2.3.4 Model Application

To evaluate the response of LULC changes on hydrological components at basin and sub-basin scales, simulations with the calibrated SWAT model have been carried out by separately considering the LULC maps of the years 1988, 2000, and 2018 as input to the model.

2.3.5 Partial Least Squares Regression (PLSR) Model

Assessing the hydrological responses using the hydrologic model is not to reveal the relationship and influence of individual LULC classes on components of water budget (Gebremicael *et al.* 2019). Pearson correlation has been applied to identify the correlation between changes in LULC classes and components of water budget at the sub-basin level at 95% significance level. Then, the PLSR model has been employed to quantify the influence of individual LULC classes on components of the water budget at the sub-basin level. PLSR relates the changes in hydrological components with the changes in LULC classes (Ayele *et al.* 2017, Shawul *et al.* 2019). It specifies the relationship between response variables, 'y' and predictor variables, '*x*,' as follows:

$$y = a + b_1x_1 + b_2x_2 + b_3x_3 \ldots\ldots\ldots\ldots b_nx_n \qquad (6)$$

where 'a' is the regression coefficients for intercept, and 'b' values are the regression coefficients (for variables '1' through 'n') computed from the data. Here, the dependent variables represent the changes in the surface runoff,

water yield, base flow, lateral flow, percolation, and evapotranspiration while the independent variables represent the changes in the cultivated land, forest evergreen, agroforestry, grassland, shrub land, and urban area.

Furthermore, the importance of independent variables on dependent variables was explained by the Variable Importance of Project (VIP) (Yan *et al.* 2013). Predictors with higher values of VIP better explain the importance of the LULC classes on the hydrological components. Gashaw *et al.* (2018) suggest VIP > 0.8 is statistically significant to explain the hydrological components. Hence, the regression coefficients (Equation 6) give the position of the influence (negative or positive effect), and the VIP values deliver information on the strength of influence for each LULC class. In this study, four PLSR models have been developed for hydrological components to maximize the prediction ability of the model: PLSR1 (surface runoff and water yield), PLSR2 (base flow and percolation), PLSR3 (lateral flow), and PLSR4 (ET). The PLSR modeling and other statistical analysis were performed using the XLSTAT tool (www.XLSTAT.com).

3. RESULTS AND DISCUSSION

3.1 Evaluation of LULC Change and Accuracy Assessment

The Landsat satellite images, in combination with supervised classification techniques, have been used to map the LULC in the study watershed in the years 1988, 2000, and 2018 and subsequently, changes in the LULC characteristics have been worked out. Around 150 or more reference ground truth locations have been used to assess the accuracy of the classification. The error matrix (Table 2) obtained from the analysis reveals the overall accuracy of 85.34% with a kappa statistic of 82.46% for the LULC map of 2018. Similarly, for the LULC maps for the years 1988 and 2000, the overall accuracy of 81.21% and 85.16% and kappa statistic of 77.23% and 82.24%, respectively have been obtained. The discrimination of forest evergreen and agroforestry has been found to be tedious and most challenging during the classification process and may remain a source of uncertainty. However, the overall accuracy achieved has met the minimum criteria for further analysis, as suggested by Ariti *et al.* (2015).

Table 2: Error matrix for the 2018 classified map

Classified data	Reference data									
	CL	FE	AF	GL	SH	UR	WR	WL	Row total	User's accuracy (%)
CL	36	1	2	5	0	2	0	0	46	78.26
FE	0	28	1	0	0	0	0	0	29	96.55
AF	2	5	37	0	0	1	0	0	45	82.22
GL	0	1	1	23	1	0	0	0	26	88.46
SH	0	0	0	1	13	0	0	0	14	92.86
UR	1	0	0	0	0	12	0	0	13	92.31
WR	0	0	0	0	0	0	5	1	6	83.33
WL	0	0	0	1	1	0	1	9	12	75.00
Column total	39	35	41	30	15	15	6	10	191	
Producer's accuracy (%)	92.31	80.00	90.24	76.67	86.67	80.00	83.33	90.00		

Note: CL: Cultivation; FE: Forest evergreen; AF: Agroforestry; SH: Shrubland; GL: Grassland; UR: Urban area; WR: Water; WL: Wetland

The areal extent and rate of change of LULC in the Gidabo watershed are shown in Figure 3 and presented in Table 3. Agroforestry, cultivated area, forest evergreen, and grassland cover a significant portion of the study watershed over the entire study period horizon. An appraisal of LULC maps for the years 1988, 2000, and 2018 suggests that the most significant changes occurred in the cultivated area, agroforestry, and forest evergreen classes during the study period from 1988 to 2018. The cultivated land increased from 19.62% to 33.36%, with a rate of change of 32.85 km^2/year from the year 1988 to 2000 while the area of agroforestry, grassland, and forest evergreen

decreased from 51.36% to 42.86%, 10.76% to 10.04%, and 15.16% to 11.97%, respectively, with a rate of change of 20.33 km^2/year, 1.72 km^2/year, and 7.63 km^2/year during the same period.

Table 3: Areal extents and rate of changes of Gidabo basin LULC classes

LULC classes	Areal extent (%)			Rate of change (km^2/year)		
	1988	2000	2018	2000-1988	2018-2000	2018-1988
CL	19.62	33.36	36.38	+32.85	+5.21	+16.80
FE	15.16	11.97	5.08	-7.63	-11.90	-10.11
AF	51.36	42.86	46.86	-20.33	+6.91	-4.51
SH	2.66	1.11	1.90	-3.72	+1.38	-0.76
GL	10.76	10.04	8.43	-1.72	-2.78	-2.34
UR	0.15	0.22	0.59	+0.17	+0.65	+0.45
WR	0.006	0.04	0.13	+0.07	+0.16	+0.12
WL	0.27	0.40	0.61	+0.30	+0.36	+0.34

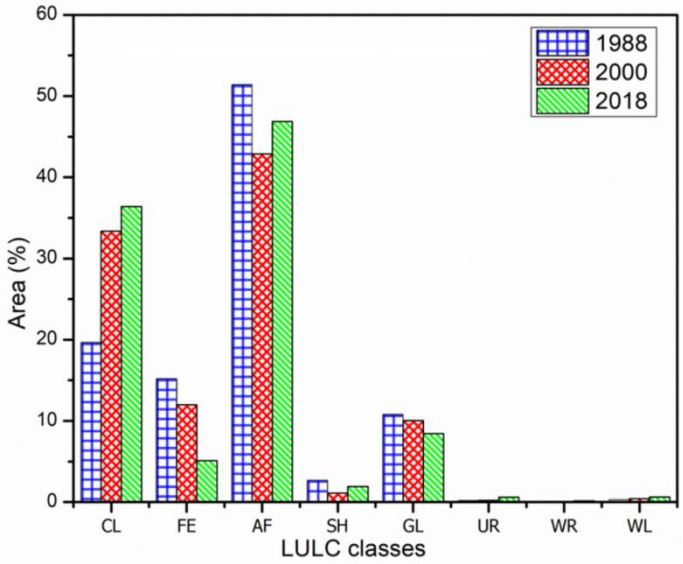

Figure 3: Areal extents of LULC types in the years 1988, 2000, and 2018

After the year 2000, the areal extent of agroforestry and shrubland started increasing from 42.86% to 46.86% and 1.11% to 1.90%, respectively, with a rate of change of 6.9 km^2/year and 1.38 km^2/year. During this period, the expansion of cultivated land was gradual from 33.36% to 36.38%, with a rate of change of 5.21 km^2/year. On the other hand, forest evergreen and the grassland cover decreased consistently from 2000 to 2018. These conditions occurred because of the growing population that triggered the demand for new agricultural land and fuelwood, which in turn, brought about the reduction in other LULC classes (Ariti *et al.* 2015, Liyew *et al.* 2019a). Nonetheless, the increased agroforestry and gradual expansion of cultivated land over the period from 2000 to 2018 exhibited that the environment was convalescing from the devastating drought and forest clearance for firewood and cultivation. During this period, the Ethiopian Government had introduced plantation program and extensive soil and water conservation measures were carried out by the public (Ariti *et al.* 2015, Liyew *et al.* 2019a). Some other authors have also observed an increase in cultivated land at the expense of forest land, grassland, and shrubland, such as those Ariti *et al.* (2015) in the Central Rift Valley of Ethiopia; Gebremicael *et al.* (2013), and Ayele *et al.* (2017) in the Upper Blue Nile basin, Ethiopia; Gashaw *et al.* (2018) in the Andassa watershed, Blue Nile basin, Ethiopia; and Liyew *et al.* (2019a) in the Upper Blue Nile basin of North-Western Ethiopia.

3.2 Calibration and Validation of the Model

The SWAT model has been calibrated and validated using the observed streamflow data of Measa and Aposto gauging sites in the Gidabo watershed. The 12 most sensitive parameters affecting the surface runoff, lateral flow, groundwater flow, and evapotranspiration in the study watershed have been selected. The optimized values of 12 influential parameters for the Aposto and Measa sub-watersheds are presented in Table 4.

Table 4: Calibrated values of sensitive parameters for Aposto, and Measa gauging sites

Parameter	Ranges	Optimized parameter values	
		Aposto	Measa
r__CN2.mgt	± 0.2	-0.108	-0.056
v__CANMX.hru	0-100	7.09	9.90
v__ESCO.hru	0-1	0.85	0.84
v__GWQMN.gw	0-5000	3690	3400
r__SOL_K.sol	± 0.8	-0.2	-0.388
v__RCHRG_DP.gw	0-1	0.591	0.13
r__SOL_Z.sol	± 0.25	0.21	0.0175
v__GW_REVAP.gw	0.02-0.2	0.076	0.079
r__SLSUBBSN.hru	0-0.2	0.161	0.1542
v__ALPHA_BF.gw	0-1	0.091	0.448
v__REVAPMN.gw	0-500	344.6	298.3
r__SOL_AWC.sol	± 0.25	-0.182	-0.137

The comparisons of hydrographs between the observed and simulated monthly streamflow during the periods of calibration and validation for the Measa and Aposto gauging sites are shown in Figures 4 and 5, respectively. It can be seen that the simulated streamflow matches well with the observed streamflow. However, some mismatch between the observed and simulated results was observed in the hydrographs, especially in low- and high-flows. This may be attributed to the uneven distribution of rain gauges, errors in stream gauges, and the weakness of the curve number method of the SWAT model. In addition, the mismatch in low-flows may have resulted from the unaccounted flow diverted for irrigation by the local community in the watershed. Also, the plot of monthly rainfall variability seems not to be corresponding to the observed monthly flows, e.g. Jan-Dec 2002 (Fig. 8). This may be attributed to the errors in rain gauges or stream gauges. The NSE, PBIAS, and R^2 during the calibration period are estimated as 0.67, -1.88, and 0.75, respectively, whereas during the validation period, these values are 0.66, -7.29, and 0.78, respectively for the Measa gauging site. Similarly, for the Aposto gauging site, these values are 0.69, 5.51, and 0.72, respectively, during the calibration period and 0.68, 4.97, and 0.69 respectively during the validation period. Moriasi *et al.* (2007) suggested that the performance of statistical criteria on monthly time step calibration is acceptable if NSE and $R^2 > 0.50$, and if PBIAS is of the order of ± 25%. Good model performance has been attained for both Measa and Aposto gauging sites during both calibration and validation stages. Hence, based on the model performance, the calibrated SWAT model has been used to assess the hydrological response of LULC changes in the Gidabo watershed.

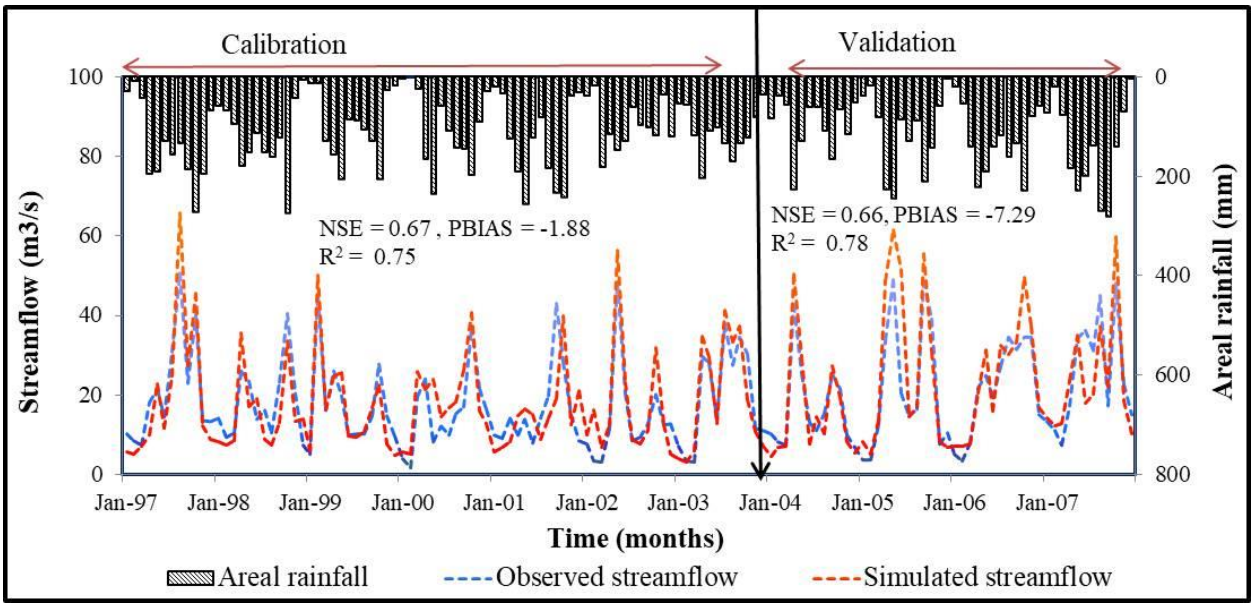

Figure 4: Calibration and validation of simulated and observed monthly streamflow at Measa gauge

Note. R^2: coefficient of determination; NSE: Nash-Sutcliffe efficiency; PBIAS: percent bias.

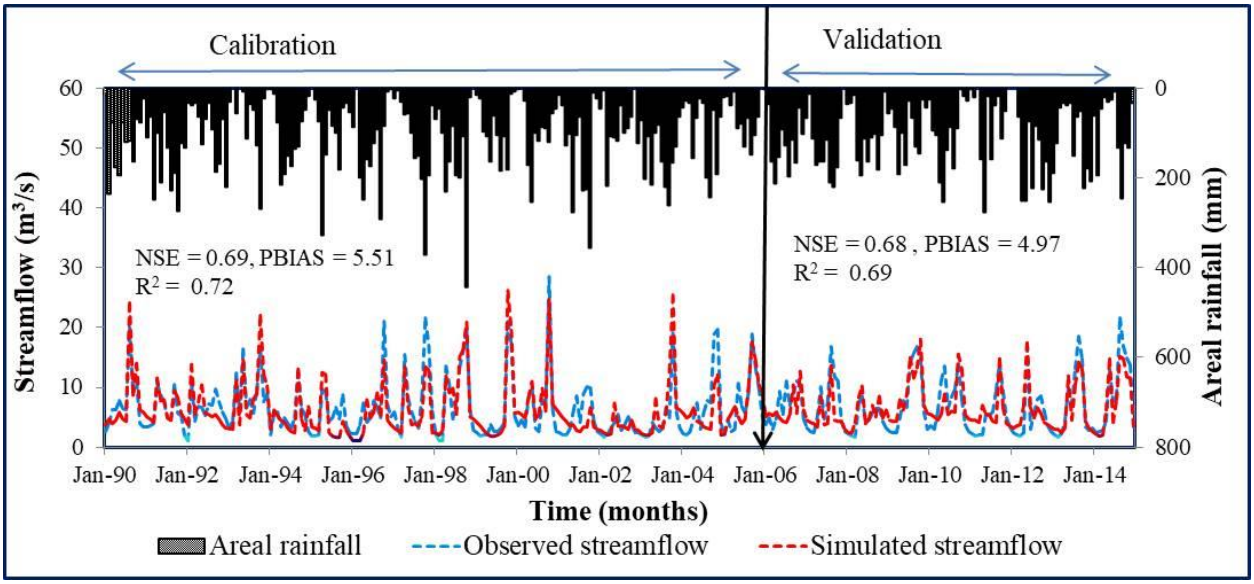

Figure 5: Calibration and validation of simulated and observed monthly streamflow at Aposto gauge

3.3 Hydrological Responses to LULC Changes at Basin Level

The yearly mean basin estimations of surface runoff, water yield, baseflow, lateral flow, percolation, and ET, and their relative changes at the basin outlet, which have been estimated from the years 1988, 2000, and 2018 LULC maps, are shown in Table 5. Following an expansion in cultivation land and urban area, and a reduction in forest evergreen, grassland, and agroforestry, the yearly mean surface runoff showed a reliably increasing pattern from 151.4 mm in 1988 to 173.1 mm in 2000 and 175.0 mm in 2018 (Table 5). Compared with the period of 2000 and 2018 (1.10%), the yearly mean surface runoff between 1988 and 2000 (14.33%) is higher. This is due to drastic expansion of cultivated land between 1988 to 2000. In contrast, the baseflow, lateral flow, and percolation showed

a decreasing trend from 89.0 mm to 79.9 mm, 69.2 mm to 65.0 mm, and 287.9 mm to 277.7 mm, respectively, between 1988 and 2018. However, the changes in water yield and ET were inconsistent. For instance, the estimated annual average ET decreased from 880.5 mm to 863.4 mm (by 1.94%) between 1988 and 2000. This decrease was mainly caused by the contraction of forest evergreen, agroforestry, grassland, and shrubland, and drastic expansion of cultivated land between 1988 and 2000. In contrast, the annual average ET was increased from 863.4 mm to 868.3 mm (by 0.57%) between 2000 and 2018, as a result of the increase in agroforestry through replantation activity, and gradual expansion of cultivation land. The water yield increased from 306.6 mm to 324.9 mm between 1988 and 2000 and diminished to 319.9 mm in 2018. The water yield in 2018 was less than that in 2000 as it is mainly the summation of surface runoff, lateral flow, and baseflow. Thus, the decrease in base flow and lateral flow and slight increment of surface runoff in 2018 reduced the total upsurge of water yield.

Table 5: Annual mean hydrological components (1988-2018) during the different LULC periods

Hydrological	Study periods			Relative changes (%)		
Components (mm)	1988	2000	2018	1988-2000	2000-2018	1988-2018
Surface Runoff	151.4	173.1	175.0	14.33	1.10	15.6
Lateral Flow	69.2	67.7	65.0	-2.17	-4.00	-6.07
Baseflow	89.0	84.1	79.9	-5.5	-4.99	-10.22
Water Yield	306.6	324.9	319.9	5.97	-1.54	4.34
Evapotranspiration	880.5	863.4	868.3	-1.94	0.57	-1.38
Percolation	287.9	281.8	277.7	-2.12	-1.42	-3.54

The results of baseflow, lateral flow and percolation (Table 5) show reduction throughout the study periods. Because the depletion in vegetation cover added to low penetration and canopy interception so that the incoming rainfall was converted to surface runoff (Nie *et al.* 2011, Ayele *et al.* 2017, Liyew *et al.* 2019b). On the other hand, the translation of forest evergreen and grassland to the cultivation and urban areas resulted in escalations in impervious surface covers (Gyamfi *et al.* 2016). Also, on cultivated land, the soil particles are easily detached by the impact of rainfall. Consequently, upper layers of the pores are clogged, which leads to a reduction in the infiltration rate. As a result, the consistent increase in surface runoff was observed (Table 5).

The results of this study are in agreement with other research studies (Gashaw *et al.* 2018) within the Andassa watershed, Blue Nile Basin, Ethiopia, (Ayele *et al.* 2017) inside the Upper Blue Nile Basin, Ethiopia, who found that cultivation lands are expanding at the cost of vegetation covers. As a result, surface runoff is enhanced, and baseflow diminished. Nie *et al.* (2011) and Gyamfi *et al.* (2016) also ascribed the overall escalation of surface runoff to the growth of urban area and cultivation and the shrinking of vegetation covers.

3.4 Response of Hydrological Components to LULC Changes at Sub-basin Level

The spatial distributions of the changes of major LULC classes and the yearly mean hydrological components between 1988 and 2018 are shown in Figures 6 and 7, respectively. Changes in land use mainly occurred in the central and southern parts of the basin (Figure 6). Cultivation land is mainly expanded to the southern and north-eastern parts of the basin at the expense of forest evergreen, agroforestry, and grassland. The most significant increase in surface runoff and decrease in groundwater flow also mainly occurred in the central and southern parts of the basin (Figure 7). The average annual surface runoff in all sub-basins was increased by 28.61 mm. Surface runoff changes in the basins increased in almost all sub-basins, especially in the central and downstream of the basin following the conversion of forest evergreen, agroforestry, and grassland to cultivated and urban areas. Nevertheless, the decrease in surface runoff has also occurred in the northwestern part of the basin concerned with the increment of agroforestry. The spatial distribution of water yield showed a nearly similar trend with surface runoff.

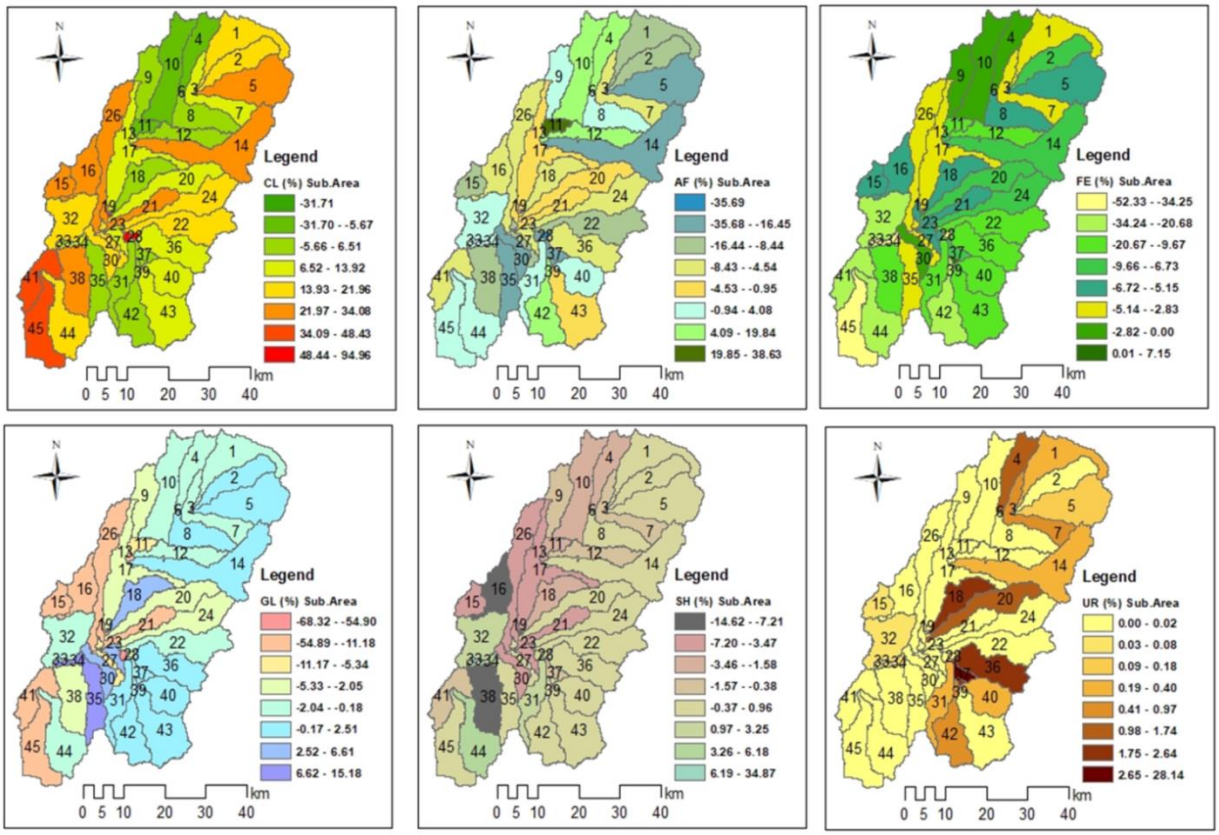

Figure 6: Spatial distributions of changes in LULC classes at sub-basin-level during the period 1988 to 2018

The baseflow in 45 sub-basins demonstrated a decreasing pattern during 1988 and 2018, with the most significant reduction in southern and central parts of the basin. Meanwhile, the yearly average ET in all sub-basins decreased by 15.13 mm, with a most extreme decrease in the southern part of the basin (Figure 7). However, in certain parts of the basin, ET increased by a maximum of 55.26 mm at sub-basin 6. Generally, ET decreased in the southern and south-eastern parts of the basin. The resilient nature of cultivation and urban area reveals a decline in the recharge rate, which appeared by the spatial trend of percolation in many sub-basins. Sub-basins which have experienced a more significant increment of cultivation and urban areas generate more surface runoff and water yield and contrasting effect to other hydrological components. Marhaento *et al.* (2017) argue that the impact of land-use changes on the water budget elements varied in different sub-basins depending on the scale of changes in LULC classes.

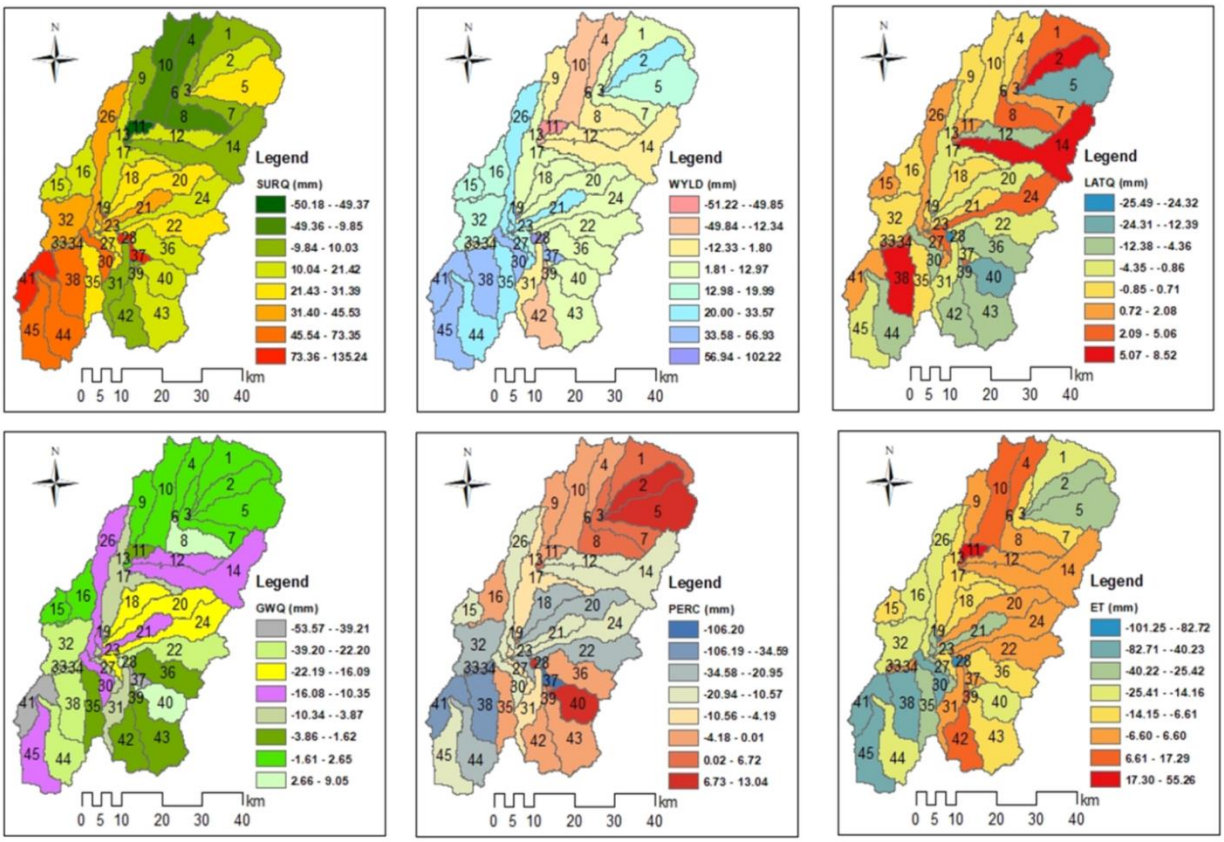

Figure 7: Spatial distributions of changes in the hydrological components at sub-basin-level during the period 1988 to 2018

Note: SURQ: Surface runoff; WYLD: Water yield; GWQ: Baseflow; LATQ: Lateral flow; PERC: Percolation; ET: Evapotranspiration

The sub-basins level (Figure 7) impacts of LULC change on hydrological elements were higher than the entire basin level (Table 5). Hence, more articulated changes of hydrological components were observed at the sub-basin level because of the uneven spatial distribution of LULC alterations. The impacts of LULC changes were more at a small scale. However, the responses of hydrological elements to LULC changes were relatively small at watershed level due to compensating effects (Gebremicael *et al.* 2019). Mwangi *et al.* (2016) also concluded that the impact of agroforestry was more at a smaller scale than the entire watershed.

3.5 Influence of Individual LULC Changes to Changes in Hydrological Components

The Pearson matrix of six LULC classes and six hydrological components are shown in Table 6. The results reveal that nearly all LULC classes have a fair association with different hydrological components. Correspondingly, appropriate correlations among the hydrological components are additionally observed. As an example, cultivated land had a positive correlation with surface runoff (0.82) and water yield (0.90) while its correlation with baseflow, lateral flow, percolation, and ET is negative (Table 6). The regression coefficients (Table 7) additionally confirmed that cultivated land influence surface runoff and water yield positively. However, its influence on baseflow, lateral flow, percolation, and ET is negative. Likewise, the correlation between surface runoff and water yield is positive, but is negative between surface runoff, water yield, and base flow, lateral flow, percolation, and ET (Table 6). Further, the Variable importance of the projection (VIP) values (Figure 8) shows that cultivated land is an essential factor for surface runoff, lateral flow and ET.

Grassland is seen to have an excellent association with surface runoff, water yield, lateral flow, and ET, with the correlation coefficient of -0.47, -0.57, +0.50, and +0.62, respectively. In contrast, grassland has a relatively low correlation with baseflow (-0.21) and percolation (-0.21). This is also attested by the regression coefficient (Table 7) that grassland influences lateral flow and ET positively, and surface runoff and water yield negatively. The positive impact of grassland on lateral flow and ET is due to a shallow vertical root system, which enables them to use water in the shallow soil that facilitates lateral flow and ET (Gyamfi *et al.* 2016). VIP values also confirm the grassland to be most impacting factor for lateral flow and ET (Figure 8).

Table 6: Pearson correlation matrix for changes in LULC and hydrological components between 1988 and 2018

Variables	CL	FE	AF	GL	SH	UR	SURQ	WYLD	GWQ	LATQ	PERC	ET
CL	**1.00**											
FE	-0.21	**1.00**										
AF	**-0.54**	-0.03	**1.00**									
GL	**-0.76**	-0.04	0.01	**1.00**								
SH	-0.28	**-0.63**	0.02	**0.39**	**1.00**							
UR	-0.13	0.07	-0.23	0.10	0.01	**1.00**						
SURQ	**0.82**	**-0.33**	**-0.67**	**-0.47**	-0.10	0.25	**1.00**					
WYLD	**0.90**	-0.20	**-0.69**	**-0.57**	-0.23	0.11	**0.95**	**1.00**				
GWQ	-0.09	**0.49**	**0.31**	-0.21	-0.26	**-0.48**	**-0.52**	-0.29	**1.00**			
LATQ	**-0.44**	0.09	0.09	**0.50**	0.06	0.00	**-0.38**	**-0.36**	-0.24	**1.00**		
PERC	-0.02	**0.38**	0.29	-0.21	-0.19	**-0.67**	**-0.48**	-0.25	**0.96**	-0.22	**1.00**	
ET	**-0.92**	0.15	**0.64**	**0.62**	0.24	0.12	**-0.87**	**-0.96**	0.09	**0.40**	0.00	**1.00**

Note: Values in bold are different from 0 with a significance level alpha=0.05. This is confirmed by the table of the p-values below (p-values < 0.0001)

Forest evergreen shows a high correlation with surface runoff, baseflow, and percolation, with the correlation coefficient of -0.33, +0.49, and +0.38, respectively. In contrast, forest evergreen shows a relatively low correlation with other hydrological components (Table 6). This is also attested by the regression coefficient (Table 7); surface runoff is influenced negatively and baseflow positively by forest evergreen. VIP values too confirm that forest evergreen is an essential contributor for baseflow and percolation. The correlation matrix reveals that the agroforestry is highly associated with surface runoff (-0.67), water yield (-0.69), baseflow (+0.31), and ET (0.64).

Table 7: PLSR coefficients - the positive and negative signs showed a position of influence

PLSR Model	Response Variables	PLSR predictors					
		CL	FE	AF	GL	SH	UR
PLSR1	SURQ	0.69	-0.87	-1.17	-0.44	-0.02	1.91
	WYLD	0.58	-0.47	-0.86	-0.50	-0.32	0.96
PLSR2	GWQ	-0.02	0.36	0.21	-0.13	-0.34	-1.37
	PERC	-0.04	0.58	0.34	-0.21	-0.56	-2.23
PLSR3	LATQ	-0.06	0.03	0.02	0.11	0.03	0.00
PLSR4	ET	-0.58	0.20	0.71	0.61	0.58	0.46

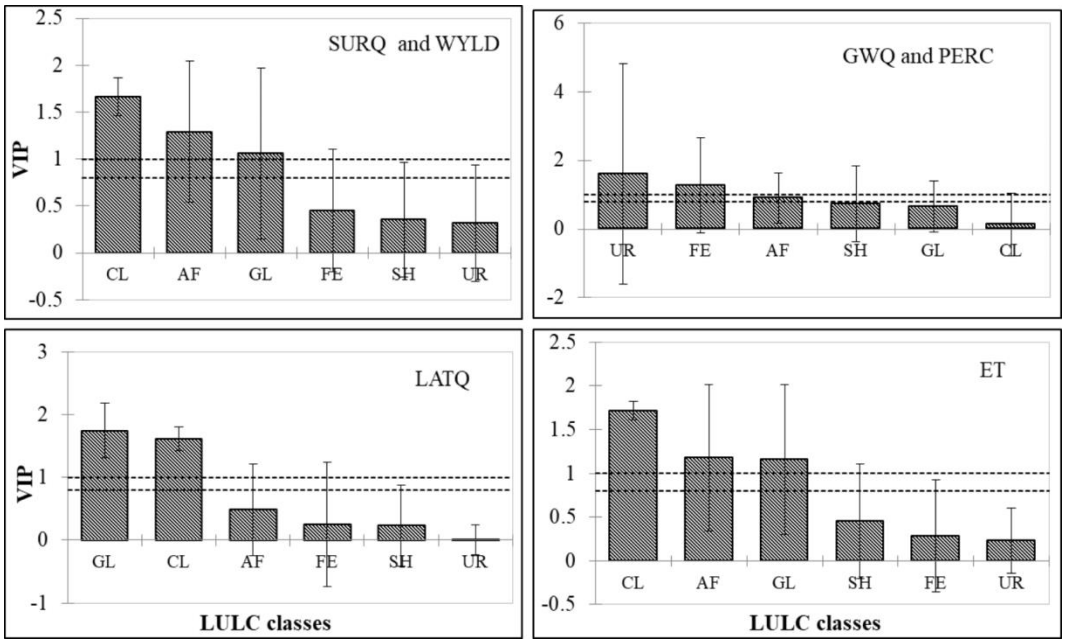

Figure 8: Variable Importance of Project (VIP) values at 95% significance level of the six LULC classes for hydrological components

Note: VIP > 0.8 is most relevant LULC classes to explain hydrological components; Horizontal dashed line showed VIP > 1, and VIP > 0.8

In general, the surface runoff and water yield are profoundly credited to change in the area of cultivation and urban areas. In contrast, baseflow, lateral flow, percolation, and ET are negatively related to change in cultivation and urban area. Moreover, baseflow, lateral flow, percolation, and ET are highly endorsed to alteration of forest evergreen, agroforestry, and grassland while surface runoff inversely correlates to it. The shrubland LULC classes also shows a positive and negative impact on all hydrological components (Table 7) though not significant statistically (Table 6), maybe because of the multicollinearity issue.

4. CONCLUSIONS

In this study, an attempt is made to assess the hydrological responses to LULC changes using the SWAT and PLSR model. The following conclusions are drawn from the study:

1. An assessment of LULC maps for 1988, 2000, and 2018 recommends that the most sizable changes happened in cultivation land, agroforestry, forest evergreen, grassland, and urban areas. The study shows an increase in a cultivated and urban area and a decline in forest evergreen, agroforestry, and grassland over the 31 years period between 1988 and 2018. However, the elevated agroforestry and gradual expansion of cultivation land over the period 2000 to 2018 validated that the environment used to be improving from devastating drought and wooded area clearing for firewood and cultivation.
2. Following an increase in cultivation and urban areas and a decline in forest evergreen, agroforestry, grassland, and shrubland, the annual mean surface runoff confirmed a persistently increasing trend from 151.4 mm in 1988 to 173.1 mm in 2000 and 175.0 mm in 2018. On the contrary, baseflow, percolation, and ET showed declining trends. More noticeable changes of hydrological components have been observed at the sub-basin scale, mainly associated with the uneven spatial distribution of LULC changes.
3. The Pearson correlation matrix confirmed nearly all LULC classes have a good relationship with different hydrological components. PLSR analysis revealed that cultivation, agroforestry, grassland, forest

evergreen, and urban areas are the most applicable variable to explain surface runoff, water yield, baseflow, and percolation for Gidabo basin. Likewise, lateral flow and ET were highly influenced via cultivation land, agroforestry, and grassland.

4. The study has attributed contributions of LULC changes to hydrological components, providing visible information that will allow stakeholders and decision-makers to make prominent choices regarding soil and water conservation measures and optimum allocation of water resources. However, the change in LULC is expected to continue in near-future and it will be crucial to examine its impact on future basin hydrology for planning future water management strategies. We also recommend further studies of the future climate change effects on the components of the water budget of Gidabo watershed.

ACKNOWLEDGEMENTS

The authors would like to express thanks to the National Meteorological Agency of Ethiopia and the Ministry of Water, Irrigation and Electricity (MoWIE) for providing the climate and hydrologic data respectively. The authors are also thankful to the United States Geological Survey (USGS) for the Landsat images and DEM data.

REFERENCES

Abbaspour, K.C., Vaghefi, S.A., and Srinivasan, R., 2017. A guideline for successful calibration and uncertainty analysis for soil and water assessment: A review of papers from the 2016 international SWAT conference. *Water*, 10 (1), 6.

Abbaspour, K.C., Yang, J., Maximov, I., Siber, R., Bogner, K., Mieleitner, J., Zobrist, J., and Srinivasan, R., 2007. Modelling hydrology and water quality in the pre-alpine/alpine Thur watershed using SWAT. *Journal of Hydrology*, 333 (2–4), 413–430.

Abdi, H., 2010. Partial least squares regression and projection on latent structure regression (PLS Regression). *WIREs Computational Statistics*, 2 (1), 97–106.

Ariti, A.T., van Vliet, J., and Verburg, P.H., 2015. Land-use and land-cover changes in the Central Rift Valley of Ethiopia: Assessment of perception and adaptation of stakeholders. *Applied Geography*, 65, 28–37.

Arnold, J.G., Srinivasan, R., Muttiah, R.S., and Williams, J.R., 1998. Large area hydrologic modeling and assessment part I: Model development. *JOURNAL OF THE AMERICAN WATER RESOURCES ASSOCIATION*, 34 (1), 73–89.

Ayele, T., Ahmed, N., Ribbe, L., and Heinrich, J., 2017. Hydrological responses to land use / cover changes in the source region of the Upper Blue Nile Basin , Ethiopia. *Science of the Total Environment*, 575, 724–741.

Baker, T.J. and Miller, S.N., 2013. Using the Soil and Water Assessment Tool (SWAT) to assess land use impact on water resources in an East African watershed. *Journal of Hydrology*, 486, 100–111.

Belihu, M., Abate, B., Tekleab, S., and Bewket, W., 2018. Hydro-meteorological trends in the Gidabo catchment of the Rift Valley Lakes Basin of Ethiopia. *Physics and Chemistry of the Earth*, 104, 84–101.

Berihun, M.L., Tsunekawa, A., and Haregeweyn, N., 2019. Exploring land use / land cover changes , drivers and their implications in contrasting agro-ecological environments of Ethiopia. *Land Use Policy*, 87, 104052.

Berihun, M.L., Tsunekawa, A., Haregeweyn, N., Meshesha, D.T., Adgo, E., Tsubo, M., Masunaga, T., Fenta, A.A., Sultan, D., Yibeltal, M., and Ebabu, K., 2019. Hydrological responses to land use/land cover change and climate variability in contrasting agro-ecological environments of the Upper Blue Nile basin, Ethiopia. *Science of the Total Environment*, 689, 347–365.

Carrascal, L.M., Galván, I., and Gordo, O., 2009. Partial least squares regression as an alternative to current regression methods used in ecology. *Oikos*, 118 (5), 681–690.

Chow , Ven T Maidment, D.R. and Mays, L.W., 1988. *Applied hydrology*. McGraw-Hill, New York.

Fang, N., Shi, Z., Chen, F., and Wang, Y., 2015. Partial Least Squares Regression for Determining the Control Factors for Runoff and Suspended Sediment Yield during Rainfall Events. *Water*, 7, 3925–3942.

Garg, V., Ramchandra, B., Kumar, P., Prasad, S., Kumar, P., and Kumar, S., 2019. Human-induced land use land cover change and its impact on hydrology. *HydroResearch*, 1, 48–56.

Gashaw, T., Tulu, T., Argaw, M., and Worqlul, A.W., 2017. Evaluation and prediction of land use/land cover changes in the Andassa watershed, Blue Nile Basin, Ethiopia. *Environmental Systems Research*, 6 (17).

Gashaw, T., Tulu, T., Argaw, M., and Worqlul, A.W., 2018. Modeling the hydrological impacts of land use/land cover changes in the Andassa watershed, Blue Nile Basin, Ethiopia. *Science of the Total Environment*, 619–620, 1394–1408.

Gebremicael, T.G., Mohamed, Y.A., Betrie, G.D., Zaag, P. Van Der, and Teferi, E., 2013. Trend analysis of runoff and sediment fluxes in the Upper Blue Nile basin : A combined analysis of statistical tests , physically-based models and landuse maps. *Journal of Hydrology*, 482, 57–68.

Gebremicael, T.G., Mohamed, Y.A., and Zaag, P. Van Der, 2019. Attributing the hydrological impact of different land use types and their long-term dynamics through combining parsimonious hydrological modelling , alteration analysis and PLSR analysis. *Science of the Total Environment*, 660, 1155–1167.

Gyamfi, C., Ndambuki, J.M., and Salim, R.W., 2016. Hydrological responses to land use/cover changes in the Olifants Basin, South Africa. *Water*, 8 (12), 588.

Legesse, D., Vallet-Coulomb, C., and Gasse, F., 2003. Hydrological response of a catchment to climate and land use changes in Tropical Africa: Case study south central Ethiopia. *Journal of Hydrology*, 275 (1–2), 67–85.

Marhaento, H., Booij, M.J., Rientjes, T.H.M., and Hoekstra, A.Y., 2017. Attribution of changes in the water balance of a tropical catchment to land use change using the SWAT model. *Hydrological Processes*, 31 (11), 2029–2040.

Mechal, A., Wagner, T., and Birk, S., 2015. Recharge variability and sensitivity to climate: The example of Gidabo River Basin, Main Ethiopian Rift. *Journal of Hydrology: Regional Studies*, 4, 644–660.

Monteith, J.L., 1965. Evaporation and environment.Symposia of the Society for Experimental Biology, 19 (2393175), 205–234.

Moriasi, D.N., Arnold, J.G., Van Liew, M.W., Bingner, R.L., Harmel, R.D., and Veith, T.L., 2007. Model Evaluation Guidelines for Systematic Quantification of Accuracy in Watershed Simulations. *Transactions of the ASABE*, 50 (3), 885–900.

Mwangi, H.M., Julich, S., Patil, S.D., McDonald, M.A., and Feger, K.H., 2016. Modelling the impact of agroforestry on hydrology of Mara River Basin in East Africa. *Hydrological Processes*, 30 (18), 3139–3155.

Neitsch, S.L., Arnold, J.G., Kiniry, J.R., and Williams, J.R., 2011. *Soil and Water Assessment Tool Theoretical Documentation Version 2009*. Texas Water Resources Institute.

Nie, W., Yuan, Y., Kepner, W., Nash, M.S., Jackson, M., and Erickson, C., 2011. Assessing impacts of Landuse and Landcover changes on hydrology for the upper San Pedro watershed. *Journal of Hydrology*, 407 (1–4), 105–114.

Niraula, R., Meixner, T., and Norman, L.M., 2015. Determining the importance of model calibration for forecasting absolute / relative changes in streamflow from LULC and climate changes. *Journal of Hydrology*, 522, 439–451.

Schilling, K.E., Gassman, P.W., Kling, C.L., Campbell, T., Jha, M.K., Wolter, C.F., and Arnold, J.G., 2014. The potential for agricultural land use change to reduce flood risk in a large watershed. *Hydrological Processes*, 28 (8), 3314–3325.

Setegn, S.G., Srinivasan, R., Dargahi, B., and Melesse, A.M., 2009. Spatial delineation of soil erosion vulnerability in the Lake Tana Basin , Ethiopia. *Hydrol. Process.*, 3750, 3738–3750.

Shawul, A.A., Chakma, S., and Melesse, A.M., 2019. The response of water balance components to land cover change based on hydrologic modeling and partial least squares regression (PLSR) analysis in the Upper Awash Basin. *Journal of Hydrology: Regional Studies*, 26, 100640.

Shi, Z.H., Ai, L., Li, X., Huang, X.D., Wu, G.L., and Liao, W., 2013. Partial least-squares regression for linking land-cover patterns to soil erosion and sediment yield in watersheds. *Journal of Hydrology*, 498, 165–176.

USDA-SCS, 1972. *National Engineering Handbook,Section 4:Hydrology*. Washington, DC.

Wagner, P.D., Kumar, S., and Schneider, K., 2013. An assessment of land use change impacts on the water resources of the Mula and Mutha Rivers catchment upstream of Pune, India. *Hydrology and Earth System Sciences*, 17 (6), 2233–2246.

WWDSE, 2007. *Study and Design of Gidabo Irrigation Project, final feasibility report*. Addis Ababa.

Yan, B., Fang, N.F., Zhang, P.C., and Shi, Z.H., 2013. Impacts of land use change on watershed streamflow and sediment yield : An assessment using hydrologic modelling and partial least squares regression. *Journal of Hydrology*, 484, 26–37.

Yan, R., Zhang, X., Yan, S., Zhang, J., and Chen, H., 2018. Spatial patterns of hydrological responses to land use / cover change in a catchment on the Loess Plateau , China. *Ecological Indicators*, 92, 151–160.

Zhang, L., Nan, Z., Xu, Y., and Li, S., 2016. Hydrological impacts of land use change and climate variability in the headwater region of the Heihe River Basin, northwest China. *PLoS ONE*, 11 (6).

Zhou, F., Xu, Y., Chen, Y., Xu, C.Y., Gao, Y., and Du, J., 2013. Hydrological response to urbanization at different spatio-temporal scales simulated by coupling of CLUE-S and the SWAT model in the Yangtze River Delta region. *Journal of Hydrology*, 485, 113–125.

Remote Sensing-based River Discharge Estimation for a Small River Flowing Over the High Mountain Regions of the Tibetan Plateau

Mulugeta Kebede Genanu [1, 2] and Lei Wang[1,*]

[1]*Key Laboratory of Tibetan Environment Changes and Land Surface Processes, Institute of Tibetan Plateau Research, Chinese Academy of Sciences, and CAS Center for Excellence in Tibetan Plateau Earth Sciences, Beijing, China*
[2]*Arba Minch Water Technology Institute, Faculty of Meteorology and Hydrology, Arba Minch University, Arba Minch, Ethiopia*
**Corresponding author*

ABSTRACT

River discharge, as one of the most essential climate variables, plays a vital role in the water cycle. Small-scale headwater catchments including high-mountain regions of Tibetan Plateau (TP) Rivers are mostly ungauged. Satellite technology shows its potential to fill this gap with high correlation of satellite-derived effective river width and corresponding in-situ gauged discharge. This study is innovative in estimating daily river discharge using modified Manning equation (Model 1), Bjerklie et al. (2003) equation (Model 2), and Rating curve approach (Model 3) by combining river surface hydraulic variables directly derived from remote sensing datasets with other variables indirectly derived from empirical equations, which greatly contributes to the improvement of river flow measurement information especially over small rivers of TP. We extracted the effective width from Landsat image and flow depth via hydraulic geometry approach. All the input parameters directly or indirectly derived from remote sensing were combined and substituted into the fundamental flow equations/models to estimate discharges of Lhasa River. The validation of all three models' results against the in-situ discharge measurements shows a strong correlation (the Nash–Sutcliffe efficiency coefficient (NSE) and the coefficient of determination (R^2) values ≥ 0.993), indicating the potentiality of the models in accurately estimating daily river discharges. Trends of an overestimation of discharge by Model 1 and underestimation by Model 2 are observed. The discharge estimation by using Model 3 outperforms Model 1 and Model 2 due to the uncertainties associated with estimation of input parameters in the other two models. Generally, our discharge estimation methodology performs well and shows a superior result as compared with previously developed multivariate empirical equations and its application for other places globally can be the focus of upcoming studies.

Keywords: *River discharge estimation, remote sensing, effective width, hydraulic relationship, Tibetan Plateau*

1. INTRODUCTION

Rivers are complex systems of natural stream water flowing in channels which have a key role in the water cycle both as the main source of water supply and transporting mechanism of surface runoff to the water bodies for many human lives and ecosystems. Meybeck et al. (1996) had classified the size of rivers based on their discharge characteristics, drainage area, and river width and according to this classification; rivers with width of 40 – 200 m are defined as small rivers, while those rivers with width of 200 – 800 m and 800 – 1,500 m are defined as medium-sized rivers and large rivers, respectively.

River discharge is one of the essential climate variables in the water cycle which regulates the climate system and indicates its changes. Even though, the necessity of river discharge information for different applications related to water resources management is well known, many basins are not still gauged and, recently the gauged ones are also declining and inaccessibility of data due to different economic and political reasons contributes to the global problem (Tarpanelli et al., 2013; Hossain et al., 2014; Gleason and Hamdan, 2015; Tourian et al., 2017; Gleason et al., 2018; Feng et al., 2019). It is particularly important to note that many small to medium sized rivers are also poorly monitored (Huang et al., 2019).

The difficulty of discharge estimation in natural channels due to the shortage and even sometimes non-existence of discharge measurements highly affects management of water resources; while the remote sensing has provided an additional opportunity to get streamflow information to efficiently monitor water resources with stage and

discharge as essential variables (Sulistioadi et al., 2015; Wang et al., 2019). The innovation of technology, knowledge, and economic assets for efficient and effective water resources monitoring with an initiatives of establishing database for large global lakes, reservoirs and rivers are increasing rapidly (e.g., Gao et al., 2015; Sichangi et al., 2016), but a due attention is not given for small rivers (Sulistioadi et al., 2015). Therefore, due to this fact the need of a special attention for space-based discharge estimation study in small-medium sized rivers (e.g., most headwater segments for large rivers) is essential and also mandatory.

A successful remote sensing based discharge estimation techniques will always depend on the accuracy of the estimated parameters that can be directly (width, slope and stage) or indirectly (velocity and bathymetry depth) obtained from satellite sensors and the techniques related with the measurement of these multiple hydraulic variables (Pan et al., 2016; Sichangi et al., 2016, 2018). The modified Manning equation, and Bjerklie model (Bjerklie et al., 2003) were selected to estimate the discharge of Lhasa River because of input data availability, inclusiveness of multiple surface hydraulic variables to represent channel morphological characteristics, simplicity and ability to compute discharge especially in non-braided channels.

2. MATERIALS AND METHODS

2.1. Description of the Study Area

The Tibetan Plateau (TP) also known as "Roof of the World" or the "Water Tower of Asia" is the home-base of major rivers flowing in the vast areas of the Asian continent covering 2.5 million km^2 areas with large cryosphere, exerts huge effects on the Earth's climate system (Cuo et al., 2014; Liu et al., 2018). The geographical location of Lhasa River basin (LRB) ranges from 29°20' - 31°15' N and 90°05' - 93°20' E along the northern ranges of the Himalayas (Fig. 1). The Lhasa River with a length of 551 km is one of the five major tributaries of the Yarlung Zangbo River. The LRB elevation ranges from 3570 m above sea level (a.s.l.) at the plain area downstream end up to 7136 m a.s.l. at the Mountains peak, with an average gradient of 2.9 % (Prasch, 2010). The basin as a typical continental plateau of semi-arid frigid region have colder climate with lowest and highest monthly air temperature of –2 °C and 15 °C occurring in January and June, respectively. The lowest and highest potential evapotranspiration of the basin also occurs during the winter and summer seasons, respectively (Shi et al., 2014). The basin's mean air-temperature annually varies between –9 °C and +10 °C, while the mean relative humidity at Lhasa station is 69 % (Singh et al., 2004; Prasch et al., 2013).

The LRB climate is highly affected by the uneven distribution and seasonal variation of annual precipitation (about 630 mm) falling during the summer monsoon months (Prasch et al., 2013; Peng et al., 2015). The basin receives its vast portion of annual total-runoff (about 90%) during the summer months and the rest during the winter months. The basin also experiences seasonally frozen ground and glaciers development that highly contributes to the overall runoff mainly in summer and its glacial coverage is about 670 km^2 (2 % of whole basin area) (Lin et al., 2008; Prasch et al., 2013). Its land use is dominantly covered by grassland with different types of vegetation and the major soil types include: Alpine meadow, shrub-steppe, and sub-alpine meadow soils (Makokha et al., 2016).

The mean flow volume of Lhasa River has been 6×10^{11} m^3 that is almost $1/8^{th}$ of the Yellow River of China (Peng and Du, 2010) and it is contributed from precipitation, melt-water and groundwater (Liu, 1999). The monthly mean runoff variation in summer season is highly affected by precipitation while during the winter season it is mainly affected by temperature (Lin et al., 2008). The Lhasa River is the main source of water for the entire growth and development of Lhasa city and rural areas in Tibet and due to its high exploitation, understanding and quantifying its water budget including the dynamic changes of streamflow in the basin by using remote sensing approaches is highly essential. In this study, the upper LRB (above the Tanggya gauge) covering an area of approximately 20,367 km^2 is considered.

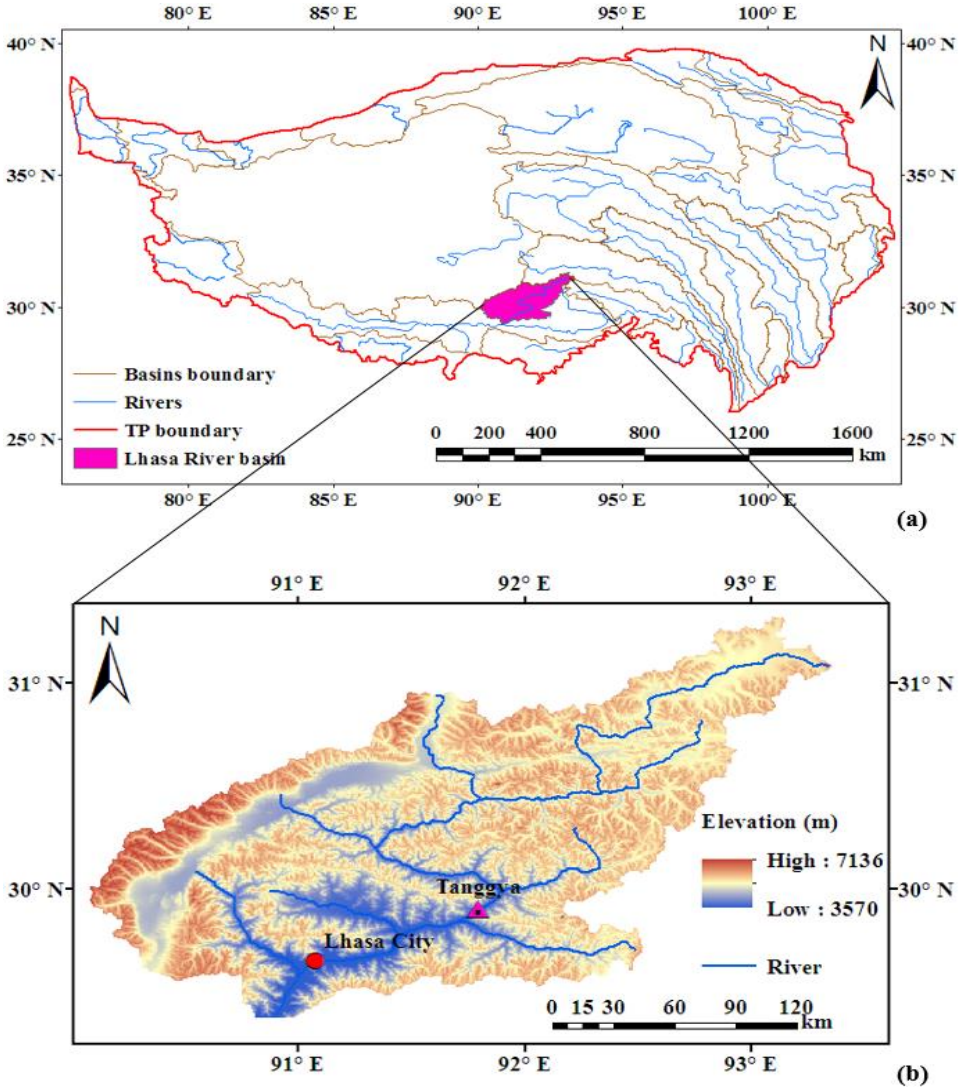

Figure 1: (a) Geographical location of the Tibetan Plateau region and (b) the elevation of the Lhasa River basin (LRB) based on the digital elevation model from the Shuttle Radar Topography Mission

2.2 In-situ Gauge Data

Observed discharge and stage data of Lhasa River at Tanggya gauging station from 1999–2018 were collected from China Ministry of Water Resources (MWR) and used to develop the hydraulic relationship (rating curve) to determine the unknown parameters in discharge estimation and also for validation of the models. Generally, from 1999 – 2013, the observed flow data at Tanggya gauge site of Lhasa River were limited and mainly available in the flooding season days and this makes limited number of Landsat images to be processed and analyzed in this period to estimate discharge as compared to the period of 2014–2018 where relatively better *in-situ* gauge data were available.

2.3 Satellite Data

The SRTM DEM tiles data over the Lhasa River basin with 30m resolution had been downloaded (https://earthexplorer.usgs.gov) and processed to extract and estimate the channel slope and the relief of LRB is shown in Fig. 1. In this study a total of 52 relatively good quality Landsat images with 30 m resolution had been accessed (https://earthexplorer.usgs.gov) and processed for capturing water surface area changes and to extract the effective in-bank width of Lhasa River by using the modified normalized difference water index (MNDWI)

approach during the study period (1999 to 2018). The quality of all downloaded Landsat images around the Lhasa River cross sections has been manually inspected and those images highly affected by clouds and snow are rejected again.

2.4. Methodology

2.4.1. Water Surface Area and Effective In-bank River Width Extraction from Landsat Images

To derive an accurate river width measurement, we firstly calculated the water surface areas across the given river reach and then divided it by the appropriate river reach length, which is a preferable method to measure width at a given river cross section (Brakenridge et al., 2007). Therefore, calculation of the Lhasa River width is done by dividing the water surface area (*A*) extracted from the Landsat images to the selected appropriate river reach length (*L*) by selecting relatively uniform river cross section to avoid error of width measurement in the braided river sections (Sichangi et al., 2016), as is shown in Eq. (1):

$$W = \frac{A}{L} \tag{1}$$

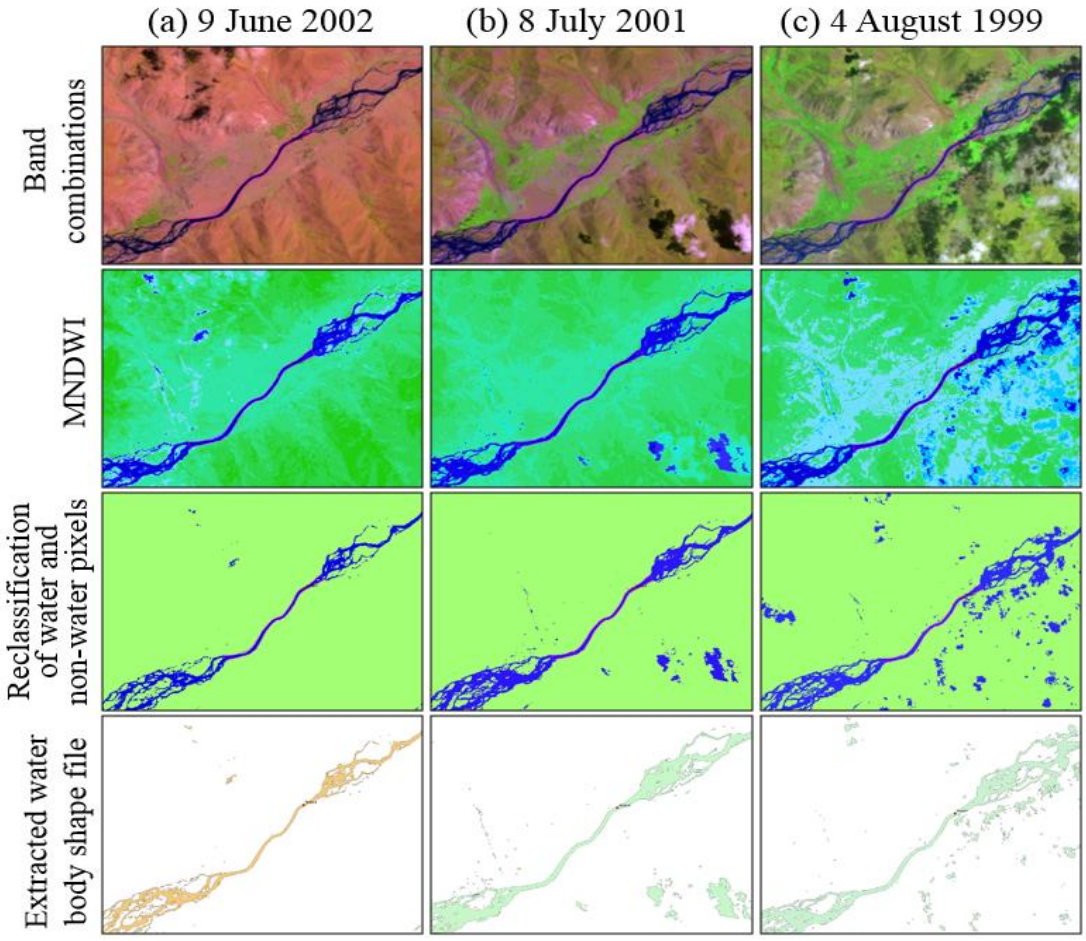

Figure 2: An examples of Landsat image classification to estimate water surface area and/or effective width of Lhasa River during 4 August 1999 (a), 8 July 2001 (b), and 9 June 2002 (c) among 52 cloud free Landsat images used in this study

Many studies had evaluated the performance of various indices for water body extraction of different river basins and found that the modified normalized difference water index (MNDWI) outperforms the other indices,

especially for rivers flowing through high hill regions in the TP (Ji et al., 2009; Duan and Bastiaanssen, 2013; Huang et al., 2018). Therefore due to this fact, we have chosen the MNDWI for detecting and measuring the changes of Lhasa River water surface area and then to calculate its effective width (Fig. 2) by using Eq. (1).

$$\text{MNDWI} = \frac{\rho_{\text{Green}} - \rho_{\text{MIR}}}{\rho_{\text{Green}} + \rho_{\text{MIR}}} \quad (2)$$

where ρ_{Green} and ρ_{MIR} are the top-of-atmosphere (TOA) reflectances for green and middle-infrared bands, respectively. Bands 2 and 5 are the corresponding bands for Landsat TM and ETM+ sensors.

2.4.2 Method of Slope (S) Estimation

We calculated the slope of the Lhasa River viably over its appropriate reach length (RL) from the SRTM DEM by extending its RL (over which discharge gauge site is located) to a sufficient distances that can accommodate the height variations so as to minimize the errors introduced in slope estimations (LeFavour and Alsdorf, 2005). The altitude of river's centreline was derived from the SRTM DEM (Fig. 3). For 252 km course of Lhasa River considered from upstream of the Zhikong dam site to its mouth at the junction of Yarlung Zangpo River, the resultant mean height error was 1.98 m km^{-1} and its standard deviation was 3.67 m km^{-1}. The average slope for this mentioned section of the channel was 0.002 m m^{-1}. By considering the LRB's topography the change in slope is estimated to be cm over km.

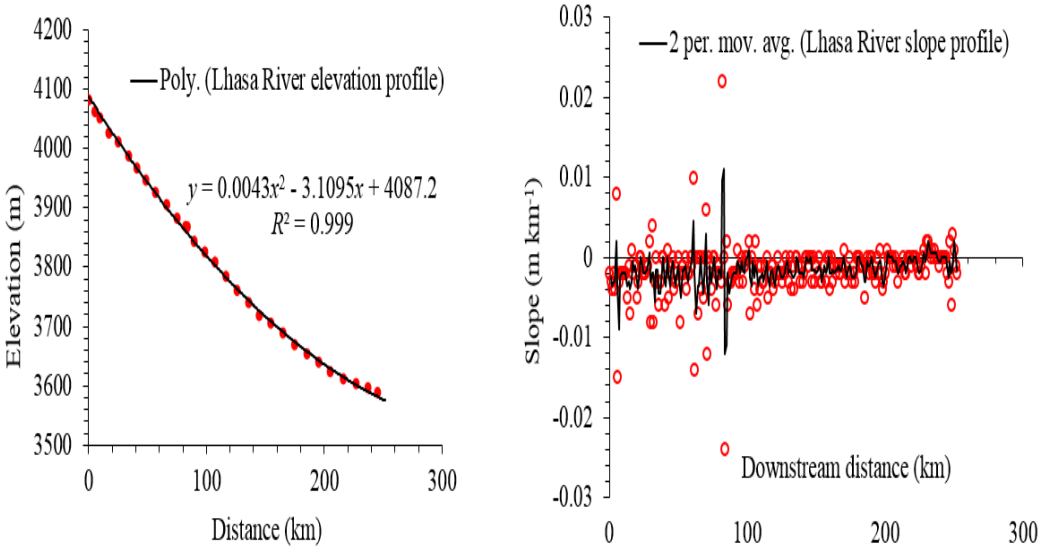

Figure 3: Lhasa River Slope derived from the water surface elevations, by measuring the change in elevation over flow distance between pixels by using the SRTM DEM data

2.4.3. Method of Roughness Coefficient (n) Estimation

The channels resistance is highly influenced by vegetation, materials involved, effect of obstruction, degree of meanders and channel irregularity (Coon, 1998). And for its estimation various approaches including visual interpretation and assigning proper tabulated values (Table 1) (Chow, 1959), the ground surveys/measurements in particular on narrower channels (Dudley et al., 1998) and the use of empirical equations/formulas (Cowan, 1956) are well known. In this study, we used high resolution Landsat images classification and band combination approach with visual interpretation to distinguish the existing channel conditions and features along the LRB Tanggya gauge site.

The detail procedure of channel roughness coefficient (n) extraction methodology through visual interpretation of Landsat imagery to distinguish the channel conditions and estimate n by using Eq.(3) can be found in Sichangi et al. (2018) which is an approach based on the Chow (1959) methodology as shown in Table 1. Therefore, the same methodology based on the context of Lhasa River morphological characteristics around the Tanggya gauging site had been applied in this study. Generally, a fair and stable channel condition (n_0) with a value of 0.025 (Albertson and Simons, 1964), minor to moderate degree of irregularity (n_1), alternating occasionally river cross-section (n_2), negligible or insignificant obstructions (n_3) to highly affect the channel flow pattern, low vegetation (n_4) with a value of 0.005, and finally minor channel meandering (n_5) with a ratio of 1.05 were used to calculate n by using Eq. (3).

$$n = (n_0 + n_1 + n_2 + n_3 + n_4)\, n_5 \qquad (3)$$

Table 8: Values for the computation of the roughness coefficient (Chow, 1959)

Channel conditions			Values
Material involved	Earth	n_0	0.025
	Rock cut		0.025
	Fine Gravel		0.024
	Course Gravel		0.027
Degree of irregularity	Smooth	n_1	0.000
	Minor		0.005
	Moderate		0.010
	Severe		0.020
Variation of channel cross-section	Gradual	n_2	0.000
	Alternating occasionally		0.005
	Alternating frequently		0.010–0.015
Relative effect of obstructions	Negligible	n_3	0.000
	Minor		0.010–0.015
	Appreciable		0.020–0.030
	Severe		0.040–0.060
Vegetation	Low	n_4	0.005–0.010
	Medium		0.010–0.025
	High		0.025–0.050
	Very high		0.050–0.100
Degree of meandering	Minor	n_5	1.000
	Appreciable		1.150
	Severe		1.300

2.4.4. Method of Depth Estimation

Moody and Troutman (2002) had formulated a regression relations (Eq. (4)–(5)) in width and depth against discharge (Q) to calculate a universal scale of width and depth for a subset of world rivers ($\hat{W} = aQ^b$ and $\check{D} = cQ^f$). Where a, b, c, and f are empirical constants, and $\hat{W}$ and $\check{D}$ are the mean width and depth, respectively.

Satellite altimetry data to estimate water level or depth of small-medium sized rivers including the Lhasa River is not available and because of this fact we had estimated the mean depth from our own effective width estimation and the derived hydraulic geometry relationships (Eq. (4)–(5)). The method is simple, practical and effective in which the widths calculated from Landsat images were utilized to compute the average depths. This was done by

manipulating Moody and Troutman's formula and putting the width data in the depth formula to calculate depth on a sub-reach scale as follows:

$$\hat{W} = 7.2\ Q^{0.50\pm0.02} \quad (a{:}2.6–20.2) \tag{4}$$

$$\check{D} = 0.27\ Q^{0.39\pm0.01} \quad (c{:}0.12–0.63) \tag{5}$$

where the ranges of *a* and *c* are as indicated above and the associated errors in Eq. (4) and Eq. (5) are 0.22 and 0.18 m, respectively.

2.4.5. Method of Discharge Estimation

There is no direct method of *in-situ* or space based river discharge estimation and rather it is calculated from the observation of hydraulic flow parameters through mathematical formulations or calibrated relationships (rating curves).

From the Manning's fundamental open channel flow equation, Sichangi et al. (2016, 2018) and Huang et al. (2018) had deduced and developed hydraulic relations which could potentially estimate discharges from space for commonly known ideal river cross-sections. In addition, for wider rivers (rivers whose width is ten times greater than their depth), the discharge can be estimated using Eq. (6) (LeFavour and Alsdorf, 2005).

$$Q = \frac{S^{\frac{1}{2}}}{n} W D^{\frac{5}{3}} \tag{6}$$

where W is width , n is channel roughness coefficient, D is depth of river flow and S is slope of the channel.

Discharge estimation based on statistically derived equations with accurately estimated input parameters is also promising nowadays and Bjerklie et al. (2003) had developed a hydraulic equation (Eq. (7)) to estimate river discharges from space with the same approach.

$$Q = 7.22 W^{1.02} D^{1.74} S^{0.35} \tag{7}$$

River discharge estimation by developing hydraulic geometry relationship along the channel cross section is also a known methodology practiced by many researchers (Leopold and Thomas, 1953; Singh and Zhang, 2008; Gleason and Smith, 2014). Therefore, we had also adopted this methodology to estimate Lhasa River discharge by developing hydraulic relationship between remote sensing based effective river width and observed discharge using Eq. (8).

$$W = aQ^{b} \tag{8}$$

where a and b are calibrated numerical constants identified in deriving the hydraulic relationship.

Therefore, Eq.(6)–(8) were used to estimate Lhasa River discharges with multiple remote sensing datasets. Then we carefully compared our discharge estimation results based on the methodology indicated in Eq. (6) (herein after Model 1) with Eq. (7) (herein after Model 2) and Eq. (8) (herein after Model 3).

2.4.6. Evaluation of Model Performance

After we estimated the Lhasa River discharge by using the three models, we evaluated their performance by using the following metrics.

$$\text{Root mean square error (RMSE)} = \sqrt{\left(\frac{\Sigma(Q_m - Q_e)^2}{k}\right)} \quad (9)$$

$$\text{Relative root mean square error (RRMSE)} = \frac{\text{RMSE}}{\overline{Q_m}} \times 100\% \quad (10)$$

$$\text{Nash–Sutcliffe efficiency coefficient (NSE)} = 1 - \frac{(Q_m - Q_e)^2}{(Q_m - \overline{Q_m})^2} \quad (11)$$

$$\text{Mean bias error (MBE)} = \frac{1}{k}\sum_1^k (Q_e - Q_m) \quad (12)$$

$$\text{Relative error (RE)} = \frac{\sum_1^k Q_e - \sum_1^k Q_m}{\sum_1^k Q_m} \times 100\% \quad (13)$$

where Q_m is the measured discharge, Q_e is the estimated discharge, $\overline{Q_m}$ denotes the mean value of measured discharge, and k represents the total number of observations.

3. RESULTS AND DISCUSSIONS

3.1. Results of River Effective Width Extracted from Landsat Image

The reach average surface water extent of Lhasa River had been measured with Landsat sensor visible and middle infrared bands in the selected non-braided section of the river around Tanggya gauging site (Fig. 3). The effective river width during the study period 1999–2018 (52 data points) had been estimated and the plot also shows its temporal variations following the hydrological wet and dry seasons in the basin. The minimum, maximum and mean effective width estimations for the 52 Landsat images processed during the study period (1999–2018) were 41.0 m, 183.0 m and 85.1 m, respectively (Fig. 4).

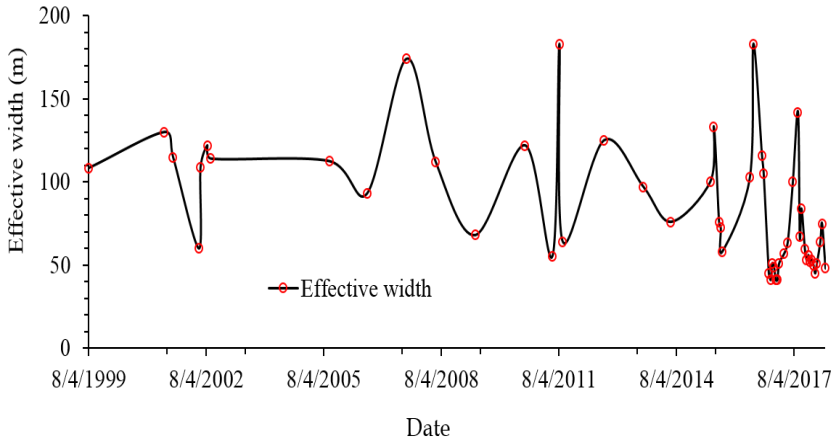

Figure 4: The time series of effective width of Lhasa River derived from 52 clouds free Landsat images during 1999–2018.

3.2. Results of Mean Depth Estimation

Monitoring of small (40–200 m wide) and medium size (200–800 m wide) rivers via satellite altimetry is very difficult because of their geographical orientation (Sulistioadi et al., 2015) and hence, due to lack of this data across Lhasa River, the mean depth was calculated by using Eq. (4) and Eq. (5). The minimum, maximum and mean depth estimations for the 52 Landsat images processed during the study period were 1.0 m, 3.4 m and 1.8 m, respectively. The variation of the mean depth also follows the hydrological wet (maximum depth) and dry seasons (minimum depth) in the basin (Fig. 5). The method of mean depth estimation used in this study was feasible especially for narrow mountainous rivers such as Lhasa, missing satellite altimetry data due to its geographic orientation.

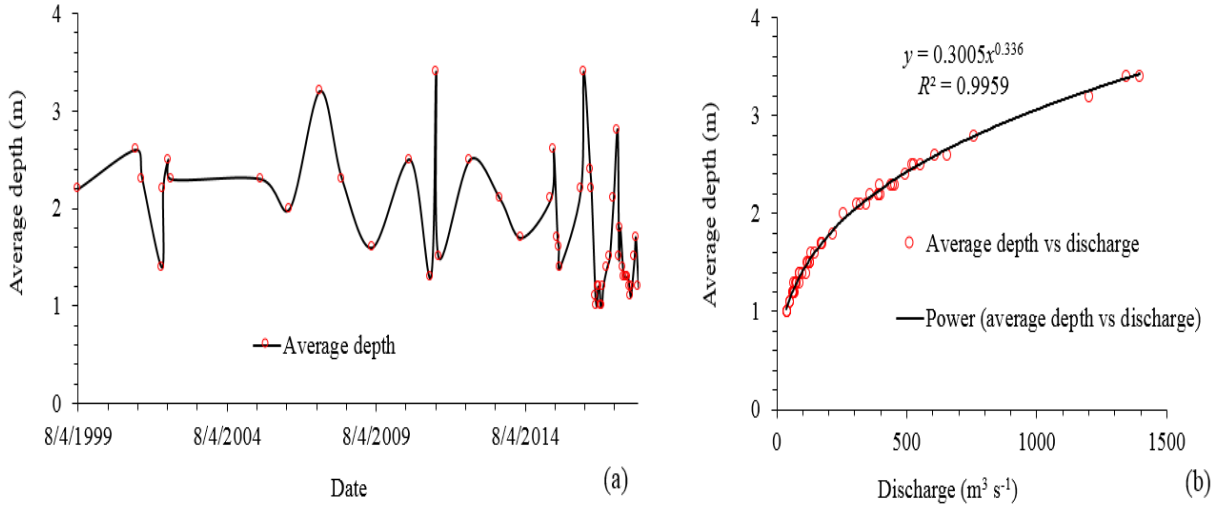

Figure 5: The time series of mean flow depth estimated from the hydraulic geometry relationship equation (a) and rating curve of estimated mean flow depth and observed discharge (b) (1999–2018).

3.3 Derivation of Hydraulic Relationships (Rating Curves)

3.3.1. Observed Stage vs Discharge Rating Curve

As shown in Fig. 6, we developed the Lhasa River rating curve by using the measured stage and discharge data at Tanggya gauge during the study period (1999–2018). The minimum, maximum and mean observed water height (stage) and discharge of Lhasa River during the study period was 1.9 m, 6.2 m and 3.7 m, and 19 m^3s^{-1}, 2080 m^3s^{-1}, 505.2 $m^3 s^{-1}$, respectively.

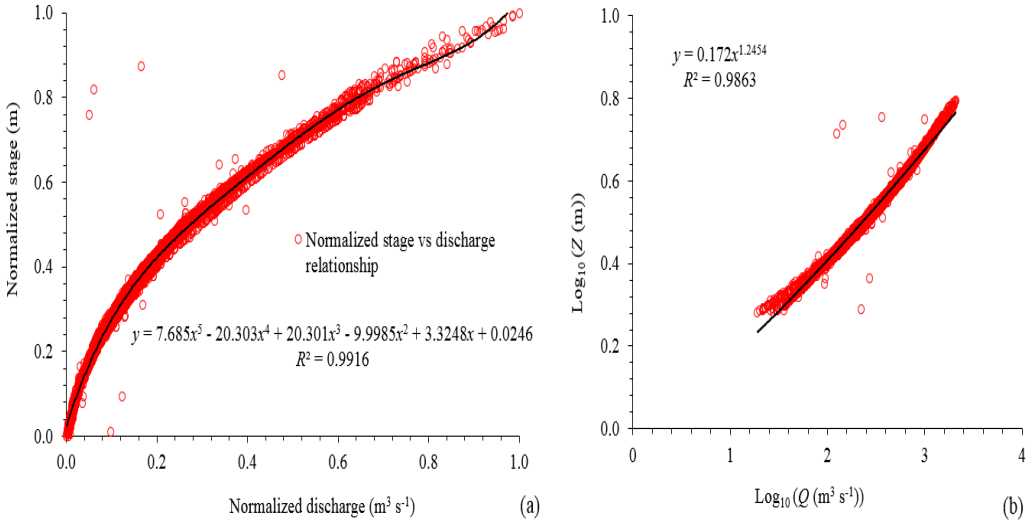

Figure 6: Scatterplots of normalized stage-discharge rating curve (a) and its logarithmic transformed curve (b) of Lhasa River developed by using the *in-situ* measurement of stage and discharge data at Tanggya gauge from 1999–2018.

3.3.2. Effective Width and Water Surface Area vs Observed Discharge Rating Curve

The rating curve showing the hydraulic relation between surface-water extents (width and/or inundation area) and the *in-situ* discharge were made and they have exponential relation with a strong correlation (Fig. 7). The two hydraulic relationships (curves) developed here can represent the potential and possibility of predicting discharges in the absence of gauge data for continuous river flow measurement over the LRB.

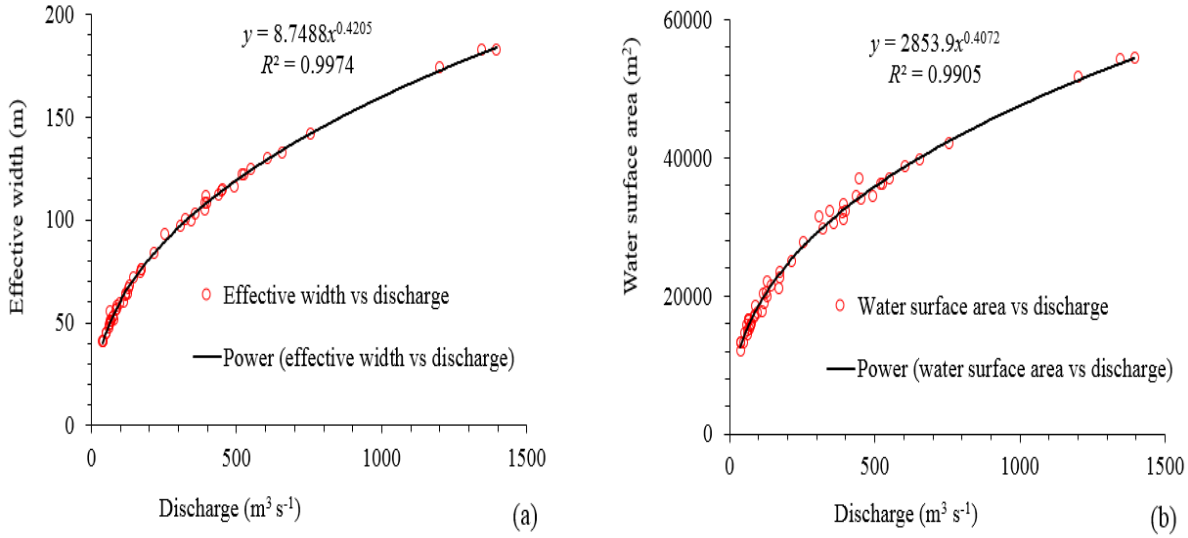

Figure 7: Scatterplots of effective width (a) and water surface inundation area (b) derived from Landsat images versus river discharge measured at Tanggya gauging station (1999–2018).

3.3.3. Effective Width and Water Surface Area vs Observed Stage Rating Curve

The river width extracted from space and stage has good correlation (Leduc et al. 2018). In this study we also developed the hydraulic relationship of water height (stage) with water surface width and area for a narrow river in a high mountain region and found a positive linear relationship (Fig. 8). The river width information can tell us about the channel hydraulic geometry in which a comparatively shallow segment of the channel gives substantially wider flow with rising stage and hence it can be used to estimate stage reliably.

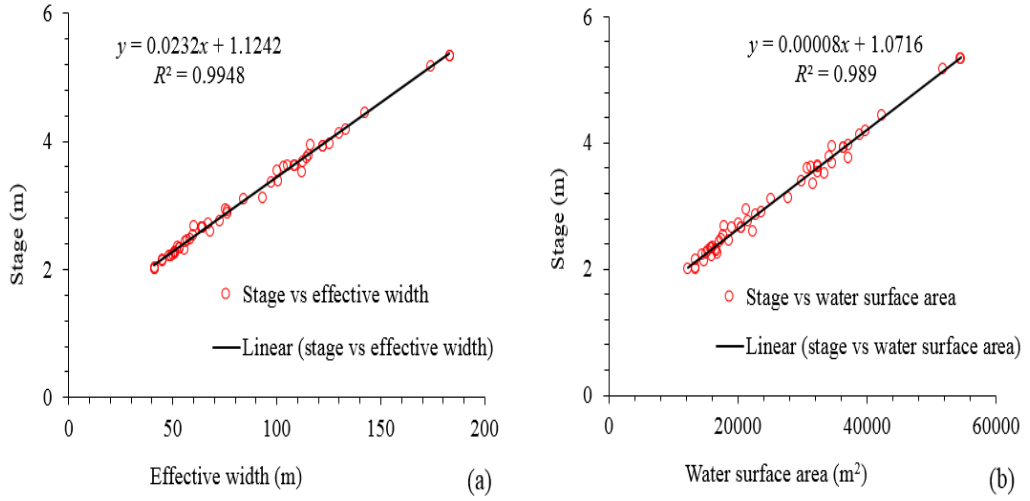

Figure 8: Scatterplots of stage- water surface inundation area (a) and stage- effective width (b) at Tanggya gauging station (1999–2018)

3.4. Discharge Estimations Using Model 1, Model 2, and Model 3 and Their Comparisons

By using Eq. (6)–(8), the estimated discharge of Lhasa River were compared via plot and their performances were also examined. In general, the results of estimated discharge values using Model 1 and Model 2 consistently correspond well with the measured ones with a reasonable accuracy and the two models capture the observed flow pattern very well. But to some extent, Model 1 generally shows an overestimation of discharge while Model 2 is always underestimating discharge (Fig. 8). Previous studies by Bjerklie et al. (2003 and 2005) and Sichangi et al. (2016) mentioned that discharge estimation by using Model 1 with more than one hydraulic flow parameter provides a promising result for many river channels and the research findings of this paper is also the first to prove that this fact works quite well for narrow mountainous region rivers with NSE values of 0.996 (Table 2). For Model 1, the temporal variation of discharge is due to the variation of river width and stage, because the estimated channel slope and roughness coefficient were temporally assumed to be constant due to limitation of data for its temporal estimation.

Model 2 is a multi-variate statistical equation of discharge estimation technique in which its performance varies for different rivers (Negrel et al., 2011). According to Sichangi et al. (2016) and Birkinshaw et al. (2014), Model 1 and 2 perform well for rivers getting a discharge below 20,000 m^3 s^{-1} by showing a strong correlation and exhibiting higher NSE and R^2 values. For Small River discharge estimation similarly also in this study, Model 1 performs well with the same agreement. With the current limitation of satellite sensors capabilities to accurately estimate some flow parameters, such as the roughness coefficient and channel slope, it is difficult to accurately estimate river discharges along a channel section and this would produce a potential error which will disturb and affect the quality of our discharge estimation. In addition, other errors might be also introduced from discharge measurement and steps of deriving rating curves.

The possible sources of uncertainties for river discharge measurement and its controlling operational factors had been studied well by different scholars (Tomkins, 2014; Peña-Arancibia et al., 2015). Therefore, many previous studies indicated that low to medium level of errors and uncertainties could be observed in extracting the input parameters from remote sensing to be used in these discharge estimation models. However, the results of our study show that the associated errors are within the acceptable range and this model can be taken as a feasible method to estimate river discharges for narrow mountainous region rivers. The discharge estimation results from Model 3 are very much consistent and closer to the observed discharge as compared with Model 1 and Model 2 estimations. In addition to this, the discharge estimation from Model 3 shows both underestimation and overestimation tendencies while the magnitude is very less (Fig. 9). Generally the three models discharge estimation results are quite comparable with the ground observations.

Model 3 discharge estimation is simply based on a hydraulic relationship (rating curve) developed between effective river width derived from high resolution Landsat image and observed discharge from Tanggya gauging station. The results of our study indicated that for narrow mountainous region channels such as Lhasa River we can accurately estimate discharge through successful extraction of river width from Landsat images. Generally the results in this study show that the discharge estimation using Model 3 outperforms over Model 1 and Model 2 for Lhasa River and the expected reasons might be the errors related with estimation of depth, slope and roughness coefficient in the other two models.

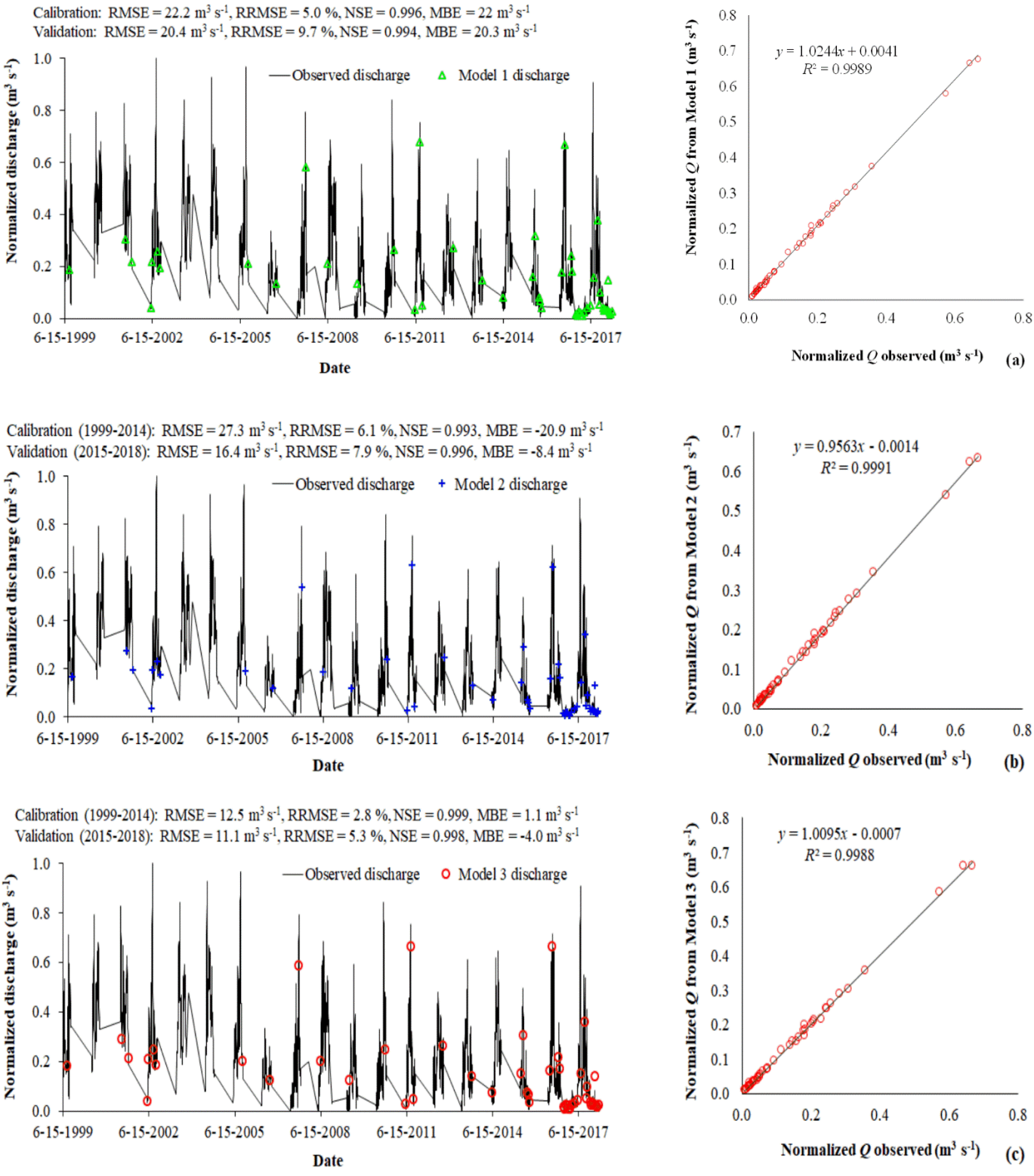

Figure 9: A comparison plot of time series of discharge estimated by using Model 1, Model 2 and Model 3 with the observed discharge data at Tanggya gauging station (1999–2018).

Model 1 and Model 2 could be taken as feasible discharge estimation equations that use multiple hydraulic parameters including river stage, width, slope, and flow resistance. The seasonal change of the river flow is mainly

due to the seasonal change in width and stage. Model 1 discharge estimation method is also promising for many rivers and flat terrains (Jarihani et al., 2015). Our research results also agree with other previously conducted research findings reporting higher accuracy of discharge estimation with an integration of multiple hydraulic flow parameters (Bjerklie et al., 2003, 2005). However, our study is unique in using river depth derived from effective width-discharge hydraulic relationship (rating curve) with other remote sensing derived parameters (*W* and *S*) to estimate discharge for narrow high mountain region channel, which outperformed the studies with a single parameter to estimate river discharge (Smith and Pavelsky, 2008; Birkinshaw et al., 2010; Tarpanelli et al., 2013a). The NSE values for all the three models used in this study range among 0.993-0.996. All the three models discharge estimation by using the normalized discharge (Q_{nor}) within the range of 0–1, computed using Eq. (14) is demonstrated in Fig. (9).

$$Q_{nor} = \frac{Q - Q_{min}}{Q_{max} - Q_{min}} \quad (14)$$

where Q is the discharge before normalization (both remote sensing discharge estimates and *in-situ* discharge measurements), Q_{min} and Q_{max} are the minimum and the maximum gauged discharges for a given gauging station in the study period, respectively.

The overall performance of our models' result against *in-situ* discharge for the whole data considered during the study period (1999–2018) shows a very good correlation with NSE value of 0.996, RRMSE of 6.84 %, MBE of -15.3 $m^3 s^{-1}$ and RMSE of 20.2 $m^3 s^{-1}$ for Model 1, NSE of 0.995, RRMSE of 7.53 %, MBE of 15.0 $m^3 s^{-1}$ and RMSE of 22.3 $m^3 s^{-1}$ for Model 2, and NSE of 0.999, RRMSE of 3.85 %, MBE of -1.1 $m^3 s^{-1}$ and RMSE of 11.4 $m^3 s^{-1}$ for Model 3 respectively (Table 2). Hence the results indicate the ability of all the three models in accurately estimating discharge especially for small narrow mountainous region channels such as Lhasa River and also the capability of Landsat to monitor the discharge, especially for this kind of rivers. Generally the overall errors in our discharge estimation models are caused by errors introduced during estimation of river *W*, *D*, *S* and *n*, and the corresponding related errors are relatively minimal and tolerable (Table 2 and Fig. 9). The comparison of discharge estimation by using Model 1, Model 2 and Model 3 with the observed discharge at Tanggya gauging station showed that the Model 3 outperforms Model 1 and 2 with greater NSE and lower RMSE and RRMSE values, while the accuracy of Model 1 and 2 is relatively low with obvious underestimation and overestimation, respectively.

Table 2: Statistical results of the RMSE, RRMSE, NSE, MBE, and RE for Model 1, Model 2 and Model 3 by using the whole data considered during the study period 1999–2018.

Model	Model performance evaluation methods				
	RMSE ($m^3 s^{-1}$)	RRMSE (%)	NSE	MBE ($m^3 s^{-1}$)	RE (%)
Model 1	20.2	6.84	0.996	15.3	5.2
Model 2	22.3	7.53	0.995	-15.0	-5.1
Model 3	11.4	3.85	0.999	1.1	0.4

The calibration and validation were done in the study period 1999–2014 and 2015–2018, respectively. The performance of all the three models discharge estimations during the calibration and validation periods shows the same pattern and signal with the corresponding observed discharge considered in the study period very closely and consistently (with NSE values greater than 0.993), demonstrating the three models capability to estimate discharges especially for small and narrow rivers in mountainous regions. Generally, trends of an overestimation of discharge by Model 1 and underestimation of discharge by Model 2 were witnessed and the overall performance results of Model 1, Model 2 and Model 3 during the calibration and validation period by using the statistical indicators is shown in Fig. 9 in detail.

4. CONCLUSIONS AND RECOMMENDATIONS

Various kinds of discharge estimation techniques making use of remote sensing datasets and their potential applications for estimating river discharge exist to date while the accuracy of those techniques depends on the accuracy of deriving surface hydraulic variables from space such as river width, stage, slope, velocity and estimated roughness coefficient (Bjerklie et al., 2003; Alsdorf et al., 2007). As a result, we evaluated three widely used hydraulic equations/models (Eq. (6)–(8) or Model 1–3, respectively) to estimate river discharges in a small and narrow high mountainous terrain region of the Lhasa River over TP by using observed discharge data and parameters derived from high resolution satellite sensors such as river width from Landsat images, slope from SRTM DEM, roughness coefficient derived from literatures and the existing channel conditions observed from Landsat image, and depth derived from an empirical width-discharge rating curve equation. For Lhasa River discharge estimation we used *in-situ* and remote sensing datasets covering the study period 1999–2018 and we had estimated the unknown variables for Lhasa River reach around the Tanggya gauging site using calibration (1999–2014) data and verified the results with the validation (2015–2018) period data.

This study is innovative in estimating daily river discharge with three different models by combining river surface hydraulic variables directly derived from remote sensing datasets with other variables indirectly derived from empirical equations, which greatly contributes to the improvement of river flow measurement information especially over small rivers of Tibetan Plateau. In spite of lack of both cross sectional and satellite altimetry observations to estimate river depth, it can be accurately derived from empirical equations and then integrated with the other remote sensing derived surface hydraulic variables (slope and width combined with rationally estimated roughness coefficient) to estimate daily river discharge, which is also one of the promising results of this paper. In addition to this, successful discharge estimation can be achieved by using width-discharge rating curve approach. The performance evaluations of the three hydraulic models used to estimate the discharge of Lhasa River were also promising and highly reliable. A strong correlation between *in-situ* discharge and estimated discharge by the three models distinguishing the seasonal pattern of discharge as well as width and depth variations had been witnessed. The performance of all the three models during the calibration and validation periods also shows the same pattern and signal with the measured discharge (with NSE values ≥ 0.993), meaning that all the three models are capable of estimating Lhasa River discharge.

The results of this study showed that the discharge estimated using Model 3 outperforms over Model 1 and Model 2 for Lhasa River and the likely reasons might be errors related to the estimation of depth, slope and roughness coefficient in the other two models. The study by Huang et al. (2018) also supports our research finding that discharge estimation based on width using Eq. (8) (Model 3) for narrow mountainous region river channels, especially for triangular cross section with short channel reach length is more accurate than discharge estimation equations based on the combination of both width from multi-spectral sensors and stage from satellite altimetry datasets.

Generally in this study, we had evaluated three discharge estimation models which are more or less similar to the Surface Water and Ocean Topography (SWOT) observation parameters based on high-resolution satellite imagery and besides this fact; we had calculated the average depth of the flow by using an empirical equation derived from width-discharge rating curve with a reasonable accuracy. The methodology proposed in this study can be taken to fill the gap in the current ground-based discharge observations and give an alternative for declined *in-situ* observing stations. Additionally, this study also illustrated that using high spatial resolution remote sensing imagery such as Landsat to extract the river width via MNDWI approach performs quite well at Lhasa River and it could be applied for river discharge estimation especially for narrow mountainous region rivers. The proposed models used in this study should be also further investigated and tested in various river channels environments with respect to the

upcoming SWOT mission, which will boost space based discharge estimations studies especially in ungauged and poorly gauged regions.

ACKNOWLEDGEMENTS

This study was financially supported by the Strategic Priority Research Program of Chinese Academy of Sciences (Grant No. XDA20060202 and XDA19070301) and the National Natural Science Foundation of China (Grant No. 91747201, 41571033). The first author wishes to thank the University of Chinese Academy of Sciences for the scholarship and Arba Minch University, Ethiopia for study leave and financial support. We would also like to thank USGS for the Landsat data and SRTM DEM data (earthexplorer.usgs.gov/).

REFERENCES

Albertson, M., & Simons D. (1964): Fluid Mechanics, in Handbook of Applied Hydrology: A Compendium of Water-Resources Technology. New York: McGraw-Hill.

Alsdorf, D., Rodríguez, E. & Lettenmaier D. (2007): Measuring surface water from space. Reviews of Geophysics, 45(2) (n/a-n/a).

Birkinshaw, S., G. M. O'Donnell, P. Moore, C. Kilsby, H. Fowler, & Berry. P (2010): Using satellite altimetry data to augment flow estimation techniques on the Mekong River. Hydrological Processes, 24(26), 3811-3825.

Bjerklie, D., S. Dingman, C. Vorosmarty, C. Bolster, & Congalton R. (2003): Evaluating the potential for measuring river discharge from space. Journal of Hydrology, 278(1–4), 17–38.

Bjerklie, D., D. Moller, L. Smith, & Dingman S. (2005): Estimating discharge in rivers using remotely sensed hydraulic information. Journal of Hydrology, 309, 191–209.

Brakenridge, G., S. Nghiem, E. Anderson, & Mic R. (2007): Orbital microwave measurement of river discharge and ice status. Water Resources Research, 43, W04405.

Chow, V.T. (1959): Open Channel Hydraulics; McGraw-Hill: New York, NY, USA.

Coon, W.F. (1998): Estimation of roughness coefficients for natural stream channels with vegetated banks; US Geological Survey: Reston, VA, USA.

Cowan, W. (1956): Estimating hydraulic roughness coefficients. Agriultural Engineering, 37(7), 473-475.

Cuo, L., Y. Zhang, F. Zhu, & Liang L. (2014): Characteristics and changes of streamflow onthe Tibetan Plateau: A review. Journal of Hydrology: Regional Studies , 2, 49–68.

Duan, Z., & Bastiaanssen W. (2013): Estimating water volume variations in lakes and reservoirs from four operational satellite altimetry databases and satellite imagery data. Remote Sensing of Environment, 134, 403–416.

Dudley, S. J., C. D. Bonham, S. R. Abt, & Fischenich J. C. (1998). Comparison of methods for measuring woody riparian vegetation density. Journal of Arid Environments, 38(1), 77-86.

Feng, D., C. J. Gleason, X. Yang, & Pavelsky T. M. (2019): Comparing discharge estimates made via the BAM algorithm in high order Arctic rivers derived solely from optical CubeSat, Landsat, and Sentinel-2 data. Water Resources Research, 55.

Gao, H. (2015): Satellite remote sensing of large lakes and reservoirs: from elevation and area to storage. WIREs WATER.

Gleason, C. J., & Hamdan A. N. (2015): Crossing the (watershed) divide: satellite data and the changing politics of international river basins. The Geographical Journal, 183(1), 2–15.

Gleason, C. J., Y. Wada, & Wang. J (2018): A Hybrid of Optical Remote Sensing and Hydrological Modeling Improves Water Balance Estimation. Journal of Advances in Modeling Earth Systems, 10(1), 2–17.

Herschy, R.W. (2002): The uncertainty in a current meter measurement. Flow Measurement and Instrumentation, 13(5–6), 281–284.

Hossain, F., A. Siddique-E-Akbor, L. Mazumder, S. ShahNewaz, S. Biancamaria, H. Lee, & Shum C. (2014): Proof of concept of an altimeter-based river forecasting system for transboundary flow inside Bangladesh. IEEE Journal of Selected Topics in Applied Earth Observations & Remote Sensing, 7, 587–601.

Huang, Q., D. Long, M. Z. Du, G. Qiao, X. Li, A. Hou, & Hong Y. (2018): Discharge estimation in high-mountain regions with improved methods using multisource remote sensing: A case study of the Upper Brahmaputra River. Remote Sensing of Environment, 219, 115–134.

Huang, Q., X. Li, P. Han, D. Long, F. Zhao, & Hou A. (2019): Validation and application of water levels derived from Sentinel-3A for the Brahmaputra River. Science China Technological Sciences.

Jarihani, A.A., J.N. Callow, T.R. McVicar, T.G. Van Niel, & Larsen J.R. (2015): Satellite-derived Digital Elevation Model (DEM) selection, preparation and correction for hydrodynamic modelling in large, low-gradient and data-sparse catchments. Journal of Hydrology, 524, 489-506.

Ji, L., L. Zhang, & Wylie B. (2009): Analysis of dynamic thresholds for the normalized difference water index. Photogrammetric Engineering & Remote Sensing, 75, 1307–1317.

LeFavour, G., & Alsdorf D. (2005): Water slope and discharge in the Amazon River estimated using the shuttle radar topography mission digital elevation model. Geophysical Research Letters, 32(17), L17404.

Leopold, L. B., & Maddock T. (1953): The hydraulic geometry of stream channels and some physiographic implications. Washington, D. C.: U.S. Geol. Surv.

Lin, X., Y. Zhang, Z. Yao, T. Gong, H. Wang, D. Chu, L. Liu, & Zhang F. (2008): The trend on runoff variations in the Lhasa River Basin. Journal of Geographical Sciences, 18, 95-106.

Liu, T. (1999): Hydrological characteristics of Yarlungzangbo River. Acta Geographica Sinica, 54(suppl.):157–164. (in Chinese).

Liu, W., F. Sun, Y. Li, G. Zhang, Y.-F. Sang, W. H. Lim, & Bai P. (2018): Investigating water budget dynamics in 18 river basins across the Tibetan Plateau through multiple datasets. Hydrology and Earth System Sciences, 22, 351–371.

Makokha, G., L. Wang, J. Zhou, X. Li, A. Wang, G. Wang, & Kuria D. (2016): Quantitative drought monitoring in a typical cold river basin overTibetan Plateau: An integration of meteorological, agricultural and hydrological droughts. Journal of Hydrology, 543, 782–795.

Meybeck, M., G. Friedrich, R. Thomas, & Chapman D. (1996): Rivers, in:Water Quality Assessments – a Guide to Use of Biota, Sediments and Water in Environmental Monitoring. In D. Chapman (Ed.), 2nd Edn., UNESCO/WHO/UNEP. 1992, Taylor and Francis, London (pp. 1- 651).

Moody, J., & Troutman B. (2002): Characterization of the spatial variability of channel morphology. Earth Surface Processes and Landforms, 27, 1251–1266.

Negrel, J., P. Kosuth, & Bercher N. (2011): Estimating river discharge from earth observation measurements of river surface hydraulic variables. Hydrology and Earth System Sciences, 15(6), 2049-2058.

Pan, F., C. Wang, & Xi. X. (2016): Constructing river stage-discharge rating curves using remotely sensed river cross sectional inundation areas and river bathymetry. Journal of Hydrology, 540, 670-687.

Peña-Arancibia, J., Y. Zhang, D. Pagendam, N. Viney, J. Lerat, A.I. van Dijk, & Frost A. (2015): Streamflow rating uncertainty: Characterisation and impacts on model calibration and performance. Environmental Modelling & Software, 63, 32–44.

Peng, D., & Du.Y. (2010): Comparative analysis of several Lhasa River basin flood forecast models in Yarlung Zangbo River. 4th International Conference on Bioinformatics and Biomedical Engineering (pp. 1-4). Chengdu, China.

Peng, D., J. Chen, & Fang. J. (2015): Simulation of summer hourly stream flow by applying TOPMODEL and two routing algorithms to the sparsely gauged Lhasa River basin in China. Water, 7,4042-4053.

Pavelsky, T. M., M. T. Durand, K. M. Andreadis, R. E. Beighley, R. C. D. Paiva, G. H. Allen, & Miller Z. F. (2014): Assessing the potential global extent of SWOT river discharge observations. Journal of Hydrology, 519, 1516–1525.

Prasch, M. (2010): Distributed Process Oriented Modelling of the Future Impact of Glacier Melt Water on Runoff in the Lhasa River Basin in Tibet. Der Ludwig-Maximilians-Universität München.

Prasch, M., W. Mauser, & Weber M. (2013): Quantifying present and future glacier melt-water contribution to runoff in a central Himalayan river basin. The Cryosphere, 7, 889–904.

Shi, H., X. Fu, J. Chen, G. Wang, & Li T. (2014). Spatial distribution of monthly potential evaporation over mountainous regions: case of the Lhasa River basin, China. Hydrological sciences journal, 59:10, 1856-1871.

Sichangi, A., L. Wang, & Hu Z. (2018). Estimation of River Discharge Solely from Remote-Sensing Derived Data: An Initial Study Over the Yangtze River. Remote Sensing, 10, 1385.

Sichangi, A., L. Wang, K. Yang, D. Chen, Z. Wang, X. Li, & Kuria D. (2016): Estimating continental river basin discharges using multiple remote sensing data sets. Remote Sensing of Environment, 179, 36–53.

Singh, V., N. Sharma, & Ojha C. (2004): The Brahmaputra Basin Water Resources (Vol. Water Science and Technology Library 47). Netherlands: Springer.

Smith, L., & Pavelsky T. (2008): Estimation of river discharge, propagation speed, and hydraulic geometry from space: Lena River, Siberia. Water Resources Research, 44(3), n/a-n/a.

Sulistioadi, Y., K.-H. Tseng, C.K. Shum, H. Hidayat, M. Sumaryono, A. Suhardiman, & Sunarso S. (2015): Satellite radar altimetry for monitoring small rivers and lakes in Indonesia. Hydrology and Earth System Sciences, 19, 341–359.

Tarpanelli, A., S. Barbetta, L. Brocca, & Moramarco T. (2013): River Discharge Estimation by Using Altimetry Data and Simplified Flood Routing Modeling. Remote Sensing, 5(9), 4145.

Tomkins, K. M. (2014): Uncertainty in streamflow rating curves: Methods, controls and consequences. Hydrological Processes, 28(3), 464–481.

Tourian, M. J., C. Schwatke, & Sneeuw N. (2017): River discharge estimation at daily resolution from satellite altimetry over an entire river basin. Journal of Hydrology, 546, 230–247.

Wang, L., A.W. Sichangi, T. Zeng, X. Li, Z. Hu, & Genanu M. (2019): New methods designed to estimate the daily discharges of rivers in the Tibetan Plateau. Science Bulletin.

Flood Vulnerability Mapping and Local Management Strategies in the Intermediate Urban Centers of Ethiopia: the Case of Adama City

Mesfin Alemu Wodnimu[1], Sitotaw Haile Erena[2,*], R. Uttama Reddy[3], Asfaw Mohamed[4]

[1]*Department of Architecture, Construction Quality and Technology Center of Excellence, Addis Ababa Science and Technology University, Addis Ababa, Ethiopia*
[2]*School of Geography and Environmental Studies, Haramaya University, Dire Dawa, Ethiopia*
[3]*Department of Geography, Jigjiga University, Jigjiga, Ethiopia*
[4]*Ethiopian Institute of Architecture Building Construction and City Development, AAU, Addis Ababa, Ethiopia*
**Corresponding author, email: sitotahaile@yahoo.com*

ABSTRACT

The economic losses and the number of people being vulnerable to natural disasters, particularly flooding have increased dramatically over the past decades. The intensity of flood vulnerability is more severe in cities of developing countries. The main objective of the study is to assess the flood vulnerability and Management system of Adama city. To meet the intended objective, the study employed multi-criteria overlay analytic hierarchy process model using Geographic information system. To identify the flood hazard map later vulnerability, various factors such as slope, distance from the river, elevation, precipitation, land cover, and population density were considered. As to hazard map is concerned, the results of the study showed that large areas of the city fall under moderate hazard zones followed by high hazard zones. The result further indicated that significant number of areas also fall under very high hazard zone. With regard to Vulnerability, and significant amount of area 1661.58 hectares and 100.17 hectares of the area is highly and very highly vulnerable to flood, respectively. Moreover, out of 18 villages, 8 of them Badhatuu (07), Abba_Gadaa (12), Odaa (08), Gurmuu (06), Barreecha (11), Biqqa (10), Gaara Luugo (03), Caffee (13) experience very high levels of flood vulnerability. As to flood management practices, the result shows that the residents of Adama city are practicing peculiar flood management strategies such as flood septic tank in their garden, improve door size and gravel filling. To this end, it is highly recommended that these locations within high and very high hazard zone needs immediate intervention and decision making for future flood hazard management and planning of the city. As urban areas expand haphazardly, such hazards and vulnerability of an urban neighborhood greatly increases the risk of flooding.

Keywords: *flood hazard, flood vulnerability, analytic hierarchy, Adama city*

1. INTRODUCTION

Disaster risk is rising throughout the world. The economic losses and the number of people who have been affected by natural disasters have increased dramatically over the past decades than both economic and population growth that could slower the economic growth of the affected country. To this effect, all nations, whether developed or underdeveloped, are exposed to disasters though varying in degrees (Pandey et al., 2007). However, there are variations in time and space of natural hazards and their impacts on affected populations (Cowan *et al*., 2014). Therefore, understanding hazards and their potential impacts is a central to promoting early action (Wilkinson *et al*., 2018).

Among others hazards, floods are the most devastating water related disasters experienced throughout the world with significant and continuously increasing cost to global economy (Perera *et al*., 2019). Ethiopia is highly prone and vulnerable to a range of natural and man-made hazards with severe human and economic impacts. Ethiopia ranks among the top 10 countries globally with the largest number of disaster-affected people, reaching 46 million between 2000 and 2019. Severe droughts, which affect 1.5 million people on average annually and recurrent flooding that impacts the lives of 250,000 people yearly, pose the greatest risks with average annual losses of US$40 million and US$200 million respectively. Climate change is expected to worsen these conditions, increasing

the frequency and intensity of hydro-meteorological events such as floods and droughts. Severe flooding in the 2020 rainy season damaged physical assets and affected peoples' lives and livelihoods.

Heavy and prolonged belg and kiremt rains between April and September 2020 led to severe flooding and landslides in many parts of Ethiopia, with Afar, Oromia, Gambella, SNNP, Somali and Amhara regions most severely affected. According to records by the National Disaster Risk Management Commission (NDRMC), 288 people died, an estimated 1,017,854 people were affected and 292,863 people were displaced by the floods, which were reportedly the most severe in decades. As a systematic local data on the floods damage is not available, the World Bank conducted a remote flood damage assessment of the 2020 floods. The analysis showed that the floods inundated in total 1.02 million ha of land, predominately in Afar region, which accounts for almost 40% of the total flooded area. The floods affected an estimated 38,600 buildings, 1,350 km of the road network and 164,000 ha of cropland. Direct flood damage to just these assets is estimated at US$ ± 357.5 million. Damage was by far the highest in Oromia region (US$ ± 116.5 million), followed by Afar (US$ ± 57.3m) and Somali region (US$ ± 44.9 million).The figure below shows the areas flooded and flood displaced people as of August 18, 2020 (OCHA Ethiopia).

Risk is the product of hazard and vulnerability that helps to identify vulnerable group (Erena and Worku, 2019). At the same time vulnerability and hazard mapping is the first activity in any type of risk management (Erena et al.,2018). Adama is among the most city of Oromia regularly affected by flood hazards. Various studies have been conducted in Adama flooding (Seid, 2005, Bulti et al., 2017). These authors have investigated the causes of flood in Adama city with respect to geomorphology, hydrology and land use changes within the city boundary with possible counter measures that can be adopted to minimize the consequences (Bulti et al., 2017). Beside to previous studies, the materialized and on-going effort of the city government regarding this aspect is not undermined. Annually the city government is allocating huge budget to stem the flood induced risk, human causalities and property damage by using structural and non- structural measures of mitigation strategies.

In Adama the occurrence of floods is more frequent and cyclical in nature. According to past historical record of flooding and the result of Adama meteorological station rainfall data, the flood return period of Adama city is less than a decade. Because of its high incidence and intensity, floods that occurred at different time have destroyed homes, public institutions, and market places with their properties, infrastructures, crops in the field, livestock and the like. Currently there are also reports of flooding from different parts of the country in which Adama city is part of that. According to NMA, among those areas which are pointed out as facing the danger of flooding this season are included some of those that experienced the disaster in previous years. With technological advances, an enormous opportunity exists to better target specific flood interventions and to site where it has greatest impact by mapping and evaluating metrics related to a variety of risk components (Tuyishimire, 2013). The general objective of the study is therefore to characterize and spatially model flood hazard and vulnerability using analytic hierarchy process (AHP) and geographic information system (GIS). This, in turn, would help to control and identify flood hotspot areas for prevention and preparedness of the early warning and emergency response mechanism.

2. MATERIALS AND METHODS

2.1. Location, Physical and Socioeconomic Characteristics of the Study Area

Adama city is one of the largest urban areas in the Oromia National regional state of Ethiopia. It is totally ordered by East Showa zone specifically bordered in the East by Olanchiti, in the West by Modjo and on the South by Sodate woreda. Adama city is located in the Great East African Rift Valley system which runs from Syria in the Middle East to Mozambique in the Southern. Astronomically, the city is positioned between $8^0$33'11'' to $8^0$36'11'' North latitudes and $39^0$11'57'' to $39^0$21'15'' East longitudes (Figure 1).

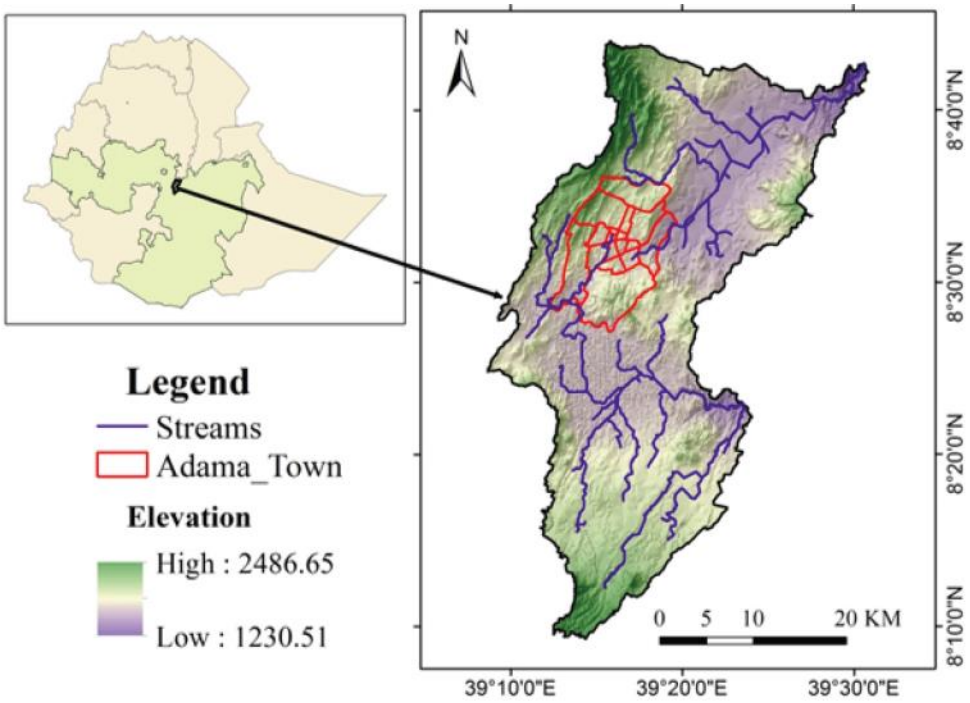

Figure 1: Location maep of the study area

Topography of the city is characterized by flat terrain that is surrounded by ridges. The plain land is covered by lacustrine sediments and reworked volcanic, while the ridges are made of volcanic rocks. The nature of topography has created three drainage sub-catchments; one that drain to Awash river and the others two closed basins, absence of appropriate drainage network, lack of natural out let and unplanned human interventions that have made the city vulnerable to natural and human-induced disasters. The track of the Addis Ababa Djibouti railway crosses the southern part of this district (CSA 2007). Adama city was built on flat and undulating fertile ground that ranges from a completely low-lying center to hilly peaks overlooking the city, each with its unique landscape sceneries. The altitude steadily declines from all of the city's outskirts to the city's core, where the slopes become mild in the heart of the city. According to the city's current master plan, the city is situated the elevation between 1500 and 1900 meters above mean sea level with an average elevation/altitude of 1700 meters above sea level.

The climate is tropical, with plenty of rain in the summer and relatively little in the winter. The average annual temperature of Adama is 20.50°C, with an annual rainfall of 808 mm. There are six sub-cities and 18 administrative kebeles in the city (the lowest admiration level) ("Socio-Economic Profile of Adama", 2019). Geographically Adama city is surrounded by plateaus, mountainous and ridged topography. These surrounding mountains are the source of flooding and made gullies from which surface moves downstream to Adama city. As a result, Flood has been the manifestation of Adama city since long past. The city's history of Flooding shows that the problem is cyclic and routine which has a long history as equal as the age of the city. Adama city is the second largest urban center in Ethiopia regarding population size, next to Finfine (Addis Ababa). Moreover, it is the first largest urban center in Oromia Region and one of few cities in the country with a threshold population of over 100,000. The city has long population survey trends which have been covered by most demographic and housing censuses and surveys since 1965G.C, when the first baseline urban demographic survey was conducted in the country. Demographic records for Adama city existed as far back as 1967, when the Central Statistics Agency launched the first nationwide demographic survey of urban centers. It was one of the 195 towns in the country that were covered by the national first and second round surveys. Since then the city has been covered by almost all major surveys and, of course, the three national population and housing censuses. In view of this, Adama city population grown

trends for the last three consecutive censuses conducted in the country showed increasing tendency. With the intention of this, the first population and housing census made that was held in May 1984, Adama town known within 77,237 population. The next census made in 1994 after ten years Adama city had 127,842 populations (female accounted 65,877). Thirdly, held that census made in 2007 after thirteen years presented 220,212 populations (female accounted 111,341).

2.2. Data Sources and Data Collection Methods

The required data for this study were collected from various sources. To identify the existing flood management practices of Adama City residents, 214 households were contacted through survey questionnaire method from purposively selected Kebeles. These Kebles are (03, 13 and 09) which were selected for the fact that they have been reported as flood vulnerable kebles by City Municipality. The population density, Precipitation, Slope, and other spatial elements that are important for vulnerability assessment were collected through different techniques and sources. Accordingly, DEM (digital elevation model) which was used for the extraction of slope and elevation, and 2020 Landsat images used to produce NDVI land cover map of the study area was downloaded from USGS (United States Geological Survey). Similarly, the 30-year precipitation data (1992-2022) of Adama was collected from Ethiopian Meteorological Agency. Moreover, other supportive primary data were also collected from Adama city municipal office document, expertise interview, focus group discussion with the society and site observations.

2.3. Methods of Data Analysis

Data obtained about the outbreak of flood was analyzed using both descriptive and analytic methods of data analysis (Yimer et al., 2017). The household survey data was also analyzed to identify the flood outbreak impact and examine the copying mechanisms of the local community. Geographic information system based multi-criteria decision analysis was used to identify the flood hazard and risk factors by assign the influencing factors weights (Malczewski, 2006) and map the risk zone of the area. A multi-criteria overlay analysis was used to identify the vulnerability of the area using relative exposure to flood, on a scale from 1 to 4. Where 1 = refers less hazard and 4 represents high hazard zone (Jiang and Eastman, 2000) was used. The major factors determining the hazard level in the study area are precipitation, slope, flow length, river distance, NDVI (as a land cover representation), elevation.

Flow length calculates the upstream or downstream distance or weighted distance along the flow path for each cell. In this case, the weight of 1 was applied to each cell. For each cell in the output raster, the result will be the number of cells that flow into it. The direction of measurement along the flow length selected the downstream that calculates the downslope distance along the flow path from each cell to a sink or outlet on the edge of the raster. Slope is an important factor in flood hazard mapping because it governs the amount of surface runoff produced from precipitation and displacement velocity of water to the riverbank. The slope and flow length factors were classified to different level ranks based on the criterion shown under Table2. Elevation is another factor used for flood hazard map of Adama city. The level of flood hazard is highly persistent in the lower or the middle course of the river. Therefore, the level of vulnerability is higher in low land areas than highland. To its effect, Elevation of the city was classified in to five classes. The distance from the river determines the level of flood inundation.

As villages are near to the river the level of flood hazard getting higher and it has negative relationships. Precipitation is another decisive factor in flood hazard mapping. The interpolated coverage of the land is determined based on the value of amount of water the points received. Therefore, as the amount of water reached the area determines the level of hazard for flood, which positively related. Normalized Difference Vegetation Index (NDVI), which the representative of the land cover of the area, also determines the formation of surface runoff and resulting flood hazard. The NDVI value ranges from 0.5- -0.18 in the given study area. As the NDVI value getting higher the abundance and coverage of the surface is very high. Therefore, it has reversal relationship between NDVI and flood hazard. The city was classified in to four in terms of population density. The population density map of each kebele was developed using different ranges of population density. Accordingly, the areas with 117.9 -

645.0 population density/km^2 range is classified less populous area while villages with 19912.1 - 37205.6 population density/km^2 are regarded as very high populous villages that later determine the level of vulnerable populations. These all individual factors of flood hazard maps were put under five classes with their respective criterion (Table 1).

Table 1: Individual Criterion classification for different variables used for flood hazard mapping

Variable	Class
Pop_density/km2	117.9–645.0
	645.1–3267.3
	3267.4–9385.6
	9385.7- 19912.0
	19912.1–37205.6
NDVI	/-0.165 - -0.0317
	/-0.0317–0.101
	0.101–0.235
	0.235–0.368
	0.368–0.502
Elvation (m)	1,230–1,561
	1,561- 1,684
	1,684–1,832
	1,832–2,049
	2,049 − 2,483
River Distance (m)	< 1000
	1000-3000
	3000-6000
	6000-10000
	> 10000
Precipitation (mm)	27.268–28.97
	28.97–30.68
	30.68–32.39
	32.39–34.10
	34.10–35.80

Weight Overlay analysis often requires the analysis of many different factors that are necessary for flood hazard mapping. It is desirable to establish the relationship of all the input factors together to identify the desirable hazard map for each site. For this study, all the weighted factor maps were overlaid using weighted overlay extension of spatial analyst tool in GIS. Finally, both flood hazard and flood risk were computed using weighted linear combination using the formula in equation 1 and 2

$H = \sum wixi$ ……. 1

$R = \sum wixi$ ……. 2

Where, H- is the composite hazard score, R – is the composite risk score, xi –is factor scores, wi is weights assigned to each factor and ∑ -- is sum of weighted factors. Flood risk of the district was analyzed from the following general risk equation.

Risk = (vulnerable population) *(Flood Hazard).

To evaluate the Multi-criteria evaluation of the flood hazard zone identification the study applied the Analytical Hierarchy Process (AHP), which allows for the detection and correction of errors made when determining the relative importance of various criteria in a site selection analysis. It also demonstrates how the AHP frames the site evaluation problem and how it might help with decisions involving a variety of criteria, diverse factors, and unknown circumstances. The consistency ratio achieved in this investigation, which was computed to be 0.0208, was shown to be consistent across paired comparisons. Only when the consistency rate derived from the consistency analysis is less than 0.10 can the comparison matrix be considered to be consistent. If not, a new comparison matrix will have to be generated (Orhan, 2021).

3. RESULTS AND DISCUSSIONS

3.1 Flood Hazard Map

Hazard is a possible source of danger that may cause injury, death, harm and economic damage. As most of hazard triggering factors are beyond the human control it is not easy to avoid hazards, but it is possible to prevent it from becoming disasters. Hence, flood hazard map is part of flood early warning system that helps to identify flood inundation zones and ultimately helps to reduce vulnerability.

Hazard map is the cumulative effect of the results of each variable considered. The specific analysis for slope, river distance, elevation, flow length, rainfall and land cover , major parts of the city fall under very low and low classes only showing that the effects of the two variables are less significant. In the same way, as to precipitation variable, which is supposed to mainly affect flood hazard, is concerned, the city boundary falls under two classes of low and moderate zones. This implies that flood hazard zones of Adama city is not majorly depend in the intensity of precipitations rather other factors affect more. Figure 2 shows that the city is experiencing all types of hazard classes with respect to each variable that range from very low to very high hazard zone. This implies that these variables are dominantly determining the hazard maps of the city.

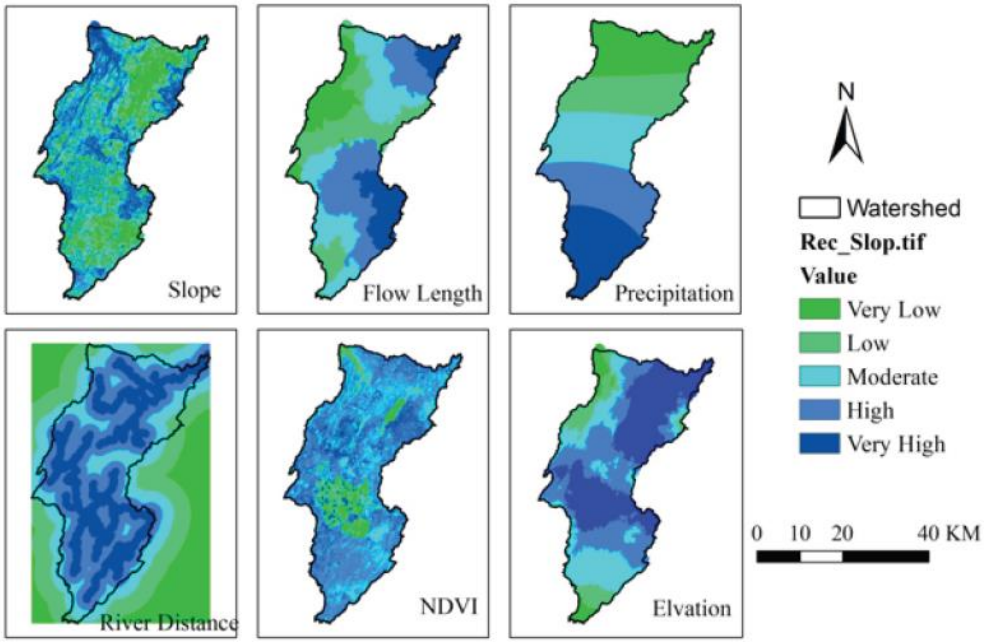

Figure 2: Map of flood hazard determining factors

The overall hazard map of the city was developed by overlaying the results of each respective variable together. The flood hazard map results of Adama city indicated that the city fall under five different hazard categories that range between very low to very high hazard zones (Figure 3).

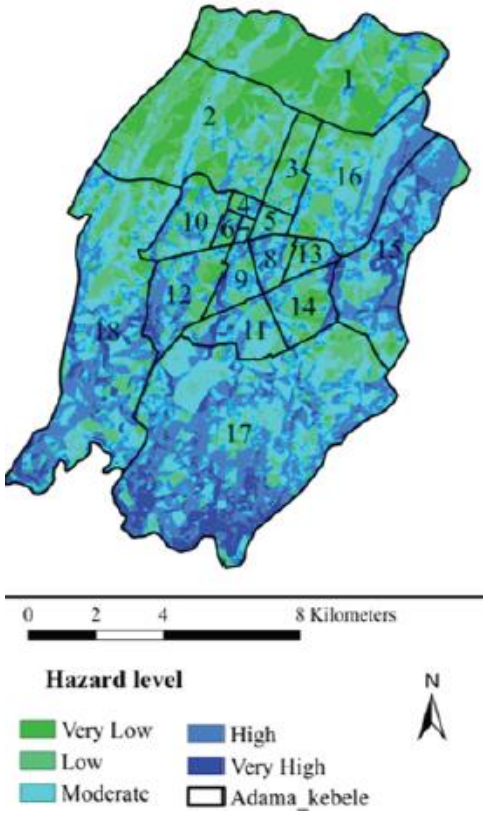

Figure 3: Flood hazard map of Adama City

As shown under Table 2 large areas of the city (4389.03 ha) fall under moderate hazard zones followed by high hazard zones (3868.02 ha). The result further indicated that significant number of areas (829.8 hae) fall under very high hazard zone. This shows that these locations within high and very hazard zone needs immediate intervention and decision making for future flood hazard management planning.

Table 2: Flood hazard map results of Adama city

Hazard level	Area (Ha)
Very low	1,240.38
Low	3,257.82
Moderate	4,389.03
High	3,868.02
Very high	829.80

As the use of crude flood hazard map is not easy for policy makers, it is important to identify places in relation to their flood hazard levels that can ultimately help to prioritize villages for flood management activities. Because of variations of each variable at different locations, the city level analysis of flood hazard map shows that the hazard distribution varies across different kebeles of the city (Figure 3). Accordingly, Bokku shaman is highly susceptible to hazard followed by Malka Adama and Daabe Solloqqe, respectively. This implies that those Kebeles needs to be prioritized for immediate intervention ad flood management planning of the city. The overall kebele level flood hazard map, with respective area coverage, of Adama city is shown in Table 3.

Table 3: Kebele level distribution of flood hazard map of Adama City

Kebele	Very low	Low	Moderate	High	Very high
Dhaka Adi	552.9	638.7	374.5	115.4	2.2
Gooro (01)	333.6	694.4	460.2	83.0	0.0
Dhadacha Araara (04)	51.0	108.4	78.8	18.1	0.0
Badhatuu (07)	0.8	21.9	14.5	12.2	0.0
Abba Gadaa (12)	6.5	26.6	38.8	13.2	0.2
Odaa (08)	0.5	23.9	12.3	18.1	0.0
Gurmuu (06)	0.0	5.6	19.0	6.2	0.1
Barreecha (11)	2.7	30.9	56.9	61.8	9.5
Biqqa (10)	3.3	52.4	59.2	64.3	13.5
Dagaaga (05)	36.1	92.8	118.5	99.4	4.1
Gaara Luugo (03)	7.8	81.5	142.2	84.2	18.9
Irreechaa (09)	28.4	120.0	116.3	181.7	35.8
Caffee (13)	6.4	45.8	50.3	16.7	8.3
Migiraa (02)	42.1	116.6	88.0	73.4	18.0
Daabe Solloqqe	7.2	145.4	318.5	513.5	113.8
Hangaatu (14)	49.7	216.3	410.1	333.5	6.8
Bokku shanan	32.8	422.9	1195.1	1421.6	442.0
Malka Adama	78.6	413.7	835.8	751.6	156.8

3.2. Population Density

The level and impacts of flood variability is determined by elements exposed to a give hazard. Flood can induce various types of vulnerabilities (Erena and Worku, 2019). These include social, economic, environmental and Institutional vulnerabilities. Population density helps to identify the possible social vulnerabilities. Accordingly, the city is classified under four classes (Very low, low, medium, high and very high) population densities (Table 3). Accordingly, most of the dawn town kebeles located at the center of the city is found to be more populous which in turn has a significant association to flood vulnerability. The overall kebele level population density of the city is depicted under (Table 4).

Table 4: Kebele level population density distribution of Adama City

Kebele	Sub-city	Tot_pop	Area	Pop. Density
Dhaka Adi	Bole	2.538	16.8345	0.150762
Gooro (01)	Bole	30.109	15.713	1.91618
Dhadacha Araara (04)	Bole	32.045	2.56021	12.5166
Badhatuu (07)	Gadaa	18.389	0.494254	37.2056
Abba Gadaa (12)	Gadaa	16.954	0.85144	19.9121
Odaa (08)	Gadaa	17.363	0.549167	31.617
Gurmuu (06)	Gadaa	11.147	0.3094	36.0278
Barreecha (11)	Bokkuu	29.646	1.61893	18.3121
Biqqa (10)	Luugoo	28.215	1.92873	14.6288
Dagaaga (05)	Dambalaa	30.252	3.51111	8.61608
Gaara Luugo (03)	Luugoo	31.421	3.34776	9.38568
Irreechaa (09)	Dambalaa	34.854	4.82008	7.231
Caffee (13)	Daabe	17.226	1.27317	13.53
Migiraa (02)	Bokkuu	21.508	3.38304	6.3576
Daabe Solloqqe	Daabe	7.083	10.9809	0.645029
Hangaatu (14)	Daabe	33.209	10.1639	3.26735
Bokku shanan	Bokkuu	6.845	35.142	0.194781
Malka Adama	Dambalaa	2.637	22.3637	0.117914

The Population density distribution indicated that Badhatuu (07) with (37.2056 people per square kilometers) is the highest in terms of population density followed by Gurmuu (06) (36.0278 people per square kilometers) and Abba Gadaa (12) (19.9121 people per square kilometers). This shows old villages located close to the mountains surrounding the city the most populous which can aggravate the occurrence of flood hazards and the vulnerabilities (Figure 4).

3.3. Vulnerability Map

Vulnerability is described as the degree to which an area, people, physical structures or economic assets are exposed to loss, injury or damage caused by the impact of the hazard (Dandapat & Panda, 2017, Erena and Worku, 2019). This means vulnerability is formed when hazard interacts with exposed and susceptible human being or assets with less capacity to resist it. As a result, a given community may have the same level of exposure to a natural hazard, but varying consequences resulted from the diverging individual and groups capacities to handle the impacts of the hazard. With this regard, the characteristics of a people and their situation that influence their capacity to predict, cope with, resist and recover from the impact of a natural hazard are also equally important

(Wisner et al., 2012, Erena and Worku, 2019). Combining the groups of population exposed to flood hazard and the flood hazard map of the city, flood vulnerability map of Adama city was developed at city level (Figure 5).

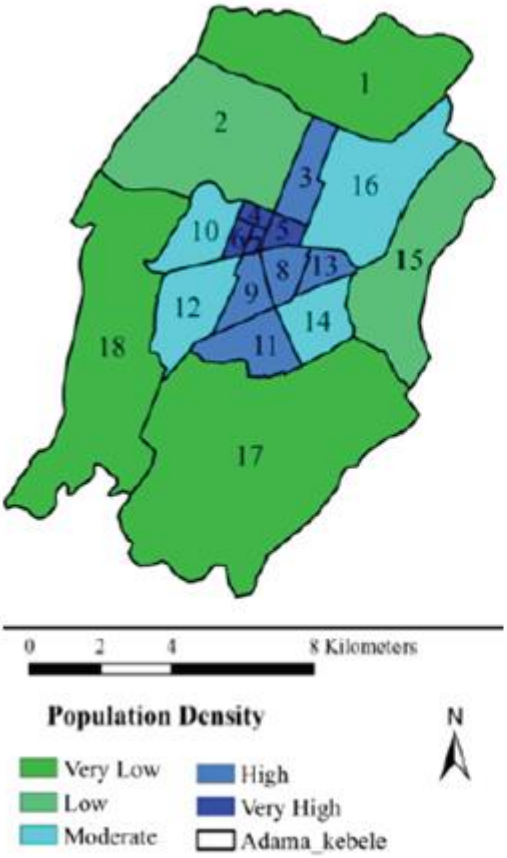

Figure 4: Population density map of Adama City

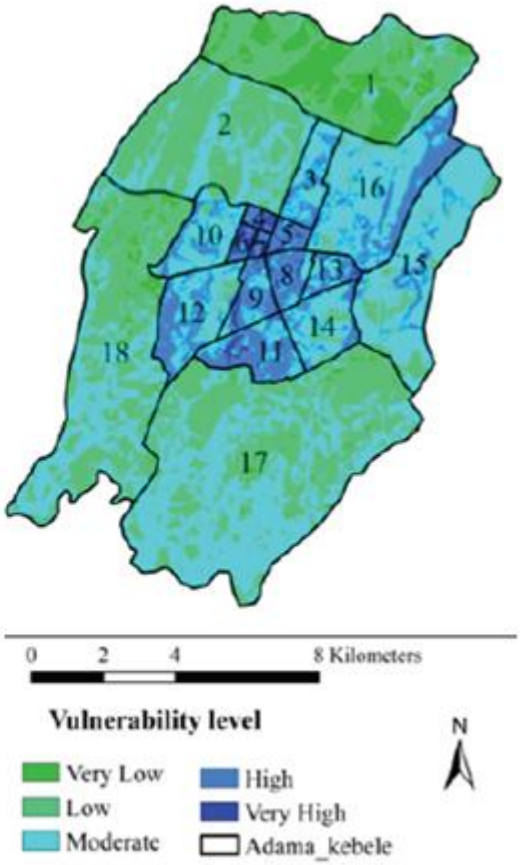

Figure 5: Flood vulnerability map Adama City

As can be referred from Figure 5 and Table 5, large areas of the city (5941.44 ha) fall under moderate flood vulnerability flowed by low (5217.66 ha) and high (1661.58 ha) vulnerability levels, respectively. Though raked last, the areas under very high vulnerability (100.17 ha) is also not undermined (Table 5).

Table 5: Flood vulnerability analysis of Adama city

Vulnerability level	Area (Ha)
Very low	664.2
Low	5217.66
Moderate	5941.44
High	1661.58
Very high	100.17

Vulnerability is the result of various factors. As a result of this study, the level of flood vulnerability varies across different Kebeles of the city for the fact that the extent and level of flood-induced damage depends on the characteristics of the affected people and infrastructure condition of the area (Choudhury et al., 2015; Kuhlicke et al., 2011). The location wise variation level of vulnerability is arise due variation in the major elements of

vulnerability. Vulnerability is expected to happen under certain conditions of hazard, exposure, susceptibility and resilience (Erena and Worku, 2018; Fuchs et al., 2012).

Vulnerability = [Hazard + Exposure + Susceptibility] – [Adaptive Capacity]

Resilience is the ability of a system to adjust to changes or threats, to avoid, mitigate or absorb potential damage, to cope with the consequences without loss or to even take advantage of opportunities (Edwards and Schneider, 2001). Exposure represents values that are present at the location where hazard can occur. It is the predisposition of a system or its elements to be affected by hazard due to its location in the hazard area. Due to variation in susceptibility, not all exposed people and material are equally vulnerable to the flood hazard. Susceptibility describes the potential of a system to be harmed by a hazardous event such as flooding, caused due to material makeup of the house, fragility of the materials, relative social or economic weaknesses and disadvantageous conditions (Cardona, 2005). In this sense Kebeles with poor drainage, slum settlement made up of poor materials, accommodating voiceless people who are marginalized because of economy and social status are found to be high flood vulnerable zones. This fact is reflected among high flood vulnerable kebeles of Adama City.

The specific Kebele level flood vulnerability map of Adama shows that out of 18villages 8 of them (Badhatuu (07), Abba_Gadaa (12), Odaa (08), Gurmuu (06), Barreecha (11), Biqqa (10), Gaara Luugo (03), Caffee (13) partly experience very high levels of flood vulnerability (Table 6).

Table 6: Kebele Level Flood Vulnerability distribution of Adama City

Kebele	Vulnerability level (area /square meter)				
	Very low	Low	Moderate	High	Very high
Dhaka Adi	5528700	10132200	1175400	0	0
Gooro (01)	0	10280700	5431500	0	0
Dhadacha Araara (04)	0	0	1593900	969400	0
Badhatuu (07)	0	0	8100	363600	121500
Abba Gadaa (12)	0	0	64800	654300	134100
Odaa (08)	0	0	5400	362700	180900
Gurmuu (06)	0	0	0	245700	63000
Barreecha (11)	0	0	335700	1187100	95400
Biqqa (10)	0	0	557100	1234800	135000
Dagaaga (05)	0	360900	2113200	1034100	0
Gaara Luugo (03)	0	0	893700	2264400	189000
Irreechaa (09)	0	283500	2362500	2175300	0
Caffee (13)	0	0	522000	670500	82800
Migiraa (02)	0	421200	2046600	914400	0
Daabe Solloqqe	0	1525500	8320500	1137600	0
Hangaatu (14)	0	496800	6264000	3402900	0
Bokku shanan	327600	16180200	18636300	0	0
Malka Adama	785700	12495600	9083700	0	0

As observed from Table 6, kebeles with high flood vulnerability level are located both at the oldest villages located at the Centre of the city and at periphery kebeles (03, 13) recently included to the City administration. This shows that the oldest kebeles are experiencing flood vulnerability because of the concentration of resources and asset in these areas supplemented with lack of adequate and maintained drainage systems. Of course, the

impervious condition of the area also contributes for the incidence of vulnerability. On the contrary kebles located at periphery were experiencing flood vulnerability due to the illegal expansion of urbanization that ultimately complicate the expansion of infrastructures and reduced provision capacity of the existing infrastructure. Moreover, the unplanned slum settlement developed in these areas also occupies flood sensitive areas located at unacceptable buffer zone areas less than 15 meters away from the river course.

The number and specific kebeles identified by this study comply with the reports of Adama City Disaster Risk Management results of May 2020 that identified all 18 kebles as flood vulnerable areas. The discrepancy in the number of villages arise as a result of multiple flood causing factor overlay used under this study which helps to rank vulnerability of the villages as very high, high, medium, low and very low. In this regard, the result of this study shall be helpful to prioritize floods with very high vulnerability level than assuming all together as the high flood vulnerable kebeles.

In addition, to measure the validity of the model, the study takes into consideration historical record of flood damage. Of the 21 flood damage record of the municipal office social affairs division report 16 of them are fall on a very highly vulnerable, which accounts about 76% as 14 and 9.5% of the point fall up on highly vulnerable and moderately vulnerable areas, respectively.

3.4. Local management Strategies

People are the scientist of their local area. Through time they have built, accumulate knowledge how to respond to their site specific challenges. Likewise, in response to spatial variation of flood hazard and vulnerabilities, People develop their own peculiar flood coping mechanisms that function in their socio-economic conditions. Accordingly, the residents of Adama city has been using seven types of flood management mechanisms against the prevailing flood hazards of the city and their surroundings (Figure 6).

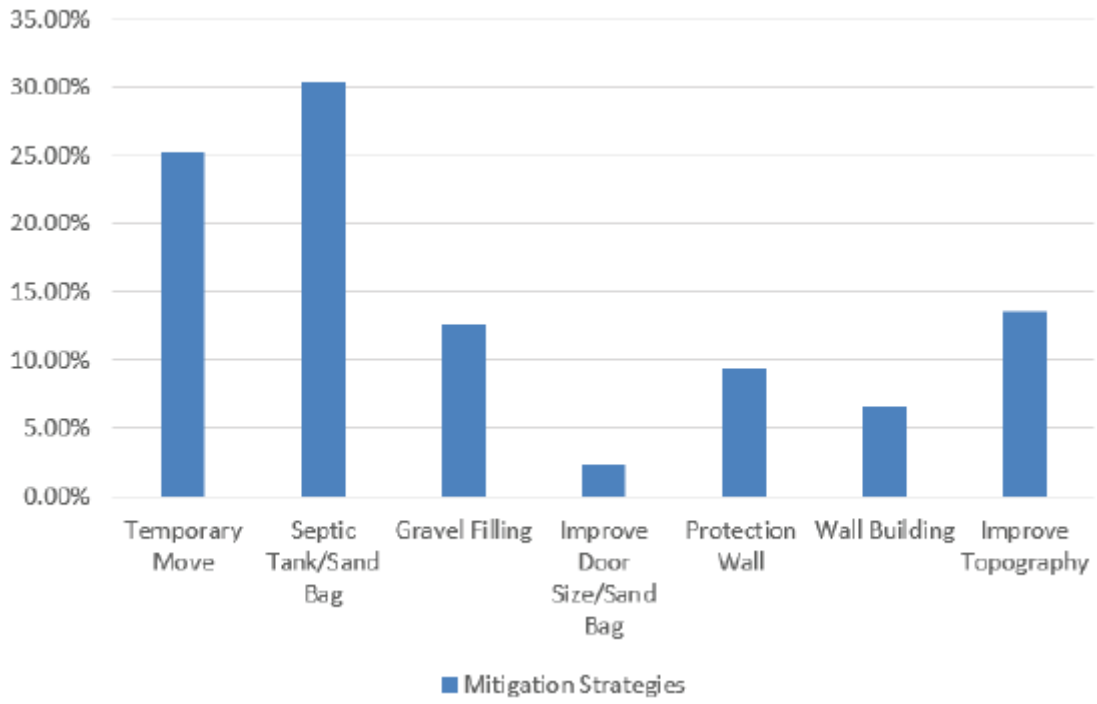

Figure 6: Local flood Management Strategy of Adama City

The result of the local flood adaptation mechanisms indicted that majority of the sample household (30.37%%) are practicing Septic Tank/Sand Bag followed by temporary move (25.23%) and Improve topography,

respectively. Some of the findings of this study such as temporary move, flood retailing wall and sand bag application as flood management practices comply with the results of other studies take place in Dire Dawa and other places (Erena and Worku, 2018; Gwimbi, 2007; Mavhura et al.,2013). However, there are peculiar flood management strategies practiced only by Adama city residents. These include, preparation of flood septic tank in their garden, improve door size and filling gravel to avoid flood inundation shall be the new finding that could be duplicated to other places facing similar problem.

4. CONCLUSION

This study has developed flood hazard and vulnerability map of Adama City with corresponding coping mechanisms practiced by city dwellers. With regard to flood mapping and vulnerability, the study employed analytic hierarchy process (AHP) with the help GIS. Various factors were employed for the development of Adama city flood hazard. Accordingly, major hazard determining factors such as precipitation, slope, flow length, river distance, NDVI, and elevation were considered to identify keble level flood hazard zones. Among these factors slope, river distance and elevation dominantly determining the hazard maps of the city. Subsequent to development of flood hazard map, the population density of the city was overlaid to generate flood vulnerability map of the City.

The analysis of flood hazard map showed that the city experiencing different level of flood hazard that rages from very low to very high rage at different parts of the Kebele. Specifically, Bokku shaman is highly susceptible to flood hazard followed by Malka Adama and Daabe Solloqqe, respectively. The hazard map further indicated that large areas of the city (4389.03 hectare) fall under moderate hazard zones followed by high hazard zones (3868.02 hectare). It also showed that significant number of areas (829.8 hectare) fall under very high flood hazard zone. The flood vulnerability result indicated that 8 out of 18 villages (Badhatuu (07), Abba_Gadaa (12), Odaa (08), Gurmuu (06), Barreecha (11), Biqqa (10), Gaara Luugo (03), Caffee (13)) partly experience very high levels of flood vulnerability. Some of These keeles are located in the inner cities while others are in the periphery areas indicating that flood vulnerability is the widely recognized challenge of the city at all levels demanding immediate and appropriate intervention.

In response of the widely disseminated and disastrous flood hazard ad vulnerability, the city dwellers have developed their own local specific flood mitigation strategies. Among these some of them such as preparing flood septic tank in the compound, improve door size and filling gravel to avoid flood inundation are unique experiences that shall contribute new knowledge to the fields of flood hazard and vulnerability management. In most cases, these locally developed flood management strategies are highly effective in normal flood conditions. However, these strategies are limited to withstand the consequences of extreme events beyond normal occurrence. Therefore, it is highly recommended that the output of the flood hazard and vulnerability map developed by this study should be properly utilized for future flood risk planning and management of Adama city.

REFERENCES

Bulti, D. T., Mekonnen, B., & Bekele, M. (2017). Assessment of Adama city flood risk using multicriteria approach. *Ethiop J Sci Sustain Dev*, *4*(1), 6-23.

Cardona, O. (2005). Indicators of disaster risk and risk management: Summary report. Inter-American Development Bank.

Chowdhury, M. M. H., & Quaddus, M. A. (2015). A multiple objective optimization based QFD approach for efficient resilient strategies to mitigate supply chain vulnerabilities: The case of garment industry of Bangladesh. *Omega*, *57*, 5-21.

Cowan T, Purich A, Perkins S, Pezza A, Boschat G, Sadler K (2014) More frequent, longer, and hotter heat waves for Australia in the twenty-first century, J. Climate 27:5851–3871

Dandapat, K., & Panda, G. K. (2017). Flood vulnerability analysis and risk assessment using analytical hierarchy process. *Modeling Earth Systems and Environment*, *3*(4), 1627-1646.

Edwards, P. N., & Schneider, S. H. (2001). Self-governance and peer review in science-for-policy: The case of the IPCC Second Assessment Report. *Changing the atmosphere: Expert knowledge and environmental governance*, 219-246.

Erena, S. H., & Worku, H. (2018). Flood risk analysis: causes and landscape based mitigation strategies in Dire Dawa city, Ethiopia. *Geoenvironmental Disasters*, *5*(1), 1-19.

Erena, S. H., & Worku, H. (2019). Urban flood vulnerability assessments: the case of Dire Dawa city, Ethiopia. *Natural Hazards*, 1-22.

Erena, S. H., Worku, H., & De Paola, F. (2018). Flood hazard mapping using FLO-2D and local management strategies of Dire Dawa city, Ethiopia. *Journal of Hydrology: Regional Studies*, *19*, 224-239.

Erena, S.H., Worku, H. (2018). Flood risk analysis: causes and landscape based mitigation strategies in Dire Dawa city, Ethiopia. Geoenvironmental Disaster Vol. 5, No. 16.

Fuchs, S., Birkmann, J., & Glade, T. (2012). Vulnerability assessment in natural hazard and risk analysis: current approaches and future challenges. *Natural Hazards*, *64*(3), 1969-1975.

Gwimbi, P. (2007). The effectiveness of early warning systems for the reduction of flood disasters: some experiences from cyclone induced floods in Zimbabwe. J.Sustain. Dev.

Jiang, H., & Eastman, J. R. (2000). Application of fuzzy measures in multi-criteria evaluation in GIS. *International Journal of Geographical Information Science*, *14*(2), 173-184.

Kuhlicke, C., Scolobig, A., Tapsell, S., Steinführer, A., & De Marchi, B. (2011). Contextualizing social vulnerability: findings from case studies across Europe. *Natural hazards*, *58*(2), 789-810.

Malczewski, J. (2006). GIS-based multicriteria decision analysis: a survey of the literature. *International journal of geographical information science*, *20*(7), 703-726.

Mavhura, E., Manyena, S., Collins, A., Manatsa, D. (2013). Indigenous knowledge, coping strategies and resilience to floods in Muzarabani, Zimbabwe. Int. J. DisasterRisk Reduct. 5, 38–48.

Pandey, S. K., Tyagi, P., & Gupta, A. K. (2007). Municipal solid waste management in Ghazipur city-A case study. *Journal of Agricultural and Biological Sciences*, *2*(6), 41-43.

Perera, D., Seidou, O., Agnihotri, J., Rasmy, M., Smakhtin, V., Coulibaly, P., & Mehmood, H. (2019). Flood early warning systems: a review of benefits, challenges and prospects. *UNU-INWEH, Hamilton*.

Wilkinson, D. A., Marshall, J. C., French, N. P., & Hayman, D. T. (2018). Habitat fragmentation, biodiversity loss and the risk of novel infectious disease emergence. *Journal of the Royal Society Interface*, *15*(149), 20180403.

Wisner, B., Gaillard, J. C., & Kelman, I. (2012). Framing disaster: Theories and stories seeking to understand hazards, vulnerability and risk. In *The Routledge handbook of hazards and disaster risk reduction* (pp. 18-33). Routledge.

Yimer, M., Hailu, T., Mulu, W., Abera, B., & Ayalew, W. (2017). A 5 year trend analysis of malaria prevalence with in the catchment areas of Felegehiwot referral Hospital, Bahir Dar city, northwest-Ethiopia: a retrospective study. *BMC research notes*, *10*(1), 1-4.

Syndicate 4:

Manufacturing and Computational Science

Fabrication of Inorganic Ceramic Membrane Water Filters

Enyew Amare Zereffa*, T. D. Zeleke

Department of Applied Chemistry, Adama Science and Technology University, P.O.Box 1888, Adama, Ethiopia
**Corresponding author, email: enyewama@yahoo.com*

ABSTRACT

Inorganic ceramic membrane is receiving more attention in recent times due to their unique characteristics which include different pore structures, hydrophilic surfaces, high chemical, thermal and mechanical stabilities which offer possibilities for application in water treatment. In the present work, cost-effective clay ceramic water filters of different designs were mixed and pressed from local clay (50, 60, and 70) %, organic burnout materials (15, 20, 25, and 35) %, grog (5, 10 and 15)% ratios plus 5% bone char by volume and sintered at temperature of 950ºC for 6hrs. For the flow rate of water that passed through the filter, fluoride and nitrite tests synthetic waters were used, while for E.coli removal efficiency test of the filter wastewater sample collected by purposive sampling methods from Modjo River was used. The analysis of the optimal performing sintered filter by X-ray diffraction revealed the existence of mixed phases such as quartz, kaolinite, mulite and ilite. The surface functional group analysis by infrared spectroscopy showed the presence of strong bands at 3696 cm^{-1}, 3622 cm^{-1}, 3450 $cm^{-1}$of hydroxyl linkages. Field emission scanning electron microscopy of fractured filter surfaces with better performance showed the formation of interconnected porous microstructure materials. The ceramic water filter developed from 50 % clay, 15% grog, 35% sawdust, and 5% bone char, (C950-50-35-15), characterized with total porosity 36.33±0.05 %, flow rate 1.91±0.55L/h and E. coli, nitrite, and fluoride removal efficiencies 99.91±0.09 %, 70.00±0.22%, and 96.8±0.41% respectively. Porosity evaluated by BET studies demonstrated an average pore size 18 nm and surface area of 7.30m^2/g.

Keywords: *Ceramic membrane, water filter, Microstructure, Porosity, Sintering*

1. INTRODUCTION

Lack of clean water is a great distress. Contaminated water causes different diseases which may lead to death millions (Clasen et al., 2004; WHO, 2019). Chemical contamination of drinking water sources is also a concern for millions of people and long-term exposure to these pollutants can have serious health implications. As an example, fluorine is a chemical contaminant that contaminates water and causes serious health problems such as dental and skeletal fluorosis (World Health Organization (WHO), 2021). Currently, many technologies such as chemical precipitation (Matlock et al., 2002), adsorption (Ali and Gupta, 2006), ion exchange (Rengaraj et al., 2001), membrane filtration (Zularisam et al., 2016), electrochemical (Vasudevan et al., 2014), phytoremediation (Rezania et al., 2015), and others (Upadhyay et al., 2014) have been widely studied to purify wastewater. Of these water treatments, membrane filtration, especially based on clay ceramic water filters have the ability to remove materials that affect appearance, bad taste and further remove contaminants that can cause disease and illness from water at large-scale (Sobsey et la., 2018). In fact, the WHO encourages their use as household water treatment systems for effective treatment of drinking water (Brown et al., 2017; Du Preez et al., 2008).

The practice of using metal oxides and ceramic membranes for purification has evolved because of their efficiencies in the inactivation of gram-positive bacteria, gram-negative bacteria and spore cells (Stoimenov et al., 2002; Schmidt et al., 2001; Lyckfildt and Ferreira, 1998; Yang et al., 2006), adsorption of heavy metals(Sharma et al., 2009), and removal of halogenated hydrocarbons, radio nuclides, organic compounds, fluoride and anions (Malay et al. 2011; Huang et al., 2011). Amongst these membranes, clays containing aluminum and iron oxide and chemically modified clays have been shown to adsorb higher amounts of fluoride by exchange of OH^- ions with F^- ions (Kofa et al., 2017). Similarly, high fluoride adsorption efficiencies by fired clay soil and fired clay soil pillared with tea leave ash has also been reported (Hauge et al., 1994; Mugs et al., 1996). Membrane filters are porous ceramic media which can also filter microbes or other pathogens from water, which can be easily regenerated after

fouling because the ceramics can withstand harsh chemical and thermal cleaning methods(Faibish and Cohen, 2001; Benito et al., 2007; Mallouk et al., 2007).

Such filter is prepared by mixing clay with pore formers, shaped into a filter in a press and fired in a furnace at elevated temperatures. The pore-formers leave small pores of different sizes, which can filter out the majority of harmful microbes (Doek et al., 2007; Rob et al., 2003 Mwabi et al., 2012; Doris, 2006; Galdiero, 2011; Yang and Tsai , 2008; Bottino, 2001). A clay water filter has many advantages due to its lightweight, portable, low-cost, requires no chemicals and is simple to use; it can be produced locally, using naturally available clay and other materials. The pore size and surface charge of a ceramic water filter determine its ability to remove particles and pathogens from water (Naddafi et al., 2015). The pathogenic microorganisms are ordered by size (Fig. 1), and the screening mechanism of the ceramic filter also depends on pore size diameter. The ceramic filter has been attractive to researchers in the last decade due to their superior thermal and chemical resistance, better mechanical strength, and good defouling properties (Jedidi, 2009). The successful application of ceramic filters for wastewater treatment is found in the chemical industry, metal industry, textile industry, food and beverage industry (Fang et al., 2021). The use of clay and fly ash as the raw materials for crack-free ceramic membrane filtration have showed good performance in the removal of heavy metals in the treatment of textile wastewater (Nasir, 2013; Palacio et al., 2009) and ceramic membranes made from clays and phosphates were suggested for use as a previous clarification step in textile water treatment (Shafiquzzaman et al., 2021). In another study, it has been shown that simple ceramic filters manufactured from clay soil and rice can be applied to remove more than 95% of iron through oxidation, co-precipitation, and filtration. The ceramic filter surface can be regenerated through periodic scrubbing to reduce surface deposits that slow down filtration rates (Bielefeldt et al., 2020).

The effort of this research was to develop a clay composite ceramic water filter from locally available materials such as clay, sawdust, grog and bone char for household water treatment and study the efficiency of the prepared filters in removing microorganisms (*E.* coli), and chemical contaminants: fluoride, and nitrite from drinking water.

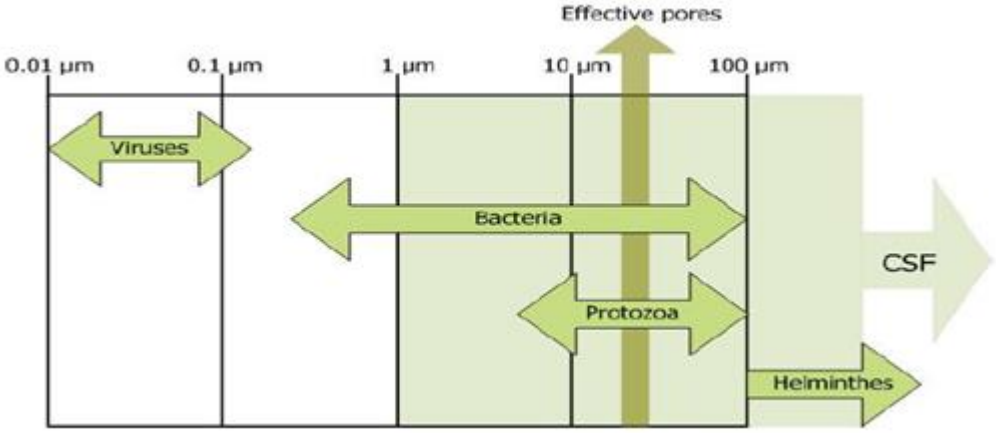

Figure 1: The order of magnitude of pathogenic microorganisms (Doris, 2006)

2. MATERIALS AND METHODS

2.1 Materials

The raw materials used for the preparation of the filters, clay, water, grog and burnout materials (i.e., hardwood sawdust) and bone char (charred at 400°C) were collected from local sources. Each of these basic materials was subjected to various physical treatments before use. The treatment included sun drying, crushing and mortar and pestle grinding of clay mortar), and sieving so that in excess of 85 percent passed through 75µm sieve size to obtain fine uniform particle size. The grog (fired clay without burnout material) was prepared from fresh dried sieved clay fired at 800°C for 6hrs.

2.2 Preparation of Filters

The preparation of different filter compositions was based on the procedure developed by Hagan et al., 2008. In a typical process, of the filters, requisite proportions of sieved clay powder, grog, bone char, and combustible matter were dry mixed thoroughly for more than 1h followed by gradual addition of water under mixing till the first signs of uniform consistency. The different wet compositions were further mixed by wedging and rolling to obtain homogenous uniform mixtures. These were then divided into pre-weighed blocks. Table 1 shows the compositions prepared. The clay mixture blocks were molded into frustum shape of dimension 20.0cm top diameter, 15.0 cm height, 10.0 cm bottom diameter and 1.10 cm wall thickness using a 2ton car jack. The shaped filters were allowed to sundry for 2 weeks. Once dried, they were sintered in a muffle furnace at 950°C for 6 hrs. This temperature was attained at a heating ramp of 5°C per minute with an intermediate stay time of 1hr at 500°C to enable removal of combustible matter and then continuing heating to the final sintering temperature with same heating ramp. After sintering, the filters were left to cool gradually until the temperature reached room temperature. The ceramic filters were removed from the muffle furnace, allowed to soak in water for 24 h and tested for their clean water flux. All the filters prepared by for this work were washed with distilled water, dried in an oven at the temperature of 100°C for 24 h, cooled, packed in plastic bags to protect them from any contamination prior to subjecting them to different tests. A typical filter prepared is shown in Fig.2.

Table 1: Composition of the different filters and the sintering temperature

S No	Filter Code	% Clay(v/v)	% Grog(v/v)	% Sawdust(v/v)	% Bone Char	Sintering Temperature (°C)
1	C950-50-15-35	50	15	35	5	950
2	C950-60-15-25	60	15	25	5	950
3	C950-70-15-15	70	15	15	5	950
4	C950-70-10-20	70	10	20	5	950
5	C950-70-5-25	70	5	25	5	950

Figure 2: Some of the prepared filters

2.3 Flow Rate

Flow rate testing is an important quality assurance step which indicates the rate at which water passes through the filter element. It was measured from the water source with the same turbidity. All the prepared filters were fully immersed in distilled water and soaked for 24 hours to ensure complete saturation at the start of the test and ensuring standardized results. Once soaked, the filters were transferred onto a flow test rack designed to drain excess water away and most importantly, to prevent overflow water from dripping into the measuring cylinders

placed below each filter. Each of the filters was filled to the brim with water and a timer started to time flow for an hour. The water level in each filter was maintained at brim throughout the duration of the test. After an hour of continuous flow, the filters were removed from the rack and the flow rate of each filter was evaluated by measuring the amount of water collected in the measuring cylinders. The flow rate of each filter was tested thrice and the values averaged.

2.4 Escherichia Coli (*E. coli*) Removal

The water used for the bacterial test was collected from Modjo River which is contaminated with pathogenic bacteria by purposive sampling technique (Ilker et al., 2016). The influent water samples were prepared by diluting (in 1:1000 ratio by taking 1 mL of the river water and diluted with 999 mL sterilize water) and filtering through Millipore 0.45-µm pore size cellulose ester filters before filtering through the ceramic filters. The E. coli concentration of the influent water and effluent water was determined in triplicate. The filters were incubated on agar for 24hours at 37°C. The log10 reduction values (LRV) were used to describe the removal efficiency in case the bacteria removal approached 100%.

2.5 Fluoride Removal Efficiency

The fluoride removal efficiency of the filters was determined using an ion-selective electrode (Expandable Ion Analyzer, Model Orion EA940, Orion Research Inc., Laboratory Products Group, and the USA). It was used to determine the fluoride removal efficiency of the filters from synthetic water samples prepared by dissolving 10mg of sodium fluoride (NaF) to obtain solutions with different fluoride concentrations: 1mg/L, 2mg/L, 3mg/L, 4mg/L, and 5mg/L solutions for the calibration of the fluoride selective electrode were prepared from the stock solution by dilution with distilled water. In order to determine the extent of adsorbed fluoride, the calibration and determination were carried out by addition of TISAB buffer. For the preparation of TISAB 500ml distilled water was taken in a 1L beaker to which 7g trisodium citrate, 56g sodium chloride, and 2g ethylenediaminetetraaceticacid were added under stirring till dissolution. To this solution, 57mL glacial acetic acid was added followed by 5M sodium hydroxide to pH 5.3 which was then transferred to a 1L volumetric flask and diluted with distilled water to the calibration mark. To 20mL each of the prepared fluoride solutions of different concentration: 1mg/L, 2mg/L, 3mg/L, 4mg/L, and 5mg/L, 2mL TISAB buffer was added for the calibration of the electrode.

In each of the triplicate filtration tests, a solution having 10mg/l of fluoride ion concentration was filtered through each filter and the filtrate analyzed for residual fluoride concentration. The potential reading of each concentration was taken and the graph of potential (E in mv) versus the logarithm of concentration (Log C in mg/L) was drawn and the slope of the graph and r^2 were calculated to check the accuracy of the measurements.

2.6 Nitrite Removal Efficiency

The removal efficiency of each filter was determined in accordance with the USEPA approved Diazotization Method* (Powder Pillows or AccuVacAmpuls) 1979; for reporting wastewater and drinking water analyses by filtering synthetic sodium nitrite solution of strength 10.98mg/L. The performance of each individual filter was evaluated in triplicate by comparing the concentration of nitrite before and after filtration and without any surface modification of the filters by acid. A stock solution of sodium nitrite (1000 mg/L) in deionized water was used to prepare a 50.0 mg/L working standard in a 100 ml volumetric flask. From this working solution, a series of calibration standards of 0.2 mg/L, 0.4 mg/L, 0.6 mg/L, 0.8 mg/L and 1.0 mg/L sodium nitrite indeionized water were prepared in 100 ml volumetric flasks.

A solution of p-nitro-aniline and 1-naphthol were prepared separately. Nitrite ions in the filtrates under acidic conditions underwent diazotization with p-nitro-aniline and formed a violet colored complex with 1-naphthol. The concentrations of nitrite after filtration were calculated from a calibration plot prepared from the standard sodium nitrite solutions.

2.7 Total Porosity

The porosity of the ceramic filters was determined in accordance with using the water absorption test (direct) method (D'ujanda, 2001). Oven dry filters were weighed in air and then saturated in distilled water at room temperature for 24 h. The wet filters were then immersed in boiling distilled water for 2 h and then allowed to cool to room temperature while being immersed for another 24 h. This was done to ensure that any entrapped air in the open pores of the filters was replaced by water. The water saturated filters were weighed while immersed in distilled water and then removed. The surfaces were wiped gently with tissue paper and the weights in air recorded. The weights of the suspending wires used for immersion were subtracted from the values recorded while determining the weights of the filters in water. Apparent porosity was then calculated using the expression:

$$P = 100\left[\frac{W_{saturate} - W_{dry}}{W_{saturated} - W_{underwater}}\right] \ldots\ldots\ldots\ldots\ldots\ldots\ldots (2)$$

Where; W-saturated is the weight of the filter when saturated with water, W-dry is the weight of the dry filter and W-under water, the weight of the filter immersed underwater. The porosity of each filter was determined in triplicate and values averaged. BET method was employed using nitrogen bearing molecular cross-sectional area of 0.162 nm² Dried filters were ground to a fine powder for surface area analysis and degassed under vacuum for 24 hours. Filters were analyzed for N2 gas adsorption and their surface area was evaluated at 77K and relative pressure range P/Po≈ 0.3-0.9.

2.8 Isoelectric Point or Zero Point Charge (pH_{zpc})

Zero point charge (pH_{zpc}) of the select filter, C950-50-15-35, was determined by using the method described by Duran-Valle, 2012. 0.1 M of 10 NaCl solutions having the initial pH values ranging from 1 to 12 was prepared in duplicate using 0.1M HCl and 0.1M NaOH, and the final pH values of the solutions were then measured, and the calculation of ΔpH was made by subtracting the initial pH values from final pH values.

3. RESULTS AND DISCUSSION

3.1 Characterization of Clay

The gravimetric method was used to determine silica (SiO_2) and alumina (Al_2O_3), whereas ferric oxide (Fe_2O_3), calcium oxide (CaO), and magnesium oxide (MgO) were estimated volumetrically. Alkalis were determined by flame photometry and the loss on ignition (LOI) was determined by heating the sample in a muffle furnace at 1000°C for 60 min followed by cooling to room temperature and recording the weight loss. The results showed that the major components of the clay were SiO_2 (47.32%), Al_2O_3 (21.88%), Fe_2O_3 (11.6%), and minor oxides were CaO (0.44%), MgO (<0.01%), Na_2O (4.18%) and K_2O (1.48%) (Table.2). This indicated that the filter material is composed of high siliceous clay. The chemical composition of the clay is shown in Table 2.

Table 2: The chemical composition of raw clay

Oxide	SiO_2	Al_2O_3	Fe_2O_3	CaO	MgO	Na_2O	K_2O	MnO	P_2O_5	TiO_2	H_2O	LOI
%	47.32	21.88	11.6	0.44	<0.01	4.18	1.48	<0.01	0.07	0.31	2.20	11.55

3.2 Removal of Nitrite

In Table 3, it is observed that all the ceramic filters prepared were able to remove a sufficient amount of nitrite from its water solutions. The filter, C950-50-15-35, incorporating 35% burnout materials removed about 76% nitrite without any need of surface modification by acid. The surface modification of the clay composite filter with the ash obtained from sawdust improved nitrite adsorption on the surface of the clay composite adsorbents (Sowmya and Meenakshi, 2013).

Table 3: Basic parameters determined by different filters

S. No	Filter Code	*E.* coli (%)	Flow Rate (L/h)	NO_2^- (%)	F^-(%)
1	C950-70-15-15	96.67±2.88	1.20±0.15	70.69±0.26	96.4±0.31
2	C950-60-15-25	98.09±1.90	1.56±0.25	73.99±0.23	93.8±0.21
3	C950-50-15-35	99.91±0.09	1.91±0.55	76.00±0.22	96.8±0.41
4	C950-70-10-20	91.9±3.87	1.63±0.31	71.42±0.32	98.6±0.20
5	C950-70-5-25	95.94±3.61	2.50±0.27	72.77±0.22	97±0.01

3.3 Removal of E. coli

The diluted Modjo river water used for filtration had more than 250 cfu *E*. coli bacteria detected in 100 ml. From Table 3, it is observed that the number of *E*. coli bacteria colonies after filtration, expressed in terms of percentage reduction of *E*. coli bacteria, ranged from 91.9±3.87 % to 99.91±0.09 %. The filter C950-70-10-20 with 91.9±3.87 % removal efficiency is termed as a high-risk filter according to the WHO water risks categories. Ceramic water filters with interconnected pores and average pore diameter less than the size of bacteria are more efficient in removing microbial colonies from contaminated water sources (Vasanth et al., 2011; Clasen et al., 2007). The obtained trends pointed out the increase of the microbial removal efficiency of the filters with the decrease in clay plus grog and an increase in the percentage composition of sawdust. This is attributed to the formation of uniform pores during sintering in the ceramic body as confirmed by the micro-structure image of the filter C950-50-15-35.

3.4 Porosity

The total porosity of the filters as a function of the percentage of burnout material content is shown in Figure 2. The data indicated that the porosity was proportional to the initial additive content of the pore-forming agent. The porosity of the prepared filters increased with an increase in the percentage of burnout material incorporated in the compositions of the filters. This is evident from the total porosity of the filter C950-50-15-35 having the highest ratio of sawdust (35%), porosity (36.33±0.05 %), and flow rate (1.91±0.55 L/h) which is in the WHO standard.

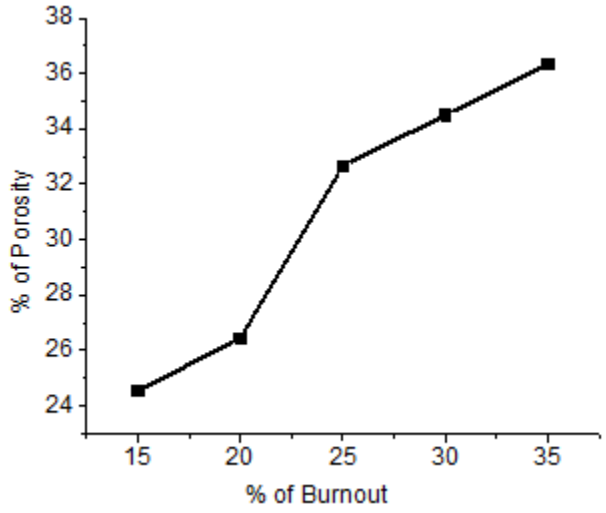

Figure 3: Percent porosity of the filters as a function of sawdust ratios

3.4.1 BET Analysis of Sintered Ceramic Filter

By analyzing the adsorption isotherms of nitrogen on the mesoporous C950-50-15-35 ceramic filter surface at increasing relative pressure, the BET surface area, pore size and volume were determined. The adsorption &

desorption isotherms characteristics of C950-50-15-35 composite classified as the Type IV isotherm in accordance to the IUPAC isotherm classification. The mesoporous structure of the developed ceramic filter element makes it a potential adsorbent material. The distribution of pore sizes for sintered C950-50-15-35 was from the Multipoint BET analysis is, in the 0.025 to 0.30 range of P/P_0, the linear plot with correlation coefficient of 0.99 was determined, with the positive slope of 5.45. The calculation of specific surface area, total pore volume and average pore diameter based on the Brunauer-Emmett-Teller (BET) method for the sintered filter were 7.30g/m^2, 0.0033 cc/g and 18 nm respectively.

3.5 Removal of Fluoride Ions

The removal efficacies of the filters are shown in Table 3. The prepared filters contain three potential deflouridation materials: fired clay, activated bone char, and thermally treated leftover sawdust or activated carbon in their ceramic structures. The main methods used in defluoridation from aqueous solutions are ion exchange and adsorption techniques (Fan et al., 2003). On average, the filters reduced the initial fluoride concentration of 10mg/L in the untreated water samples to a residual 0.68mg/L in the filtered water which is greater than 95% removal efficiency. The high fluoride removal efficacies of the filters sintered at 950°C might be due to the exchangeable hydroxyl ions from clay, bone char, and activated carbon in the ceramic bodies.

3.6. Zero point charge (pH_{zpc})

The isoelectric point, pH_{PZC}, of the filter C950-50-15-35 (Table 4) indicated that its surface was neutral (pH_{PZC}= 8.5). This indicated that the adsorption affinity of many negatively charged species including fluoride ions would be feasible in the WHO recommended range (6.5-8.5) for drinking water (Doke et al., 2013). The pH of the filtered water revealed that the filter was resistant to both acid and base (Bottino et al., 2001).

Table 4: The pH change results of filter C950-50-15-35 for Zero point charge determination

Initial (pH)	Final (pH)	ΔpH	Initial (pH)	Final (pH)	ΔpH	Initial (pH)	Final (pH)	ΔpH
1	7.19	6.19	5	7.5	2.5	9	7.4	-1.6
2	6.99	4.99	6	8.0	2.0	10	7.3	-2.7
3	6.79	3.79	7	7.66	0.66	11	6.9	-4.1
4	6.66	2.66	8	7.8	0.2	12	6.7	-5.3

3.7 X-Ray Diffraction and Energy Dispersive X-Ray Analysis

Fig.4. shows the XRD patterns of raw clay and the filter C950-50-15-35. The major peaks of the fired filter are associated with those of quartz (2θ = 20.76, 27.08 and 49. 97). Other peaks of the raw clay are related to kaolinite (2θ =12.47 and 24.32), and muscovite (2θ = 32.02 and 36.15). The kaolinite phase of raw clay transformed into metakaolinite, which is an amorphous material and, consequently, displays no XRD peaks in the fired clay (Carty et al., 1998)

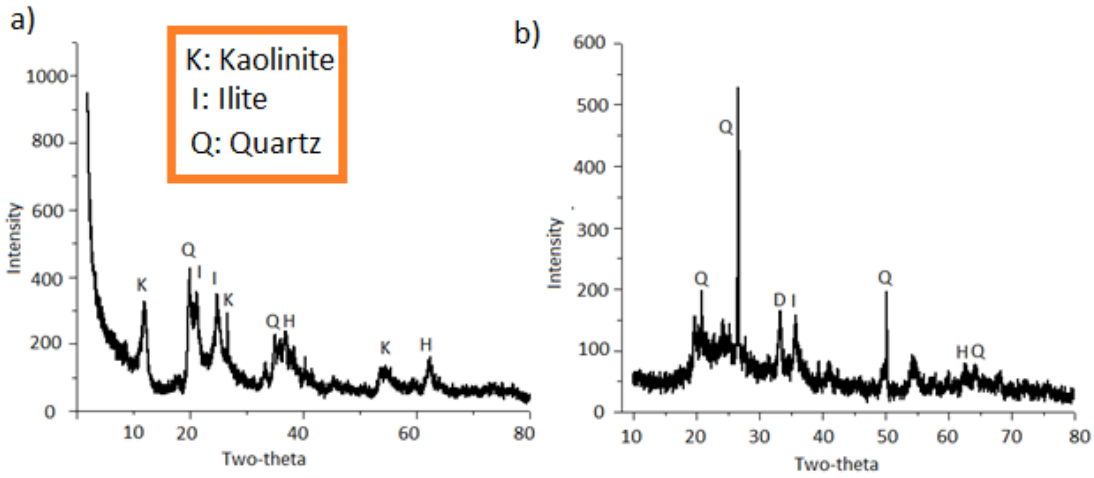

Figure 4: XRD patterns of (a) raw clay and (b) filter C950-50-15-35

The energy dispersive spectrometry (EDS) analysis (Fig.5) revealed that the major elements in the filter were like calcium (Ca), aluminum (Al), silicon (Si), oxygen (O), iron (Fe), carbon (C) and phosphorous (P). The presence of other elements like copper (Cu) and tin (Sn) may be due to the adsorption of other ions on the surfaces of the filter from the contaminated water during filtration.

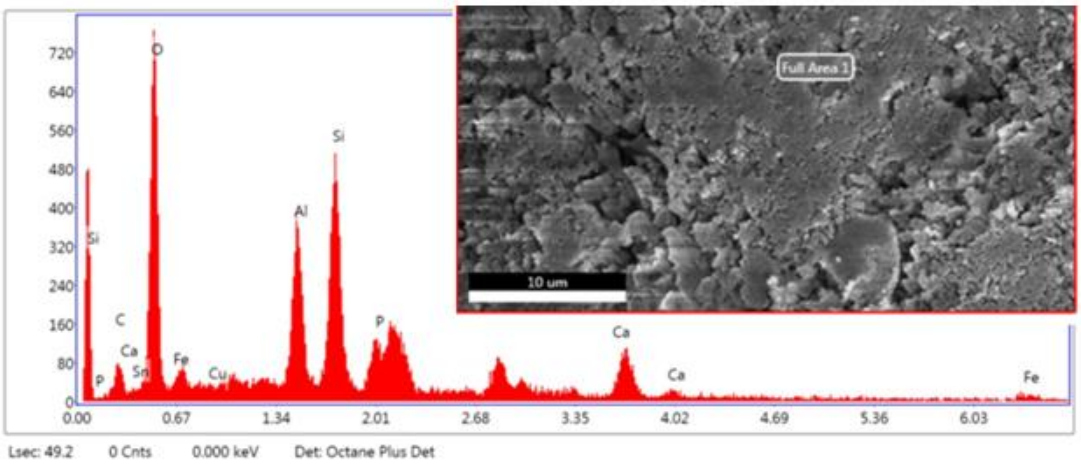

Figure 5: EDS spectrum of filter C950-50-15-35

3.8. Microstructure of the filters

The desired flow rate and microbial removal efficiency of sintered filters are influenced by the formation of defects created in the bulk body during the sintering process. The microstructures of the filters by investigated Field Emission electron microscopy are shown in Figure 6. From the figure, it is observed that the differences in structures of the filters are a direct consequence of the variations of the ratios of clay to sawdust. The filter C950-60-15-25 showed the presence of uniform porous structures, filter C950-50-15-35 showed a fine and interconnected uniform porous microstructure and filter C950-70-5-25 showed minor cracks in the microstructure, the presence of which affected both the flow rate and *E*. coli removal efficiency. The filter C950-70-10-20 showed a large cracks microstructure with uneven pores distribution. The presence, distribution, and connectivity of pores are observed on, C950-70-15-15, filter micrograph. The pore size in the sintered filtered, both at the external and the fractured inner surface, are nearly similar.

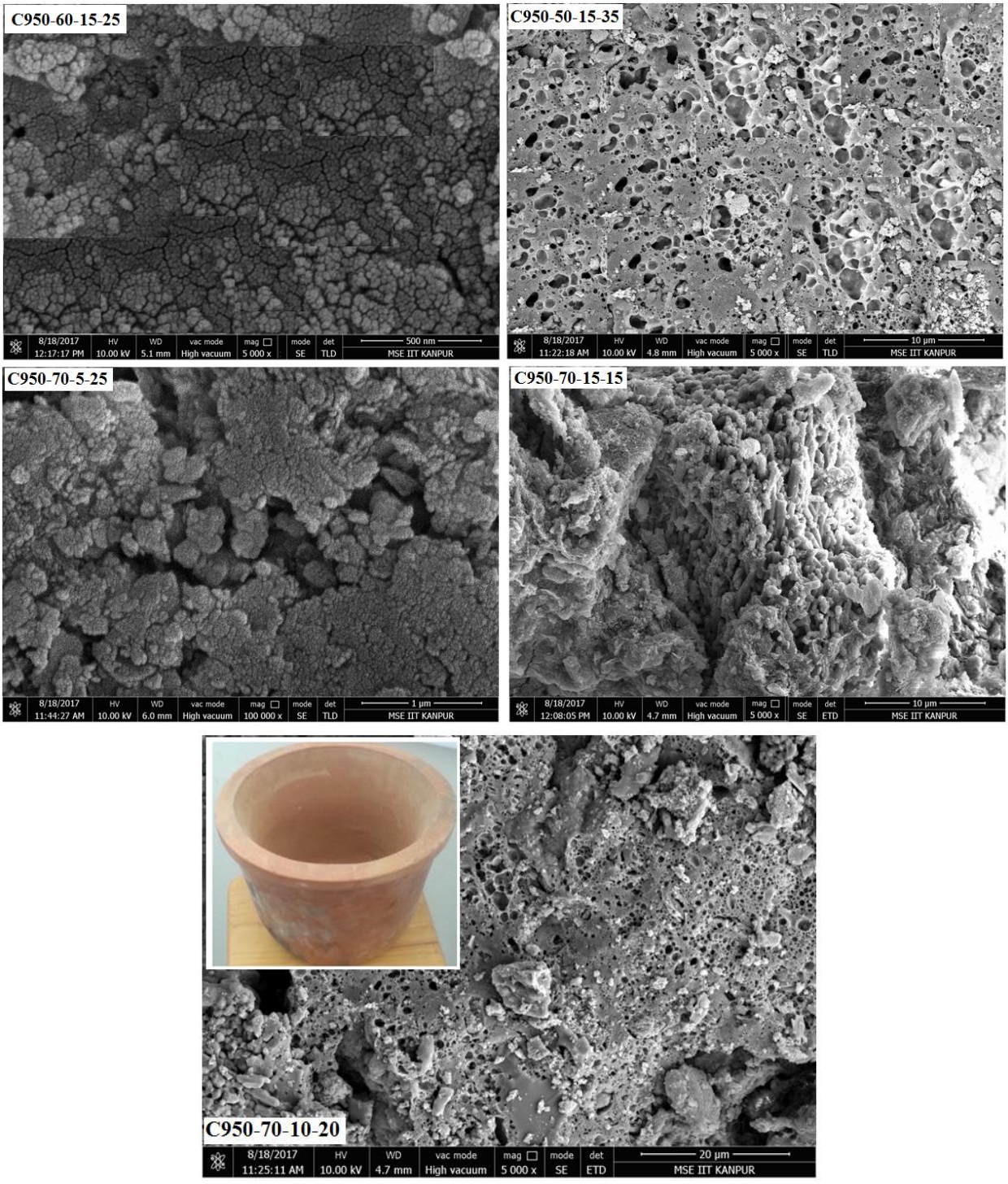

Figure 6: Microstructures of the sintered filters by FESEM

3.9 FT-IR Analysis

FTIR spectra of one select filter, C950-60-25-15, before and after filtration of NaF solution of concentration are shown in Fig. 7a and 7b. The presences of coupled vibrations are appreciable due to the availability of various groups. Most of the bands such as 3696cm^{-1}, 3622 cm^{-1}, 3450 cm^{-1}, 1033 cm^{-1}, 917 cm^{-1}, 795 cm^{-1}, 692cm^{-1}, 533cm^{-1} and 466cm^{-1} showed the presence of kaolinite. As seen in the spectra of the filter prior to NaF filtration

(Fig.7a), the vibration observed at ~917 cm^{-1} is attributed to the possibility of the presence of hematite (Farmer, 1974) whereas, the vibrations at 3622cm^{-1}, ~1631 cm^{-1} and 1033 cm^{-1} are attributed to the presence of gypsum and that at ~693 $cm^{-1}$is attributed to the possible presence of calcite. The strong triplet peaks at 3696 cm^{-1}, 3622 cm^{-1} and 3450$cm^{-1}$are associated with hydroxyl groups. However, the broadband at 3450 cm^{-1} and the band at 1633 $cm^{-1}$are suggestive of the water of hydration in the filter.

The FT- IR spectra also revealed the differences between the functional groups in the filter before and after filtration of the fluoride contaminated water solution. It was observed that the hydroxyl groups present on the filter surface were mainly involved in the sorption of fluoride. Anion exchange and electrostatic interaction were suggested as the main mechanisms involved in the sorption of fluoride on the filter. The changes in the stretching frequency of fluoride-treated filter material compared to untreated filter material confirm the chemical modification.

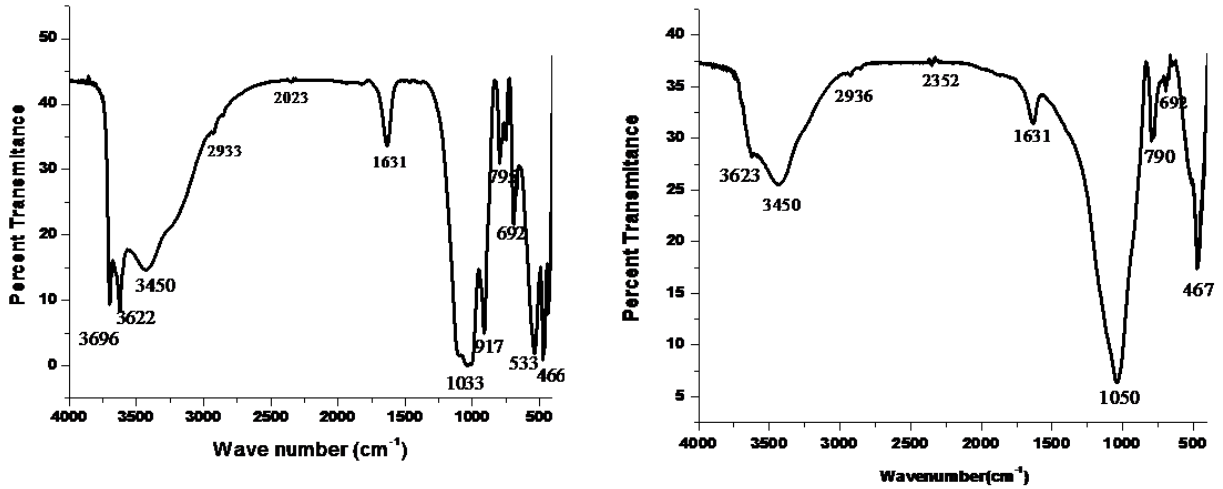

Figure 7: FT-IR spectrum of filter C950-60-25-15 before (a) filtration of NaF (10mg/L) solution (b)after filtration of NaF (10mg/L) solution

4. CONCLUSIONS

In this work, five ceramic water filters were fabricated by varying the ratios of clay, binder, and burnout and bone chare, and sintered at 950ºC. The efficiency of the filters for water purification was evaluated by determining their efficacies to remove *E.* coli, nitrite and fluoride ions from synthetic and contaminated river water samples. It is clearly evidenced that the performance levels of the filters are an influence of their compositional variations with respect to the ratios of clay, grog, and sawdust. The filter C950-50-15-35 showed the best overall performance, able to remove *E.* coli 99.70±2.4 % and possessing a good flow rate 1.91±0.55 L/h. It is also concluded from the microstructures of the filters that there is a room for further refining the structure by slightly fine-tuning the interplay of the ratio of clay to grog to sawdust.

ACKNOWLEDGMENTS

The researchers would like to acknowledge Adama Science and Technology University Research Affairs for the financial support and OSHO Fluoride Removal Technology Center for providing laboratory facilities.

REFERENCES

Ali I., Gupta V., (2016), Advances in water treatment by adsorption technology. Nat. Protoc, 1, 2661–2667.

Benito J., Sanchez M., Pena P., Rodríguez M., (2017), Development of a new high porosity ceramic membrane for the treatment of bilge water, Desalination, 214, 91-101

Bielefeldt A., Kowalski K., Schilling C., Schreier S., Kohler A., Summers R., (2020), Removal of the virus to protozoan sized particles in point-of-use ceramic water filters. Water Research, 44, 1482-88.

Bottino A., Capannelli C., Del Borghi A., Colombino M., Conio O., (2001), Water treatment for drinking purpose: ceramic microfiltration application, Desalination, 141,75-79.

Brown J., Sobsey M., ProumS:.,(2007), Improving household drinking water quality, Use of ceramic water filters in Cambodia.WSP Field notes. Phnom Penh, Cambodia: WSP.

Carty W.M., Senapati U., (1998), Porcelain-Raw Materials, Processing, Phase Evolution, and Mechanical Behavior, Journal of the American Ceramic Society, 8: 3-20.

Clasen T., Brown J., Collin S., Suntura O., Cairncross S., (2004), Reducing Diarrhea Through The Use of Household-Based Ceramic Water Filters: A Randomized, Controlled Trial in Rural Bolivia, American Journal of Tropical Medicine and Hygiene, 70, 651-657.

Clasen T., Schmidt W., Rabie T., Roberts I., Cairncross S., (2007), Interventions to improve water quality for preventing diarrhea: a systematic review and meta-analysis.BMJ, 334, 782

Doek S., Simon B., Dik B., Bas H., (2007), Particle Removal from Surface Water with Ceramic Microfiltration. Leeuwarden: The Netherlands.

Doke M. K., AmolChavan R., Nalawade, Ejazuddin M., (2013), Kinetics and Equilibrium Isotherm for adsorption of Basic Blue Dye onto Activated Charcoal prepared from Bhagar Seed Husk, J. Matter and Environmental Science,3, 374-383.

Doris V., (2006): Aqua for All Post bus 1072 3430 BB Nieuwegein Department of Water Management Faculty of the Civil Engineering Delft University of Technology, Kiwa Water Research Groningerhaven, 1- 76.

Du Preez M., Conroy R. M., Wright J. A., Moyo S., Potgieter N., Gundry S.W., (2008), Use of Ceramic Water Filtration in the Prevention of Diarrheal Disease: a Randomized Controlled Trial in Rural South Africa and Zimbabwe. American Journal of Tropical Medicine and Hygiene, 79, 696-701.

Faibish R., and Cohen Y., (2001), Fouling-resistant ceramic-supported polymer membranes for ultrafiltration of oil-in-water microemulsions, Journal of Membrane Science,185, 129-143.

Fang J., Qin G., Wei W., Zhao X., (2011), Preparation and characterization of tubular supported ceramic microfiltration membranes from fly ash, Separation and Purification Technology, 80, 585-590.

Fan X., Parker D., Smith M., (2003), Adsorption kinetics of fluoride on low-cost materials," Water Research, 37, 4929–4937.

Hagan J., Harley N., Pointin D., Sampson M., Vanna S., Smith K., (2009), Resource Development International. Cambodia: Ceramic Water FIlter Handbook.

Hagan J., Harley N., Pointing D., Sampson M., Soam V., (2008), Ceramic Water Filter Handbook, Resource Development International, Cambodia.

Hauge S., Osterberg R., Bjorvatn K., Selvig A., (1994), Defluoridation of drinking water with pottery: effect of firing temperature, Scandinavian Journal of Dental Research, 102, 329–333.

Huang Y., Shih Y., Chang C., (2011), Adsorption of fluoride by waste iron oxide: The effects of solution pH, major coexisting anions, and adsorbent calcination temperature. J. Hazard. Mater, 186, 1355–1359.

Ilker E., Rukayya A., (2016), Comparison of Convenience Sampling and Purposive Sampling. Department of Biostatistics, Near East University, Nicosia-TRNC, Cyprus American Journal of Theoretical and Applied Statistics; 5, 1-4.

Jedidi I., Saïdi S., Khmakem S., Larbot A., Elloumi-Ammar, N., Fourati, A., Charfi, A., Amar R.B.,(2009), New ceramic microfiltration membranes from mineral coal fly ash, Arabian Journal of Chemistry, 2, 31- 39.

Kofa P., Gomdje H., Telegang C., NdiKoungou S., (2017), Removal of Fluoride from Water by Adsorption onto Fired Clay Pots: Kinetics and Equilibrium Studies, Journal of Applied Chemistry, 2017,1-7.

Lyckfildt O., Ferreira F., (1998), Processing of porous ceramics by starch consolidation, Journal of the European Ceramic Society, 18, 131-140.

Malay K., Salim J., (2011), Comparative Study of Batch Adsorption of Fluoride Using Commercial and Natural Adsorbent, Research Journal of Chemical Sciences,1, 68-75.

Mallouk, W., Lukens, D., Shuh, D., (2007), Removal of pertechnetate from simulated nuclear waste streams using supported zerovalent iron, Chemistry of Materials, 19, 5703-5713.

Matlock, M.M., Howerton, B.S., Atwood, D.A., (2002), Chemical precipitation of heavy metals from acid mine drainage. Water Res, 36, 4757–4764.

Mugs G., Zewge F., Socher M., (1996), Preliminary investigations on the defluoridation of water using fired clay chips, Journal of African Earth Science, 21, 479-482.

Mwabi J.K., Mamba B.B., Momba M., (2012), Removal of Escherichia coli and fecal coliforms from surface water and groundwater by household water treatment devices/systems: A sustainable solution for improving water quality in rural communities of the Southern African Development Community Region. Int. Journal of Environmental Research and Public Health, 9,139–170.

Naddafi K., MahvI A., Nasseri S., Kokhtari M., Zeraati H., (2005), Evaluation of the efficiency of clay pots in the removal of water impurities. Iranian Journal of Environmental Health Science and Engineering, 2, 12–16.

Nasir Subriyer, (2013), Treatment of domestic water using the ceramic filter from natural clay and fly-ash Journal of Engineering studies and research,19, 71-75.

Palacio L., Bouzerdi Y., Ouammou M., Albizane A., Bennazha J., Hernández A., Calvo J., (2009), Ceramic membranes from Moroccan natural clay and phosphate for industrial water treatment, Desalination, 245, 501-507.

Schmidt H., Koch D., Grathwohl G., Colombo P., (2001), Micro and macroporous ceramics from preceramic precursors, Journal of the American Ceramic Society. 84, 2252-2255.

Shafiquzzaman M., Azam S., Nakajima J., Bari H., (2011), Investigation of arsenic removal performance by a simple iron removal ceramic filter in rural households of Bangladesh, Desalination, 265, 60– 66.

Sharma C., Srivastava V., Singh K., Kaul N., Weng H., (2009), Nano-adsorbents for the removal of metallic pollutants from water and wastewater, Environmental Technology, 30, 583-609.

Sobsey M. D., Stauber C. E., Casanova L. M., Brown J. M., Elliott M. A.,(2008), Point of Use Household Drinking Water Filtration: A Practical, Effective Solution for Providing Sustained Access to Safe Drinking Water in the Developing World. Environmental Science and Technology, 42, 4261-4267.

Sowmya A., Meenakshi S., (2013), Removal of nitrate and phosphate anions from aqueous solutions using strong base anion exchange resin. Desalination and Water Treatment, 51, 7145-7156.

Stoimenov P. K., Klinger R. L., Marchin G. L., Klabunde K. J., (2002), Metal oxide nanoparticles as bactericidal agents, Langmuir, 18, 6679-6686.

Rezania S., Ponraj M., Talaiekhozani A., Mohamad S.E., Din M.F.M., Taib S.M., Sabbagh F., Sairan F.M., (2015), Perspectives of phytoremediation using water hyacinth for removal of heavy metals, organic and inorganic pollutants in wastewater, Journal of Environmental Management,163, 125–133.

Rengaraj S., Yeon K.H., Moon S.H., (2001), Removal of chromium from water and wastewater by ion exchange resins. Journal of Hazardous Materials, 87, 273–287.

Rob D., Xanat F., Melanie P., Georges T., (2003), Point-of-use water treatment technology investigations in Nepal. Clean Water for Nepal, Inc, Cambridge, MA 02139.

Upadhyay R.K., Soin N., Roy S.S., (2014), Role of graphene/metal oxide composites as photocatalysts, adsorbents, and disinfectants in water treatment: A review. RSC Adv. 4, 3823–3851

Vasanth D., Pugazhenthi G., Uppaluri R., (2011), Fabrication and properties of low-cost ceramic microfiltration membranes for separation of oil and bacteria from its solution. Journal of Membrane Science, 379, 154-163.

Vasudevan S., Oturan M.A., (2014), Electrochemistry: As cause and cure in water pollution—An overview, Environmental Chemistry Letters,12, 97–108.

WHO, (2009), Diarrhoea: Why Children Are Still Dying and What Can Be Done, New York: United Nations Children's Fund. WHO, (2011), Guidelines for drinking-water quality.

Yang G., Tsai C., (2008), Effects of starch addition on characteristics of porous ceramic membrane substrates, Desalination, 233, 129–136.

Yang S., Ryu I., Kim Y., Kim K., Jang K., Russell P., (2006), Nanoporous membranes with ultrahigh selectivity and flux for the filtration of viruses, Advanced Materials18, 709-712.

Zularisam A.W., Ismail A.F., Salim R., (2006), Behaviours of natural organic matter in membrane filtration for surface water treatment—A review. Desalination, 194, 211–231.

Front End Passive Safety System for Vehicle Collisions: Design and Analysis

Kibru Aregahegn*, Ramesh Babu Nallamothu

Mechanical Engineering Department, Adama Science and Technology University, P.O.Box 1888, Adama, Ethiopia
**Corresponding author, email: kibruaregahegn2412@gmail.com*

ABSTRACT

Road crashes are hard-nosed affairs that can have a very negative influence on vehicles and vehicle occupants involved in them. Efforts to improve road safety, particularly vehicle safety, have been made in numerous ways. But these systems are not effective in low-income countries because these systems require some advanced system and infrastructure inroads. In this work a new front-end, the passive safety system is designed, modeled using CATIA V5R20, and installed on a Geo-Metro sedan vehicle which is developed under NCAC, by applying boundary conditions and testing the effectiveness and functionality of the system by using LS-DYNA. One free rotation wheel is fitted horizontally at the vehicle's lower front left and right corners, respectively, in the specified passive safety mechanism. In non-perpendicular forward collisions, the wheels are the vehicle's first point of contact; the collision force component parallel to the impact surface causes the wheel to rotate, causing the vehicle to roll in the direction of the parallel force component. The simulation of the vehicle indicates that the vehicle with a device at 45 degrees and 35km/h impact to the PCB-R diverts the harmful energy (about 69 kKJ) into non-harmful energy than the vehicle tested without a device, and in addition, it increases the displacement of the vehicle about 447 mm into negative y-direction. For occupant response, the resultant rotational acceleration measured at the C.G accelerometer indicates for the vehicle equipped with a device was lower than the vehicle without a device. Generally, we can conclude that the vehicle with a device diverted to the safest place and the probability of occurrence of rear-end collision decreased, and the harm to the parts and occupant decreased. The stability of vehicle for the vehicle with a device was improved.

Keywords: *Front-end passive safet, vehicle collision, LS-DYNA, Geo-Metro, Non-perpendicular, Harmful/non-harmful Energy*

1. INTRODUCTION

Traffic accidents expanded periodically at an alarming rate and it was a genuine issue all through the globe especially in developing countries like Ethiopia (Deme, 2019). A road traffic accident (RTA) is an incidence that occurs or begins on a public way or road, resulting in the death or injury of one or more individuals, with at least one moving vehicle involved.

Collisions between cars, vehicles and pedestrians, and vehicles and wildlife or immovable obstructions are all included in RTA (Woldu et al., 2020). Every year, around 1.35 million people's lives are cut short as a result of a road traffic accident around the world. This special issue examines the history and background of car safety systems while also highlighting modern advances (Sabarinath, 2020). The traditional approach to active and passive safety systems is to supply their functionality only during the phase in which they are used (Waghe and S Y, G, 2014). The problem will be modeled using computer-aided parametric design software to specify all coordinate values and geometrical details. This CATIA data will then be transferred to FEM software for pre-processing, solution, and post-processing. Finally, results pertaining to energies, acceleration, and displacements with various loads and boundary conditions in various accidental situations will be generated and interpreted (Yadav and Pradhan, 2014).

2. MATERIALS AND METHODS

Modeling and Assembling of the Components

The wheel has a rim-type structure, as shown in Fig. 1, to reduce weight and material utilization without sacrificing performance. The wheel is fastened to the car's body frame using the mounting plates. The caps protect the interior of the rim-style wheel, preventing dust from entering. The passive safety system is assembled with a wheel, top mounting plate, top cap, bottom mounting plate, and bottom cap, as illustrated in Fig. 1.

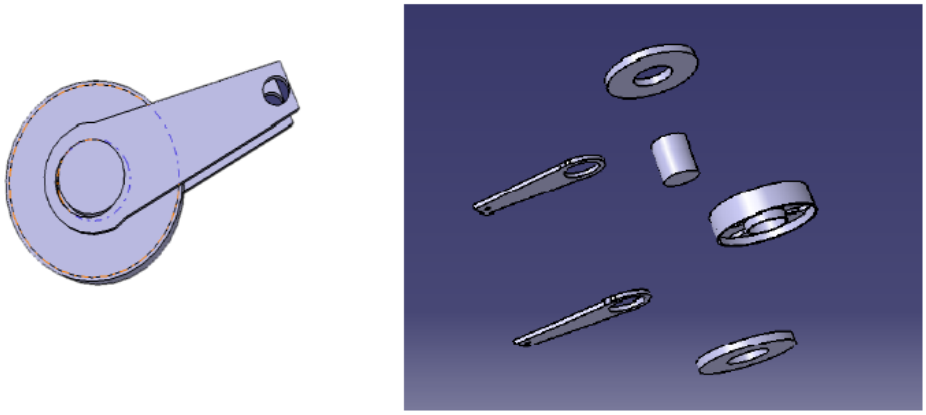

Figure 1: Front-end passive collision safer systems in assembly order

Selection of Models

Vehicle Model Selection

For simulations involving the impact of a sedan, passenger car, a 632.8 kg small car model known as Geo Metro developed and validated by NCAC (National Crash Analysis Center) was utilized. Selected vehicle model is given in Fig. 2.

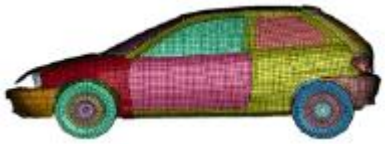

Figure 2: Vehicle model

Guardrail Model

Portable concrete barriers (PCBs) that are modeled under the National Crash Analysis Center (NCAC) are used as colliding material. The model of guardrail is shown in Fig.3.

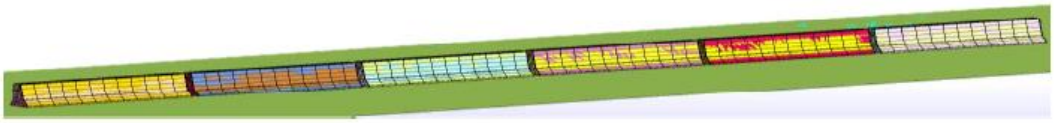

Figure 3: Guardrail model

Installation of Front-End Passive Safety System

Fig. 4 demonstrates the configuration and assembly of front end passive safety systems at the two front sides of the front end chassis outline next to the bumper.

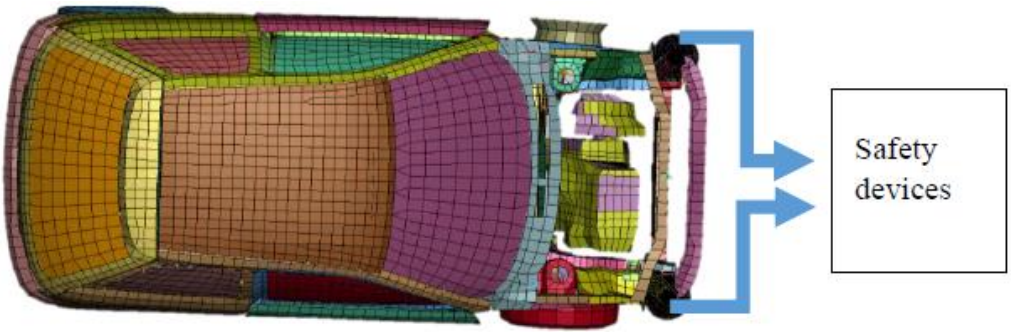

Figure 4: Front-end passive collision safety system installed on bumper location

Simulation of the Designed System Using LS-DYNA

There are three basic steps in the technique for explicit dynamic analysis:

- ✓ Create the model
- ✓ Apply loads and get the solution
- ✓ Review the results

For the analysis of the modeled and assembled parts of the front-end passive safety systems, first, we have to save them in IGES format in CATIA so that our systems will become readable in LS DYNA for further analysis. The front-end passive safety system for Geo metro (reduced model) is designed by using CATIA V5R20 software as per the dimensions.

Systems of Consistent Units

The finite element code will accept any units that are input without error checking. Thus, if engineering units are input using an inconsistent system of units, or a left-handed coordinate system is used, the results will be flawed. The modeler should be careful with units of force, mass, and density.

Mesh Quality

The dependability of crash simulation findings is generally greatly impacted by the mesh quality, element choice, and number of nodes and elements of a vehicle model (big numbers meaning greater structural details but high computing cost). Quality parameters and their allowable minimum and maximum values are given in Table 1.

Table 1: Quality parameters and their allowable minimum and maximum value

Quality parameter	Allowable mn/max
Aspalt ratio	5
Warpage	15
Jacobian	0.6
Minimum side length	5
Maximum side length	12
Minimum triangular internal angle	15
Maximum triangular internal angle	120
Triangles	5

Mesh Generation

For the time being, mixed elements of linear quadrilateral and triangular elements were employed, with an average element size of 3 for the front-end passive safety system and an element size of 1 for the rest of the model. The overall mesh of the vehicle with a system is illustrated in Fig. 5.

Figure 5: Mesh generation for the whole vehicle

Element Formulation

The completed model contains approximately 205 parts, 205 materials, and 16260 elements and 19216 nodes for normal vehicle test and 512 parts, 510 materials and 24,000 elements, and 25,800 nodes for a vehicle with device test. The model's structural components and specific element kinds include:

- ✓ Solid elements
- ✓ Shell elements

Material Properties and Thickness of the Front-end Passive Safety System

Table 2: Material and section definition of the designed system

Vehicle item	Mass density (kg/mm^3)	Young's modulus (GPa)	Poisons ratio	Yield stress (GPa)
Flywheel	7.890e-09	2.00e+05	0.30	300
Mounting plate	6.8 e-09	1.89e+5	0.28	200
Shaft	7.890e-09	2.00e+05	0.30	300

Table 3: Section definition of the designed system

Vehicle components	Thickness in mm (from design result)
Flywheel	47.6
Mounting plate	0.46
Shaft	15.6

Vehicle Components Constrain

The designed front-end passive safety system is jointed into the vehicle front-end frame at the bumper location by a CONSTRAINED NODAL-RIGID BODY. The designed system mounting plate and shaft are joined by constrained EXTRA-NODE-SET. But between the shaft and the rotating wheel which is allowed to rotate freely on the shaft upon impact, constrained JOINT- REVOLUTE is created as the following Fig. 6. To reduce the motion space, all of the vehicle components of the simplified model were joined together using different constraint types within the FE program, LS-DYNA (LS-Pre-Post).

Figure 6: JOINT-REVOLUTE between a shaft and rotating fly-wheel

Verification of the results

For verification of the result obtained, we use the comparison of the results with and without the system for the same parameter and boundary condition and compared with each other.

Configuration of vehicle and guard rail

For the first scenario i.e. at a normal speed of the vehicle the following configuration is set up.

A. At an angle of impact of 45 degrees and low speed (35km/h):

Figure 7: Simulation configuration of a vehicle with a barrier

B. Vehicle test at large collision angle 70 degrees:

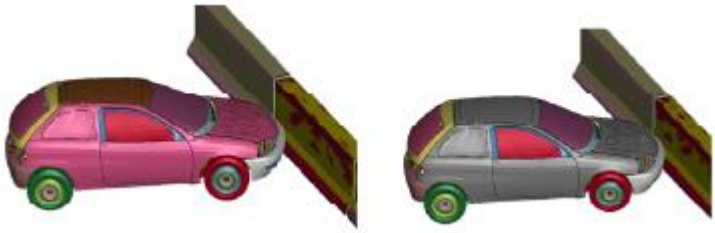

Figure 8: Vehicle crash configuration at large collision angle

The third scenario is when a vehicle makes a collision with a rigid body (PCB-B barrier) at high impact force i.e. the initial vehicle velocity is too high. The following configuration is to test the vehicle at high speed.

C. At an impact angle of 45 degrees and High-speed (120 km/hr)

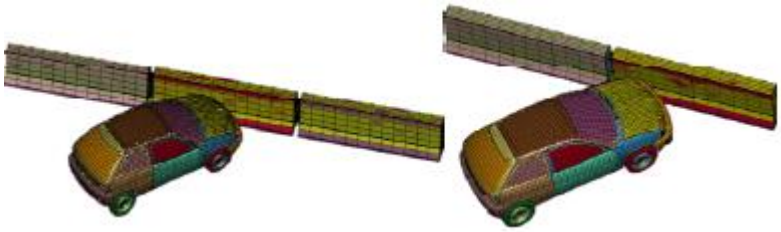

Figure 9: Vehicle crash configuration at a high vehicle speed

Vehicular Response

Crash testing companies must adhere to the processes outlined in the handbook while evaluating safety hardware (MASH). According to MASH, the recommended departure angle should be less than 60% of the initial impact angle. The following Table 4 lists the preferred exit angles specified by MASH.

Table 4: MASH's preferred maximum exit angles

Impact angle	20	30	40	50	60	70	80	90	100
Preferred maximum exit angle	12	18	24	30	36	42	40	54	60

The car's yaw, pitch, and roll were used to examine the orientation and stability of the vehicle during a collision, as shown in Fig. 10. Pitch and roll angles were used to assess the vehicle's stability during the impact, while the yaw angle showed how far the vehicle was deflected. According to MASH regulations, pitch and roll angles shouldn't be greater than 75 degrees because they can indicate shaky vehicle behavior.

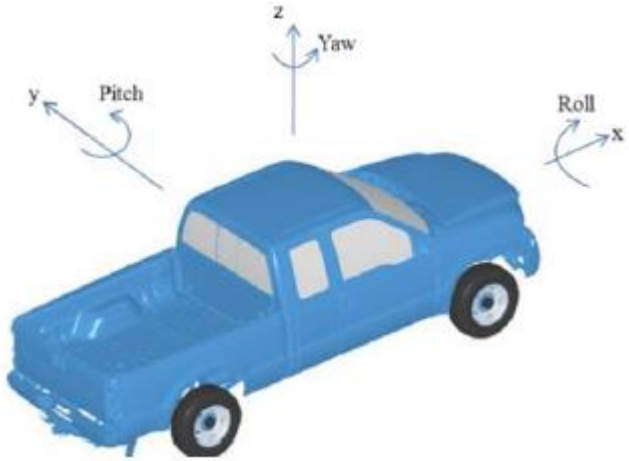

Figure 10: Definition of yaw, pitch, and roll

3. RESULTS AND DISCUSSION

Impact at an Angle of 45 Degrees and 35 km/h

Fig. 11 shows the energy curves of a Geo- metro small vehicle with and without a front-end passive safety system. The Figure shows that for a vehicle without a system, the kinetic energy is decreased from 409 kJ to 160 kJ and the internal energy of the vehicle increases from 0 kJ to approximately 219 kJ. But for a Geo-Metro vehicle test with a system, the energy curve indicates that the kinetic energy decreases from 410 kJ to approximately 225 kJ and the internal energy is increased from 0 kJ to 150 kJ.

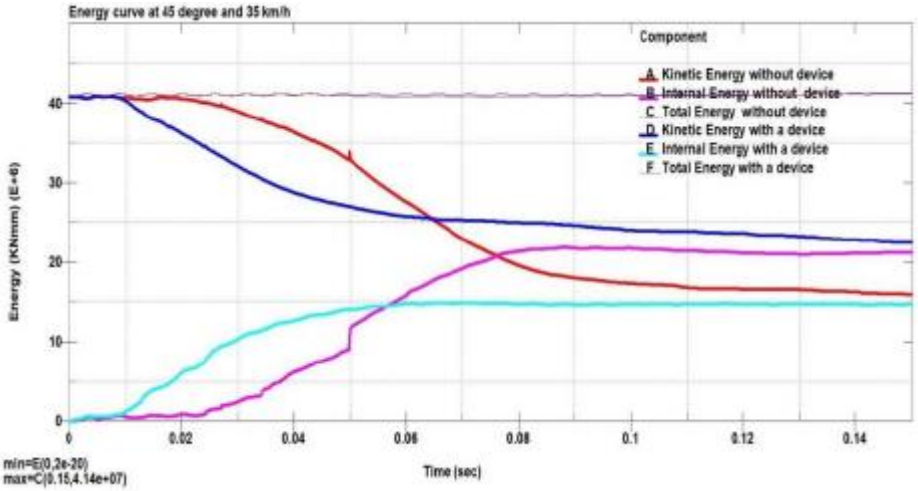

Figure 11: Energy curves of a vehicle collision at an angle of 45 degrees and 35 km/h

When we compare the increase in internal energy of the vehicle with and without a system, there are approximately (219 kJ-150 kJ) equal to 69 kJ of internal energy increase for a vehicle without a system, and this means that for a vehicle with a device 69 kJ of harmful force is diverted to the safest place by the rotation of wheels during the collision.

Energy ratio above 0.7% means the simulation result total energy is not conserved and there is more total energy loss and gain, this violates the conservation of energy. The energy ratio curve is below 0.7% for the vehicle with and without a system simulation result. So there is no more total energy gain or loss under the simulation process and the theorem of energy conservation is met under this.

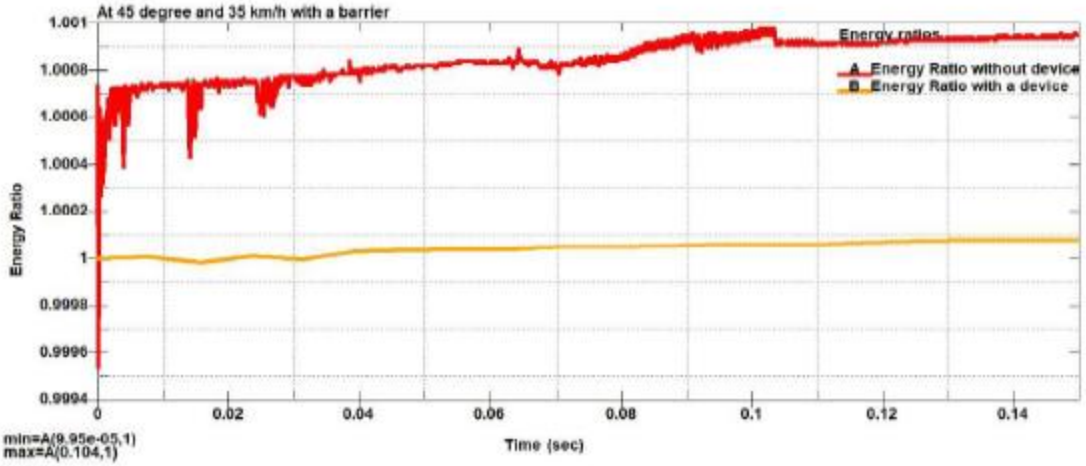

Figure 12: Energy ratio vs time

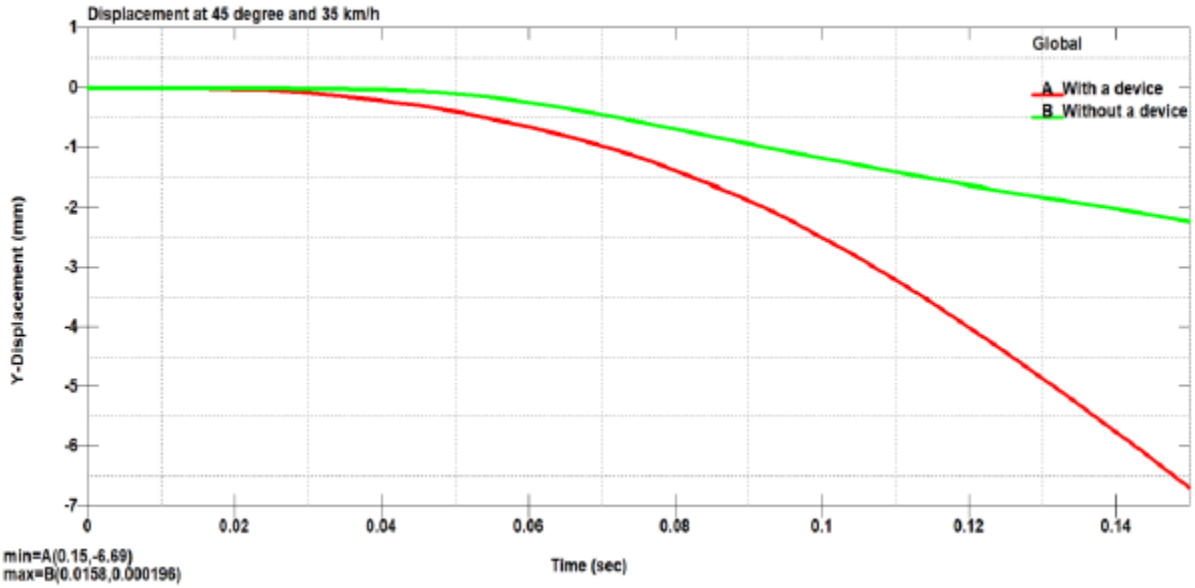

Figure 13: Y- displacement-time graph of vehicle collision to a barrier

Vehicle simulation without a system moves 222 mm in the negative y-direction. But when we see a displacement-time graph of the vehicle simulated with a system, it moves 669 mm in the negative y-direction. The vehicle with a system moves 446 mm more distance in the y-direction when compared to the vehicle without a system.

This more distance movement of vehicle with a system in the negative y-direction indicates that at the time of impact, the wheel is rotated by the non-perpendicular force and the rotation of the flywheel directs the vehicle to the negative y-direction and gives the driver more time to react to the brake and it gives the possibility to avoid the rear-end collision.

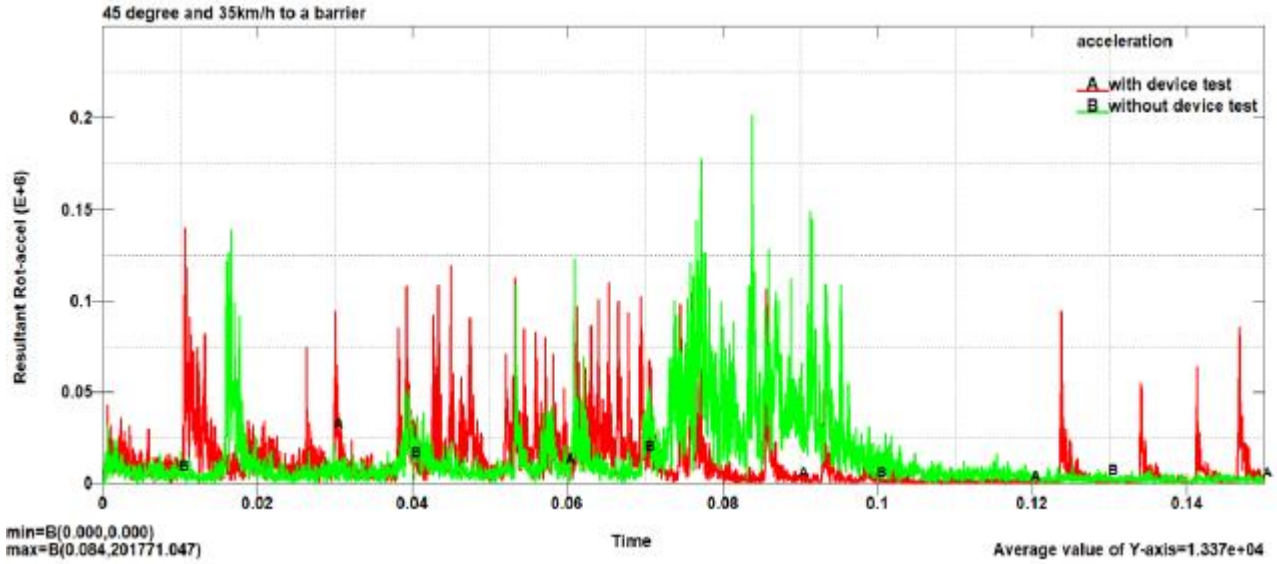

Figure 14: Resultant rotational acceleration time histories

From Fig. 14 we see that the peak rotational acceleration for the simulation without a system test is higher than the peak rotational acceleration for the simulation with a system. From Figure 4.4 above, we can see that the peak acceleration for the vehicle without a system is much higher than the vehicle without a system. So the impact force on the passenger's decreased when a vehicle is equipped with a system.

Fig. 15 shows the vehicle's response to the impact force during a crash into a PCB-R barrier at a speed of 35km/h and 45 degrees with a system (a) and without a system (b). X and Y-rotational displacement of a vehicle without a system is more when compared to the vehicle with a system simulation result. This pitch and roll of the vehicle indicate the vehicle without a system is more unstable than the vehicle with a system. But when we see z-rotational displacement the vehicle with a system rotates more along the z-axis than the vehicle without a system. This rotation of the vehicle along the z-axis indicates the rotation of the flywheel directs the vehicle away from the surface of the barrier. But this yaw motion must be within a specified limit, if the vehicle intrudes into another vehicle lane there may be an occurrence of dangerous collision with another vehicle. So as specified by MASH the vehicle's exit angle must be lower than 60% of its entering angle. So the yaw angle is measured by the 3 node angle measurement method and we get an exit angle of 12.44 degrees which is below 27 degrees, so the exit angle is within the specified limit.

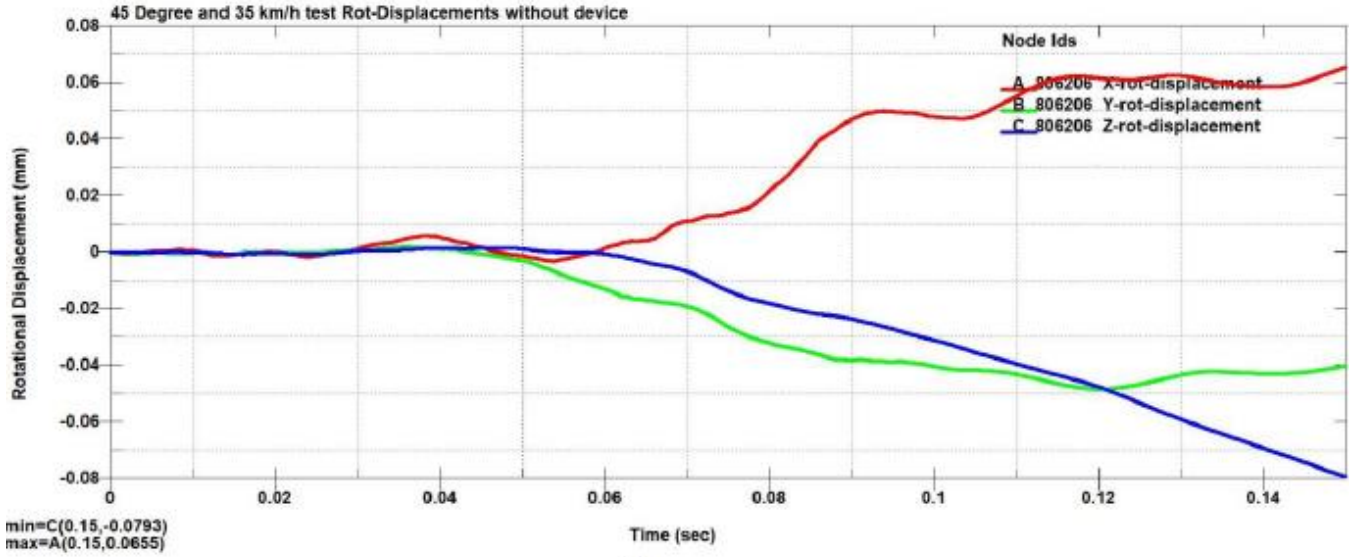

(a)

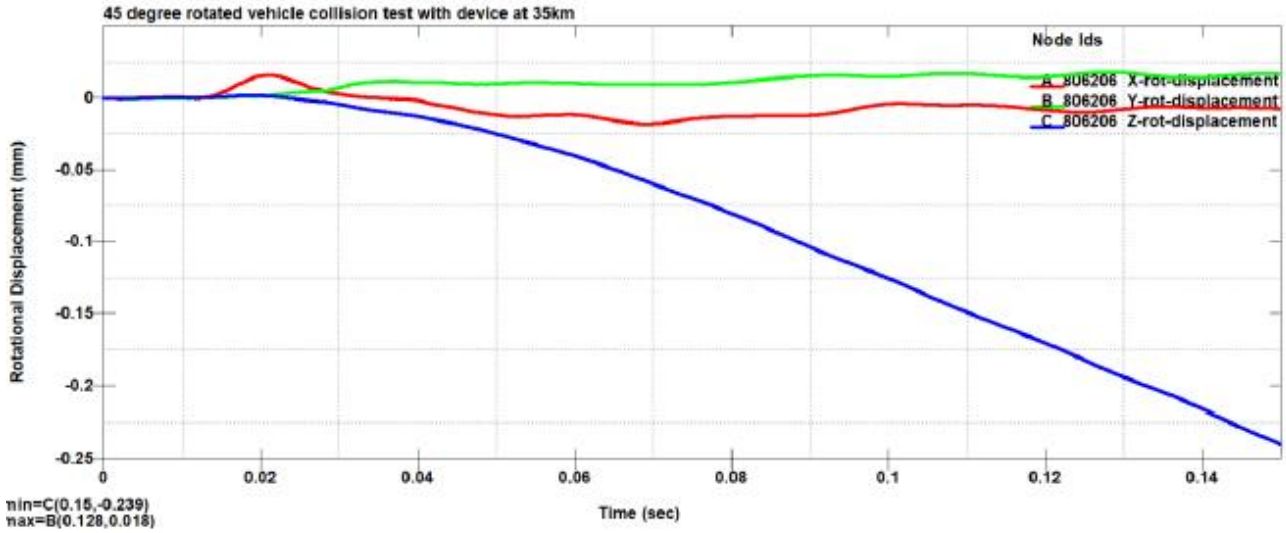

(b)

Figure 15: Yaw, pitch, and roll displacement of the vehicle

Vehicle Test at Large Collision Angle (70 Degree)

The vehicle simulated without a system at a large collision angle interacts into a guard rail jumps to the air leaves the ground, experiences more damage, and stops. At large angles i.e. at 70 degrees the Geo-Metro small vehicle with a system collision with a PCR-B barrier makes a swing slide motion along the collision surface. The vehicle collision angle is 70 degrees but the vehicle stop angle is 74 degrees, which indicates that the vehicle swing slides along a collision surface. But a vehicle with a system is stable and doesn't leave the ground and there is minimum damage to the barrier and the vehicle parts as shown in Fig. 16 (b). But for the vehicle without a system, the vehicle leaves the ground and the guard rail is deflected more when compared to a vehicle with a system test as shown in the following Fig. 16 (a).

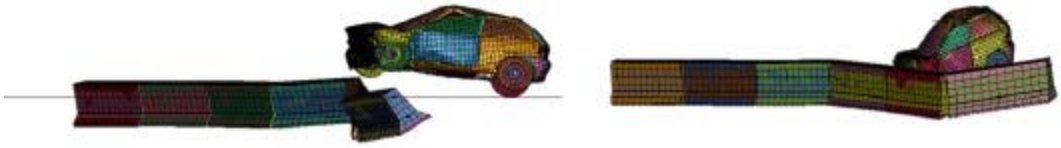

Figure 16: Vehicle swing slide at large collision angle

At an Impact Angle of 45 Degrees and High-Impact Force (120 Km/h.)

The crash impact force is too great, the structure can't handle it and is damaged, and the severity of the accident on the people can be mitigated by controlled crumpled structure deformation, safety belts, and airbags (if available).

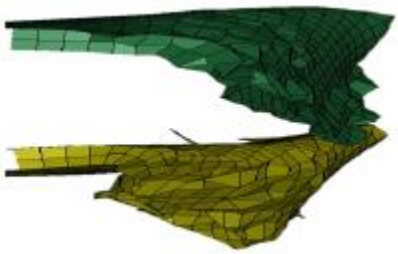

Figure 17: Mounting plate fails at high impact force

The failing of the mounting plate as shown in Fig. 17 is happened from the side of the rail, because of that from the rail end the mounting plate is hollow and the strength is less from this end of the parts.

Vehicular Responses

The following table is a list of the value of some of the yaw angles done to check at different speeds and impact angles to see whether the vehicle under impact with a device intrude into another adjacent lane or not.

Table 5: Impact speed, impact angle, and their yaw angle

Impact angle	Impact speed (km/h)		
	35	50	70
30	14.46	9.14	11.79
50	14.2417	12.79	-
70	Swing-slide (81.12)	Swing slide (79.2)	Swing slide (76.9) and mounting plate starts to fail

From the Table value, we can generally conclude that the vehicle under normal speed with a system does not intrude into an adjacent lane the contact to the barrier is smooth and redirection of the vehicle is also smooth like a plane landing on the ground.

The Hourglass Energy in Crash Simulation

The hourglass energy must be controlled low to the total energy of the vehicle (Tang et al., 2016).

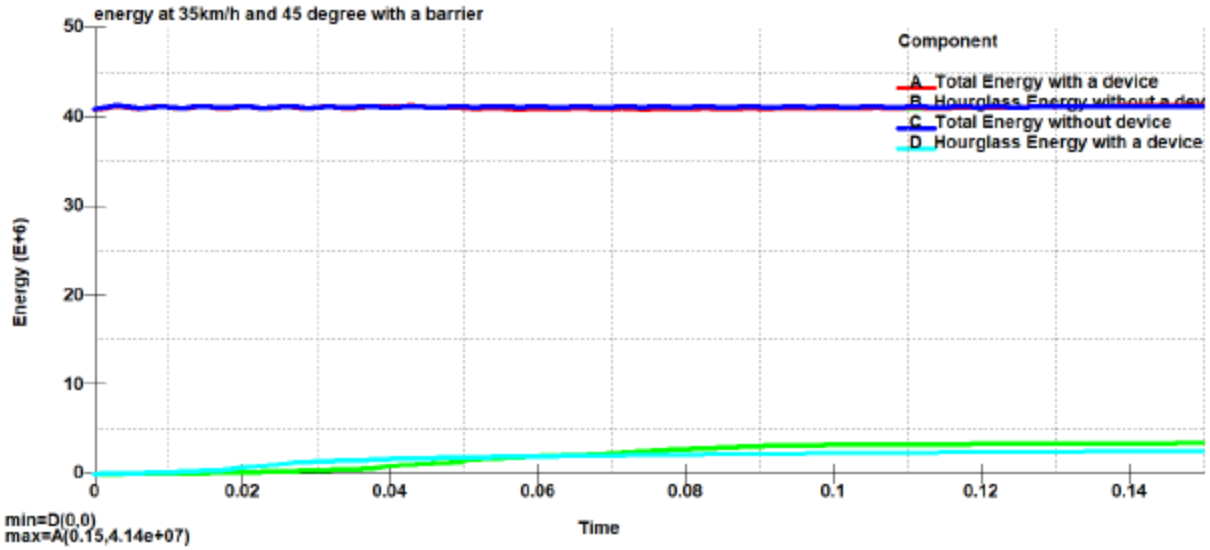

Figure 18: Hourglass energy vs time when compared to total energy

Fig. 18 depicts the hourglass energy vs time curve when compared to the total energy of the vehicle in a collision to a barrier at 35 km/h and 45 degrees. For the test with and without a system, the hourglass energy is low. We can generally conclude that the hourglass energy is low for all simulation, because of that the hourglass energy is unstable when mesh size, element formulation, and type of integration method is varied.

4. CONCLUSIONS

From the simulation result of the collision simulation of a Geo-Metro small vehicle test with a PCR-B barrier at different test criteria, we can generally conclude that The planned and modeled front-end passive safety system for automobiles may effectively divert collision force and partially convert harmful force into non-harmful force, considerably reducing the severity of the crash and saving lives and repair costs. Even if a rear-end collision cannot be prevented, it increases the driving distance after its first collision with a pickup truck and a set of roadside barriers, providing pursuing cars considerably more room and time to brake and slow down. This reduces the severity of rear-end collisions and saves lives. It is straightforward, inexpensive, and simple to implement into contemporary automotive designs without compromising the crumple zone structure's functionality; rather, it works effectively to protect and compliment it.

REFERENCES

Deme. D. (2019): Road Traffic Accident in Ethiopia from 2007/08-2017/18 (Since Ethiopia Millennium). 18(January).

Jordan, P. (2010): A Brief Introduction to Safety Barriers.

Liu, Y. P. (2013): Simulation of vehicle's frontal crash with a dummy inside. Advanced Materials Research, 760–762(Iccsee), 1244–1249.

Luo, Q., Chen, X., Yuan, J., Zang, X., Yang, J., & Chen, J. (2020): Study and Simulation Analysis of Vehicle Rear-End Collision Model considering Driver Types. Journal of Advanced Transportation, 2020.

Moravčík, L., & Jaśkiewicz, M. (2016): Intelligent Safety Vehicle Systems. Autobusy: Technika, Eksploatacja, Systemy Transportowe, 17(11), 106–115.

Namazi, E., Li, J., & Lu, C. (2019): Intelligent Intersection Management Systems Considering Autonomous Vehicles: A Systematic Literature Review. IEEE Access, 7, 91946–91965.

Prentkovskis, O., Sokolovskij, E., & Bartulis, V. (2010): Investigating traffic accidents: A Collision of two motor vehicles. Transport, 25(2).

Puthan, P., Thalya, P., & Lubbe, N. (2018): Active and passive safety passenger car technologies: Potentials to save lives in India. Conference Proceedings International Research Council on the Biomechanics of Injury, IRCOBI, 2018-April(April), 11–16.

Rathod Balasaheb S, S. M. R. (2014): A Case Study on Design of a Flywheel for Punching Press Operation. International Journal of Engineering and Advanced Technology (IJEAT), 3(4), 32–35.

Rebelo, P. M. (2016): Design Study of a Side Intrusion Beam for Automotive Safety. Instituto Superior T´ecnico, Lisboa, Portugal.

Sabarinath, P. (2020): Passive Safety System for Side Impact in Cars. Shanlax International Journal of Arts, Science, and Humanities, 7(4), 115–120.

Safety, V. (2018): Vehicle Safety 2018.

Satinder Singh & Beant Singh. (2014): Design Optimization and Statistical Crash Analysis of Chassis Frame for Off-Road Vehicle. International Journal of Automobile Engineering Research and Development (IJAuERD), 4(6), 9–14.

Tadege, M. (2020): Determinants of fatal car accident risk in Finote Selam town, Northwest Ethiopia. BMC Public Health, 20(1), 1–8.

Tang, Z., Liu, F. J., Guo, S. H., Chang, J., & Zhang, J. J. (2016): Evaluation of coupled finite element/meshfree method for a robust full-scale crashworthiness simulation of railway vehicles. Advances in Mechanical Engineering, 8(4), 1–13.

Woldu, A. B., Desta, A. A., & Woldearegay, T. W. (2020): Magnitude and determinants of road traffic accidents in Northern Ethiopia: A cross-sectional study. BMJ Open, 10(2), 1–9.

Waghe, R., & S Y, G. (2014): Study of Active and Passive Safety Systems and Rearview Mirror Impact Test. International Journal of Mechanical Engineering, 1(3), 5–10.

Yadav, S., & Pradhan, S. K. (2014): Investigations into dynamic response of automobile components during crash simulation. Procedia Engineering, 97, 1254–1264.

Design, Construction and Performance Evaluation of Tractor Drawn Potato Planter

Sagni Bedassa Miressa*

Department of Agricultural Engineering, Ambo University, Ambo, Ethiopia
**Corresponding author, email: sagnibedassa5805@gmail.com*

ABSTRACT

Potato can play an important role in improving food security and cash income of smallholder potato growers in Ethiopia. The country has a very high potential for potato production as 70% of the 10 million hectares of arable land is located in the mid and high altitudes, which is suitable for potato production. Potato planting in Ethiopia has been accomplished by traditional methods to planting the potato tubers on the field, which is labour intensive, time consuming and giving low yields of potato per hectare. This is due to lack of suitable row planting machine. In order to solve above problem, this study aimed to design and development of automatic potato planter which capable of plantings potato tubers in rows at desired depth and spacing. The developed tractor drawn potato planter machine consists of trapezoidal shape hopper, fertilizer hopper, cup feed seed metering mechanism, shovel type furrow opener, ground wheel and furrow covering device. The physical properties of five varieties of potato were studied. The sphericity result was 79.27 % to 86.6 %. The angles of repose of all varieties were nearly equal to 35.5º. The seed rate was calibrated and observed that 2,009.5 kg/ha which is laying in the acceptable range of 19 to 23 quintal/ha. The preliminary test conducted at speed of 3.0, 3.5 and 4.0 km/h speed show good seed rate but 3.5 km/h speed gave better operation result than other operating speed the cost of fabrication of the planter was estimated approximately 10,927.07 ETB Birr.

Keywords: *Speed, Seed rate, Potato, Planter, Fertilizer hopper, Design, Physical properties*

1. INTRODUCTION

Potato can play an important role in improving food security and cash income of smallholder potato growers in Ethiopia. The country has a very high potential for potato production as 70% of the 10 million hectares of arable land is located in the mid and high altitudes, which is suitable for potato production (FAO, 2008). In Ethiopia total production from potato was 943,233 tons with an average productivity of 13.5 tones/ha. The area under potato was 70,132 ha cultivated by 1.4 million households in the main cropping season of 2015/16 (CSA, 2016).

Potato planters have two types of potato dropping mechanisms. The automatic potato planter consists of a hopper for each row and cups with chain drive mechanism. In automatic planter, metering mechanism used is either cup type or picker wheel type. In cup type automatic planter, a slow-moving belt having two rows of cups for each row of potato.

The semi-automatic potato planter consists of a hopper, metering disc and furrow openers (Anonymous, 1991). However, the potato sub-sector in Ethiopia is relatively undeveloped and has been faced with low productivity with less than 10 tones/ha. There is potential for yields of 13.5 tones/ha, which are being attained by progressive farmers using quality seed potato of improved varieties coupled with improved management practices, under the same rain-fed conditions. Therefore, this study is aimed at and initiated with the objective of designing the best performing tractor drawn potato planter.

Most of the potato manual operations are requiring high amount of labor. The main constraint to enhance the productivity and quality of vegetable crops in Ethiopia is lack of Mechanization. As our population continues to increase, it required more food, but this can only be achieved by increasing level of mechanization. Traditional methods to planting the potato tubers on the field, which improper potato placement and spacing labour intensive, time consuming and low yields of potato per hectare. Therefore, necessary to develop a low-cost tractor operated row potato planter that will reduce tedious and drudgery and increasing productivity of potato.

The main objective of this study was to design, construction and performance evaluation of tractor drawn potato planter and the specific objectives were to find the physical properties of potato tuber related to multi-row potato planter and to design and development of tractor drawn potato planter.

A potato planter ranges from automatic to semi-automatic to the ones which are tractor drawn. Manual method of potato planting, results in low seed placement, spacing efficiencies and serious back for the farmer which limits the size of field that was planted. So, there must be implements that match with the tractor power. It's the importance of design of potato row planter was to increase production of potato through uniform distribution of potato seed in the field saving the time, resources and money per hectare.

2. MATEDRIALS AND MEDTHODS

This deals with the materials used and method followed in conducting experiments of the proposed study leading to design and development automatic potato planter for sowing of potatoes.

2.1 Materials

The selection of materials was based on durability, cost and availability, strength and rigidity, weight and friction.

Table 1: Different component's part, specification and material

S. No	Components	Specification	Material
1	Ground wheel	Wheel diameter 600 mm, rim width 35 mm.	Rubber tire
2	Seed hopper	Rectangular at the top and trapezoidal at the bottom with dimensions 400x500x500 mm and 500x300x200 mm. Two number seed boxes provided of the same size of seed box.	MS sheet 18 gauge
3	Seed metering mechanism	Cup metering mechanism,18 cups around peripheral, distance between cups 100 mm.	MS sheet 18 gauge
4	Chain and Sprockets	Sprockets 45 teeth and 15 teeth 60 mm diam. chain pitch12.5 mm, total chain length 2037.5 mm.	Steel
5	Frame	Total length and width - 1,500 and 1000 mm respectively.	MS square pipe 60x60x3 mm
6	Tyne type of furrow opener	Adjustable row to row spacing and depth up to 15 mm, height of shank 200 mm, rake angle 120º	Medium carbon steel
7	Seed tube	Diameter 250 mm, thickness 2 mm	MS sheet 18 gauge
8	Ridger	MS. flat 70x6 mm having length and width 175 and 70 mm respectively.	Mild steel flat bar
9	Cups	Diameter 200 mm, thickness 3 mm	MS sheet metal
10	Three-point hitch system	-	Mild steel bar
11	Nuts and bolts	-	Low carbon steel
12	Ball bearing	Diameter 24 mm	

2.2 Methods

The methods were followed the following procedures.

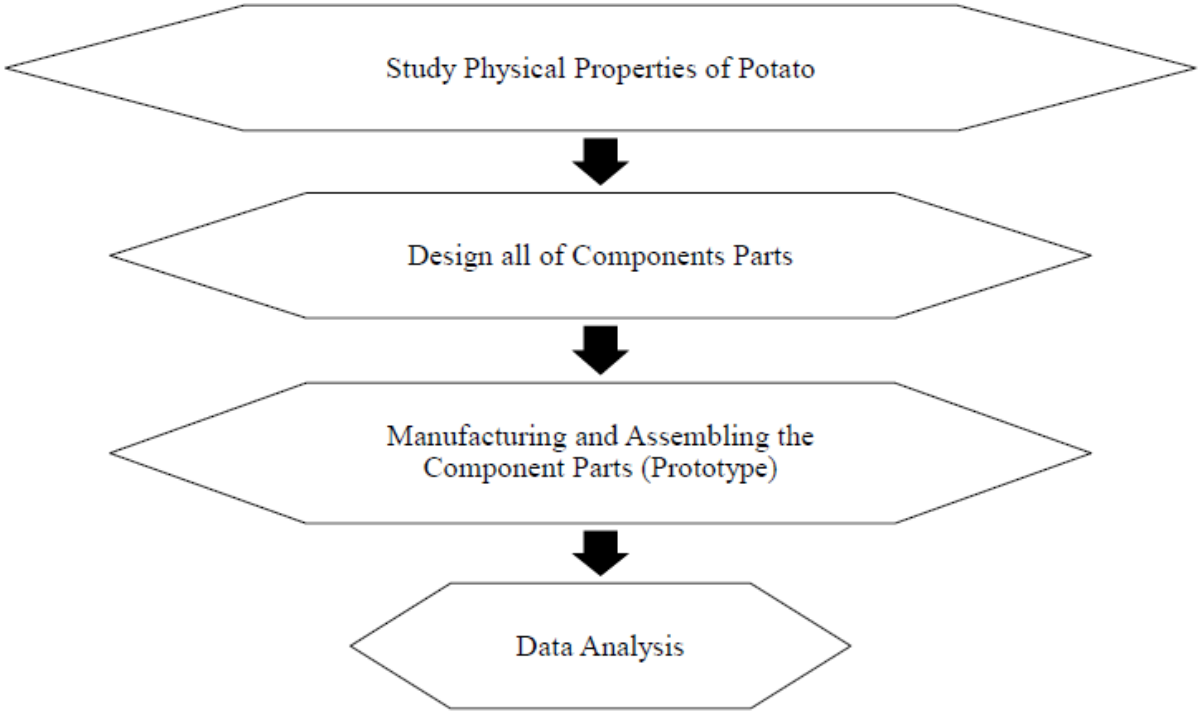

Figure 1: The steps followed to design potato planter

2.3 Physical Properties of Potato

Instrument used for determination of physical properties of tubers: Hopper, cone and Vernier caliper. The physical properties of tubers are important factors for the design of potato planter. Physical Properties of tubers were size, shape, bulk density and angle of repose. The size was calculated by equations (Mohsenin, 1986).

Size = $\sqrt[3]{}$ ((length x width x thickness))
Shape index, k = L^2/ (W x T) x 100
Bulk density (kg/m^3) = (weight of sample, kg)/ (volume occupied by the sample, m^3)
Angle of repose, $\Theta = \tan^{-1}(2H/D)$

where: L = Mean length (mm), D = Mean width (mm), T= Mean thickness (mm), Vm = Mean volume (mm^3) and Dg = Mean geometric diameter (mm).

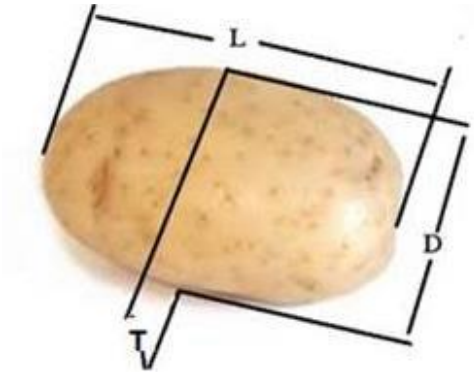

Figure 2: Potato seed

2.4 Design Analysis of Major Components of the Planter

This assumption was on the basis literature reviews essential for the design that the three bottom ridged planters also be used as two-row for potato planter. Power source was tractor which has 40 hp.

Brake horse power (BHP) = 40 hp (YTO tractor available in MARC).

2.4.1 Design of the Seed Hopper

The volume of hopper was calculated (Klenin *et al.*, 1985):

Volume of hopper =weight of potato tubers/bulk density of potato tubers

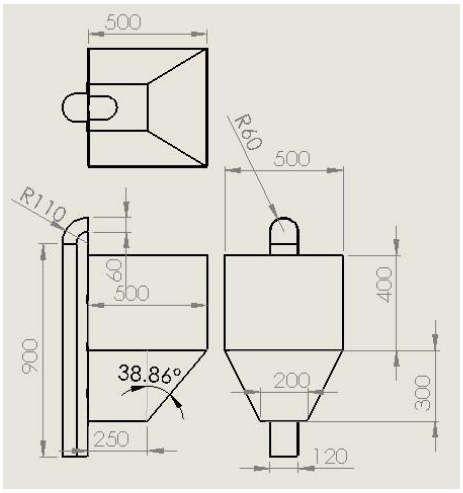

Figure 3: Isometric view seed hopper (all dimensions are in mm)

2.4.2 Design of Main Frame

Design was based on the stresses produced in the frame. The consideration was given on lightweight mainframe but strong enough. To withstand the imposed loading during operation appropriate material sections and strength were kept in view for resistance against bending and twisting.

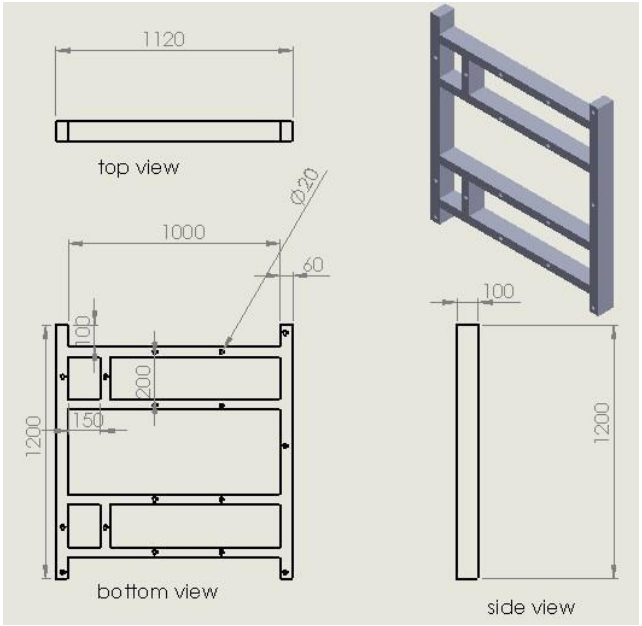

Figure 4: Isometric view of main frame (all dimensions are in mm)

2.4.3 Seed Metering Mechanism

The feed cup type seed metering was selected for the machine for sowing of this for five different potato varieties. The dimensions of each feed cup were decided by maximum size of potato tubers from five varieties can

be put in the feed cups considering the mean geometric diameter of the potato tubers and shape cup was determined based on shape index of potato seed.

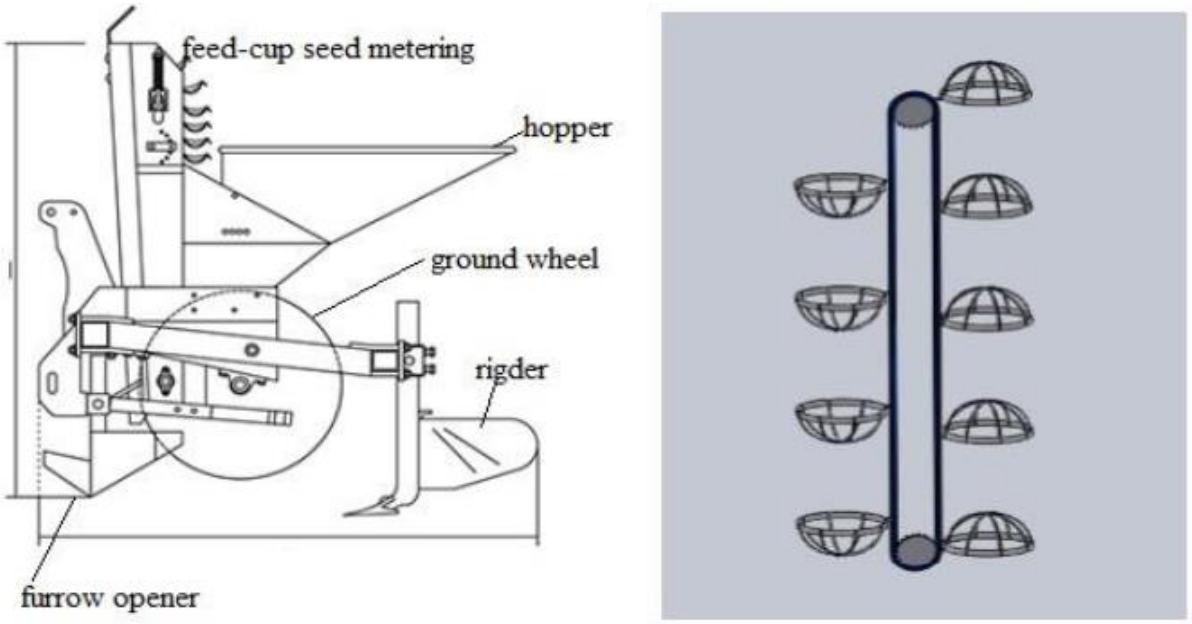

Figure 5: A schematic diagram of the feed cup metering mechanism

2.4.4 Design of Ridger

The ridger was one of the important parts of the planter; it covers the potato seed and forms a ridge of suitable dimensions for proper growth of crop. As the planter was design for two rows, three ridgers are provided. As the planter moves further, the ridger attachment then covers the seeds and makes a ridge. The ridger consists of tyne, shovel and wings.

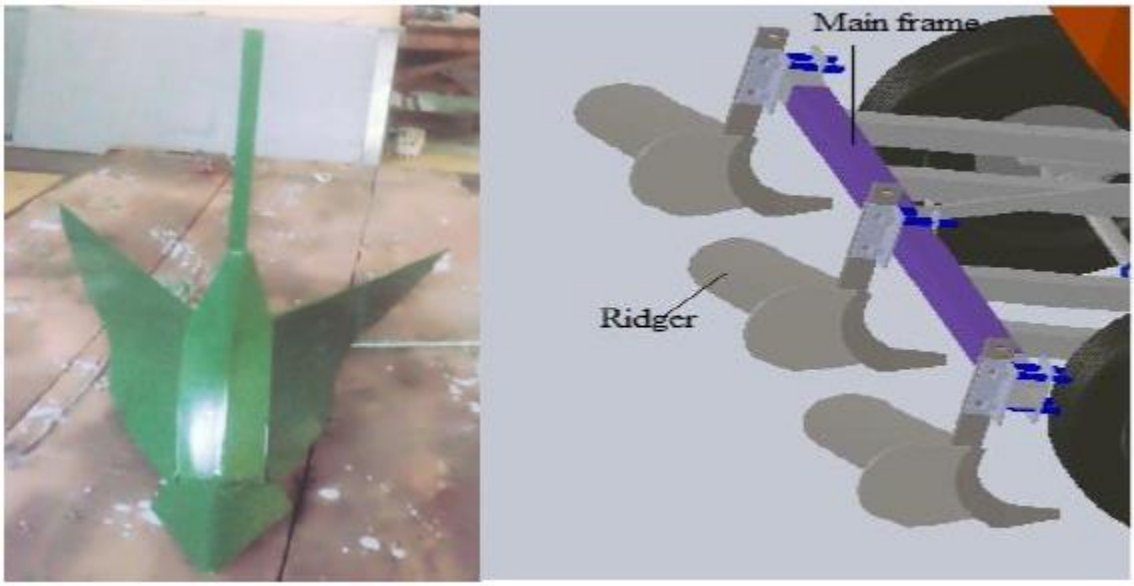

Figure 6: Ridger

2.4.5 Granular Fertilizer Application

A variable rate fertilizer metering mechanism was designed by changing the speed of the feed shaft for use in variable rate fertilizer applicator.

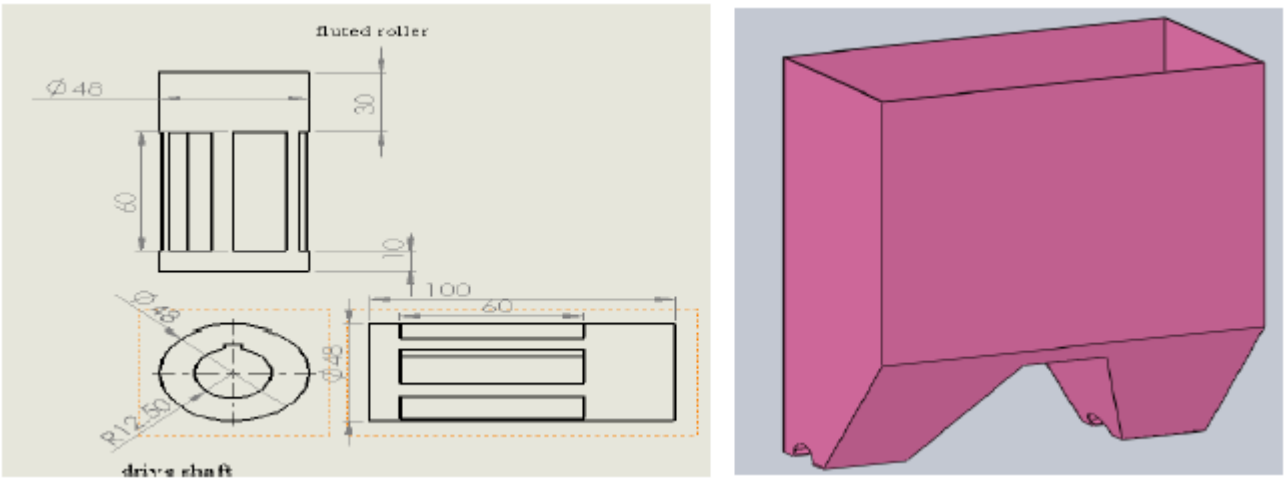

Figure 7: Fertilizer metering mechanism

2.5 Performance Evaluation of Potato Planter

In order to evaluate the performance of potato planter, it was essential to conduct tests such as seed rate, seed distribution, seed placement.

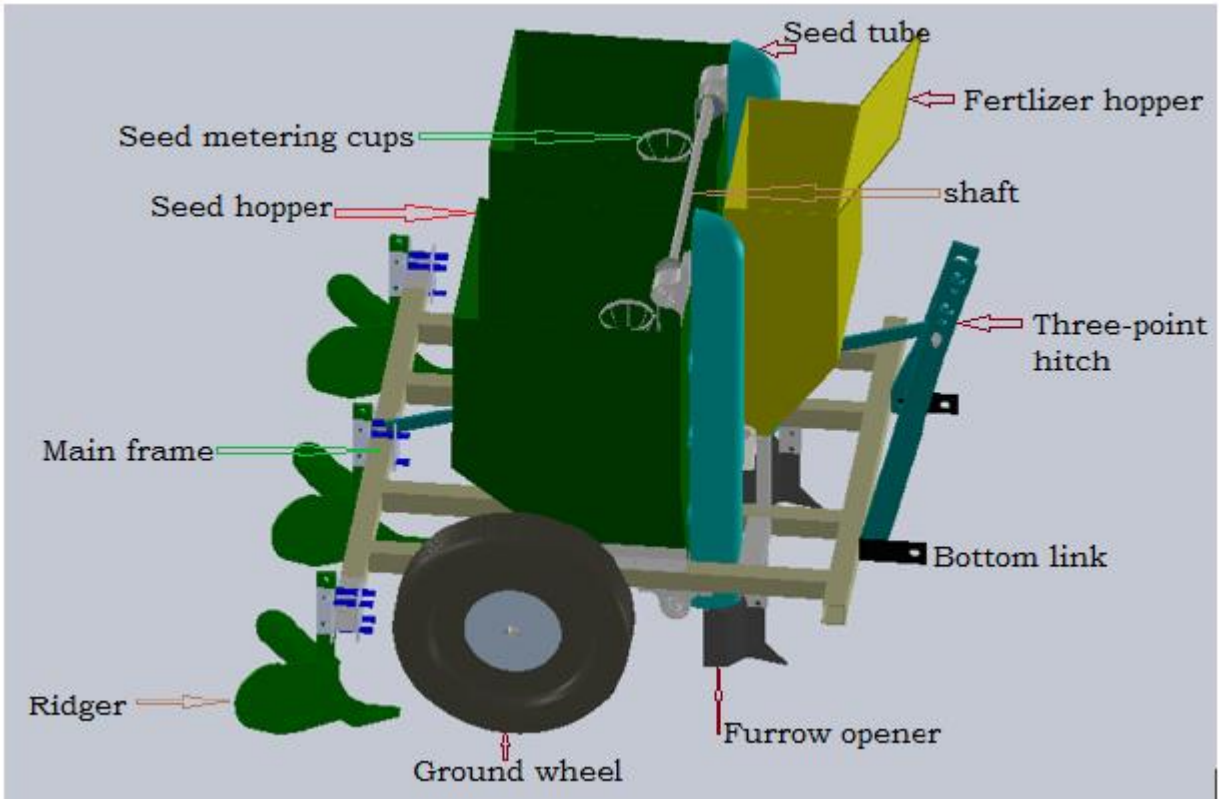

Figure 8: Diagram of the prototype potato planter

2.6 Working Principle of Potato Planter

For operating the potato planter in the field, three-point linkage of planter was attached to the tractor with the help of pin. Seed hopper filled with good quality of potato seeds. The whole unit was taken to field having well prepared seedbed. The potato planter was operated by tractor. The potato planter consists of chain and cup type

seed metering mechanism, which gets drive from the ground wheel. As the planter moves forward, the chain and cup assembly start moving through the seed hopper in which seeds are stored. As the chain moves up it carries seeds in the cup, which are located at some distance from each other. As the chain moves further up the cup gets invert inside a chute which drops the seed to the ground. At the same time the furrow opener opens up a furrow in which the seeds are planted. As the planter moves further, the ridger attachment then covers the seeds and makes a ridge.

2.7 Laboratory Tests

2.7.1 Calibration of Planter

It is used to determine the seeding rate obtainable at different hopper capacity and the variation among furrow openers when the machine was stationary.

2.7.2 Mechanical Damage Test

The percentage of damage of seeds during calibration was found out by rotating the ground wheel for 10 revolutions. The metered seed were identified and treated as damaged seeds were weighed separately and percentage damage was calculated as follows:

Damage percentage = Weight of damaged seed /Total weight of seed x 100

2.7.3 Seed Germination Test

Three samples of 100 seeds each were taken randomly and kept in the seed germinator on water-soaked germination paper and water was sprinkled every day. The germination percentages of potato seeds were determined before and after the laboratory tests of metering systems (Belcher et al., 1995).

The moisture content (Dry basis) was determined by (Belcher et al., 1995):

$$Moisture\ content\ (\%) = \frac{W_w - W_d}{W_d}$$

Where: W_w = Mass of wet soil sample and W_d = Mass of dry soil sample.

3. RESULTS AND DISCUSSIONS

A tractor drawn potato planter was designed and fabricated. The physical properties of potato seed were determined and used for the design of various components of planter. The performance of developed machine was evaluated in the laboratory as well as in the field.

3.1 Physical Properties of the Seeds

In order to get some of the physical properties of the potato seed, 100 sample seeds were of randomly taken from different variety of potato and their length, width and thickness were measured using digital vernier caliper. Geometric diameter and sphericity were calculated.

Table 2: Mean values of physical properties of five different potato varieties

Physical properties	Unit	Different variety of potato available in Ethiopia					
		Jalene	Chala	Belete	Gera	Gudene	Average
Mean Length	mm	53.86	58.96	63.55	60.61	53.96	58.18
Mean Width	mm	48.26	44.81	50.89	46.51	44.81	47.05
Mean Thickness	mm	43.84	38.47	42.39	39.37	39.15	40.64
Geometric mean Diameter	mm	50.88	46.88	51.56	48.05	45.57	48.58
Volume	mm^3	59665.50	53217.47	71781.25	58110.64	49565.36	58468.00
Sphericity	%	86.6	79.51	81.13	79.27	84.46	82.19
Angle of response	^{o}	38	37	34	33	35.5	35.5

The obtained shape index was compared with the recommended limits and classified into different classes (k, from 100 to 160 as round, 160 to 240 as oval, 240 to 340 as long, and higher than 340 as very long). The shape index of potato tubers was calculated by (Singh*et al*, 2004):

$$Shape\ index, k = \frac{Lm^2}{D * T} * 100$$

Laboratory Performance of Potato Planter

The newly developed tractor operated potato planter was tested in the laboratory to evaluate its performance. The results are discussed in the following paragraphs.

Hopper Filling Effect on Mechanical Damage

Three replications were carried out for calibrating the potato planter in the laboratory. Table 3 indicates the effect of hopper filling on seed damage for different observation varied with the hopper filling (full, ½ fill and ¼ fill). The percent of external damage of the seeds were tested at three levels of hopper fills.

Table 3: Effect of hopper filling on seed damage (in %) of potato seeds

Operating speed ($km.h^{-1}$)	No	¼ hopper fill	½ hopper fill	Complete hopper fill
3	3	1.78	2.26	3.94
3.5	3	3.12	3.89	4.52
4	3	3.56	4.01	4.92
cv		32	28	11
mean		2.83	3.38	4.46
standard deviation		0.927	0.977	0.492

The correlation between seed damage at different level of hopper fill and operating speed was showed in Fig. 9. The data obtained from the testing were analyzed, first and second-degree polynomial regression showed good correlation between seed damage and operating speed in all trials, high coefficient of determination (R^2 = 0.988, R^2 = 1 and R^2 = 1) were observed with ¼ fill, ½ fill and completed fill, respectively.

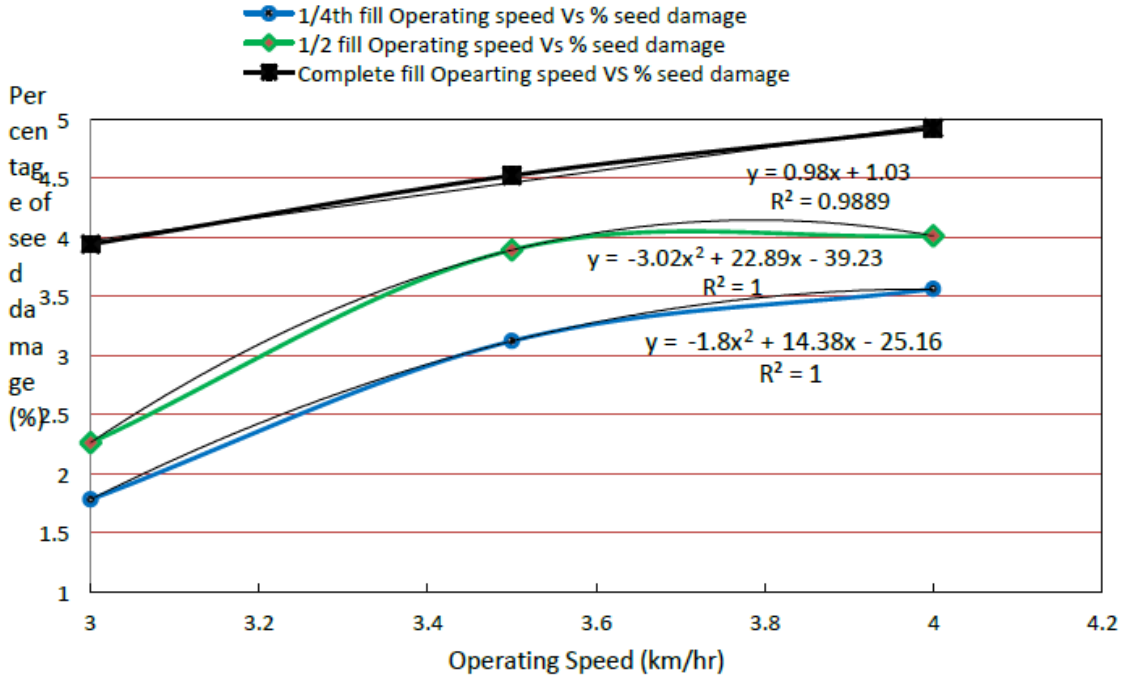

Figure 9: Effects of planter forward speeds on seeds damage

Hopper Filling Effect on seed rate

Table 4 indicates the effect of hopper filling on seed rate (kg/ha) of potato seeds for different observation varied with the hopper filling (full, ½ fill and ¼ fill). The seed rate of the planter seeds was tested at three levels of hoppers fills. The coefficient of variation (CV) is the ratio of the standard deviation to the mean. The higher the CV, the less the precision of the experiment will be for a determined parameter. From Table 4, the speed increased the mechanical damage of potato seed increase. The mechanical damage of seed was due to higher rotational speed of the metering roller at high speed. At high rotational speed the cup strikes the seeds with greater impact resulting in mechanical damage.

Table 4: Effect of hopper filling on seed rate (in $kg.ha^{-1}$) of potato seeds

Replication	¼ fill	½ fill	Complete fill
1	1,956	2,003	2,094
2	1,963	2,019	2,101
3	1,969	2,028	2,114
CV	0.33	0.63	0.48
Mean	1,963	2,016.6	2,103
Standard dev.	6.50	12.66	10.15

Seed rate increased with the increase in hopper fill as shown in Table 3.3. The mean seed rate from the calibration were observed 1962.67, 2016.67, 2103 kg/ha at 36 rpm tractor at 3rd gear speed. The increase in seed rate with the increase in hopper fill might be due to decrease in exposure time to pick the seed and due to slip of seed from the cup due to higher speed of metering device.

This may be due to the hopper's sizes were larger and their shapes were different, e.g. trapezoidal, there would have been significant variations among the means of the respective parameters due to the weight of the seeds, the potential greater variability of the potato seeds in size and shape, and the friction between the metering chain and potato seeds at the picking zone (due to speed of revolution).

4. CONCLUSION AND RECOMMENDATIONS

A prototype of tractor drawn potato planter was developed for sowing operation suitable for medium (model) farmers and to evaluate its performance. The planter consists of seed metering mechanism, seed tube, furrow openers, drive wheel and power transmission. In Preliminary test tractor drawn potato planter was operated with 3.0, 3.5 and 4 km/h speed. The following conclusions are made from the study of tractor drawn potato planter.

- The planter was evaluated in laboratory as well as in real field condition.
- The seed rate for seeds affected by the speed of operation and they were recorded for speed (km/h) of 3.0, 3.5, 4.0 were 1962.67, 2016.67 and 2103.0 kg/ha respectively.
- The meter seed were observed average mechanical damage at different hopper filling level (¼ fill, ½ fill and full fill) were 2.83, 3.38 and 4.46% in of potato seeds respectively.
- The cost of fabrication of the planter was estimated approximately to be 10,927.07 ETB.

The following suggestions help improve the performance of developed tractor drawn potato planter.

- Popularization of the new potato planter technology need to be made.
- Systematic, coordinated and relentless efforts be made to get the planter adopted, effectively and efficiently used by the farmers
- Number of rows covered be increased to improve field capacity and field efficiency of developed tractor drawn potato planter.
- The planter may be tested for different other related crops and feedback received may be used for further design refinements, if any.
- Grade potato before planting so, to solve this problem make adjustable seed metering cup for all size of potato seeds, if any.

ACKNOWLEDGMENTS

A special thanks is due to my advisor Dr. Amana Wako for all his help. I would also like to extend thanks to staffs of Agricultural Engineering Research Directorate (AERD) at Melkassa Agricultural Research Center (MARC) for their indispensable advice and assistances during the research work.

REFERENCES

ASABE, (2011).The measured performance values of the Agricultural machinery. *American Society of Agricultural and Biological Engineers*, New York, USA

Berga, L., Gebremedhin, W., Terrisa, J. and Bereke, T. (1994). 'Potato agronomy research. Proceedings of the 2nd National Horticultural Workshop of Ethiopia', December 1-3, 1992, Institute of Agricultural Research and Food and Agriculture Organization, Addis Ababa, Ethiopia

CSA. (2016). Agricultural sample survey 2015/16. Volume I. Report on area and production of major crops for private peasant holdings, meher season. statistical bulletin 578, Central Statistical Agency, Addis Ababa, Ethiopia.

CASCAPE. (Capacity building for scaling up of evidence-based best practices in agricultural production in Ethiopia) (2015). Best Fit Practice Manual for Potato Production and Utilization. working paper 8.

Culpin C. (1986) "Farm machinery". Eleventh edition. Great Britain. 117-250

Hancock, J. N.; Swetnam, Larry D.; and Benson, F. J., "Calculating Farm Machinery Field Capacities" (1991). Agricultural Engineering Extension Publications. 20

Ismail Z, E. and A.E. Abou El –Magd., (1991)." Evaluation of mechanical potato planting". Mis J. Agric.Eng., 11(1): 3-18.

Mulatu and Hirpa. (2010). 'Improving potato seed tuber quality and producer's livelihoods in Hararghe, Eastern Ethiopia', *Journal of New Seeds*, **7**(3), pp.31–51.

Singh, R. D. (2004). Tractor mounted semi-automatic two-row belt type potato planter ridger. *Agricultural Engineering Today*, 28: 69-74.

Analyzing Sustainable Manufacturing Practices in Leather Industry

Sisay Addis*

School of Mechanical and Industrial Engineering, Debre Markos University, Ethiopia
**Corresponding author, email: sisayaddis123@gmail.com*

ABSTRACT

The leather industry is identified as the priority sector in Ethiopia's industrial development strategy for accelerating sustainable development. However, reliable guideline is not existed to guarantee the successful implementation of sustainable manufacturing practices (SMPs). A framework that explains the process and pathways to guide the implementation of SMPs is lacking. Hence, this study aims to analyze and identify effective SMPs that may specifically help in the leather industry of Ethiopia. Initially, the common sustainable manufacturing practices are collected from literature under five dimensions (social, economic, environmental, technical and regulatory) and validated with focus groups. The study adopts the fuzzy Delphi method (FDM) to arrive at a valid set of practices and the fuzzy decision-making trial and evaluation laboratory (FDEMATEL) to analyze the proposed practices. The findings demonstrate that technical performance and social development are the most critical dimensions to facilitate effective implementation of sustainable manufacturing in the leather industry. Clearly, focusing on these two dimensions will effectively improve the implementation of sustainable manufacturing in the leather. Finally, this study sheds some light on the future research and contribute towards both social and scientific means.

Keywords: *sustainable manufacturing practices, fuzzy Delphi method, DEMATEL, leather industry*

1. INTRODUCTION

Ethiopia is among the least developed countries and faces significant challenges in developing a sustainable and self-supporting economy (UN, 2021). To accelerate sustainable growth and social progress, the leather and leather products industry is identified as one of the priority sectors in Ethiopia's industrial development strategy. However, progress has been disappointing, with low levels of labor productivity, slow development of productive capacities, low levels of human capital formation, and persistent underperformance in human wellbeing (Ghebretekle, 2015; Grumiller and Raza, 2019). Grumiller and Raza (2019) noted that although the leather tanning sector has made significant contributions to the economy and jobs in Ethiopia, it has also created severe environmental and social issues due to the vast quantity of gaseous, liquid, and solid wastes that it generates. Leather processing is recognized as being among the most severe threats to the natural environment because of its industrial processes and harmful working conditions (Śmiechowski and Lament, 2017, Jayanthi et al., 2019). These issues notwithstanding, studies synergizing sustainability and leather tanning concepts from the context of the least developed countries have received less attention.

Leather tanning that transforms skins and hides into a durable substance is a polluting and resource-intensive process (Bacardit et al., 2015; Sathish et al., 2019; Chojnacka et al., 2021). Bacardit et al. (2015) noted the processing of 1000 kilograms of raw salted hide generates roughly 22 cubic meters of wastewater with significant concentrations of contaminants, approximately 730 kilograms of solid waste, and 40 kilograms of emissions. Leather processing is expected to produce 200 times more waste than total product output and has a negative impact by diminishing green areas, increasing air and land pollution, and severely threatening the community, leading to resource scarcity and biodiversity loss (Dixit et al., 2015; Chojnacka et al., 2021). For instance, the residual chromium is highly toxic, yet chrome tanning is used in 85 percent of the processes in the leather industry because it is inexpensive (Karuppiah et al., 2021). Karuppiah et al. (2021) highlighted that the leather industry generates 4 million tons of solid waste annually, including almost 600,000 metric tons of chromium waste. In Ethiopia, Amabye (2015) discovered that due to the dumping of tannery effluents, the waters in the nearby river

contain 2333 times more chromium than the surrounding groundwater. The results also revealed that the chromium content poses a risk to crops cultivated with this water and pollutes shallow subterranean waters.

There is a need to transition to a sustainable way of thinking that encompasses the economic, social, and environmental dimensions of sustainability primarily because of the pressure applied by stakeholders and buyers in global markets (Moktadir et al., 2018; Omoloso et al., 2021). The ideal way to make the transition to sustainability in leather production is to embrace sustainable manufacturing practices (SMPs) (Jayanthi et al., 2019; Omoloso et al., 2021). SMPs transform the production system and promote pollution reduction solutions, potentially lowering manufacturing costs by reducing input costs or reducing spillover effects (Almeida et al., 2017; Gupta et al., 2018; Machado et al., 2020). SMPs are also related to creating a closed-loop paradigm that includes reducing, reusing, recycling, and recovering. SMPs are an essential component of sustainable leather manufacturing, which entails using resource-efficient and environmentally friendly industrial technologies and processes (Dixit et al., 2015). SMPs in the leather sector is impossible unless cleaner technology is adopted to prevent and mitigate pollution challenges. Hence, the present study considers a holistic framework of SMPs that integrates the social, economic, environmental, regulatory and technical aspects. The objectives of this study are to develop a valid set of SMP attributes in leather tanning based on qualitative data, to determine the causal interrelationships among the attributes and linguistic preferences and to provide the driving SMPs for improving the transition under uncertainty.

2. LITERATURE REVIEW

SMPs are defined as the integration of processes and systems that enable the production of high-quality products while consuming fewer resources, being safer for employees and the communities in which enterprises operate, and mitigating environmental and social impacts (Shankar et al., 2017; Machado et al., 2020). Hence, SMPs are actions that the manufacturing industry takes to protect the environment and improve people's quality of life when conducting business activities. SMPs aim to balance economic prosperity, ecosystem viability, and social development, and they require a change in technology by manufacturers and the support of regulatory authorities.

Social development deals with the management of human beings and social capital. It consists of health and safety issues (e.g., safe working conditions and educational opportunities), civil rights (e.g., worker rights and associational freedom) and community (e.g., philanthropic initiatives and public awareness) (Cooper et al., 2018). The tanning industry is recognized as one of the most severe threats to the neighboring community, and its industrial processes affect employees. Tannery workers often suffer from various health issues, such as pathogens, chronic headaches, respiratory disease, and skin problems (Ghebretekle, 2015; Dwivedi et al., 2019). The primary concern of social sustainability is protecting workers against dangerous chemical contaminants present at work, which may harm their health. Uddin et al. (2019) reported that harmful working conditions cause a severe health risk to workers and the living conditions in the neighboring community. Yusuf (2013) noted that social aspects have a significant impact on tanning operations and play a significant role in the decision-making processes of tanneries. Śmiechowski & Lament (2017) reported that social challenges, such as the lack of education and training, the lack of public awareness creation, and the lack of adequate use of personal protective equipment, significantly hinder the implementation of SMPs. Dwivedi et al. (2019) noted that SMPs could be achieved by implementing socially related adjustments, which in turn could be achieved by employing innovative and sufficient manufacturing technologies. There exists a strong link between social aspects and leather industry SMPs. Zahraee et al., (2022) highlighted using targeted education and training initiatives, a sustainable transformation in local economies can be facilitated. Hence, the social aspects of sustainability, such as developing education and training, raising public awareness, installing proper first aid facilities, and ensuring the proper use of personal protective equipment, are major issues for facilitating the successful implementation of SMPs.

Economic gains are important for organizations to reap financial benefits such as reduced costs, higher revenues, an improved reputation, and competitiveness (Dwivedi et al., 2019). The leather tanning industry has a substantial

economic impact, but it suffers from tannery wastes produced during leather manufacturing (Dixit et al., 2015; Padda & Asim, 2019). Zuriaga-Agusta et al. (2015) found that SMPs can assist leather companies in increasing turnover and market share by reducing ecological hazards and effects while increasing productivity. Wahga et al. (2018) asserted that businesses must be innovative, opportunistic, and proactive in acquiring the resources and capabilities required to take advantage of environmentally relevant market possibilities. Abdel-Baset et al. (2019) reported that SMPs help minimize waste and reduce costs; furthermore, they can be used to promote economic gains and guarantee the efficient utilization of resources. In addition, demand from environmentally aware consumers can drive revenues and be a source of competitive advantage. However, Dwivedi et al. (2019) emphasized that the expense of adapting to SMPs is increasing exponentially, which is a major concern for the leather industry. Negash et al. (2021) stated that economic viability is a key obstacle that substantially impacts organizational performance and the transition to SMPs. It can also have an impact on the foundations of the manufacturing process (Yusuf 2013). Hence, transitioning to SMPs is the way to reduce negative environmental consequences, but economic sustainability should be researched to understand the best possible ways to maximize profits in the leather industry.

Environmental practices in the tanning industry are recognized as being among the most severe threats to the natural ecosystem because of the industry's manufacturing processes and the toxicity of the substances that are used (Chojnacka et al., 2021; Karuppiah et al., 2021). Despite its considerable economic impact, the poor image of the leather industry is fueled by the environmental impact of tannery effluents, including wastewater, toxic chemicals, the indiscriminate disposal of solid wastes, and gaseous emissions (Dixit et al., 2015). Karuppiah et al. (2021) found that the leading source of environmental issues is the challenges posed by the waste and emissions released during tanning processes and reducing the impact of waste on the environment. Tannery effluent treatment requires sophisticated technological infrastructure to minimize waste and protect the environment. Dwivedi et al. (2019) noted that using various mechanisms and infrastructures to achieve SMPs and create a sustainable working environment has become imperative. However, SMPs in the leather industry are hampered by a lack of nearby recycling centers, illegal waste disposal, the open-air combustion of leather trimmings, and inadequate waste collection infrastructure (Mihai and Grozavu, 2019; Omoloso et al. 2021). Therefore, the role of environmental aspects in a hierarchical model for the transition to sustainable leather processing needs further investigation.

Regulatory support and policies are required to control the toxic emissions of gaseous, liquid, and solid wastes from the leather industry (Mihai and Grozavu, 2019). Shankar et al. (2017) highlighted that while developed nations have more severe environmental control measures to monitor the production and disposal of industrial waste, the developing world bears the burden of rising demand for tanned leather exports. The discharge of untreated emissions from leather tanning facilities is an issue, especially in the leather sector of the developing world, causing significant environmental degradation as untreated sewage is spilled into neighboring reservoirs (Grumiller and Raza, 2019, Jayanthi et al., 2019). Countries have different discharge limit parameters for the leather industry. In various countries, tannery wastes are subject to general industrial waste discharge legislation rather than specific limits (Dixit et al., 2015). Certain legislative authorities regulate the quality of the treated wastes, while others regulate the quality of the receiving water bodies. Some establish the maximum impurity levels that can be discharged into a receiving water body per day, while others regulate the total volume of wastewater discharged (Gupta et al., 2018). Numerous tanneries have been ordered to cease their operations due to their failure to adhere to pollution control system regulations, while many of them have been forced to pay large sums of money to compensate for the damage caused by groundwater salinization (Chojnacka et al., 2021). Machado et al. (2020) argued that improvements in regulatory compliance are among the advantages of SMPs. The primary intent of regulatory policies is to ensure the highest level of safety, health and environmental consent. Thus, integrating and implementing regulatory aspects are essential to achieve SMPs because businesses that follow these regulations are more likely to be sustainable.

Technical performance that involves technologies, expertise, and knowledge helps promote the transition to sustainability in organizations (Karuppiah et al., 2021; Negash et al., 2021). There are some concerns about combining technical evaluations in regard to research on SMP strategies. Dixit et al. (2015) found that technical suitability and commercial feasibility are critical for the transition to SMPs and environmentally friendly waste processing during leather production. The leather sector, which has been widely criticized for its negative environmental impacts, has many opportunities to adopt SMPs by utilizing the best technologies and processes (Dixit et al., 2015; Sathish et al., 2019; Karuppiah et al., 2021). Śmiechowski & Lament (2017) found that manufacturing methods and technical capabilities influence the environmental performance of the leather industry and that these factors play an important role in tanneries' decision-making processes. However, technical barriers are the fundamental obstacle to achieving SMPs. For instance, Karuppiah et al. (2021) noted that a lack of technologies and technical skills inhibits the implementation of SMPs, and the leather industry is mainly focused on preventing pollution using in-process control measures. Most leather processing enterprises use less advanced technology and release untreated effluents that have a significant negative impact on the health and safety of both humans and the environment (Garai, 2014). Technological development minimizes chemical consumption in processes and recycles chemical effluents. Uddin et al. (2019) highlighted that the adoption of the right technical attributes and technology provides significant leverage to enhance prospective industry expansion. Gupta et al. (2018) argued that sustainable development in leather tanning will be impossible unless new approaches to pollution prevention and mitigation are developed. Hence, SMPs are important possible pathways for achieving sustainability. Technical qualities comprise certain crucial elements in leather production, such as human resources or expertise, which are essential aspects, as they manage the production processes to achieve SMP goals. The study collected initial practices (IPs) under each aspect.

3. MATERIALS AND METHODS

3.1 Case Background

The leather industry in Ethiopia is one of the leading sectors that can accelerate economic development by creating job opportunities, generating revenue through exports, and providing investment opportunities (MIE, 2014). Its contribution to the national economy is increasing, contributing $27.8 million from leather exports in 1998/99 and $131.5 million fifteen years later in 2013/14 (Brautigam et al., 2018). Currently, there are 34 registered tanneries in Ethiopia, and the industry has seen significant expansion in recent years, with the potential to quickly boost output (ECCSA, 2019). However, in Ethiopia, tanneries generate approximately 150 tons of solid waste and 12,500 m^3 of liquid waste per day; the upsurge in the leather industry increases the waste discharged to the surrounding environment without treatment (Amabye, 2015; Grumiller and Raza, 2019). The government's increasing pressure has prompted tanneries to spend heavily on waste treatment plants in recent years, but the pollution concerns remain unsolved (Ghebretekle, 2015; Grumiller and Raza, 2019). For instance, only one out of the 34 tanneries can comply with requirements and be certified by the Leather Working Group. This independent auditor conducts tannery inspections and promotes tighter environmental criteria. Ghebretekle (2015) found that the solid and liquid hazardous wastes from Ethiopian tanneries contain substances and other contaminants that are detrimental to human wellbeing and the environment. The toxic substances in rivers also affect the health of animals as hazardous wastes are ingested with polluted water. Furthermore, Grumiller and Raza (2019) noted that the sector is characterized by low pay and inadequate worker safety, which contributes to significant employee turnover and increases companies' training expenditures.

Ethiopia has a legislative framework in place to decrease tanning's environmental impact, although regulations are frequently not followed. Current waste management is mainly characterized by the burning of waste at several locations and the disposal of mixed waste in an unsecured landfill. The landfill sites are a source of negative public and environmental consequences. Since many tanneries are now located in metropolitan areas, the severity of the

problem has grown (Grumiller and Raza, 2019). Demand from environmentally aware consumers is also constrained because of low environmental sustainability and irresponsible and outdated waste treatment methods. Hence, SMPs should be implemented to ensure a better future for society, the economy, and the environment. Manufacturing industries are increasingly required to adopt sustainability practices to gain competitive advantages while also securing the aspects of sustainability (Shankar et al., 2017). Nevertheless, the leather industry in Ethiopia faces problems due to fewer interventions of cleaner production techniques in operations, leading to profit reductions at the enterprise level and becoming a barrier to the country's economic development and its safeguarding of the environment (Ghebretekle, 2015; Grumiller and Raza, 2019). Hence, this study seeks to explore the transition to SMPs in the Ethiopian tanning industry context, and it can be of assistance to practitioners who are attempting to improve their strategies in terms of SMPs.

3.2 Data Collection and Analytical Methods

Fig. 1 illustrates the study framework, including the analytical steps. A set of practices containing an initial set of 24 practices was derived from the literature review. Then, a linguistic evaluation questionnaire was sent to a panel of experts. An expert panel of 13 people participated in this research, with backgrounds ranging from being the CEOs of enterprises in the leather tanning sector (6 CEOs) to being experts in Ethiopia's leather industry development institute (7 experts). The experts were experienced researchers of the leather industry development institute and engaged in benchmarking leather companies. The opinions of the experts were solicited in two rounds to operationalize the FDM and FDEMATEL. Round one was carried out on 05 November 2021. Then, with a 45 days gap, round two was carried out on 20 December 2021. In round one, the list of 24 proposed practices and their descriptions were presented to the experts. This study employed a hybrid method that used fuzzy set theory and the Delphi method to validate the practices gathered from the literature. The Delphi technique screened out nonsignificant criteria from the 24 initial practices derived from the literature review, and fuzzy set theory resolved the uncertainty arising from the experts' viewpoints. In round two, the experts were provided FDEMATEL questionnaires, and interviews were conducted based on the valid criteria identified in the first-round FDM analysis. The interviews were conducted to verify the accuracy of the data and strengthen the reliability of the data source. The FDM and FDEMATEL procedures are as follows.

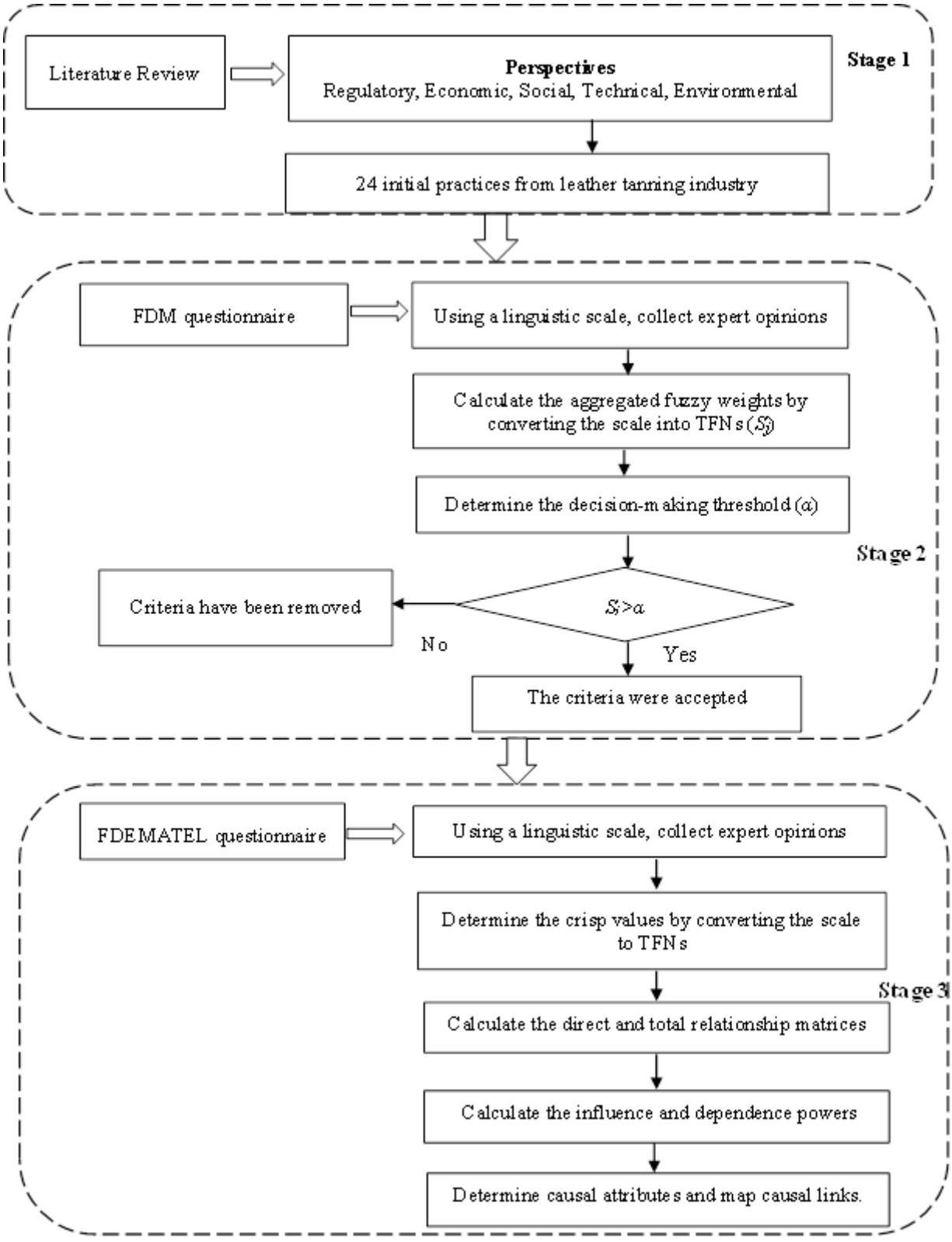

Figure 1: Study framework including analytical steps

3.2.1 Fuzzy Delphi Method

The FDM included the following steps. First, utilizing a Likert scale, expert evaluation scores regarding the relevance of each practice were collected. Second, using Table 1, the evaluations were converted into TFNs. Third, it was determined whether expert consensus was achieved for each practice by meeting the consensus threshold level, updating practices based on the consensus level, taking into account expert opinions, and eliminating unaccepted practices (Bui et al., 2022). The steps are as follows.

Table 1: Linguistic terms and TFNs

Linguistic terms	TFNs		
Very high (VH)	0.75	1.00	1.00
High (H)	0.50	0.75	0.10
Medium (M)	0.25	0.50	0.75
Low (L)	0.00	0.25	0.50
Very low (VL)	0.00	0.00	0.25

The aggregated respondent evaluation scores were computed using the geometric mean, and the fuzzy weight (FW_j) of each criterion was calculated using Equation (1).

$$\mathrm{FW_j} = \left\{ l_y = min(l_{xy}), m_y = \left(\prod_1^n m_{xy}\right)^{1/n}, \text{and } u_y = max(u_{xy}) \right\} \quad (1)$$

where $\mathrm{FW_j}$ denotes the criterion's assessment score, y is the expert-rated criterion j, n denotes the number of experts, and *ly*, m_y, and u_y denote the TFNs' lower, medium, and upper values, respectively. Each criterion's aggregated fuzzy weights were defuzzified (S_j), and a threshold (α) was set to eliminate nonsignificant criteria. If $S_j < \alpha$, the j^{th} criterion was rejected; if $S_j \geq \alpha$, the j^{th} criterion was accepted. In this situation, α is the average of the defuzzified weights.

$$S_j = \frac{\sum FW_j}{3},\ j = 1, 2, 3, \ldots m \quad (2)$$

$$\alpha = \frac{\sum S_j}{n},\ x = 1, 2, 3, \ldots n \quad (3)$$

3.2.2 Fuzzy Decision-Making Trial and Evaluation Laboratory

Experts use linguistic characteristics such as very low, low, medium, high, and very high to measure their perception of the pairwise influence of the practices. Thus, this study employed fuzzy set theory to address the uncertainty created by the experts' fuzziness in their decision-making. The linguistic preferences were transformed into the corresponding TFNs, as shown in Table 1. The FDEMATEL was employed to identify the causal effects of the interrelationships among the practices (Bui et al., 2022). The FDEMATEL procedure is as follows.

$$\begin{aligned} S &= \left(s\tilde{z}_{1ij}^{f}, s\tilde{z}_{2ij}^{f}, s\tilde{z}_{3ij}^{f} \right) \\ &= \left[\left(z_{1ij}^{f} - minz_{1ij}^{f} \right) \Big/ \Delta_{\min}^{\max}, \left(z_{2ij}^{f} - minz_{2ij}^{f} \right) \Big/ \Delta_{\min}^{\max}, \left(z_{3ij}^{f} - minz_{3ij}^{f} \right) \Big/ \Delta_{\min}^{\max} \right], \end{aligned} \quad (4)$$

where $\Delta_{\min}^{\max} = \max z_{3ij}^{f} - minz_{1ij}^{f}$

The left (slt) and right (srt) normalized values were then computed (Equation (5)), as well as the overall normalized crisp value (Equation (6)).

$$\left(\mathrm{slt}_{ij}^{n}, \mathrm{srt}_{ij}^{n}\right)=\left(sz_{2ij}^{f}\Big/\left(1+sz_{2ij}^{f}-sz_{1ij}^{f}\right), sz_{3ij}^{f}\Big/\left(1+sz_{3ij}^{f}-sz_{2ij}^{f}\right)\right) \quad (5)$$

$$\mathrm{s}_{ij}^{f}=[slt_{ij}^{f}\left(1-slt_{ij}^{f}\right)+(srt_{ij}^{f})^{2}]/(1-slt_{ij}^{f}+srt_{ij}^{f}). \quad (6)$$

The subjective judgments of n assessors were then aggregated, and the synthetic value was calculated.

$$\tilde{z}_{ij}^{f}=\frac{1}{f}\left(\tilde{z}_{ij}^{1}+\tilde{z}_{ij}^{2}+\tilde{z}_{ij}^{3}+\ldots+\tilde{z}_{ij}^{f}\right). \quad (7)$$

Next, we obtained an initial direct relation matrix (IDRM), IDRM $=\left[\tilde{z}_{ij}^{f}\right]_{n\times n}$, where z_{ij} indicates the extent to which criterion *i* influences criterion *j*. Then, we standardized the IDRM $\mathrm{X}=[\mathrm{X}_{ij}]_{n\times n}$ $i, j=1,2,\cdots,n$ as follows:

$$\mathrm{X}=\omega\times\mathrm{Z}, \quad (8)$$

where $\omega=\frac{1}{\max_{1\le i\le f}\sum_{j=1}^{f}\tilde{z}_{ij}^{f}}$.

The total relation matrix was then calculated as follows:

$$\mathrm{Y}=\lim_{\mathrm{f}\to\infty}\left(\mathrm{X}+X^{2}+\cdots+X^{f}\right)^{\mathrm{n}}=\mathrm{X}\left(\mathrm{I}-\mathrm{X}\right)^{-1}. \quad (9)$$

An interrelationship map was constructed from the values of (D + R, D - R) to map the causal links. The x-axis (D + R) represents "importance," and the y-axis (D - R) represents "prominence." The y-axis represents "relation" and divides the criteria into cause and effect categories. (D R) was in the effect group if it was negative; if it was positive, it was in the cause group.

$$\mathrm{D}=[\sum_{i-1}^{n}X_{ij}]_{n\times n}=[X_{i}]_{n\times 1} \quad (10)$$

$$\mathrm{R}=[\sum_{j-1}^{n}X_{ij}]_{n\times n}=[X]_{1\times n} \quad (11)$$

4. RESULTS

4.1 Validity of the Measures

As a result of the experts' assessment, 15 criteria were approved, while nine were rejected. Equations (1)-(3) were utilized to eliminate invalid criteria with a threshold of 0.514 using the FDM. The FDM analysis results for the 24 initial practices are provided in appendix 1, and Table 2 lists the accepted criteria, which have been renamed.

Table 2: Validated measures

Aspects	Criteria	Weight
Regulatory support(A1)	P1. National plans	0.663
	P2. Level of compliance	0.580
	P3. Regular supervision	0.532
Economic practices (A2)	P4. Resource utilization and economy	0.640
	P5. Tax exemptions	0.658
	P6. Incentives	0.567
Social practices (A3)	P7. Developing education and training	0.522
	P8. Public awareness creation	0.691
	P9. Health and safety	0.550
Technical performance (A4)	P10. Green designing	0.552
	P11. Site waste management plans	0.650
	P12. Electro-oxidation	0.658
Environmental practices (A5)	P13. Waste elimination	0.645
	P14. Landfill spaces saved	0.643
	P15. Environmental management	0.706
	Threshold value	0.514

4.2 Interrelationships between Sustainable Leather Processing Attributes

The FDEMATEL questionnaire was created using the fifteen validated criteria from the FDM analysis. The experts' judgments of the pairwise influence between the aspects and between criteria were collected on linguistic scales, as indicated in Table 1. The study interviewed the same experts to see whether there were any interrelationships between aspects and between criteria for practical changes. The experts' linguistic preferences were analyzed using the FDEMATEL approach and transformed into TFNs. Equations (4)-(6) normalized the TFNs into crisp values. Then, we combined the subjective evaluations of the respondents and used Equation (7) to calculate the synthetic value. Equation (8) was used to obtain the IDRM and standardize it, and Equation (9) was used to obtain the complete relation matrix (Table 3). Equations (10) and (11) were used to build cause-and-effect diagrams. Table 4 shows how the driving and dependency power of the aspects were determined.

Table 3: Total relation matrix aspects

	A1	A2	A3	A4	A5
A1	2.448	2.131	2.355	2.281	2.527
A2	2.175	2.102	2.138	2.121	2.361
A3	2.531	2.272	2.509	2.398	2.687
A4	2.711	2.452	2.625	2.619	2.865
A5	2.585	2.377	2.541	2.513	2.800

Table 4: Causal-effect interrelationship among aspects

	D	R	D+R	D-R
A1	11.741	12.451	24.192	(0.710)
A2	10.897	11.334	22.231	(0.437)
A3	12.397	12.167	24.565	0.230
A4	13.273	11.932	25.204	1.341
A5	12.816	13.240	26.056	(0.424)

Fig. 2 shows the cause-and-effect diagram of the aspects and shows that technical performance (A4) and social development (A3) are part of the cause group. The effect group includes environmental protection (A5), regulatory improvement (A1), and economic gains (A2). The following is the relationship between the various aspects: Technical performance has a significant impact on environmental protection and a moderate impact on social development and regulatory improvement, but it has little impact on economic gains. Environmental protection is strongly influenced by social development, and regulatory gains are moderately affected by social development.

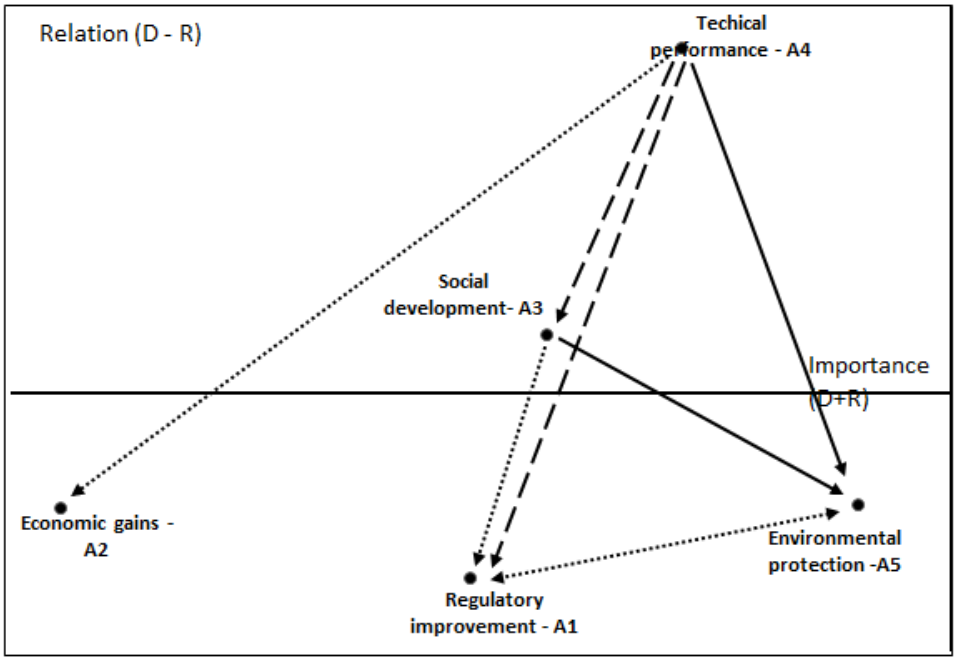

Figure 2: Cause and effect diagram for aspects

Similarly, the FDEMATEL steps were repeated, and the total interrelationship matrix (Table 5) and the driving and dependency power of the criteria (Table 6) were determined.

Table 5: Total relation matrix of practices

	P1	P2	P3	P4	P5	P6	P7	P8	P9	P10	P11	P12	P13	P14	P15
P1	0.29	0.27	0.27	0.27	0.26	0.28	0.26	0.28	0.28	0.29	0.30	0.27	0.30	0.25	0.29
P2	0.28	0.32	0.29	0.28	0.29	0.30	0.28	0.30	0.33	0.31	0.31	0.30	0.32	0.26	0.33
P3	0.26	0.27	0.30	0.27	0.27	0.29	0.26	0.28	0.30	0.28	0.30	0.29	0.29	0.25	0.29
P4	0.24	0.24	0.24	0.27	0.26	0.23	0.25	0.26	0.27	0.28	0.27	0.26	0.26	0.23	0.26
P5	0.19	0.21	0.21	0.20	0.25	0.24	0.20	0.22	0.22	0.21	0.24	0.21	0.23	0.18	0.22
P6	0.20	0.21	0.22	0.22	0.21	0.26	0.18	0.20	0.23	0.24	0.24	0.23	0.24	0.19	0.23
P7	0.27	0.28	0.26	0.26	0.28	0.27	0.30	0.28	0.31	0.30	0.29	0.30	0.28	0.25	0.30
P8	0.26	0.27	0.26	0.27	0.26	0.27	0.27	0.30	0.30	0.28	0.29	0.28	0.29	0.24	0.29
P9	0.24	0.26	0.27	0.25	0.27	0.27	0.26	0.25	0.31	0.29	0.29	0.27	0.27	0.24	0.30
P10	0.32	0.31	0.33	0.32	0.32	0.33	0.30	0.32	0.36	0.36	0.36	0.34	0.35	0.30	0.35
P11	0.28	0.29	0.28	0.28	0.29	0.30	0.28	0.29	0.32	0.32	0.34	0.30	0.31	0.26	0.31
P12	0.30	0.29	0.29	0.31	0.29	0.31	0.28	0.29	0.33	0.33	0.32	0.33	0.33	0.26	0.33
P13	0.20	0.21	0.23	0.22	0.20	0.22	0.19	0.23	0.23	0.21	0.24	0.22	0.30	0.17	0.23
P14	0.18	0.18	0.19	0.16	0.17	0.17	0.14	0.16	0.19	0.17	0.18	0.15	0.20	0.20	0.20
P15	0.24	0.23	0.24	0.22	0.24	0.23	0.22	0.24	0.26	0.25	0.26	0.24	0.23	0.22	0.28

Table 6: Causal-effect interrelationship among practices

	D	R	D+R	D-R
P1	4.155	3.773	7.927	0.382
P2	4.513	3.856	8.369	0.657
P3	4.206	3.894	8.100	0.312
P4	3.778	3.826	7.604	(0.048)
P5	3.218	3.882	7.100	(0.664)
P6	3.288	3.957	7.245	(0.669)
P7	4.278	3.616	7.894	0.662
P8	4.129	3.909	8.038	0.220
P9	4.038	4.244	8.282	(0.205)
P10	4.971	4.114	9.085	0.857
P11	4.455	4.230	8.685	0.224
P12	4.599	3.969	8.568	0.630
P13	3.271	4.189	7.460	(0.918)
P14	2.645	3.502	6.147	(0.858)
P15	3.610	4.192	7.801	(0.582)

Fig. 3 shows a cause-and-effect diagram of the criteria in which the criteria are divided into four quadrants. Quadrant 1, or the linkage/causal criteria, has great power and is crucial to the shift to SMPs. Quadrant 2, often known as the dependent criteria, has much power but is not as important to the system. Quadrant 3, also known as the autonomous criteria, has a low level of dependency and is somewhat detached from the rest of the system. Quadrant 4, often known as the independent criterion, may be enhanced only indirectly by improving quadrant 1. P10, P12, P2, P11, and P3 are in quadrant 1, i.e., the linkage criteria; P7, P1, and P8 are in quadrant 2, i.e., the dependent criteria; P4, P15, P13, P6, P5, and P14 are in quadrant 3, i.e., the autonomous criteria; and P9 is in quadrant 4, i.e., the independent criteria. Quadrant 1 criteria with strong dependent and driving power are essential for the industry to monitor and evaluate practical improvements in the transition.

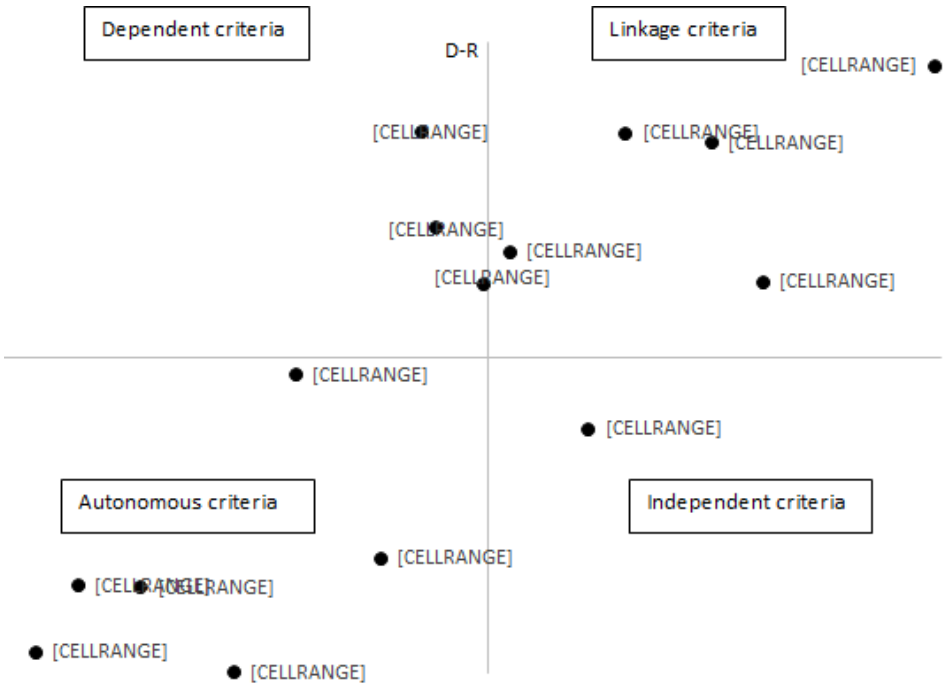

Figure 3: Cause and effect diagram for criteria

5. DISCUSSION

This study identified that in the transition to SMPs in leather processing, technical performance and social development are the focal aspects to improve environmental protection, economic gains, and environmental regulations. The findings indicated that technical and social attributes drive the transition to sustainability in leather tanning, and improvement in these aspects is required to manage SMPs.

Technical performance has the highest level of importance in the transition to SMPs. It drives improvements in solving severe environmental and social issues resulting from the gaseous, liquid and solid wastes generated from leather tanning. This finding also suggests that technical performance is a causal factor that affects all aspects of the model. The results confirmed the argument that the transition to SMPs in the leather sector is impossible unless the existing technical performance is enhanced by systematizing the available knowledge to prevent and mitigate pollution challenges (Gupta et al., 2018). In Ethiopia, the majority of leather processing enterprises use outdated technology and discharge untreated pollutants that harm both humans and the environment. A case study on one tannery indicated that the neighboring river had 2333 times more chromium than the surrounding groundwater due to the dumping of untreated effluents (Amabye, 2015). Adopting the correct technical qualities and technology can help accelerate the transition to SMPs. Nevertheless, long-term growth in the leather sector will be unachievable until new pollution control and mitigation approaches are introduced. Tannery effluent treatment requires sophisticated technological infrastructure capable of minimizing waste and protecting the environment. Currently, the application of SMPs is hampered by a lack of technologies and technical abilities, and the leather industry is primarily focused on pollution avoidance at the source through in-process control techniques (Karuppiah et al., 2021). As a result of technological advancements, the chemicals used in operations are optimized, and the effluents generated by chemical operations are recycled (Moktadir et al., 2020). In summary, the theoretical framework for the transition to sustainability indicated that improving technical performance leads to socially harmless, eco-friendly, and economically viable solutions to manage SMPs.

Social development is also a driving factor in addressing concerns about the transition to sustainability. Social development advancements contribute to the elevation of current SMP difficulties such as low labor productivity, low human capital formation, and continuous underperformance in human wellbeing. The finding also indicated that social development could lead to environmentally friendly tanning and reduce polluting methods that affect employees, consumers, and the surrounding community. Furthermore, social development is interrelated with environmental and regulatory improvement. For example, raising public knowledge about the environmental consequences of waste disposal among communities aids in implementing emission reduction measures and improves the firm's total environmental impact. The implementation of SMPs is severely hindered by social obstacles, such as a lack of education and training, the absence of public awareness, and the improper use of personal protection equipment (Śmiechowski & Lament, 2017). Knowledge about SMPs was shown to be the priority driver due to their high positive impact on implementing SMPs in the leather industry (Chang et al., 2016; Almeida et al., 2017). Thus, SMPs could be achieved by implementing socially related adjustments, which in turn could be achieved by employing innovative and sufficient manufacturing technologies (Dwivedi et al., 2019). In summary, the social aspects of the transition, such as developing education and training, raising public awareness, installing proper first aid facilities, and ensuring appropriate personal protective equipment, can facilitate the successful implementation of SMPs.

However, the argument that the regulatory aspect is a dimension that must be considered a driver to force the leather industry to implement SMPs and organizational sustainability in the leather sector is not confirmed in this study (Moktadir et al., 2018; Karuppiah et al. 2021). In the context of the least developed countries, regulatory practices are found to have a high level of importance but low driving power. Hence, they are essential but not sufficient.

6. CONCLUSION

The leather tanning industry in Ethiopia faces challenges in adopting SMPs due to the lack of technical capabilities and social development, making the transition to sustainability difficult. The industry has created severe environmental and social issues by diminishing green areas, increasing air and land pollution, and severely threatening the community, leading to biodiversity loss. Yet, a framework that explains the process and pathways to guide the transition to SMPs is lacking. This study proposed an integrated framework for the transition to SMPs, identifying the aspects that effectively enhance the transition and providing practical insights into the Ethiopian leather tanning industry. The framework guides the transition to SMPs in leather tanning and suggests pathways to socially harmless, eco-friendly, and economically viable solutions. Expert opinions were used to develop a valid set of SMP attributes, to investigate their causal interrelationships, and to identify criteria for practical improvement based on their interdependence. The study employed a hybrid method integrating fuzzy set theory, the FDM, and the FDEMATEL. Fuzzy set theory was applied to collect experts' linguistic preferences in the form of qualitative information and to translate it into comparable crisp values. FDM analysis was conducted to eliminate invalid criteria, and the FDEMATEL method was used to determine the relationships between the attributes.

The findings indicate that solid technical performance promotes the transition to SMPs and drives socially and environmentally responsible business practices within the leather industry. Hence, it will be essential to build technical capabilities and create a knowledge base to influence environmental performance. Adopting the right technical attributes and technology provides significant leverage to enhance the transition to SMPs. In addition, the empirical results indicate that social development is interrelated with environmental and regulatory improvement and leads to environmentally friendly tanning and reduces polluting methods that affect employees, consumers, and the surrounding community. Hence, social development plays a driving role in addressing concerns about the transition to SMPs. For decision-makers in the least developed countries who wish to develop strategies for implementing SMPs, the driving practices include green design, electro-oxidization, site waste management plans, regular supervision, and increasing the level of regulatory compliance.

Hence, this study contributes to our understanding of the transition by building a valid hierarchical model and determining the causal links between SMP attributes in leather tanning. This study investigates the dynamics of sustainability transition attributes in leather tanning and identifies the driving factors in adopting SMPs. Theoretical and practical contributions are discussed. The driving SMPs for improving the transition are identified as green design, electro-oxidization, site waste management plans, regular supervision and increasing the level of regulatory compliance. This study can serve as a resource for decision-makers seeking to incorporate sustainable practices.

This study has limitations. First, the presented attributes were collected from the literature, which could lead to an overdependence on existing studies. Thus, expanding the number of literature sources and attributes should be considered. Second, the study was limited to 13 experts in Ethiopia. Third, Ethiopia has the highest livestock population in Africa and is endowed with a vast potential for a low-cost supply of hides and skins. Thus, Ethiopia's tanning industry has unique characteristics; the results might not apply to other countries. A comparison study is required in the future to obtain more appropriate and conclusive results.

REFERENCES

Abdul-Rashid, S. H., Sakundarini, N., Ghazilla, R. A. R., & Thurasamy, R. (2017): The impact of sustainable manufacturing practices on sustainability performance: Empirical evidence from Malaysia. *International Journal of Operations & Production Management*, 37(2), 182-204

Almeida, C. M., Agostinho, F., Huisingh, D., & Giannetti, B. F. (2017): Cleaner Production towards a sustainable transition. Journal of Cleaner Production, 142, 1-7.

Amabye, T. G. (2015): Plant, soil and water pollution due to tannery effluent a case study from Sheb Tannery PLC, Wukro Tigray, Ethiopia. Science, 3(5), 47-51.

Bacardit, A., Baquero, G., Sorolla, S., & Ollé, L. (2015): Evaluation of a new sustainable continuous system for processing bovine leather. Journal of cleaner production, 101, 197-204.

Brautigam, D., Weis, T., & Tang, X. (2018): Latent advantage, complex challenges: Industrial policy and Chinese linkages in Ethiopia's leather sector. China Economic Review, 48, 158-169.

Bui, T. D., Tseng, J. W., Tseng, M. L., & Lim, M. K. (2022): Opportunities and challenges for solid waste reuse and recycling in emerging economies: A hybrid analysis. Resources, Conservation and Recycling, 177, 105968.

Chang, R. D., Zuo, J., Soebarto, V., Zhao, Z. Y., Zillante, G., & Gan, X. L. (2016): Sustainability transition of the Chinese construction industry: Practices and behaviors of the leading construction firms. Journal of management in engineering, 32(4), 05016009.

Chojnacka, K., Skrzypczak, D., Mikula, K., Witek-Krowiak, A., Izydorczyk, G., Kuligowski, K., & Kułażyński, M. (2021): Progress in sustainable technologies of leather wastes valorization as solutions for the circular economy. Journal of Cleaner Production, 313, 127902.

Cooper, J., Stamford, L., & Azapagic, A. (2018): Social sustainability assessment of shale gas in the UK. Sustainable Production and Consumption, 14, 1-20.

Dwivedi, A., Agrawal, D., & Madaan, J. (2019): Sustainable manufacturing evaluation model focusing leather industries in India: a TISM approach. Journal of Science and Technology Policy Management, 10(2), 319-359.

Dixit, S., Yadav, A., Dwivedi, P. D., & Das, M. (2015): Toxic hazards of leather industry and technologies to combat threat: a review. Journal of Cleaner Production, 87, 39-49.

ECCSA (2019): Short Investment Profile of Leather Sector in Ethiopia, http://ethiopianchamber.com/Data/Sites/1/2012%20EC/Attachments/Ethiopian%20Leather%20Sector%20Profile.pdf (accessed on: October 19, 2021)

Garai, J. (2014): Environmental aspects and health risks of leather tanning industry: a study in the Hazaribag area. Chinese Journal of Population Resources and Environment, 12(3), 278-282.

Ghebretekle, T. B. (2015): Industrial pollution control and management in Ethiopia: a case study on Almeda textile factory and Sheba leather industry in Tigrai Regional State (Doctoral dissertation, University of Warwick).

Grumiller, J., & Raza, W., (2019): The Ethiopian Leather and Leather Products Sector: An Assessment of Export Potentials to Europe and Austria. OFSE, Vienna.

Gupta, S. K., Gupta, S., & Gayathiri, S. (2018): "Pollution prevention" is the key to drive sustainability: Preliminary findings from a tannery unit in India. Management of Environmental Quality: An International Journal, 29(3), 416-426.

Jayanthi, D., Victor, J. S., Chellan, R., & Chellappa, M. (2019): Green processing: minimising harmful substances in leather making. Environmental Science and Pollution Research, 26(7), 6782-6790.

Karuppiah, K., Sankaranarayanan, B., Ali, S. M., Jabbour, C. J. C., & Bhalaji, R. K. A. (2021): Inhibitors to circular economy practices in the leather industry using an integrated approach: Implications for sustainable development goals in emerging economies. Sustainable Production and Consumption, 27, 1554-1568.

Machado, C. G., Winroth, M. P., & Ribeiro da Silva, E. H. D. (2020): Sustainable manufacturing in Industry 4.0: an emerging research agenda. International Journal of Production Research, 58(5), 1462-1484.

Mihai, F. C., & Grozavu, A. (2019): Role of waste collection efficiency in providing a cleaner rural environment. Sustainability, 11(23), 6855.

Moktadir, M. A., Rahman, T., Rahman, M. H., Ali, S. M., & Paul, S. K. (2018): Drivers to sustainable manufacturing practices and circular economy: A perspective of leather industries in Bangladesh. J. of Cleaner Production, 174, 1366-1380.

Negash, Y. T., Hassan, A. M., Tseng, M. L., Wu, K. J., & Ali, M. H. (2021): Sustainable construction and demolition waste management in Somaliland: Regulatory barriers lead to technical and environmental barriers. Journal of Cleaner Production, 297, 126717.

Omoloso, O., Mortimer, K., Wise, W. R., & Jraisat, L. (2021): Sustainability Research in the Leather Industry: a critical review of progress and opportunities for future research. Journal of Cleaner Production, 125441.

Padda, I. U. H., & Asim, M. (2019): What determines compliance with cleaner production? An appraisal of the tanning industry in Sialkot, Pakistan. Environmental Science and Pollution Research, 26(2), 1733-1750.

Sathish, M., Madhan, B., & Rao, J. R. (2019): Leather solid waste: An eco-benign raw material for leather chemical preparation–A circular economy example. Waste Management, 87, 357-367.

Shankar, K. M., Kannan, D., & Kumar, P. U. (2017): Analyzing sustainable manufacturing practices–A case study in Indian context. Journal of Cleaner Production, 164, 1332-1343.

Śmiechowski, K., & Lament, M. (2017): Impact of Corporate Social Responsibility (CSR) reporting on pro-ecological actions of tanneries. Journal of Cleaner Production, 161, 991-999.

Uddin, S., Ali, S. M., Kabir, G., Suhi, S. A., Enayet, R., & Haque, T. (2019): An AHP-ELECTRE framework to evaluate barriers to green supply chain management in the leather industry. International Journal of Sustainable Development & World Ecology, 26(8), 732-751.

UN, (2021): The least developed countries report 2021. https://unctad.org/system/files/official-document/ldc2021overview_en.pdf retrieved on March 6, 2022.

Wahga, A. I., Blundel, R., & Schaefer, A. (2018): Understanding the drivers of sustainable entrepreneurial practices in Pakistan's leather industry: A multi-level approach. International Journal of Entrepreneurial Behavior & Research, 24(2), 382-407.

Yusuf, A. (2013): Assessment on Corporate Social Responsibility. Practices and determinants: a comparative study conducted in Addis Ababa tannery and Awash tannery. Addis Ababa University. Retrieved Mai 15, 2017 from http://file:///C;/Users/User/Desktop/AbdulhamidYusuf.pdf.

Zuriaga-Agustí, E., Galiana-Aleixandre, M. V., Bes-Piá, A., Mendoza-Roca, J. A., Risueño-Puchades, V., & Segarra, V. (2015): Pollution reduction in an eco-friendly chrome-free tanning and evaluation of the biodegradation by composting of the tanned leather wastes. Journal of Cleaner Production, 87, 874-881.

Zahraee, S. M., Shiwakoti, N., & Stasinopoulos, P. (2022): Agricultural biomass supply chain resilience: COVID-19 outbreak vs. sustainability compliance, technological change, uncertainties, and policies. Cleaner Logistics and Supply Chain, 4, 100049.

Hybrid Nonlinear Controller Design for Quadrotor under Multiple Disturbances

Kalkidan Yirmed Tsegaw*

Department of Electrical and Computer Engineering, Faculty of Technology, Debretabor University, P.O.Box 272, Debretabor, Ethiopia,
**Corresponding author, email: dn.kalkidan23@gmail.com*

ABSTRACT

Due to the quadrotor's under-actuated nonlinear system, coupling, parametric uncertainties, actuator faults, and external disturbances, designing controller algorisms for stabilization, take-off, hover, and landing and tracking the desired trajectories is a challenging task.In this research, we design a hybrid nonlinear control method by using integral backstepping combined with the super twisting sliding mode control (IBSTSMC) to stabilize the quadrotor attitude and to accomplish the task of trajectory tracking subject to several disturbances such as parametric uncertainties, actuator faults, and external disturbance. Integral backstepping controller makes the controller immune to mismatched uncertainties, and the super-twisting algorithm is used to guarantee the sliding surface can reach the equilibrium point in a shorter time and to attenuate the chattering problem. Finally, the IBSTSMC is designed to track the correct trajectory command aim at numerous disturbances; and improved particle swarm optimization (PSO) is utilized to determine the optimal values of the proposed control parameters. Furthermore, the entire system stability is investigated using the Lyapunov stability criterion. Finally, MATLAB simulations under various conditions are carried out for verification, and the results indicate the effectiveness and robustness of the control strategy.

Keywords: *multiple disturbances, nonlinear control, quadrotor, super twisting algorithm, trajectory tracking*

1. INTRODUCTION

Recently, as the small unmanned aerial vehicle (UAV) family (Lee, 2018), the quadrotor is becoming a popular topic among researchers and scholars because of its vertical take-off and landing, autonomous hovering, autonomous control and low-cost manufacturability with reduced mechanical complexity so on (Zou & Zhu, 2017). Additionally, it is quite useful in a number of crucial applications, including military surveillance, search-and-rescue operations, agricultural mapping, disaster monitoring, and similar ones.

However, it is difficult to control a quadrotor UAV for position trajectory tracking on account of the following essential reasons (Serra et al., 2016; L. Wang & Jia, 2014; Zhao & Yang, 2016): 1) The quadrotor is known as an open-loop unstable system with nonlinearity and strong coupling between the translational and rotational dynamics; 2) There always exist some parameterized uncertainties in the model dynamics that severely affect the robustness of a controller; 3) The actuator faults threaten the system's stability and reliability; 4) The quadrotor typically operates outdoors in the presence of external disturbances. In a word, how to develop an effective robust flight controller that performs well in practice while ensuring asymptotic stability in theory is still a significant challenge because of the multiple disturbances.

Studies employed linear control techniques, such as proportional-integral-derivative control (PID), for the sake of simplicity and practicability (Li & Li, 2011; Pratama et al., 2018), linear quadratic regulator (LQR) (Rinaldi et al., 2013) and H_∞ control (Basak & Prempain, 2014) in designing the quadrotor controller in early quadrotor helicopters research stage. By linearizing the dynamic model and ignoring the irrelevant details, the linear control technology was employed to stabilize the quadrotor's attitude. Due to this, the quadrotor's performance in terms of tracking precision, robustness against disturbances, etc., was poor and even unacceptable.

A growing number of nonlinear control methods have been used and have performed better in some areas as a result of the advancement of control technology and the widespread use of quadrotors. In (Sreenath et al., 2005), a controller is designed for the quadrotor based on the concept of non-linear dynamic inversion. Significant

numerical simulations have been presented by the authors. However, the controller's performance is extremely susceptible to state disruptions. A unique form of variable structure control called sliding mode control (SMC) (Utkin, 2019) has shown effective for controlling uncertain nonlinear systems. In this control mechanism, the system states are brought to a predefined sliding manifold by switching between two structures. The state space or error state space of the system is used to define the sliding manifold. A lyapunov function is defined as part of the controller design process and is used to evaluate the system stability. The order of the system is reduced and it becomes immune to all matched uncertainties and disturbances when the states reach the sliding manifold. Also, the SMC can provide faster dynamics and has been widely used for controlling uncertain nonlinear systems (Lu & Hwang, 2012; Mondal & Mahanta, 2012; Rafiq et al., 2012) due to its robustness and simplicity. However, only the matched uncertainty and disturbance can be rejected by the sliding mode controller. For mismatched uncertainty, the controller can be effective only under certain conditions or by combination with other methods, but generally it fails. Furthermore, the SMC's Lyapunov function cannot be defined in a systematic way. Moreover, conventional SMCs can be applied to decoupled systems only. Underactuated systems are highly coupled systems to which typical SMCs cannot be directly applied. The high frequency oscillations known as chattering, which can lead to instability and system damage, are another significant undesirable characteristic that SMCs to face with. Numerous studies are being conducted to remove chattering (Mondal & Mahanta, 2012; Rafiq et al., 2012).

In nonlinear systems with matched and mismatched disturbances, the backstepping (BS) control methodology has recently gained popularity (Wang & Liu, 2018). The fundamental concept behind backstepping technology is the recursive selection of appropriate functions of state variables as virtual control inputs. After choosing the final control input, the stability of the entire system is guaranteed. An integrated action is combined with a backstepping controller to increase the controller's ability to counteract disruptions in the steady state. Traditional backstepping controls, however, are not very robust against disturbances and parametric variation.

In recent years, numerous control mechanisms have been put out in an effort to improve robustness. A robust nonlinear controller that combines the sliding mode control approach and the backstepping control technique was suggested by (Chen et al., 2016). Investigations are made into the controller's robustness to model uncertainty and external disturbances. However, the sliding mode control causes the inevitable oscillations. A dynamic surface control (DSC) and backstepping control technique for uncertain parameters was suggested (Chen et al., 2017), and the radial basis function neural network (RBFNN) was used to approximation the unknown external disturbance. However, this paper does not consider the effect of actuator faults on the quadrotor system. In(Avram et al., 2018) a fault-tolerant control of the system was achieved and an adaptive backstepping control approach for quadrotor UAV actuator faults was presented. However, the external disturbance is not taken into account in this paper. In Shao et al. (2018), an extended state observer (ESO) based robust dynamic surface trajectory tracking controller was shown for a quadrotor UAV to deal with the parametric uncertainties and external disturbances. However, this paper does not consider the effect of actuator faults on the system. In (Hu et al., 2018), an adaptive backstepping control strategy was given for actuator faults, parameterized uncertainties and external disturbances of the quadrotor UAV and the stability analysis was given in theory. However, the proposed method is used in the attitude tracking, and is not used in the trajectory tracking directly. An integral backstepping sliding mode controller is proposed for quadrotor helicopter under external uncertain disturbances in (Jia et al., 2017). The outcomes of the simulation showed the controller's ability to reject both matched and mismatched disturbances. PSO-based integral sliding mode control (PSO-ISMC) solution for the cart-inverted pendulum system in (Shima & Bashir, 2021). Traditional PSO algorithm is having the disadvantage problem of falling into local extreme values, the issue of not obtaining a globally optimal solution, and the problem of finding the best fitness.

In this paper, a novel control methodology combined with integral backstepping and super-twisting sliding mode is proposed for the quadrotor trajectory tracking problem under multiple disturbances. And the main contributions of this paper are summarized as follows:

- A new integral backstepping super twisting sliding mode controller is developed for the quadrotor trajectory tracking control with the parametric uncertainties, actuator fault and external disturbance.
- The stability of the closed-loop system is guaranteed using the lyapunov stability criterion, and the stability conditions are used to design the controller parameters.
- Improved particle swarm optimization (PSO) is utilized to determine the optimal values of IBSTSMC.
- MATLAB simulations are performed to validate the effectiveness of the proposed scheme.

2. MATERIALS AND METHODS

2.1 The Quadrotor UAV Model

This subsection establishes the quadrotor UAV model with the various disturbances. The quadrotor's centre of gravity is located where the body axis originates. And it is a rigid body when the flexible of the mechanical structure is neglected. Thrust and drag forces are related to the squares of the propeller's speed. Its motion can be separated into rotational motion and spatial translational motion. Take into account the parametric uncertainties with the unknowable external disturbances described by (Bingöl & Güzey, 2022; Xiong & Zhang, 2016):

$$
\begin{aligned}
\ddot{\mathrm{X}} &= \frac{1}{m+\Delta m}(\cos\phi\sin\theta\cos\psi+\sin\phi\sin\psi)U_1-\frac{k_1\dot{x}}{m+\Delta m}+D_x(\mathrm{t})\\
\ddot{\mathrm{Y}} &= \frac{1}{m+\Delta m}(\cos\phi\sin\theta\sin\psi-\sin\phi\cos\psi)U_1-\frac{k_2\dot{y}}{m+\Delta m}+D_y(\mathrm{t})\\
\ddot{\mathrm{Z}} &= \frac{1}{m+\Delta m}(\cos\phi\cos\theta)U_1-g-\frac{k_3\dot{z}}{m+\Delta m}+D_z(\mathrm{t})\\
\ddot{\phi} &= \dot{\theta}\dot{\psi}\frac{I_y+\Delta I_y-I_z-\Delta I_z}{I_x+\Delta I_x}+\frac{J_r}{I_x+\Delta I_x}\Omega_r\dot{\theta}+\frac{l}{I_x+\Delta I_x}U_2-\frac{k_4 l}{I_x+\Delta I_x}\dot{\phi}+D_\phi(\mathrm{t})\\
\ddot{\theta} &= \dot{\psi}\dot{\phi}\frac{I_z+\Delta I_z-I_x-\Delta I_x}{I_y+\Delta I_y}+\frac{J_r}{I_y+\Delta I_y}\Omega_r\dot{\phi}+\frac{l}{I_y+\Delta I_y}U_3-\frac{k_5 l}{I_y+\Delta I_y}\dot{\theta}+D_\theta(\mathrm{t})\\
\ddot{\psi} &= \dot{\phi}\dot{\theta}\frac{I_x+\Delta I_x-I_y-\Delta I_y}{I_z+\Delta I_z}+\frac{1}{I_z+\Delta I_z}U_4-\frac{k_6}{I_z+\Delta I_z}\dot{\psi}+D_\psi(\mathrm{t})
\end{aligned}
\qquad (1)
$$

Where, (ϕ,θ,ψ) are three Euler angles, indicating roll, pitch and yaw, respectively; (x, y, z) are three positions of quadrotor in space; m is the total mass of the quadrotor; g is the acceleration of gravity; l is the half-length of the quadrotor; (I_x,I_y,I_z) are the inertias of the quadrotor with respect to axes; J_r is the inertia of the propeller; $k_i(\mathrm{i}=1,2,...,6)$ are the drag coefficients; $\mathrm{D}_i(\mathrm{i}=\mathrm{x},\mathrm{y},\mathrm{z},\phi,\theta,\psi)$ are external disturbances; Δ denote parametric uncertainties;

The external disturbances can be characterized by two parts:

$$D_i = D_{i,const} + D_{i,\mathrm{sto}}(\mathrm{i}=x,y,z,\phi,\theta,\psi) \qquad (2)$$

Where, $D_{i,const}$ (static wind, unmodeled dynamic errors) represents the unknown constant disturbances changing slowly along time.

$D_{i,\mathrm{sto}}$ (Stochastic wind, uncertain measurement noise) represents the fast varying and unknown stochastic disturbances with the assumption that corresponds to uniform distribution.

$U_i(\mathrm{i}=1,2,3,4)$ are the virtual control inputs defined as:

$$\begin{bmatrix} U_1 \\ U_2 \\ U_3 \\ U_4 \end{bmatrix} = \begin{bmatrix} \mathrm{F}_1+\mathrm{F}_2+\mathrm{F}_3+\mathrm{F}_4 \\ \mathrm{F}_4-\mathrm{F}_2 \\ \mathrm{F}_3-\mathrm{F}_1 \\ k_q(-\mathrm{F}_1+\mathrm{F}_2-\mathrm{F}_3+\mathrm{F}_4)/k_l \end{bmatrix} \tag{3}$$

Where, $F_i = k_l\Omega_i^2(\mathrm{i}=1,2,3,4)$ are thrusts generated by four rotors, and k_l is the lift coefficient, k_q is the drag coefficient; $\Omega_r = \Omega_1 - \Omega_2 + \Omega_3 - \Omega_4, \Omega_i(\mathrm{i}=1,2,3,4)$ are the angular speed of the propeller i. The input of the system is altitude control (U_1), roll control (U_2), pitch control (U_3) and yaw control (U_4). We consider the actuator faults represented by loss of effectiveness (LOE) to the rotors. For instance, the structural damage to a propeller would result in a partial loss of thrust generated by the corresponding rotor. Thus, the actuator faults under consideration are modelled as follows:

$$\varpi_i = (1-\varepsilon_i)\omega_i, i=1,2,3,4 \tag{4}$$

Where, ω_i represents the commanded rotor angular velocity, ϖ_i is the actual rotor angular velocity, and $\varepsilon_i \in (0,1]$ is an unknown constant characterizing the occurrence of a partial LOE fault in rotor i; and the relationship between rotor angular velocity and control inputs are treated as follows:

$$\begin{aligned} \mathrm{U}_1 &= k_l(\varpi_1^2+\varpi_2^2+\varpi_3^2+\varpi_4^2) \\ \mathrm{U}_2 &= k_l(\varpi_4^2-\varpi_2^2) \\ \mathrm{U}_3 &= k_l(\varpi_3^2-\varpi_1^2) \\ \mathrm{U}_4 &= k_q(\varpi_1^2-\varpi_2^2+\varpi_3^2-\varpi_4^2) \end{aligned} \tag{5}$$

Substituting (4) into (5), we can obtain as follows:

$$\begin{aligned} \mathrm{U}_1 &= k_l[(1-\varepsilon_1)^2\omega_1^2+(1-\varepsilon_2)^2\omega_2^2+(1-\varepsilon_3)^2\omega_3^2+(1-\varepsilon_4)^2\omega_4^2] \\ \mathrm{U}_2 &= k_l[(1-\varepsilon_4)^2\omega_4^2-(1-\varepsilon_2)^2\omega_2^2] \\ \mathrm{U}_3 &= k_l[(1-\varepsilon_3)^2\omega_3^2-(1-\varepsilon_1)^2\omega_1^2] \\ \mathrm{U}_4 &= k_q[(1-\varepsilon_1)^2\omega_1^2-(1-\varepsilon_2)^2\omega_2^2+(1-\varepsilon_3)^2\omega_3^2-(1-\varepsilon_4)^2\omega_4^2] \end{aligned} \tag{6}$$

Assumption1. It is assumed that the roll, pitch and yaw angle satisfy the conditions $|\phi(\mathrm{t})| < \pi/2, |\theta(\mathrm{t})| < \pi/2$, and $|\psi(\mathrm{t})| < \pi$ for $t \geq 0$.

Assumption2. In general, the parameter disturbance $D_i(\mathrm{t}) = \left[D_x, D_y, D_z, D_\phi, D_\theta, D_\psi\right]^T$ is assumed bounded uncertainty, i.e. $|D_i(\mathrm{t})| \leq \beta_i$ where β_i is positive constant. This assumption is also authentic for matched and mismatched uncertainties when there is knowledge about the uncertain terms based on systems states.

In this subsection, three different types of disturbances in quadrotor UAV flight are taken into consideration. They are the parametric uncertainties, actuator fault and external disturbance, respectively. Next, a quadrotor UAV model with several disturbances is established. Integral backstepping super twisting sliding mode controller will be designed for the quadrotor UAV model in the manner described below in order to control the quadrotor's stability.

2.1 Integral Backstepping Super Twisting Sliding Mode Controller Design

In the controller design, the double loops structure is utilized. The quadrotor's trajectory tracking issue can be separated into position loop and attitude loop problems. The position loop is slow dynamic that it controls the quadrotor to follow the given reference trajectory using the thrust forces. The position loop includes: the height subsystem, the x-axis subsystem and the y-axis subsystem. The attitude loop is fast dynamic that accounts for regulating the orientation to timely track the desired attitude produced by the position loop. The attitude loop includes the roll subsystem, the pitch subsystem and the yaw subsystem. The roll and pitch angle are gained though virtual input (U_x, U_y) inverse design.

There are both internal and external disturbances in each subsystem. The causes of internal disturbance include: the uncertain parameters and the actuator faults. The quadrotor UAV's exposure to external disturbance is primarily due to wind-related effects, unmodeled dynamic errors and uncertain measurement noise.

For the purpose of designing controllers, the system equations are rewritten in state space representation. And the state space model adopted by the control system is $\dot{X}_s = f(\mathrm{X}_s, \mathrm{U})$, where X_s is the state vector and U is the control input vector. The state vector is selected as $\mathrm{X}_s = [\phi \quad \dot{\phi} \quad \theta \quad \dot{\theta} \quad \psi \quad \dot{\psi} \quad z \quad \dot{z} \quad x \quad \dot{x} \quad y \quad \dot{y}]$. In the design of the controller the state variables are selected as:

$$x_1 = \phi, x_2 = \dot{\phi}, \mathrm{x}_3 = \theta, \mathrm{x}_4 = \dot{\theta}, \mathrm{x}_5 = \psi, \mathrm{x}_6 = \dot{\psi}, \quad \mathrm{x}_7 = z, \mathrm{x}_8 = \dot{z}, \mathrm{x}_9 = x, \mathrm{x}_{10} = \dot{x}, \mathrm{x}_{11} = y, \mathrm{x}_{12} = \dot{y}.$$

The state equations can be described as:

$$\dot{X}_s = f(\mathrm{X}_s, \mathrm{U}) = \begin{bmatrix} x_2 \\ \mathrm{x}_4\mathrm{x}_6 a_1 + \mathrm{x}_4 \Omega_r a_2 + b_1 U_2 - r_1 x_2 + D_\phi(\mathrm{t}) \\ \mathrm{x}_4 \\ \mathrm{x}_2\mathrm{x}_6 a_3 + \mathrm{x}_2 \Omega_r a_4 + b_2 U_3 - r_2 x_4 + D_\theta(\mathrm{t}) \\ \mathrm{x}_6 \\ \mathrm{x}_2\mathrm{x}_4 a_5 + b_3 U_4 - r_3 x_6 + D_\psi(\mathrm{t}) \\ \mathrm{x}_8 \\ b_4 \cos x_1 \cos x_3 U_1 - g - r_4 x_8 + D_z(\mathrm{t}) \\ \mathrm{x}_{10} \\ b_5 U_x U_1 - r_5 x_{10} + D_x(\mathrm{t}) \\ \mathrm{x}_{12} \\ b_6 U_y U_1 - r_6 x_{12} + D_y(\mathrm{t}) \end{bmatrix} \tag{7}$$

$$a_1 = \frac{I_y + \Delta I_y - I_z - \Delta I_z}{I_x + \Delta I_x}, a_2 = \frac{J_r}{I_x + \Delta I_x}, \mathrm{b}_1 = \frac{l}{I_x + \Delta I_x}, r_1 = \frac{k_4 l}{I_x + \Delta I_x}, r_3 = \frac{k_6}{I_z + \Delta I_z}, r_5 = \frac{k_1}{m + \Delta m}$$

Where $a_3 = \frac{I_z + \Delta I_z - I_x - \Delta I_x}{I_y + \Delta I_y}, a_4 = \frac{J_r}{I_y + \Delta I_y}, \mathrm{b}_2 = \frac{l}{I_y + \Delta I_y}, r_2 = \frac{k_5 l}{I_y + \Delta I_y}, r_4 = \frac{k_3}{m + \Delta m}, r_6 = \frac{k_2}{m + \Delta m}$

$$a_5 = \frac{I_x + \Delta I_x - I_y - \Delta I_y}{I_z + \Delta I_z}, \mathrm{b}_3 = \frac{1}{I_z + \Delta I_z}, b_4 = b_5 = b_6 = \frac{1}{m + \Delta m}$$

$$\begin{aligned} U_x &= \cos x_1 \sin x_3 \cos x_5 + \sin x_1 \sin x_5 \\ U_y &= \cos x_1 \sin x_3 \sin x_5 - \sin x_1 \cos x_5 \end{aligned} \tag{8}$$

We can find the desired roll and pitch angles corresponding to *Ux* and *Uy* by using (8) as:

$$\begin{cases} \phi_d = \arcsin(U_x \sin(\psi_d) - U_y \cos(\psi_d)) \\ \theta_d = \arcsin\left(\dfrac{U_x \cos(\psi_d) + U_y \sin(\psi_d)}{\cos(\psi_d)}\right) \end{cases} \tag{9}$$

A higher order linear switching function can be replaced in place of nonlinear switching function to reduce chattering significantly. Super-twisting sliding mode control introduces for the sliding variables to reach the sliding surface in finite time as well as reach them without chattering. And the continuous super-twisting control law *Ust*(*t*) comprises two parts. The first part, indicated by W(t), is defined by its discontinuous first-time derivative dW(t)/dt; whereas the second part is a continuous function of the sliding variable (Shi et al., 2019). The super-twisting sliding mode control is given by (10), and it is a simplified form derived from the fact that the system is linearly dependent on the control.

$$\begin{cases} U_{st}(\mathrm{t}) = \mathrm{W}(\mathrm{t}) - \mathrm{k}_1 |s|^{1/2} \, sign(\mathrm{s}) \\ \dot{\mathrm{W}}(\mathrm{t}) = -\mathrm{k}_2 \, sign(\mathrm{s}) \end{cases} \tag{10}$$

The following are the necessary conditions for finite-time convergence:

$$\begin{cases} |\Delta(\mathrm{X}_s, \mathrm{U}, \mathrm{t})| < \zeta \\ 0 \le h_{\min} \le \dfrac{\partial \dot{s}}{\partial U} \le h_{\max} \end{cases} \tag{11}$$

Following that, the super-twisting algorithm's parameters can be constrained to:

$$\begin{cases} \mathrm{k}_1^2 \ge \dfrac{4\zeta}{h_{\min}^2} \cdot \dfrac{h_{\max}(\mathrm{k}_2 + \zeta)}{h_{\min}(\mathrm{k}_2 - \zeta)} \\ \mathrm{k}_2 > \dfrac{\zeta}{h_{\min}} \end{cases} \tag{12}$$

The control aim is to design an appropriate control law so that the state trajectory $X_{sd} = [\phi_d \quad \theta_d \quad \psi_d \quad z_d \quad x_d \quad y_d]^T$ of the quadrotor system can track desired reference trajectory. Each of the six degrees of freedom (DOF) that can be controlled by the quadcopter's control system is described in a similar manner, however only one DOF is taken into account here for the sake of simplicity. And let's start with the IBC's methodical design, which is described as follows:

Step 1: Defining the tracking error: $e_1 = \phi_d - \phi$ (13)

The derivative of the tracking error is shown as follows:

$$\dot{e}_1 = \dot{\phi}_d - \dot{\phi} \tag{14}$$

The first Lyapunov function is selected as:

$$V_1(e_1,\eta_1)=\frac{1}{2}e_1^2+\frac{1}{2}\lambda_1\eta_1^2 \quad (15)$$

Where $\eta_1=\int_0^t e_1(\tau)\,\mathrm{d}\tau$ (16)

The derivative of $V_1(e_1,\eta_1)$ is:

$$\dot{V}_1(e_1,\eta_1)=e_1\dot{e}_1+\lambda_1\eta_1 e_1=e_1(\dot{\phi}_d-\dot{\phi}+\lambda_1\eta_1) \quad (17)$$

If we set the virtual control z_ϕ of $\dot{\phi}$ as: $\mathrm{z}_\phi=\dot{\phi}_d+\lambda_1\eta_1+c_1e_1$ (18)

Where c_1 and λ_1 are positive constants, then: $\dot{V}_1(e_1,\eta_1)=-c_1e_1^2\le 0$ (19) $\dot{V}_1(e_1,\eta_1)$ is a negative semi-definite. Therefore, the control law will asymptotically stabilize the system.

Step 2: Set the tracking-error of $\dot{\phi}$ as:

$$e_2=\mathrm{z}_\phi-\dot{\phi}=\dot{\phi}_d+\lambda_1\eta_1+c_1e_1-\dot{\phi} \quad (20)$$

Then for roll angle ϕ, use equation (20) as dynamic sliding surface as:

$$S_\phi=e_2=\mathrm{z}_\phi-\dot{\phi}=\dot{\phi}_d+\lambda_1\eta_1+c_1e_1-\dot{\phi} \quad (21)$$

Considering the augmented lyapunove function:

$$V_2(\mathrm{e}_1,\mathrm{s}_\phi,\eta_1)=\frac{1}{2}(\mathrm{e}_1^2+\mathrm{s}_\phi^2+\lambda_1\eta_1^2) \quad (22)$$

$$\dot{V}_2(\mathrm{e}_1,\mathrm{s}_\phi,\eta_1)=\mathrm{e}_1\dot{\mathrm{e}}_1+\mathrm{s}_\phi\{\ddot{\phi}_d+c_1(-\lambda_1\eta_1-c_1\mathrm{e}_1+\mathrm{e}_2)+\lambda_1\mathrm{e}_1-x_4x_6a_1-a_2\Omega_r x_4-b_1U_2+r_2x_2-D_\phi\}+\lambda_1\eta_1\mathrm{e}_1 \quad (23)$$

The chosen law for the attractive surface is the time derivative in (20) satisfies $(\mathrm{s}_\phi\dot{\mathrm{s}}_\phi<0)$,

$$\begin{aligned}\dot{\mathrm{s}}_\phi&=-q_1|\mathrm{s}|^{1/2}.\mathrm{sgn}(\mathrm{s}_\phi)-q_2\int_0^t\mathrm{sgn}(\mathrm{s}_\phi(\tau))d\tau=\ddot{\phi}_d+\lambda_1\dot{\eta}_1+c_1\dot{\mathrm{e}}_1-\ddot{\phi}\\&=\ddot{\phi}_d+c_1(-\lambda_1\eta_1-c_1\mathrm{e}_1+\mathrm{s}_\phi)+\lambda_1\mathrm{e}_1-x_4x_6a_1-a_2\Omega_r x_4-b_1U_2+r_1x_2-D_\phi\end{aligned} \quad (24)$$

Then, the control input U_2 is extracted as:

$$U_2=\frac{1}{b_1}\{q_1|\mathrm{s}_\phi|^{1/2}.\mathrm{sgn}(\mathrm{s}_\phi)+q_2\int_0^t\mathrm{sgn}(\mathrm{s}_\phi(\tau))d\tau+\ddot{\phi}_d+c_1(-\lambda_1\eta_1-c_1\mathrm{e}_1+\mathrm{s}_\phi)+\lambda_1\mathrm{e}_1-x_4x_6a_1-a_2\Omega_r x_4+r_1x_2-D_\phi\} \quad (25)$$

The same steps are followed to extract U3, U4, U1, U_x and U_y using the following dynamic sliding surface/manifold in eq. (26).

$$\begin{cases}S_\theta=\dot{\theta}_d+\lambda_2\eta_2+c_3e_3-\dot{\theta}\\S_\psi=\dot{\psi}_d+\lambda_3\eta_3+c_5e_5-\dot{\psi}\\S_z=\dot{z}_d+\lambda_4\eta_4+c_7e_7-\dot{z}\\S_x=\dot{x}_d+\lambda_5\eta_5+c_9e_9-\dot{x}\\S_y=\dot{y}_d+\lambda_6\eta_6+c_{11}e_{11}-\dot{y}\end{cases} \quad (26)$$

So the control input U3, U4, U1, U_x and U_y are extracted as:

$$U_3 = \frac{1}{b_2}\{q_3 |s_\theta|^{1/2}.\mathrm{sgn}(s_\theta) + q_4 \int_0^t \mathrm{sgn}(s_\theta(\tau))d\tau + \ddot{\theta}_d + c_3(-\lambda_2\eta_2 - c_3 e_3 + s_\theta) + \lambda_2 e_3 - x_2 x_6 a_3 - a_4 \Omega_r x_2 + r_2 x_4 - D_\theta\} \quad (27)$$

$$U_4 = \frac{1}{b_3}\{q_5 |s_\psi|^{1/2}.\mathrm{sgn}(s_\psi) + q_6 \int_0^t \mathrm{sgn}(s_\psi(\tau))d\tau + \ddot{\psi}_d + c_5(-\lambda_3\eta_3 - c_5 e_5 + s_\psi) + \lambda_3 e_5 - x_2 x_4 a_5 + r_3 x_6 - D_\psi\} \quad (28)$$

$$U_1 = \frac{1}{b_4 \cos x_1 \cos x_3}\{q_7 |s_z|^{1/2}.\mathrm{sgn}(s_z) + q_8 \int_0^t \mathrm{sgn}(s_z(\tau))d\tau + \ddot{z}_d + c_7(-\lambda_4\eta_4 - c_7 e_7 + s_z) + \lambda_4 e_7 + g + r_4 x_8 - D_z\} \quad (29)$$

$$U_x = \frac{1}{b_5 U_1}\{q_9 |s_x|^{1/2}.\mathrm{sgn}(s_x) + q_{10} \int_0^t \mathrm{sgn}(s_x(\tau))d\tau + \ddot{x}_d + c_9(-\lambda_5\eta_5 - c_9 e_9 + s_x) + \lambda_5 e_9 + r_5 x_{10} - D_x\} \quad (30)$$

$$U_y = \frac{1}{b_6 U_1}\{q_{11} |s_y|^{1/2}.\mathrm{sgn}(s_y) + q_{12} \int_0^t \mathrm{sgn}(s_y(\tau))d\tau + \ddot{y}_d + c_{11}(-\lambda_6\eta_6 - c_{11} e_{11} + s_y) + \lambda_6 e_{11} + r_6 x_{12} - D_y\} \quad (31)$$

Where, $q_1, q_2, q_3, q_4, q_5, q_6, q_7, q_8, q_9, q_{10}, q_{11}, q_{12}, c_1, c_3, c_5, c_7, c_9, c_{11}, \lambda_1, \lambda_2, \lambda_3, \lambda_4, \lambda_5, \lambda_6$ are parameters of IBSTSMC and are positive constants.

2.2 Tuning of IBSTSMC Parameters Using Improved PSO

The PSO is a type of population-based algorithm and swarm intelligence technique that is typically employed as an optimization tool. Each particle of the population is a candidate solution. In PSO, each particle moves across the search (solution) space by changing its velocity in accordance with its own and the experiences of the other particles. Each particle tries to imitate the traits of their successful peers in order to improve them. Additionally, each particle has a memory to continuously track its prior best position (denoted as pbest) and corresponding fitness. The population's most fit particle is referred to as gbest. Three steps are involved in the basic PSO algorithm, namely, generating particles' positions and velocities, velocity update, and finally, position update. First, by using the design upper, $x_{\max}$ and lower, $x_{\min}$ bound values, the initial positions x_i^k and velocities v_i^k of particles are randomly produced, as expressed in the following equations,

$$\begin{aligned} x_i^k &= x_{\min} + rand(x_{\max} - x_{\min}) \\ v_i^k &= x_{\min} + rand(x_{\max} - x_{\min}) \end{aligned} \quad (32)$$

In Eq. (32), the subscript and the superscript mean the *i*th particle at iteration k, respectively, while *rand* is a uniformly distributed random variable that can take any value between 0 and 1. The second step is to update each particle's velocity using the following equations:

$$v_i^{k+1} = w.v_i^k + n_1.rand.(\mathrm{pbest} - x_i^k) + n_2.rand.(g\ \mathrm{best} - x_i^k) \quad (33)$$

Traditional PSO, however, suffers from the disadvantages of falling into local extreme values, failing to establish a globally optimal solution, and unable to determine the best fitness. A new PSO equation is developed by combining two types of inertia weights, namely the linear decreasing inertia weight and the chaotic inertia weight, in order to address the shortcomings of traditional PSO (Nkwanyana & Wang, 2020).

Linear Decreasing Inertia Weight: $\mathrm{w}_l = w_{\max} - \frac{w_{\max} - w_{\min}}{I_{\max}} * t$ (34)

Chaotic inertia weight: $w_c = (w_{\max} - w_{\min}) \frac{I_{\max} - I}{I_{\max}} + w_{\min} z$ (35)

The first step is to combine two inertia weights:

$$\mathrm{w} = \mathrm{w}_l + w_c = [w_{\max} - \frac{w_{\max} - w_{\min}}{I_{\max}} * t] + [(w_{\max} - w_{\min}) \frac{I_{\max} - I}{I_{\max}} + w_{\min} z]$$

$$\mathrm{w} = \frac{I_{\max} * w_{\max} - (w_{\max} - w_{\min})t + (w_{\max} - w_{\min})I_{\max} - I + I_{\max} * w_{\min} z}{I_{\max}} \quad (36)$$

Where, z is logistic mapping, Wmax - maximum weight, Wmin - minimum weight, Imax - maximum iteration.

The next step is to introduce a control factor (α) that will help to control the output fitness by varying it into the suitable values. The control factor is added as the exponential function, therefore: w becomes w^{α}. Then the equation (33) becomes the equation (37):

$$v_i^{k+1} = w^{\alpha}.\mathrm{v}_i^k + n_1.rand.(\mathrm{pbest} - x_i^k) + n_2.rand.(g\ \mathrm{best} - x_i^k) \quad (37)$$

Three weight factors, namely: inertia weight factor w^{α}, self-confidence factor n_1, and swarm confidence factor n_2, are combined in Eq. (37) to affect the particles direction. Lastly, the position of each particle is updated using its velocity vector as Eq. (38).

$$x_i^{k+1} = x_i^k + v_i^{k+1} \quad (38)$$

Until a stopping criterion is achieved, repeat steps (i) velocity update, (ii) location update, and (iii) fitness calculations. In this study, the control parameters are determined by minimizing a cost function that is defined by the Integral Time Absolute Error (ITAE) performance index.

$$ITAE = \int_0^T t\,|e(\mathrm{t})|dt \quad (39)$$

Compared to the IAE (integral of the absolute error) or the ISE (integral square error) performance indices, the ITAE performance index has the advantage of causing smaller overshoots and oscillations (Biswas et al., 2014). In this work, the following values are assigned for controller parameter optimization:

- Population/swarm size = 30.
- The number of maximum iterations = 30.
- Control factor, α = -10.
- The self, swarm confident and inertia weight factors, n_1 and n_2 = 2 and w =1.5.
- The simulation time is equal to 30 seconds.

3. RESULTS AND DISCUSSION

In this section, MATLAB simulations are carried out in order to demonstrate the effectiveness of the controllers proposed in this paper. Simulations are divided into three parts, regulation task /setpoint tracking task, typical trajectory tracking including taking-off, hovering and landing; and helix trajectory tracking with multiple disturbance. The nominal parameters of the adopted quadrotor model are shown in Table 1 as a result of parametric

estimation and actual measurement of the quadrotor. The integral backstepping super twisting sliding mode controller's (IBSTSMC) parameters are shown in Table 2.

Table 1: The parameter value of the quadrotor (Jia et al., 2017)

Parameter	Value		Parameter	Value	Parameter
g(m/s^2)	9.81	Jr (kg.m^2)	2.8385e-5	k5(N/m/s)	5.5670e-4
m(kg)	0.486	k1 (N/m/s)	5.5670e-4	k6(N/m/s)	5.5670e-4
Ix (kg.m^2)	3.827e-3	k2 (N/m/s)	5.5670e-4	k_l(N.s2)	2.9842e-3
Iy (kg.m^2)	3.827e-3	k3 (N/m/s)	5.5670e-4	k_q(N.m.s^2)	3.2320e-2
Iz (kg.m^2)	7.6566e-3	k4 (N/m/s)	5.5670e-4	l(m)	0.23

Table 2: Optimal parameters of controllers

Parameter	Value	Parameter	Value	Parameter	Value	Parameter	Value
q_1	6.89	q_7	2.47	c_1	13.85	λ_1	0.0019
q_2	0.32	q_8	1.13	c_3	14.73	λ_2	0.0008
q_3	6.92	q_9	1.18	c_5	1.93	λ_3	0.06
q_4	0.003	q_{10}	0.002	c_7	3.23	λ_4	0.0004
q_5	6.6	q_{11}	1.76	c_9	2.17	λ_5	0.0034
q_6	0.53	q_{12}	0.89	c_{11}	2.02	λ_6	0.0007

3.1. Case I: Regulation Task/Set Point Tracking Task

For the regulation task, and the linear position variations are described by the equations below:

$$\begin{cases} x_d = \begin{cases} 2, 0 < t \le 10, \\ 3, 10 < t \le 20, \\ 5, 20 < t \end{cases} \\ y_d = \begin{cases} 1, 0 < t \le 10, \\ 2, 10 < t \le 20, \\ 4, 20 < t \end{cases} \\ z_d = 4, \\ \psi_d = \pi / 6 \end{cases} \tag{40}$$

We consider model uncertainty 20% and the rotor suffers from a 2% LOE (loss of effectiveness) in the thrust. And the external disturbances referring Eq. (2), including constant slide wind and the stochastic measurement noise corresponding to uniform distribution are modelled as:

$$\begin{cases} D_{j(j=x,y,z)} = \begin{cases} D_{1,cont} + D_{1,sto}, 5 \le t \le 12 \\ 0, else \end{cases} \\ D_{j(j=\phi,\theta,\psi)} = \begin{cases} D_{2,cont} + D_{2,sto}, 18 \le t \le 25 \\ 0, else \end{cases} \end{cases} \tag{41}$$

Where, $\begin{cases} D_{1,cont} = 0.25 \\ -0.01 \le D_{1,\text{sto}} \le 0.01 \end{cases}$ and $\begin{cases} D_{2,cont} = 0.01 \\ -0.005 \le D_{2,sto} \le 0.005 \end{cases}$

From Figs. 1a and b, it is evident that the x and y positions of the quadrotor are converging to their desired value very precisely despite the presence of multiple disturbances. And from the time response of x and y, it can also be concluded that the proposed method provides a good tracking response in terms of faster convergence with very less overshoot. Moreover, both controllers gave small steady state error (i.e. $x=2.988e^{-6}$ and $y=-0.00047$). A similar trend can be observed in the altitude and yaw angle responses as seen from Figs. 1c and d, respectively at small steady state error (i.e. $x=3.875e^{-6}$ and $y=-4.595e^{-5}$). As a result, the undesired chattering phenomenon will very much be alleviated.

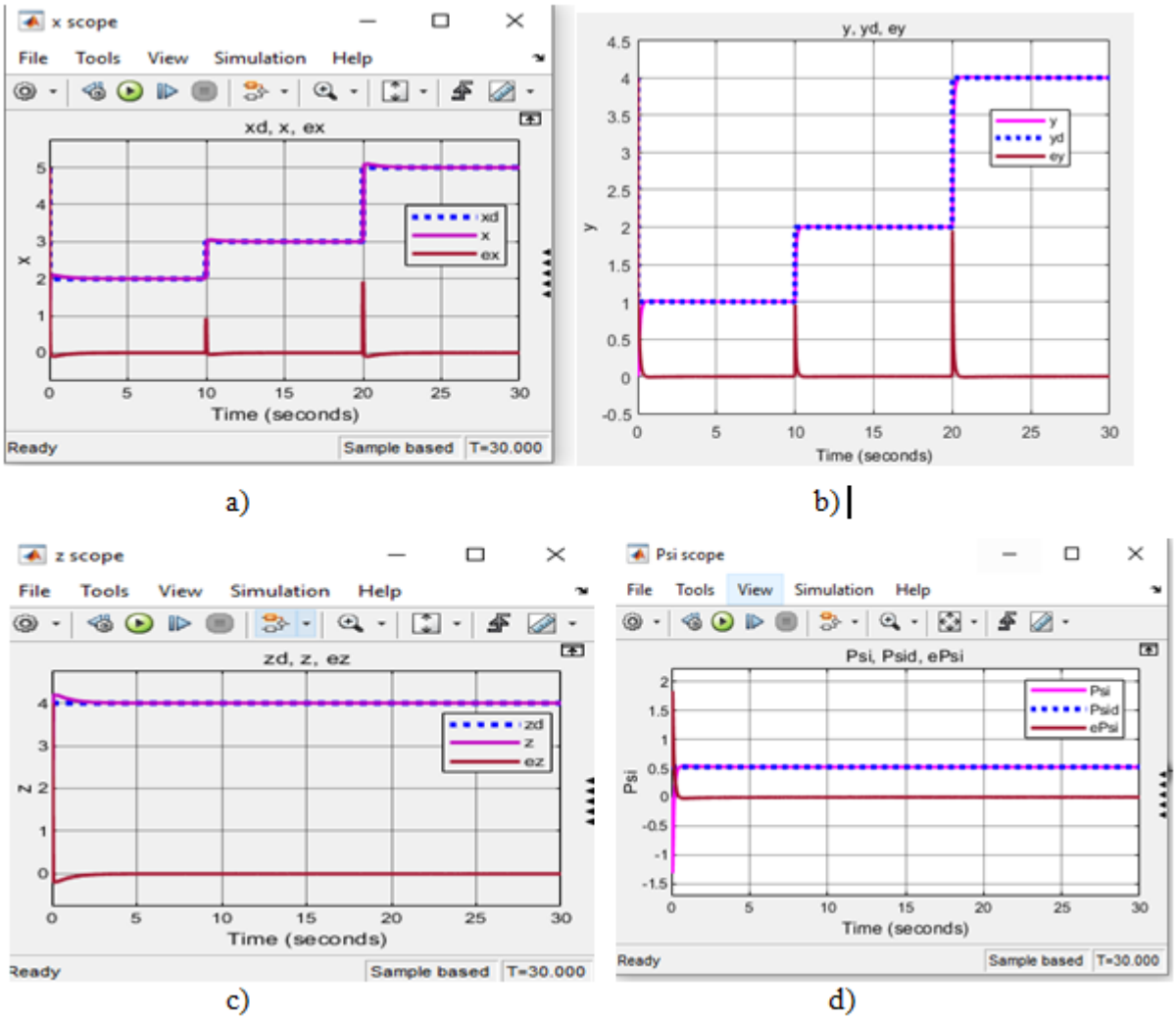

Figure 1: Time response of case I: (a) Time response of x motion, (b) Time response of y motion, (c) Time response of z motion, (d) Time response of ψ rotation

3.2. Case II: Typical Trajectory Tracking

Considering the characteristics of the quadrotor, the typical trajectory consisted of three parts, i.e., taking-off, hovering and landing. The reference flight trajectory parameters are shown below.

And we consider model uncertainty 30%; the rotor suffers from a 3% LOE (loss of effectiveness) in the thrust and the magnitude of external disturbances in eq. (41) increased by 20%. From Fig.2 (a)-(d), it is obvious that the proposed method provides a good tracking response when beginning the manoeuvring flight, namely the flight phase of taking-off and landing. Since the proposed control strategy combines the advantages of both backstepping

and sliding mode control, its position tracking errors shown in Fig.2 (a)-(d) converge to zero in a shorter time and oscillate in smaller amplitude. On the other hand, during the steady flight, namely the flight phase of hovering in the trajectory, the nonlinear dynamic characteristics are hidden because the attitude and angular velocity approximately equal zero.

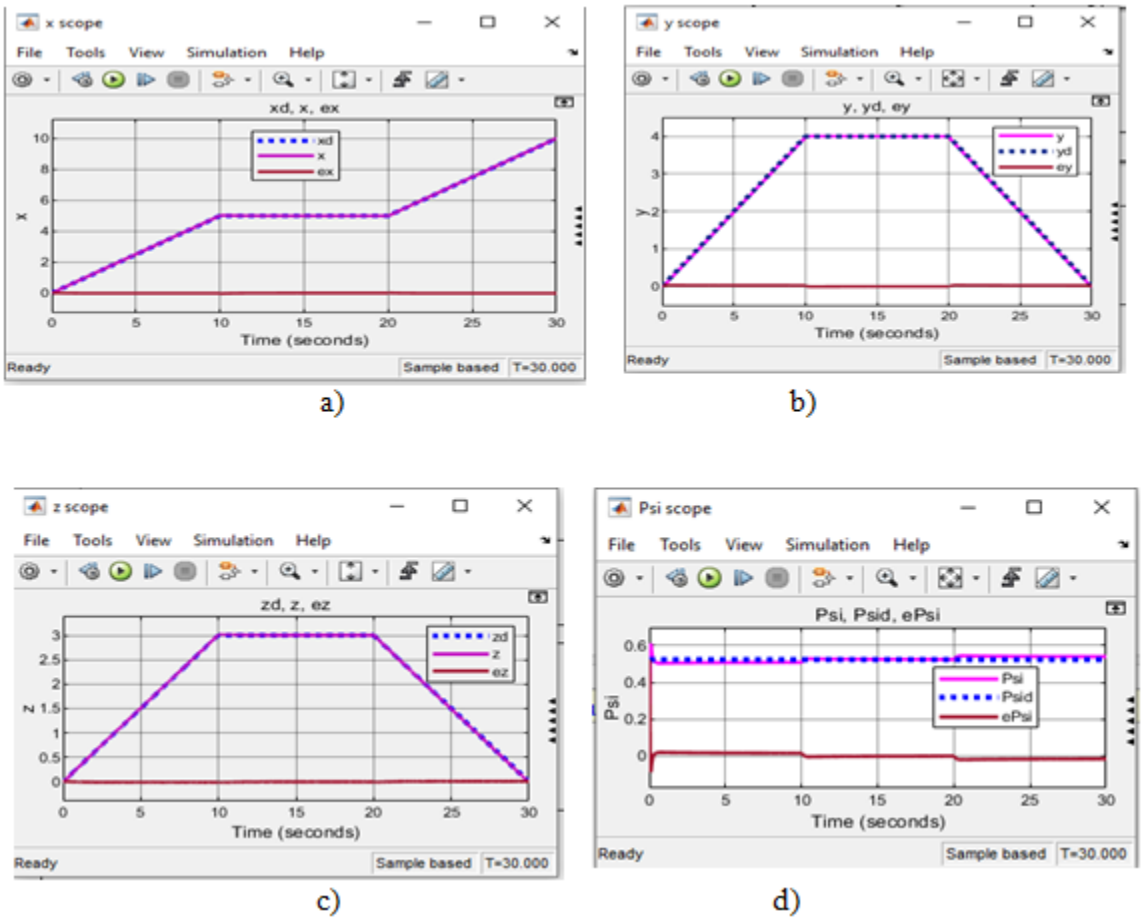

Figure 2: Time response of case II: (a) Time response of x motion, (b) Time response of y motion, (c) Time response of z motion, (d) Time response of ψ rotation

$$\begin{cases} x_d(t) = \begin{cases} 0.5t, 0 \le t < 10, \\ 5, 10 \le t < 20, \\ 0.5t - 5, 20 \le t < 30, \end{cases} \\ y_d(t) = \begin{cases} 0.4t, 0 \le t < 10, \\ 4, 10 \le t < 20, \\ -0.4t + 12, 20 \le t < 30, \end{cases} \\ z_d(t) = \begin{cases} 0.3t, 0 \le t < 10, \\ 3, 10 \le t < 20, \\ -0.3t + 9, 20 \le t < 30, \end{cases} \\ \psi_d = \pi / 6. \end{cases} \tag{42}$$

3.3. Case III: Trajectory Tracking Task

This task involves the use of a time-varying trajectory to evaluate the effectiveness of the proposed IBSTSMC. In the trajectory tracking task, the objective is to track a time varying trajectory in a finite time with chattering attenuation despite the multiple disturbances. The desired trajectory is defined as follows in the Cartesian space:

$$\begin{cases} x_d = 5\cos(0.1t) + 5 \\ y_d = 5\sin(0.1t) + 5 \\ z_d = 0.3t \\ \psi_d = \pi / 6 \end{cases} \tag{43}$$

We consider model uncertainty 30%; the rotor suffers from a 3% LOE (loss of effectiveness) in the thrust and the magnitude of external disturbances in eq. (41) increased by 20%; and the controller parameters are selected the same as taken for the regulation task.

From the time response of x, y, z and ψ given in Figs. 3(a)-(d), it can also be concluded that the proposed method provides a good tracking response in terms of faster convergence with very less overshoot. Moreover, both controllers gave small steady state error (i.e. x=0.00495, y=-0.00091, z=-0.008933 and ψ=0.009131). Finally, from the simulation results, it can be concluded that the proposed methodology caters to the *x*, *y* position, altitude, and attitude control problem of the quadrotor in the presence of multiple disturbances. The IBSTSMC not only provides finite time convergence of the tracking error but also ensures attenuation of the undesired chattering phenomena, which is the main drawback of a conventional sliding mode controller. This makes the application of the proposed controller more suitable for practical applications.

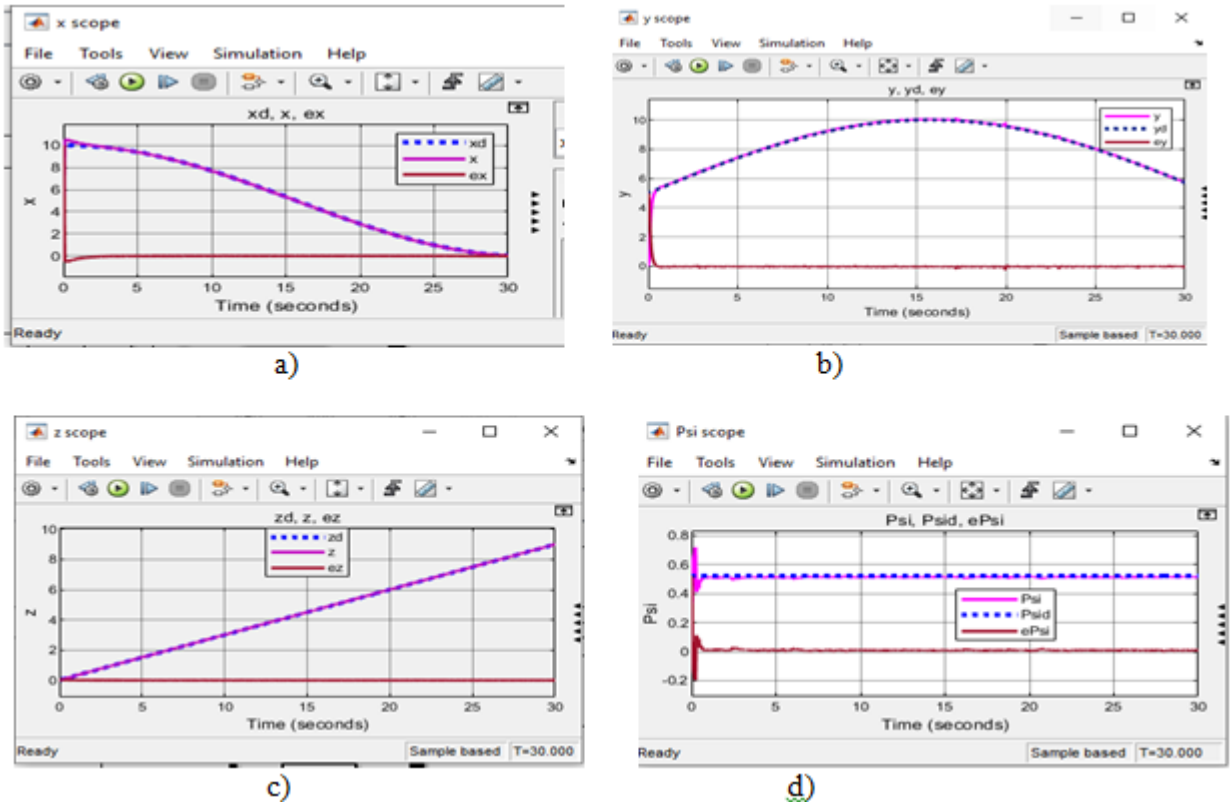

Figure 3: Time response of case III: (a) Time response of x motion, (b) Time response of y motion, (c) Time response of z motion, (d) Time response of ψ rotation

4. CONCLUSION

This paper shows a nonlinear integral backstepping super twisting sliding mode controller (IBSTSMC) trajectory tracking control scheme for a quadrotor UAV. This strategy has been developed taking into account parametric uncertainties, actuator faults, and external disturbances. The stability of the system is proved by the Lyapunov stability criterion. The super twisting algorithm's convergence is examined. The simulation results demonstrate the system's ability to respond quickly and with great tracking accuracy to multiple disturbances. In a word, the effectiveness of the proposed method has been validated by using the 6-DOF quadrotor UAV theoretical and simulation verification. In the future, the proposed control scheme will be conducted an experimental verification using a quadrotor system.

REFERENCES

Avram, R. C., Zhang, X., & Muse, J. (2018). Nonlinear Adaptive Fault-Tolerant Quadrotor Altitude and Attitude Tracking with Multiple Actuator Faults. *IEEE Transactions on Control Systems Technology*, *26*(2), 701–707.

Basak, H., & Prempain, E. (2014). Low order H∞ controllers for a quadrotor UAV. In *2014 UKACC International Conference on Control, CONTROL 2014 - Proceedings* (pp. 127–132).

Bingöl, Ö., & Güzey, H. M. (2022). Finite-Time Neuro-Sliding-Mode Controller Design for Quadrotor UAVs Carrying Suspended Payload. *Drones*, *6*(10), 1–27.

Biswas, P., Maiti, R., Kolay, A., Das Sharma, K., & Sarkar, G. (2014). PSO based PID controller design for twin rotor MIMO system. *International Conference on Control, Instrumentation, Energy and Communication, CIEC 2014*, 56–60.

Chen, F., Jiang, R., Zhang, K., Jiang, B., & Tao, G. (2016). Robust Backstepping Sliding-Mode Control and Observer-Based Fault Estimation for a Quadrotor UAV. *IEEE Transactions on Industrial Electronics*, *63*(8), 5044–5056.

Chen, M., Shao, S. Y., & Jiang, B. (2017). Adaptive Neural Control of Uncertain Nonlinear Systems Using Disturbance Observer. *IEEE Transactions on Cybernetics*, *47*(10), 3110–3123.

Hu, Q., Shao, X., & Guo, L. (2018). Adaptive fault-Tolerant attitude tracking control of spacecraft with prescribed performance. *IEEE/ASME Transactions on Mechatronics*, *23*(1), 331–341.

Jia, Z., Yu, J., Mei, Y., Chen, Y., Shen, Y., & Ai, X. (2017). Integral backstepping sliding mode control for quadrotor helicopter under external uncertain disturbances. *Aerospace Science and Technology*, *68*(May), 299–307.

Lee, T. (2018). Geometric Control of Quadrotor UAVs Transporting a Cable-Suspended Rigid Body. *IEEE Transactions on Control Systems Technology*, *26*(1), 255–264.

Li, J., & Li, Y. (2011). Dynamic analysis and PID control for a quadrotor. *2011 IEEE International Conference on Mechatronics and Automation, ICMA 2011*, 573–578.

Lu, C. H., & Hwang, Y. R. (2012). Hybrid sliding mode position control for a piston air motor ball screw table. *ISA Transactions*, *51*(3), 373–385.

Mondal, S., & Mahanta, C. (2012). A fast converging robust controller using adaptive second order sliding mode. *ISA Transactions*, *51*(6), 713–721.

Nkwanyana, T. B., & Wang, Z. (2020). Improved Particle Swarm optimization Base on the Combination of Linear Decreasing and Chaotic Inertia Weights. *Proceedings - 2020 12th International Conference on Computational Intelligence and Communication Networks, CICN 2020*, *1*, 460–465.

Pratama, G. N. P., Cahyadi, A. I., & Herdjunanto, S. (2018). Robust proportional-derivative control on SO(3) for transporting quadrotor with load uncertainties. *IAENG International Journal of Computer Science*, *45*(2), 275–284.

Rafiq, M., Rehman, S. U., Rehman, F. U., Butt, Q. R., & Awan, I. (2012). A second order sliding mode control design of a switched reluctance motor using super twisting algorithm. *Simulation Modelling Practice and Theory*, *25*, 106–117.

Rinaldi, F., Chiesa, S., & Quagliotti, F. (2013). Linear quadratic control for quadrotors UAVs dynamics and formation flight. *Journal of Intelligent and Robotic Systems: Theory and Applications*, *70*(1–4), 203–220.

Serra, P., Cunha, R., Hamel, T., Cabecinhas, D., & Silvestre, C. (2016). Landing of a quadrotor on a moving target using dynamic image-based visual servo control. *IEEE Transactions on Robotics*, *32*(6), 1524–1535.

Shao, X., Liu, J., Cao, H., Shen, C., & Wang, H. (2018). Robust dynamic surface trajectory tracking control for a quadrotor UAV via extended state observer. *International Journal of Robust and Nonlinear Control*, *28*(7), 2700–2719.

Shi, S., Xu, S., Zhang, B., Ma, Q., & Zhang, Z. (2019). Global second-order sliding mode control for nonlinear uncertain systems. *International Journal of Robust and Nonlinear Control*, *29*(1), 224–237.

Shima, T. J., & Bashir, H. A. (2021). Pso-based integral sliding mode controller for optimal swing-up and stabilization of the cart inverted pendulum system. *Nigerian Journal of Technological Development*, *18*(2), 88–97.

Sreenath, K., Giordano, V., & Lewis, F. L. (2005). Avoiding Shared Resource Conflicts in Mobile Sensor Networks. *IFAC Proceedings Volumes (IFAC-PapersOnline)*, *16*(August 2008), 263–268.

Utkin, V. I. (2019). Sliding Modes in Control Optimization. *J. of Chemical Information and Modeling*, 53(9).

Wang, L., & Jia, H. (2014). The trajectory tracking problem of quadrotor UAV: Global stability analysis and control design based on the cascade theory. *Asian Journal of Control*, *16*(2), 574–588.

Wang, R., & Liu, J. (2018). Trajectory tracking control of a 6-DOF quadrotor UAV with input saturation via backstepping. *Journal of the Franklin Institute*, *355*(7), 3288–3309.

Xiong, J. J., & Zhang, G. (2016). Sliding mode control for a quadrotor UAV with parameter uncertainties. *Proceedings - 2016 the 2nd International Conference on Control, Automation and Robotics, ICCAR 2016*, 207–212.

Zhao, D. J., & Yang, D. G. (2016). Model-free control of quad-rotor vehicle via finite-time convergent extended state observer. *International Journal of Control, Automation and Systems*, *14*(1), 242–254.

Zou, Y., & Zhu, B. (2017). Adaptive trajectory tracking controller for quadrotor systems subject to parametric uncertainties. *Journal of the Franklin Institute*, *354*(15), 6724–6746.

Constructing Birth Weight Prediction Model Based on Maternal Determinate in Ethiopia Using Ensemble Machine Learning Algorithm

Gizachew Mulu Setegn*, Abebe Alemu, Belayneh Endalamaw

Department of Computer Science, Debark University, Debark, Ethiopia
**Corresponding author, email: gizachewdku@gmail.com*

ABSTRACT

Birth weight is the first weight of a baby after born and is classified into three groups namely normal birth weight, low birth weight, and macrosomia (high birth weight). Abnormal birth weight is still a double burden problem that is associated with long-term and short-term consequences such as obesity, diabetes, heart disease with fetal and neonatal mortality and morbidity, inhibited growth, cognitive delays, and chronic diseases later in life. This study aims to develop a birth weight prediction model in the case of Ethiopia using homogeneous ensemble machine learning algorithms. This study was conducted following a design science research approach. The dataset was collected from the Ethiopian demographic health survey (EDHS), and preprocessed by applying data cleaning, transformation, and well-prepared to improve its quality for ML tasks and wrapper and filter features selection techniques were conducted. Four different homogenous ensemble classification algorithms such as Random forest, Bagged decision tree, Catboost, and Extra tree was employed to build the predictive model with a training and testing dataset split ratio of 80/20 and a total of 13443 instances with 23 features. This study was implemented using Python 3.7, HTML embedded in anaconda distribution, and Heroku–based cloud computing platform with flask API.The performance of the models was evaluated and compared using the standard metrics; accuracy, precision, recall, F1_score, cross-validation, and the overall accuracy of random forest scored a classification accuracy of 82.2%; cat boost scored a classification accuracy of 80.1%; bagged decision tree scored a classification accuracy of 87.2% and Extra tree scored classification accuracy of 90.7%. The experimental result shows that the extra tree ensemble algorithm registers the best performance with 90.7% accuracy and the researcher decided to use extra tree ensemble algorithms to the rest for further use in the development of artifacts, model deployment, risk factor analysis, and generating rules. The most determinant risk factors of abnormal birth weight were identified using feature importance. Some of them are the mode of delivery, abortion, maternal occupation, maternal anemia during pregnancy, malaria during pregnancy, number of antenatal visits, marital status, and birth order.

Keywords: *Birth Weight, Cloud Computing, Ensemble Learning, Design Science*

1. INTRODUCTION

Health is one of humanity's worldwide problems and the healthcare sector contains different types of information about patients' medical records. Medical data analysis plays a vital role in decision-making and management in healthcare (Senthilkumar & Paulraj, 2015). Birth weight is an important health indicator of maternal and infant that affects the infant's physical, survival, and mental growth. It also indicates the past and present health status of the mothers (Adams & Muenke, 2008). Depending on birth weight (BW), the neonates are grouped into three categories by World Health Organization (WHO) based on specific threshold values, that are normal (birth weight ≥2.5 kg < 4.0 kg), too light (low birth weight (birth weight < 2.5 kg) or macrosomia (birth weight ≥ 4.0 kg). The last two birth weights (low birth weight and macrosomia) are named abnormal birth weight. Abnormal Birth can be defined as structural or functional abnormalities of an infant, including metabolic and psychological disorders, which cause mortality and disability among mothers, infants, and children under five years of age that result in long-term disability, and negatively affect individuals, families, healthcare systems, and societies (Adams & Muenke, 2008). An abnormal birth weight baby is more likely exposed to many health defects and needs special care and facilities than a baby with normal birth weight (Abubakari et al., 2015).

Abnormal birth weight (low birth weight and macrosomia) may cause the current and future burden of chronic diseases for infants (Abubakari et al., 2015). Studies have shown consequences such as high infant mortality and

childhood growth failure as a part of short-term consequences of abnormal birth weight and adult coronary heart disease and type 2 diabetes, obesity, and insulin resistance (Abubakari et al., 2015) considered a long-term risk of abnormal birth weight (Abubakari et al., 2015). In addition, abnormal birth weight is associated with negative maternal and neonatal outcomes, complex deliveries, and obesity epidemics, with related problems during childhood, adolescence (Mengesha et al., 2017), adulthood, and abnormality during delivery and increased risk of several complications, particularly maternal and/or fetal trauma during birth and neonatal hypoglycemia, postpartum hemorrhage, prolonged labor, skeletal injuries, and respiratory problems (Dube Jara, 2014). Being abnormal birth weight is related to fetal and neonatal morbidity and mortality (Dube Jara, 2014; Lake & Olana Fite, 2019). The chance of the infant to outlive, encounter healthy growth, and advancement was highly decided by birth weight (Mehare & Sharew, 2020).

Abnormal birth weight (low birth weight and macrosomia) is still an important public health problem (Mehare & Sharew, 2020). It is a growing problem in most developing countries, such as Ethiopia and it directly or indirectly contributes to morbidity, mortality, and disability in Ethiopia as well as in the world and leads to economic and social burdens to modify the major risk factor of abnormal birth weight. Over 20 million infants in the world are born each year with low birth weights 17% of all births in the developing world, out of which 6% are observed in the developed world and 21% in developing countries (Talie et al., 2019). The level of fetal macrosomia significantly shifts over diverse geographic districts with recurrence extending from 0.5% to 15% in 23 developing nations In Africa, Asia, and Latin America 95.6 percent of them are in developing countries. Globally, "macrosomia affects 3 to 15% of all pregnancies" (Biratu et al., 2018). In the developed world the prevalence of macrosomia is ranging from 5 to 20% of all births (Henriksen, 2008). In Ethiopia, a different study was done in the area of abnormal birth weight from singleton live birth hospital records and EDHS datasets using a different methodology. The incidence of low birth weight was around 10.3 %to 34.1% (Talie et al., 2019) in dangla, with 18% in the Kambata-Tembaro zone to 34.1% Dilla Town, Southern Ethiopia (Mehare & Sharew, 2020), and findings from recent studies have also shown that macrosomia prevalence in Ethiopia ranges from 6.7% to 19.1% (Tiruneh et al., 2020) in a different district within(Mengesha et al., 2017), 7.54% Newborns Delivered in University of Gondar referral hospital (Mengesha et al., 2017) 19.1% in Mekelle city (Tela et al., 2019) 11.86% in Hawassa city (Biratu et al., 2018).

However, previous studies on abnormal birth weight low birth (Biratu et al., 2018; Talie et al., 2019; Biratu et al., 2018; Hassen et al., 2020) and macrosomia (Dube Jara, 2014; Biratu et al., 2018; Shigemi et al., 2018; Ye et al., 2020) were conducted using observational studies like a cohort, case-control, and cross-sectional studies with a very small proportion of the datasets up to 1152 neonates-maternal delivered in select hospitals and limited to a certain region or area. Besides, in those studies, data analysis was conducted by using statistical techniques and the researcher used SPSS for data cleaning, compiling using binary logistic regression to identify the factors associated with abnormal birth weight. Gestational age, gender of the neonate, Sex of the child, previous history of fetal macrosomia, post-maturity, and no maternal complication was significant with fetal macrosomia. As a result, this may underestimate and/or overestimate the prevalence of abnormal birth weight and its risk factor.

Studies (Feng et al., 2019; Karthiga, 2019; Kuhle et al., 2018) also, propose to investigate the use of machine learning-based solutions to improve the prediction of fetal macrosomia from prenatal ultrasound and fetal parameters imaging measurements to identify potential risks before delivery without considering the maternal determinate for abnormal birth weight (macrosomia) and the author unable to assess the maternal determinate for the prevalence of macrosomia. Similarly, the other research works (Senthilkumar & Paulraj, 2015; Dineva & Atanasova, 2020; Demelash et al., 2015; Kumlachew et al., 2018) introduced ensemble machine learning and data mining models on the prediction of low birth weight and its associated risk factor. Studies (Feng et al., 2019; Mengesha et al., 2017; Biratu et al., 2018; Hassen et al., 2020) apply statistical and machine learning techniques to predict birth weight but the disadvantage of using statistical and machine learning algorithm techniques is its

tendency for overfitting, generation of the model with high variation, Logistic regression need long training time, support vector machine achieves poor performance when working with noise data, naive Bayes failure to predict rare events and decision tree need long training time and not easy for result interpretation (Dineva & Atanasova, 2020).

Therefore, the absence of significant attempts that has been done so far in this area in Ethiopia shows the importance of applying homogenous ensemble machine-learning techniques that have the ability to improve the performance of the prediction model by removing variance and bias from the data by designing one optimal predictive and affect infant health and also lack of artifact that predict infant birth weight to reduce the complications before delivery, mortality, and morbidity of infant and mothers and the absence of use the full rule to understand the relationship between the attribute to formulate policy related to abnormal birth weight to reduce risk of abnormal birth weight and Due to the absence of multi-class prediction model and relevant feature that cause abnormal birth (maternal malaria during pregnancy, maternal anemia level, number of children per birth) to develop the model, the previous researcher and created prediction model is incomplete for new unseen data prediction using model prototype and the previous researcher focused on binary class and a limited number of attribute this limitation leads maternal and infant mortality, morbidity of as well as an economic and social burden to modify the major risk factor of abnormal birth weight.

Moreover, most of the available studies in Ethiopia for birth weight were limited to a certain region or area even if the data is available at EDHS about abnormal birth weight (Dineva & Atanasova, 2020; Demelash et al., 2015; Kumlachew et al., 2018. This study, hence, aims to construct a birth weight prediction model based on maternal determinants in Ethiopia using an ensemble machine learning algorithm by investigating the following research questions (1) What are the determinants attributes that influence the presence of abnormal birth weight in Ethiopia? (2) Which homogenous ensemble machine learning technique is more appropriate to construct a model to predict birth weight? (3) What are the associated risk factors that influence the occurrence of abnormal birth weight in Ethiopia? (4) What are the important rules that may shape strategies and policies toward preventing and/or reducing abnormal birth weight in Ethiopia? (5) To what extent does the design artifact and deployed model predict birth weight?

2. MATERIALS AND METHODS

2.1 Data Collection

In this study, secondary data sources from Ethiopian Demographic Health Survey (EDHS) that were analyzed by quantitative methods at a central statistical agency and collected in 2005, 2011 and 2016 were used.

2.2 Data Preprocessing

The extracted datasets from EDHS consist of a total of 13443 instances. with 32 features. all these features are not relevant for constructing a predictive model that can predict birth weight in Ethiopia, data preprocessing methods such as data profiling, data cleaning, data transformation, and feature selection methods were applied. The missing values were handled using the mode imputation for ordinal variables and the modal value for nominal variables. Redundant data were removed manually. Data normalization was applied to make the analysis process manageable and cost-efficient for the feature that contains different values like continuous and categorical values in the dataset; such as birth weight, body mass index, wealth index, marital status, occupation, preterm, number of tetanus injections, and number of living children were transformed into discrete values using data smoothing technique (binning discretization technique). Then, feature selection methods were applied to select the relevant features to construct the birth weight prediction model. In this study, two types of feature selection methods (wrapper and filter) were applied to get an important feature. As a result, the forward feature selection method registered the highest performance of 83.9% accuracy using RandomForestClassifier (Table 1).

Table 1: Feature selection results

No	Mutual information feature selection	Chi^2 feature selection	F classifcation feature selection	Step forward feature selection	Step backward feature selection
0	Region	Region	Age in 5-year groups	Age in 5-year groups	Age in 5-year groups
1	Educational level	Type of place of residence	Region	Region	Region
2	Religion	Educational level	Type of place of residence	Number of visits	Type of place of residence
3	Frequency of reading newspapers or magazine	Religion	Educational level	Educational level	Frequency of reading newspaper or magazine
4	Birth order number	No of household members	Religion	Religion	Educational level
5	Sex of child	Frequency of reading newspaper or magazine	No of household members	No of household members	Religion
6	Number of living children	Birth order number	Frequency of reading newspaper or magazine	No of household members	No of household members
7	Ever had a terminated pregnancy	Child is twin	Birth order number	Birth order number	Frequency of reading newspaper or magazine
8	Type of cooking fuel	Sex of child	Child is twin	Child is twin	Birth order number
9	Body mass index	No of living children	Sex of child	Sex of child	Sex of child
10	Anemia level	Anemia level	No of living children	No of tetanus injections before birth	No of living children
11	Fever/cough: government hospital	Body mass index	Anemia level	Ever had a terminated pregnancy	No of tetanus injections before birth
12	Gestational age < 37	Type of cooking fuel	Source of drinking water	Delivery by cesarean section	Type of cooking fuel
13	Iodine intake	Alcoholic drink	Ever took an alcoholic drink	Anemia level	Current marital status
Accuracy	70%	71%	79%	83.90%	69%

We also include recommended additional nine features by domain experts (antenatal care professionals in the University of Gondar specialized hospital). Such as place of residence, iodine intake, wealth index, current marital status, respondent occupation, body mass index, preterm, cigarette smoking, and during pregnancy took fansidar for malaria[38] are not included in the feature selection techniques.

2.3 Prediction Model

To construct a multi-class birth weight prediction model in Ethiopia, we applied and test the chosen ensemble algorithms (Random forest, bagged decision tree, extra tree, and cat boost), to predict birth weight and find the best between them to develop artifacts and deploy the model. To build a predictive model, 13443 instances and 23 features selected by the forward feature selection method and domain experts are used. To evaluate the performance of the model; the performance of each predictive model was evaluated using accuracy, precision, recall, F1- score, K-fold cross-validation, and ROCAUC were used due to its relatively low bias and variations. This means the data are randomly partitioned equally into ten parts.

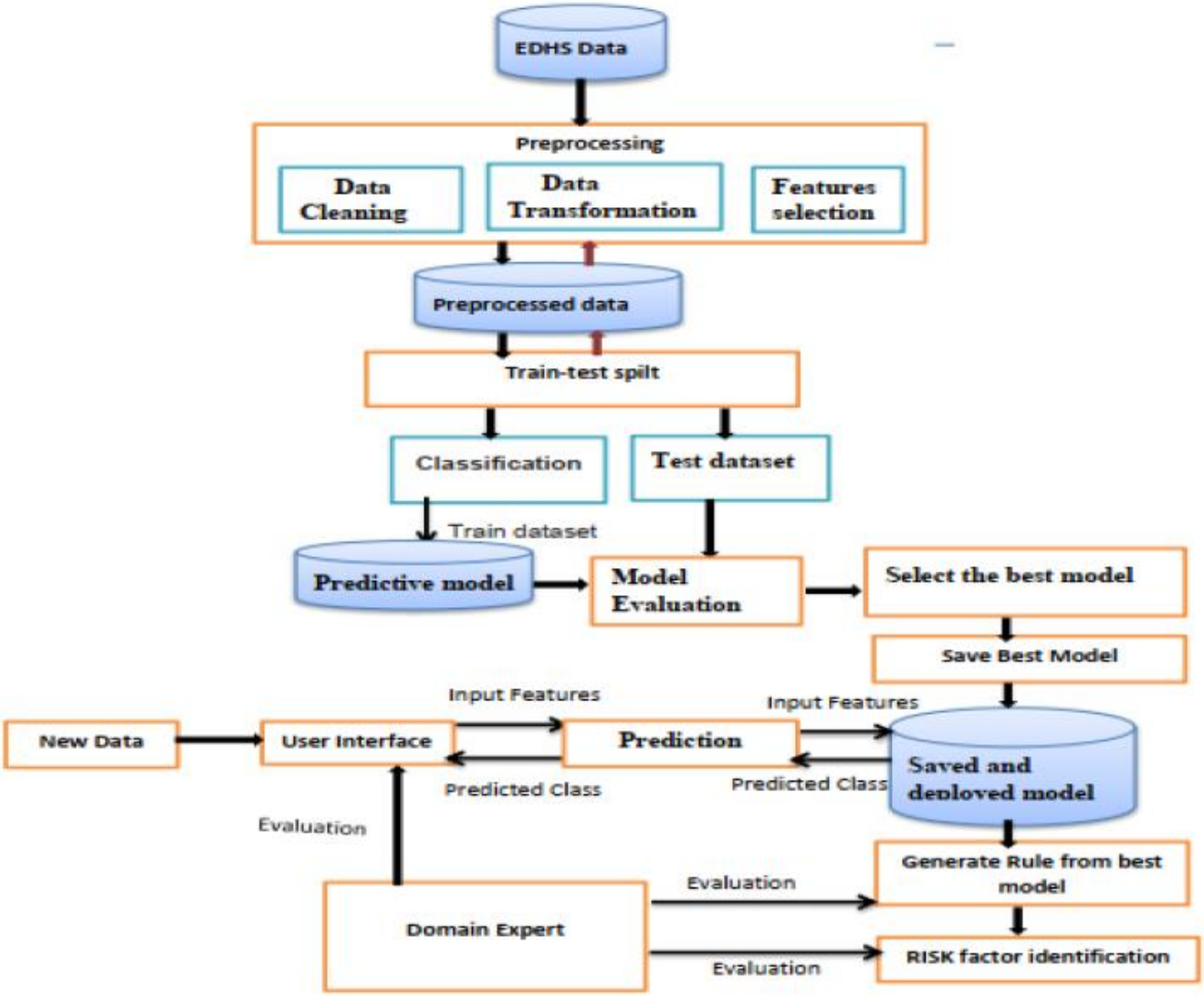

Figure 1: The overall process and proposed model architecture

3. RESULTS AND DISCUSSION

3.1 Determinant factors to Presence of Abnormal Newborn Birth Weight in Ethiopia

To answer this question related to this section, logistic regression techniques with p-values and domain expert evaluation were used.

Table 2: Risk Factor for Low Birth Weight Using P-Values

Feature	Coefficient	2.50%	97.50%	OR	p-value
v013	0.030143366	0.926084	1.0166409	0.970306	0.236
v024	0.032557491	0.953586	0.9825642	0.967967	0.969
v025	0.332157673	1.253167	1.5505989	1.393973	0.897
v027	0.075529284	0.876342	0.9811209	0.927253	0.160
v106	0.196872325	0.775996	0.8692397	0.821295	0.000
v130	0.139539273	1.111053	1.1897819	1.149744	0.064
v136	0.006740892	0.952478	1.0641437	1.006764	0.791
v157	0.106220599	0.830712	0.9733914	0.899226	0.000
bord	0.088533679	1.049993	1.1368752	1.092571	0.027
b0	0.782690717	0.303777	0.6880319	0.457174	0.000
b4	0.363682606	0.637877	0.7574823	0.695112	0.000
v228	0.037720011	0.901176	1.1966130	1.038440	0.018
m1	0.002732387	0.965759	1.0411286	1.002736	0.252
m17	0.376806273	1.279306	1.6607923	1.457622	0.007
m49a	0.513951487	1.035265	2.6999825	1.671885	0.017
hw57	0.204289123	0.733844	0.9056344	0.815227	0.000
v463a	0.774514163	1.228165	3.8324608	2.169538	0.389
v501	0.098621315	1.037524	1.1739868	1.103648	0.258
v716	0.656925653	0.305752	0.8790878	0.518443	0.018
v445	0.043212467	0.957239	1.1389735	1.04416	0.409
v223	0.039651176	0.623947	1.4805106	0.961125	0.484
v166	0.000207833	0.994482	1.0059669	1.000208	0.686
v190	0.028974279	0.927071	1.0179352	0.971441	0.213

Table 3: Risk Factor for Macrosomia Using P-Values

Feature	Coefficient	2.50%	97.50%	OR	p-value
v013	-0.03014	0.926084	1.016641	0.970306	0.205
v024	-0.03256	0.953586	0.982564	0.967967	0.000
v025	0.332158	1.253167	1.550599	1.393973	0.000
v027	-0.07553	0.876342	0.981121	0.927253	0.009
v106	-0.19687	0.775996	0.86924	0.821295	0.000
v130	0.139539	1.111053	1.189782	1.149744	0.000
v136	0.006741	0.952478	1.064144	1.006764	0.812
v157	-0.10622	0.830712	0.973391	0.899226	0.009
bord	0.088534	1.049993	1.136875	1.092571	0.000
b0	-0.78269	0.303777	0.688032	0.457174	0.000
b4	-0.36368	0.637877	0.757482	0.695112	0.000
v228	0.037720	0.901176	1.196613	1.038440	0.602
m1	0.002732	0.965759	1.041129	1.002736	0.887
m17	0.376806	1.279306	1.660792	1.457622	0.000
m49a	0.513951	1.035265	2.699982	1.671885	0.036
hw57	-0.20429	0.733844	0.905634	0.815227	0.000
v463a	0.774514	1.228165	3.832461	2.169538	0.008
v501	0.098621	1.037524	1.173987	1.103648	0.002
v716	-0.656930	0.305752	0.879088	0.518443	0.015
v445	0.043212	0.957239	1.138973	1.04416	0.330
v223	-0.039650	0.623947	1.480511	0.961125	0.857

Feature	Coefficient	2.50%	97.50%	OR	p-value
v166	0.000208	0.994482	1.005967	1.000208	0.943
v190	-0.02897	0.927071	1.017935	0.971441	0.224

As a result, the most determinate risk factors that cause low birth weight are birth order, abortion, mode of delivery, and unique factors that cause macrosomia are antenatal visits during pregnancy, frequency of reading newspapers, smoking cigarettes, and marital status. As the result of the logistic regression risk factor that causes both low and macrosomia are maternal malaria during pregnancy and maternal occupation was the most determinate risk factor for abnormal birth weight.

3.2 Appropriate Homogenous Ensemble Machine Learning Techniques: Birth Weight Prediction Model

To answer the related question, four experiments for four predictive models involving Random Forest, Bagging, Extra Tree, and cat boost classifier algorithms are constructed in all attributes using 80% train and 20% test dataset with default parameters of the algorithm. The experiments showed that the Extra tree is the best classification algorithm to develop the multi-class prediction model that can predict the type of newborn birth weight because it registers better performance with 90.7% and 76% of objective and subjective evaluation respectively. The researcher decided to use Extra Tree for further use in the development of artifacts and deployment of the model using flask API with the Heroku platform and the generation of useful rules for policymakers.

Table 4: Model performance

Ensemble algorithm	Target class	Correctly classified	Evaluation metrics	Incorrectly classified	Error rate (%)
Random forest	Low birth weight	394	Accuracy = 82.2% Precision = 80%	112	17.8
	Normal weight	1309	Recall= 79.9% F1_score = 79.9%	193	
	Macrosomia	510	Cross validation = 87.4% ROC = 97.7%	171	
Extra tree	Low birth weight	430	Accuracy = 90.7% Precision = 90.8%	76	9.3
	Normal weight	1432	Recall = 79.9% F1_score = 79.9%	70	
	Macrosomia	577	Cross validation = 87.4% ROC = 97.7%	104	
Bagged decision tree	Low birth weight	377	Accuracy = 87.2% Precision = 88.9%	129	12.8
	Normal weight	1440	Recall = 88.3% F1_score = 89.5%	62	
	Macrosomia	529	Cross validation = 94.7% ROC = 99.8%	152	
Catboost	Low birth weight	307	Accuracy = 80.1% Precision = 82.2%	199	19.1
	Normal weight	1424	Recall = 72.6% F1_score = 75.9%	78	
	Macrosomia	425	Cross validation = 84.3% ROC = 99.2%	256	

3.3 Rules to Shape Strategies and Policies to Prevent and/or Reduce Abnormal Birth Weight

Here, we used all the features that we used to develop the predictive model to investigate the interaction between the relevant feature to generate interesting and useful prediction rules using the Extra tree ensemble algorithm to know the presence of abnormal birth weight in Ethiopia. The most important rules that were also validated by domain experts are:

1) If region is "Addis Ababa", reading newspaper is "Not at all", a child is a twin "Single", education level is "Primary ", birth order is "one", the number of tetanus injections during pregnancy is "two", marital status is "Married", age is "25-29, religion is " orthodox " "less than once a week ", body mass index is "normal weight", number of households is "1-3", sex of the child is "female" then low birth weight baby will be born.
2) If region is "Addis Ababa", reading newspaper is "Not at all", a child is a twin "Single", education level is "Primary ", birth order is "one", the number of tetanus injections during pregnancy is "two", marital status is "Married", age is "25-29, religion is " orthodox " "less than once a week ", body mass index is "normal weight", the number of households is "1-3", sex of a child is "male", maternal Anemia during pregnancy is "no anemia" then normal birth weight baby will be born. C. If region is "Dire Dawa", education level is "Primary ", antenatal visits during pregnancy is "one", the number of households is "4-6", age is "25-29", the number of tetanus injections during pregnancy is "two, birth order is "two", maternal wealth index is "Poor", sex of a child is "Female", maternal Anemia during pregnancy is "no", iodine intake is "no salt", then the macrosomic baby will be born.

3.4 Birth Weight Predicting Extent of the Design Artifact and Deployed Model

For this, the predictive model was deployed on the cloud for potential users. The artifact was designed using the Extra Tree ensemble model and Flask web application framework with HTML and deployed on Heroku. All potential users can access (https://birthprediction.herokuapp.com/) the developed artifact validated by the domain expert that predicts birth weight and the designed artifact and deployed model achieves 76% accuracy at subjective evaluation by the domain expert.

4. CONCLUSION

According to the WHO birth weight (normal, low birth weight, and macrosomia) are strong predictors of maternal and neonatal health and development. Abnormal birth weight (low birth weight and macrosomia) is the main factor that causes the current and future problem of chronic diseases and Complications during delivery that leads to risk factors for neonatal morbidity and mortality. According to World Health Organization (WHO), abnormal birth weight is defined as weight at birth less than 2,500 grams as low birth weight and birth weight greater than 4000g as high birth weight (macrosomia). This study was conducted using design science methodology. The proposed model was constructed using homogeneous ensemble machine learning algorithms namely random forest scored a classification accuracy of 82.2%; cat boost scored a classification accuracy of 80.1%; bagged decision tree scored a classification accuracy of 87.2% and Extra tree scored a classification accuracy of 90.7%. The evaluation result shows the proposed extra tree model provides effective classification with 23 relevant features. After building a multi-class prediction model for birth weight, we identify the most associated risk factor for abnormal birth weight using logistic regression and extracted important rules using the best-performed ensemble algorithm (extra tree). The result of the extra tree with the ID3 model reveals so many interesting rules and the rules that were generated show different risk factors for abnormal birth weight in Ethiopia design artifact and deploy the model to reuse the extra tree classification algorithm and graphical user interface was designed using the selected model Finally, we recommend that future researchers conduct a predictive model that includes maternal determinate like chronic disease and genetic factors to predict birth weight in addition to socio-

demographic factors, Identifying the most determinant risk factors using fetal parameters with Sociodemographic factors using ensemble machine learning techniques.

ACKNOWLEDGMENTS

We would like to acknowledge the Ethiopian central statistics for providing us with the data with its description.

REFERENCES

Abubakari, A., Kynast-Wolf, G., & Jahn, A. (2015). Prevalence of abnormal birth weight and related factors in Northern region, Ghana. *BMC Pregnancy and Childbirth*, *15*(1), 1–8.

Access, O. (2019). *Low birth weight: prevalence and associated factors among newborns at hospitals in Kambata-Tembaro zone, southern Ethiopia 2018*. *8688*, 1–8.

Adams, D., & Muenke, M. (2008). Birth Defects. *Encyclopedia of Infant and Early Childhood Development*, *1–3*, 192–203.

Biratu, A. K., Wakgari, N., & Jikamo, B. (2018). Magnitude of fetal macrosomia and its associated factors at public health institutions of Hawassa city , southern Ethiopia. *BMC Research Notes*, *December*.

Demelash, H., Motbainor, A., Nigatu, D., Gashaw, K., & Melese, A. (2015). Risk factors for low birth weight in Bale zone hospitals , South-East Ethiopia : a case – control study. *BMC Pregnancy and Childbirth*, 1–10.

Dineva, K., & Atanasova, T. (2020). Systematic look at machine learning algorithms - Advantages, disadvantages and practical applications. *International Multidisciplinary Scientific GeoConference Surveying Geology and Mining Ecology Management, SGEM*, *2020-August*(2.1), 317–324.

Dube Jara, T. W. (2014). Factors Associated with Macrosomia among Neonates Delivered at Debre Markos Referral Hospital, Northwest Ethiopia, 2014: A Case Control Study. *Journal of Diabetes & Metabolism*, *5*(12).

Feng, M., Wan, L., Li, Z., Qing, L., & Qi, X. (2019). Fetal Weight Estimation via Ultrasound Using Machine Learning. *IEEE Access*, *7*, 87783–87791.

Hassen, H. Y., Gebreyesus, S. H., Endris, B. S., & Roro, M. A. (2020). *Development and Validation of a Risk Score to Predict Low Birthweight Using Characteristics of the Mother : Analysis from BUNMAP Cohort in Ethiopia*. *Lmic*.

Henriksen, T. (2008). The macrosomic fetus: A challenge in current obstetrics. *Acta Obstetricia et Gynecologica Scandinavica*, *87*(2), 134–145.

Karthiga, S. (2019). *Machine Learning Model to Predict Birth Weight of New Born using Tensorflow*. 71–90.

Kuhle, S., Maguire, B., Zhang, H., Hamilton, D., Allen, A. C., Joseph, K. S., & Allen, V. M. (2018). Comparison of logistic regression with machine learning methods for the prediction of fetal growth abnormalities: A retrospective cohort study. *BMC Pregnancy and Childbirth*, *18*(1), 1–10.

Kumlachew, W., Tezera, N., & Endalamaw, A. (2018). Below normal birth weight in the Northwest part of Ethiopia. *BMC Research Notes*, *11*(1), 1–7.

Lake, E. A., & Olana Fite, R. (2019). Low Birth Weight and Its Associated Factors among Newborns Delivered at Wolaita Sodo University Teaching and Referral Hospital, Southern Ethiopia, 2018. *International J. of Pediatrics*, *2019*, 1–7.

Mehare, T., & Sharew, Y. (2020). Prevalence and Associated Factors of Low Birth Weight among Term Newborns in Dilla Town, Southern Ethiopia. *International Journal of Pediatrics*, *2020*, 1–7.

Mengesha, H. G., Wuneh, A. D., Weldearegawi, B., & Selvakumar, D. L. (2017). Low birth weight and macrosomia in Tigray, Northern Ethiopia: Who are the mothers at risk? *BMC Pediatrics*, *17*(1), 1–9.

Senthilkumar, D; Paulraj, S. (2015). Prediction of Low Birth Weight Infants and Its Risk Factors Using Data Mining Techniques. *Proceedings of the 2015 International Conference on Industrial Engineering and Operations Management Dubai, United Arab Emirates (UAE)*, *3*, 186–194.

Shigemi D., Yamaguchi S., Aso S., Yasunaga H. (2019). Predictive model for macrosomia using maternal parameters without sonography information. The Journal of Maternal-Fetal & Neonatal Medicine, 32(22), 3859–3863.

Talie, A., Taddele, M., & Alemayehu, M. (2019). Magnitude of Low Birth Weight and Associated Factors among Newborns Delivered in Dangla Primary Hospital, Amhara Regional State, Northwest Ethiopia, 2017. *Journal of Pregnancy*, *2019*.

Tela, F. G., Bezabih, A. M., Adhanu, A. K., & Tekola, K. B. (2019). Correction: Fetal macrosomia and its associated factors among singleton live-births in private clinics in Mekelle city, Tigray, Ethiopia (BMC Pregnancy and Childbirth (2019) 19 (219). *BMC Pregnancy and Childbirth*, *19*(1), 1–6.

Tiruneh, T., Shiferaw, E., & Enawgaw, B. (2020). Prevalence and associated factors of anemia among full-term newborn babies at University of Gondar comprehensive specialized hospital, Northwest Ethiopia: A cross-sectional study. *Italian Journal of Pediatrics*, *46*(1).

Yadav, S. S., & Jadhav, S. M. (2019). Machine learning algorithms for disease prediction using Iot environment. *International Journal of Engineering and Advanced Technology*, *8*(6), 4303–4307.

Ye, S., Zhang, H., Shi, F., Guo, J., Wang, S., & Zhang, B. (2020). Ensemble Learning to Improve the Prediction of Fetal Macrosomia and Large-for-Gestational Age. *Journal of Clinical Medicine*, *9*(2), 380.

Optimization of Pressure Vessel Design Problem Using Four Metaheuristic Optimization Techniques: a Comparative Study

Getaw Ayay*, Ashenafi Abuye, Fasikaw Kibrete, Lemmi Girma, Dereje Engda

Mechanical Engineering Deparment, Addis Ababa Science and Technology University, Addis Ababa, Ethiopia
**Corresponding author, email: getaw.ayay@aastustudent.edu.et*

ABSTRACT

Many engineering optimization problems have nonlinear objective problems with intense equality and inequality constraints and various decision variables. Different conventional deterministic optimization methods have been developed and adopted to search for optimal solutions to such engineering problems. However, conventional optimization methods have limitations for solving high-dimensional, multi-modal and highly constrained engineering optimization problems. As an alternative way, metaheuristic algorithms are preferred to find an optimal solution for such optimization problems by trial and error in an acceptable computational time. Metaheuristic algorithms are suitable tools to determine the optimum solutions to engineering optimization problems due to their efficiency, reliability and relatively low computing time. In this work, a comparative study of harmony search, cuckoo search, firefly and particle swarm optimization algorithms are performed on a pressure vessel design optimization problem. This study's result indicates that the cuckoo search algorithm outperforms with 0.096% below the average cost of the pressure vessel. Therefore, it is recommended to make pressure vessel design optimization using cuckoo search algorithms.

Keywords: *cuckoo search, firefly, harmony search, metaheuristic algorithm, particle swarm optimization, pressure vessel design*

1. INTRODUCTION

Many engineering optimization problems have nonlinear objective problems with intense equality and inequality constraints along with various decision variables. Various conventional deterministic optimization methods have been developed and adopted to search for the optimal solutions of such engineering problems. However, conventional optimization methods have limitations for solving high-dimensional, multi-modal and highly constrained engineering optimization problems. As an alternation way, heuristic algorithms are preferred to find an optimal solution for such optimization problems by trial and error in an acceptable computational time [1].

Metaheuristic optimization algorithms, also called approximation optimization algorithms, are high-level heuristic algorithms used to solve difficult and complex optimization problems [2]. Metaheuristic algorithms are stochastic search process inspired by the nature that intelligently carry out the diversification (exploration) and exploitation in the solution space aiming to find near optimal solutions [3]. Metaheuristic algorithms differ from deterministic methods in the following three aspects: using a population of individuals in the search domain, using the direct fitness information instead of function derivatives and other related knowledge, and using probabilistic rather than deterministic rules. Flexible and easily applicable structure of these algorithms has made them very popular in recent years [4]. Many metaheuristic algorithms have been developed in the literature. Some of the well-known techniques are Simulated Annealing, Bee Algorithms, Ant Colony Optimization, Firefly Algorithms, Genetic Algorithm, Particle Swarm Optimization, Cuckoo Search Algorithm, Harmony Search Algorithm, and many more [5]. These methods do not require the derivatives of the objective function and constraints. Having in common processes of natural evolution, these algorithms share many similarities: each maintains a population of solutions which are evolved through random alterations and selection. The differences between these procedures lie in the representation technique utilized to encode the candidates, the type of alterations used to create new solutions, and the mechanism employed for selecting new patterns.

In this study, four metaheuristic optimization algorithms, namely, cuckoo search algorithm, firefly algorithm, harmony search algorithm and particle swarm optimization are used to solve the pressure vessel design optimization problem for the purpose of comparison.

2. MATERIAL AND METHODS

The pressure vessel design problem is one of a standard optimization problem in mechanical engineering design optimization. It has been optimized since 1988 using different optimization techniques. The optimization of pressure vessel design problem has two parts. The first part is optimum design problem formulation which has problem description, data and information collection, definition of design variables, optimization criterion, and formulation of constraints. The second part is metaheuristic algorithms which are used to search the optimum design variables. Four metaheuristic algorithms (cuckoo search, firefly, harmony search and particle swarm optimization) are adopted and redesigned. The algorithms were carried out using MATLAB and PYTHON software in the design optimization processes of the pressure vessel problem.

2.1 Problem Formulation of Pressure Vessel Design Optimization Problem

The pressure vessel design optimization problem has been published by different authors since 1988. The problem is well described by Sandgren in 1988 [6]. The pressure vessel is made of carbon steel ASME SA203 grade B. The given information are the length of the shell to be no longer than 20 feet, the working pressure of the vessel is 3,000 psi, a minimum volume of 750 $feet^3$, the thickness of the shell and head is not to be less than and exceed 1.1 and 2, and 0.6 and 2 inches, respectively. Minimizing the total manufacturing cost is the objective of the design for the pressure vessel.

The total cost of the pressure vessel is written as follows which is taken from [6];

$$\min f(x) = 0.6224x_1x_3x_4 + 1.7781x_2{x_3}^2 + 3.1611{x_1}^2x_4 + 19.8621{x_1}^2x_3$$

The design variables are thickness of shell x_1, thickness of head x_2, radius x_3 and length x_4 of pressure vessel. The above function is subjected to the following constraints [6];

$$g_1(x) = 0.0193x_3 - x_1 \leq 0$$

$$g_2(x) = 0.00954x_3 - x_2 \leq 0$$

$$g_3(x) = 1296000 - \pi{x_3}^2x_4 - \frac{4\pi}{3}{x_3}^3 \leq 0$$

$$g_4(x) = x_4 - 240 \leq 0$$

The lower and upper bound of the design variables redefined from the given information;

$1.1 \leq x_1 \leq 2;\ 0.6 \leq x_2 \leq 2;\ 62.9 \leq x_3 \leq 103.6;\ \ 0 \leq x_4 \leq 240$

2.2 Metaheuristic Algorithms

Four nature inspired metaheuristic algorithms are adopted and designed for the optimization of the pressure vessel design problem. Their basic nature inspiring behavior and pseudocodes are discussed as follows.

2.2.1 Harmony Search Algorithm

Harmony Search Algorithm (HSA) is a new population-based metaheuristic algorithm inspired from the musical process of searching for a best harmony with repeated trails considering their experience [5]. HSA was first developed by Zong Woo Geem in 2001 [7]. Harmony search is a music-based metaheuristic optimization

algorithm. In HS algorithm, the optimality in an optimization process is analogous to the harmony in musician's improvisations. In the basic HS algorithm, each musician (= decision variable) plays (= generates) a note (= a value) for finding a best harmony (= global optimum) all together. The HS algorithm is capable of solving continuous variable problems and combinatorial problems [8].

According to [9], the standard HS algorithm considers five main control parameters. These are the harmony memory size (HMS), the harmony memory consideration rate (HMCR), the pitch adjustment rate (PAR), the band width (BW), and the number of improvisation (NI). HMS is the total number of harmonies stored in the harmony memory (HM). HMCR indicates the balancing between the value of exploration and exploitation, which varies between 0 and 1. If HMCR is too small, only few best harmonies are selected and it may cause slower convergence. If this rate is close to 1, almost all the harmonies are used in the harmony memory, and then other harmonies are not explored well. This can lead to potentially wrong solutions. Therefore, HMCR is taken between [0.7, 0.95] to prevent this problem [8]. The PAR is a parameter which determines the requirements for further adjustment according to BW parameters, which varies between 0 and 1. A small PAR can slow the convergence time of HS, whereas a high PAR can act as a random search process. Therefore, PAR is taken in the range [0.1, 0.5] [10]. The termination criterion is the maximum NI. These parameters are responsible for exploration and exploitation.

The general procedure of harmony search algorithm for optimization are as follows [2][7][11]:

Step 1: Initialize a Harmony Memory (HM). These parameters are the harmony memory size (HMS), the harmony memory considering rate (HMCR), the pitch adjusting rate (PAR) and the maximum the number of improvisations (NI).

Step 2. Improvise a new harmony from the HM. Improvise a new harmony from the HM based on HMCR, PAR, and randomization.

Step 3. Update the harmony memory. If the new harmony is better than the worst harmony in the HM, the new harmony is saved to in the HM and the existing worst harmony is discarded.

Step 4. Terminating criterion controlling. Repeat Steps 2 and 3 until a certain stopping criterion (maximum number of iterations) is satisfied. When the stopping criterion is satisfied, the algorithm is terminated.

The pseudocode of the Harmony Search Algorithm is provided in Table 1.

Table 1: Pseudocode of HS Algorithm

Algorithm 1: Pseudo code of the Harmony Search algorithm (HSA)

Begin;
Define objective function $f(x)$, $x=(x1, x2, \ldots, xd)^T$
Define Harmony Memory Considering rate (HMCR)
Define Pitch adjusting rate (PAR) and other parameters
Generate Harmony Memory with random harmonies
while (t<max number of iterations)
  while (i<=number of variables)
    if *(rand*<HMCR*),*
      Choose a value from HM for the variable i
        if *(rand*<PAR*),*
          Adjust the value by adding certain amount
        end if
      else
        Choose a random value
      end if
    end while
    Accept the New Harmony (solution) if better
  end while
  Find the current best solution
End

HS algorithm is easy to implement, discover the optimal solution potential solution rapidly and finds a good enough solution in a reasonable amount of computational time [11]. However, the local search ability of the standard HS algorithm is weak. To mitigate this deficiency, the various variants of HAS have been developed in last few years. For instance, Ref. [12] developed an improved adaptive harmony search (IAHS) algorithm whose parameters are adjusted adaptively, and proposed model has the favorable abilities of accuracy and escaping local minimums. Zhou et al. [13] proposed the selective acceptance novel global harmony search (SANGHS) algorithm which combines the novel global harmony search (NGHS) algorithm with a selective acceptance mechanism.

2.2.2 Cuckoo Search Algorithm

Cuckoo search (CS) is one amongst the most recent nature-inspired metaheuristics that is developed in 2009 by Xin-She [14]. CS relies on the brood parasitism of cuckoo species which is enhanced by Lévy flights. Recent studies show that CS is potentially much more efficient than PSO, genetic algorithms, and other algorithms [15].

There are three idealized rules used to simplify the description of the standard Cuckoo Search. These are each cuckoo lays one egg at a time, and dumps it in a randomly chosen nest, the best nests with high-quality eggs will be carried over to the next generations and the number of available host nests is fixed, and the egg laid by a cuckoo is

discovered by the host bird with a probability Pa∈(0,1). In this case, the host bird can either get rid of the egg, or simply abandon the nest and build a completely new nest [16].

There is no difference among eggs, cuckoos, and nests i.e., "egg = cuckoo = nest" [15]. The egg laying strategy by Cuckoo and protection mechanism by the host species are two different mechanisms to modify the solutions. The egg laying strategy by Cuckoo is determined by their vector difference ($\mathbf{x}_j - \mathbf{x}k$) at time t which is [15];

$$\mathbf{x_i^{t+1}} = \mathbf{x_i^t} + \alpha s \otimes H(Pa - \epsilon) \otimes (\mathbf{x_j^t} - \mathbf{x_k^t})$$

Wherex_j^t and x_k^t are two different solution vectors, randomly selected from the population for i = 1, 2, ..., n, Pa∈ [0,1] is probability of discovery of a cuckoo's egg, s is a step size with the random permutation of solution differences, α is scaled by a scaling factor and ⊗ is entry-wise multiplications [15] and $\alpha > 0$ is the step size scaling factor [16].

The protection mechanism is to avoid egg contamination by the host species by flying far away to make a nest. This is determined by a global random walk using Lévy flights [15].

$$\mathbf{x_i^{t+1}} = \mathbf{x_i^t} + \alpha L(s - \beta)$$

The Lévy probability distribution $L(s - \beta)$ can be determined using the power-law distribution with an exponent $0 \leq \beta \leq 2$.

$$L(s - \beta) \sim \frac{\beta \Gamma(\beta) \sin\left(\pi\beta/2\right)}{\pi} * \frac{1}{s^{1+\beta}}$$

The value of gamma function is determined by;

$$\Gamma(\beta) = \int_0^\infty z^{q-1} e^u \, du$$

Mantegna's algorithm is used to determine Lévy flights [15]. The step size s can be analyzed in Mantegna's algorithm by two Gaussian distributions U and V via the following equations [15].

$$s = \frac{U}{|V|^{1/\beta}}$$

where $U \sim N(0, \sigma^2)$ and $V \sim N(0,1)$

$U \sim (0, \sigma^2)$ is the samples are made from a Gaussian normal distribution with a zero mean and a variance of σ^2. The variance can be calculated by [15];

$$\sigma^2 = \left[\frac{\Gamma(1+\beta)}{\beta\Gamma((1+\beta)/2)} * \frac{\sin(\pi\beta/2)}{2^{(\beta-1)/2}}\right]^{1/\beta}$$

The number of host nests (or the population size n) and the probability Pa have used n = 5, 10, 15, 20, 30, 40, 50, 100, 150, 250, 500 and pa = 0, 0.01, 0.05, 0.1, 0.15, 0.2, 0.25, 0.3, 0.4, 0.5. The sufficient values of n, Pa, β and α are 15 to 40, 0.25, 1.5 and 0.01 respectively for most optimization problems [15].

Table 2: Pseudocode of Cuckoo Search via Lévy Flights Algorithm [15].

Objective function $f(x)$, $x = (x_1, \ldots, x_d)^T$
Generate initial population of n host nests x_i
while (t<MaxGeneration) or (stop criteria)
Get a cuckoo randomly
Generate a solution by Levy flights
Evaluate its solution quality or objective value f_i
Choose a nest among n (say, j) randomly
if $f_i < f_j$,
Replace j by the new solution i
end
A fraction (P_a) of worse nests ae abandoned
New nests/solutions are built/generated
Keep best solutions (o nests with quality solutions)
Rank the solutions and find the current best
Update $t \leftarrow t + 1$
end while
Postprocess results and visualization

Cuckoo Search code can be split into seven parts for simplicity which are the objective function, simple bounds, selection of solution, Lévy flights, the main loop, initial population and initialization [15]. The number of iterations, number of nests (or different solutions) n and discovery rate of alien eggs/solutions pa are 2000, 25 and 0.25, respectively.

2.2.3 Firefly Algorithm

The firefly algorithm (FA) is a nature-inspired metaheuristic optimization algorithm developed by Xin-She Yang at Cambridge University in 2007 that is inspired by the flashing behavior of fireflies [17][18]. The flashing light of fireflies is an amazing sight in the summer sky in the tropical and temperate regions. There are about two thousand firefly species, and most fireflies produce short and rhythmic flashes. The pattern of flashes is often unique for a particular species. The flashing light is produced by a process of bioluminescence, and the true functions of such signaling systems are still debated. However, two fundamental functions of such flashes are to attract mating partners (communication) and to attract potential prey [19]. It originally designed to solve can be applied for solving the hardest optimization problems [20].

In the FA, there are two important issues: the variation of light intensity and formulation of the attractiveness. For simplicity, it can always assume that the attractiveness of a firefly is determined by its brightness or light intensity which in turn is associated with the encoded objective function [21]. Three rules are used to model fireflies' behavior and govern the algorithm.

The light intensity of a firefly is affected or determined by the landscape of the fitness function.

1) All fireflies are unisex so that one firefly will be attracted to other fireflies regardless of their sex;
2) Their attractiveness is proportional to their brightness, thus for any two flashing fireflies, the less bright one will move towards the brighter one. The attractiveness is proportional to the brightness and they both decrease as their distance increases. If there is no brighter one than a particular firefly, it will move randomly; and

3) The brightness of a firefly is affected or determined by the landscape of the objective function. For a maximization problem, the brightness can simply be proportional to the value of the objective function. Other forms of brightness can be defined in a similar way to the fitness function in genetic algorithms [22].

The pseudocode of the Firefly Algorithm is provided in Table 3.

Table 3: Pseudocode of Firefly Algorithm

Algorithm 3: Pseudo code of the Firefly Algorithm (FA)

Begin;
Objective function $f(X)$, $X = (x1, \ldots, xd)^T$
Initialize population on fireflies x_i $(i = 1,2, \ldots, n)$
Define the light absorption coefficient γ
While (t < MaxGeneration)
for i = 1 : n all n fireflies
  for j = 1 : n (all n fireflies)
    Light intensity I_i) at x_i is determined by $f(x_i)$
    if ($I_j > I_i$)
    Move firefly i towards j in all d dimensions
    end if
    Attractiveness varies with distance r via $exp(-\gamma r)$
    Evaluate the new solution and update light intensity
  end for j
end for i
Rank the fireflies and find the current global best
End while
Post-process of results and visualization

2.2.4 Particle Swarm Algorithm

Particle swarm optimization originated by Dr. Kennedy and Eberhart in 1995. Particle swarm optimization is one of the metaheuristic types of optimization created from flocks of birds or fish flocks [23][24]. The group of birds was considered as they randomly distributed to search for food somewhere. From those flock of birds, one bird moves in the shortest distance to get food, other birds flock towards the piece of food. As such, the piece of food is considered as the optimal value while each bird is taken as a particle. Therefore, the birds' flocking behavior can be express follows:

For velocity case : $V_{i,j}^{k+1} = V_{i,j}^{k} + c_1 r_1 (x_{lbest\ i,j}^{k} - x_{i,j}^{k}) + c_2 r_2 (x_{gbest\ j}^{k} - x_{i,j}^{k})$

For position case: $X_{i,j}^{k+1} = X_{i,j}^{k} + X_{i,j}^{k+1}$

where $V_{i,j}^{k}$ is the inertia, $c_1 r_1 (x_{lbest\ i,j}^{k} - x_{i,j}^{k})$ is a personal influence on optimization, and $c_2 r_2 (x_{gbest\ j}^{k} - x_{i,j}^{k})$ is social influence by each particle; r_1 and $r_2$are two random numbers uniformly distributed in the range (1, 0), but modified the random value for uniform distribution from limited value [0,1] and (-1,1) [25]; c_1 and r_2 are two parameters representing the particle's confidence in itself (cognition) and in the swarm (social behavior), respectively.

Table 4: Pseudocode of Particle Swarm Algorithm

Algorithm 4: Pseudo code of the Particle Swarm Algorithm (PSO)

```
For each particle
   Initialize particle
END
Do
   For each particle
      Calculate fitness value
      If the fitness value is better than the best fitness value (pBest) in history
         set current value as the new pBest
   End
   Choose the particle with the best fitness value of all the particles as the gBest
   For each particle
      Calculate particle velocity according equation (a)
      Update particle position according equation (b)
   End
```

3. RESULTS AND DISCUSSION

The results obtained from CS, FA, HS and PSO are shown in Table 5. All the four methods are original versions without any modification. The numbers of iterations are 2000 for all algorithms. CS and FA were done using MATLAB whereas HS and PSO using Python.

Table 5: Best Solution of Pressure Vessel Optimization Problem

Design Variables	CS (MATLAB)	FA (MATLAB)	HS (Python)	PSO (Python)
x_1	1.21397	1.213978859398094	1.217	1.214
x_2	0.600066	0.600067510834431	0.601	0.600
x_3	62.9	62.9	63.046	62.9
x_4	20.3600531	20.360702455217410	19.723	20.612
g_1	2.000E-12	-8.9E-06	0	0
g_2	4.000E-12	-1.5E-06	0	0
g_3	-4.657E-09	-8.07433	-497	-3132.816
g_4	-219.6399469	-219.639	-220.277	-219.5
f(x)	7125.03475581715	7125.114589835030	7139.170	7138.165
Total Iteration	2000	2000	2000	2000

The total cost of the pressure vessel determined by the four methods has an average value of 7131.871. The minimum and maximum cost is obtained by cuckoo search and harmony search optimization algorithms, respectively. The result shows that cuckoo search is the most efficient method 0.096% below the average cost on the other hand harmony search is the lowest efficient method 0.102% above the average cost. The CS, FA, HS and PSO has accomplished the minimum cost value without violating all constraints.

4 CONCLUSION

In this study, the manufacturing cost minimization of the pressure vessel was optimized based on the four different metaheuristic optimization method; cuckoo search, firefly, harmony search and particle swarm optimization algorithms. The algorithms were designed for 2000 iterations. From the four algorithms, cuckoo search approach is the most efficient algorithm than other approaches. Therefore, optimization of pressure vessel problems shall be preferably conducted by cuckoo search algorithm. Further in-depth researches for modification purposes are recommended and detailed parametric studies are needed for these algorithms to obtain best result.

ACKNOWLEDGMENTS

We would like to thank Addis Ababa Science and Technology University, Ambo University, Debre Birhan University, and Gondar University for giving the chance to study our PhD.

REFERENCES

[1] J. Zhang, M. Xiao, L. Gao, and Q. Pan, "Queuing search algorithm: A novel metaheuristic algorithm for solving engineering optimization problems," *Appl. Math. Model.*, vol. 63, pp. 464–490, 2018.
[2] H. N. Ghafil and K. Jármai, "Dynamic differential annealed optimization: New metaheuristic optimization algorithm for engineering applications," *Appl. Soft Comput. J.*, vol. 93, p. 106392, 2020.
[3] E. H. Houssein, M. R. Saad, F. A. Hashim, H. Shaban, and M. Hassaballah, "Lévy flight distribution: A new metaheuristic algorithm for solving engineering optimization problems," *Eng. Appl. Artif. Intell.*, 94:103731, 2020.
[4] S. Yılmaz and E. U. Küc, "A new modification approach on bat algorithm for solving optimization problems," *Appl. Soft Comput.*, vol. 28, pp. 259–275, 2015.
[5] M. Dubey, V. Kumar, M. Kaur, and T. P. Dao, "A Systematic Review on Harmony Search Algorithm: Theory, Literature, and Applications," *Math. Probl. Eng.*, vol. 2021, no. Article ID 5594267, p. 22 pages, 2021.
[6] E. Sandgren, "Nonlinear integer and discrete programming in mechanical design," *Proc. ASME Des. Eng. Tech. Conf.*, vol. 112, no. June 1990, pp. 95–105, 1988.
[7] Z. W. Geem, J. H. Kim, and G. V. Loganathan, "A New Heuristic Optimization Algorithm: Harmony Search," *Simulation*, vol. 76, no. 2, pp. 60–68, 2001.
[8] X. Yang, "Harmony Search as a Metaheuristic Algorithm," in *Music-Inspired Harmony Search Algorithm*, vol. 191, Springer, Berlin, Heidelberg, 2009, pp. 1–18.
[9] B. Thamaraikannan and V. Thirunavukkarasu, "Design optimization of mechanical components using an enhanced teaching-learning based optimization algorithm with differential operator," *Math. Probl. Eng.*, vol. 2014, 2014.
[10] L. V. Enikeeva, E. N. Shvareva, and I. M. Gubaydullin, "Gravitational search and harmony search algorithms for solving the chemical kinetics optimization problems," *Eng. J.*, vol. 25, no. 6, pp. 107–121, 2021.
[11] X. Z. Gao, V. Govindasamy, H. Xu, X. Wang, and K. Zenger, "Harmony search method: Theory and applications," *Comput. Intell. Neurosci.*, vol. 2015, no. Article ID 258491, p. 10 pages, 2015.
[12] Z. Li-min, "An Improved Adaptive Harmony Search Algorithm," in *Proceedings of the 2015 International Conference on Computational Science and Engineering*, 2015, pp. 54–59.
[13] H. Li, P. C. Shih, X. Zhou, C. Ye, and L. Huang, "An improved novel global harmony search algorithm based on selective acceptance," *Appl. Sci.*, vol. 10, no. 6, pp. 1–20, 2020.
[14] X.-S. Yang, "Cuckoo Search," *Nature-Inspired Optim. Algorithms*, pp. 129–139, 2014.
[15] X.-S. Yang and X.-S. He, *Bat algorithm and cuckoo search algorithm*. Elsevier Ltd, 2020.
[16] X. S. Yang and S. Deb, "Cuckoo search: Recent advances and applications," *Neural Computing and Applications*, vol. 24, no. 1. pp. 169–174, Aug. 22, 2014.
[17] Tajmiruzzaman and Asadujjaman, "Artificial Bee Colony, Firefly and Bat Algorithm in Unconstrained Optimization," *Int. Conf. Mech. Ind. Energy Eng.*, 2016.
[18] V. Kumar and D. Kumar, "A Systematic Review on Firefly Algorithm: Past, Present, and Future," *Arch. Comput. Methods Eng.*, vol. 28, no. 4, pp. 3269–3291, 2021.
[19] X. S. Yang, "Firefly algorithms for multimodal optimization," *Lect. Notes Comput. Sci. (including Subser. Lect. Notes Artif. Intell. Lect. Notes Bioinformatics)*, vol. 5792 LNCS, pp. 169–178, 2009.
[20] I. Fister, I. Fister, X. Yang, and J. Brest, "A comprehensive review of fire fly algorithms," *Swarm Evol. Comput.*, vol. 13, no. 1, pp. 34–46, 2013.
[21] X. S. Yang, "Firefly algorithm, stochastic test functions & design optimization," *Int. J. Bio-Inspired Comput.*, 2(2): 78–84, 2010.
[22] H. S. Gebremedhen, D. E. Woldemichael, and F. M. Hashim, "A firefly algorithm based hybrid method for structural topology optimization," *Adv. Model. Simul. Eng. Sci.*, vol. 7, no. 1, 2020.
[23] M. Hajžman, R. Bulín, Z. Šika, and P. Svatoš, "Usage of the particle swarm optimization in problems of mechanics," *Appl. Comput. Mech.*, vol. 10, no. 1, pp. 15–26, 2016.
[24] K. E. Parsopoulos and M. N. Vrahatis, "Unified Particle Swarm Optimization for Solving Constrained Engineering Optimization Problems," *Proc. - 2005 IEEE Swarm Intell. Symp. SIS 2005*, vol. 3612, pp. 582–591, 2005.
[25] H.P. Dai, D.D. Chen, & Z. S. Zheng, "Effects of random values for particle swarm optimization algorithm," *Algorithms*, 11(2), 2018.

Small Ball Tracking with Trajectory Prediction

Shambel Ferede[1,*], Xuemei Xie[2], Chen Zhang[2], Jiang Du[2], Guangming Shi[2]

[1]*College of Computing and Informatics, Assosa University, Assosa, Ethiopia*
[2]*School of Artificial Intelligence, Xidian University, Xi'an, 710071, China*
**Corresponding author, email: shambel@asu.edu.et*

ABSTRACT

Small ball tracking with trajectory prediction is proposed to track small balls when the athletes playing with them at sports field. Due to its significant detection quality on the tracking performance, CFED is selected as a detector for the tracking process. The proposed tracking technique is based on Deep SORT and improved it for the tracking of small balls. Due to lack of appearance information for small balls, deep SORT can't track them well. To solve this problem, the designed algorithm incorporates motion, frames storage and directional information to indicate the trajectory. The last various frames that have matched detections are retained for re-identifying when the small ball reappears and this can solve the problem of ID failure, and also direction judgment is added to solve object overlap problem. Trajectory is used to indicate the motion and direction of small balls in the small ball tracking process. A set of trajectories are engendered from the set of small balls to locate the small balls using its trajectory and to predict the locations of the missed balls. The small balls tracking experiment implemented on a collection of proposed BALL datasets. The experimental result of the small ball tracking performance is evaluated in comparison with deep SORT based on the metrics evaluation. The experimental result displays that the proposed improvement effectively decreases the number of identity switches from 137 to 111, track fragmentation from 496 to 420, false detections from 891 to 809 and similarly the number of missed detections reduces from 1201 to 725. Thus, there is significant increment in the number of small ball tracking accuracy from 49.5 to 62.7 and precision from 66.2 to 67.3.

Keywords: *object tracking, small object tracking, intelligent physical education, computer vision*

1. INTRODUCTION

When the players are playing rhythmic gymnastics balls at the sports ground, and if the tutor or coach wants to manage or know whether players are playing based on the standard rule, it is difficult to comprehend the trajectory of the entire small balls with eyes simultaneously. For this, it is necessary to engage computer vision application or technology to assist tracking these small balls, since it is very essential for intelligent physical education (IPE) and to step up the sports industry as a whole by connecting with such sophisticated technologies. It is used to support the coaches to easily handle the accuracy of the actions by the players; the proposed task is to track small balls with trajectory prediction as shown in Fig. 1.

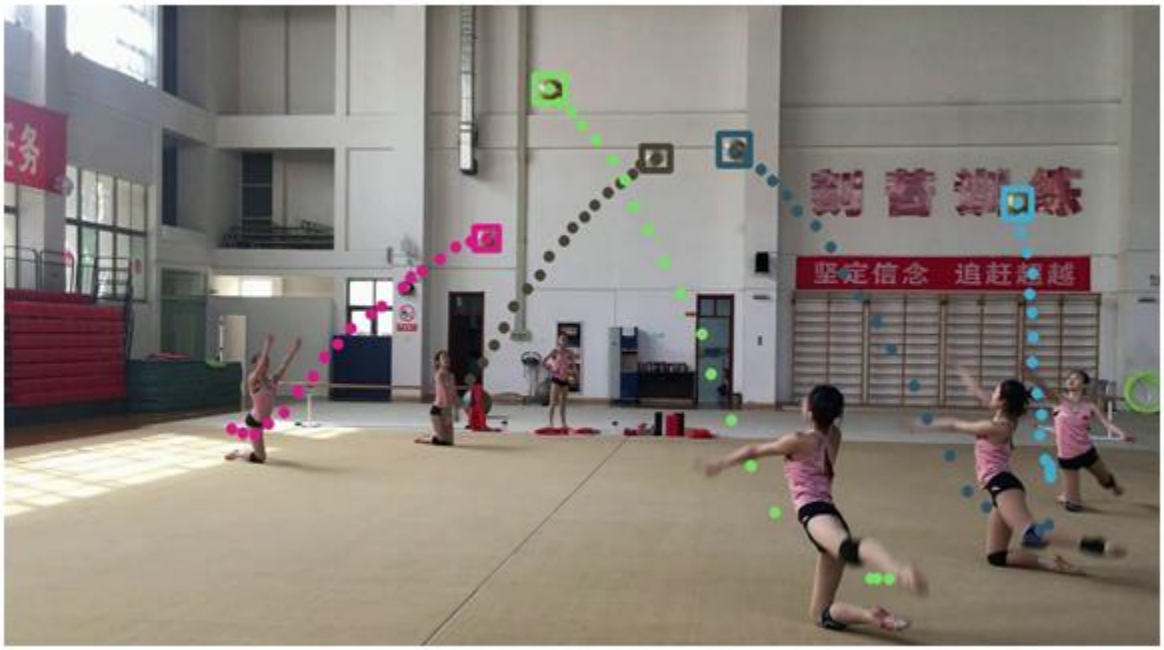

Figure 1: Sample result of the proposed small ball tracking task

The solution to this task is multiple object tracking. It is a classical computer vision task that aims to identify and track different objects within a video, without any prior knowledge about the appearance and the number of targets (Ciaparrone, 2020). It has been applied in various real-world applications, *e.g.* robotics, self-driving vehicles, and traffic control (Luo et al., 2019; Christoph et al., 2017; Rachna, 2017). However, the balls we track are very small. Small objects tracking is a challenging task, particularly when considering different complex situations (Liu et al., 2019).

Considering that in group event, multiple balls are shown in a single frame, multiple object tracking can be adopted to our task, which is a classical and challenging computer vision problem that targets to locate and track various objects within a video sequence, without any particular experience or knowledge about the amount of targeted objects and its appearance (Ciaparrone, 2020). In the current era, due to the development of deep convolutional neural network (CNN), significant improvement has been made in multiple objects tracking task (Want, 2019; Bewley et al., 2016; Wojke, 2017; Chen et al., 2018; Braso and Taixe, 2020; Zhang et al., 2020; Chen and Tsotsos, 2019; Voigtlaender et al., 2019, Bergmann et al., 2019; Zhang, et al., 2019; Zhou, 2019). Among them, simple online and real-time tracking (SORT) (Bewley et al., 2016) explores an approach to multiple objects tracking, which focuses on association of objects efficiently for online and real-time applications. However, SORT faces a difficulty in tracking through occlusions, since the employed association metric is accurate only when employing accurate state estimation. To overcome this issue. Deep SORT (Wojke, 2017) solves this problem by replacing the association metric with a more informed metric that combines motion and appearance information of the target objects.

However, existing methods could not achieve a good performance in the proposed small ball tracking task. On the one hand, tracking the ball (Chakraborty and Meher, 2013; Kamble et al., 2019) is not merely a complex task with the cause of shadows, occlusions, false detections, changes in motion of balls, and playground conditions. In addition, they further clarified many other challenges in the ball tracking process, including occlusion of balls by players, texture speed, unexpected high speed of events, dynamic sport environment, ball size variation, color and shape. On the other hand, the targeting balls in our scenario are very small. Tracking small objects is a difficult task, in particular when diverse real time and complicated situations are considered (Liu, et al., 2019). The main

problem of small object tracking is that small objects exhibit merely blurry and flexible physical phenomena. Compared with ordinary sized objects, they tend to be more easily lost because of lens shaking and other limitations. As mentioned earlier, small objects are characterized by a small number of pixels in the image. They consist insufficient information to learn or model properly, and because of their small size, they may not be accurately exemplified.

To overcome those challenges, we improve Deep SORT (Wojke, 2017) for the proposed small ball tracking task with trajectory prediction. Deep SORT tracks objects through longer periods of occlusions by integrating motion and appearance information. While, the appearance information of small balls is very limited.

To exploit the suitable manner for small ball tracking, the following two methods are proposed. Initially, when the ball leaves the instance, we store the last several frames which have matched the detections and these stored frames can be used for recognizing or re-identifying the small balls when it occurs. This will solve problem of ID failure in the tracking process. Next, in order to solve the objects staggered problem, we include direction judgement which can control the direction of balls. Hence, if a staggered problem happens between two objects, we can manage the direction to persist on their tracks.

The experimental results demonstrate that the proposed technique flourished better outcome on the proposed BALL dataset by integrating motion, directional information, and frames storage. The contributions of this paper are: (1) Proposed a novel small ball tracking task that is challenging and significant for IPE; (2) Proposed to incorporate frames storage and directional information in the tracking process in order to make it effective to re-identify the tracked balls; (3) Set up the small BALL tracking dataset.

2. METHODOLOGY

This section deals with the methods used to track small balls, which has the following subsections: small ball detection about the preferred detector details, improvements based on deep SORT i.e. the proposed modifications, frames storage and direction judgment, and trajectory.

2.1 Small Ball Detection

In order to gain advantages from the rapid development of CNN-based detection, CFED is applied to the small ball detection (Shambel Ferede et al., 2019) framework. CFED is designed depending on SSD (Liu et al., 2016) and modified to detect small objects in a suitable manner. CFED adds a new prediction layer on conv3_3, and deletes other layers after the conv3_3 layer in the SSD to match the size of the receiving field and the ball.

In order to improve the features of the prediction layer, CFED (Shambel Ferede et al., 2019) adds a channel feature enhancement module which magnifies the importance of each convolution kernel in the feature layer. In order to effectively compute the channel enhancement, CFED squeezes the spatial dimension of the input feature map into a feature vector. The feature vector designating the significance weight is important to fine-tune the feature map of each of the channels. This method enables CFED to amplify the variance between the target feature and the repetitive feature, and as a result the target feature will be more distinguishable. CFED has accomplished excellent performance on small ball detection.

Therefore, throughout the proposed small ball tracking task we use CFED as a detector to get advantage from its detection quality, which will have a significant influence on the performance of small ball tracking.

2.2 Improvements based on Deep SORT

Deep SORT (Wojke, 2017) incorporates the object appearance information to increase the tracking performance of SORT (Bewley et al., 2016), since SORT has a large number of IDs relatively, and the engaged association metric is accurate only when state estimation ambiguity is low. Consequently, SORT has a difficulty in tracking through occlusions. Deep SORT resolves this problem by substituting the association metric with a more learned metric that integrates the motion and the object appearance information. Deep SORT uses a convolutional

network that has been trained to differentiate pedestrians on an extensive person re-identification dataset. It tracks objects within occlusions for a longer period of time and effectively decreases the quantity of identity switches.

The purpose of this study is to track small moving balls in rhythmic gymnastics. The methodology is based on Deep SORT and we modify it in an appropriate manner to track small balls. All balls in the organized dataset are too small, resulting in unsatisfactory tracking evaluations of Deep SORT (see section 3.2 for details). The following technical strategies are proposed to gain better tracking performance.

First, when the ball disappeared from the instance, we will accumulate the last number of frames that have matched detections. Therefore, once the ball appears, we can use the accumulated frames to re-identify or recognize the small balls and here the ID failure will be solved. Second, we have added direction judgment to solve the staggered problem of objects. When two objects overlap, we will determine the direction to remain their trajectory.

Furthermore, the tracking scheme of the proposed tracking technique is derived from deep SORT (Wojke, 2017). Therefore, the tracking structure is designated on the eight-dimensional state space $(x, y, \gamma, h, \dot{x}, \dot{y}, \dot{\gamma}, \dot{h})$ which contains the bounding box midpoint (center) position (x, y), aspect ratio γ, height h, and their corresponding velocities in picture coordinates. We apply a standard Kalman filter with persistent velocity motion and linear observation model, where we take the bounding coordinates (x, y, γ, h) as observations of the state of object.

The relationship among the predicted Kalman states and newly-attained measurements is elucidated by using Hungarian algorithm. The mathematical formula is computed by combining motion and direction information of the object through the integration of two suitable metrics. To incorporate motion information, we apply Euclidian distance among predicted Kalman states and a new arrived measurements.

$$d^{(1)}(i, j) = \sqrt{\left(x_i - x_j\right)^2 + \left(y_i - y_j\right)^2}, \tag{1}$$

where (x_i, y_i) denotes the center of the i-th track bounding box, and (x_j, y_j) the j-th detection bounding box.

We incorporate direction distance metric into the assignment problem using the cosine distance between two balls' slope. Primarily, the slope is calculated as follows:

$$slope(a) = \frac{y}{x}, \tag{2}$$

where α represents for bounding box and x, y denotes the center of the bounding box.

The formula of cosine distance is as follows:

$$d^{(2)}(i, j) = \frac{\|i\|_2 \|j\|_2 - i \cdot j}{\|i\|_2 \|j\|_2}, \tag{3}$$

where i stands for the slope of i-th track bounding box and j represents the slope of j-th detection.

In grouping, both metrics balance each other by serving diverse aspects of the assignment problem. Both metrics are integrated using a weighted sum to build the association problem:

$$c_{i,j} = \lambda d^{(1)}(i, j) + (1 - \lambda) d^{(2)}(i, j). \tag{4}$$

The impact of each metric on the joined association cost can be controlled by hyper-parameter λ.

Algorithm 1 is restructured from Deep SORT (Wojke, 2017) for the tracking task of targeted small balls as a matching algorithm to reduce track uncertainty and track fragmentation. As input, we have track T indices, detection D *indices*, maximum age A_{max}, and maximum cost C_{max}.

Algorithm 1 Matching Algorithm

Input: Track indices $T = \{1, ..., N\}$, Detection indices $D = \{1, ..., M\}$, Maximum age A_{max}, Maximum cost C_{max}

1: Compute Cost Matrix $C = [c_{(i,j)}]$ using (4)
2: Initialize set of matches $M \leftarrow \varnothing$
3: Initialize set of unmatched detections $U \leftarrow D$
4: for $n \in \{1, ..., A_{max}\}$ do
5: Select tracks by age $T_n \leftarrow \{i \in T \mid a_i = n\}$
6: $[x_{(i,j)}] \leftarrow$ min_cost_matching (C, T_n, U)
7: $M \leftarrow M \{(i, j) \mid x_{(i,j)} \leq C_{max}\}$
8: $U \leftarrow U\backslash\{j \mid x_{i,j} > C_{max}\}$
9: store_current_detection (i, j)
10: end for
11: return M, U

In line 1 the association cost matrix is calculated and then the linear assignment problem increasing age is resolved by rehearsing over track age n. The subset of tracks T_n that have not been linked in the last n frames with detection is selected in line 5, and in line 6 the linear assignment among tracks in T_n and unmatched detections U are resolved. The number of matched detections is updated in line 7 and similarly the set of unmatched detections are modified in line 8. The current accumulated detections are stored in line 9 and then after end, we return in line 11.

2.3 Frames Storage and Direction Judgement

As described before, to obtain better tracking efficacy in the suggested small ball tracking task, we have added direction information and frames storage. Then after the matched detections and unmatched detections are adjusted, we will retain the last number of frames if the object will be kept out of instance. The stored frames will have been used for re-identification or recognition of the small balls when it occurs in the instance and the miss ID problem will be solved.

In the proposed small ball tracking system several difficulties will occur, such as occlusion, shadowing, deformation and others. Athletes play balls with each other by throwing or dribbling the balls. As a result, there will be staggering difficulty when players play the balls. To solve the object staggering problem, we add the object direction information. If there is a staggering problem among two objects, we can find the direction information of the objects through finding the slope as Eq. (4) and we will have to control the direction to proceed in their tracks.

2.4 Trajectory

In the proposed small ball tracking task, we use trajectories to point toward the direction and movement of the balls. When the ball is occluded by a player in the frame, it loses its shape. Consequently, it may be missed in the ball's generation process. In order to focus on this, a trajectory is applied that a set of trajectories are created from a number of balls. It is greatly easier to locate the small ball using its trajectory and assist to identify the vanished small ball locations due to shadowing, occlusion, and other problems. When the players play balls by throwing them to other players in a distance, the balls may pass in a parabolic path. Therefore, the distance can be solved by

analyzing the 2D scattering of the balls. The trajectory of the ball is shown by clear dotted lines and bounding boxes, to describe from whom it was thrown or bounced and who will receive it.

3. EXPERIMENTS

3.1 Dataset

We setup the proposed BALL dataset for the experiment, as shown in Fig. 2. We collected the dataset by shooting several videos while the athletes were playing with balls at Shaanxi Provincial Sports Training Center. The resolution of all videos is 1920×1080 and we captured one target image per 10 frames. The entire dataset contains 1,754 images and we use the procedure and detection result of CFED (Shambel Ferede et al., 2019). In the BALL dataset, the balls are distributed in various positions and have different shapes. Fig. 2 shows the ball in different scenes. The ball will be deformed when squeezed, the ball will be blurred due to quick throw, and the ball will be blocked when the player takes the ball. In addition, the features of the ball may not be recognized when there is a shadow

Figure 2: The proposed BALL dataset examples' in different scenes. The ball is shown as deformed, occluded or blurred while moving.

3.2 Evaluation of Tracking Results

We evaluate the tracking efficiency of the designed small ball tracker on the organized small BALL dataset. The performance of the tracker is assessed based on the challenging test sequences contrasting with Deep SORT (Wojke, 2017). For the proposed tracker input we use a detector provided by (Luo et al. 2021). In order to provide an improved performance, the modified deep SORT is implemented on an organized collection of BALL datasets. The proposed small ball tacking implementation has been done using a single NVIDIA GTX-1080Ti GPU (12 GB memory), CUDA 8.0, cuDNNv6.0 with Intel Core i7-7700k@4.2GHz.

Evaluation is performed on a test sequences, using $\lambda = 0.5$, maximum age $A_{max} = 30$ frames and maximum cost $C_{max} = 0.5$. The detection of (Luo et al., 2021) has been thresholded at a confidence score of 0.3. Evaluation is performed according to the following metrics based on (Wojke, 2017; Bernardin and Stiefelhagen, 2008).

MOTA is the summarization of the general tracking accuracy in terms of identity switches, false positives and false negatives (Bernardin and Stiefelhagen, 2008). MOTP is the entire tracking precision in terms of bounding box overlap between ground-truth and reported location (Bernardin and Stiefelhagen, 2008). IDs is the number of times that reports identity of a ground-truth track variations. FM is the number of times a track is interrupted by a failure detection. FP is the number of false detections, and FN is the number of neglected or missed detections.

The experimental results are presented on Table 1 based on the proposed evaluation metrics. In comparison with deep SORT, the proposed improvement successfully decreases the amount of identity switches from 137 to 111. Because of maintaining object identities through different challenges, e.g. occlusions, deformations and misses, track fragmentation declines significantly from 496 to 420.

Furthermore, the experimental result demonstrates that the number of false detections decreases from 891 to 809 and the number of failure or missed detections falls from 1201 to 725. As a result, there is consequential increase in the percentage of small ball tracking accuracy from 49.5 to 62.7 and the percentage of precision from 66.2 to 67.3.

Table 1: Tracking results on proposed ball dataset in comparison with deep SORT

	MOTA(+)	MOTP(+)	IDs(-)	FM(-)	FP(-)	FN(-)
Deep SORT [11]	49.5	66.2	137	496	891	1201
Proposed	62.7	67.3	111	420	809	725

For evaluation measures with (+), higher scores represent better performance; while for evaluation measures with (-), lower scores represent better performance.

Generally, in Table 1, we compare the tracking results of proposed method in comparison with deep SORT on proposed ball dataset. The result shows that we are able to tack small balls effectively due to the integration of temporal and direction information.

Figure 3: Some results of the proposed small ball tracking ouputs

Fig. 3 indicates that some results of the proposed small ball tracking results in different scenes. The small ball tracking process is shown by using the spotted trajectory lines are used to indicate the tracking process of the small balls in order to specify where the ball is, who throws the ball, and who will receive the ball. In addition, to identify a specific ball in a video, each of the trajectory lines and bounding boxes has various color.

4. CONCLUSION

This paper proposes a small ball tracking with trajectory prediction by adopting Deep SORT that integrates direction information with motion and frames storage. Due to this, the proposed method can track the small balls with better performance on BALL dataset. Therefore, this work has an incredible significance for modern intelligent physical education.

ACKNOWLEDGMENT

This work is supported by Natural Science Foundation (NSF) of China (61836008, 61632019).

REFERENCES

Bergmann, P. et al. (2019): Tracking Without Bells and Whistles, IEEE/CVF International Conference on Computer Vision (ICCV), Seoul, South Korea. 2019: 941-951.

Bernardin, K. and Stiefelhagen, R. (2008): Evaluating multiple object tracking performance: the clear mot metrics, Journal on Image and Video Processing, 246309.

Bewley, A. et al. (2016): Simple online and real-time tracking, IEEE International Conference on Image Processing (ICIP), Phoenix, AZ, USA. 2016: 3464-3468.

Braso, G. and Taixe, L. (2020): Learning a Neural Solver for Multiple Object Tracking, IEEE/CVF Conference on Computer Vision and Pattern Recognition (CVPR), Seattle, WA, USA. 6246-6256.

Chakraborty, B. and Meher S. (2013): A real-time trajectory-based ball detection-and-tracking framework for basketball video, Journal of Optics, 42(2): 156-170.

Chen, B. and Tsotsos, J. (2019): Fast Visual Object Tracking using Ellipse Fitting for Rotated Bounding Boxes, IEEE/CVF International Conference on Computer Vision Workshop (ICCVW), Seoul, Korea (South). 2281-2289.

Chen, L. et al. (2018): Real-Time Multiple People Tracking with Deeply Learned Candidate Selection and Person Re-Identification, IEEE International Conference on Multimedia and Expo (ICME), San Diego, CA, USA. 1-6.

Christoph F., et al. (2017): "Detect to Track and Track to Detect" in Proceeding of ICCV.

Ciaparrone, G. et al. (2010): Deep Learning in Video Multi-Object Tracking: a Survey, Neurocomputing, 381: 61-88.

Kamble, P. et al. (2019): A deep learning ball tracking system in soccer videos, Opto-Electronics Review, 27(1): 58-69.

Liu, C. et al. (2019): Aggregation Signature for Small Object Tracking, arXiv preprint: 1910.10859, 10.

Liu, W., et al. (2016): SSD: single shot multibox detector[C], In: LEIBE B, MATAS J, SEBE N, WELLING M (eds) Computer Vision – ECCV 2016. ECCV 2016. Lecture Notes in Computer Science, Springer, 9905: 21-37.

Luo, W. et al. (2019): Trajectories as Topics: Multi-Object Tracking by Topic Discovery, IEEE Transactions on Image Processing, 28(1): 240-252.

Luo, W. et al. (2021): Multiple object tracking: A literature review, Artificial Intelligence, 293: 103448.

Rachna, V. (2017): Review of Object Detection and Tracking Methods, International Journal of Advance Engineering and Research Development, 4(10): 569-578.

Shambel Ferede et al. (2019): Channel Feature Enhanced Detector for Small Ball Detection, In: LIN Z et al. (eds) Pattern Recognition and Computer Vision. PRCV 2019. Lecture Notes in Computer Science, Springer: vol 11857. 3-13.

Voigtlaender P. et al. (2019): MOTS: Multi-Object Tracking and Segmentation, IEEE/CVF Conference on Computer Vision and Pattern Recognition (CVPR), Long Beach, CA, USA. 7934-7943.

Want, Z. et al. (2019): Towards Real-Time MultiObject Tracking, arXiv preprint: 1909.12605, 9.

Wojke, N. (2017): Simple Online and Real-time Tracking with a Deep Association Metric, IEEE International Conference on Image Processing (ICIP), Beijing, China. 3645-3649.

Zhang, W. et al. (2019): Robust multi-modality multi-object tracking, IEEE/CVF International Conference on Computer Vision (ICCV), Seoul, South Korea. 2365-2374.

Zhang, Y. et al. (2020): A Simple Baseline for Multi-Object Tracking, arXiv preprint: 2004.01888, 2020: 17.

Zhou, X. (2019): Tracking Objects as Points[C] // In VEDALDI A, BISCHOF H, BROX T, et al. (eds) Computer Vision – ECCV 2020. ECCV 2020. Lecture Notes in Computer Science, Springer. vol 12349. 2020: 474-490.